

Metal-organic Assemblies for Multifunctional Electrochromic Materials and Devices

By

Indulekha M.

10CC17A39014

A thesis submitted to the
Academy of Scientific and Innovative Research
for the award of degree of
DOCTOR OF PHILOSOPHY

in

SCIENCE

Under the supervision of
Dr. A. Ajayaghosh



**CSIR-National Institute for Interdisciplinary Science and Technology
(CSIR-NIIST)
Thiruvananthapuram-695019**



Academy of Scientific and Innovative Research
AcSIR Headquarters, CSIR-HRDC Campus, Sector 19, Kamla Nehru Nagar
Ghaziabad, U.P.-201 002, India

January 2023

Dedicated to Achan, Amma

Freddy and My Dear.



राष्ट्रीय अंतर्विषयी विज्ञान तथा प्रौद्योगिकी संस्थान
NATIONAL INSTITUTE FOR INTERDISCIPLINARY SCIENCE AND TECHNOLOGY

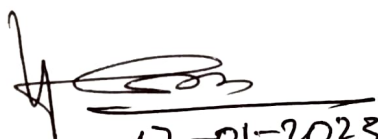
वैज्ञानिक तथा औद्योगिक अनुसंधान परिषद् | Council of Scientific and Industrial Research

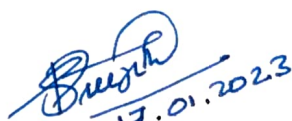
इंडस्ट्रियल एस्टेट पी ओ, पाप्पनमकोड, तिरुवनंतपुरम, भारत – 695 019 | Industrial Estate P O, Pappanamcode, Thiruvananthapuram, India – 695 019

CERTIFICATE

This is to certify that the work incorporated in this Ph.D. thesis entitled, “**Metal-organic Assemblies for Multifunctional Electrochromic Materials and Devices**”, submitted by **Ms. Indulekha M.**, to the Academy of Scientific and Innovative Research (AcSIR) in fulfilment of the requirements for the award of the Degree of *Doctor of Philosophy in Sciences*, embodies original research work carried out by the student. We further certify that this work has not been submitted to any other University or Institution in part or full for the award of any degree or diploma. Research materials obtained from other sources and used in this research work has been duly acknowledged in the thesis. Images, illustrations, figures, tables etc., used in the thesis from other sources, have also been duly cited and acknowledged.


Indulekha M.
17/01/2023


17-01-2023
Dr. A Ajayaghosh
(Supervisor)


17.01.2023
Dr. Sreejith Shankar
(Co-Supervisor)


STATEMENTS OF ACADEMIC INTEGRITY

I, Indulekha M., a Ph.D. student of the Academy of Scientific and Innovative Research (AcSIR) with Registration No. 10CC17A39014 hereby undertake that, the thesis entitled “*Metal-organic Assemblies for Multifunctional Electrochromic Materials and Devices*” has been prepared by me and that the document reports original work carried out by me and is free of any plagiarism in compliance with the UGC Regulations on “*Promotion of Academic Integrity and Prevention of Plagiarism in Higher Educational Institutions (2018)*” and the CSIR Guidelines for “*Ethics in Research and in Governance (2020)*”.


17/01/2023
Indulekha M.

17-01-2023
Thiruvananthapuram

It is hereby certified that the work done by the student, under our supervision, is plagiarism free in accordance with the UGC Regulations on “*Promotion of Academic Integrity and Prevention of Plagiarism in Higher Educational Institutions (2018)*” and the CSIR Guidelines for “*Ethics in Research and in Governance (2020)*”.


17-01-2023
Dr. A. Ajayaghosh

17-01-2023
Thiruvananthapuram



17.01.2023
Dr. Sreejith Shankar

17-01-2023
Thiruvananthapuram

DECLARATION

I, **Indulekha M.**, bearing AcSIR Registration No. 10CC17A39014 declare that my thesis entitled “*Metal-organic Assemblies for Multifunctional Electrochromic Materials and Devices*” is plagiarism free in accordance with the UGC Regulations on “*Promotion of Academic Integrity and Prevention of Plagiarism in Higher Educational Institutions (2018)*” and the CSIR Guidelines for “*Ethics in Research and in Governance (2020)*”.

I would be solely held responsible if any plagiarised content in my thesis is detected, which is violative of the UGC regulations 2018.


Indulekha M.

17-01-2023

Thiruvananthapuram

ACKNOWLEDGEMENTS

*It is with immense pleasure and immense respect that I place on record my deep sense of gratitude to my research supervisor **Dr. A. Ajayaghosh**, for giving me an opportunity to work under his guidance. His valuable suggestions and motivation have carried me through all the stages of my PhD work. I would like to express my sincere gratitude to **Dr. Sreejith Shankar** my co-supervisor, for suggesting the research topic and for his inspiring guidance throughout my research career. His valuable advice and scientific approach have helped me to a great extent to complete my research work.*

I wish to thank Dr. Anantharamakrishnan and Dr. A. Ajayaghosh, Present and former Directors, CSIR-NIIST Thiruvananthapuram, for providing the necessary facilities for carrying out the research work.

I would like to express my gratitude Dr. K. V. Radhakrishnan, Dr. P. Sujatha Devi, and Dr. Narayanan Unni present and former Heads of the Division and Section, Chemical Sciences and Technology Division and Photosciences and Photonics Section for their endless support.

I would like to acknowledge Dr. R. Luxmi Varma, Dr. C. H. Suresh, and Dr. V. Karunakaran the former and present AcSIR coordinators, CSIR-NIIST for the timely help and advice for the academic procedures of AcSIR.

I am very thankful to Dr. Vijayakumar C., Dr. Biswapriya Deb, and Dr. Bhoje Gowd E. (my Doctoral Advisory Committee members) for their help, support, suggestion, and encouragement during my doctoral advisory meetings.

I like to thank all the AcSIR faculty members of CSIR-NIIST for their help and support during the coursework period.

My sincere thanks are due to:

- *Dr. V. K. Praveen, Dr. Joshy Joseph, Dr. K. Yoosaf, Dr. Suraj Soman, Dr. Ishita Neogi, Dr. Adersh Asok, Dr. Rakesh K. Mishra, Dr. Manas Panda and Dr. Animesh Samanta, present and former Scientists of Photosciences and Photonics Section for their encouragement and help.*
- *Dr. Rakhi and Ms. Anjana for helping me out with the capacitance part of my research work.*
- *Dr. Jubi John for helping me with the synthesis part of my thesis.*
- *Dr. Saju Pillai, Dr. Hareesh U. S., and Mr. Peer Mohamed A. for helping me with the XPS analysis and BET surface area measurements.*
- *Mr. Chandrakanth C. K., Mr. Kiran J. S., Mr. Robert Philip for general help, and Mr. Harish Raj V, Mr. Amal raj, and Mr. Kiran Mohan for morphology and XRD analysis.*
- *Mrs. Saumini Mathew for recording NMR spectra, and Mrs. S. Viji for mass spectral analysis.*
- *Mr. Nayan Dev Madhavan and Ms. Ranjana Venugopal for helping me with the film and device fabrication part.*

- *Ms. Manjusha, Ms. Shyama, Ms. Delna, Ms. Arathi, Ms. Anila and Ms. Sarga (MSc project students/summer interns) for helping me to carry out some of my lab work.*
- *Dr. Samrat, Dr. Sudheesh, Dr. Arindam, Dr. Hifsudheen, Dr. Satyajit, Dr. Saranya, Dr. Gourab Das, Dr. Sandip Chakraborty, Mr. Vijayakumar, Ms. Anjali Nirmala., Ms. Anagha Thomas, Mr. Lingamoorthy, Mr. Dipak Patra, Ms. Priyanka, Ms. Anjali Anand, Ms. Lekshmi. L, Mr. Sidha Lingeshwar, Ms. Annie Prasad, Ms. Anisha Mathew, Ms. Greeshma V.S, Ms. Haritha Jayaraj, Ms. Athulya B.S, Mr. P. Sri Bala Jeya Krishna Sri, Ms. Sruthi S Nair, Ms. Ashwathi N. V., and other present and former SS/AG group members for their love, care and support throughout my research period.*
- *Ms. Vyshna Priya, Mr. Sourav Chandra Pradhan, Ms. Anooja, Mr. Nandu A, Mr. Vibhu Darshan, Ms. Kavya Rajeev, Ms. Anjali K Sajeev, Ms. Sruthi Poovattil, Mr. Rishad Baig, Mr. Sanoop, Ms. Rani Mol, Ms. Megha Paul, Ms. Tessy, Mr. Manikandan, Ms. Pavithra V Prabhu, Mr. Navin Jacob, Mr. Arjun V. Prakash, Ms. Hasna, Ms. Suja Former and present members of CSTD & friends at CSIR-NIIST.*
- *Dr. Arya J.S, Dr. Gayathri Prabhu, Dr. Silja Abraham, Dr. Anjali B.R, Dr. Hanna B, Dr. Vijitha, Dr. Ramya P.R, Dr. Anjali, Dr. Sumitha Paul, Dr. Jayanthi, Dr. Tanwishta Ghosh, Dr. Sreejith, Dr. Sajena and Dr. Nitha P.R, my seniors for all the support and help throughout my research.*
- *Dr. Gayathri Prabhu and Dr. Silja Abraham for clarifying all my doubts during the research.*
- *Shibu, Susu, Sheba, Vishnu Oman, Neethi and Nishna, my dearest friends at NIIST for giving me the best five years of life here and all the good memories of friendship that I cherish throughout my life.*
- *Jesna, Jeena, and Henna my friends at IISER-Bhopal for their friendship and support.*
- *Dr. K.P Sudheer and Mrs. Shyni, for being local guardian and for all support and care.*
- *My parents (Mr. Raghu Raman M. and Mrs. Sayija M.P.), and my little brother (Dr. Kiran Dae M) for their endless caring love and support.*
- *Dr. Vishnu Prasoodanan P. K., my life partner for understanding all my stress during my research and bringing back a smile on my face. Your care support and love helped me to move forward with courage. Thank you for everything.*
- *DST-Inspire for the financial assistance*
- *Lastly and most importantly I thank the Almighty....*

Indulekha Mukkatt

TABLE OF CONTENTS

Certificate	i
Statement of academic integrity	ii
Declaration	iii
Acknowledgement	iv
Table of contents	vi
List of abbreviations	xiv
List of tables	xvii
List of figures	xviii
Preface	xxxviii

CHAPTER 1

Multifunctional Electrochromic Materials and Their Applications

1.1	Abstract	1
1.2	Introduction	2
1.3	History of Electrochromism	2
1.4	Applications of Electrochromic Materials	3
1.5	Electrochromic Devices	4
1.6	Performance Characteristics of Electrochromic Materials	5
1.6.1	Optical Contrast	5
1.6.2	Response Time	5
1.6.3	Cycling Life	5
1.6.4	Coloration efficiency	6
1.6.5	Write-Erase efficiency	6
1.6.6	Optical memory	6
1.7	Classifications of EC Materials	6
1.7.1	Transition Metal Oxides	6
1.7.2	Prussian Blue	7
1.7.3	Viologens	8

1.7.4	Conjugated Conducting Polymers	8
1.7.5	Metal Coordination Complexes and Polymers	10
1.8	Terpyridine-based Metal-Organic Materials for Electrochromic Applications	11
1.9	Bipyridine-based Metallopolymers for Electrochromic Applications	19
1.10	Metal-Organic Systems based on other Acceptor-type Ligands for Electrochromic Applications	23
1.11	Multifunctional Applications of Electrochromic Materials	29
1.11.1	Electrochromic Sensors	29
1.11.2	Electrochromic Batteries and Supercapacitors	34
1.12	Objectives and Organization of the Thesis	42
1.13	References	44

CHAPTER 2

Ligand Structure Dependent Molecular Permeability and Spectroelectrochemical Diversification in Electrochromic Metallopolymer

2.1	Abstract	55
2.2	Introduction	56
2.3	Results and Discussions	64
2.3.1	Synthesis and Characterization	64

2.3.2	Spectroelectrochemical Diversification in the Film State	72
2.3.3	Molecular Permeability in the Film State	78
2.3.4	Electrochromic Devices	81
2.3.5	Creation of Patterns and Images	89
2.4	Conclusions	89
2.5	Experimental section	90
2.5.1	Materials and Methods	90
2.5.2	NMR Spectroscopy	90
2.5.3	FTIR Spectroscopy	90
2.5.4	ESI-HRMS and MALDI-TOF Analyses	91
2.5.5	UV-Vis Spectroscopy	91
2.5.6	Thickness Measurements	91
2.5.7	X-ray Photoelectron Spectroscopy	91
2.5.8	Atomic Force Microscopy and Roughness Estimation	91
2.5.9	Cyclic Voltammetry	92
2.5.10	Spectroelectrochemical Analysis	92
2.5.11	Molecular Permeability Studies	92
2.6	Synthesis	93

2.7	Synthesis of the Coordination Polymers for Spray Coating	97
2.8	Fabrication of MPNFs by Spray Coating the MPs on FTO substrates	97
2.9	Fabrication of Electrochromic Devices	97
2.9.1	Synthesis of Gel Electrolyte	97
2.9.2	ECD Fabrication	97
2.10	References	98

CHAPTER 3

Electrochromic Energy Storage and Tunable Capacitive Behaviour of Fe(II)

Coordinated Metallopolymers

3.1	Abstract	107
3.2	Introduction	108
3.3	Results and Discussion	116
3.3.1	Synthesis and Characterization	116
3.3.2	Electrochemistry and Spectroelectrochemistry	123
3.3.3	Capacitance	127
3.3.4	BET Surface Area and Conductivity	135
3.4	Conclusions	138
3.5	Experimental Section	139

3.5.1	General Methods and Instrumentation	139
3.5.2	Molecular Characterization	140
3.5.3	Absorption and Emission Spectroscopy	140
3.5.4	Morphological Analyses, Thickness Measurements and Thermal Characterization	140
3.5.5	Powder X-ray Diffraction	141
3.5.6	X-ray Photoelectron Spectroscopy (XPS)	141
3.5.7	Electrochemistry and Spectroelectrochemical Analyses	141
3.5.8	Synthesis	141
3.5.9	Syntheses of the Metallopolymers	142
3.5.10	Preparation of the Electrodes and Electrochemical Measurements	142
3.5.11	Determination of Resistivity and Electrical Conductivity by 4-Probe Measurements	142
3.5.12	Computational Calculations	143
3.5.13	BET Surface Area Measurements	143
3.6	References	143

CHAPTER 4

Metal ion Dependent Capacitance Modulation in Electrochromic Metallopolymers

Derived from Near Iso-structural Coordination Complexes

4.1	Abstract	155
4.2	Introduction	156
4.3	Results and Discussion	165
4.3.1	Synthesis and characterization	165
4.3.2	Photophysical Studies	174
4.3.3	Electrochemical and Electrochromic Studies	176
4.3.4	DFT Calculations	181
4.3.5	Capacitance Measurements	182
4.3.6	Galvanostatic Charge-Discharge (GCD) Measurements	186
4.3.7	Electrochemical Impedance Spectroscopic (EIS) Investigations	187
4.3.8	BET Surface Area Experiments	189
4.4	Conclusion	195
4.5	Experimental Section	196
4.5.1	Materials and Methods	196
4.5.2	Molecular Characterization	196

4.5.3	Absorption Spectroscopy	196
4.5.4	Thermogravimetric Analyses (TGA)	197
4.5.5	Wide-angle X-ray Diffraction (WAXD) analyses	197
4.5.6	Transmission Electron Microscopy (TEM)	197
4.5.7	Raman Spectroscopy	197
4.5.8	Cyclic Voltammetry	197
4.5.9	X-ray Photoelectron Spectroscopy	198
4.5.10	BET Surface Area and Porosity Analysis	198
4.5.11	Synthesis and Characterization	198
4.5.12	Preparation of Electrodes and Electrochemical Measurements	201
4.5.13	Determination of Resistivity and Electrical Conductivity via four-Probe Measurements	202
4.6	References	202
	Abstract	211
	List of Publications	212
	List of Conferences attended	212

List of Abbreviations

ECDs	Electrochromic devices
MLCT	Metal to ligand charge transfer
FTO	Fluorine tin oxide
AgCl	Silver chloride
^t Bu ₄ PF ₆	Tetra butyl ammonium hexafluorophosphate
°C	Degree celsius
CHCl ₃	Chloroform
E _{1/2}	Half-wave potentials
CE	Coloration efficiency
λ	Wavelength
Δ%T _{max}	Maximum change in transmittance
Q _d	Charge ejected or injected per unit area
CDCl ₃	Deuterated chloroform
CV	Cyclic voltammogram
MeOH	Methanol
DCM	Dichloromethane
DFT	Density functional theory
MPNFs	Metallosupramolecular polymer network films
LiClO ₄	Lithium perchlorate
eV	Electron volt
E _{ox}	Oxidation potential
E _{red}	Reduction potential
PC	Propylene carbonate
PMMA	Polymethyl methacrylate

EIS	Electrochemical impedance spectroscopy
TMS	Trimethylsilane
Pt	Platinum
^t BuOH	Tertbutanol
AFM	Atomic force microscopy
FTIR	Fourier transform infrared
PXRD	Powder X-ray diffraction
TCO	Transparent conducting oxide
GCD	Galvanic charge discharge
EDL	Electrical double layer
I-V	Current-Voltage
HRMS	High resolution mass spectroscopy
MOF	Metal organic framework
C	Cell capacitance
CP	Coordination polymer
Br ⁻	Bromine
P(OEt) ₃	Triethyl phosphite
PF ₆	Hexafluorophosphate
DMSO	Dimethyl sulfoxide
Pd	Palladium
TGA	Thermogravimetric analysis
TEM	Transmission electron microscopy
V	Voltage
TBAPF ₆	Tetra butyl ammonium hexafluorophosphate
M	Molar
mA	Milliampere

mg	Milligram
mL	Millilitre
mV	Millivoltage
mM	Millimolar
s	Seconds
ESR	Equivalent series resistance
MeOH	Methanol
MO	Molecular orbital
S	Siemens
μ M	Micromolar
nm	Nanometer
NMR	Nuclear magnetic resonance
BET	Brunauer Emmet and Teller
PCP	Porous coordination polymer
F	Farad
μ L	Microlitre
THF	Tetrahydrofuran
min	Minute
h	Hour
KOH	Potassium hydroxide
A	Area
R	Resistance
t	Thickness

List of Tables

1	Table 2.1	Redox potentials of the CPs in solution and film state	71
2	Table 2.2	Optical and spectroelectrochemical properties of the films and devices	87
3	Table 3.1	Comparison of the volumetric capacitance (max) and energy density (max) reported for different materials	133
4	Table 4.1	Electrochemical redox potentials of the metal complexes Mn-L, Fe-L and Co-L	176
5	Table 4.2	Areal capacitance of the metallopolymer derived supercapacitors at varying scan rates	185
6	Table 4.3	Characteristics and performance of the coordination polymers and coordination polymer derived supercapacitors	190
7	Table 4.4	Electrical conductivity of the coordination polymers determined from four-probe measurements	192

List of Figures

1	Figure 1.1	Photographs of a) electrochromic smart windows produced by Sageglass, b) electrochromic windows in aircrafts and c) rear-view mirror from Gentex, and d) printable and flexible electrochromic displays designed by Siemens.	3
2	Figure 1.2	Schematic representation of the device architecture in conventional ECDs.	4
3	Figure 1.3	Structure of the donors and acceptors used for the synthesis of conjugated conducting polymers via electro or chemical polymerization.	9
4	Figure 1.4	Chemical structure of different conjugated conducting polymers and its color switches based on measured CIE color coordinates.	10
5	Figure 1.5	Chemical structure of terpyridine ligand 22 and its octahedral metal complex 23.	12
6	Figure 1.6	a) Chemical structure of the triphenylamine-terpyridine based metallopolymers ($p\text{-ML}_n$, $M = \text{Ru, Fe}$; $n = 1\text{--}3$). b) Photographs showing the color changes in the corresponding thin films upon applying 0V and 2 V, respectively.	12
7	Figure 1.7	a) Chemical structure of the polymer polyCo. Photograph of b) MeOH solution of polyCo and the thin films at c) pH 7 and d) pH 13, upon application of different potentials. The corresponding transmittance changes are also shown.	13
8	Figure 1.8	a) The chemical structure of the ligand TPA-TPY and b) the switching stability of the nanosheet based device at a pulse width of 5s for 500 cycles. c) Photographs showing the color changes in the electrochromic device fabricated from the Fe(II-terpyridine) nanosheets at 0 V, 2.2 V, and 3.4 V.	14
9	Figure 1.9	Chemical structure of a) the terpyridine-based ligand 3-tpy and b) the coordination nanosheet 3tpy-Fe. c) Cyclic voltammogram of 3tpy-Fe in a solid-state ECD and the corresponding device architecture. d) Photograph showing the color switching in the ECD (-2V – 3V).	15
10	Figure 1.10	a) Chemical structure of heterobimetallic [Fe(II)/Os(II)] supramolecular polymer HBP. b) Photographs of the electrochromic	16

device at 0 V, 1.8 V and 2.5 V. c) Switching stability of device up to 100 cycles at a pulse width of 5 s. d) Photographs showing the proof-of-concept voltage-tunable multicolor flowerpot electrochromic display prototypes.

- 11 Figure 1.11 a) Chemical structure of the ligand L-TPA. b) A schematic representation of electrochromic device architecture fabricated from L-TPA-Fe or L-TPA-Ru layers and the corresponding photographs of the devices fabricated from c) L-TPA-Fe and e) L-TPA-Ru at 0 V (left) and 1.5 V (right). The corresponding transmittance changes at d) 578 nm (blue line) and at 885 nm (gray line) for L-TPA-Fe and f) at 498 nm (red line) and 896 nm (black line) for L-TPA-Ru at a pulse width of 2.5 s. 17
- 12 Figure 1.12 a) Chemical structure of the heterometallic polymer polyOsRuFe. b) Photographs of the films fabricated from polyOsRuFe at different applied potentials. The corresponding changes in oxidation states of the metal ions are also shown. 18
- 13 Figure 1.13 a) Chemical structure of the terpyridine ligand HL. b) Spectroelectrochemical profiles of the thin films fabricated from Pt(II) complexed HL upon applying potentials in the range 0 V and 1.4 V. Changes in c) transmittance at 820 nm and d) current under double-potential steps of 0 V and 1.4 V at a pulse width of the 20 s. 19
- 14 Figure 1.14 Figure 1.14: (a-b) Chemical structure of the metal-bipyridine complexes Bipy(1-4)-Fe. c) Schematic representation of the electrochromic device architecture (top) and the photographs showing the color changes in device fabricated using Bipy1-Fe and Bipy2-Fe (bottom), -3.0 V- +3.0 V, 5 s pulse width). d) Spectroelectrochemical switching of Bipy2-Fe in a potential window of 0.55 V – 1.45 V at a 1 s pulse width, showing stable electrochromic switching. 20
- 15 Figure 1.15 a-b) Chemical structure of the metal bipyridine complexes (Bipy1-Os and Bipy2-Fe). c) Schematic representation of electrochromic device fabricated from a combination of Bipy1-Os and Bipy2-Fe. d) 21

Photographs showing the three colored states of Bipy 1.2 upon applying 2 V, -2 V, and 2.8 V after 500, 1000, and 2000 cycles.

- 16 Figure 1.16 a) Chemical structure of the bipyridine ligand L-bip. b) Photographs showing the color changes in the ECD fabricated from Ru(II) coordinated L-bip upon applying 0 V (left) and 0.6 V (purple), and c) the corresponding transmittance changes at 578 nm. d) Stability data for the device (>20000 cycles) at a pulse width of 3 s. Adapted with permission from ref 54. 22
- 17 Figure 1.17 a) Schematic representation of the synthesis of dual-branched hexagonal coordination nanosheets using the ligand L-3Phn and Fe(II). b) Reversible color change in the electrochromic device fabricated from L-3Phn - (Fe(II)) nanosheets upon application of 0 V (top) and 1.5 V (bottom). c) Cycling stability of the device at a pulse width of 15 s for 15000 switchings. 23
- 18 Figure 1.18 a-b) Chemical structure of the Salen-based ligands Poly 1 and Poly 2. Photographs showing the color changes in the ECDs fabricated from Poly 1 c) with topology 1 and e) topology 2. d) and f) The corresponding schematic representation of the ECDs of topology 1 and topology 2, respectively. 24
- 19 Figure 1.19 a) Chemical structure of the terpyridine appended Fe-phthalocyanine FePc-Tp. Photographs showing the color change in b) the film state of FePc-Tp ITO/glass and c) the device state. d) Cycling stability of the ECD (578 nm) upon applying 2.5 V and -2.1 V at a pulse width of 15 s. 26
- 20 Figure 1.20 a) Chemical structure of the porphyrin ligand TPP. Absorbance changes at neutral (black), oxidized (red), and reduced (blue) states of b) H₂TPP, c) CuTPP, and d) AgTPP. 27
- 21 Figure 1.21 a) Chemical structure of the dibenzoeilatin ligand Ldb. b) Schematic representation of the ECDs fabricated from Ldb-Cu polymeric films and c) the corresponding changes in absorbance upon applying -3 V 28

- and 1 V at a pulse width of 5 s. d) Photographs showing the color changes in the device using the same potential window.
- 22 Figure 1.22 a) Chemical structure of the benzenetetramine ligand BTA and a schematic representation of the synthetic scheme of Ni-BTA. b) Transmittance changes observed for Ni-BTA films upon application of 0 V and 0.6 V, and c) the corresponding photographs of the film at initial (blue), bleached and colored states. 29
- 23 Figure 1.23 a) Changes in absorbance of PW with the addition of different concentrations of NaClO (0 – 75 μ M). b) Photographs showing the color of (1) PB, (2) PB converted into colorless PW, and (3) PW converted back to PB with different amounts of NaClO (1.5 - 5.6 mM). 30
- 24 Figure 1.24 a) Schematic representation of fabrication of electrochromic sensor using PANI-modified ITO electrode. b) Color changes in the electrochromic sensor at different concentrations of E. coli. 31
- 25 Figure 1.25 a) Schematic representation of the EC biosensor device based on iridium oxide MIP. b) Visual detection of chlorpyrifos upon application of voltage and the corresponding concentration range. c) Smartphone-based detection of chlorpyrifos. 32
- 26 Figure 1.26 Schematic representation of strain sensor and electrochromic device on hand skin and the corresponding device response. 33
- 27 Figure 1.27 a) Schematic illustration of the closed bipolar electrode (CBE)-based electrochromic sensor. b) Color change in reporter cells upon detection of lactate, glucose, and uric acid each at a concentration of 2.5 mM. c) Chronoamperometric data obtained from glucose (black); lactate (red); and uric acid (blue). 34
- 28 Figure 1.28 a) Schematic representation of the zinc ion electrochromic battery (ZIEB) prototype. b) Digital images of an LED (0.5 V) powered by the ZIEB with 1.23 V open circuit potential. c) Changes in %T before and after discharging. d) Cycling stability of ZIEB prototype. 35

- 29 Figure 1.29 a) Schematic representation of the flexible electrochromic battery consisting of PET/ITO as substrate, WO₃ film as cathode, Al sheet as anode, and absorptive glass mat (AGM) as a separator, and aluminum trichloride (AlCl₃) as electrolyte. b) Photographs of the flexible device in charged and discharged states. c) Discharging curve at a constant current density of 0.5 A g⁻¹ and the corresponding photographs of the device. 36
- 30 Figure 1.30 a) Schematic representation of the hybrid Zn²⁺/Al³⁺ electrochromic battery architecture. b) Near-infrared transmittance spectrum of the device and its experimentally measured open circuit voltage (inset). c) Photographs of LED powered by the device after 1 minute and up to 80 minutes showing the discharge efficiency. d) Photographs showing the charging process of the completely discharged device. e) Transmittance spectra of the prototype device on applying 0.1 V and 1.2 V showing efficient electrochromic switching. 37
- 31 Figure 1.31 Photograph of the (a) beached and (b) colored (powering an LED) bifunctional PB/Al electrochromic device. c) Cycling stability of the PB/Al device and (d) the corresponding changes in transmittance before and after bleaching. 38
- 32 Figure 1.32 (a-b) Schematic illustration of the electrostatic double-layer mechanism of energy storage and electrochemical pseudocapacitance using c) redox reactions on the electrode surface or d) ion intercalation process. 39
- 33 Figure 1.33 a) Molecular structure of the Ni-MOF Ni₃(HITP)₂ and b) the corresponding space-filling diagram of Ni₃(HITP)₂. c) Cyclic voltammetry of Ni₃(HITP)₂ based electrode at a scan rate of 10 mV s⁻¹ with increasing cell voltage. d) Capacitance retention under repeated cycling at a current density of 2 A g⁻¹ for 10,000 cycles. 40
- 34 Figure 1.34 Schematic representation of the solid-state electrochromic energy storage devices: a) device architecture with plain ITO/glass and b) device architecture with an ion storage layer, TiO₂/ITO/glass). c) 41

Areal capacitance of the device with TiO₂ ion storage layer, measured at different current densities (0.06 to 1 mA cm⁻²). d) GCD cycling stability for the device with TiO₂ ion storage layer, at a current density of 0.06 mA cm⁻².

- 35 Figure 1.35 a) Electrochemical redox reaction occurring at working and counter electrodes in the asymmetric supercapacitor with a sandwich configuration of metallosupramolecular polymers as cathodic material and Prussian blue as anodic material using a non-aqueous electrolyte. b) Volumetric capacitance of poly Fe and poly Ru based asymmetric supercapacitors at different current densities. c) Cycling stabilities of poly Fe and poly Ru based asymmetric supercapacitors up to 10000 charge-discharge cycles. d) Photograph of an LED powered by a polyRu-based capacitor. 42
- 36 Figure 2.1 a) Chemical structure of the ligands 1 and 2. b) Photographs of the thin films fabricated by dip coating solutions of Fe-1-MEPE (deep blue, 30 mM), Fe-2-MEPE (dark green, 14 mM), and Co-2-MEPE (red, 14 mM). 58
- 37 Figure 2.2 a) Chemical structure of the terpyridine-based ligands 3a,b and the corresponding coordination nanosheets. Electrochromic color switching in b) Fe-3a (blue to yellow) and c) Fe-3b nanosheets (blue to yellow). d) Schematic representation of the hybrid electrochromic device and e) photographs upon application of 2 V and 1 V. 59
- 38 Figure 2.3 Cyclic voltammograms (CVs) at different scan rates and the corresponding spectroelectrochemistry of materials obtained by simultaneous deposition of isostructural a) Os and Fe complexes, c) Co and Fe complexes and d) Co, Os, and Fe complexes (3M) on ITO. Insets show photographs of ECDs demonstrating the color change due to oxidation and reduction of corresponding metal centers. b) Representative structure of the monolayer constructed from the metal complexes of ligand 4. 60

- 39 Figure 2.4 a) Chemical structure of the metal complexes 5-8. c) Two consecutive redox switching and the corresponding color changes for the metallopolymeric assemblies constructed from the complexes 5-8. 61
- 40 Figure 2.5 a) Chemical structure of the imidazolium-linked terpyridine ligand 9. b) Schematic representation of formation of three-dimensional metal-organic coordination assemblies via layer-by-layer deposition. c) Transmittance change and the corresponding photographs and d) switching stability of the assemblies upon applying potentials of -2 V and 3.2 V in the device state. 62
- 41 Figure 2.6 a) Molecular structures of the terpyridine ligands used in this study. b) A schematic illustration of the structure of the coordination polymers. The core (Ph, TPE, Thio) is shown in red, the coordinating terpyridines are shown in blue and Fe(II) is shown in pink. The corresponding metallopolymeric assemblies are denoted as Fe(II)-Ph-TPy, Fe(II)-TPE-TPy and Fe(II)-Thio-TPy. 65
- 42 Figure 2.7 Concentration (5-30 μM) dependent UV-vis spectra of a) Fe(II)-Ph-TPy, c) Fe(II)-TPE-TPy and e) Fe(II)-Thio-TPy in MeOH. The linear correlation between the MLCT band intensity and concentration for b) Fe(II)-Ph-Tpy (λ_{MLCT} : 578 nm), d) Fe(II)-TPE-Tpy (λ_{MLCT} : 580 nm) and f) Fe(II)-Thio-Tpy (λ_{MLCT} : 584 nm). 66
- 43 Figure 2.8 UV-vis spectra of the assemblies formed by spray coating methanol solutions (0.3 mM) of the ligands containing 2 equivalents of FeCl_2 : a) Ph-Tpy, b) TPE-Tpy and c) Thio-Tpy. The MLCT wavelengths are also shown. The exponential increase in the absorbance of the MLCT bands with the number of deposition steps and the corresponding photographs of FTO-glass substrates (3 cm \times 3 cm) after 9 deposition steps are shown in the insets. $R^2 > 0.99$ for all fits. d) The change in the thickness of the spray coated films with the number of deposition steps for the assemblies obtained using Fe(II) MPs of Ph-Tpy, (red), TPE-Tpy (blue) and Thio-Tpy (green). $R^2 > 0.99$ for all fits. 67

- 44 Figure 2.9 AFM images ($10\ \mu\text{m} \times 10\ \mu\text{m}$) of the MPNFs constructed from a) 68
Fe(II)-Ph-Tpy, b) Fe(II)-TPE-Tpy and c) Fe(II)-Thio-Tpy after 9
deposition steps. The thickness of the assemblies was $165 \pm 6\ \text{nm}$.
- 45 Figure 2.10 Cyclic voltammograms of the assemblies formed by spray coating the 69
methanol solutions (0.3 mM) of the ligands containing 2 equivalents
of FeCl_2 : a) Ph-Tpy, b) TPE-Tpy and c) Thio-Tpy. The exponential
increase in the current densities (d-f) and the linear correlation
between current densities and film thickness (g-i) for the assemblies
constructed from d,g) Fe(II)-Ph-Tpy, e,h) Fe(II)-TPE-Tpy and f,i)
Fe(II)-Thio-Tpy with the number of deposition steps.
- 46 Figure 2.11 CVs of the MPNFs ($56.5 \pm 1.5\ \text{nm}$, 5 deposition steps) constructed 70
from a) Fe(II)- Ph-Tpy, b) Fe(II)-TPE-Tpy and c) Fe(II)-Thio-Tpy at
varying scan rates: $10\ \text{mV s}^{-1}$ (red) - $600\ \text{mV s}^{-1}$ (blue). Linear
correlation between the current densities and scan rate (d,e,f) and
exponential correlation between the current densities and square root
of scan rate (g,h,i) for the MPNFs of d,g) Fe(II)-Ph-Tpy, e,h) Fe(II)-
TPE-Tpy and f,i) Fe(II)-Thio-Tpy. $R^2 > 0.99$ for all fits.
- 47 Figure 2.12 CVs of the metallopolymers Fe(II)-Ph-Tpy (red), Fe(II)-TPE-Tpy 71
(blue) and Fe(II)-Thio-Tpy (green) in a) solution ($15\ \mu\text{M}$ in
acetonitrile) and b) on FTO substrates ($165 \pm 6\ \text{nm}$, 9 deposition
steps). The experiments were carried out at a scan rate of $100\ \text{mV s}^{-1}$,
using glassy carbon (solution) / modified FTO substrate (film),
Ag/AgCl and platinum wire as working, reference and counter
electrodes, respectively. $0.1\ \text{M}\ \text{tBu}_4\text{NPF}_6$ in acetonitrile was used as
the supporting electrolyte.
- 48 Figure 2.13 Transmittance spectra of the metal-organic assemblies showing the 73
beaching of the MLCT bands during electrochemical oxidation of the
assemblies constructed from a) Fe(II)-Ph-Tpy, b) Fe(II)-TPE-Tpy
and c) Fe(II)-Thio-Tpy. The spectra of the assemblies in their reduced
and oxidized states are shown in red and blue, respectively. The color
pallets of the corresponding assemblies are shown in the insets.

- 49 Figure 2.14 Chromoabsorptometry of the assemblies constructed from a) Fe(II)-Ph-Tpy, b) Fe(II)-TPE-Tpy and c) Fe(II)-Thio-Tpy at different switching times (pulse width). The change in transmittance (%) during coloration (blue) and bleaching (red) of the CPNFs constructed from d) Fe(II)-Ph-TPy, e) Fe(II)-TPE-TPy and f) Fe(II)-Thio-TPy at different pulse width (1-10 s). 74
- 50 Figure 2.15 The response times for the assemblies of a) Fe(II)-Ph-Tpy, b) Fe(II)-TPE-Tpy and c) Fe(II)-Thio-Tpy at a pulse width of 10 s. The experiments (at λ_{MLCT} : 578 nm for Fe(II)-Ph-Tpy, 580 nm for Fe(II)-TPE-Tpy and 584 nm for Fe(II)-Thio-Tpy) were carried out using the modified FTO substrate as the working electrode, Ag/AgCl as reference electrode and platinum wire as counter electrode. 0.1 M tBu_4NPF_6 in acetonitrile was used as the supporting electrolyte. 76
- 51 Figure 2.16 High resolution XPS data confirming the N 1s peaks for ligands a) Ph-TPy, d) TPE-TPy and g) Thio-TPy. High resolution XPS data confirming the (b,e,h) Fe 3p_{1/2} and Fe 3p_{3/2} and (c,f,i) N 1s peaks for the MPNFs of (b,c) Fe(II)-Ph-TPy, (e,f) Fe(II)-TPE-TPy and (h,i) Fe(II)-Thio-TPy. 77
- 52 Figure 2.17 a) Molecular structures of the redox probes Q1-Q3. Cyclic voltammograms of the molecular probes Q1 and Q2 (1.3 mM) obtained using MPNFs of Fe(II)-Ph-TPy (red), Fe(II)-TPE-TPy (blue), and Fe(II)-Thio-TPy (green) as working electrodes at a film thickness of (b,c) 10.5 ± 0.5 nm, (d,e) 29.5 ± 0.5 nm, and (f,g) 39.5 ± 0.5 nm. 79
- 53 Figure 2.18 Cyclic voltammograms of the molecular probe Q3 (1.3 mM) obtained using MPNFs of Fe(II)-Ph-TPy (red), Fe(II)-TPE-TPy (blue), and Fe(II)-Thio-TPy (green) as working electrodes at a film thickness of 10.5 ± 0.5 nm. 80
- 54 Figure 2.19 Electrochromic switching in solid state devices fabricated from the Fe(II) MPs of a) Fe(II)-Ph-Tpy, b) Fe(II)-TPE-Tpy and c) Fe(II)- 81

Thio-Tpy. The MPs were spray coated on 3 cm × 3 cm FTO glass substrates.

- 55 Figure 2.20 Transmittance spectra of the ECDs showing the bleaching of the MLCT bands during electrochemical oxidation of the assemblies constructed from a) Fe(II)-Ph-Tpy, b) Fe(II)-TPE-Tpy and c) Fe(II)-Thio-Tpy. 82
- 56 Figure 2.21 Chromoabsorptometry of the assemblies constructed from (a,d) Fe(II)-Ph-Tpy, (b,e) Fe(II)-TPE-Tpy and (c,f) Fe(II)-Thio-Tpy at different pulse widths (a-c) and by applying different double potential steps (d-f). Double potential steps of -2.0 V - +2.0 V and -3.0 V - +3.0 V were used at intervals of ±0.1 V. 83
- 57 Figure 2.22 The dependence of change in %Transmittance on a) pulse width and b) change in applied potential window for the ECDs of Fe(II)-Ph-TPy (red), Fe(II)-TPE-TPy (blue) and Fe(II)-Thio-TPy (green). 84
- 58 Figure 2.23 The response times for the devices of a) Fe(II)-Ph-Tpy, b) Fe(II)-TPE-Tpy and c) Fe(II)-Thio-Tpy at a pulse width of 10 s. 86
- 59 Figure 2.24 Stability of the ECDs constructed from a) Fe(II)-Ph-Tpy, b) Fe(II)-TPE-Tpy and c) Fe(II)-Thio-Tpy up to 1000 continuous switchings at 5 s pulse width and a potential window of -3.0 V - +3.0 V at room temperature. d) The variation in stability with the number of switchings: Fe(II)-Ph-Tpy: red, Fe(II)-TPE-Tpy: blue and Fe(II)-Thio-Tpy: green. 87
- 60 Figure 2.25 Decay of transmittance (%) of the ECDs based on Fe(II)-Ph-TPy (red), Fe(II)-TPE-TPy (blue) and Fe(II)-Thio-TPy (green) under an open circuit potential. All devices were subjected to a potential of +3.0 V for ensuring complete oxidation before switching the potential off. 88
- 61 Figure 2.26 Electrochromic images created by masking 3 cm × 3 cm FTO-glass substrates during the spray coating process of a) Fe(II)-Ph-Tpy, b) Fe(II)-TPE-Tpy and c) Fe(II)-Thio-Tpy. 89

62	Figure 3.1	a) Schematic illustration of a 3D - COF and the corresponding chemical structure of the monomer. b) SEM image of the hollow spheres. c) Specific capacitance upon varying the current density. d) Cyclic stability of the 3D - COF.	109
63	Figure 3.2	a) 3D view of the conjugated microporous polymers TAT-CMP-1 and TAT-CMP-2. b) The corresponding nitrogen adsorption and desorption isotherms. c) Cycling stability at a current density of 10 A/g. d) Galvanostatic charge–discharge curves of TAT-CMP-1.	110
64	Figure 3.3	a) A space-filling model of the MOF Ni-HAB. Blue, grey, green and white spheres represent N, C, Ni and H atoms, respectively. b) Areal capacitance of Ni-HAB electrodes at different mass loadings. c) Gravimetric and volumetric capacitance of Ni-HAB pellets at different mass loadings of 9, 35 and 65 mg cm ⁻² . d) Cycling stability at 10 A g ⁻¹ .	111
65	Figure 3.4	a) Simulated structure of of the coordination polymer Ni ₃ BHT. b) Temperature dependent electrical conductivity of Ni ₃ BHT pellets. c) Gravimetric and volumetric capacitance for electrodes fabricated from Ni ₃ BHT at different scan rates and d) the cycling stability at a scan rate of 30 mV s ⁻¹ .	112
66	Figure 3.5	a) Crystal structure of the MOF Cu-CAT and b) SEM images of nanowire arrays grown on a filter paper. c) Cycling stability of the capacitor electrode at 800 mV s ⁻¹ . d) Specific capacitance at various current densities for electrodes fabricated from Cu-CAT nanowire arrays and Cu-CAT powder.	113
67	Figure 3.6	a) Schematic representation of P5ICA/WO ₃ nanocomposites. b) Color change in the electrochromic supercapacitor device during charging and discharging. c) Specific capacitance of the electrode fabricated from P5ICA/WO ₃ nanocomposites under different current densities. d) Galvanic charge discharge stability at 0.1 mA cm ⁻² .	114
68	Figure 3.7	a) Structure of the iron polypyridyl complex used as electrochromic layer in an electrochromic–hybrid supercapacitor (EHSC). b)	115

- Schematic representation showing the device architecture. c) Absorption spectra and photographs at five different potentials during charging. d) Stability of the electrochromic-hybrid supercapacitor at a current density of 0.88 A g^{-1} .
- 69 Figure 3.8 A ball-and-stick model showing the molecular structures of the terpyridine ligands a) Fe(II)-Ph-TPy, b) Fe(II)-TPE-TPy and c) Fe(II)-Thio-TPy. The metallopolymers were synthesized by mixing FeCl_2 and the corresponding ligand in a 2:1 molar ratio and were precipitated from water as their PF_6 salts. 116
- 70 Figure 3.9 UV-Vis spectra of a) Ph-TPy (red) and Fe(II)-Ph-TPy (blue), b) TPE-TPy (red) and Fe(II)-TPE-TPy (blue), and c) Thio-TPy (red) and Fe(II)-Thio-TPy (blue), in methanol ($c = 15 \mu\text{M}$). Photographs of the ligand (red border) and metallopolymer (blue border) solutions under visible light are shown in the insets. Emission spectra of d) Ph-TPy (red) and Fe(II)-Ph-TPy (blue), e) TPE-TPy (red) and Fe(II)-TPE-TPy (blue), and f) Thio-TPy (red) and Fe(II)-Thio-TPy (blue), in methanol ($c = 15 \mu\text{M}$). 118
- 71 Figure 3.10 FT-IR spectra of a) Ph-TPy (black) and Fe(II)-Ph-TPy (red), b) TPE-TPy (black) and Fe(II)-TPE-TPy (red), and c) Thio-TPy (black) and Fe(II)-Thio-TPy (red). The spectra were recorded in the solid state (KBr, neat). 119
- 72 Figure 3.11 AFM images (a-c) and 3D topographies (d-f) of the metallopolymers coated on freshly cleaved mica: (a,d) Fe(II)-Ph-TPy, (b,e) Fe(II)-TPE-TPy and (c,f) Fe(II)-Thio-TPy. 120
- 73 Figure 3.12 Powder X-ray diffraction spectra of a) Fe(II)-Ph-TPy, b) Fe(II)-TPE-TPy, and c) Fe(II)-Thio-TPy. 120
- 74 Figure 3.13 Thermogravimetric curves of a) Ph-TPy (black) and Fe(II)-Ph-TPy (red), b) TPE-TPy (black) and Fe(II)-TPE-TPy (red), and c) Thio-TPy (black) and Fe(II)-Thio-TPy (red). 121

- 75 Figure 3.14 High resolution XPS data confirming the Fe 3p_{1/2} and Fe 3p_{3/2} (left) and N 1s peaks for the metallopolymers: a) Fe(II)-Ph-TPy, b) Fe(II)-TPE-TPy, and c) Fe(II)-Thio-TPy. 122
- 76 Figure 3.15 Raman spectra of a) Ph-TPy (black) and Fe(II)-Ph-TPy (red), b) TPE-TPy (black) and Fe(II)-TPE-TPy (red), and c) Thio-TPy (black) and Fe(II)-Thio-TPy (red). 123
- 77 Figure 3.16 Cyclic Voltammograms of a) Fe(II)-Ph-TPy, b) Fe(II)-TPE-TPy, and c) Fe(II)-Thio-Tpy at varying scan rates between 10 (red) and 300 (blue) mV s⁻¹. 124
- 78 Figure 3.17 The dependence of current on the scan rates (d-f) and square root of the scan rates (g-i) for (d,g) Fe(II)-Ph-TPy, (e,h) Fe(II)-TPE-TPy, and (f,i) Fe(II)-Thio-TPy. CVs (See Figure 3.14) were obtained using the corresponding metallopolymer modified FTO as working electrode, Ag/AgCl as reference electrode and Pt wire as counter electrode. 125
- 79 Figure 3.18 UV-Vis spectra of the metallopolymers drop-casted on FTO substrates confirming the bleaching of the MLCT bands during the electrochemical oxidation of the assemblies constructed from a) Fe(II)-Ph-TPy, b) Fe(II)-TPE-TPy, and c) Fe(II)-Thio-Tpy. The spectra corresponding to the reduced and oxidized states are shown in red and blue, respectively. The photographs of the observed color pallets are shown in the insets. 1 represents the reduced ground state and 2 represents the oxidized state. The corresponding chromaticity coordinates obtained upon reversible redox switching for (d) Fe(II)-Ph-TPy, (e) Fe(II)-TPE-TPy and (f) Fe(II)-Thio-TPy. 126
- 80 Figure 3.19 The response times obtained upon reversible redox switching for (a) Fe(II)-Ph-TPy, (b) Fe(II)-TPE-TPy and (c) Fe(II)-Thio-TPy. 128
- 81 Figure 3.20 a) CV loops obtained from the symmetric supercapacitors fabricated from Fe(II)-Ph-TPy (red), Fe(II)-TPE-TPy (blue), and Fe(II)-Thio-TPy (green) at a scan rate of 100 mV s⁻¹. b) Galvanostatic charge-discharge curves of the supercapacitors fabricated from Fe(II)-Ph-

TPy (red), Fe(II)-TPE-TPy (blue), and Fe(II)-Thio-TPy (green) electrodes at a constant potential window (0.0 – 1.0 V) and current density (1.0 A g⁻¹). c) Comparison of the volumetric capacitance calculated from the GCD curves at different current densities for d) Fe(II)-Ph-TPy (red), e) Fe(II)-TPE-TPy (blue), and f) Fe(II)-Thio-TPy (green). Cycling stability of the symmetric supercapacitors derived from Fe(II)-Ph-TPy (red), Fe(II)-TPE-TPy (blue), and Fe(II)-Thio-TPy (green), at a constant current density of 1.0 A g⁻¹.

- 82 Figure 3.21 CV loops obtained from the symmetric supercapacitors fabricated from a) Fe(II)-Ph-TPy, b) Fe(II)-TPE-TPy, and c) Fe(II)-Thio-TPy at different scan rates. The red traces in (a) – (c) correspond to the CVs obtained at 5 mV s⁻¹ and the blue ones correspond to those at 200 mV s⁻¹. 130
- 83 Figure 3.22 Galvanostatic charge-discharge curves of the supercapacitors fabricated from a) Fe(II)-Ph-TPy, b) Fe(II)-TPE-TPy, and c) Fe(II)-Thio-TPy at different current densities at a constant potential window (0.0 – 1.0 V) and different current densities: 2.0 A g⁻¹ (brown), 1.0 A g⁻¹ (yellow), 0.75 A g⁻¹ (green), 0.50 A g⁻¹ (blue), and 0.25 A g⁻¹ (red). 130
- 84 Figure 3.23 Comparison of charge-discharge times (a-e) and volumetric capacitance (f-j) in symmetric supercapacitor cells fabricated from Fe(II)-Ph-TPy (blue), Fe(II)-TPE-TPy (orange), and Fe(II)-Thio-TPy (green). The charge discharge times were obtained at a constant potential window (0.0 – 1.0 V). The current densities were (a,f) 0.25 A g⁻¹, (b,g) 0.50 A g⁻¹, (c,h) 0.75 A g⁻¹, (d,i) 1.0 A g⁻¹, and (e,j) 2.0 A g⁻¹. 132
- 85 Figure 3.24 Comparison of the supercapacitor performance of different materials reported in literature: a) Ragone Plot (volumetric energy density Vs 134

- volumetric power density) and b) volumetric capacitance vs volumetric energy density.
- 86 Figure 3.25 a) Nyquist plots of the symmetric supercapacitors derived from Fe(II)-Ph-TPy (red), Fe(II)-TPE-TPy (blue), and Fe(II)-Thio-TPy (green) based electrodes obtained using electrochemical impedance spectroscopy (EIS). Inset: Equivalent Circuit of the best performing Fe(II)-TPE-TPy based supercapacitor. b) shows the corresponding zoomed-in image. 135
- 87 Figure 3.26 (a) BET surface area of the metallopolymers. The pore size distribution obtained from BET surface area analysis for b) Fe(II)-Ph-TPy, c) Fe(II)-TPE-TPy, and d) Fe(II)-Thio-TPy. 136
- 88 Figure 3.27 I-V characteristics of a) Fe(II)-Ph-TPy, b) Fe(II)-TPE-TPy, and c) Fe(II)-Thio-TPy, obtained from 4-probe measurements. 137
- 89 Figure 3.28 Energy-minimized structures confirming the octahedral coordination modes in the metallopolymers using model ligand systems for a) Fe(II)-Ph-TPy, b) Fe(II)-TPE-TPy, and c) Fe(II)-Thio-TPy. 139
- 90 Figure 4.1 a) Structure of the MOF Ni₃(HITP)₂. b) Charge discharge cycles at various current densities. c) CVs at a scan rate of 10 mV s⁻¹ with increasing voltage. d) Cycling stability at 2 A g⁻¹. 158
- 91 Figure 4.2 a) SEM images of Co-LMOF. b) The charge–discharge curves and c) specific capacitance at different current densities. d) Cycling stability at 2A g⁻¹. 159
- 92 Figure 4.3 a) SEM image of a) pure α-Ni(OH)₂ and b) α-Ni(OH)₂/graphite composite. c) Capacitance vs current density for pure α-Ni(OH)₂ (black) and α-Ni(OH)₂/graphite composite (red). d) Cycling stability at 10A g⁻¹. 160
- 93 Figure 4.4 a) Structure of Ni-MOF viewed along the a axis. b) SEM image of Ni-MOF showing its layered structure. c) Specific capacitance 161

- measured at different current densities for the supercapacitor electrode fabricated from the Ni-MOF. d) Cycling stability of the electrode fabricated from Ni-MOF measured at 2 A g^{-1} .
- 94 Figure 4.5 a) Molecular structure of ultrathin 2D Co-MOF nanosheet. b) SEM images of the Co-MOF nanosheets. c) Specific capacitances of ultrathin, micro-nano and bulk Co-MOF at different current densities. d) Cycling stability at 2 A g^{-1} using 3.0 M KOH electrolyte. 162
- 95 Figure 4.6 Structure of pCDB-EDOT polymer. b) Areal capacitance of pCDB-EDOT at various current densities. c) The color change of the electrochromic supercapacitor device at different voltages. d) The galvanic charge-discharge curves of pCDB-EDOT-based electrochromic supercapacitor devices at a current density of 1 mA cm^{-2} initially (black) and after 5000 cycles (red). 163
- 96 Figure 4.7 a) Scanning electron micrograph of a mesoporous V_2O_5 double-gyroid film on FTO substrate. b) The specific capacitance and charge-discharge cycles at 10 A g^{-1} . c) Photographs of the electrochromic supercapacitor device displaying color change upon charge (0 V) and discharge (3.5 V). 164
- 97 Figure 4.8 a) Scheme showing the molecular structures of the bipyridine ligand L and the corresponding coordination complexes $[\text{ML}_3](\text{PF}_6)_2$ ($\text{M} = \text{Mn, Fe, Co}$). b) Schematic representation of the formation of the metallopolymers. Three metallopolymers M-L-Pd ($\text{M} = \text{Mn, Fe, Co}$) were prepared by cross-linking the free pyridines on the complexes M-L ($\text{M} = \text{Mn, Fe, Co}$) with Pd(II) in a 1:3 ratio. 167
- 98 Figure 4.9 FT-IR spectra of (a) Mn-L (dotted) and Mn-L-Pd (solid), (b) Fe-L (dotted) and Fe-L-Pd (solid) and (c) Co-L (dotted) and Co-L-Pd (solid). The spectra were recorded in the solid state (KBr, neat). The peaks (wave number in cm^{-1}) corresponding to C=N ring stretching and in plane C-H deformation are provided in each spectrum (black: complex; grey: coordination polymer). 168

- 99 Figure 4.10 Thermogravimetric curves of the metal complexes (black, a) Mn-L, 169
b) Fe-L, c) Co-L) and the coordination polymers (red, a) Mn-L-Pd,
b) Fe-L-Pd, c) Co-L-Pd).
- 100 Figure 4.11 Powder X-ray diffraction spectra of a) Mn-L (blue) and Mn-L-Pd 170
(red), b) Fe-L (blue) and Fe-L-Pd (red), and c) Co-L (blue) and Co-
L-Pd (red). Comparison with the powder XRD pattern (green)
generated from the single crystal data of a structurally related
molecule is shown to indicate structural similarity.
- 101 Figure 4.12 TEM and high magnification TEM images of a,d) Mn-L-Pd, b,e) Fe- 171
L-Pd and c,f) Co-L-Pd.
- 102 Figure 4.13 Energy dispersive X-ray (EDX) spectra (from TEM) of a) Mn-L-Pd, 172
b) Fe-L-Pd, c) Co-L-Pd, qualitatively confirming the presence of the
metal ions (Mn, Fe, Co and Pd) in the metallopolymers.
- 103 Figure 4.14 High resolution XPS data for (a-c) Mn-L-Pd, (d-f) Fe-L-Pd and (g-i) 173
Co-L-Pd. The left panels (a,d,g) correspond to the high resolution
spectra for Pd, the middle ones (b,e,h) correspond to those for N and
the right ones (c,f,i) correspond to those for Mn, Fe and Co
respectively.
- 104 Figure 4.15 Raman spectra of the coordination polymers: Mn-L-Pd (red), Fe-L- 174
Pd (blue) and Co-L-Pd (green).
- 105 Figure 4.16 Photographs of the thin films obtained by spin-coating the 175
metallopolymers Fe-L-Pd (left), and Co-L-Pd (right) on FTO
substrates.
- 106 Figure 4.17 a) UV-vis absorption spectra of the metal complexes Mn-L (red 175
trace), Fe-L (blue trace) and Co-L (green trace). The complexes were
dissolved in a 1:1 mixture of CD_2Cl_2 and MeOH and the final
concentration was adjusted to 15 μM . b) Changes in the UV-vis
absorption spectra of a CD_2Cl_2 / MeOH solution (50 μM) of the metal
complex Fe-L (red trace), upon successive addition of a THF solution
(50 μM) of $\text{PdCl}_2(\text{PhCN})_2$. The blue trace represents the spectrum

upon addition of an excess of $\text{PdCl}_2(\text{PhCN})_2$ (just before the precipitation of the metallopolymer).

- 107 Figure 4.18 Cyclic Voltammograms of a) Mn-L, c) Fe-L, and e) Co-L at a scan rate of 100 mV s^{-1} and b) Mn-L-Pd, d) Fe-L-Pd and f) Co-L-Pd under various scan rates ($50 - 500 \text{ mV s}^{-1}$). 177
- 108 Figure 4.19 The exponential (a,c,e) and linear (b,d,f) dependence of current on the scan rates and square root of the scan rates for (a,b) Mn-L-Pd, (c,d) Fe-L-Pd, and (e,f) Co-L-Pd. The data is derived from the corresponding cyclic voltammograms. 178
- 109 Figure 4.20 a) Cyclic voltammograms of the spin-coated films of Fe-L-Pd: as prepared (red), after 25,000 cycles (blue), and after 50,000 cycles (green) of electrochemical switching. b) Electrochromic switching stability of the Fe-L-Pd films ($\lambda_{\text{MLCT}} = 590 \text{ nm}$). 180
- 110 Figure 4.21 The response time obtained upon reversible redox switching of the spin-coated film of Fe-L-Pd (thickness = 23 nm). 180
- 111 Figure 4.22 a) Chromoabsorptometry of the assemblies constructed by spin-coating Fe-L-Pd (thickness = 23 nm) at different switching times (pulse width) and b) the corresponding change in transmittance (%) at different pulse width (0.25-10 s). 181
- 112 Figure 4.23 Energy minimized structures of a) Mn-L-Pd, b) Fe-L-Pd and c) Co-L-Pd obtained using Density Functional Theory (DFT) at the B3LYP/6-31G (d,p) level, corroborating the near octahedral geometries for all three metal complexes. 182
- 113 Figure 4.24 a) Cyclic Voltammograms obtained from the symmetric supercapacitors based on Mn-L-Pd (red), Fe-L-Pd (blue), and Co-L-Pd (green) at a scan rate of 5 mV s^{-1} . b) Galvanostatic Charge-Discharge curves of symmetric supercapacitors based on Mn-L-Pd (red), b) Fe-L-Pd (blue), and Co-L-Pd (green) electrodes at a constant potential window ($0.0 - 1.0 \text{ V}$) and current density (1.0 mA cm^{-2}). c) Comparison of the areal capacitance obtained for Mn-L-Pd (red), Fe-

L-Pd (blue) and Co-L-Pd (green) derived capacitors at different scan rates.

- 114 Figure 4.25 Cyclic Voltammograms obtained from the symmetric 184
supercapacitors based on a) Mn-L-Pd, b) Fe-L-Pd, and c) Co-L-Pd at
different scan rates. The red traces in (a) – (c) correspond to the CVs
obtained at 5 mV s^{-1} and the blue ones correspond to those at 200 mV s^{-1} .
d) Comparison of the areal capacitance obtained for Mn-L-Pd (red), Fe-L-Pd (blue) and Co-L-Pd (green) derived capacitors at
different scan rates.
- 115 Figure 4.26 Galvanostatic charge-discharge curves of symmetric supercapacitors 187
based on a) Mn-L-Pd, b) Fe-L-Pd, and c) Co-L-Pd electrodes at a
constant potential window (0.0 – 1.0 V) and different current
densities: 2.0 A g^{-1} (purple), 1.0 A g^{-1} (red), 0.75 A g^{-1} (green), 0.50 A g^{-1} (yellow), and 0.25 A g^{-1} (blue).
- 116 Figure 4.27 a) Nyquist plots of the symmetric supercapacitors derived from Mn- 188
L-Pd (red), Fe-L-Pd (blue), and Co-L-Pd (green) based electrodes
obtained using electrochemical impedance spectroscopy (EIS). The
inset shows the corresponding equivalent circuit of the best
performing Co-L-Pd based supercapacitor and b) shows the
corresponding zoomed-in image.
- 117 Figure 4.28 Cycling performance (stability) of the symmetric supercapacitors 189
derived from Mn-L-Pd (red), Fe-L-Pd (blue), and Co-L-Pd (green),
at a constant current density of 1.0 A g^{-1} .
- 118 Figure 4.29 (a) BET adsorption (solid circles) and desorption (open circles) 191
isotherms for Mn-L-Pd (red), Fe-L-Pd (blue), and Co-L-Pd (green).
Pore size distribution in (a) Mn-L-Pd, (b) Fe-L-Pd and (c) Co-L-Pd,
obtained from adsorption isotherms.
- 119 Figure 4.30 I-V characteristics of a) Mn-L-Pd, b) Fe-L-Pd and c) Co-L-Pd, 192
obtained from 4-probe measurements. The red, blue and green colors
show the results from three independent measurements.

120 Figure 4.31 Comparison of the capacitance normalized to the BET surface area. 194

The values are plotted directly from the references or calculated from available data on capacitance and specific surface area. The normalized capacitance in the plot is limited to a maximum of $150 \mu\text{Fcm}^{-2}$ for clarity. A few electrode materials with the surface area normalized capacitance $>150 \mu\text{Fcm}^{-2}$ have been reported (CNT: $239.3 \mu\text{Fcm}^{-2}$, 3D porous graphene with noncarbeneous additives: $792.7 \mu\text{Fcm}^{-2}$, $184.0 \mu\text{Fcm}^{-2}$, MOFs and MOF derived carbon: $261.1 \mu\text{Fcm}^{-2}$, $1449.9 \mu\text{Fcm}^{-2}$, $726.0 \mu\text{Fcm}^{-2}$, $869.5 \mu\text{Fcm}^{-2}$, $909.0 \mu\text{Fcm}^{-2}$).

PREFACE

Electrochromic materials are a family of smart materials that change their optical properties in terms of absorbance, reflectance, or emission via an electrochemical redox process under the application of an electric voltage. The tunable optical properties of these materials directly reflect on the light and heat transmission properties of the surface on which they are immobilized, leading to energy efficiency in indoor lighting and cooling. Integration of other functions with electrochromism would be one strategy towards multifunctional smart applications. In this context, combining electrochromism and energy-storage is an interesting perspective and such electrochromic energy storage smart windows can not only adjust the sunlight and solar heat via the application of a small electric field but also can be used as energy-storage devices at the same time. Several classes of electrochromic materials - transition metal oxides, viologen, conjugated conducting polymers, metal coordination complexes, etc. are reported in the literature. Most majority of these report qualify as EC material for their academic impact, but practically suffer from low to moderate efficiency, inferior redox, photochemical and cycling stability, write-erase inefficiency and laborious processability. Hence the current research in the field is actively driven by the quest for new generation EC materials with uncompromising performance. Coordination-based metal-organic thin films are, therefore, a relatively less investigated class of electrochromic materials, with excellent prospects in terms of optical contrast, ease of switching, redox reversibility, facile processability, low power consumption, and high cycle life. The current thesis aims at developing new metal-organic systems with highly efficient EC properties and the fabrication of the corresponding solid-state electrochromic devices as well as applying them as energy storage systems. Until recently, carbon-based materials such as activated carbon, carbon nanotubes, graphite, etc., were exclusively used as active electrode materials in supercapacitors. Out of all the non-carbon materials, metal organic materials that combine the functional advantages of both organic and inorganic materials, are one of the less investigated class of electrode materials, that too as pyrolytic precursors for carbon in electrochemical storage devices. Metal organic materials having exceptionally large surface areas and tunable porosity along with structural and morphological versatilities have triggered recent interest to investigate the electrochemical feasibility of using metal organic systems as electrode materials in supercapacitors. The thesis also aims at developing metallopolymer based thin film or micro-supercapacitors with a unique coherence of high volumetric capacitance, energy densities and cycling stability.

The thesis has been divided into four chapters. In the **first chapter**, an overview of electrochromism, its applications, and different type of electrochromic materials have been discussed. We focused on reviewing literature reports on metal-organic electrochromic systems based on different ligands such as terpyridine, bipyridine, and other acceptor-type ligands. Multifunctional applications of electrochromic systems such as sensing, energy storage, and battery are also discussed.

In the **second chapter**, we synthesized three tetra-terpyridine ligands with variations in their core architecture (phenyl vs. tetraphenylethynyl vs. bithiophene) to create spray-coated electrochromic assemblies of iron(II) based coordination polymer network films on transparent conducting oxide substrates. These thin films exhibited molecular permeability and spectroelectrochemical properties that are in turn dictated by the ligand structure. Electrochromic films with high coloration efficiencies (up to 1050 cm²/C) and superior optical contrast (up to 76%) with a concomitant color-to-color redox transition were readily achieved.

In the **third chapter**, we report three electrochromic metallopolymer-based electrode materials containing Fe²⁺ with high volumetric capacitance and energy densities in a symmetric two-electrode supercapacitor set-up. These metallopolymers exhibited volumetric capacitance up to 866.2 F cm⁻³ at a constant current density of 0.25 A g⁻¹. The volumetric capacitance (Fe(II)-TPE-TPy: 544.6 F cm⁻³ > Fe(II)-Ph-TPy: 313.8 F cm⁻³ > Fe(II)-Thio-TPy: 230.8 F cm⁻³ at 1 A g⁻¹) and energy densities (Fe(II)-TPE-TPy: 75.5 mWh cm⁻³ > Fe(II)-Ph-TPy : 43.6 mWh cm⁻³ > Fe(II)-Thio-TPy: 31.2 mWh cm⁻³) followed the order of the electrical conductivity of the metallopolymers, and are among the best values reported for metal-organic systems.

In the **fourth chapter**, we report the use of electrochromic metallopolymers obtained from near-isostructural metal (Mn²⁺, Fe²⁺, Co²⁺) bipyridine coordination complexes as electrode materials in a symmetric supercapacitor test cell. The variation in the central metal ion (Mn²⁺, Fe²⁺, Co²⁺) was found to dictate the capacitive performance of the metallopolymers obtained via Pd(II) cross-linking of the otherwise nearly identical parent coordination complexes. The central metal ion not only influences the porosity, BET surface area (6.46 (Mn), 10.36 (Fe) and 29.72 (Co) m²g⁻¹) and hence the areal capacitance, but also the performance parameters like cycling stability and charge discharge kinetics as well as the charge transfer mechanism. A 3:4:5 ratio for the areal capacitance values (9.1 (Mn), 12.2 (Fe), and 15.4 (Co) mFcm⁻² at a scan rate of 5 mVs⁻¹) corroborates the modulative effect of the metal center in the capacitive characteristics of the metallopolymers.

Multifunctional Electrochromic Materials and Their Applications



1.1 Abstract

Stimuli-induced control and modulation of the functional properties of molecular assemblies have revolutionized several aspects of modern materials science. Electrochromic materials, in this regard, are a class of smart chromogenic materials capable of exhibiting different optical or colored states under electrical stimulation. Ever since its discovery, electrochromic materials have shown huge potential towards various multifunctional applications including energy saving smart windows, smart mirrors, wearable devices, display technologies, consumer electronics, sensors, etc. Therefore, the design and development of novel electrochromic materials with high thermal and photochemical stabilities, high contrast ratio, fast and reversible switching, high coloration efficiency, low voltage of operation, and easy processability is driving the current research interest in this field. This introductory chapter aims at providing an overview of electrochromism, types of electrochromic materials, electrochromic thin films and devices and their multifunctional applications. The objectives and the outlook of the thesis are presented towards the end of this chapter.

1.2 Introduction

The development of responsive materials has been a thrust area of research in various interdisciplinary approaches towards the realization of smart materials.^{1,2} The possibilities for modulating the optical properties of chemical systems from nano to macroscopic levels under electrically stimulated conditions have therefore led to a watershed moment in the area of optoelectronic materials and devices.^{3,4} The active research in the field over the past couple of decades has been mainly due to the increasing demand for smart technology applications such as smart windows, optical memory devices, improved display technologies, and sensors.⁵

Chromism is the reversible change in the color of a substance upon the application of external stimuli such as electric field, temperature, light, pH, etc. Electrochromism is the reversible color change between two redox states of a chemical species under the application of an electrical voltage.^{6,7} The term “electrochromism” was first coined by Platt in 1961 and was first demonstrated by S. K. Deb using WO_3 thin films.⁸ Electrochromic materials are classified into three types: (a) type I electrochromic materials that are soluble in both oxidized and reduced states, (b) type II materials that form the film in one redox state and is soluble in another state, and (c) type III materials that form a solid film on the electrode surface and are not soluble in any of the redox states.⁶ Metal oxides, Prussian blue, metallopolymers, conducting polymers, and polymeric viologens are included under the type III classification.

1.3 History of Electrochromism

In 1953, an internal document at Balzers AG in Liechtenstein gave a description of electrically induced color changes in the films of tungsten oxide immersed in sulfuric acid. In 1969, Deb at American Cyanamid Corporation demonstrated the reversible color change in the films of WO_3 .^{8,9} At the same time, Palatnik, Malyuk, and Belozarov from the former Soviet Union also reported the electrochromic nature of Niobium oxide.¹⁰ During 1970s, research in this area was driven by their potential application in information displays. MNCs like Canon, IBM, Philips, the American Cyanamid Corporation, and Zenith Radio were also interested in EC research.^{11–13} In the latter part of the 1970s, the interest in electrochromic materials faded temporarily, due to the rise of the liquid crystal technology. In the mid-1980s, interest in EC materials was revamped with the emergence of improved fenestration technologies. The term “smart window” was introduced in 1984 and attracted immediate global attention.¹⁴ The first electrochromic device based on WO_3 films was reported by Deb and the corresponding energy-saving smart windows were conceptualized by Lampert, Granqvist and co-workers.¹⁵

1.4 Applications of Electrochromic Materials

Applications of electrochromic materials include smart windows, that are used in regulating solar radiation for energy management, glare reduction, indoor comfort and aesthetic attraction.¹⁶ Such systems also find applications in displays such as price tags, signages, advertisement boards, etc.⁶ They are also used in antiglare car mirrors, sunglasses, and electrochromic strips for charge indicators (**Figure 1.1**).¹⁷ The whole planet is getting heated up due to enhanced levels of CO₂ in the atmosphere that effectively triggers the greenhouse effect and has led to the disastrous phenomenon of global warming. The present scenario demands a judicious use of energy through smart systems as 30-40% of the total energy is rejected by the buildings through glass installations such as windows and doors. This context signifies the use of smart windows that modulate heat and light transmission leading to energy efficient buildings.

Prerequisites for such applications include several materials properties and performance parameters such as high contrast ratio and coloration efficiency, reversibility write-erase efficiency, and cycle life. For example, electrochromic materials in display devices need fast response, whereas, smart windows may need optimal response time of up to several minutes.

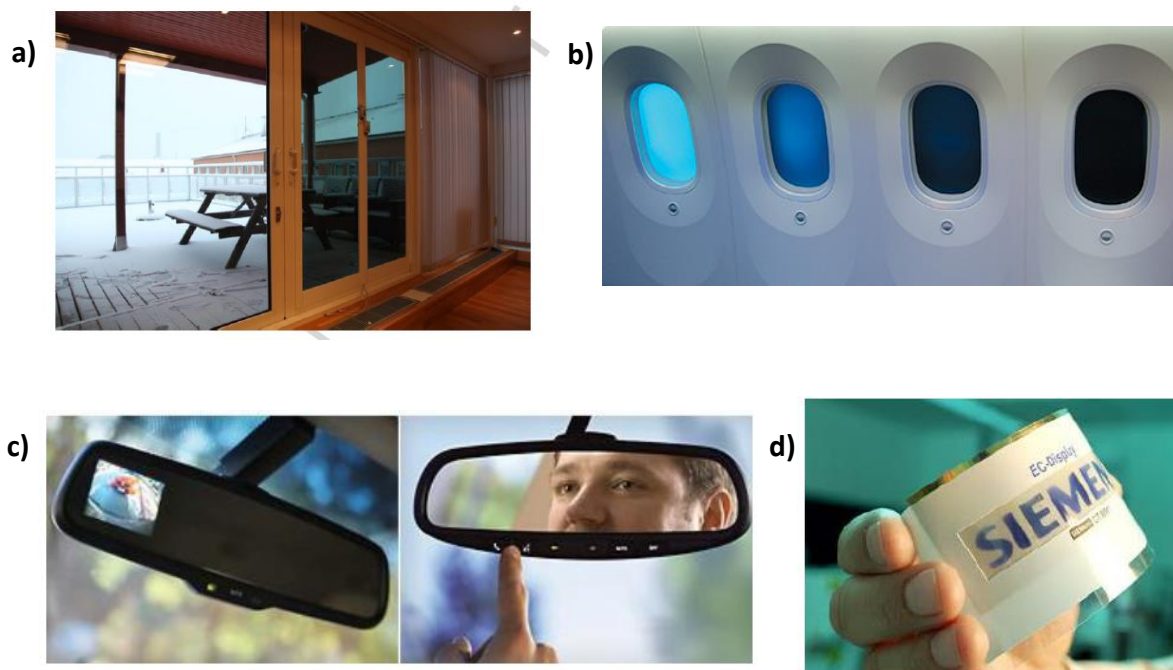


Figure 1.1: Photographs of a) electrochromic smart windows produced by Sageglass, b) electrochromic windows in aircrafts and c) rear-view mirror (both from Gentex), and d) printable and flexible electrochromic displays designed by Siemens.

In addition, the applications may either be in the visible region (for example, smart windows, automotive sunroofs, domestic appliances, and ophthalmic lenses) or in the infrared region (for example, satellite thermal control.).¹⁸ Electrochromic windows have been installed in several iconic buildings worldwide. Lawrence Berkeley Laboratories have installed smart windows for their office rooms in Oakland. National Renewable Energy Laboratories (NREL) has devoted R & D on the development of prototypes for self-powered electrochromic displays using the electrochromic devices integrated with photovoltaic cells.¹⁹

1.5 Electrochromic Devices

An electrochromic device consists of two electrodes separated by an electrolyte layer (**Figure 1.2**). The electrolyte may be liquid, semi-solid, or solid and should have properties such as high ionic conductivity, wide potential window of operation, low volatility, and thermal and chemical stabilities.¹⁶

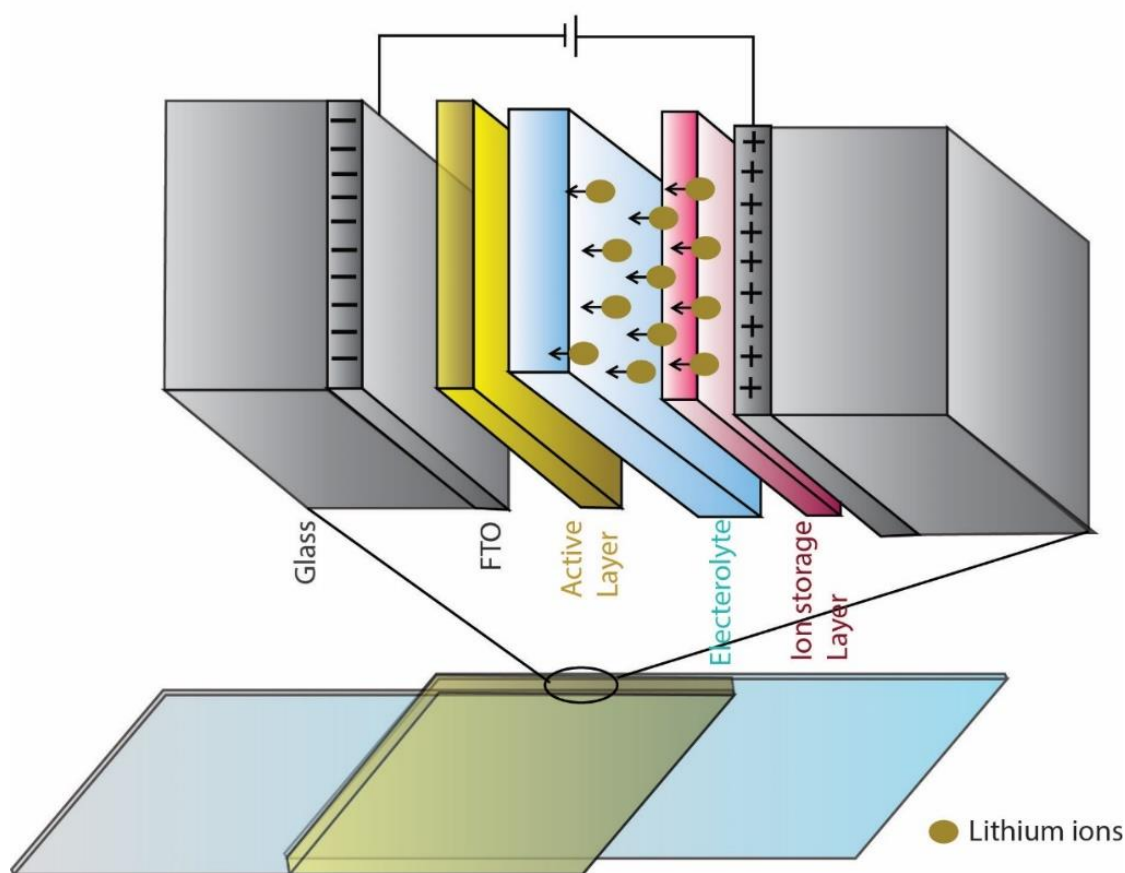


Figure 1.2: Schematic representation of the device architecture in conventional ECDs.

The electrodes consist of electrically conducting film coated on glass such as ITO or Fluorine doped Tin Oxide (FTO) or on a flexible PET substrate. The specific application of the electrochromic device determines the nature of the electrodes used. For example, transparent

electrodes are required for window applications.²⁰ Fabricating the device with optically transparent electrodes such as ITO or FTO usually provides transparency and visibility. An ion storage layer is occasionally used to balance the charges that are transported from the electrochromic layer through the electrolyte. The ion storage layer may or may not be electrochromic depending on the application. A complimentary electrochromic coating could be optionally used at the counter electrode that improves the overall coloration efficiency of the ECDs. NiO, CeO₂, and IrO₂ are commonly used inorganic ion storage materials.²¹ Typically, the required external voltage is in the range 2.0 – 4.0 V in a parallel plate capacitive architecture.

1.6 Performance Characteristics of Electrochromic Materials

Performance parameters such as optical contrast, response time, cycling life, coloration efficiency, write-erase efficiency, and optical memory are used to evaluate the electrochromic properties in film or device states. The key parameters are briefly discussed below.

1.6.1 Optical Contrast: It is defined as the difference in transmittance between the two redox states of an electrochromic device, and it is an essential parameter in evaluating the electrochromic material.²² It is reported as percentage transmittance change ($\Delta\%T$) at a specific wavelength or over a specified range of wavelength. Optical contrast can be modulated by the thickness and morphology of the electrochromic layer. Generally, EC materials with high optical contrast are necessary for practical applications.

1.6.2 Response Time: Response time defines the time required for switching between colored and bleached states or between multiple-colored states. It is generally calculated from the time needed for the optical change to become 95% of the ultimate change in %T. The response time of electrochromic materials is mainly dependent on factors such as the ionic conductivity of the electrolyte, ionic diffusion through the electro-active thin films, electrical conductivity of the electrodes, the magnitude of the applied potential and thickness, and morphology of the electrochromic film. The response time of the device can be different from one application to another. For display applications, fast switching is desirable and for smart window applications long switching time of up to several minutes may be optimal.

1.6.3 Cycling Life: It is defined as the number of write-erase cycles that can be performed before any significant extent of degradation occurs.²³ When an ECD is repeatedly cycled, device failure eventually occurs due to many reasons such as degradation of the electro-active species, irreversible redox reactions at extreme potentials, secondary reactions due to the presence of water or oxygen, and the resistive heating with the system. The cycling stability of

an ECD depends on the device structure, environmental conditions, applied voltage, and redox stability of the materials.

1.6.4 Coloration efficiency: Coloration efficiency is defined as the change in optical density per unit area of the electrode for a given wavelength. It is calculated using the following equation

$$\eta = \Delta OD / Q_d = \log [T_b / T_c] / Q_d$$

where η (cm^2/C) is the coloration efficiency at a given wavelength and T_b and T_c are the percentage transmittance at bleached and colored states respectively.²⁴ It is usually higher for organic materials than for inorganic ones because of their higher molar absorption coefficients. Nature of the material, applied potential, film fabrication process and electrolyte interaction are some of the factors that affect the coloration efficiency.

1.6.5 Write-Erase efficiency: This parameter defines the fraction of the originally formed colored state that can subsequently be electrochemically bleached. For a successful display, the efficiency must approach 100%.

1.6.6 Optical memory: It is defined as the time the electrochromic material retains its electronic state after the electric field is switched off. ECDs with long optical memory are power efficient because no power supply is required to retain the new electrochromic state. The electrochemical stability of the reduced/oxidized state of the EC material and the slow movement of electrons and electrolyte ions inside the device enhance the optical memory. In general, solid ECDs show long optical memory than liquid ECDs because of the restricted movement of electrons and ions through the ECDs.

1.7. Classification of EC Materials

Electrochromic materials are generally classified into the following classes: Transition metal oxides, Prussian blue, viologens, conjugated conducting polymers, and metal coordination complexes/polymers.⁶

1.7.1 Transition Metal Oxides

The oxides of transition metals such as iridium, rhodium, ruthenium, cobalt, manganese, nickel, palladium, cerium, titanium, molybdenum, and tungsten have emerged as potential electrochromic materials over the past three to four decades.²² Among them, tungsten (VI) trioxide (WO_3) is the first and most studied electrochromic material. Initially, WO_3 films (W^{VI})

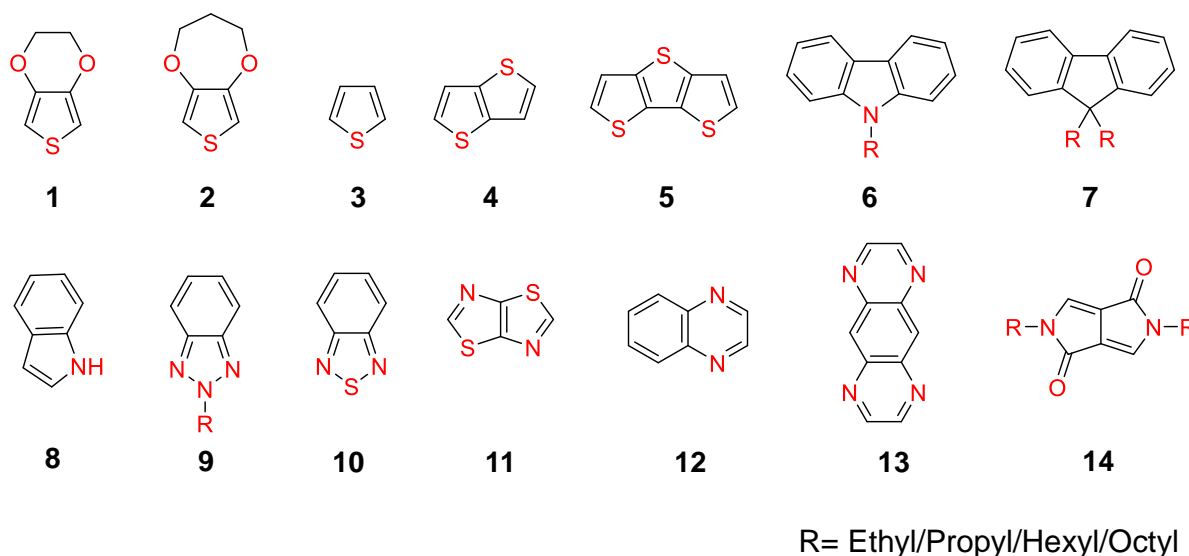


Figure 1.3: Structure of the donors and acceptors used for the synthesis of conjugated conducting polymers via electro or chemical polymerization.

The optical bandgap (E_g) between the highest-occupied π -electron band (the valence band) and the lowest unoccupied band (the conduction band) determines the electrochromic properties in conducting polymers.⁶ The oxidation or reduction process due to the insertion of counter ions, performed on a conducting polymer is referred to as doping, where the oxidation of a polymer is known as ‘p-doping’ and the reduction is known as ‘n-doping’. Since conjugated conducting polymers have an unsaturated π -bonded structure, addition or removal of an electron is facile, without significantly perturbing the σ -bonded backbone.³¹ The D-A type conjugated polymers contain electron-rich and electron-deficient functionalities that exhibit lower band gaps and wider bandwidths when compared to their corresponding parent homopolymers made of either D or A units only.³² Modification of structure and ratio of electron-rich and electron-poor moieties on the polymer chain could offer a balance of short- and long-wavelength absorption bands and thus lead to a high degree of color tunability.

In this regard, polythiophenes, that show red color in their reduced form (undoped) and blue color in its oxidized form (doped), are used for electrochromic applications because of the ease of synthesis, stability, and processability.³³ Polythiophene-based electrochromic systems with tunable colors are prepared by changing the substituents on the monomers or by using various thiophene analogues. Poly[(3,4-ethylenedioxy)thiophene] (PEDOT) is an analog of thiophene and PEDOT derivatives have characteristically low band gap than polythiophene or alkyl-substituted polythiophenes owing to the presence of two electron-donating oxygen atoms adjacent to the thiophene ring. PEDOT is a widely investigated electrochromic polymer that exhibits a deep blue color in its neutral state and changes to a light blue transmissive state upon

oxidation.³⁴ PEDOT shows excellent stability and conductivity in the doped state when compared to other substituted polythiophenes. Polypyrroles are yet another class of extensively investigated conjugated electrochromic polymers, and exhibit a yellow-green ($\lambda_{\text{max}} = 420 \text{ nm}$) neutral insulating state and blue-violet ($\lambda_{\text{max}} = 670 \text{ nm}$) doped conductive state.³⁵ Polypyrrole-based electrochromic systems can be easily synthesized with a varying range of optoelectronic properties via simple alkyl or alkoxy substitution. Multicolor electrochromism in conjugated conducting polymers has been achieved by tuning the band gap through copolymerization and chemical modification of monomers.¹⁷ **Figure 1.4** shows how the structural modification of the monomer unit results in tuning the band gap leading to multicolor electrochromism in conjugated conducting polymer-based systems.

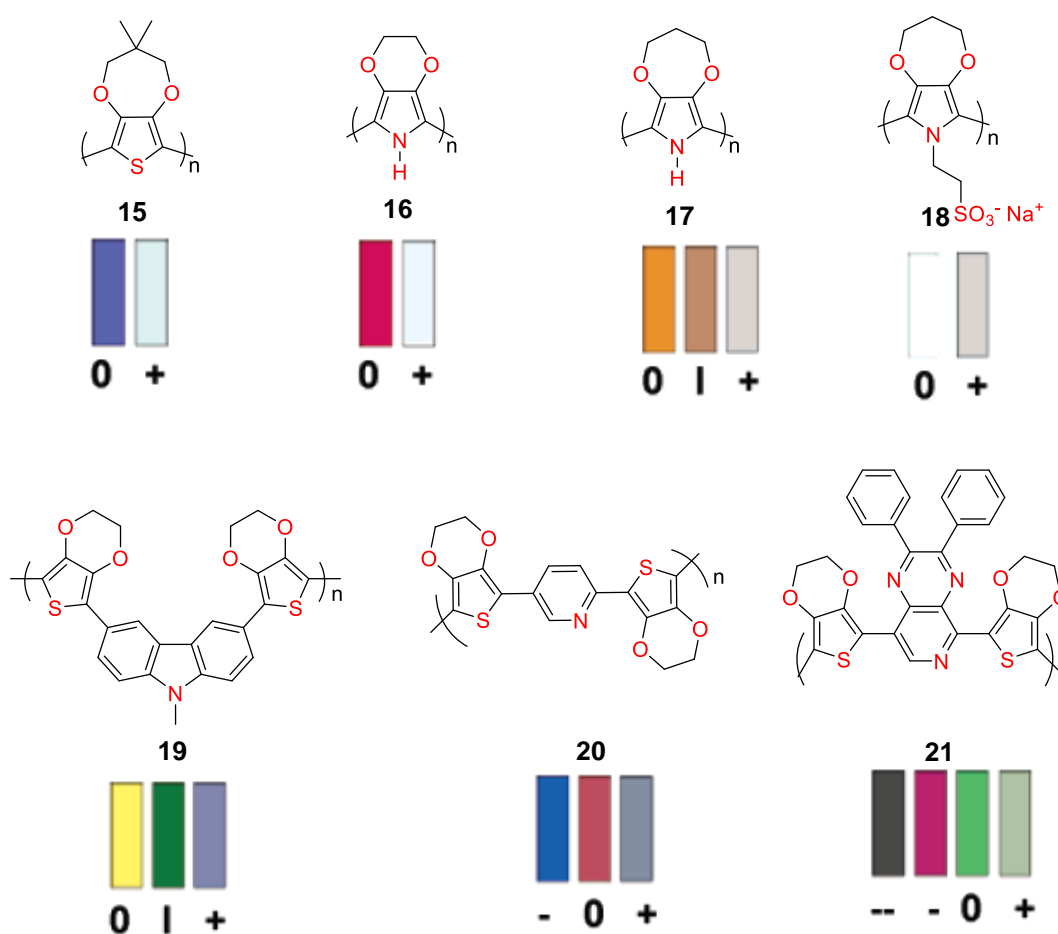


Figure 1.4: Chemical structure of different conjugated conducting polymers and its color switches based on measured CIE color coordinates. Adapted with permission from ref 17.

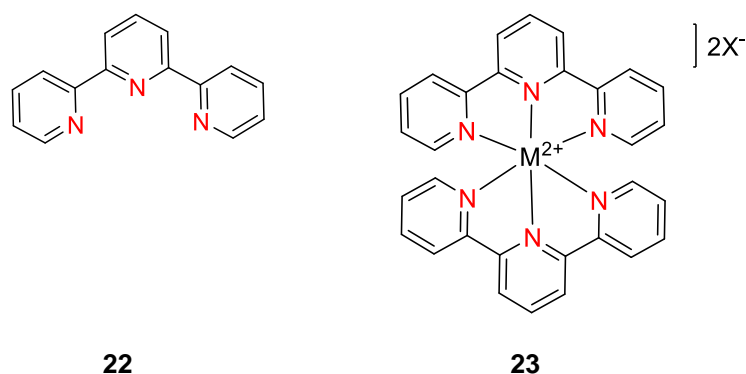
1.7.5 Metal Coordination Complexes and Polymers

Transition-metal complexes generally show electronic transitions such as ligand-centered transitions, metal-centered transitions, and those resulting from the interaction of metal ions and ligands (charge transfer transitions).⁶ These transitions involve valence electrons, and the

chromophoric characteristics are altered upon redox reactions involving the metal center. Charge transfer transitions can be classified into ligand-to-metal charge transfer transitions (LMCT) and metal-to-ligand charge transfer transitions (MLCT).³⁶ Between two different ligands, ligand-to-ligand charge transfer transitions (LLCT) are also possible. Transition-metal complexes-based electrochromism involves the MLCT transitions that result in perceivable spectral changes in the visible region. Metal coordination complexes and polymers possess multiple well-defined reversible metal redox processes and the electronic absorptions are defined by the redox states. This is one of the reasons for using metal - organic systems for electrochromic applications.³⁷ These metal complexes show favorable electrochromic switching due to fast redox reactivity and good electron conductivity. They also possess structural benefits emanating from the presence of a delocalized π electron system, rigid ligand network, and stability.³⁸ These systems also benefit from a large number of fabrication possibilities such as polymerization, dip coating, spin coating, drop casting, spray coating, layer-by-layer deposition, and printing. Color can be tuned in the RGB color space via the choice of ligands, metal, or ligand-metal combinations, and ligand structure modifications.³⁹ Different types of ligands such as terpyridine, bipyridine, phenanthroline, porphyrin, etc. are used to generate electrochromic metal complexes and polymers, and are discussed in detail in the following sections.

1.8. Terpyridine-based Metal-Organic Materials for Electrochromic Applications

Terpyridine is a tridentate ligand with high affinity to several transition metal ions (**Figure 1.5**). Terpyridine and its derivatives are chemically and thermally stable and coordinates the metal ion in an octahedral geometry. Such metal-organic assemblies generally exhibit characteristic optical and electrochemical profiles including metal-to-ligand charge transfer (MLCT) in the visible region and reversible redox reactions.⁴⁰ Electrochromic films fabricated from such metal-organic systems show excellent electrochromic properties such as low switching potential, high optical contrast and coloration efficiency, and fast switching kinetics.⁴¹ A few representative reports on terpyridine-based electrochromic metal-organic systems are discussed in this section.



$M = Fe^{2+}, Ru^{2+}, Os^{2+}, Co^{2+}, Zn^{2+},$ or Ni^{2+} and $X =$ anion

Figure 1.5: Chemical structure of the terpyridine ligand **22** and its octahedral metal complex **23**.

Tao *et al.* have synthesized EC films using electrochemical polymerization of triphenylamine appended terpyridine coordinated to Fe and Ru metal centers (**p-ML_n**, **Figure 1.6a**). Electropolymerized ruthenium films showed a color change from orange-red to yellow, while the iron-based films showed an optical transition between purple and blue (**Figure 1.6b**).

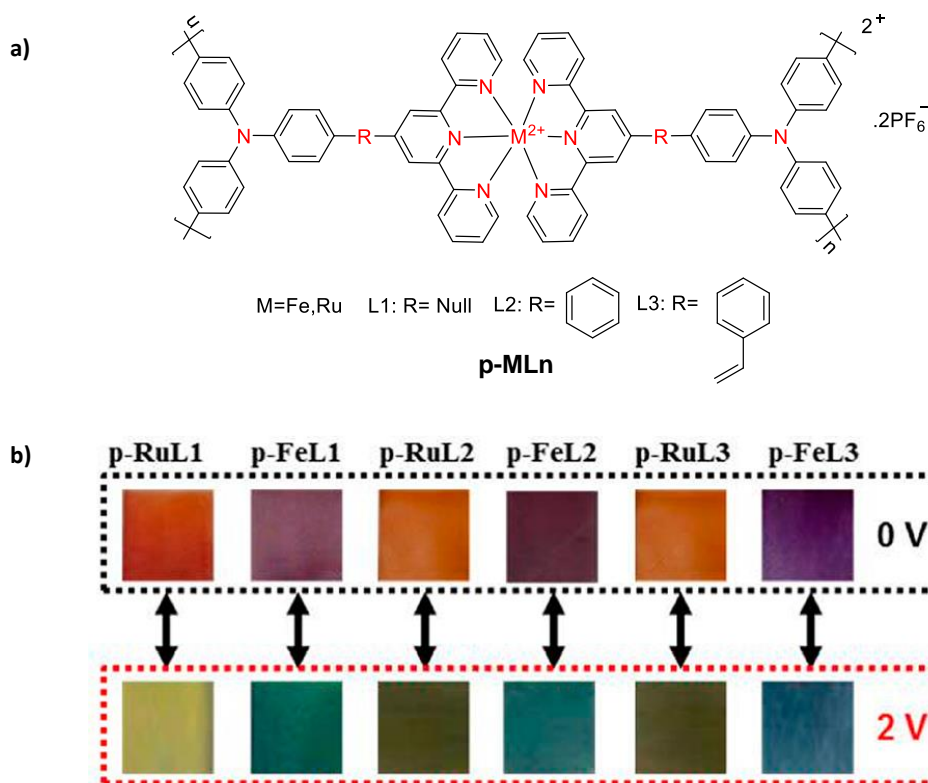


Figure 1.6: a) Chemical structure of the triphenylamine-terpyridine based metallopolymers (**p-ML_n**, $M = Ru, Fe$; $n = 1-3$). b) Photographs showing the color changes in the corresponding thin films upon applying 0V and 2 V, respectively. Adapted with permission from ref 42.

The short and rigid ligand structure was shown to enhance intramolecular charge transfer from triphenylamine and metal ions thereby stabilizing the metal ions in the higher oxidized state, resulting in a longer memory retention (11.4 min) and stability up to 300 cycles with 10% loss in optical density.⁴²

Higuchi and co-workers have developed a Co (II)-based metallo-supramolecular polymer (**polyCo**) that exhibited black-to-transmissive electrochromism (**Figure 1.7a,b**). The electrochromic property was tuned by changing the pH of the aqueous electrolyte. Increasing the pH from 7 to 13 enhanced the optical contrast of the film from 18% to 74% (**Figure 1.7b,d**).⁴³ Such drastic enhancement was found to originate from the weakened d-d* transition in Co(II), resulting from the interactions between the aqueous electrolyte system and **polyCo**. The film exhibited a fast response time at pH 7 (3.3 s for bleaching and 6 s for coloration). Electrochromic stability up to 100 switching cycles with 94% retention of the initial transmittance change was observed for the **polyCo** film.

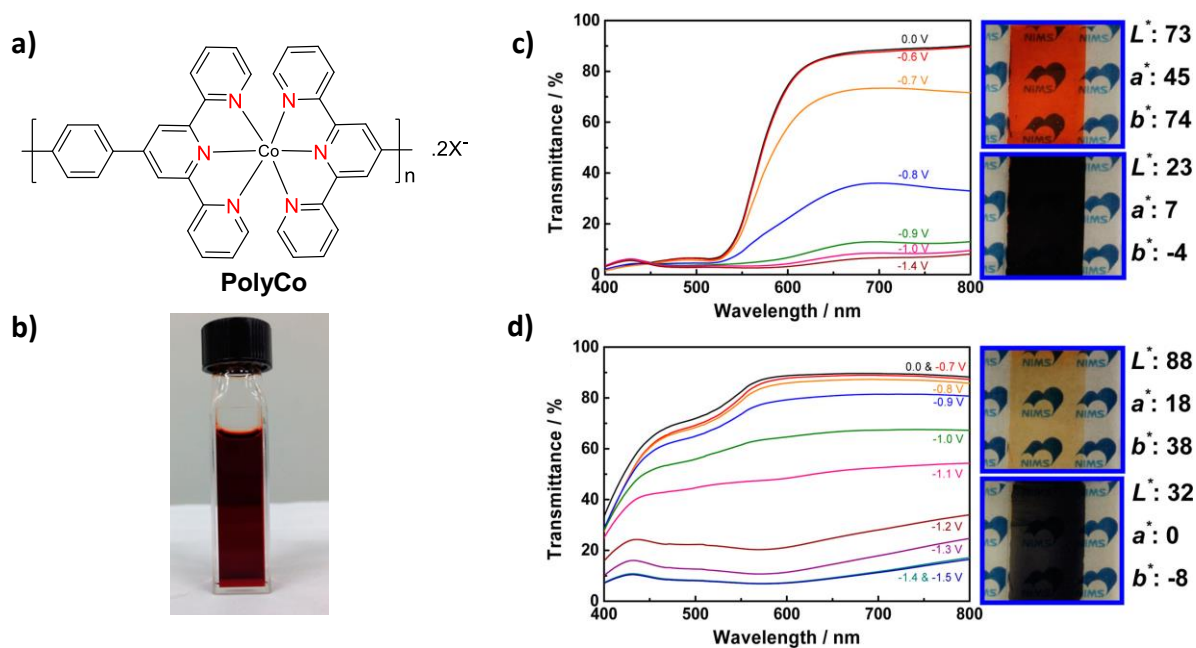


Figure 1.7: a) Chemical structure of the polymer **polyCo**. Photograph of b) MeOH solution of **polyCo** and the thin films at c) pH 7 and d) pH 13, upon application of different potentials. The corresponding transmittance changes are also shown. Adapted with permission from ref 43.

Electrochromic metal-organic nanosheets have been prepared by liquid-liquid interfacial synthesis using an organic solution of the ligand and an aqueous metal salt solution. In this context, Nishihara *et al.* have prepared Co^{2+} and Fe^{2+} nanosheets using liquid/liquid interfacial synthesis and demonstrated reversible redox reactions with visually perceivable color changes. Nanosheets exhibited a fast response time (0.54 s) and good durability over 1000 cycles. Dual

electrochromic device was also fabricated by modifying the counter and working electrode with Co^{2+} and Fe^{2+} nanosheets, respectively.⁴⁴

Zhang and co-workers have demonstrated multicolor electrochromism using Fe(II)-terpyridine-nanosheets synthesized by liquid-liquid interfacial self-assembly of the ligand **TPA-TPY** (**Figure 1.8a**) and $\text{Fe}(\text{BF}_4)_2$. The film was found to exhibit a color change from purple-red to orange-yellow to green with stability exceeding 500 cycles (**Figure 1.8b,c**). The optical contrast in the film state was found to be $>22\%$ with a fast-switching time (0.5 s for coloration and 0.4 s for bleaching).⁴⁵ The device was fabricated using the nanosheet (1.9 cm^2) as the electrochromic layer and blank ITO as a counter electrode with PMMA / LiClO_4 electrolyte in between. The device exhibited a switching time of 1 s for coloration and 0.9 s for decoloration and excellent stability with a constant optical contrast over 500 cycles.

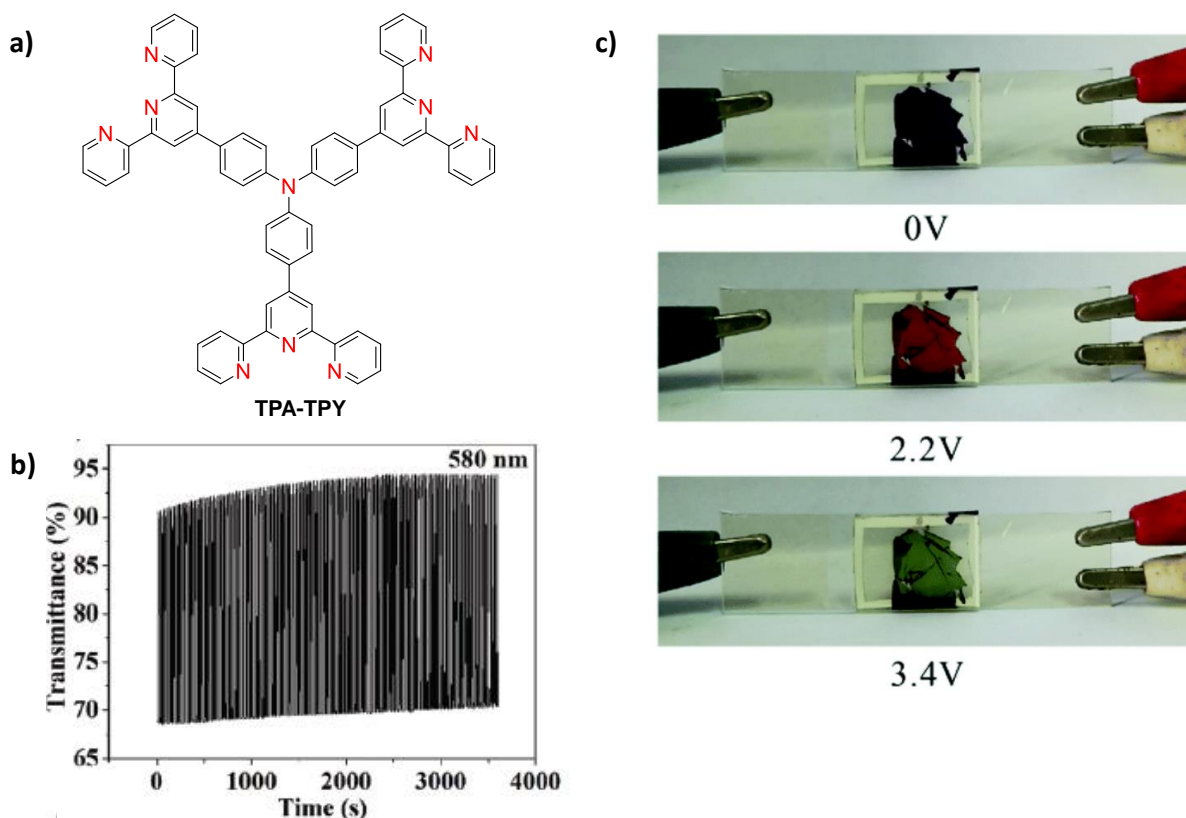


Figure 1.8: a) The chemical structure of the ligand **TPA-TPY** and b) the switching stability of the nanosheet based device at a pulse width of 5s for 500 cycles. c) Photographs showing the color changes in the electrochromic device fabricated from the Fe(II-terpyridine) nanosheets at 0 V, 2.2 V, and 3.4 V. Adapted with permission from ref 45.

Chakraborty *et al.* have recently reported a non-conjugated terpyridine-based ligand (**3tpy**, **Figure 1.9a**) and Pink-colored coordination nanosheets (**3tpy-Fe**, **Figure 1.9b**) were obtained using liquid-liquid interfacial polymerization technique. ECDs fabricated from **3tpy-Fe**

exhibited a pink to colorless transition with high optical contrast (>53%) and coloration efficiency (>470 cm² C⁻¹, **Figure 1.9c,d**).

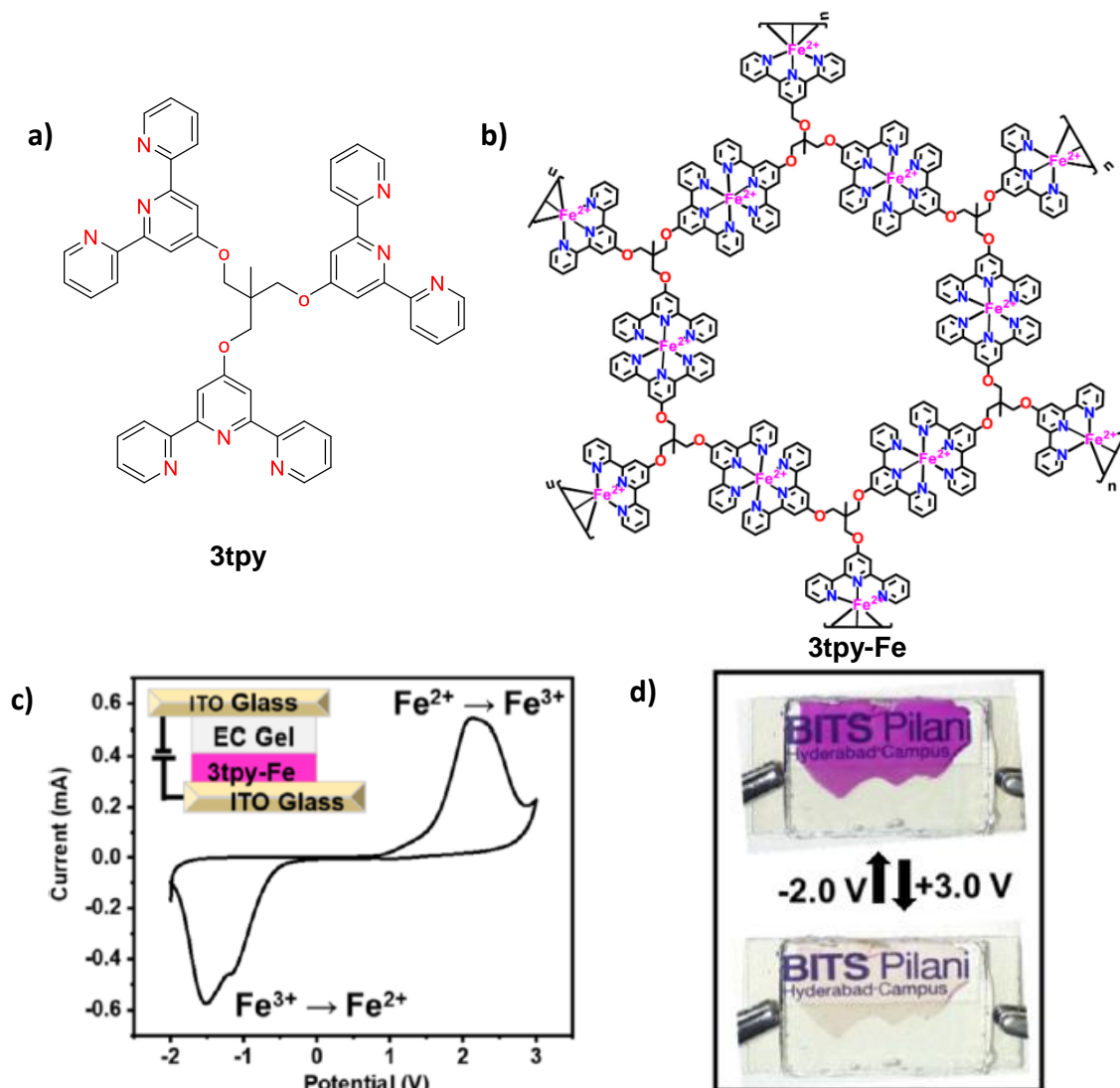


Figure 1.9: Chemical structure of a) the terpyridine-based ligand **3-tpy** and b) the coordination nanosheet **3tpy-Fe**. c) Cyclic voltammogram of **3tpy-Fe** in a solid-state ECD and the corresponding device architecture. d) Photograph showing the color switching in the ECD (-2V – 3V). Adapted with permission from ref 46.

The device switched with a reasonably fast kinetics. Response time of 1.15 s (coloration) and 2.49 s (bleaching) with stability up to 1000 cycles were observed. Compared to its conjugated bis-terpyridine analogue that recovered 90% of its colored state within 15 min, **3tpy-Fe** based devices exhibited an improved EC memory with 50% retention of its colorless state for 25 min.⁴⁶ This is most likely due to the presence of a non-conjugated ligand that prevents the electron transfer inside the **3tpy-Fe** films and a corresponding fast electron conduction through the conjugated bond in the bis-terpyridine analogue.

Voltage-tunable multicolor ECDs using a single metallosupramolecular polymer was reported by Higuchi and co-workers by alternatively positioning Os and Ru metal centers in a linear polymeric chain. Heterobimetallic supramolecular polymers (**HBP**, **Figure 1.10a**) with different counter anions were synthesized (BF_4^- , Cl^- , PF_6^- , and OAc^-), however, **HBP-OAc** alone was found to be soluble in methanol and insoluble in acetonitrile, which was found to be the best combination for the preparation of EC films.

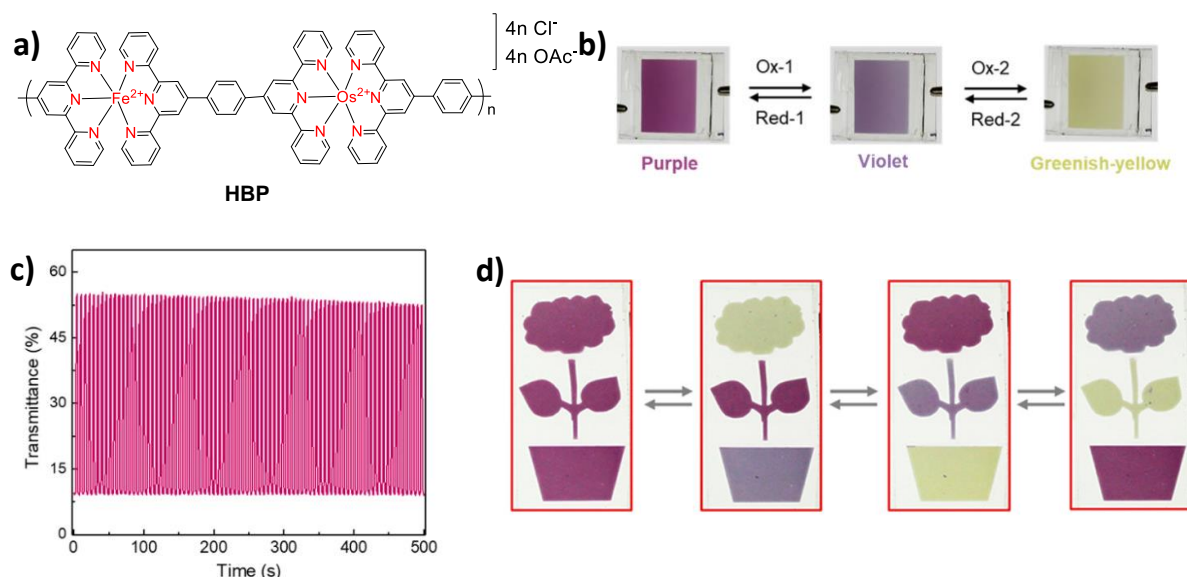


Figure 1.10: a) Chemical structure of heterobimetallic [Fe(II)/Os(II)] supramolecular polymer **HBP**. b) Photographs of the electrochromic device at 0 V, 1.8 V and 2.5 V. c) Switching stability of device up to 100 cycles at a pulse width of 5 s. d) Photographs showing the proof-of-concept voltage-tunable multicolor flowerpot electrochromic display prototypes. Adapted with permission from ref 47.

The film thus fabricated via spray coating showed a purple to violet to greenish-yellow transition upon stepwise application of 0 V, 0.7 V and 1.0 V with stability up to 10000 switching cycles and 52% optical contrast at 575 nm (**Figure 1.10b,c**).⁴⁷ The same optical transitions were also observed for the solid-state ECDs fabricated using **HBP-OAc**. The device exhibited stability up to 100 switching cycles and fast response time (0.98 s for coloration and 1.45 s for bleaching). A prototype of a flower with leaves in a flower pot was demonstrated as a proof-of-concept for voltage-tunable multi-color electrochromic displays (**Figure 1.10d**). The same group also synthesized similar Cr(III)-based metallosupramolecular polymers (**polyCr**), that exhibited a four-color electrochromism (yellow, magenta, blue, and navy). A cycling stability for more than 100 cycles with a maximum contrast of 86.1% at 780 nm under a potential window of 0.2 – 1.8 V was observed for **polyCr** based EC films.⁴⁸

A metallo-supramolecular polymer (**L-TPA-Fe** or **L-TPA-Ru**) containing redox-active Fe(II) or Ru(II) metal centers and 4,4-bis(2,2':6,2''-terpyridinyl)-phenyl-triphenylamine (**L-TPA**, **Figure 1.11a**) as a ligand has been shown to exhibit visible to NIR electrochromism with color change from dark brown to greenish and red to light green, respectively (**Figure 1.11c,e**). The metallo-supramolecular polymers in their film state showed an optical contrast of 80% in the NIR region and 52% in the visible region.⁴⁹ The corresponding solid-state device exhibited cycling stability exceeding 4000 cycles, with high optical contrast in the visible (50% at 578 nm) and NIR regions (77% at 885 nm) (**Figure 1.11d,f**).

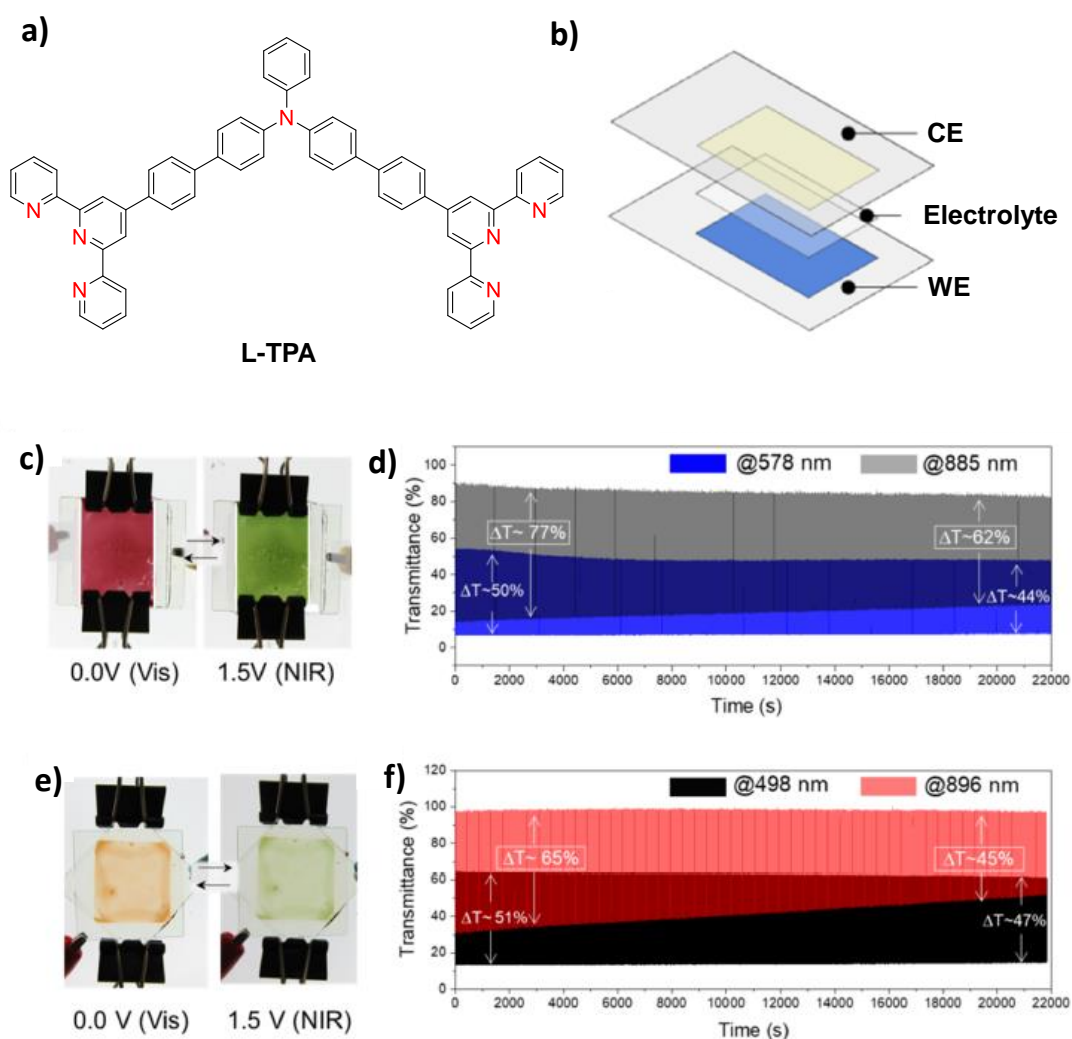


Figure 1.11: a) Chemical structure of the ligand **L-TPA**. b) A schematic representation of electrochromic device architecture fabricated from **L-TPA-Fe** or **L-TPA-Ru** layers and the corresponding photographs of the devices fabricated from c) **L-TPA-Fe** and e) **L-TPA-Ru** at 0 V (left) and 1.5 V (right). The corresponding transmittance changes at d) 578 nm (blue line) and at 885 nm (gray line) for **L-TPA-Fe** and f) at 498 nm (red line) and 896 nm (black line) for **L-TPA-Ru** at a pulse width of 2.5 s. Adapted with permission from ref 49.

Quad-color electrochromic switching has been reported using a metallocupramolecular polymer comprising of Os(II), Ru(II), and Fe(II) (**polyOsRuFe**) metal centers coordinated to terpyridines (**Figure 1.12a**). The metal ions were introduced via stepwise coordination of each metal ion to 2,2':6',2''-terpyridine (tpy) units. Spin-coated **polyOsRuFe** film exhibited a color change from magenta to brown to yellow and green depending on the oxidation of each metal center (**Figure 1.12b**). The **polyOsRuFe** based thin film on ITO/glass exhibited stable switching for more than 300 cycles under the application of a double-potential step (0 V and 1.2 V).⁵⁰

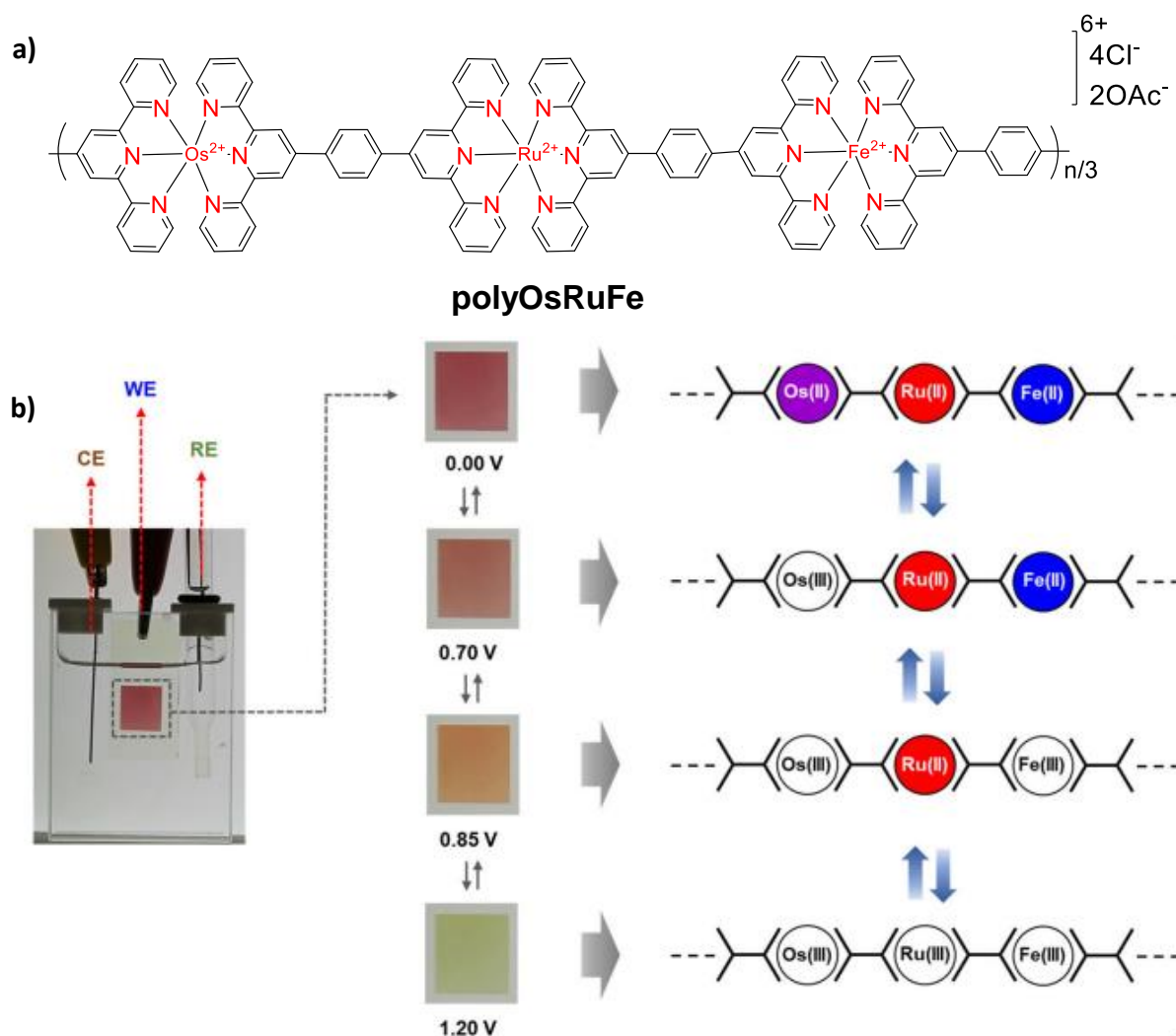


Figure 1.12: a) Chemical structure of the heterometallic polymer **polyOsRuFe**. B) Photographs of the films fabricated from **polyOsRuFe** at different applied potentials. The corresponding changes in oxidation states of the metal ions are also shown. Adapted with permission from ref 50.

Liu *et al.* have fabricated an electrochromic film via the oxidative electropolymerization of a Pt(II) complexed terpyridine appended with triphenylamine (**HL**, **Figure 1.13a**). Upon

application of 1.4 V, the polymer film exhibited a color change from orange to greenish-black characterized by a decrease in its MLCT band concomitant with the formation of a new band at 820 nm (**Figure 1.13b**).⁵¹ The NIR absorption was found to be due to the complete oxidation of triphenylamine moieties resulting in the formation of the corresponding dication. High coloration efficiency (363.3 cm²/C) and optical contrast (>88% at 820 nm) were observed for the electrochromic films (**Figure 1.13c,d**). Switching the potentials between 0 V and 1.4 V at a pulse width of 20 s revealed moderate stability up to 45 cycles with a $\Delta\%T$ of 86%.

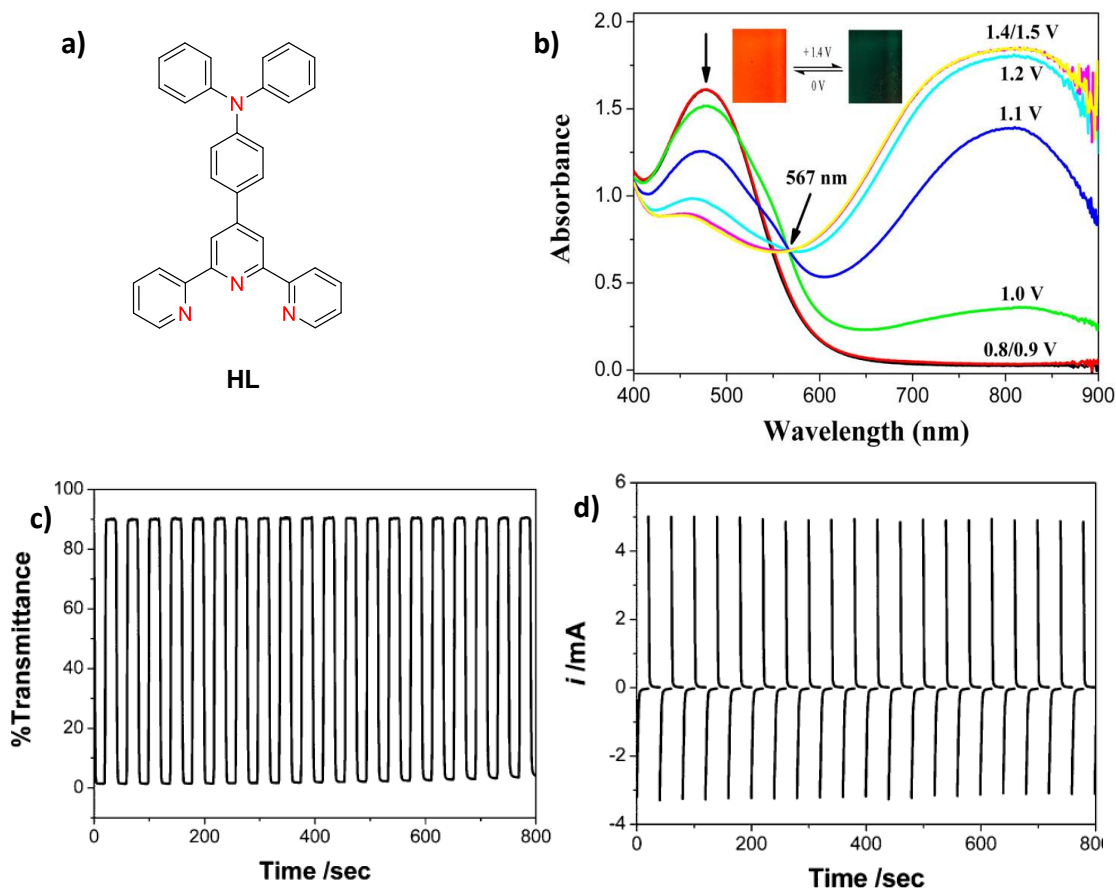


Figure 1.13: a) Chemical structure of the terpyridine ligand **HL**. b) Spectroelectrochemical profiles of the thin films fabricated from Pt(II) complexed **HL** upon applying potentials in the range 0 V and 1.4 V. Changes in c) transmittance at 820 nm and d) current under double-potential steps of 0 V and 1.4 V at a pulse width of the 20 s. Adapted with permission from ref 51.

1.9. Bipyridine-based Metal-Organic Materials for Electrochromic Applications

2,2'-Bipyridine (2,2'-bipy) is a bidentate chelating ligand that forms complexes with most transition metal ions such as Fe(II), Co(II), Mn(II), Ru(II), and so forth.⁴¹ The versatile nature of the bipyridine ligand, including high coordinating ability, color tunability by changing the

metal or ligand structure, and easy synthesis make it a good candidate for metal-organic materials based electrochromic systems. Selected examples of metal-bipyridine systems for electrochromic applications are discussed in this section.

van der Boom and co-workers have demonstrated the formation of electrochromic coordination-based molecular assemblies using alternative dip coating of metal polypyridyl complexes (**Bipy(1-4)-Fe**, **Figure 1.14a,b**) and a Pd(II) salt on ITO coated glass substrates. These coatings exhibited high coloration efficiencies ($1488 \text{ cm}^2 \text{ C}^{-1}$) and switching stability (3×10^4 cycles, **Figure 1.14c,d**).⁵²

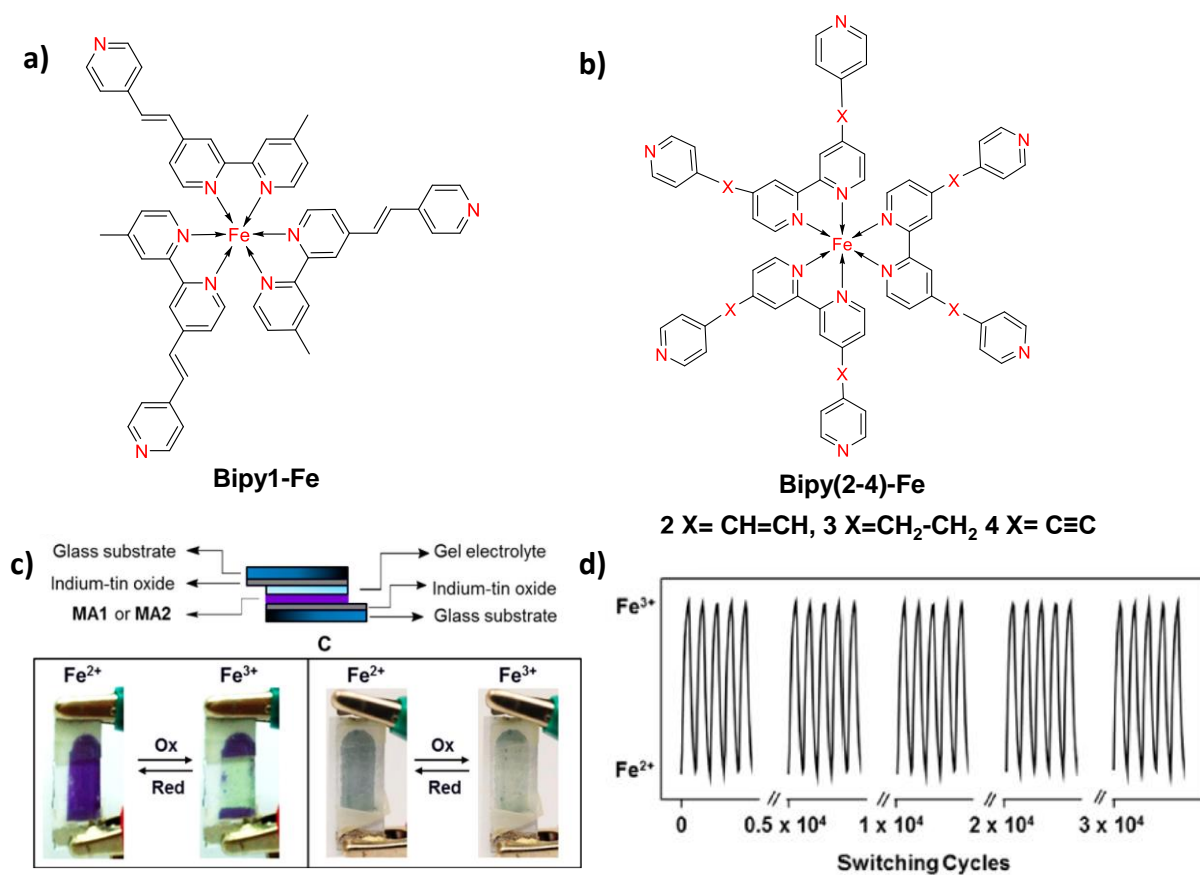


Figure 1.14: (a-b) Chemical structure of the metal-bipyridine complexes **Bipy(1-4)-Fe**. c) Schematic representation of the electrochromic device architecture (top) and the photographs showing the color changes in device fabricated using **Bipy1-Fe** and **Bipy2-Fe** (bottom), -3.0 V- +3.0 V, 5 s pulse width). d) Spectroelectrochemical switching of **Bipy2-Fe** in a potential window of 0.55 V – 1.45 V at a 1 s pulse width, showing stable electrochromic switching. Adapted with permission from ref 52.

Later, the formation of metal organic assemblies was demonstrated by iterative spin-coating of dilute solutions of the polypyridyl complexes and the Pd(II) salt ($\text{Pd}(\text{PhCN})_2\text{Cl}_2$) onto a

transparent conductive oxide surface. Using three different metal ions (Fe, Ru, Os), a large area of RGB color space was shown to be covered and was also extended to flexible substrates. The ECDs fabricated using the spin coated films showed an optical contrast of 40-50% and switching stability up to 1500 cycles.^{52a} The fabrication technique was further extended to stepwise spray coating of the components and the use of a metal grid on PET resulted in a decrease in the potential window, whereas the additional ion storage layer was found to augment the switching stability (1500 cycles).^{52a}

Solid polymer electrolytes (SPE), though very promising for electrochromic applications, have several challenges associated with switching times and redox stability. In this regard, an ECD based on similar metal-organic coatings using an ultraviolet cross-linked polymer as a solid-state electrolyte has been reported. The solid electrolyte comprised of acetonitrile, propylene carbonate, poly(methyl methacrylate), lithium perchlorate, 1,6-hexanediol-diacrylate, and Omnirad-184 (photoinitiator). Three metal-bipyridine-based molecular assemblies were used for fabricating the ECDs (**Bipy1-Os**: red, **Bipy2-Fe**: grey, and **Bipy 1.2**: Bordeaux red, **Figure 1.15a-d**).

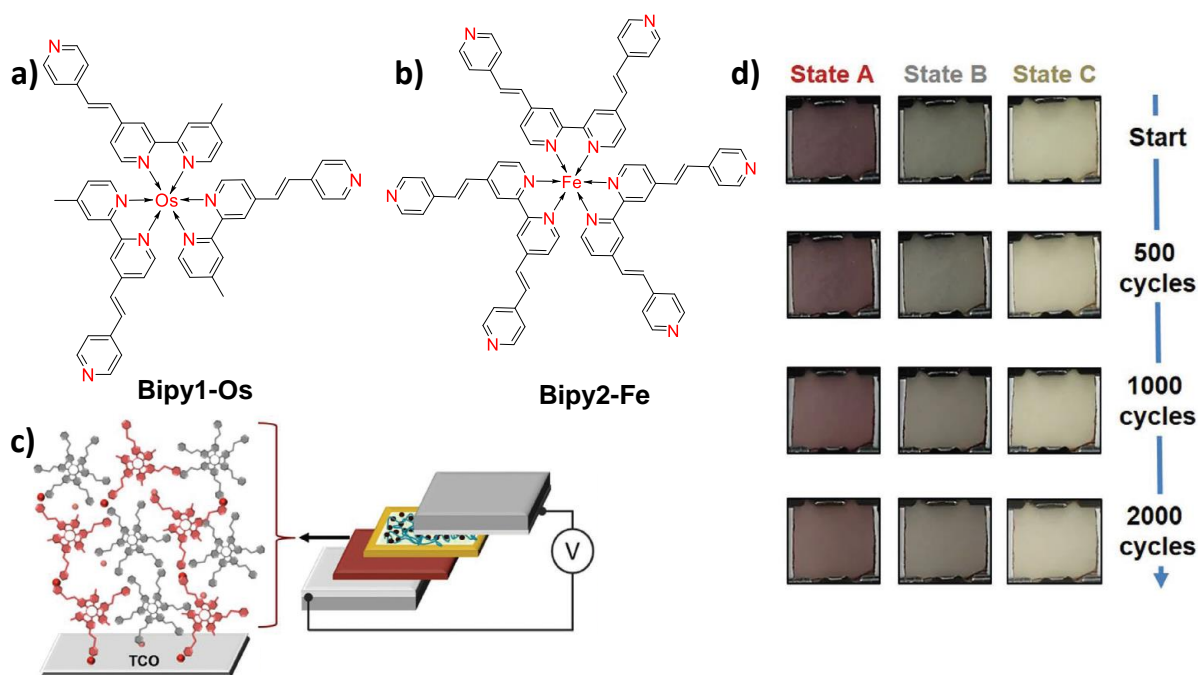


Figure 1.15: a-b) Chemical structure of the metal bipyridine complexes (**Bipy1-Os** and **Bipy2-Fe**). c) Schematic representation of electrochromic device fabricated from a combination of **Bipy1-Os** and **Bipy2-Fe**. d) Photographs showing the three colored states of **Bipy 1.2** upon applying 2 V, -2 V, and 2.8 V after 500, 1000, and 2000 cycles. Adapted with permission from ref 53.

Surprisingly, **Bipy1-Os** was found to be stable up to 4500 redox cycles with a typically low switching time ($t_{\text{bleach}} = 0.6$ s, $t_{\text{color}} = 0.4$ s).⁵³ Heating of the devices (100 °C) for 24 h in air did not have any effect on device performance. The bimolecular assemblies **Bipy 1.2** showed multicolor electrochromism (Bordeaux red, light gray, and off-white) with a switching time of 2.8 s and stability up to 2000 cycles.

Low operational voltage is a prerequisite to increase the lifetime of ECDs since the application of larger potential windows has been shown to degrade the conducting electrodes. In this regard, Higuchi *et al.* have synthesized an electron-rich tetrakis(*N*-methylbenzimidazolyl)bipyridine (**L-bip**, **Figure 1.16a**) ligand and the electrochromic device fabricated using Ru(II) coordinated **L-bip** exhibited a color change from violet to light greenish yellow in a potential window of 0 V – 0.6 V (**Figure 1.16b**).⁵⁴ The device was found to have excellent cycling stability exceeding 20000 cycles with an optical contrast of 54% and a coloration efficiency of 571 cm²/C (**Figure 1.16c,d**).

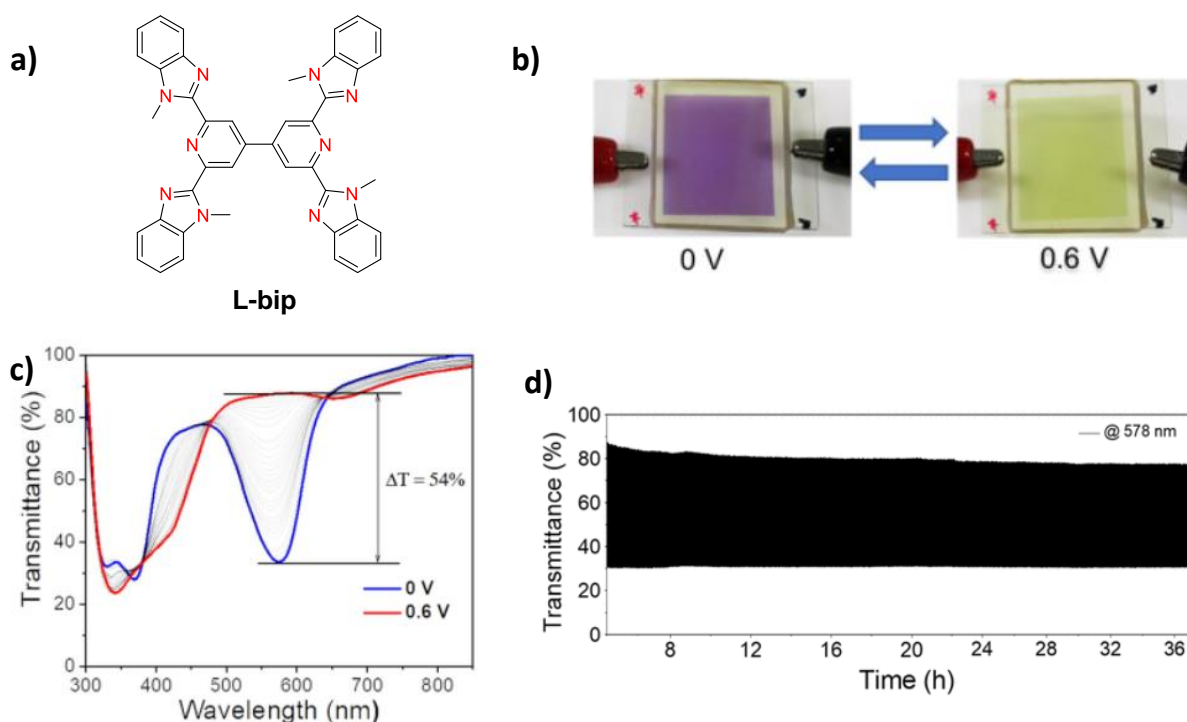


Figure 1.16: a) Chemical structure of the bipyridine ligand **L-bip**. b) Photographs showing the color changes in the ECD fabricated from Ru(II) coordinated **L-bip** upon applying 0 V (left) and 0.6 V (purple), and c) the corresponding transmittance changes at 578 nm. d) Stability data for the device (>20000 cycles) at a pulse width of 3 s. Adapted with permission from ref 54.

1.10. Metal-Organic Systems based on other Acceptor-type Ligands for Electrochromic Applications

Apart from terpyridine and bipyridine based ligands, several other nitrogen and oxygen-based acceptor-type ligands such as phenanthroline, porphyrin, phthalocyanines, salen, etc. have been explored for electrochromic applications. Phenanthroline is a bidentate ligand similar to 2,2'-bipyridine with two nitrogen donors, and can coordinate with different metal ions. Higuchi and co-workers have synthesized a dual-branched hexagonal coordination nanosheet using a phenanthroline ligand (**L-3Phn**, **Figure 1.17a**) coordinated to Fe(II) using liquid-liquid interfacial synthesis.⁵⁵ Using the Langmuir-Blodgett (LB) method, the thickness of the monolayer was estimated to be 2.5 nm. The polymeric film showed a color change from red to colorless with a contrast ratio of 56% and 3.3 s bleaching and 2.9 s coloration times (**Figure 1.17b**). The electrochromic device fabricated using the coordination nanosheet exhibited high durability exceeding 15000 cycles with an optical contrast of 57% (**Figure 1.17c**).

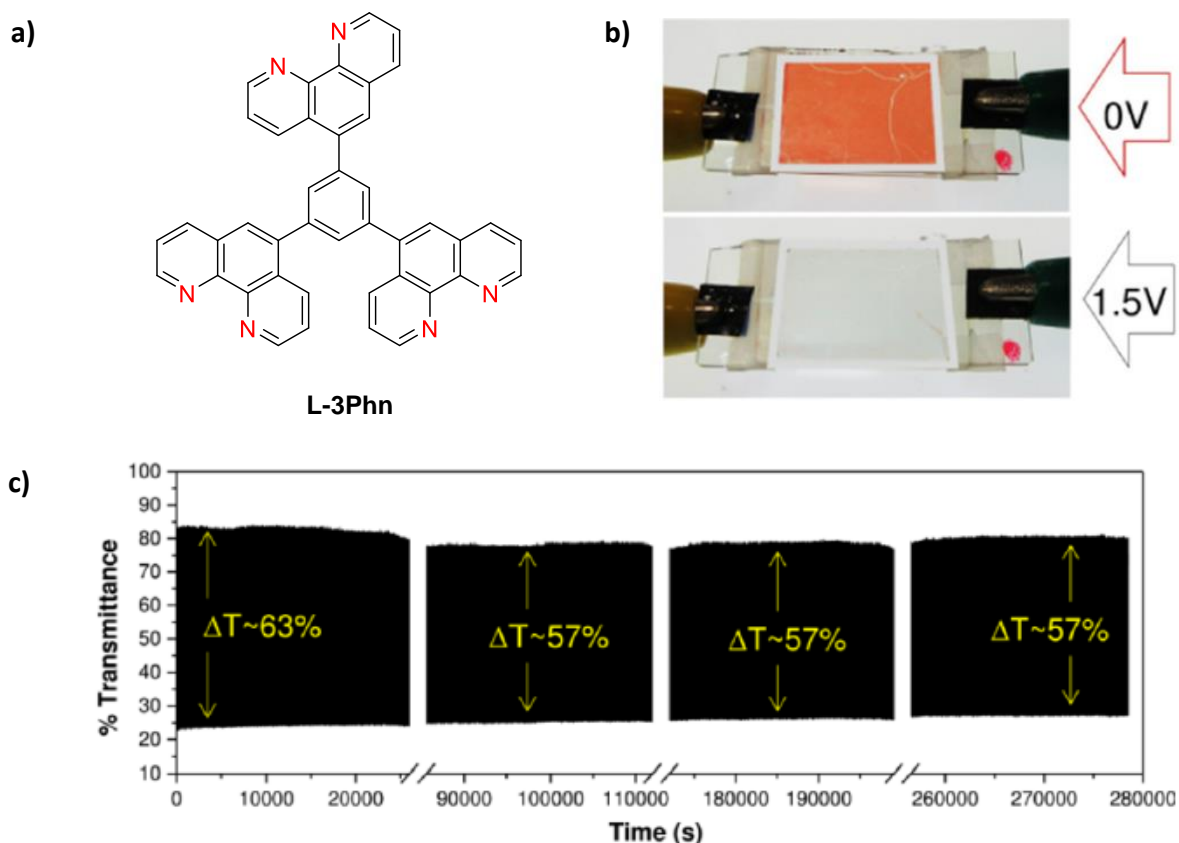


Figure 1.17: a) Structure of an Fe(II) coordinating ligand **L-3Phn** and Fe(II). b) Reversible color change in the electrochromic device fabricated from **L-3Phn** - (Fe(II)) nanosheets upon application of 0 V (top) and 1.5 V (bottom). c) Cycling stability of the device at a pulse width of 15 s for 15000 switchings. Adapted with permission from ref 55.

Salen is a tetradentate ligand that can coordinate metals and stabilize them in various oxidation states and are used for electrochromic applications. Freire *et al.* have fabricated two thin films using poly [Ni(salen)] metal complexes featuring the absence/presence of methyl substituents in the imine bridge (**Poly 1** and **Poly 2**, respectively, (**Figure 1.18a,b**)).⁵⁶

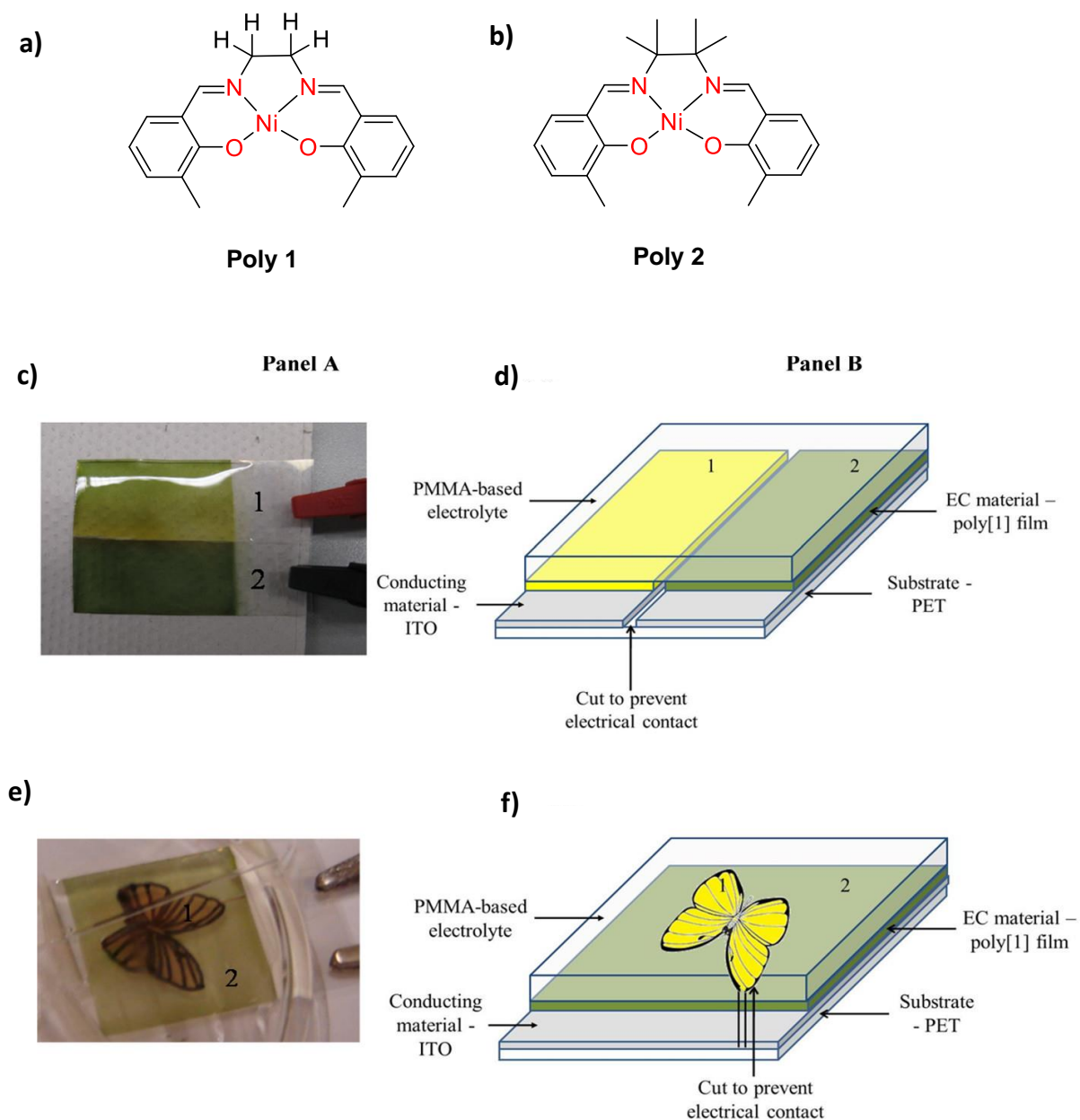


Figure 1.18: a-b) Chemical structure of the Salen-based ligands **Poly 1** and **Poly 2**. Photographs showing the color changes in the ECDs fabricated from **Poly 1**, c) with topology 1 and e) topology 2. d) and f) The corresponding schematic representation of the ECDs of topology 1 and topology 2, respectively. Adapted with permission from ref 56.

While **Poly 1** based film showed a color change between yellow and green states with stability up to 9000 redox cycles and coloration efficiency of $75.55 \text{ cm}^2\text{C}^{-1}$ with an optical contrast of

58.5%, the one fabricated from **Poly 2** exhibited a color change from green to russet with the same optical contrast (58.5%) and moderate stability. Devices with different shapes were also fabricated from **Poly 1**; the device with a simple shape (topology 1) showed high optical contrast of 88.7% and redox durability of 3000 cycles; however the butterfly shape (typology 2) was found to be stable up to 1250 cycles with a charge loss of 58.9% (**Figure 1.18c,d**).

Subsequently the same research group developed polymeric nanocomposites containing a [Ni(salen)] complex and TiO₂ nanoparticles that showed enhanced electrochemical activity when compared to bare poly[Ni(salen)] based system. This observations was found to be due to the presence of large electroactive surface coverages in the polymeric nanocomposites.⁵⁷ The film exhibited a color change from yellow to green and was found to switch for 10000 redox cycles with a charge loss of only 7.3%, that was comparably lower than that for the bare film (13.7%) with an improvement of 16.7% in optical contrast.

Phthalocyanines are tetra-azatetra benzo derivatives of porphyrins in which a coordinating metal atom either lies at the center of the ligand or between the two rings of the phthalocyanine in a sandwich-type complex. Phthalocyanines are macrocyclic compounds in which modification of the substituents attached to the peripheral ring and coordinating metal atoms result in the tuning of absorption and emission properties. These ligands show high chemical and thermal stabilities, and a reversible redox chemistry, and can be used for electrochromic applications. The phthalocyanines coordinate with metals like Fe(II), Zn(II), Cu(II), and Ni(II) to form peripherally tetra-substituted polymer complexes (**PCs**),⁵⁸ that electropolymerize on the working electrode during oxidation. Thus, the **PCs** were coated over ITO-glass using electropolymerization and were found to change its color from green to blue with a switching time of 12 s.⁵⁹ The films of metallophthalocyanines containing Ni, Cu, and those without any metal (**MPCs**; M = 2H⁺ (**H₂PC**); Ni²⁺ (**NiPC**) and Cu²⁺ (**CuPC**)) were also fabricated by electropolymerization of the amino substituents. **H₂PC** film exhibited a color change from cyan to light yellow with an optical contrast of 40% and low stability after repetitive CV cycles.⁶⁰ **NiPC** and **CuPC** films showed a color change from cyan to red with a low optical contrast of 20% but higher stability compared to phthalocyanines without metal ions (**H₂PC**).

Park *et al.* have reported the electrochromic properties of a terpyridine appended iron phthalocyanine (**FePC-Tp**) in their film and device states (**Figure 1.19a-c**). The film was found to absorb in a broad range of visible and near-infrared regions and exhibited a color change from dark blue to transparent green upon application of a potential window of 0 V – 1.2 V.⁶¹

Switching stability up to 1000 cycles with coloration efficiencies of $211.4 \text{ cm}^2 \text{ C}^{-1}$ and $346.7 \text{ cm}^2 \text{ C}^{-1}$ were observed for the film and device states, respectively (**Figure 1.19d**).

Sener and co-workers have incorporated EDOT in Zn(II) metallophthalocyanines and investigated the electrochromic properties of the electropolymerized films. A color change from greenish-yellow to dark blue was observed with an optical contrast of 44% and fast switching time of 2.5 s. The electropolymerized copolymer was further capable of sensing the presence of glucose as well. In yet another report, Zhang *et al.* have demonstrated the electrochromic properties of a copper phthalocyanine-PANI composite film that exhibited better EC properties when compared to the bare PANI film. The introduction of copper phthalocyanine nanostructures was found to improve the diffusion of the counter anion within the film, leading to a concomitant increase in the contact area for better charge transfer. The **CuPc-PANI** composite film showed switching stability up to 500 redox cycles and an optical contrast of 58%.⁵⁹

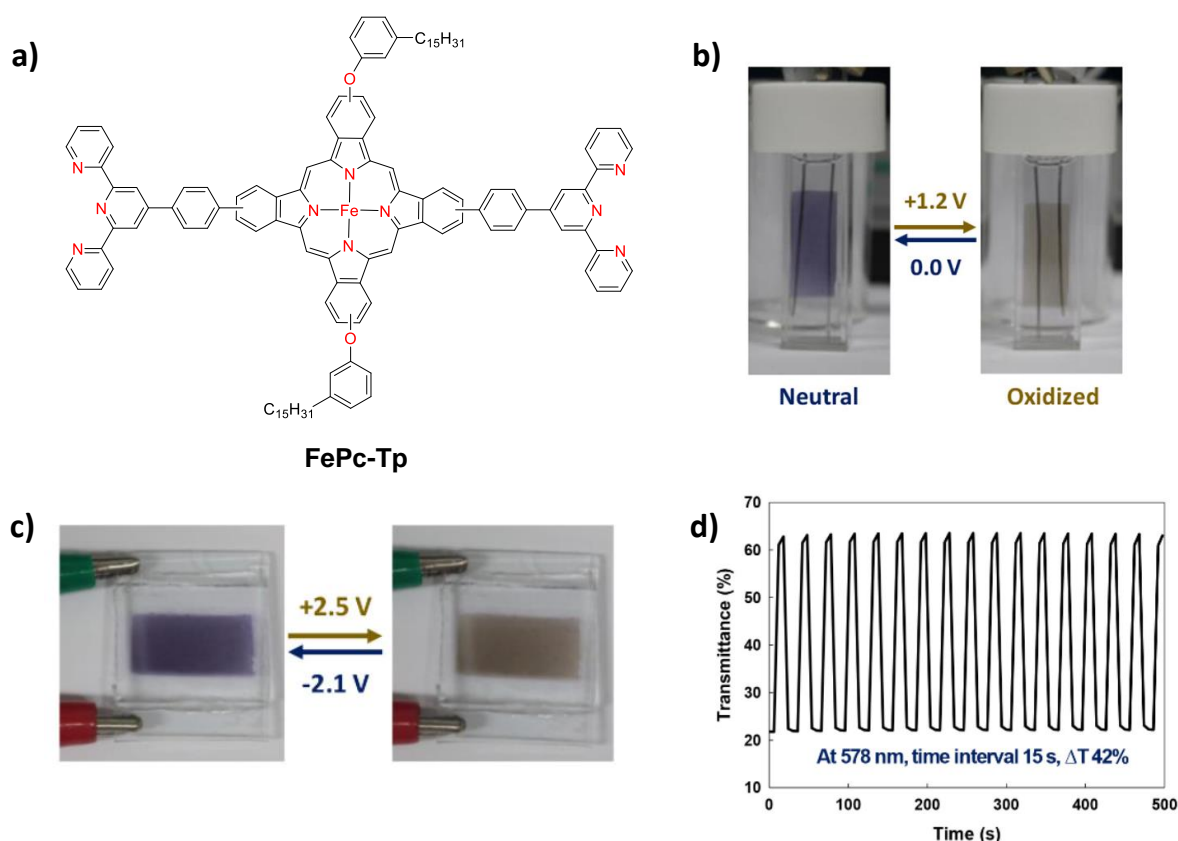


Figure 1.19: a) Chemical structure of the terpyridine appended Fe-phthalocyanine **FePc-Tp**. Photographs showing the color change in b) the film state of **FePc-Tp** ITO/glass and c) the device state. D) Cycling stability of the ECD (578 nm) upon applying 2.5 V and -2.1 V at a pulse width of 15 s. Adapted with permission from ref 61.

Porphyrins belong to yet another family of ligands comprising a tetrapyrrole porphine (**TPP**, **Figure 1.20a**) nucleus with substituents at four meso positions and eight β positions of the pyrroles and are highly colored naturally occurring pigments. The 18 π -electron porphyrin system and its metal complexes were found to be redox active under electrochemical conditions.⁶² The free porphyrin features a reddish-purple color due to the presence of the Sorret band emanating from the ring structure (**Figure 1.20b-d**). Upon oxidation, the color changed to green with a shift in the Sorret band from 418 to 440 nm, with a relatively strong absorption at 650 nm.⁶³ After reduction, the Sorret band was found to be red-shifted and a yellow color was observed. Electrochemical investigations using Ag(II), Fe(III), and Mn(III) complexes indicated that metal centered redox processes led to the observed color changes. Porphycene is a constitutional isomer of porphyrin and Hisaeda *et al.* have fabricated films of Ru(III)-porphycene by oxidative electropolymerization that showed a blue to olive green EC switching. The color change was found to be reversible and stable up to 5×10^3 cycles with a coloration efficiency of $178 \text{ cm}^2 \text{ C}^{-1}$ at 609 nm.⁶⁴

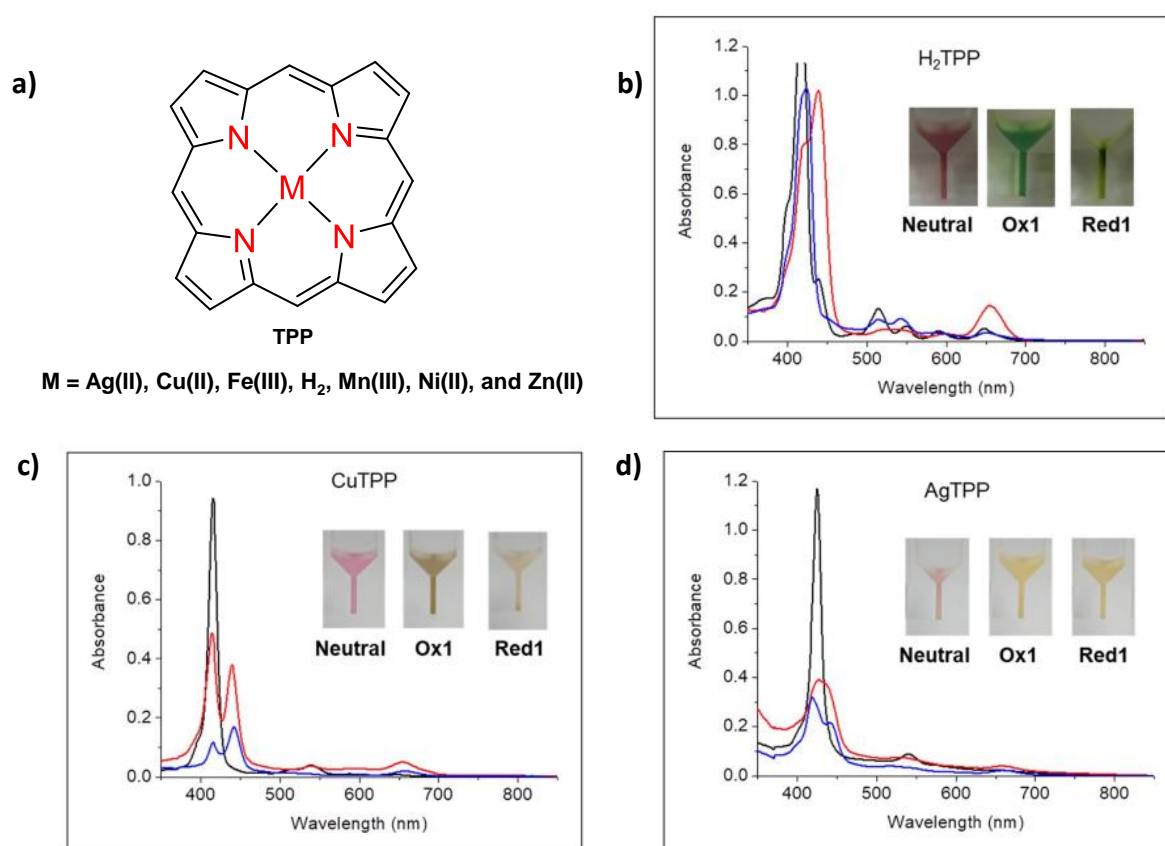


Figure 1.20: a) Chemical structure of the porphyrin ligand **TPP**. Absorbance changes at neutral (black), oxidized (red), and reduced (blue) states of b) **H₂TPP**, c) **CuTPP**, and d) **AgTPP**. Adapted with permission from ref 62.

Higuchi and co-workers have fabricated an electrochromic device using a Cu(I)-based metallo-supramolecular polymer having dibenzoeilatin as ligand (**Ldb**, **Figure 1.21a**), that showed a green to black electrochromism. The device was found to be stable up to 500 redox cycles with a low switching time of 1.35 s for bleaching and 1.04 s for coloration (**Figure 1.21b-d**).⁶⁵

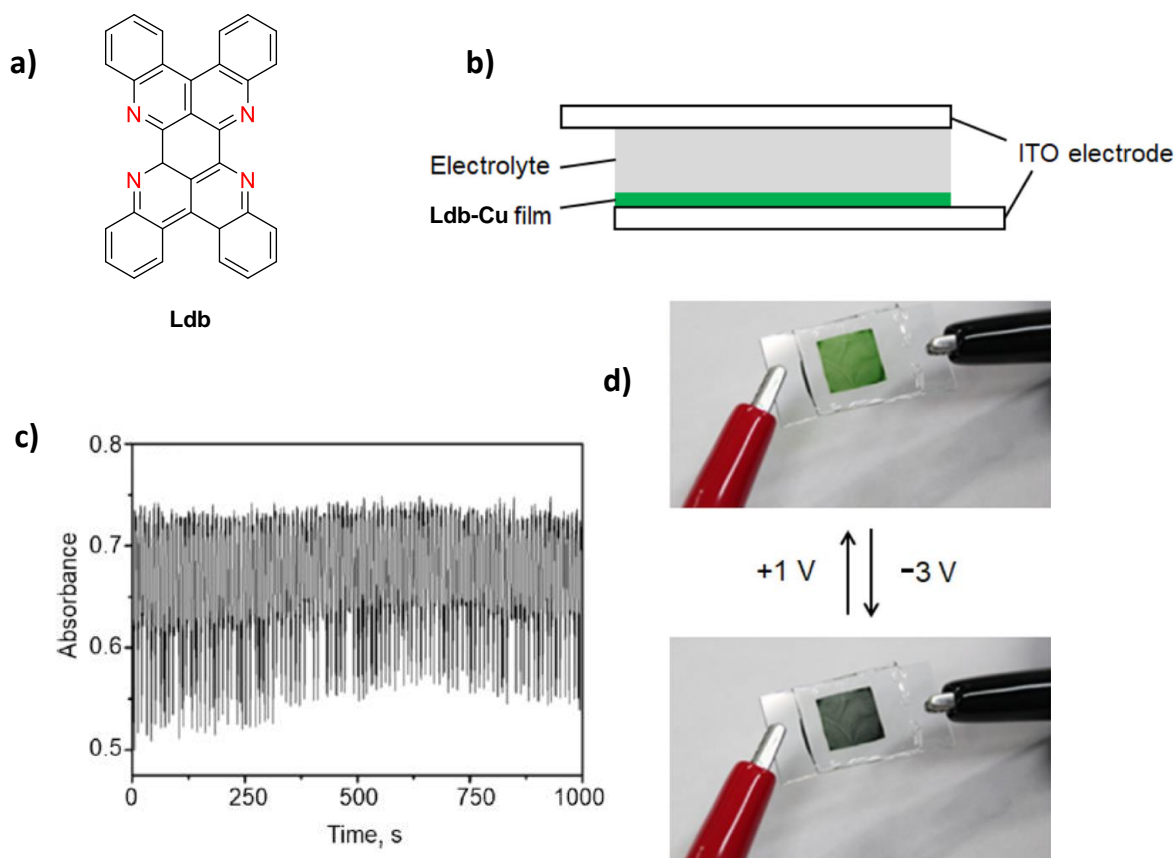


Figure 1.21: a) Chemical structure of the dibenzoeilatin ligand **Ldb**. B) Schematic representation of the ECDs fabricated from **Ldb-Cu** polymeric films and c) the corresponding changes in absorbance upon applying -3 V and 1 V at a pulse width of 5 s. d) Photographs showing the color changes in the device using the same potential window. Adapted with permission from ref 65.

Dioximes are chelating ligands that coordinate transition metal ions through hydroxyl and azomethine groups to form square-planar, square-pyramidal and octahedral complexes. A macrocyclic Co(II) complex of dioxime based ligand has been reported to exhibit metal-centered electrochromism with a color switching from a bleached state to a green state. The film was found to be stable up to 100 redox cycles with a maximum optical contrast of 86.8%.⁶⁶

Lee *et al.* have synthesized a 1D-conjugated coordination polymer containing 1,2,4,5-benzenetetramine (**BTA**, **Figure 1.22a**) as ligand and Ni as a metal center. **Ni-BTA** films were

fabricated using a chemical bath deposition method and exhibited an optical contrast of 61.3% and stability up to 10000 electrochemical cycles (**Figure 1.22b,c**). A color change from blue to transparent to brown with a coloration efficiency of $223.6 \text{ cm}^2 \text{ C}^{-1}$ was observed for these thin films (**Figure 1.22**).⁶⁷

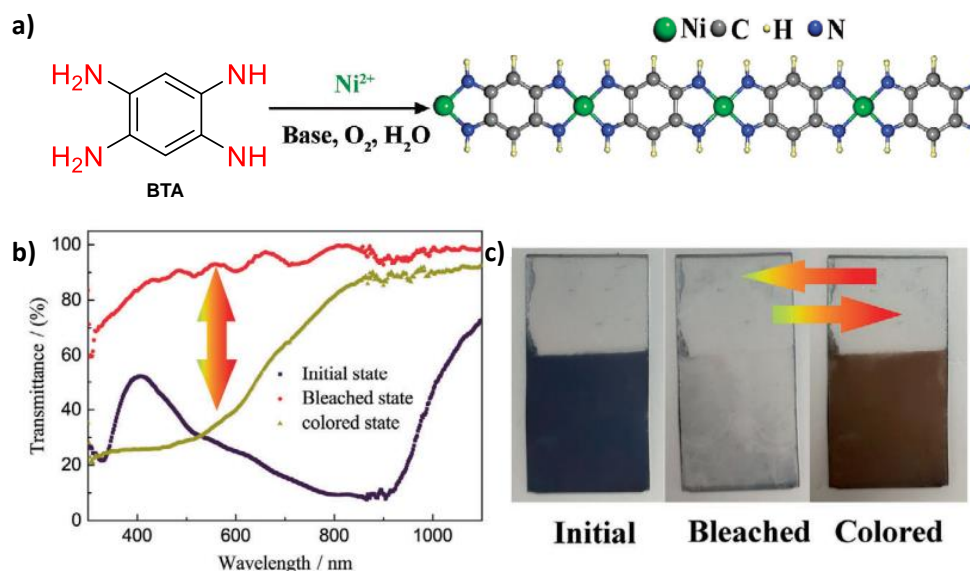


Figure 1.22: a) Chemical structure of the benzenetetramine ligand **BTA** and a schematic representation of the synthetic scheme of **Ni-BTA**. b) Transmittance changes observed for **Ni-BTA** films upon application of 0 V and 0.6 V, and c) the corresponding photographs of the film at initial (blue), bleached and colored states. Adapted with permission from ref 67.

1.11. Multifunctional Applications of Electrochromic Materials

Electrochromic materials are capable of changing their color during an electrochemical redox process along with ion insertion. Integration of other functions with electrochromism has attracted tremendous interest over the past few years due to diverse multifunctional applications of such smart systems. In this context, multifunctional EC materials find application in smart windows, energy storage, sensors, etc. and are described in the forthcoming sections.

1.11.1 Electrochromic Sensors

Exposure of electrochromic materials to certain gases, vapors, and other analytes has been shown to result in a change in its electronic structure and optical spectra, which in turn is accompanied by a change in conductivity. This property of EC materials is promising towards an alternative for conventional sensors. Electrochromic sensors provide an optical readout that depends on the potential applied to the working electrode. Electrochromic materials including transition metal oxides, conjugated conducting polymers, Prussian blue, and viologens are used

for sensing applications. A few examples of electrochromic sensors are discussed in this section.

Prussian blue (**PB**) or ferric hexacyanoferrate is often used to evaluate urea concentration by monitoring the accompanying changes in **PB** absorption. Determination of urea is crucial in food, clinical and environmental analysis since high concentration of urea is considered to be harmful to children and pregnant women and causes health disorders such as intestinal bleeding or dehydration.⁶⁸ An electrochromic transition between **PB** and its reduced form Prussian white (**PW**) is readily achieved by changing the electric potential applied to **PB** or **PW** layer. This potential depends on the concentration of ions (namely NH_4^+ , K^+ , Cs^+ , and Rb^+), that promotes **PB** conversion into **PW**. The concentration of NH_4^+ can be determined from the changes in the absorption spectrum of **PB**. In this regard, Ramanavicius *et al.* have fabricated a glass/ITO/**PB**-urease biosensor that exhibited the highest sensitivity towards urea (7-30 mM) and the biosensor response was more than 50% during a period of 41 days.⁶⁹

Electrodeposited **PB** film and magnesium (Mg) was used as cathode and anode electrodes for constructing a fast-charging/recharging battery with high power-density for visual detection of reactive oxygen species (ROS) with high sensitivity. Proteins, nucleic acids, and lipids can be directly oxidized by strong ROS including $\cdot\text{OH}$, ClO^- , ONOO^- , etc. NaClO was used to monitor the concentration of ROS in real time.⁷⁰ **PW** was re-oxidized to be **PB** in the presence of NaClO with a low detection limit of 0.22 μM , thereby making the device a versatile ROS sensor (**Figure 1.23**).

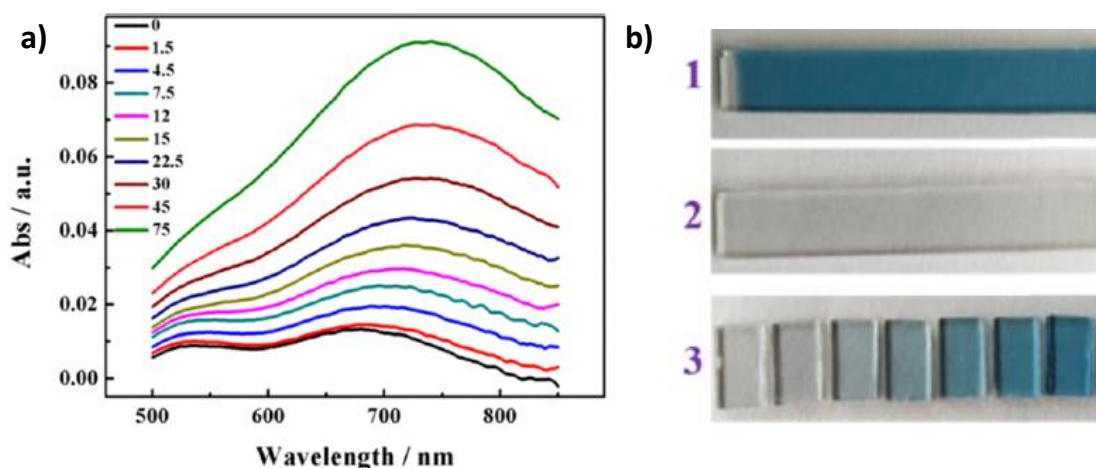


Figure 1.23: a) Changes in absorbance of **PW** with the addition of different concentrations of NaClO (0 – 75 μM). b) Photographs showing the color of (1) **PB**, (2) **PB** converted into colorless **PW**, and (3) **PW** converted back to **PB** with different amounts of NaClO (1.5 - 5.6 mM). Adapted with permission from ref 70.

Shahrokhian *et al.* have developed a novel electrochromic sensor based on **PANI**-modified ITO electrodes for the visual and fast detection of *E.coli* in water samples. Applying a constant potential of 0.2 V to the working electrode led to an electrochromic color change from yellow to blue.⁷¹ *E.coli* was captured using specific antibodies on the **PANI**-coated ITO electrode and their presence on the electrode surface resulted in an enhanced electrical resistance (**Figure 1.24**). This increase in resistance dampened the electrochromic response of the film and with increasing *E.coli* concentration the larger resistance of film led to the retention of the initial yellow color.

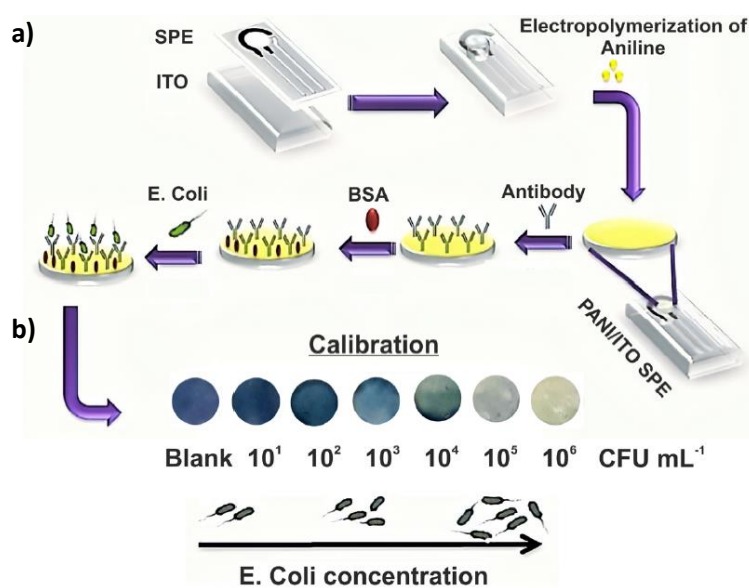


Figure 1.24: a) Schematic representation of fabrication of electrochromic sensor using **PANI**-modified ITO electrode. b) Color changes in the electrochromic sensor at different concentrations of *E. coli*. Adapted with permission from ref 71.

Biosensors are powerful analytical tools in food technology since they allow for simple, low-cost, and reliable determination of glucose. Toppare *et al.* have synthesized a D-A-D altering monomer comprising electropolymerized furan and thiazolothiazole units. A redox enzyme, glucose oxidase, was immobilized on the polymer surface for the detection of glucose. Glucose oxidase catalyzes the oxidation of β -glucose to D-glucono- δ -lactone that spontaneously hydrolyzes into gluconic acid and hydrogen peroxide. The limit of detection (LOD) and sensitivity values were found to be 12.8×10^{-3} mM and $65.44 \mu\text{A mM}^{-1} \text{cm}^{-2}$, respectively.⁷²

Polyazomethine has been reported as an electrochromic material and has the capability to sense ascorbic acid (vitamin C). The visible color of the electroactive polyazomethine thin film was found to change from light gray to green upon electrochemical oxidation.⁷³ The sensitivity was

found to be $24.2 \mu\text{A mM}^{-1}$ with an estimated detection limit of $7.1 \mu\text{M}$ at a signal-to-noise ratio of 3.

Molecularly imprinted polymers (MIPs) have been used as recognition elements in biomimetic sensors and recognition sites in the MIP lead to excellent sensitivity and selectivity. One such MIP sensing device was reported for the detection of chlorpyrifos using electrochromic iridium oxide. Chlorpyrifos is a pesticide extensively used in agriculture, households, and urban applications. The device exhibited a color change from blue-black to transparent upon oxidation. However, electrochemical oxidation was found to be hindered in the presence of chlorpyrifos, thereby limiting the electrochromic color changes (**Figure 1.25**).⁷⁴ Smartphone-based detection was further developed and an ultra-low detection limit of 0.1 pM was observed.

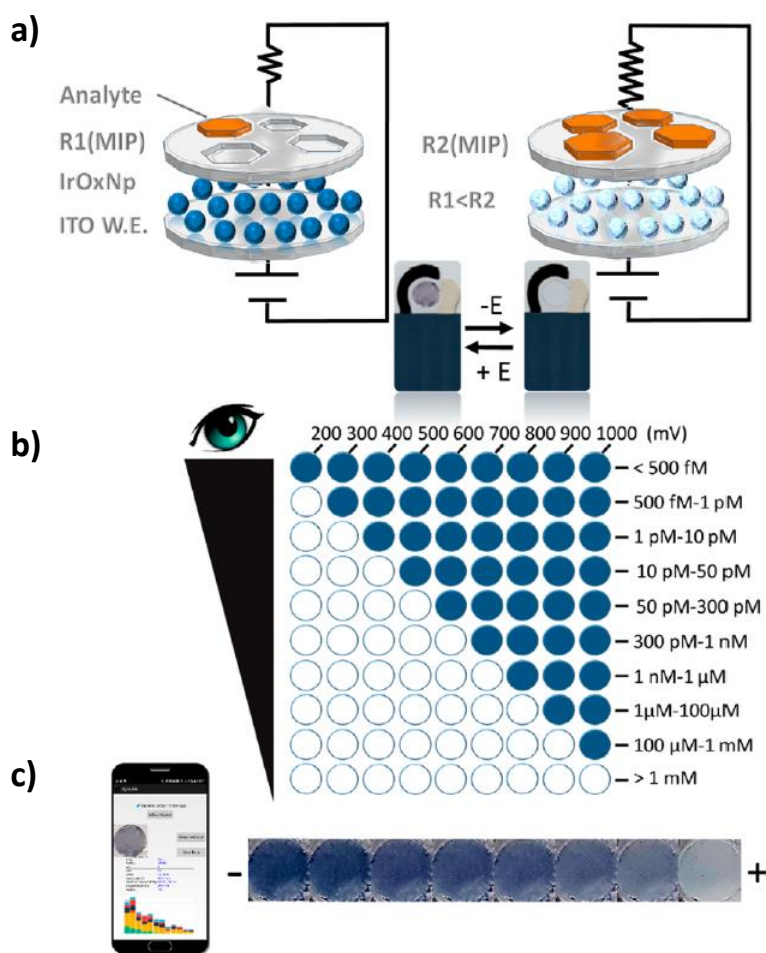


Figure 1.25: a) Schematic representation of the EC biosensor device based on iridium oxide MIP. b) Visual detection of chlorpyrifos upon application of voltage and the corresponding concentration range. c) Smartphone-based detection of chlorpyrifos. Adapted with permission from ref 74.

Jeong and co-workers have incorporated a strain sensor with an electrochromic device fabricated from thin films of polyaniline nanofibers and V_2O_5 that showed changes in color from yellow to dark blue upon the application of an electric voltage. The device was integrated into the skin via an Arduino circuit for monitoring color changes with variations in applied strain. The fabricated strain sensor exhibited high transparency (77%), and durability (10000 stretch/release cycles) with a fast response and good gauge factor (GF) of 5.2 up to 50% strain.⁷⁵ (Figure 1.26).

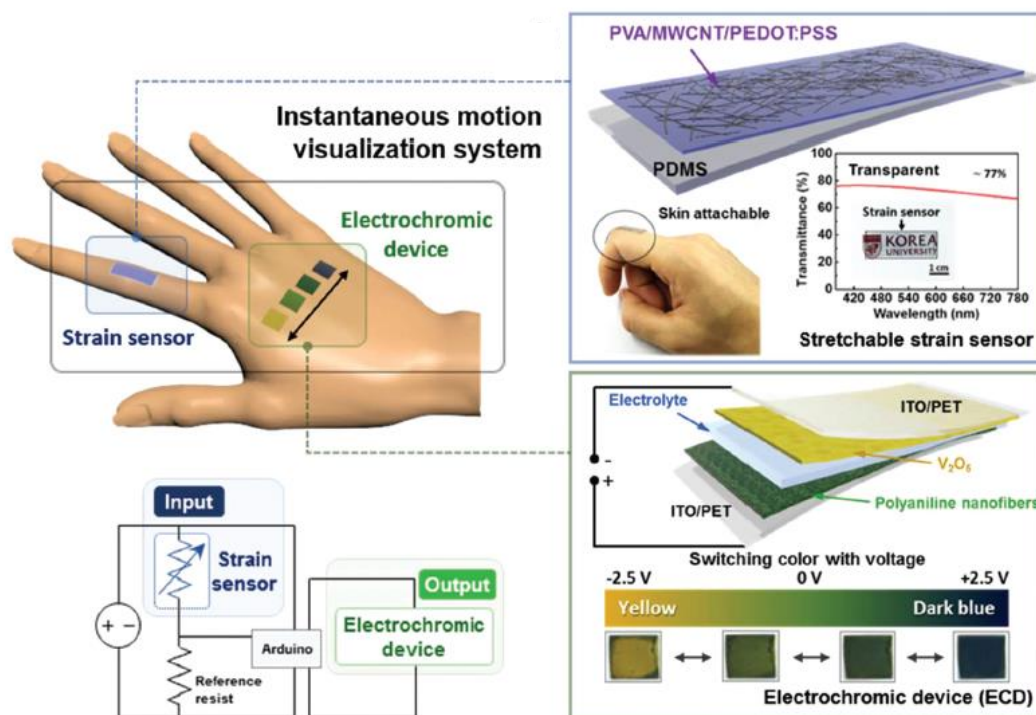


Figure 1.26: Schematic representation of strain sensor and electrochromic device on hand skin and the corresponding device response. Adapted with permission from ref 75.

Bohn *et al.* have developed a closed bipolar electrode (**CBE**)-based electrochromic device for sensing multiple metabolites such as lactate, glucose, and uric acid. The analytical cell comprised of a redox mediator (methyl viologen) combined with a specific oxidase (Eg: lactate oxidase, glucose oxidase, or uricase, **Figure 1.27a**). The extent of color change in the **CBE** electrode was found to directly correlate to the concentration of metabolites in the analytical cell.⁷⁶ Electrons generated in the cell were transported through the **CBE** to a reporter cell and subsequent reduction of methyl viologen (MV^{2+}) resulted in a colorless-to-purple transition at the reporter cell (**Figure 1.27b,c**). The color change was recorded by a smartphone for RGB analysis.

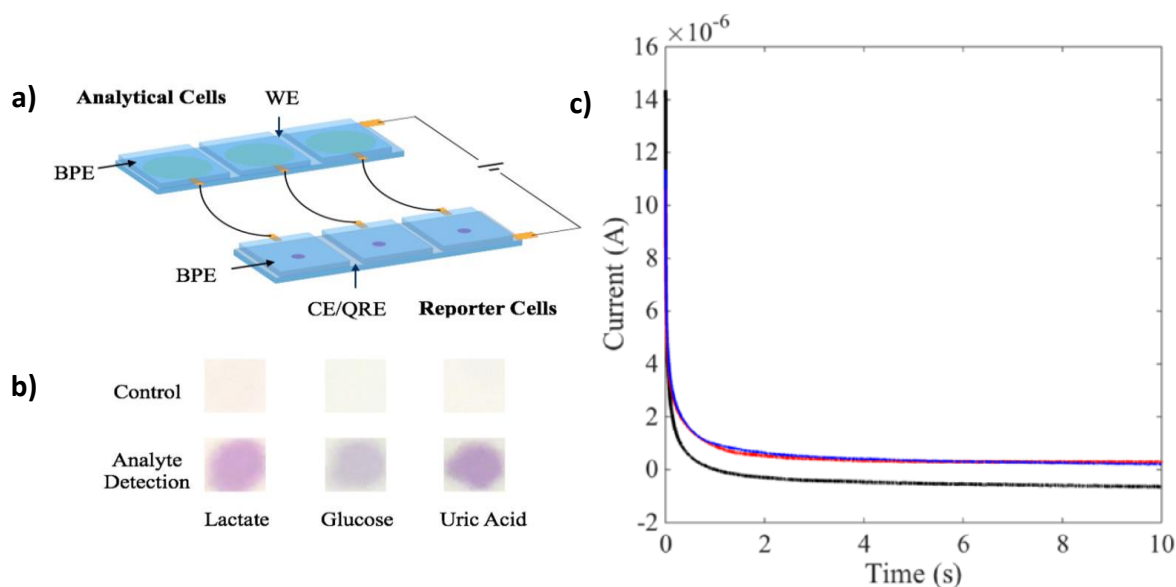


Figure 1.27: a) Schematic illustration of the closed bipolar electrode (CBE)-based electrochromic sensor. b) Color change in reporter cells upon detection of lactate, glucose, and uric acid each at a concentration of 2.5 mM. c) Chronoamperometric data obtained from glucose (black); lactate (red); and uric acid (blue). Adapted with permission from ref 76.

1.11.2 Electrochromic Batteries and Supercapacitors

Electrochemical energy storage devices, such as supercapacitors and batteries, have been extensively studied in recent years because of their huge potential in applications such as electronics, electric vehicles, aerial vehicles, electric tools, and machines. Electrochromic (EC) energy storage devices are highly desirable and have attracted research interests recently. A recent trend in the field of electrochemical energy storage is therefore, to combine energy storage and electrochromic functions in a single device. Recent literature on electrochromic batteries and supercapacitors are discussed in this section.

Elezzabi *et al.* have developed an electrochromic aqueous rechargeable battery using Ti-substituted tungsten molybdenum oxide (MTWO, **Figure 1.28a**). Zn^{2+} are used as intercalating ions because of their low redox potential, low cost, high gravimetric capacity, and safe operational benefits. The MTWO cathode exhibited a high optical contrast of 62% and an areal capacity of 260 mA h m^{-2} upon Zn^{2+} insertion.⁷⁷ The fabricated zinc ion electrochromic battery (ZIEB) prototype delivered a high open circuit potential of 1.2 V and cycling stability up to 100 cycles (**Figure 1.28b-d**). The same group has also synthesized colloidal V_3O_7 nanoparticles with a yellow oxidized state and a grayish-blue reduced state for electrochromic Zn-based battery displays. This Zn- V_3O_7 electrochromic battery display exhibited short switching times and an optical contrast of 21% at 632.8 nm with an open circuit potential (OCP) of 1.38 V.⁷⁸

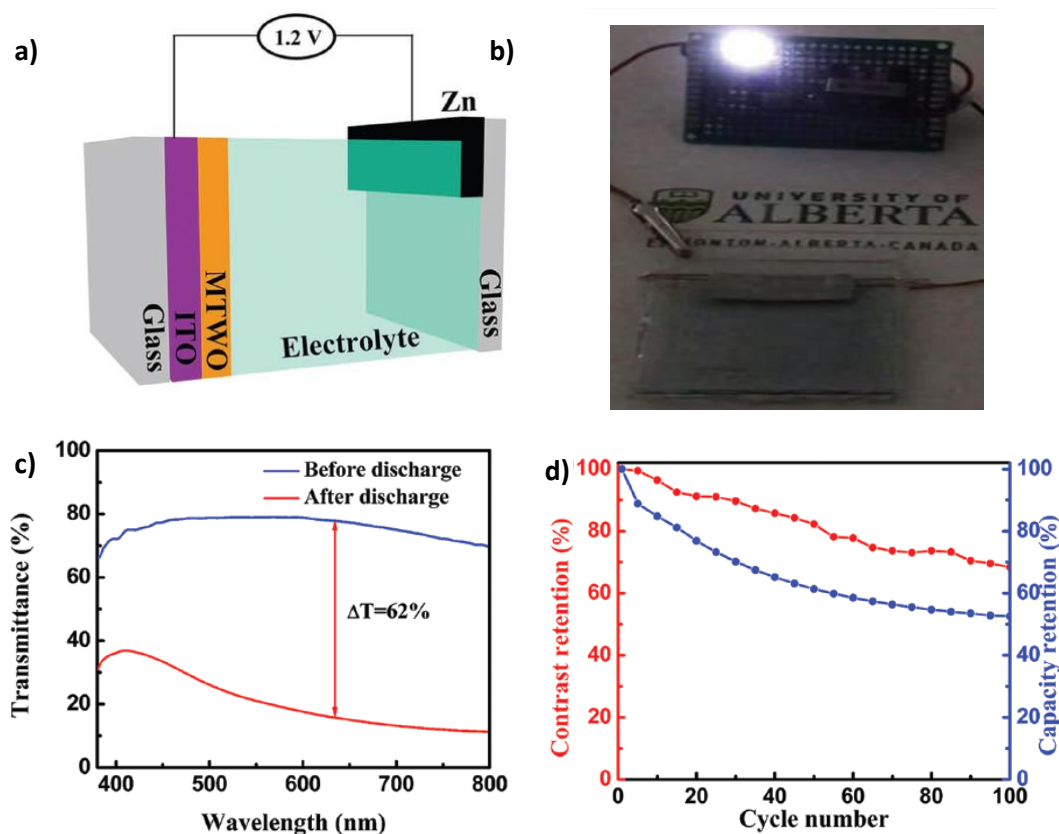


Figure 1.28: a) Schematic representation of the zinc ion electrochromic battery (ZIEB) prototype. b) Digital images of an LED (0.5 V) powered by the ZIEB with 1.23 V open circuit potential. c) Changes in %T before and after discharging. d) Cycling stability of ZIEB prototype. Adapted with permission from ref 77.

A flexible electrochromic battery (ECB) consisting of PET/ITO as substrate, WO_3 film as cathode, Al sheet as anode, and absorptive glass mat (AGM) as a separator, and aluminum trichloride (AlCl_3) as electrolyte was reported by Zhu and co-workers (**Figure 1.29a**).⁷⁹ The electrochromic battery exhibited a color change between white (bleached state) and dark blue (colored state) with a high specific capacity of 142 mA h g^{-1} (**Figure 1.29b,c**). Moreover, the ECB retained $>92\%$ of its capacity after 40 bending cycles with bending angles of $0\text{--}80^\circ$.

Wang *et al.* have developed a polypyrrole-based bi-functional electrochemical device that exhibited electrochromism and self-rechargeable battery characteristics. A color change from black to yellow with an optical contrast of 59% (698.5 nm) was observed for the ECD. The battery characteristics included a capacity of $75.25 \text{ mA h g}^{-1}$ at a constant current density of 1.0 A g^{-1} and an open-circuit voltage of 0.94 V. The capacity of the device was found to be proportional to electrochromic color changes.⁸⁰

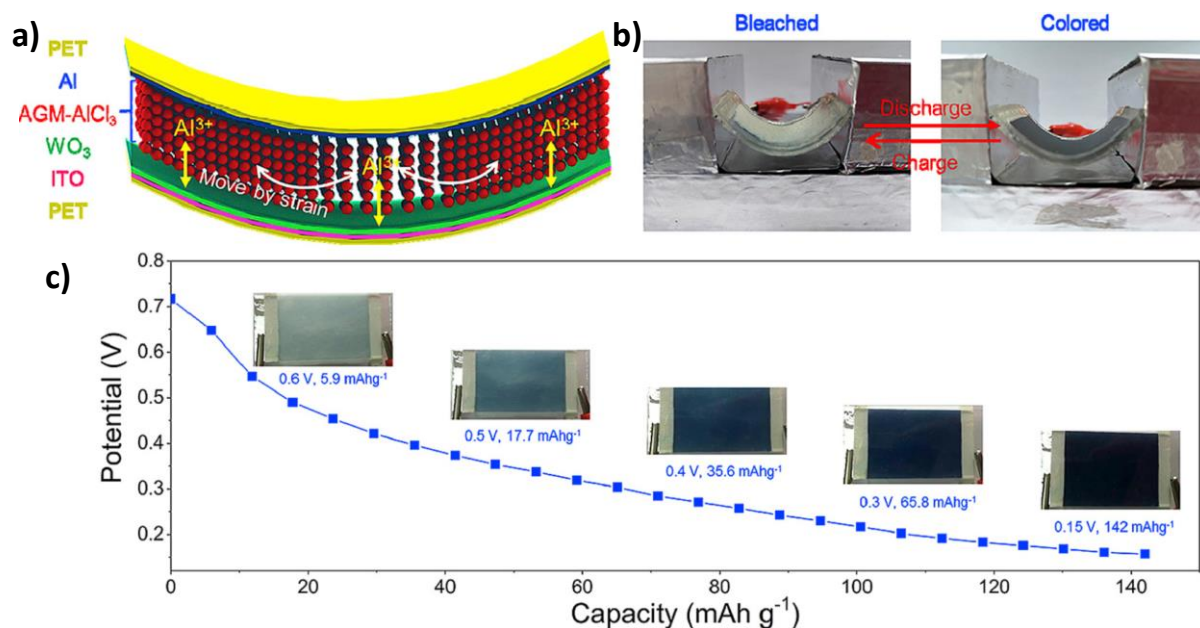


Figure 1.29: a) Schematic representation of the flexible electrochromic battery consisting of PET/ITO as substrate, WO₃ film as cathode, Al sheet as anode, and absorptive glass mat (AGM) as a separator, and aluminum trichloride (AlCl₃) as electrolyte. b) Photographs of the flexible device in charged and discharged states. c) Discharging curve at a constant current density of 0.5 A g⁻¹ and the corresponding photographs of the device. Adapted with permission from ref 79.

An aqueous hybrid Zn²⁺/Al³⁺ electrochromic battery system that exhibited incredible electrochromic properties such as a fast-switching time (0.5 s) and high optical contrast (88%) has been fabricated by Elezzabi and co-workers (**Figure 1.30a-d**).⁸¹ An areal capacity of 185.6 mA h m⁻² at a current density of 0.5 mA cm⁻² along with a high optical contrast (77%, **Figure 1.30b**) was obtained for the battery. The prototype device was characterized by an open circuit voltage (OCV) of 1.15 V (**Figure 1.30b, inset**) and was able to power a 0.5 V light-emitting diode (LED) for 80 min (**Figure 1.30c**).

Zhao *et al.* have developed an Al-tungsten oxide electrochromic battery in which the level of energy stored was determined using variations in the color of the device.⁸² With trace amount of H₂O₂, the battery showed a high specific capacity of 429 mA h g⁻¹, by combining the structural benefits and valence state changes of tungsten oxide. The battery was found to charge to its near maximum within eight seconds and is 1000 times faster than conventional batteries. A bi-functional PB/Al device that showed electrochromism and self-rechargeable battery properties also demonstrated by Sun and co-workers. Aluminium was used to reduce Prussian blue (PB, blue in color) to Prussian white (PW, colorless) and was reversed by spontaneous

oxidation of PW to PB using the dissolved oxygen in the electrolyte. Therefore, the battery was found to automatically self-recharge by reacting with dissolved oxygen and regaining the **PB** cathodic state after discharging (**Figure 1.31a,b**).⁸³ The optical contrast of the device was found to be 52.2% at 670 nm and a capacity of 75 mA h g⁻¹ was obtained with cycling stability up to 50 cycles (**Figure 1.31c,d**).

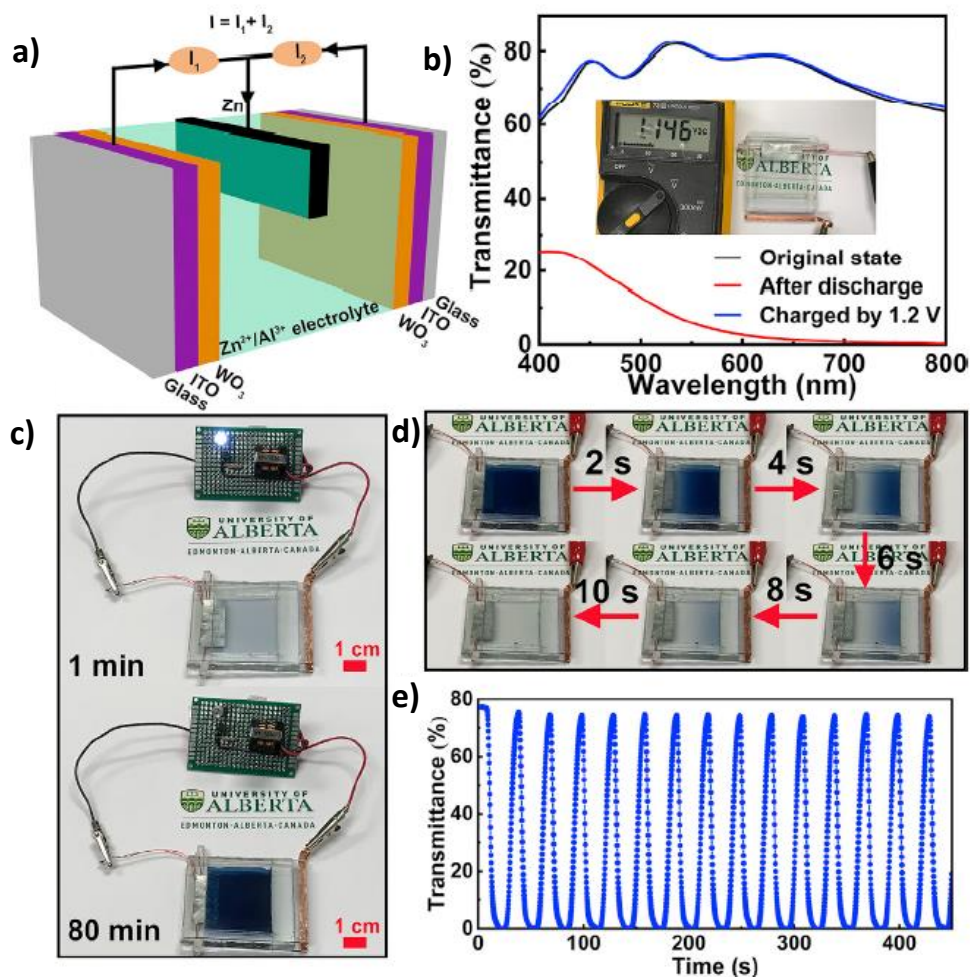


Figure 1.30: a) Schematic representation of the hybrid Zn²⁺/Al³⁺ electrochromic battery architecture. b) Near-infrared transmittance spectrum of the device and its experimentally measured open circuit voltage (inset). c) Photographs of LED powered by the device after 1 minute and up to 80 minutes showing the discharge efficiency. d) Photographs showing the charging process of the completely discharged device. e) Transmittance spectra of the prototype device on applying 0.1 V and 1.2 V showing efficient electrochromic switching. Adapted with permission from ref 81.

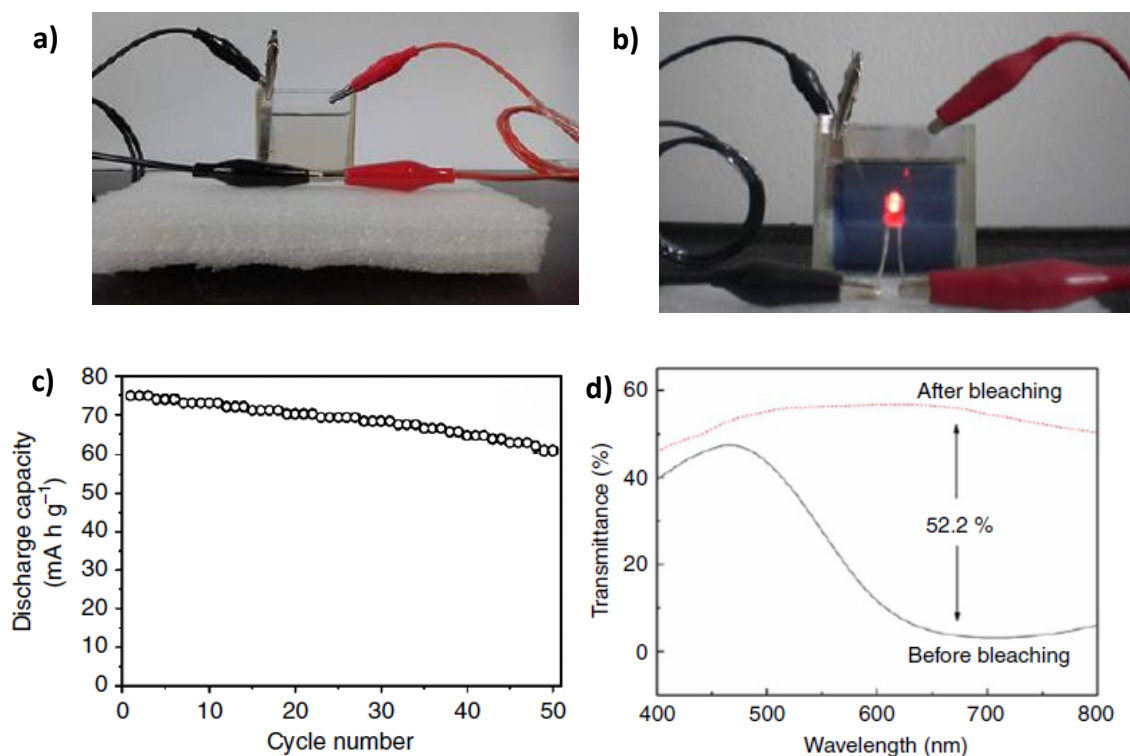


Figure 1.31: Photograph of the (a) bleached and (b) colored (powering an LED) bi-functional **PB/Al** electrochromic device. c) Cycling stability of the **PB/Al** device and (d) the corresponding changes in transmittance before and after bleaching. Adapted with permission from ref 83.

While batteries have high energy densities, supercapacitors possess better power densities. Therefore, supercapacitors can quickly discharge their stored energy, whereas batteries store more energy for a longer time in the same amount of material. Supercapacitors store electrical energy based on two mechanisms:

- 1) Electrostatic double-layer capacitance: Electrostatic storage of the electrical energy achieved by separation of charge in a Helmholtz double layer at the interface between the surface of a conductor electrode and an electrolytic solution electrolyte (**Figures 1.32a - b**).
- 2) Electrochemical pseudocapacitance: Electrochemical storage of electric energy, which is achieved by electron transfer due to redox reactions on the electrode surface (**Figure 1.32c**) or intercalation process (**Figure 1.32d**).⁸⁴

Carbon-based materials such as activated carbon, carbon nanotubes, graphite, etc., are used as active electrode materials in supercapacitors. For the last few years, there has been an increase in the use of non-carbon materials, including metal oxides, conducting polymers, viologens, metal chalcogenides, metal-organic frameworks, etc., either exclusively or in combination with carbon as active electrode materials. Out of all the non-carbon materials, metal-organic

materials that combine the functional advantages of both organic and inorganic materials, are one of the less investigated classes of electrode materials, most likely due to their lower conductivity. However, their exceptionally large surface areas and tunable porosity have triggered the recent interest in investigating the electrochemical feasibility of using metal-organic systems as electrode materials in supercapacitors.

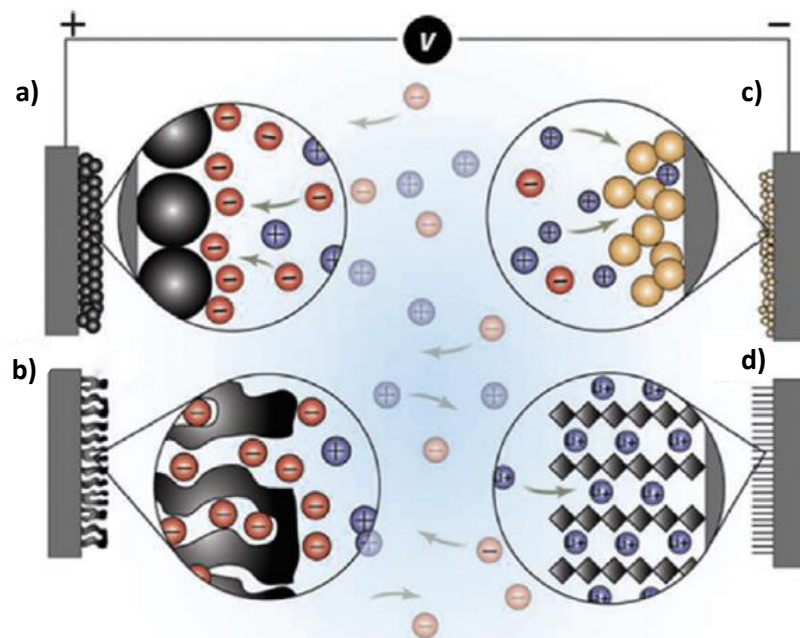


Figure 1.32: (a-b) Schematic illustration of the electrostatic double-layer mechanism of energy storage and electrochemical pseudocapacitance using c) redox reactions on the electrode surface or d) ion intercalation process. Adapted with permission from ref 84.

Dinca *et al.* have reported the first example of a supercapacitor made of Ni hexaaminotriphenylene ($\text{Ni}_3(\text{HITP})_2$, **Figure 1.33a,b**) metal-organic framework as active material without any conductive additives. $\text{Ni}_3(\text{HITP})_2$ based electrical double layer capacitor featured a surface area normalized capacitance of $18 \mu\text{F cm}^{-2}$ and a gravimetric capacitance of 111 F g^{-1} at a current density of 0.05 A g^{-1} with charge-discharge cycling stability up to 10000 cycles with only a 10% reduction in capacitance (**Figure 1.33c,d**).⁸⁵

A comparison of the capacitive performance of $\text{Ni}_3(\text{HITP})_2$ and $\text{Cu}_3(\text{HHTP})_2$ (HHTP = 2,3,6,7,10,11-hexahydroxytriphenylene) using 1 M NEt_4BF_4 in acetonitrile as electrolyte was demonstrated by Forse and co-workers. A similar specific capacitance ($110\text{--}114 \text{ F g}^{-1}$) at low current density ($0.04\text{--}0.05 \text{ A g}^{-1}$) was observed for $\text{Cu}_3(\text{HITP})_2$ based electrodes. This observation is indicative of similar capacitive performance for two nearly isostructural frameworks independent of the identity of the metal node and organic linker. $\text{Cu}_3(\text{HHTP})_2$ exhibited good charge-discharge stability up to 30000 cycles with a modest capacitance

retention of 81%.⁸⁶ Bao *et al.* have reported conductive hexaaminobenzene-derived two-dimensional metal–organic frameworks (**Ni-HAB**) with exceptionally high volumetric and areal capacitance. **Ni-HAB** pellets of 50 μm thickness exhibited a volumetric capacitance of 760 F cm^{-3} and an areal capacitance of 3.7 F cm^{-2} .⁸⁷

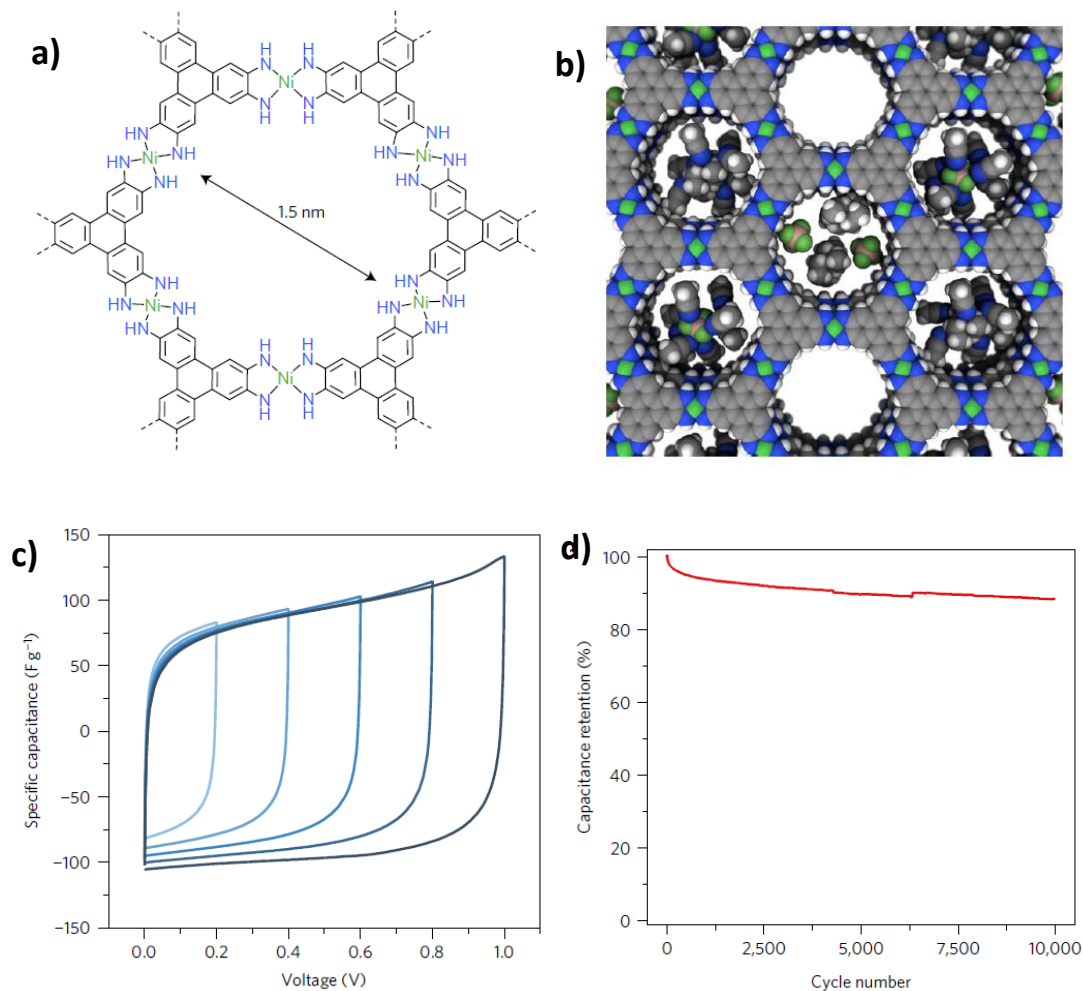


Figure 1.33: a) Molecular structure of the Ni-MOF **Ni₃(HITP)₂** and b) the corresponding space-filling diagram of **Ni₃(HITP)₂**. c) Cyclic voltammetry of **Ni₃(HITP)₂** based electrode at a scan rate of 10 mV s^{-1} with increasing cell voltage. d) Capacitance retention under repeated cycling at a current density of 2 A g^{-1} for 10,000 cycles. Adapted with permission from ref 85.

Electrochromic electrode materials reversibly change their color during the Faradaic reactions that occur with charge transfer. The charge state of electrochromic energy storage devices can be easily detected by monitoring the accompanying color changes and quantitatively determined by optical transmittance measurements. Such multifunctional materials combine the properties of optical modulation and energy storage within a single system. van der Boom *et al.* have integrated an electrochromic–hybrid supercapacitor (EHSC), comprising an Fe complex as an electrochromic metal-organic layer and multi-walled carbon nanotubes (MWCNTs) and

a conductive polymer (PEDOT: PSS) as a capacitive layer.⁸⁸ The amount of available charge was denoted by the color of the metal-organic complexes. A specific capacitance of 10.7 F g^{-1} with high energy and power densities (2.2 W h kg^{-1} and 2529 W kg^{-1}) were observed for the electrochromic supercapacitor. The prototype device was found to be stable for up to 1000 consecutive charging-discharging cycles with a short charging time (2 s).

Zenkina and co-workers have fabricated electrochromic energy storage devices based on monolayers of Co(II), Os(II), and Fe(II) metal (M) complexes of 4'-(pyridin-4-yl)-2,2':6',2''-terpyridine ligand (L) with a ML_2 stoichiometry by depositing individually or simultaneously three complexes together on a template layer. It was noted that incorporation of a TiO_2 layer on the counter electrode improved the capacitive performance to 4.4 mF cm^{-2} (2.2 F g^{-1}) at a constant current density of 0.06 mA cm^{-2} and stability up to 5000 cycles (Figure 1.34).⁸⁹

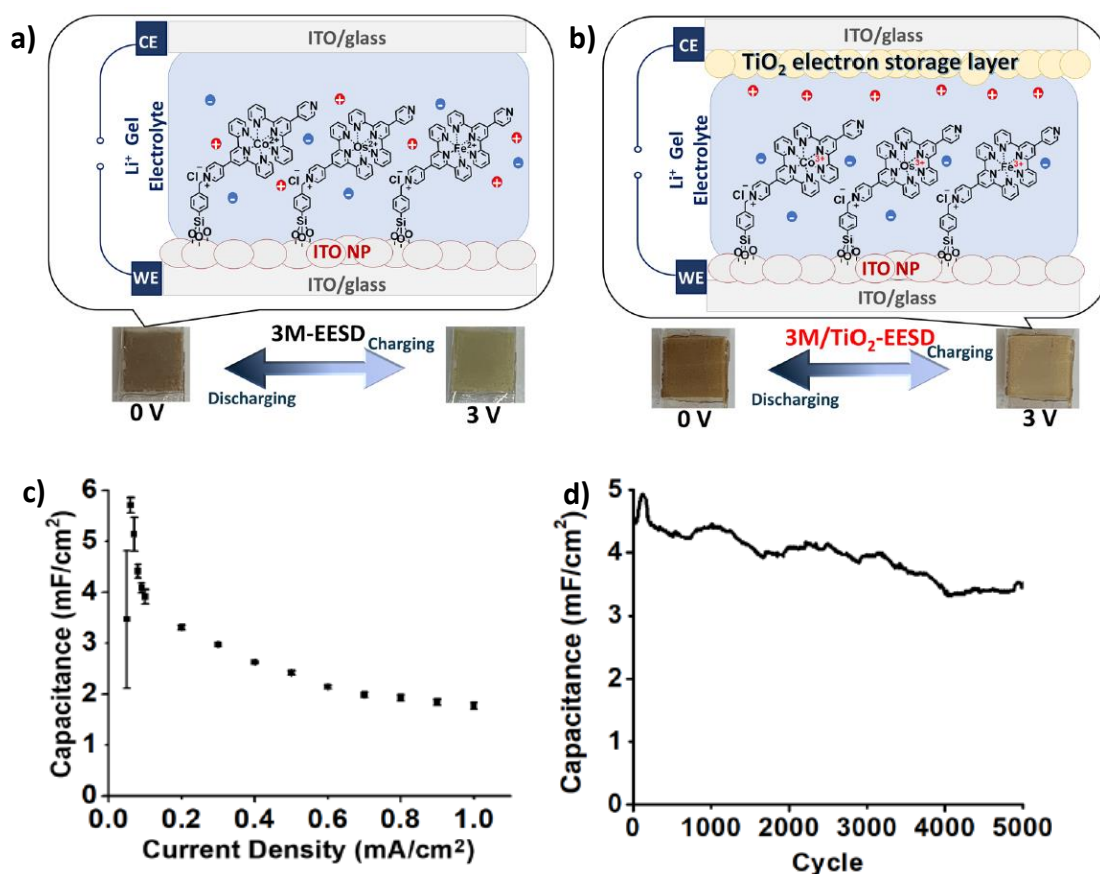


Figure 1.34: Schematic representation of the solid-state electrochromic energy storage devices: a) device architecture with plain ITO/glass and b) device architecture with an ion storage layer, ($\text{TiO}_2/\text{ITO}/\text{glass}$). c) Areal capacitance of the device with TiO_2 ion storage layer, measured at different current densities (0.06 to 1 mA cm^{-2}). d) GCD cycling stability for the device with TiO_2 ion storage layer, at a current density of 0.06 mA cm^{-2} . Adapted with permission from ref 89.

An asymmetric supercapacitor with a sandwich configuration of Fe(II) and Ru(II) based (**polyFe** and **polyRu**) metallocupramolecular polymers as cathodic material and Prussian blue as anodic material using a non-aqueous electrolyte was reported by Higuchi and co-workers (**Figure 1.35a**). These asymmetric devices showed volumetric capacitance of 39 ± 2 and $65 \pm 5 \text{ F cm}^{-3}$ with an energy density of 10.6 mW cm^{-3} and 17.8 mW cm^{-3} , respectively for **polyFe** and **polyRu**, at a power density of 0.7 W h cm^{-3} (**Figure 1.35b**).⁹⁰ Good cycling stability up to 10000 GCD cycles at a current density of 10 A cm^{-3} was also observed (**Figure 1.35c**). **polyRu**-based supercapacitor was further used to light up an LED (**Figure 1.35d**).

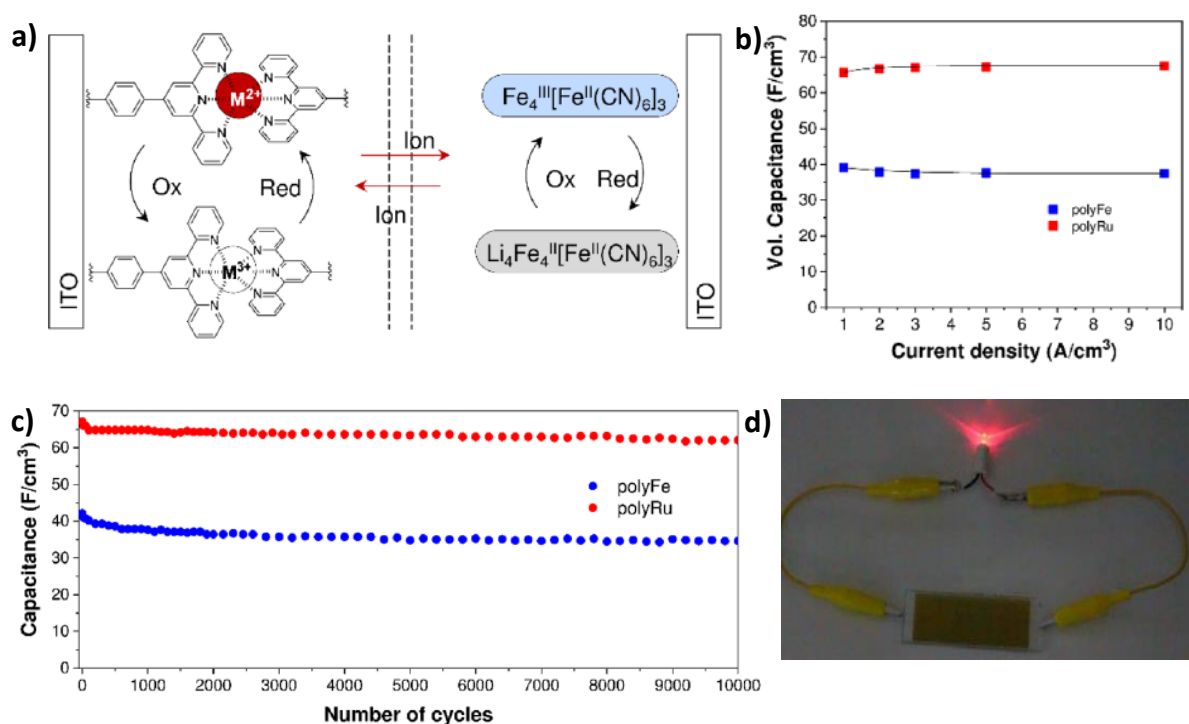


Figure 1.35: a) Electrochemical redox reaction occurring at working and counter electrodes in the asymmetric supercapacitor with a sandwich configuration of metallocupramolecular polymers as cathodic material and Prussian blue as anodic material using a non-aqueous electrolyte. b) Volumetric capacitance of **poly Fe** and **poly Ru** based asymmetric supercapacitors at different current densities. c) Cycling stabilities of **poly Fe** and **poly Ru** based asymmetric supercapacitors up to 10000 charge-discharge cycles. d) Photograph of an LED powered by a **polyRu**-based capacitor. Adapted with permission from ref 90.

1.12. Objectives and Organization of the Thesis

The thesis aims at developing new multifunctional metal-organic systems with efficient EC properties such as high thermal and photochemical stabilities, high contrast ratio, fast and reversible switching, high coloration efficiency, low voltage of operation, and easy

processability. The multifunctional applications and modulation of electrochromic and energy storage properties in these materials by changing the ligand structure, core of the ligand, and metal center were envisaged. Studies and experiments were planned accordingly and the outcome are organised in various chapters (chapters 1, 2, 3 and 4) as described.

Different classes of electrochromic materials, and their multifunctional applications as sensors, batteries, and supercapacitors are discussed in **Chapter 1**. Majority of these materials practically suffer from low to moderate efficiency, inferior redox, photochemical and cycling stabilities, write-erase inefficiency, and laborious processability. Hence, we focused on developing new-generation molecule-based nanoscale metal-organic assemblies as homogeneous thin film electrochromic systems, their fabrication into electrochromic devices (ECDs) and exploration of their charge storage properties. With these objectives, in the **second chapter**, we synthesized three tetra-terpyridine ligands with variations in their core architecture (phenyl vs. tetraphenylethynyl vs. bithiophene) to create spray-coated electrochromic assemblies of iron(II) based coordination polymer network films on transparent conducting oxide substrates. These thin films exhibited molecular permeability and spectroelectrochemical properties that are in turn dictated by the ligand structure. Electrochromic films and devices with high coloration efficiencies (up to $1050 \text{ cm}^2 \text{ C}^{-1}$) and superior optical contrast (up to 76%) with a concomitant color-to-color redox transition were readily achieved. In the **third chapter**, we report three electrochromic metallopolymer-based electrode materials containing Fe^{2+} with high volumetric capacitance and energy densities in a symmetric two-electrode supercapacitor set-up. These metallopolymers exhibited volumetric capacitance up to 866.2 F cm^{-3} at a constant current density of 0.25 A g^{-1} . The volumetric capacitance and energy densities followed the order of the electrical conductivity of the metallopolymers, and are among the best values reported for metal-organic systems. In the **fourth chapter**, we report the use of electrochromic metallopolymers obtained from near-isostructural metal (Mn^{2+} , Fe^{2+} , Co^{2+}) bipyridine coordination complexes as electrode materials in a symmetric supercapacitor test cell. The central metal ion not only influences the porosity, BET surface area and hence the areal capacitance, but also the performance parameters such as cycling stability and charge discharge kinetics as well as the charge transfer mechanism. A 3:4:5 ratio for the areal capacitance values corroborates the modulative effect of the metal center in the capacitive characteristics of the metallopolymers.

1.13 References

- (1) Aida, T.; Meijer, E. W.; Stupp, S. I. Functional Supramolecular Polymers. *Science*. **2012**, *335*, 813–817.
<https://doi.org/10.1126/science.1205962>.
- (2) Stuart, M. A. C.; Huck, W. T. S.; Genzer, J.; Müller, M.; Ober, C.; Stamm, M.; Sukhorukov, G. B.; Szleifer, I.; Tsukruk, V. V.; Urban, M.; Winnik, F.; Zauscher, S.; Luzinov, I.; Minko, S. Emerging Applications of Stimuli-Responsive Polymer Materials. *Nat. Mater.* **2010**, *9*, 101–113.
<https://doi.org/10.1038/nmat2614>.
- (3) Beaujuge, P. M.; Reynolds, J. R. Color Control in π -Conjugated Organic Polymers for Use in Electrochromic Devices. *Chem. Rev.* **2010**, *110*, 268–320.
<https://doi.org/10.1021/cr900129a>.
- (4) van Der Boom, M. E. Nanostructured Molecular Materials for Device-Quality, Highly Efficient Electrooptic Poled Polymers. *Angew. Chem., Int. Ed.* **2002**, *41*, 3363–3366.
[https://doi.org/10.1002/1521-3773\(20020916\)41:18<3363::AIANIE3363>3.0.CO;2-V](https://doi.org/10.1002/1521-3773(20020916)41:18<3363::AIANIE3363>3.0.CO;2-V).
- (5) Ostroverkhova, O. Organic Optoelectronic Materials: Mechanisms and Applications. *Chem. Rev.* **2016**, *116*, 13279–13412.
<https://doi.org/10.1021/acs.chemrev.6b00127>.
- (6) Mortimer, R. J. Electrochromic Materials. *Annu. Rev. Mater. Res.* **2011**, *41*, 241–268.
<https://doi.org/10.1146/annurev-matsci-062910-100344>.
- (7) Cai, G.; Wang, J.; Lee, P. S. Next-Generation Multifunctional Electrochromic Devices. *Acc. Chem. Res.* **2016**, *49*, 1469–1476.
<https://doi.org/10.1021/acs.accounts.6b00183>.
- (8) Deb, S. K. A Novel Electrophotographic System. *Appl. Opt.* **1969**, *8*, 192.
<https://doi.org/10.1364/ao.8.s1.000192>.
- (9) Deb, S. K. Optical and Photoelectric Properties and Colour Centres in Thin Films of Tungsten Oxide. *Philos. Mag.* **1973**, *27*, 801–822.
<https://doi.org/10.1080/14786437308227562>.
- (10) Özer, N.; Chen, D.-G.; Lampert, C. M. Preparation and Properties of Spin-Coated Nb₂O₅ Films by the Sol-Gel Process for Electrochromic Applications. *Thin Solid Films* **1996**, *277*, 162–168.
[https://doi.org/10.1016/0040-6090\(95\)08011-2](https://doi.org/10.1016/0040-6090(95)08011-2).
- (11) Hajimoto, Y.; Hara, T. Coloration in a WO₃ Film. *Appl. Phys. Lett.* **1976**, *28*, 228–229.
<https://doi.org/10.1063/1.88707>.

- (12) Chang, I. F.; Gilbert, B. L.; Sun, T. I. Electrochromic Systems for Display Applications. *J. Electrochem. Soc.* **1975**, *122*, 955–962.
<https://doi.org/10.1149/1.2134377>.
- (13) Chang, I. F. Electrochromic and Electrochromic Materials and Phenomena. *Nonemissive Electrooptic Displays* **1976**, 155–196.
https://doi.org/10.1007/978-1-4613-4289-2_10.
- (14) Svensson, J. S. E. M.; Granqvist, C. G. Electrochromic Coatings for “Smart Windows.” *Sol. Energy Mater.* **1985**, *12*, 391–402.
[https://doi.org/10.1016/0165-1633\(85\)90033-4](https://doi.org/10.1016/0165-1633(85)90033-4).
- (15) Granqvist, C. G. *Handbook of Inorganic Electrochromic Materials*; Elsevier, 1995.
- (16) Neo, W. T.; Ye, Q.; Chua, S. J.; Xu, J. Conjugated Polymer-Based Electrochromics: Materials, Device Fabrication and Application Prospects. *J. Mater. Chem. C* **2016**, *4*, 7364–7376.
<https://doi.org/10.1039/c6tc01150k>.
- (17) Argun, A. A.; Aubert, P.-H.; Thompson, B. C.; Schwendeman, I.; Gaupp, C. L.; Hwang, J.; Pinto, N. J.; Tanner, D. B.; MacDiarmid, A. G.; Reynolds, J. R. Multicolored Electrochromism in Polymers: Structures and Devices. *Chem. Mater.* **2004**, *16*, 4401–4412.
<https://doi.org/10.1021/cm049669l>.
- (18) Yen, H. J.; Liou, G. S. Solution-Processable Triarylamine-Based Electroactive High Performance Polymers for Anodically Electrochromic Applications. *Polym. Chem.* **2012**, *3*, 255–264.
<https://doi.org/10.1039/c1py00346a>.
- (19) Rosseinsky, D. R.; Mortimer, R. J. Electrochromic Systems and the Prospects for Devices. *Adv. Mater.* **2001**, *13*, 783–793.
[https://doi.org/10.1002/1521-4095\(200106\)](https://doi.org/10.1002/1521-4095(200106)).
- (20) Goldner, R. B.; Seward, G.; Wong, K.; Haas, T.; Foley, G. H.; Chapman, R.; Schulz, S. Completely Solid Lithiated Smart Windows. *Sol. Energy Mater.* **1989**, *19*, 17–26.
[https://doi.org/10.1016/0165-1633\(89\)90020-8](https://doi.org/10.1016/0165-1633(89)90020-8).
- (21) Azens, A.; Granqvist, C. G. Electrochromic Smart Windows: Energy Efficiency and Device Aspects. *J. Solid State Electrochem.* **2003**, *7*, 64–68.
<https://doi.org/10.1007/s10008-002-0313-4>.
- (22) Thakur, V. K.; Ding, G.; Ma, J.; Lee, P. S.; Lu, X. Hybrid Materials and Polymer Electrolytes for Electrochromic Device Applications. *Adv. Mater.* **2012**, *24*, 4071–4096.
<https://doi.org/10.1002/adma.201200213>.

- (23) Wen, R.-T.; Niklasson, G. A.; Granqvist, C. G. Sustainable Rejuvenation of Electrochromic WO₃ Films. *ACS Appl. Mater. Interfaces* **2015**, *7*, 28100–28104.
<https://doi.org/10.1021/acsami.5b09035>.
- (24) Yao, D. D.; Rani, R. A.; O'Mullane, A. P.; Kalantar-zadeh, K.; Ou, J. Z. Enhanced Coloration Efficiency for Electrochromic Devices Based on Anodized Nb₂O₅/Electrodeposited MoO₃ Binary Systems. *J. Phys. Chem. C* **2014**, *118*, 10867–10873.
<https://doi.org/10.1021/jp5017888>.
- (25) Deb, S. K. Opportunities and Challenges in Science and Technology of WO₃ for Electrochromic and Related Applications. *Sol. Energy Mater. Sol. Cells* **2008**, *92*, 245–258.
<https://doi.org/10.1016/j.solmat.2007.01.026>.
- (26) Zhang, J.; Tu, J. P.; Xia, X. H.; Qiao, Y.; Lu, Y. Solar Energy Materials & Solar Cells An All-Solid-State Electrochromic Device Based on NiO / WO₃ Complementary Structure and Solid Hybrid Polyelectrolyte. *Sol. Energy Mater. Sol. Cells* **2009**, *93*, 1840–1845.
<https://doi.org/10.1016/j.solmat.2009.06.025>.
- (27) Assis, L. M. N.; Leones, R.; Kanicki, J.; Pawlicka, A.; Silva, M. M. Prussian Blue for Electrochromic Devices. *J. Electroanal. Chem.* **2016**, *777*, 33–39.
<https://doi.org/10.1016/j.jelechem.2016.05.007>.
- (28) Itaya, K.; Shibayama, K.; Akahoshi, H.; Toshima, S. Prussian-blue-modified Electrodes: An Application for a Stable Electrochromic Display Device. *J. Appl. Phys.* **1982**, *53*, 804–805.
<https://doi.org/10.1063/1.329997>.
- (29) Madasamy, K.; Velayutham, D.; Suryanarayanan, V.; Kathiresan, M.; Ho, K.-C. Viologen-Based Electrochromic Materials and Devices. *J. Mater. Chem. C* **2019**, *7*, 4622–4637.
<https://doi.org/10.1039/C9TC00416E>.
- (30) Welsh, T. A.; Draper, E. R. Water Soluble Organic Electrochromic Materials. *RSC Adv.* **2021**, *11*, 5245–5264.
<https://doi.org/10.1039/D0RA10346B>.
- (31) Baran, D.; Balan, A.; Celebi, S.; Esteban, B. M.; Neugebauer, H.; Sariciftci, N. S.; Toppare, L. Processable Multipurpose Conjugated Polymer for Electrochromic and Photovoltaic Applications. *Chem. Mater.* **2010**, *21*, 2978–2987.
<https://doi.org/10.1021/cm100372t>.
- (32) Lv, X.; Li, W.; Ouyang, M.; Zhang, Y.; Wright, D. S.; Zhang, C. Polymeric Electrochromic Materials with Donor–Acceptor Structures. *J. Mater. Chem. C* **2017**, *5*, 12–28.

- <https://doi.org/10.1039/C6TC04002K>.
- (33) Nicho, M. E.; Hu, H.; López-Mata, C.; Escalante, J. Synthesis of Derivatives of Polythiophene and Their Application in an Electrochromic Device. *Sol. Energy Mater. Sol. Cells* **2004**, *82*, 105–118.
<https://doi.org/10.1016/j.solmat.2004.01.009>.
- (34) Hu, Y.; Liu, X.; Jiang, F.; Zhou, W.; Liu, C.; Duan, X.; Xu, J. Article Functionalized Poly (3,4-Ethylenedioxy Bithiophene) Films for Tuning Electrochromic and Thermoelectric Properties. *J. Phys. Chem. B* **2017**, *121*, 9281–9290.
<https://doi.org/10.1021/acs.jpcc.7b05217>.
- (35) Camurlu, P. Polypyrrole Derivatives for Electrochromic Applications. *RSC Adv.* **2014**, *4*, 55832–55845.
<https://doi.org/10.1039/C4RA11827H>.
- (36) Celiesiute, R.; Ramanaviciene, A.; Gicevicius, M.; Ramanavicius, A. Electrochromic Sensors Based on Conducting Polymers, Metal Oxides, and Coordination Complexes. *Crit. Rev. Anal. Chem.* **2019**, *49*, 195–208.
<https://doi.org/10.1080/10408347.2018.1499009>.
- (37) Rowley, N. M.; Mortimer, R. J. New Electrochromic Materials. *Sci. Prog.* **2002**, *85*, 243–262.
<https://doi.org/10.3184/003685002783238816>.
- (38) Mortimer, R. J.; Dyer, A. L.; Reynolds, J. R. Electrochromic Organic and Polymeric Materials for Display Applications. *Displays* **2006**, *27*, 2–18.
<https://doi.org/10.1016/j.displa.2005.03.003>.
- (39) Xiong, S.; Yin, S.; Wang, Y.; Kong, Z.; Lan, J.; Zhang, R.; Gong, M.; Wu, B.; Chu, J.; Wang, X. Organic/Inorganic Electrochromic Nanocomposites with Various Interfacial Interactions: A Review. *Mater. Sci. Eng. B* **2017**, *221*, 41–53.
<https://doi.org/10.1016/j.mseb.2017.03.017>.
- (40) Hofmeier, H.; Schubert, U. S. Recent Developments in the Supramolecular Chemistry of Terpyridine–Metal Complexes. *Chem. Soc. Rev.* **2004**, *33*, 373–399.
<https://doi.org/10.1039/B400653B>.
- (41) Schubert, U. S.; Eschbaumer, C. Macromolecules Containing Bipyridine and Terpyridine Metal Complexes: Towards Metallosupramolecular Polymers. *Angew. Chem., Int. Ed.* **2002**, *41*, 2892–2926.
[https://doi.org/10.1002/1521-3773\(20020816\)41:16<2892::AID-ANIE2892>3.0.CO;2-6](https://doi.org/10.1002/1521-3773(20020816)41:16<2892::AID-ANIE2892>3.0.CO;2-6).

- (42) Fan, C.; Ye, C.; Wang, X.; Chen, Z.; Zhou, Y.; Liang, Z.; Tao, X. Synthesis and Electrochromic Properties of New Terpyridine–Triphenylamine Hybrid Polymers. *Macromolecules* **2015**, *48*, 6465–6473.
<https://doi.org/10.1021/acs.macromol.5b00493>.
- (43) Hsu, C. Y.; Zhang, J.; Sato, T.; Moriyama, S.; Higuchi, M. Black-to-Transmissive Electrochromism with Visible-to-Near-Infrared Switching of a Co(II)-Based Metallo-Supramolecular Polymer for Smart Window and Digital Signage Applications. *ACS Appl. Mater. Interfaces* **2015**, *7*, 18266–18272.
<https://doi.org/10.1021/acsami.5b02990>.
- (44) Takada, K.; Sakamoto, R.; Yi, S.-T.; Katagiri, S.; Kambe, T.; Nishihara, H. Electrochromic Bis(Terpyridine)Metal Complex Nanosheets. *J. Am. Chem. Soc.* **2015**, *137*, 4681–4689.
<https://doi.org/10.1021/ja510788b>.
- (45) Kuai, Y.; Li, W.; Dong, Y.; Wong, W.-Y.; Yan, S.; Dai, Y.; Zhang, C. Multi-Color Electrochromism from Coordination Nanosheets Based on a Terpyridine-Fe(II) Complex. *Dalt. Trans.* **2019**, *48*, 15121–15126.
<https://doi.org/10.1039/C9DT02980J>.
- (46) Roy, S.; Chakraborty, C. Interfacial Coordination Nanosheet Based on Nonconjugated Three-Arm Terpyridine: A Highly Color-Efficient Electrochromic Material to Converge Fast Switching with Long Optical Memory. *ACS Appl. Mater. Interfaces* **2020**, *12*, 35181–35192.
<https://doi.org/10.1021/acsami.0c06045>.
- (47) Bera, M. K.; Ninomiya, Y.; Higuchi, M. Constructing Alternated Heterobimetallic [Fe(II)/Os(II)] Supramolecular Polymers with Diverse Solubility for Facile Fabrication of Voltage-Tunable Multicolor Electrochromic Devices. *ACS Appl. Mater. Interfaces* **2020**, *12*, 14376–14385.
<https://doi.org/10.1021/acsami.9b21966>.
- (48) Yoshida, T.; Ninomiya, Y.; Higuchi, M. Reversible Four-Color Electrochromism Triggered by the Electrochemical Multi-Step Redox of Cr-Based Metallo - Supramolecular Polymers. *RSC Adv.* **2020**, *10*, 10904–10909.
<https://doi.org/10.1039/D0RA00676A>.
- (49) Mondal, S.; Chandra Santra, D.; Ninomiya, Y.; Yoshida, T.; Higuchi, M. Dual-Redox System of Metallo-Supramolecular Polymers for Visible-to-Near-IR Modulable

- Electrochromism and Durable Device Fabrication. *ACS Appl. Mater. Interfaces* **2020**, *12*, 58277–58286.
<https://doi.org/10.1021/acsami.0c18109>.
- (50) Bera, M. K.; Ninomiya, Y.; Higuchi, M. Stepwise Introduction of Three Different Transition Metals in Metallo-Supramolecular Polymer for Quad-Color Electrochromism. *Commun. Chem.* **2021**, *4*, 56.
<https://doi.org/10.1038/s42004-021-00495-1>.
- (51) Qiu, D.; Bao, X.; Zhao, Q.; Yang, Q.; Feng, Y.; Wang, H.; Yang, C.; Liu, K. Near-IR Electrochromic Film Prepared by Oxidative Electropolymerization of the Cyclometalated Pt(II) Chloride with a Triphenylamine Group. *Inorg. Chem.* **2015**, *54*, 8264–8270.
<https://doi.org/10.1021/acs.inorgchem.5b00782>.
- (52) Shankar, S.; Lahav, M.; van der Boom, M. E. Coordination-Based Molecular Assemblies as Electrochromic Materials: Ultra-High Switching Stability and Coloration Efficiencies. *J. Am. Chem. Soc.* **2015**, *137*, 4050–4053.
<https://doi.org/10.1021/jacs.5b00429>.
- (52a) Eloul Dov, N.; Shankar, S.; Cohen, D.; Bendikov, T.; Rechav, K.; Shimon, L. J. W.; Lahav, M.; Van Der Boom, M. E. Electrochromic Metallo–Organic Nanoscale Films: Fabrication, Color Range, and Devices. *J. Am. Chem. Soc.* **2017**, *139*, 11471–11481.
<https://doi.org/10.1021/jacs.7b04217>.
- (53) Malik, N.; Lahav, M.; van der Boom, M. E. Electrochromic Metallo–Organic Nanoscale Films: A Molecular Mix and Match Approach to Thermally Robust and Multistate Solid-State Devices. *Adv. Electron. Mater.* **2020**, *6*, 2000407.
<https://doi.org/https://doi.org/10.1002/aelm.202000407>.
- (54) Santra, D. C.; Mondal, S.; Yoshida, T.; Ninomiya, Y.; Higuchi, M. Ru(II)-Based Metallo-Supramolecular Polymer with Tetrakis(N-Methylbenzimidazolyl)Bipyridine for a Durable, Nonvolatile, and Electrochromic Device Driven at 0.6 V. *ACS Appl. Mater. Interfaces* **2021**, *13*, 31153–31162.
<https://doi.org/10.1021/acsami.1c07275>.
- (55) Mondal, S.; Ninomiya, Y.; Yoshida, T.; Mori, T.; Bera, M. K.; Ariga, K.; Higuchi, M. Dual-Branched Dense Hexagonal Fe(II)-Based Coordination Nanosheets with Red-to-Colorless Electrochromism and Durable Device Fabrication. *ACS Appl. Mater. Interfaces* **2020**, *12*, 31896–31903.
<https://doi.org/10.1021/acsami.0c05921>.

- (56) Nunes, M.; Araújo, M.; Fonseca, J.; Moura, C.; Hillman, R.; Freire, C. High-Performance Electrochromic Devices Based on Poly[Ni(Salen)]-Type Polymer Films. *ACS Appl. Mater. Interfaces* **2016**, *8*, 14231–14243.
<https://doi.org/10.1021/acsami.6b01977>.
- (57) Nunes, M.; Moura, C.; Hillman, A. R.; Freire, C. Multicolour Electrochromic Film Based on a TiO₂@poly[Ni(Salen)] Nanocomposite with Excellent Electrochemical Stability. *Langmuir* **2017**, *33*, 6826–6837.
<https://doi.org/10.1021/acs.langmuir.7b01380>.
- (58) Akyüz, D.; Demirbaş, Ü.; Koca, A.; Çelik, F.; Kantekin, H. Electrochemistry, Electropolymerization and Electrochromism of Novel Phthalocyanines Bearing Morpholine Groups. *J. Mol. Struct.* **2020**, *1206*, 127674.
<https://doi.org/10.1016/j.molstruc.2019.127674>.
- (59) Göktuğ, Ö.; Soganci, T.; Ak, M.; Şener, M. K. Efficient Synthesis of EDOT Modified ABBB-Type Unsymmetrical Zinc Phthalocyanine: Optoelectrochromic and Glucose Sensing Properties of Its Copolymerized Film. *New J. Chem.* **2017**, *41*, 14080–14087.
<https://doi.org/10.1039/C7NJ03250A>.
- (60) Demir, F.; Bıyıklıoğlu, Z.; KOCA, A. Electrochromism of Electropolymerized Metallophthalocyanines. *J. Electrochem. Soc.* **2014**, *161*, G1–G6.
<https://doi.org/10.1149/2.002403jes>.
- (61) Arockiam, J. B.; Son, H.; Han, S. H.; Balamurugan, G.; Kim, Y.-H.; Park, J. S. Iron Phthalocyanine Incorporated Metallo-Supramolecular Polymer for Superior Electrochromic Performance with High Coloration Efficiency and Switching Stability. *ACS Appl. Energy Mater.* **2019**, *2*, 8416–8424.
<https://doi.org/10.1021/acsaem.9b01022>.
- (62) Cogal, S.; Kiristi, M.; Ocakoglu, K.; Oksuz, L.; Oksuz, A. U. Electrochromic Properties of Electrochemically Synthesized Porphyrin/3-Substituted Polythiophene Copolymers. *Mater. Sci. Semicond. Process.* **2015**, *31*, 551–560.
<https://doi.org/10.1016/j.mssp.2014.12.036>.
- (63) Durantini, J.; Morales, G. M.; Santo, M.; Funes, M.; Durantini, E. N.; Fungo, F.; Dittrich, T.; Otero, L.; Gervaldo, M. Synthesis and Characterization of Porphyrin Electrochromic and Photovoltaic Electropolymers. *Org. Electron.* **2012**, *13*, 604–614.
<https://doi.org/10.1016/j.orgel.2012.01.004>.
- (64) Abe, M.; Futagawa, H.; Ono, T.; Yamada, T.; Kimizuka, N.; Hisaeda, Y. An Electropolymerized Crystalline Film Incorporating Axially-Bound Metalloporphyrines:

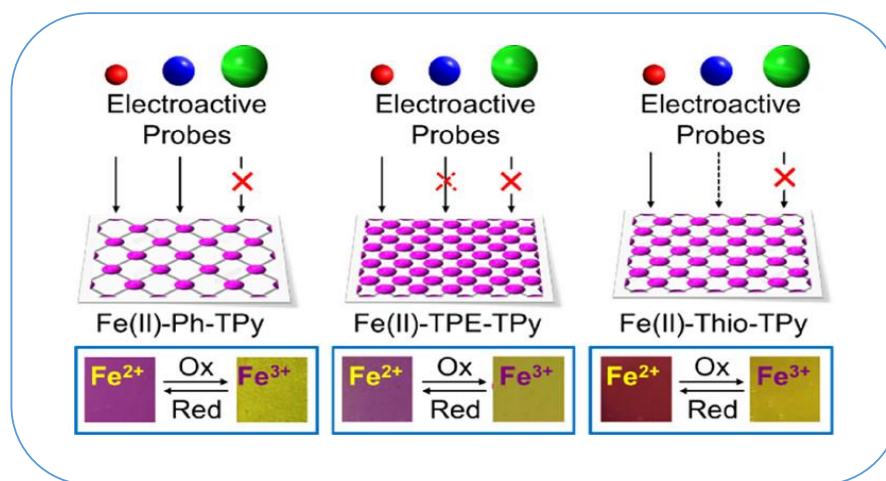
- Remarkable Reversibility, Reproducibility, and Coloration Efficiency of Ruthenium(II/III)-Based Electrochromism. *Inorg. Chem.* **2015**, *54*, 11061–11063. <https://doi.org/10.1021/acs.inorgchem.5b02129>.
- (65) Hossain, M.; Chakraborty, C.; Rana, U.; Mondal, S.; Holdt, H.-J.; Higuchi, M. Green-to-Black Electrochromic Copper(I)-Based Metallo-Supramolecular Polymer with a Perpendicularly Twisted Structure. *ACS Appl. Polym. Mater.* **2020**, *2*, 4449–4454. <https://doi.org/10.1021/acsapm.0c00559>.
- (66) Soganci, T.; Baygu, Y.; Kabay, N.; Dumlu, G.; Gök, Y.; Ak, M. Synthesis of a Carbazole Substituted Unusual Cobalt(II)Dioxime Complex to Design Conducting Polymers with Caged Metal Centers for Enhanced Optical and Electrical Properties. *New J. Chem.* **2020**, *44*, 18616–18624. <https://doi.org/10.1039/D0NJ03931D>.
- (67) Cai, G.; Cui, P.; Shi, W.; Morris, S.; Lou, S. N.; Chen, J.; Ciou, J.-H.; Paidi, V. K.; Lee, K.-S.; Li, S.; Lee, P. S. One-Dimensional π -d Conjugated Coordination Polymer for Electrochromic Energy Storage Device with Exceptionally High Performance. *Adv. Sci.* **2020**, *7*, 1903109. <https://doi.org/10.1002/advs.201903109>.
- (68) Valiūnienė, A.; Virbickas, P.; Medvikytė, G.; Ramanavičius, A. Urea Biosensor Based on Electrochromic Properties of Prussian Blue. *Electroanalysis* **2020**, *32*, 503–509. <https://doi.org/10.1002/elan.201900556>.
- (69) Ratautaite, V.; Samukaite-Bubniene, U.; Plausinaitis, D.; Boguzaitė, R.; Balciunas, D.; Ramanaviciene, A.; Neunert, G.; Ramanavicius, A. Molecular Imprinting Technology for Determination of Uric Acid. *Int. J. Mol. Sci.* **2021**, *22*, 5032. <https://doi.org/10.3390/ijms22095032>.
- (70) Zhai, Y.; Li, Y.; Zhang, H.; Yu, D.; Zhu, Z.; Sun, J.; Dong, S. Self-Rechargeable-Battery-Driven Device for Simultaneous Electrochromic Windows, ROS Biosensing, and Energy Storage. *ACS Appl. Mater. Interfaces* **2019**, *11*, 28072–28077. <https://doi.org/10.1021/acsami.9b08715>.
- (71) Ranjbar, S.; Nejad, M. A. F.; Parolo, C.; Shahrokhian, S.; Merkoçi, A. Smart Chip for Visual Detection of Bacteria Using the Electrochromic Properties of Polyaniline. *Anal. Chem.* **2019**, *91*, 14960–14966. <https://doi.org/10.1021/acs.analchem.9b03407>.

- (72) Soylemez, S.; Kaya, H. Z.; Udum, Y. A.; Toppare, L. A Multipurpose Conjugated Polymer: Electrochromic Device and Biosensor Construction for Glucose Detection. *Org. Electron.* **2019**, *65*, 327–333.
<https://doi.org/10.1016/j.orgel.2018.11.001>.
- (73) Yeh, L.-C.; Huang, T.-C.; Lai, F.-Y.; Lai, G.-H.; Lo, A.-Y.; Hsu, S.-C.; Yang, T.-I.; Yeh, J.-M. Synthesis of Electroactive Polyazomethine and Its Application in Electrochromic Property and Electrochemical Sensor. *Surf. Coatings Technol.* **2016**, *303*, 2807-2982.
<https://doi.org/10.1016/j.surfcoat.2016.03.094>.
- (74) Capoferri, D.; Álvarez-Diduk, R.; Del Carlo, M.; Compagnone, D.; Merkoçi, A. Electrochromic Molecular Imprinting Sensor for Visual and Smartphone-Based Detections. *Anal. Chem.* **2018**, *90*, 5850–5856.
<https://doi.org/10.1021/acs.analchem.8b00389>.
- (75) Park, H.; Kim, D. S.; Hong, S. Y.; Kim, C.; Yun, J. Y.; Oh, S. Y.; Jin, S. W.; Jeong, Y. R.; Kim, G. T.; Ha, J. S. A Skin-Integrated Transparent and Stretchable Strain Sensor with Interactive Color-Changing Electrochromic Displays. *Nanoscale* **2017**, *9*, 7631–7640.
<https://doi.org/10.1039/C7NR02147J>.
- (76) Xu, W.; Fu, K.; Bohn, P. W. Electrochromic Sensor for Multiplex Detection of Metabolites Enabled by Closed Bipolar Electrode Coupling. *ACS Sensors* **2017**, *2*, 1020–1026.
<https://doi.org/10.1021/acssensors.7b00292>.
- (77) Li, H.; McRae, L.; Firby, C. J.; Elezzabi, A. Y. Rechargeable Aqueous Electrochromic Batteries Utilizing Ti-Substituted Tungsten Molybdenum Oxide Based Zn²⁺ Ion Intercalation Cathodes. *Adv. Mater.* **2019**, *31*, 1807065.
<https://doi.org/10.1002/adma.201807065>.
- (78) Zhang, W.; Li, H.; Al-Hussein, M.; Elezzabi, A. Y. Electrochromic Battery Displays with Energy Retrieval Functions Using Solution-Processable Colloidal Vanadium Oxide Nanoparticles. *Adv. Opt. Mater.* **2020**, *8*, 1901224.
<https://doi.org/10.1002/adom.201901224>.
- (79) Sun, S.; Tang, C.; Jiang, Y.; Wang, D.; Chang, X.; Lei, Y.; Wang, N.; Zhu, Y. Flexible and Rechargeable Electrochromic Aluminium-Ion Battery Based on Tungsten Oxide Film Electrode. *Sol. Energy Mater. Sol. Cells* **2020**, *207*, 110332.
<https://doi.org/10.1016/j.solmat.2019.110332>.
- (80) Yang, B.; Ma, D.; Zheng, E.; Wang, J. A Self-Rechargeable Electrochromic Battery Based on Electrodeposited Polypyrrole Film. *Sol. Energy Mater. Sol. Cells* **2019**, *192*, 1–7.
<https://doi.org/10.1016/j.solmat.2018.12.011>.

- (81) Li, H.; Firby, C. J.; Elezzabi, A. Y. Rechargeable Aqueous Hybrid Zn²⁺/Al³⁺ Electrochromic Batteries. *Joule* **2019**, *3*, 2268–2278.
<https://doi.org/10.1016/j.joule.2019.06.021>.
- (82) Zhao, J.; Tian, Y.; Wang, Z.; Cong, S.; Zhou, D.; Zhang, Q.; Yang, M.; Zhang, W.; Geng, F.; Zhao, Z. Trace H₂O₂-Assisted High-Capacity Tungsten Oxide Electrochromic Batteries with Ultrafast Charging in Seconds. *Angew. Chem., Int. Ed.* **2016**, *55*, 7161–7165.
<https://doi.org/10.1002/anie.201602657>.
- (83) Wang, J.; Zhang, L.; Yu, L.; Jiao, Z.; Xie, H.; Lou, X. W. (David); Wei Sun, X. A Bi-Functional Device for Self-Powered Electrochromic Window and Self-Rechargeable Transparent Battery Applications. *Nat. Commun.* **2014**, *5*, 4921.
<https://doi.org/10.1038/ncomms5921>.
- (84) Yang, P.; Sun, P.; Mai, W. Electrochromic Energy Storage Devices. *Mater. Today* **2016**, *19*, 394–402.
<https://doi.org/10.1016/j.mattod.2015.11.007>.
- (85) Sheberla, D.; Bachman, J. C.; Elias, J. S.; Sun, C.-J.; Shao-Horn, Y.; Dincă, M. Conductive MOF Electrodes for Stable Supercapacitors with High Areal Capacitance. *Nat. Mater.* **2017**, *16*, 220–224.
<https://doi.org/10.1038/nmat4766>.
- (86) Gittins, J. W.; Balhatchet, C. J.; Chen, Y.; Liu, C.; Madden, D. G.; Britto, S.; Golomb, M. J.; Walsh, A.; Fairen-Jimenez, D.; Dutton, S. E.; Forse, A. C. Insights into the Electric Double-Layer Capacitance of Two-Dimensional Electrically Conductive Metal-Organic Frameworks. *J. Mater. Chem. A* **2021**, *9*, 16006–16015.
<https://doi.org/10.1039/d1ta04026j>.
- (87) Feng, D.; Lei, T.; Lukatskaya, M. R.; Park, J.; Huang, Z.; Lee, M.; Shaw, L.; Chen, S.; Yakovenko, A. A.; Kulkarni, A.; Xiao, J.; Fredrickson, K.; Tok, J. B.; Zou, X.; Cui, Y.; Bao, Z. Robust and Conductive Two-Dimensional Metal-Organic Frameworks with Exceptionally High Volumetric and Areal Capacitance. *Nat. Energy* **2018**, *3*, 30–36.
<https://doi.org/10.1038/s41560-017-0044-5>.
- (88) Eisenberg, O.; Algavi, Y. M.; Weissman, H.; Narevicius, J.; Rybtchinski, B.; Lahav, M.; van der Boom, M. E. Dual Function Metallo–Organic Assemblies for Electrochromic–Hybrid Supercapacitors. *Adv. Mater. Interfaces* **2020**, *7*, 2000718.
<https://doi.org/10.1002/admi.202000718>.

-
- (89) Laschuk, N.; Ebralidze, I.; Easton, E.; Zenkina, O. Systematic Design of Electrochromic Energy Storage Devices Based on Metal–Organic Monolayers. *ACS Appl. Energy Mater.* **2021**, *4*, 3469–3479.
<https://doi.org/10.1021/acsaem.0c03218>.
- (90) Mondal, S.; Yoshida, T.; Maji, S.; Ariga, K.; Higuchi, M. Transparent Supercapacitor Display with Redox-Active Metallo-Supramolecular Polymer Films. *ACS Appl. Mater. Interfaces* **2020**, *12*, 16342–16349.
<https://doi.org/10.1021/acsami.9b23123>.

Ligand Structure Dependent Molecular Permeability and Spectroelectrochemical Diversification in Electrochromic Metallopolymers



2.1. Abstract

Designing surface-confined molecular assemblies capable of expressing the slight variations in their chemical structure in modulating their functional properties is a challenge. In this study, we used three tetra-terpyridine ligands with variations in their core architecture (phenyl vs tetraphenylethynyl vs bithiophene) to create spray-coated electrochromic assemblies of iron(II) based coordination polymer network films on transparent conducting oxide substrates. These thin films exhibited molecular permeability and spectroelectrochemical properties that are in turn dictated by the ligand structure. Electrochromic films with high coloration efficiencies (up to 1050 cm²/C) and superior optical contrast (up to 76%) with a concomitant color-to-color redox transition were readily achieved. These functional switching elements were further integrated into sandwich-type electrochromic cells with coloration efficiencies up to 641 cm²/C that exhibited a contrast ratio >56%, attractive ON-OFF ratios, fast switching kinetics, and high operational stability. Almost every measurable spectroelectrochemical property (redox window, optical contrast, switching kinetics, voltage response, cycling stability, and coloration efficiency) of the films and devices is a function of the ligand structure that coordinates the same metal ion. While exhibiting a ligand structure induced porosity and spectroelectrochemical diversification, these assemblies also allow for the creation of electrochromic patterns and images without the need for expensive lithographic techniques or printing.

2.2. Introduction

A major contribution to the vicious problem of global warming originates from increasing energy demand. The solution, hence, demands more adept energy utilizing and efficient smart systems, which could further open the doors for future industrial growth.^{1,2} Therefore, new materials with designed functions are to be actively explored for driving next-generation clean and efficient energy technologies.³⁻⁵ In this context, electrochromic devices (ECDs) that belong to the family of smart devices with a low energy footprint are envisioned to contribute to efficient energy utilization and management, especially for regulating indoor energy consumption.^{6,7} Electrochromic materials are a class of ‘smart materials’ that can change their optical properties under the application of an electric voltage. The tunable optical properties of electrochromic materials can be linked to the transmission of light and heat, leading to efficient indoor lighting and cooling, aesthetics as well as glare reduction. For instance, the dynamic modulation of heat and light transmission through smart windows could be directly correlated to the energy consumption in maintaining the indoor temperature and visibility; thus a significant portion of domestic energy consumption could be reduced. Further, the energy released during the switching process may be utilized for lighting or storage applications.

While a number of materials are being explored for electrochromic color switching, the real-world applications of such systems are hindered by exorbitant cost, low optical contrast, moderate to low efficiency, laborious processibility, slow color switching and relatively low cycle life.⁸⁻¹⁰ Metal oxides and conjugated polymers have been extensively investigated as efficient electrochromic materials.¹¹⁻¹³ The large-scale application of the former class of materials, though one among the best reported EC systems,^{9,14} is limited by the high cost of vacuum processing. Therefore, solution processible materials that change color efficiently with low applied voltages are of contemporary interest.¹⁵

In contrast to the deeply investigated and well documented organic polymers and inorganic metal oxides, hybrid metal-organic materials are yet under-explored for their potential towards electrochromic smart applications. While the inorganic EC materials are comparably more stable, the organic ones exhibit better energy efficiency and processability. A judicious combination of better stability, high efficiency, facile processability and high performance is rarely accomplished with either organic or inorganic electrochromic materials. Hence rational design of hybrid metal-

organic assemblies would be the best deterrent against the disadvantages of the well-studied organic and inorganic electrochromic materials.

Coordination-based metal-organic thin films are a relatively less investigated class of electrochromic systems, with excellent prospects in terms of optical contrast, ease of switching,^{16,17} redox reversibility, facile processibility,^{18,19} low power consumption, and high cycle life.²⁰⁻²² While the rational design of porous materials has opened up exciting avenues for several applications,^{23,24} nanoscopic control over the internal structure of surface-confined porous metal-organic networks with in-plane periodicity is scarcely reported.²⁵ Owing to their rich structural diversities, metallosupramolecular coordination polymers have attracted immense attention in catalysis, carbon capture,²⁶ color switching,²⁷ sensing, adsorption and separation, nanoarchitectonics, etc.²⁸⁻

30

Transition metal coordination complexes and their polymers exhibit electrochromic properties due to metal to ligand charge transfer, intervalence charge transfer, intra ligand excitation and visible region electronic transitions. A few reports on bipyridyl complexes $[M(\text{bipy})_3]^{2+}$ ($M = \text{Fe}, \text{Ru}, \text{Os}$), that are coloured in M^{II} (ground) state and colorless in the M^{III} (oxidized) state, clearly demonstrates the potential of these class of materials as candidates for practical EC systems. The design of ligands with delocalized π electron and rigid networks, in general, possess fast redox reactivity, stability and reversibility. Color tunability can be readily achieved by changing the metal ion, the ligand structure or the metal-ligand combination. These complexes and polymers can also be easily processed from their solutions and allows for different fabrication methods under non-stringent conditions. Metal-organic systems, that were previously considered to be an alternative to conventional and matured organic and inorganic electrochromic materials, has thus become a front runner as the candidate of choice for real world smart applications. Electrochromic color tunability in such metallosupramolecular polymers has been achieved using modular approaches, and their structure property relationship has been established.³¹⁻³⁴

Kurth *et al.* have reported the synthesis of metallosupramolecular polyelectrolytes (MEPEs) self-assembled from 1,4-bis[2,6-bis(2-pyridyl)pyrimidin-4-yl]benzene **1** and 5,5'-bis[2,6-bis(2-pyridyl)pyrimidin-4-yl]-2,2'-bithiophene) **2**, coordinated by Fe(II) and Co(II). Thin films of these metallopolymers were fabricated by dip coating on transparent conducting indium tin oxide (ITO) glass substrates that formed deep blue, intense green and red assemblies for Fe-**1**-MEPE, Fe-**2**-

MEPE and Co-2-MEPE respectively. Green to red and blue to colorless electrochromism were observed for Fe-2-MEPE and Fe-1-MEPE, respectively, confirming the effect of electrochromic properties on ligand structure (**Figure 2.1**).³¹ The Fe-MEPEs showed a reversible redox behavior corresponding to Fe^{II}/Fe^{III} transitions at 0.86 and 0.82 V with redox stability up to 50 switching cycles. Fe-2-MEPE exhibited near IR (1500 nm) absorption in the oxidized state due to ligand to metal charge transfer transitions in the bithiophene spacer.

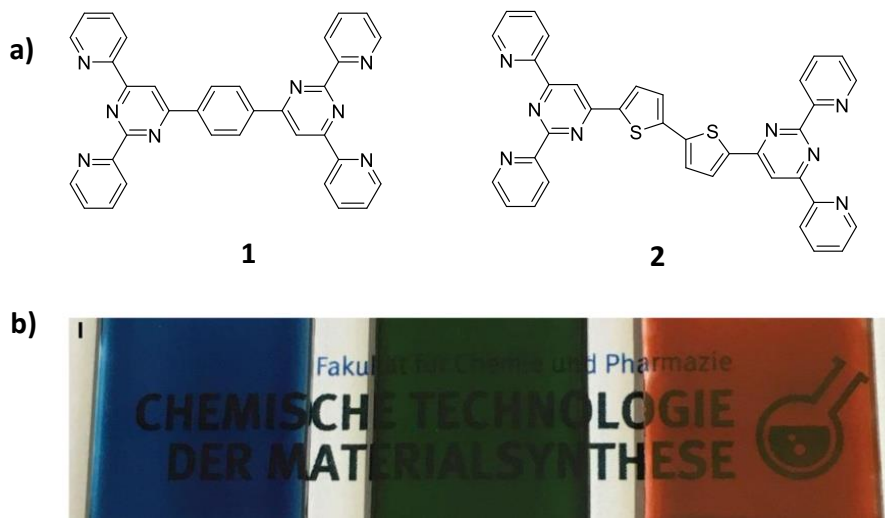


Figure 2.1. a) Chemical structure of the ligands **1** and **2**. b) Photographs of the thin films fabricated by dip coating solutions of Fe-1-MEPE (deep blue, 30 mM), Fe-2-MEPE (dark green, 14 mM), and Co-2-MEPE (red, 14 mM). Adapted with permission from ref 31.

Tunable spectroelectrochemical properties were also achieved using multi-metalated surface-confined assemblies.^{35,36} Nishihara and coworkers have synthesized electrochromic metallopolymer nanosheets comprising 1,3,5-tris(4-(2,2':6',2''-terpyridyl)phenyl)benzene **3** and Fe²⁺ or Co²⁺ as coordinating metal ions using a liquid/liquid interfacial strategy. Upon depositing on an indium tin oxide (ITO) electrode, the nanosheet showed a distinctive color change from blue to yellow and orange to purple for Fe-**3** and Co-**3** respectively. A hybrid device comprising of the thin films of Fe-**3** and Co-**3** showed “dual” electrochromism upon applying 2 V and 1 V, respectively (**Figure 2.2**).⁴²

Zenkina *et al.* have fabricated electrochromic devices that showed color to color transitions via the deposition of two or three metal complexes of the terpyridine **4** on ITO pre-covered with a templating 4-(chloromethyl)-phenylsiloxane layer (**Figure 2.3**). Upon application of suitable

potentials, Os–Fe systems exhibited two distinct color-to-color transitions: from orange-reddish to wasabi-green, and then to anzac-yellow (**Figure 2.3a**). Co–Fe ECDs showed only one-color transition from gray to brass-yellow upon oxidation of the iron species (**Figure 2.3b**).³⁵ While simultaneous deposition of equimolar Co(II), Os(II), and Fe(II) complexes resulted in higher Co(II) loading that results in insignificant color change, which is only perceptible by close observation. Co–Fe ECDs was found to possess a high coloration efficiency of 1583 cm²/C at 600 nm and a low switching time of 1.2 s and 1.4 s for coloration and bleaching, respectively.

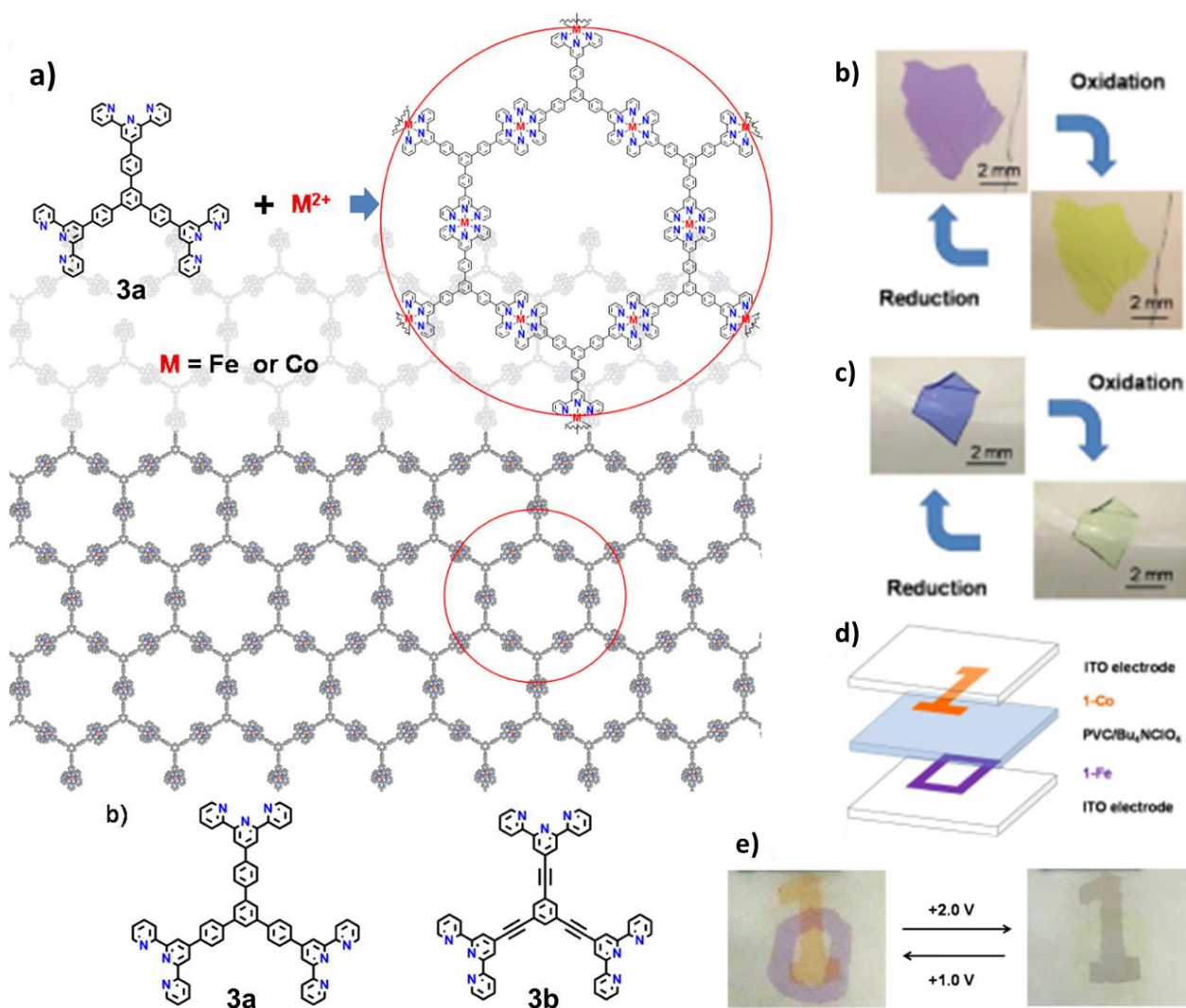


Figure 2.2. a) Chemical structure of the terpyridine-based ligands **3a,b** and the corresponding coordination nanosheets. Electrochromic color switching in b) Fe-**3a** (blue to yellow) and c) Fe-**3b** nanosheets (blue to yellow). d) Schematic representation of the hybrid electrochromic device and e) photographs upon application of 2 V and 1 V. Adapted with permission from ref 42.

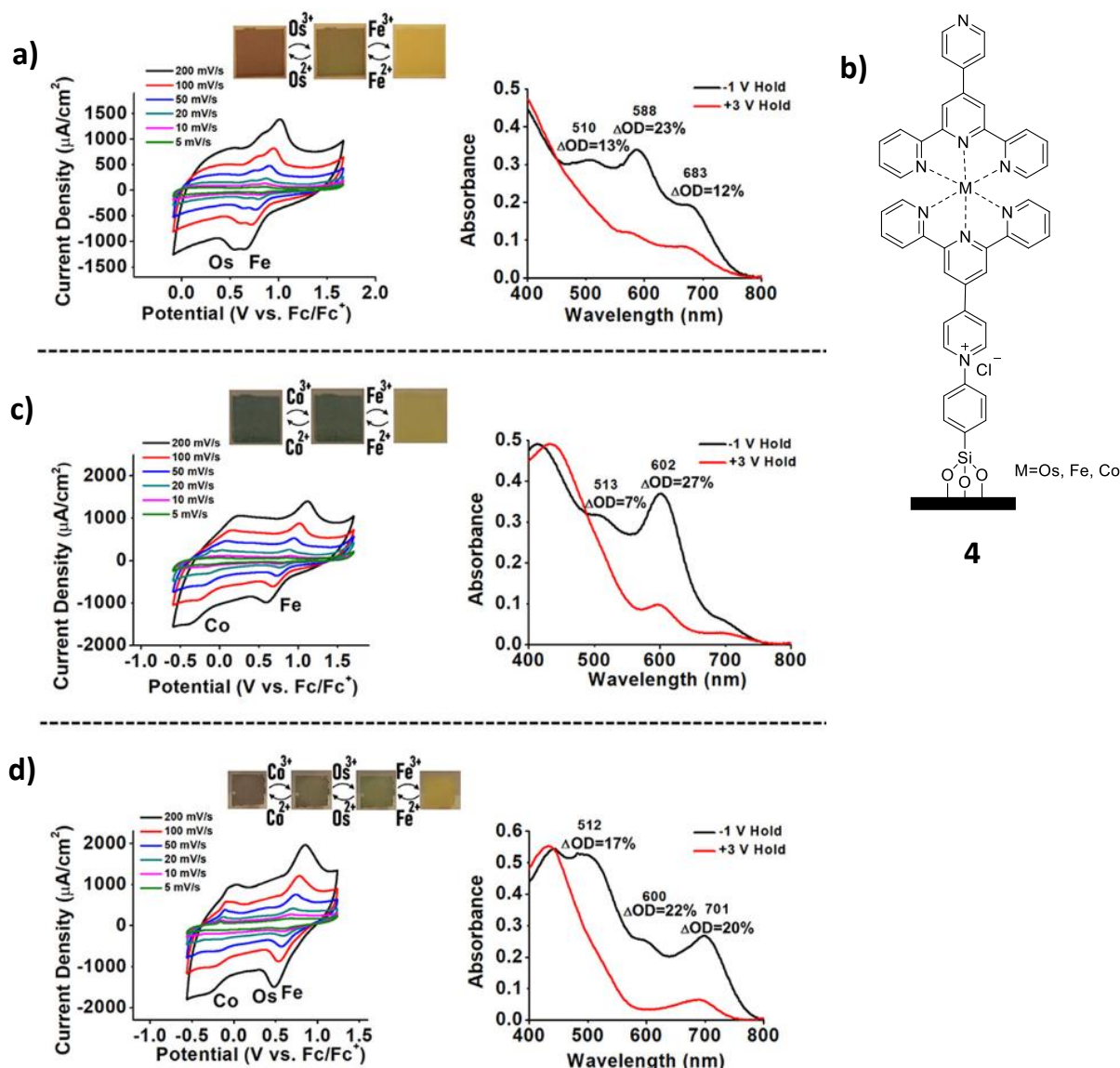


Figure 2.3. Cyclic voltammograms (CVs) at different scan rates and the corresponding spectroelectrochemistry of materials obtained by simultaneous deposition of isostructural a) Os and Fe complexes, c) Co and Fe complexes and d) Co, Os, and Fe complexes (3M) on ITO. Insets show photographs of ECDs demonstrating the color change due to oxidation and reduction of corresponding metal centers. b) Representative structure of the monolayer constructed from the metal complexes of ligand **4**. Adapted with permission from ref 35.

Shankar *et al.* have reported electrochromic molecular assemblies from bipyridine based Fe(II) complexes **5-8** with different pyridine-bipyridine bond order ($\text{H}_2\text{C}-\text{CH}_2$, $\text{HC}=\text{CH}$, $\text{C}\equiv\text{C}$) and the number of pyridine moieties using a layer-by-layer deposition process (**Figure 2.4a**). Thin films

constructed from palladium cross-linked assemblies of the Fe(II) complex **6** showed excellent coloration efficiency of $1488 \text{ cm}^2/\text{C}$ at 591 nm with exceptional stability exceeding 1.12×10^5 redox cycles. The thin films exhibited typical color to colorless transitions corresponding to $\text{Fe}^{2+/3+}$ redox switching (**Figure 2.4 b**). Electrochromic devices fabricated from these metallopolymeric assemblies also exhibited a similar color change from colored to transmissive states.¹⁶

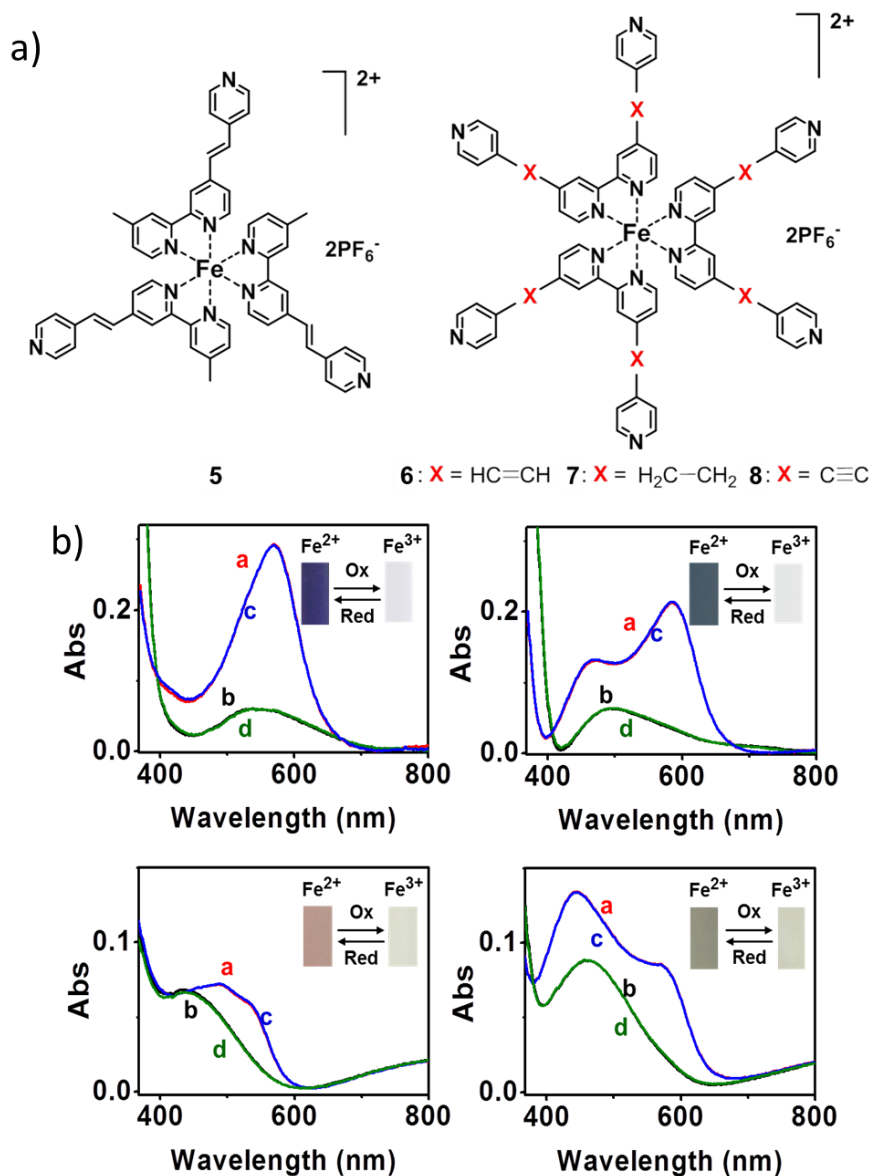


Figure 2.4. a) Chemical structure of the metal complexes **5-8**. c) Two consecutive redox switching and the corresponding color changes for the metallopolymeric assemblies constructed from the complexes **5-8**. Adapted with permission from ref 16.

The same group later extended this strategy by varying the central metal ion of the polypyridyl complexes (Os, Ru, and Fe) and electrochromic coatings that covered a large area of RGB color space were achieved by forming mixed assemblies of these complexes.¹⁷ The thin films thus obtained showed typically low voltage of operation (-2.5 V to 3 V), high coloration efficiency (474 cm²/C) and excellent switching stabilities up to 4000 cycles. Choudhury and coworkers have recently reported an electrochromic device containing a novel imidazolium-linked terpyridine ligand **9** coordinated to Fe(II), forming three-dimensional metal-organic coordination assemblies using a layer-by-layer dip coating method. The device exhibited a purple to colorless transition upon applying electric voltage (-2 V to 3.2V) with a reasonably high coloration efficiency of 275 cm²/C, optical contrast (40%) and cycling stabilities up to 4500 redox switchings (**Figure 2.5**).³⁷

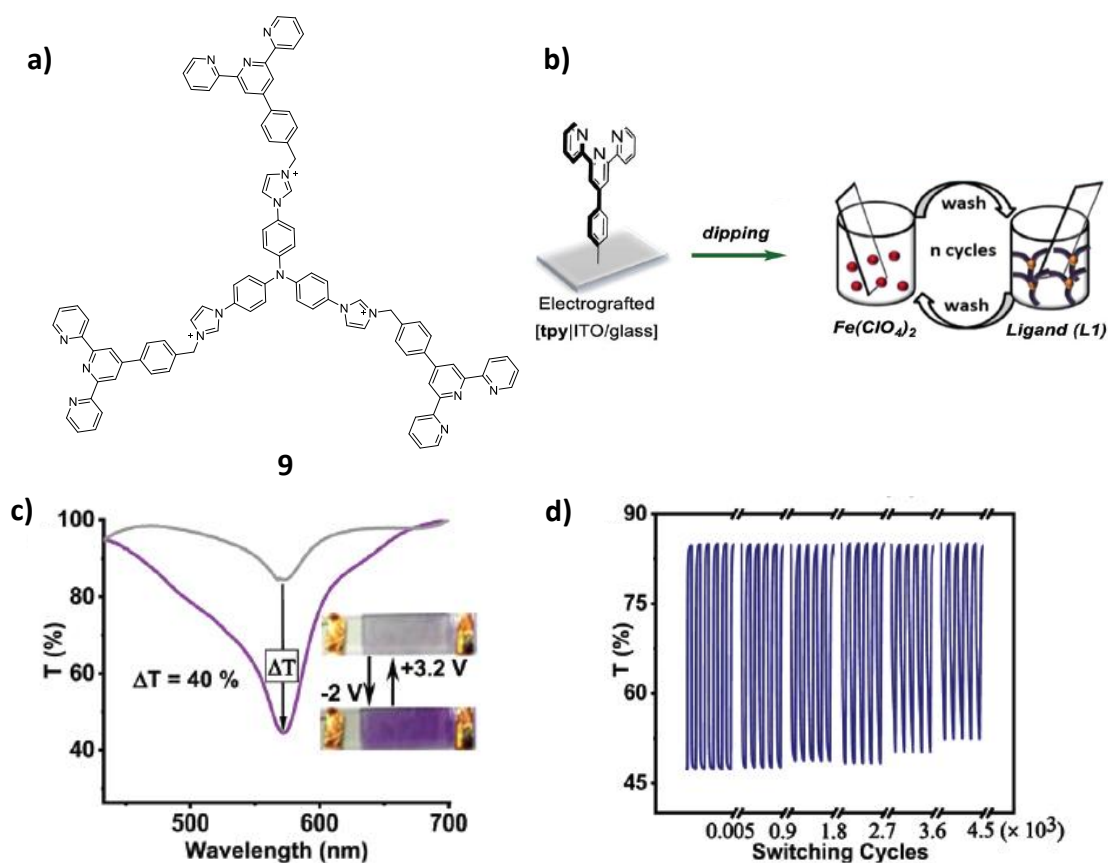


Figure 2.5. a) Chemical structure of the imidazolium-linked terpyridine ligand **9**. b) Schematic representation of formation of three-dimensional metal-organic coordination assemblies via layer-by-layer deposition. c) Transmittance change and the corresponding photographs and d) switching stability of the assemblies upon applying potentials of -2 V and 3.2 V in the device state. Adapted with permission from ref 37.

While ditopic terpyridine ligand systems are extensively investigated as electrochromic materials, metal ion induced electrochromic assemblies of tetratopic terpyridines have rarely been reported. Structural modification using electron-withdrawing/donating groups may have a predictable impact on the electrochromic attributes of such materials. In this regard, the effect of the interaction of metal ions with conducting polymers on their electrochromic activity for the detection of Cu(II) has been reported.³⁸ However, electrochemical diversification based on small variations in the core architecture of the otherwise similar molecular components in their thin film states are hard to predict. A fundamental understanding of the internal structure, porosity, and transport of electrons or materials within electrochromic thin films mandated at effectively modulating their properties is in need of attention.^{39,40} Combined with complex electron and mass transfer processes, a diverse electro-optical behavior of such systems, while efficiently modulating their smart response, is extremely difficult to achieve.⁴¹

In this study, we demonstrate the use of simple Fe(II) metallocupramolecular polymer network films (MPNFs)⁴² derived from tetra-terpyridine ligands **Ph-TPy**, **TPE-TPy** and **Thio-TPy** (**Figure 2.6a**) leading to electrochromic redox active interfaces with control over their permeability and electro-optical properties. These electrochromic (EC) assemblies are deeply colored in their reduced ground state (Fe^{2+}), whereas electrochemical oxidation (Fe^{3+}) leads to a reversible change in color to yellow. Exceptionally high coloration efficiencies (CE up to $1050 \text{ cm}^2/\text{C}$) were obtained for the spray coated films. While this metallopolymers are among the rare examples of octahedral iron terpyridine based EC materials showing a color-to-color transition, electrochromic devices (ECDs) fabricated from these nanoscopic films ($165 \pm 6 \text{ nm}$ thick) exhibited high coloration efficiencies (up to $641 \text{ cm}^2/\text{C}$), cycling stability (1000 redox switchings) and optical contrast (up to 56%). The films and devices were found to switch colors with relatively low response times (0.5-3 s). This study provides one of the first examples of metallopolymers with similar solution electrochemistry, where designed variations in ligand structure dictates the spectroelectrochemical signature (redox potential, optical contrast, response time, voltage response, cycling stability, and coloration efficiency) and molecular permeability of the surface confined assemblies in both film and device configurations.

2.3. Results and Discussion

2.3.1. Synthesis and Characterization

Three tetraterpyridine-based ligands (**Ph-TPy**, **TPE-TPy**, and **Thio-TPy**; **Figure 2.6a**) with variations in their central core (phenyl, tetraphenyl ethynyl and bithiophene) were synthesized by palladium catalyzed Suzuki coupling of the corresponding tetrabromo compound **13**, **16** or **17** with the boronic acid derivative of terpyridine **12**. The details regarding the synthetic procedure and characterization are provided in the experimental section. Metallopolymers of these tetraterpyridine-based ligands (**Fe(II)-Ph-TPy**, **Fe(II)-TPE-TPy**, and **Fe(II)-Thio-TPy**; **Figure 2.6b**) were prepared using Fe(II) as the coordinating metal. Typically, a methanolic solution containing 2 equiv. of FeCl₂·4H₂O was added to a chloroform solution of the corresponding ligand and stirred for a few minutes to obtain the spray coatable solution of the metallosupramolecular polymers. The formation of the metallopolymers was confirmed by the emergence of characteristic MLCT bands in the UV–vis spectra along with a concomitant decrease in ligand emission. Increasing the concentration above 300 μM in any solvent led to instantaneous precipitation, further corroborating the formation of the metallopolymers. FT- IR showed a shift of C=C stretching vibrations from 1582–1585 to 1600–1603 cm⁻¹, which is characteristic for the metal complexation of terpyridine ligands.

As prepared methanolic solutions of the Fe(II) metallopolymers (0.3 mM) were spray-coated to generate multilayer assemblies. In a typical procedure, the solution of the corresponding metallopolymer was sprayed using a semi-automated dispensing system that dispenses fluids in a preprogrammed pattern onto freshly cleaned FTO glass substrates at a line speed of 150 mm/s and a ptp speed of 200 mm/s. 10 consecutive sprays of the metallopolymer solutions was considered as one deposition step. The electroactive components of these assemblies are well defined coordination complexes bridged by Fe(II) centers.⁴³ Terpyridine ligands generally bind divalent metal ions to form bis terpyridine complexes with a defined D_{2d} symmetry and near octahedral geometry. Such metal terpyridine assemblies form metallopolymer network films (MPNFs) and are known to exhibit one electron redox behavior generally characterized by a highly colored ground state (Fe²⁺) and an almost transparent oxidized state (Fe³⁺). The intense color in the ground

state of these metallopolymers is characterized by strong metal to ligand charge transfer (MLCT) with high molar extinction coefficients ($\epsilon \sim 3 - 5 \text{ M}\cdot\text{cm}^{-1}$ in methanol solutions, **Figure 2.7**).⁴⁴

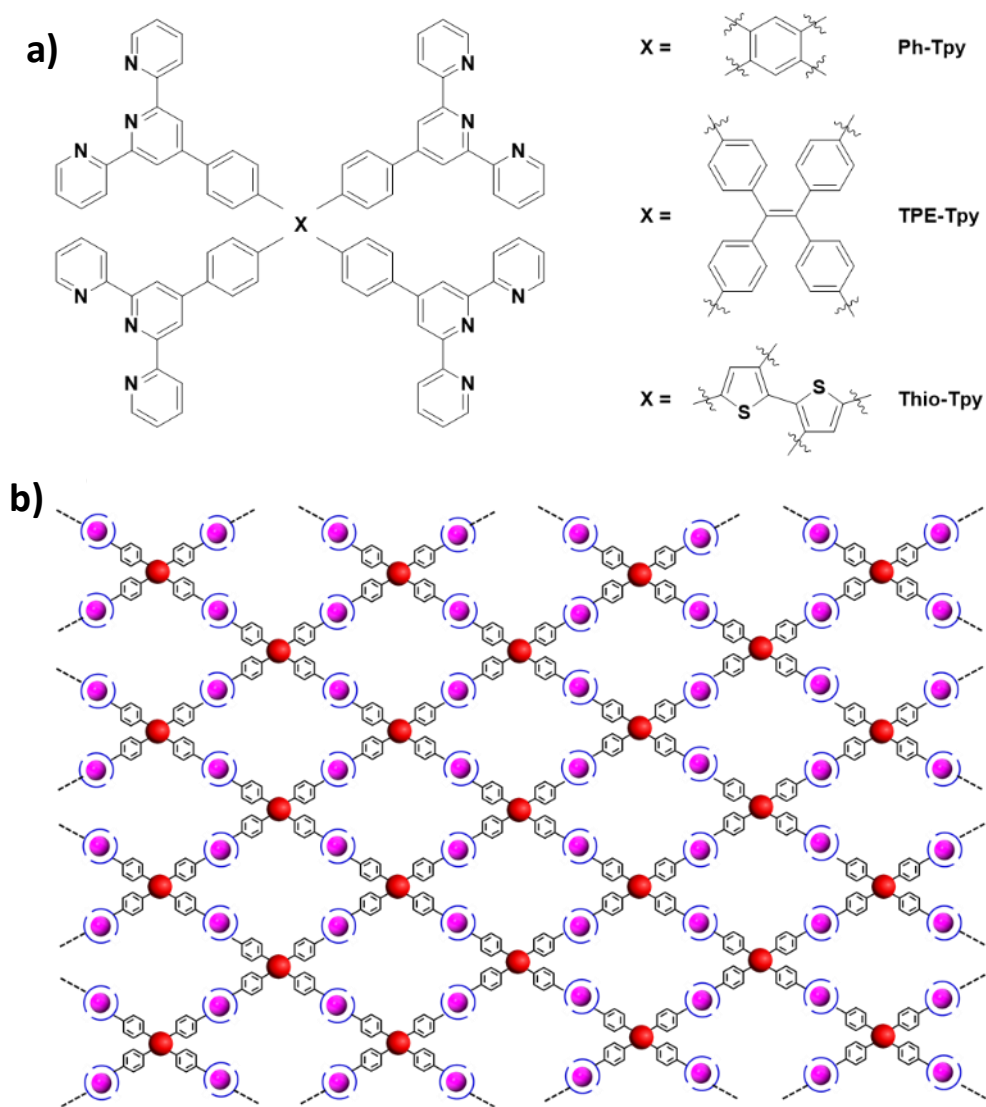


Figure 2.6. a) Molecular structures of the terpyridine ligands used in this study. b) A schematic illustration of the structure of the coordination polymers. The core (Ph, TPE, Thio) is shown in red, the coordinating terpyridines are shown in blue and Fe(II) is shown in pink. The corresponding metallopolymers are denoted as **Fe(II)-Ph-TPy**, **Fe(II)-TPE-TPy** and **Fe(II)-Thio-TPy**.

The metallosupramolecular assemblies were characterized using UV-vis spectroscopy, atomic force microscopy (AFM), X-ray photoelectron spectroscopy (XPS), electrochemistry and spectroelectrochemistry, in addition to thickness measurements using profilometer. *Ex situ*

absorption spectra measured after alternate deposition steps and thickness measurements confirmed a ligand structure independent exponential growth model for these nanoscopic assemblies (**Figure 2.8a-d**).

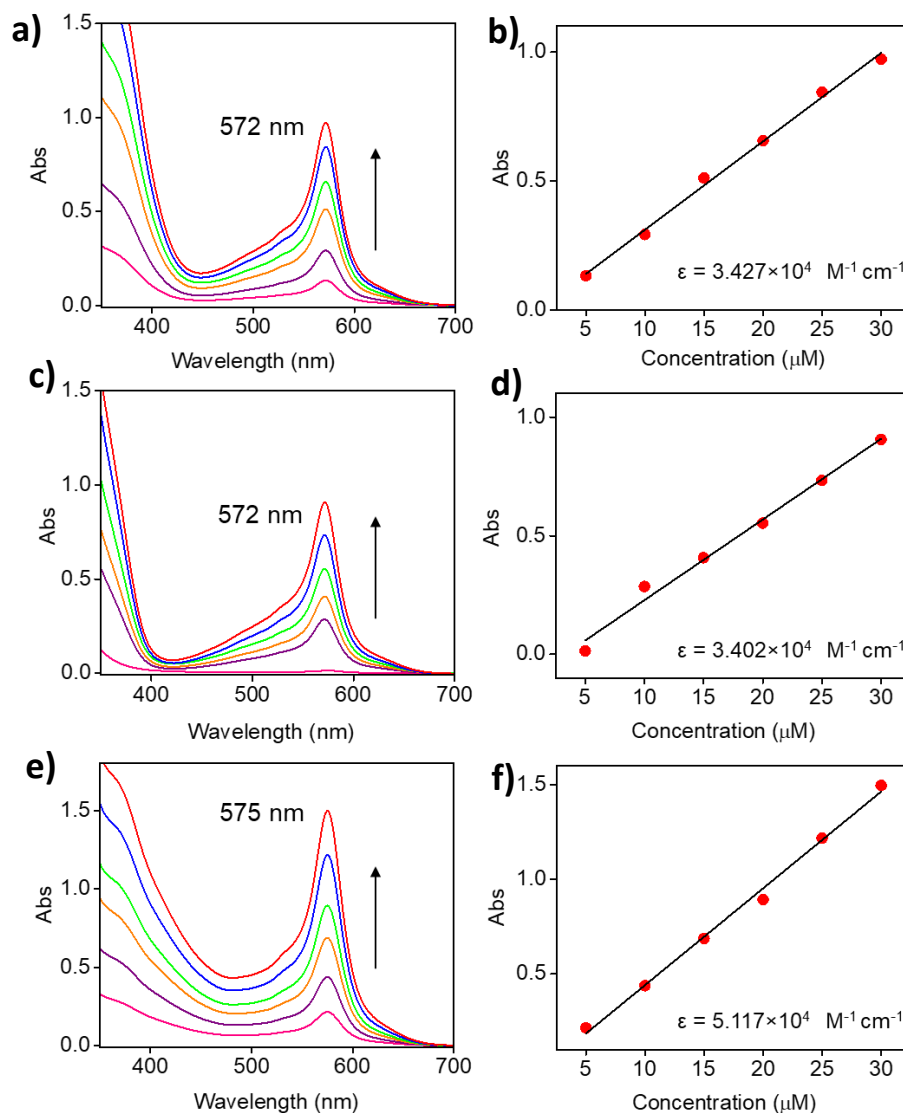


Figure 2.7. Concentration (5-30 μM) dependent UV-vis spectra of a) **Fe(II)-Ph-Tpy**, c) **Fe(II)-TPE-Tpy** and e) **Fe(II)-Thio-Tpy** in MeOH. The linear correlation between the MLCT band intensity and concentration for b) **Fe(II)-Ph-Tpy** (λ_{MLCT} : 578 nm), d) **Fe(II)-TPE-Tpy** (λ_{MLCT} : 580 nm) and f) **Fe(II)-Thio-Tpy** (λ_{MLCT} : 584 nm). The corresponding molar extinction coefficients are calculated from the slopes of the Abs vs concentration plots. The experiments were conducted in quartz cuvettes at room temperature. The corresponding measurement using MeOH provided the baseline.

The intensity of the characteristic λ_{MLCT} (578 nm for **Fe(II)-Ph-Tpy**, 580 nm for **Fe(II)-TPE-Tpy** and 584 nm for **Fe(II)-Thio-Tpy**) and thickness of the metallopolymers increased exponentially with deposition steps (**Figure 2.8**). A second MLCT band at wavelengths <400 nm was also observed for all these thin films (**Figure 2.8 a-c**). The variations in the core group resulted in different shades of purple to brownish colors for these coordination polymer network films (**Figure 2.8a-c**, insets).

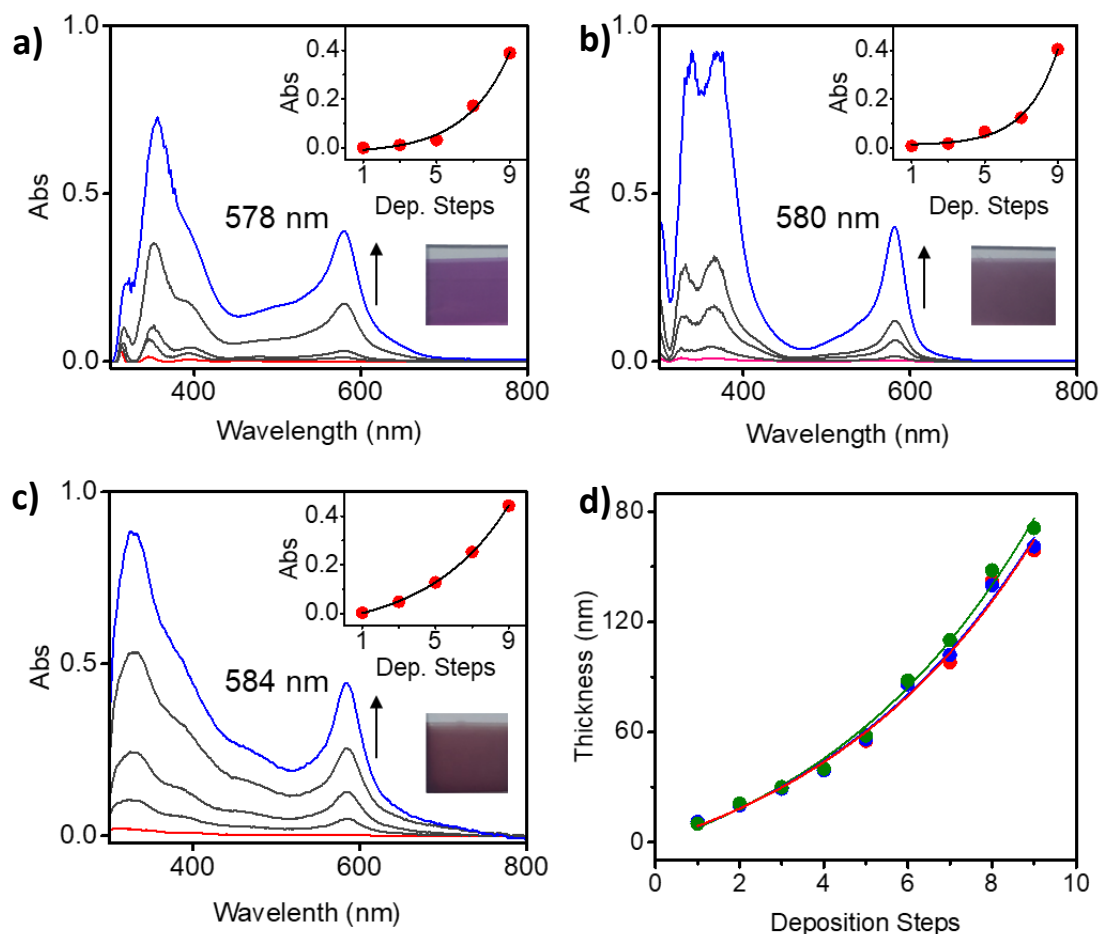


Figure 2.8. UV-vis spectra of the assemblies formed by spray coating methanol solutions (0.3 mM) of the ligands containing 2 equivalents of FeCl_2 : a) **Ph-Tpy**, b) **TPE-Tpy** and c) **Thio-Tpy**. The MLCT wavelengths are also shown. The exponential increase in the absorbance of the MLCT bands with the number of deposition steps and the corresponding photographs of FTO-glass substrates ($3 \text{ cm} \times 3 \text{ cm}$) after 9 deposition steps are shown in the insets. $R^2 > 0.99$ for all fits. d) The change in the thickness of the spray coated films with the number of deposition steps for the assemblies obtained using Fe(II) MPs of **Ph-Tpy**, (red), **TPE-Tpy** (blue) and **Thio-Tpy** (green). $R^2 > 0.99$ for all fits.

AFM images showed grain like morphologies for all the MPNFs (**Figure 2.9**). The films of **Fe(II)-Thio-TPy** were found to be composed of uniformly sized grains (45 ± 5 nm), while the others exhibited a larger size distribution. The films obtained from **Fe(II)-TPE-TPy** revealed the prevalence of clustered grains. Consequently, these films had a comparably higher roughness ($R_{\text{rms}}\sim 35$ nm), while those based on **Fe(II)-Ph-TPy** and **Fe(II)-Thio-TPy** exhibited a slightly smaller roughness ($R_{\text{rms}} = 23 \pm 2$ nm), after 9 deposition steps. All the MPNFs appeared rather free of defects to the naked eye (**Figure 2.8**, insets).

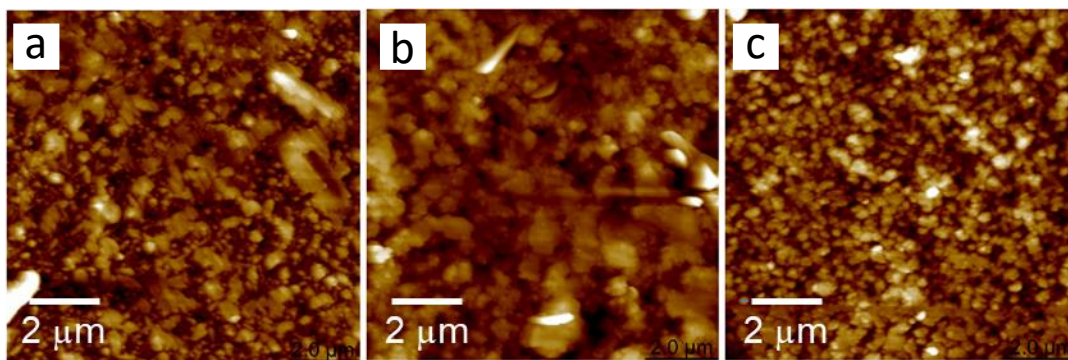


Figure 2.9. AFM images ($10\ \mu\text{m} \times 10\ \mu\text{m}$) of the MPNFs constructed from a) **Fe(II)-Ph-TPy**, b) **Fe(II)-TPE-TPy** and c) **Fe(II)-Thio-TPy** after 9 deposition steps. The thickness of the assemblies was 165 ± 6 nm.

The cyclic voltammograms of the assemblies also corroborated a similar deposition pattern characterized by an exponential increase in the current density with the number of deposition steps (**Figure 2.10a-f**). A linear correlation between the thickness of the assemblies and current densities up to nine deposition steps suggests that nearly all metal centers remain electroactive at least until a thickness of 165 ± 6 nm (**Figure 2.10g-i**). The current densities for all the assemblies, in both oxidative and reductive directions, vary linearly with scan rate ($10\text{-}600\ \text{mVs}^{-1}$) and exponentially with the square root of scan rate (**Figure 2.11**). This observation is indicative of a surface confined electrochemical redox process that is not limited by slow diffusion.⁴⁴

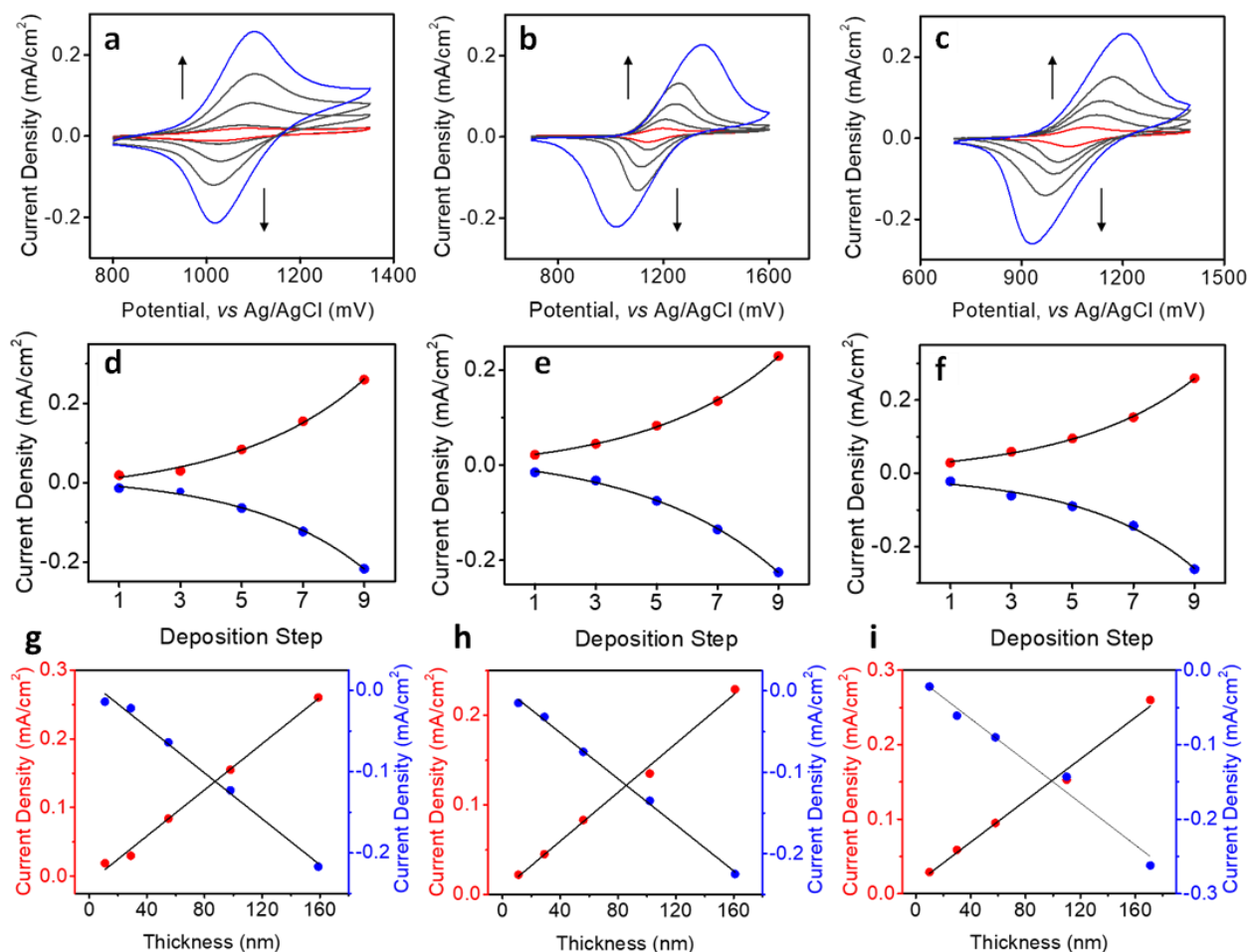


Figure 2.10. Cyclic voltammograms of the assemblies formed by spray coating the methanol solutions (0.3 mM) of the ligands containing 2 equivalents of FeCl_2 : a) **Ph-Tpy**, b) **TPE-Tpy** and c) **Thio-Tpy**. The exponential increase in the current densities (d-f) and the linear correlation between current densities and film thickness (g-i) for the assemblies constructed from d,g) **Fe(II)-Ph-Tpy**, e,h) **Fe(II)-TPE-Tpy** and f,i) **Fe(II)-Thio-Tpy** with the number of deposition steps. The current densities in the oxidative and reductive directions are shown in red and blue circles, respectively. $R^2 > 0.99$ for all fits. The CV experiments were carried out using the modified FTO substrate as the working, Ag/AgCl as reference and platinum wire as counter electrodes, at a scan rate of 100 mV s^{-1} . $0.1 \text{ M } ^t\text{Bu}_4\text{PF}_6$ in acetonitrile was used as the supporting electrolyte.

While the growth models, thickness, and overall morphologies of the coordination-based assemblies are found to be more or less unaffected by the variations in the core structure of the parent ligands, the electrochemical and spectroelectrochemical profiles indeed depend on the

ligand structure. For instance, all the Fe(II) metallopolymers in solution (acetonitrile, 15 μM) exhibited similar redox potentials, however, the oxidation and reduction potentials of the films obtained after nine deposition steps were distinctly different, with a larger peak-to-peak separation (**Figure 2.12, Table 2.1**).

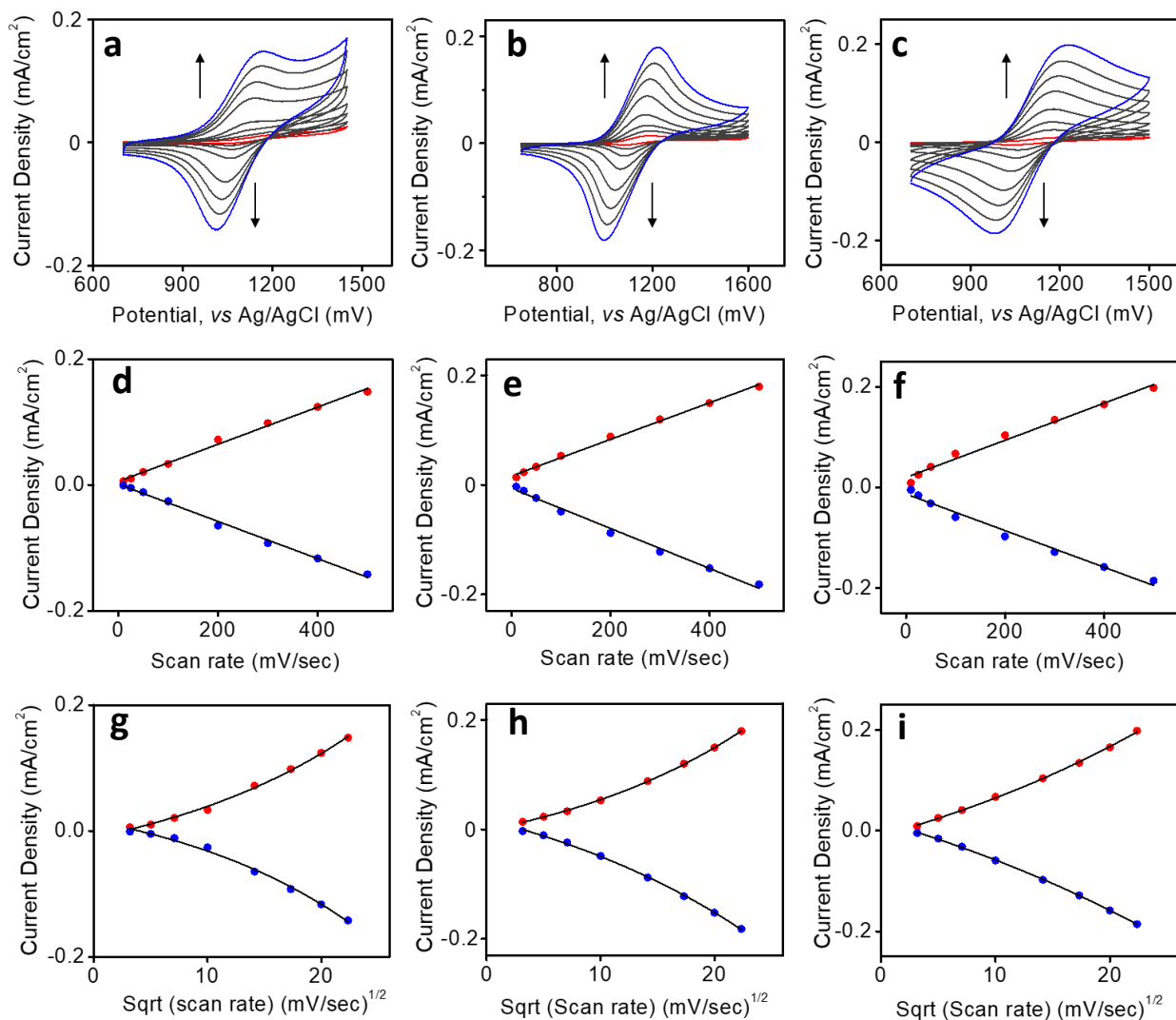


Figure 2.11. CVs of the MPNFs (56.5 ± 1.5 nm, 5 deposition steps) constructed from a) **Fe(II)-Ph-TPy**, b) **Fe(II)-TPE-TPy** and c) **Fe(II)-Thio-TPy** at varying scan rates: 10 mV s^{-1} (red) - 600 mV s^{-1} (blue). Linear correlation between the current densities and scan rate (d,e,f) and exponential correlation between the current densities and square root of scan rate (g,h,i) for the MPNFs of d,g) **Fe(II)-Ph-TPy**, e,h) **Fe(II)-TPE-TPy** and f,i) **Fe(II)-Thio-TPy**. $R^2 > 0.99$ for all fits.

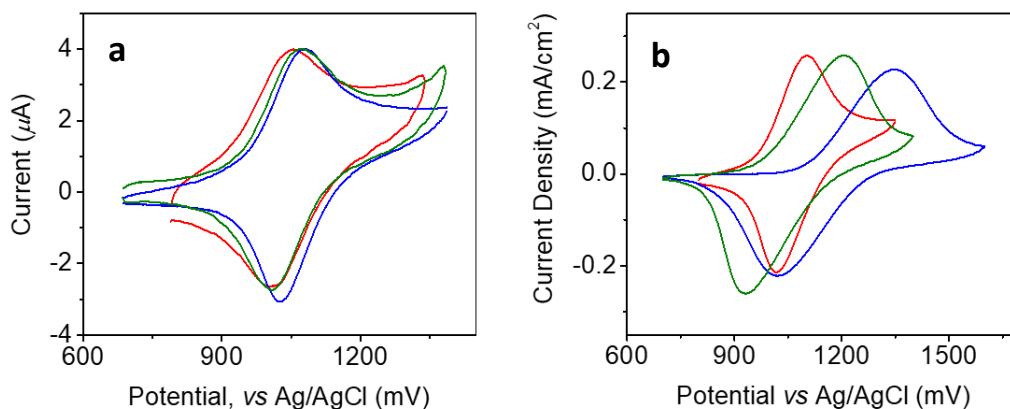


Figure 2.12. CVs of the metallopolymer **Fe(II)-Ph-TPy** (red), **Fe(II)-TPE-TPy** (blue) and **Fe(II)-Thio-TPy** (green) in a) solution (15 μM in acetonitrile) and b) on FTO substrates (165 \pm 6 nm, 9 deposition steps). The experiments were carried out at a scan rate of 100 mV s^{-1} , using glassy carbon (solution) / modified FTO substrate (film), Ag/AgCl and platinum wire as working, reference and counter electrodes, respectively. 0.1 M tBu_4NPF_6 in acetonitrile was used as the supporting electrolyte.

Table 2.1. Redox potentials of the CPs in solution and film state.^a

CP	E_{ox} (V)	E_{red} (V)	Peak to Peak sepn. (V)	$E_{1/2}$ (V)
Fe(II)-Ph-TPy (soln) ^b	1.06	1.01	0.05	1.04
Fe(II)-Ph-TPy (film) ^c	1.10	1.02	0.08	1.06
Fe(II)-TPE-TPy (soln) ^b	1.08	1.02	0.06	1.05
Fe(II)-TPE-TPy (film) ^c	1.21	1.02	0.19	1.12
Fe(II)-Thio-TPy (soln) ^b	1.08	1.01	0.07	1.05
Fe(II)-Thio-TPy (film) ^c	1.35	0.93	0.42	1.14

^aSee **Figure 2.12**. ^bThe experiments were carried out at a scan rate of 100 mV s^{-1} , using glassy carbon, Ag/AgCl and platinum wire as working, reference and counter electrodes, respectively. 15 μM solutions of the CPs were used. 0.1 M Bu_4PF_6 in acetonitrile was used as the supporting electrolyte. ^cThe experiments were carried out at a scan rate of 100 mV s^{-1} , using CPNF modified FTO, Ag/AgCl and platinum wire as working, reference and counter electrodes, respectively. 0.1 M Bu_4PF_6 in acetonitrile was used as the supporting electrolyte.

After nine deposition steps, the molecular assemblies constructed using **Fe(II)-Ph-Tpy**, **Fe(II)-TPE-Tpy** and **Fe(II)-Thio-Tpy** exhibited characteristic $\text{Fe}^{2+/3+}$ redox couple with half-wave potentials ($E_{1/2}$) of 1.06 V, 1.12 V and 1.14 V, respectively (**Figure 2.12b**, **Table 2.1**). This single

electron redox process is accompanied by a visually perceivable change in color. While many Fe oligopyridine systems generally exhibit a color-to-colorless redox behavior,³⁷ we observed typical color-to-color transitions. Electrochemical oxidation leads to a decrease in the intensity of the MLCT bands with a concomitant increase in ligand-centered charge transfer transitions, leading to a yellow color in the oxidized state (**Figure 2.13**). The effect of the variations in ligand structure was evident in the optical contrast at λ_{MLCT} and was found to be higher for the assemblies constructed from **Fe(II)-Ph-Tpy** (>76%), followed by those from **Fe(II)-Thio-Tpy** (>60%) and **Fe(II)-TPE-Tpy** (~40%) upon switching within a potential window of 0.8 V – 1.3 V (**Figure 2.13**).

2.3.2. Spectroelectrochemical Diversification in the Film State

The spectroelectrochemical properties of the assemblies were investigated using double potential steps and were recorded as optical changes over time (**Figure 2.14**). Response time defined as the time required for the change in transmittance ($\Delta\%T$) to become 90-95% of the maximum change in transmittance ($\Delta\%T_{\text{max}}$). However, switching time is often reported as the time taken for the coloring/bleaching process of an EC material. These parameters are experimentally determined by correlating the time required for the specific change in the corresponding optical properties at an applied potential using chromoabsorptometric techniques. The overall pulse width dependent changes in the contrast ratios of **Fe(II)-TPE-Tpy** MPNFs was found to be due to the combined effect of increase in %T during bleaching (oxidation) and a concomitant decrease in %T during coloration (reduction, **Figure 2.14b, 2.14e**). However, %T during coloration of **Fe(II)-Ph-Tpy** and **Fe(II)-Thio-Tpy** based films were found to be more or less independent of pulse width (>2 s, **Figure 2.14a,c, 2.14d,f**). Therefore, the overall changes in contrast ratios for these films stem almost exclusively from the increase in %T during bleaching (oxidation). Thus, the ligand structure is directly expressed in the ease of redox reactions in these MPNFs: oxidation and reduction are equally demanding for the films of **Fe(II)-TPE-Tpy**; near complete reduction of Fe^{3+} centers to Fe^{2+} is facile even at low switching times (2 s) in **Fe(II)-Ph-Tpy** and **Fe(II)-Thio-Tpy** based films; the oxidation process ($\text{Fe}^{2+} \rightarrow \text{Fe}^{3+}$), on the other hand, is rather difficult when the pulse width is low.

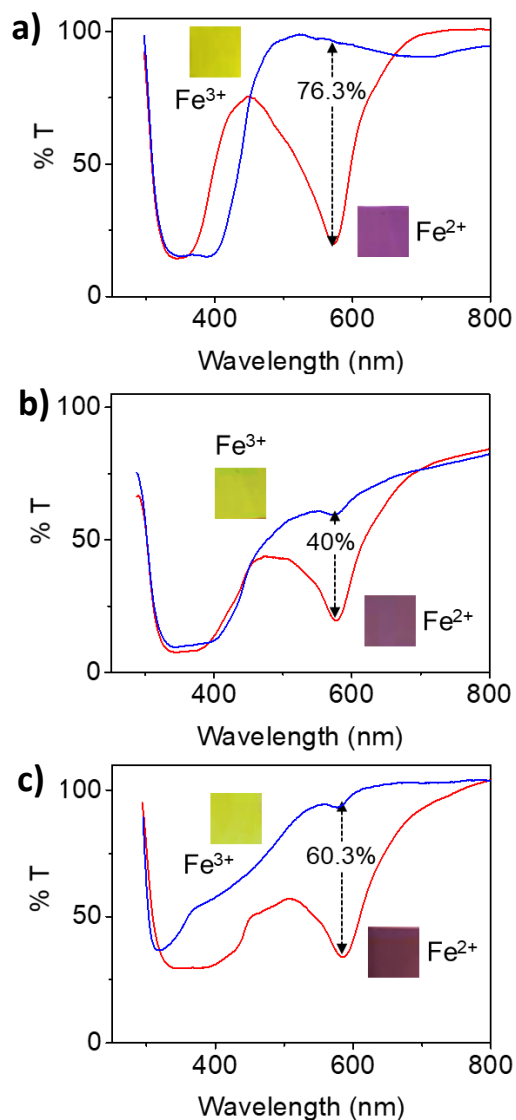


Figure 2.13. Transmittance spectra of the metal-organic assemblies showing the bleaching of the MLCT bands during electrochemical oxidation of the assemblies constructed from a) **Fe(II)-Ph-Tpy**, b) **Fe(II)-TPE-Tpy** and c) **Fe(II)-Thio-Tpy**. The spectra of the assemblies in their reduced and oxidized states are shown in red and blue, respectively. The color pallets of the corresponding assemblies are shown in the insets. The experiments (at λ_{MLCT} : 578 nm for **Fe(II)-Ph-Tpy**, 580 nm for **Fe(II)-TPE-Tpy** and 584 nm for **Fe(II)-Thio-Tpy**) were carried out using the modified FTO substrate as the working electrode, Ag/AgCl as reference electrode and platinum wire as counter electrode. 0.1 M tBu_4NPF_6 in acetonitrile was used as the supporting electrolyte. A potential window of 0.8 V – 1.3 V was used for all experiments.

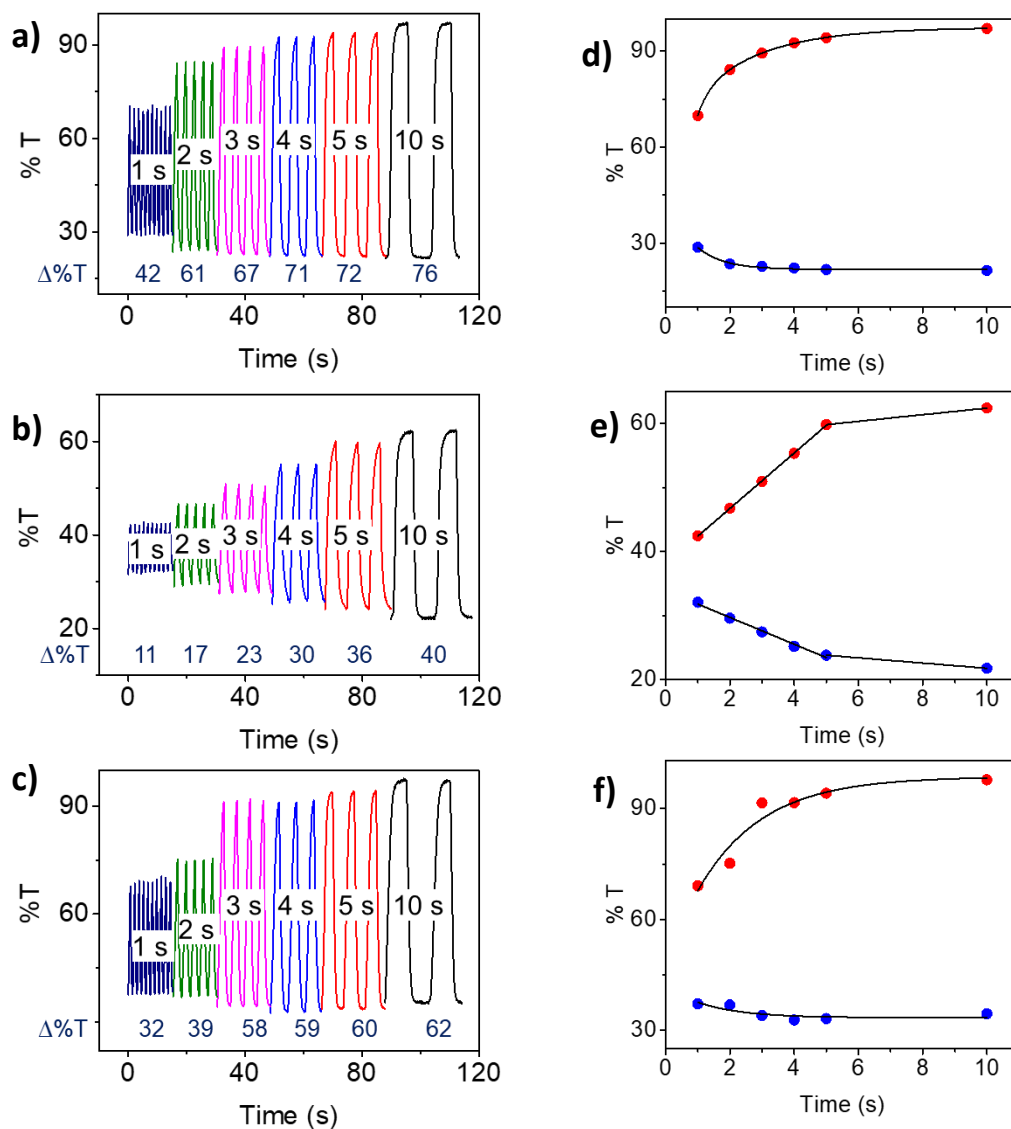


Figure 2.14. Chromoabsorptometry of the assemblies constructed from a) **Fe(II)-Ph-Tpy**, b) **Fe(II)-TPE-Tpy** and c) **Fe(II)-Thio-Tpy** at different switching times (pulse width). The change in transmittance (%) during coloration (blue) and bleaching (red) of the CPNFs constructed from d) **Fe(II)-Ph-Tpy**, e) **Fe(II)-TPE-Tpy** and f) **Fe(II)-Thio-Tpy** at different pulse width (1-10 s). The change in %T, rounded to the nearest whole number, at each pulse width is given below the corresponding switching cycle. The experiments (at λ_{MLCT} : 578 nm for **Fe(II)-Ph-Tpy**, 580 nm for **Fe(II)-TPE-Tpy** and 584 nm for **Fe(II)-Thio-Tpy**) were carried out using the modified FTO substrate as the working electrode, Ag/AgCl as reference electrode and platinum wire as counter electrode. 0.1 M tBu_4NPF_6 in acetonitrile was used as the supporting electrolyte. A potential window of 0.8 V – 1.3 V was used for all experiments.

The response time (time taken for >90% of the color to switch in oxidative and reductive directions) was also found to be a function of the ligand structure. The MPNFs based on **Fe(II)-Ph-Tpy** exhibited response times of 1.6 s and 1 s for bleaching and coloration, respectively, at a pulse width of 10 s (**Figure 2.15a**). The response times, under identical operational conditions, for **Fe(II)-TPE-Tpy** and **Fe(II)-Thio-Tpy** based assemblies were comparably higher: 2.6 s (bleaching), 1.4 s (coloration) and 2.9 s (bleaching), 1.4 s (coloration), respectively (**Figure 2.15b,c**). The observed fast coloration may be attributed to rapid injection of electrons (reduction, $\text{Fe}^{3+} \rightarrow \text{Fe}^{2+}$) and counter ions into the films as compared to electrochemically slower rejection of electrons (oxidation, $\text{Fe}^{2+} \rightarrow \text{Fe}^{3+}$) back to the electrode and counter ions into the electrolyte during bleaching.⁴⁵⁻⁴⁷

An equally important parameter that determines the performance of electrochromic systems is their coloration efficiency. Coloration efficiency (CE, η) is defined as the change in optical density per unit charge ejected or injected per unit area of the active electrode and may be calculated from the following equation:

$$\text{CE } (\eta) = \frac{\log (T_{\text{colored}}/T_{\text{bleached}})}{Q_d}$$

where, T_{colored} and T_{bleached} are the transmittance in the colored and bleached states, respectively, and Q_d is the charge ejected or injected per unit area of the active electrode. The molecular assemblies used in this study were found to have high coloration efficiencies (at λ_{MLCT}), but dictated by the core architecture of the parent ligands: **Fe(II)-Ph-Tpy** (1049.5 cm^2/C) > **Fe(II)-TPE-Tpy** (756.5 cm^2/C) > **Fe(II)-Thio-Tpy** (473.8 cm^2/C).

The subtle differences in the spectroelectrochemical properties of the assemblies with similar modes of deposition may be attributed to the differences in their internal arrangement and structure. XPS spectra of all three ligands **Ph-Tpy**, **TPE-Tpy** and **Thio-Tpy** showed the characteristic peak corresponding to the binding energy of N 1s at 398.8 eV (**Figure 2.16.a, d,g**). Characteristic peaks corresponding to Fe^{2+} 2p_{3/2} (708.85 ± 0.05 eV) and Fe^{2+} 2p_{1/2} (721.55 ± 0.05 eV) were unambiguously observed in the XPS spectra of **Fe(II)-Ph-Tpy**, **Fe(II)-TPE-Tpy** and **Fe(II)-Thio-Tpy** (**Figure 2.16.b,e h**). However, two peaks corresponding to N 1s (398.65 ± 0.15 eV, 399.75 ± 0.15 eV) were observed for the MPs as opposed to a single peak in the spectra of the parent ligands

(**Figure 2.16.c,f,i**). This observation is indicative of incomplete coordination of the terminal terpyridines. The ratio of the two N 1s peak areas is a direct measure of the extent of coordination in these assemblies.

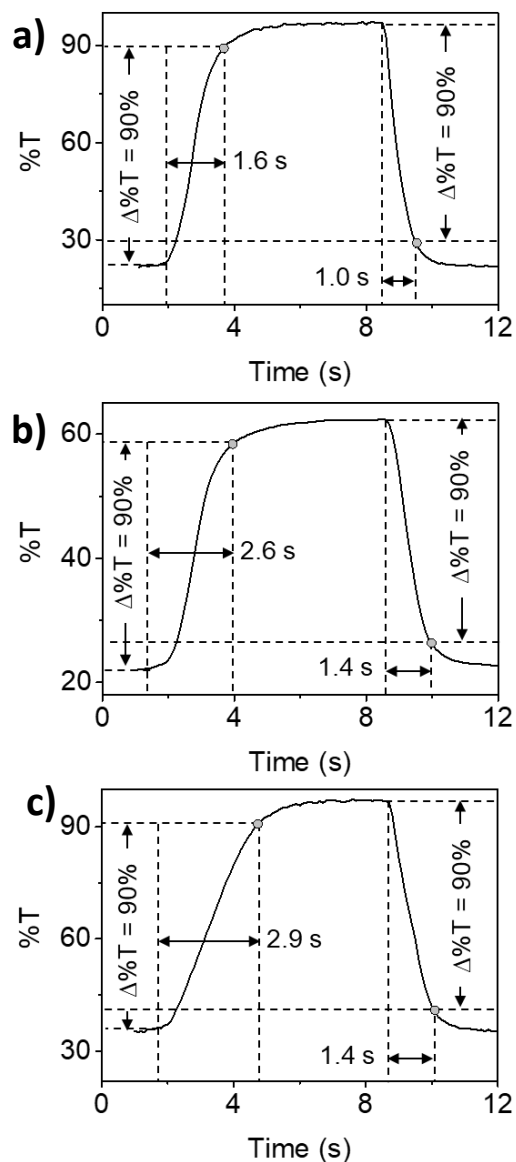


Figure 2.15. The response times for the assemblies of a) **Fe(II)-Ph-Tpy**, b) **Fe(II)-TPE-Tpy** and c) **Fe(II)-Thio-Tpy** at a pulse width of 10 s. The experiments (at λ_{MLCT} : 578 nm for **Fe(II)-Ph-Tpy**, 580 nm for **Fe(II)-TPE-Tpy** and 584 nm for **Fe(II)-Thio-Tpy**) were carried out using the modified FTO substrate as the working electrode, Ag/AgCl as reference electrode and platinum wire as counter electrode. 0.1 M tBu_4NPF_6 in acetonitrile was used as the supporting electrolyte. A potential window of 0.8 V – 1.3 V was used for all experiments.

While the MPNFs of **Fe(II)-Ph-Tpy** and **Fe(II)-Thio-Tpy** showed an approximately 1:1 ratio of the coordinated and free tpy-nitrogens, **Fe(II)-TPE-Tpy** exhibited a ratio of $\sim 1:2.5$. Therefore, the ligand structure determines the extent of coordination ($c = 0.3$ mM in MeOH) of the terminal terpyridines, that in turn is most likely expressed in the electro-optical properties of the assemblies. The possible effect of the signal depth (~ 20 nm vs film thickness of 165 ± 6 nm) is excluded as comparable data were obtained from both the films and isolated powders of the coordination polymers.

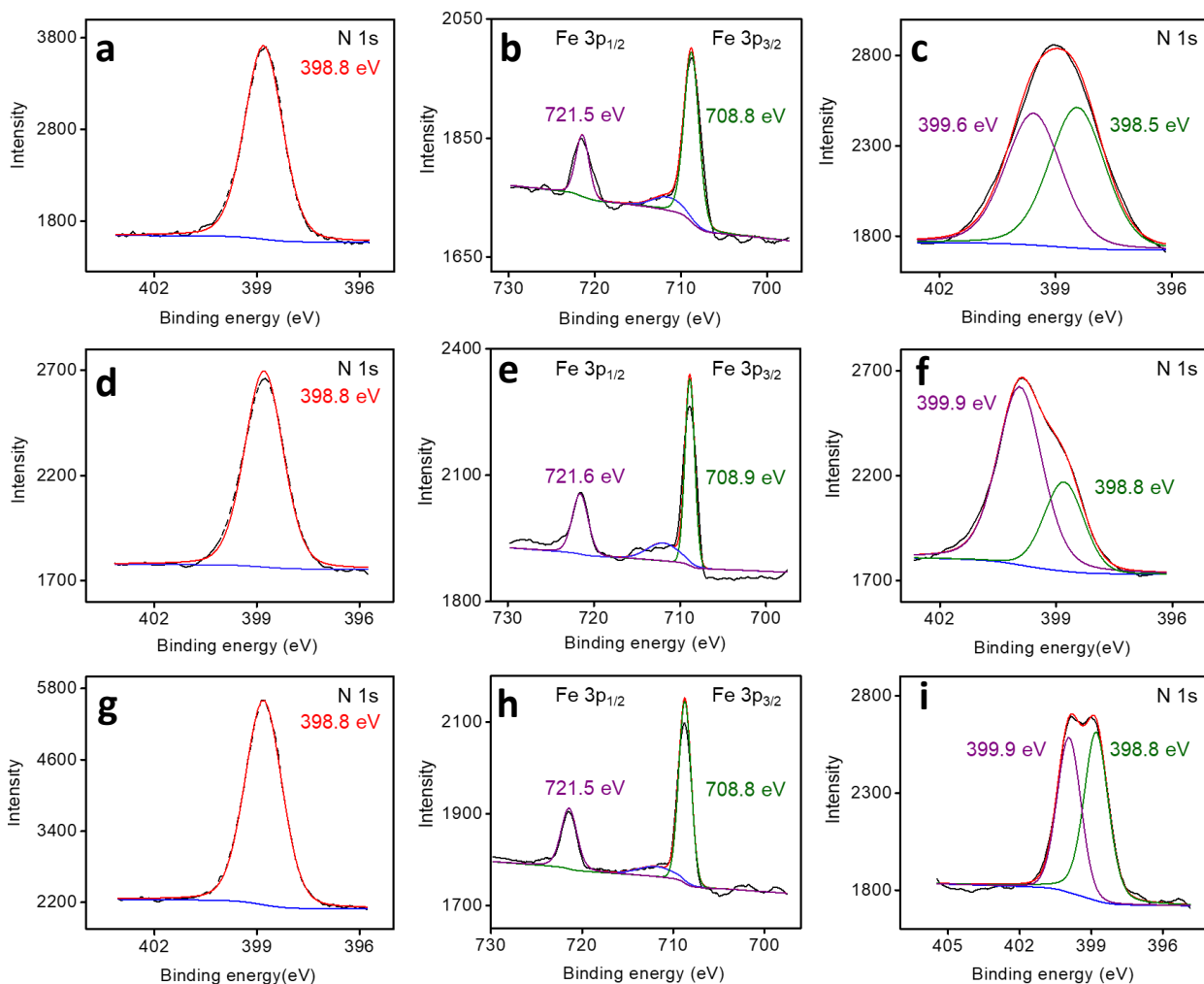


Figure 2.16. High resolution XPS data confirming the N 1s peaks for ligands a) **Ph-Tpy**, d) **TPE-Tpy** and g) **Thio-Tpy**. High resolution XPS data confirming the (b,e,h) Fe 3p_{1/2} and Fe 3p_{3/2} and (c,f,i) N 1s peaks for the MPNFs of (b,c) **Fe(II)-Ph-Tpy**, (e,f) **Fe(II)-TPE-Tpy** and (h,i) **Fe(II)-Thio-Tpy**. The binding energy corresponding to each peak and their assignments are provided in each figure.

2.3.3. Molecular Permeability in the Film State

The observations in the previous sections are indicative of the differential molecular permeability of these thin films. We, therefore, decided to explore the molecular permeability of these MPNFs using the cyclic voltametric response of three quinone-based redox probes of different molecular dimensions at identical concentrations (1.3 mM, **Figure 2.17.a**). Size-selective transfer of molecular probes through surface confined thin films have been explored based on known cavity size and molecular dimensions of the probes.⁴⁸⁻⁵¹ However, MPNFs with small variations in their core architecture as in this study, that do not necessarily reflect their internal arrangements and resulting pore sizes, are generally challenging as thin film molecular sieves.^{52,53} Three sets of MPNFs with varying thicknesses were used to assess their molecular sieving properties.⁵⁴ The current density corresponding to the redox peaks of the molecular probes gives a direct evidence for the extent of permeation.

Small-sized 1,4-benzoquinone **Q1** was found to permeate all the assemblies irrespective of their thickness (up to 39.5 ± 0.5 nm, **Figure 2.17b,d,f**) and porosity, whereas bulkier 3,3',5,5'-tetratert-butylidiphenylquinone **Q3** was found not to traverse through any of the thin films (minimum thickness of 10 nm, **Figure 2.18**). This size exclusion is indicative of a porosity of the assemblies that ranges between the molecular dimensions of the probes **Q1** and **Q3**. High degree of selective permeation was observed for a probe **Q2** of molecular size in between those of **Q1** and **Q3** (**Figure 2.17c,e,g**). The amount of **Q1** that reached the FTO surface was dependent on both the film thickness⁵⁵⁻⁵⁷ and the core structure of the ligand. At a thickness of 10.5 ± 0.5 nm (one deposition step), the films constructed from **Fe(II)-Ph-TPy** allowed more of **Q1** to permeate as compared to those of **Fe(II)-TPE-TPy** and **Fe(II)-Thio-TPy** (**Figure 2.17b**). As the thickness of the films increased (29.5 ± 0.5 nm, 39.5 ± 0.5 nm), their permeability decreased. However, a higher extent of permeability was consistently observed for **Fe(II)-Ph-TPy** based films, followed by **Fe(II)-Thio-TPy** and the lowest permeability was observed for the films of **Fe(II)-TPE-TPy** (**Figure 2.17d,f**), irrespective of the film thickness. This result gave a first indication for the existence of larger pores or higher porosity for the films based on **Fe(II)-Ph-TPy**, followed by **Fe(II)-Thio-TPy** and **Fe(II)-TPE-TPy** and was further confirmed by using a second molecular probe **Q2** of slightly larger dimension.

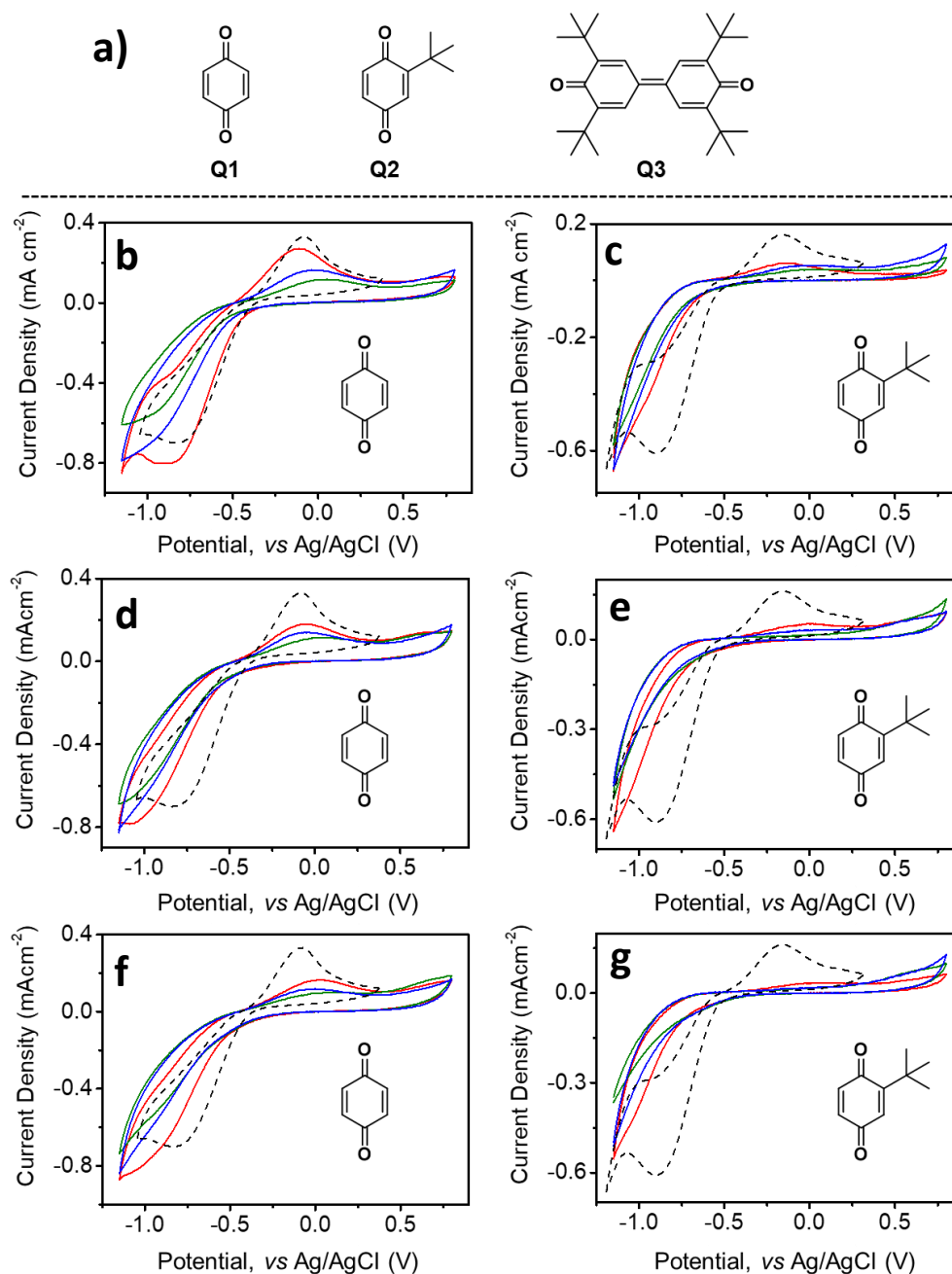


Figure 2.17. a) Molecular structures of the redox probes **Q1-Q3**. Cyclic voltammograms of the molecular probes **Q1** and **Q2** (1.3 mM) obtained using MPNFs of **Fe(II)-Ph-TPy** (red), **Fe(II)-TPE-TPy** (blue), and **Fe(II)-Thio-TPy** (green) as working electrodes at a film thickness of (b,c) 10.5 ± 0.5 nm, (d,e) 29.5 ± 0.5 nm, and (f,g) 39.5 ± 0.5 nm. Ag/AgCl and platinum wire were used as the reference and counter electrodes, respectively. $0.05 \text{ M } ^t\text{Bu}_4\text{NPF}_6$ in acetonitrile was used as the supporting electrolyte. The thickness of the assemblies was estimated from profilometer measurements. The chemical structures of the quinones are shown in the insets.

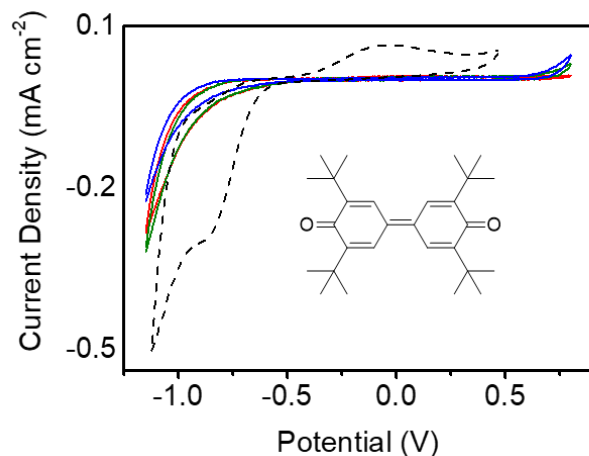


Figure 2.18. Cyclic voltammograms of the molecular probe **Q3** (1.3 mM) obtained using MPNFs of **Fe(II)-Ph-TPy** (red), **Fe(II)-TPE-TPy** (blue), and **Fe(II)-Thio-TPy** (green) as working electrodes at a film thickness of 10.5 ± 0.5 nm.

At a thickness of 10.5 ± 0.5 nm (one deposition step), all the films were permeable to the probe **Q2** in the order: **Fe(II)-Ph-TPy** > **Fe(II)-Thio-TPy** > **Fe(II)-TPE-TPy** (**Figure 2.17c**). Increasing the thickness to 29.5 ± 0.5 nm (three deposition steps) resulted in selective permeation of the probe **Q2**. The films based on **Fe(II)-Ph-TPy** and **Fe(II)-Thio-TPy** were still permeable (**Fe(II)-Ph-TPy** > **Fe(II)-Thio-TPy**) and that based on **Fe(II)-TPE-TPy** did not allow the probe to penetrate as indicated by the absence of the peaks in the corresponding CV (**Figure 2.17e**). At a still higher film thickness (39.5 ± 0.5 nm, four deposition steps), only the films based on **Fe(II)-Ph-TPy** was found to be permeable (**Figure 2.17g**). The size selective permeation achieved in these molecular assemblies suggests their porosity to be in the order: **Fe(II)-Ph-TPy** > **Fe(II)-Thio-TPy** > **Fe(II)-TPE-TPy**. The distorted shapes of the cyclic voltammograms are most likely due to the diffusive nature of mass transport. Two mechanisms may be operating under these experimental conditions: a charge transfer mechanism, whereby the probes get oxidized at the thin film – solution interface or a diffusive mechanism, whereby the probes get oxidized at the thin film – FTO interface.⁵⁸⁻⁶⁰ The former mechanism may be excluded based on the following observations: (i) redox peaks of the probes are observed in most of the CVs, and (ii) other charge transfer peaks are absent in the CVs. The selective molecular sieving is achieved by a favorable interplay of differential porosity emerged from a combined effect of available percolation pathways and interconnection of pores of varying diameters, that underlines the ligand structure effect on the internal structure of the MPNFs.

2.3.4 Electrochromic Devices

Solid state electrochromic devices (ECDs) were fabricated from these MPNFs (thickness = 165 ± 6 nm), in order to investigate the effect of ligand structure on electrochromic performance. The MPNF-modified FTO substrates ($3.0 \text{ cm} \times 3.0 \text{ cm}$) were rinsed in dry acetonitrile and dried under a flow of argon. The bare FTO substrates were placed on top of these modified substrates and was held tight with an insulating 2-sided gorilla tape (thickness $< 200 \mu\text{m}$) at each end to prevent short circuits as well as to hold the setup together. The gel electrolyte ($\text{LiClO}_4 + \text{PMMA} + \text{PC}$) was then injected using a syringe to form a sandwich type architecture and was dried in an air oven at 60°C for 10 min. The sandwich cells were then sealed. The ends were connected to a potentiostat/galvanostat and the electrochromic properties of the solid-state set-up were studied. The devices switched reversibly between a characteristic transparent colored state (Fe^{2+}) and a transparent yellow state (Fe^{3+}) upon the application of double step potentials between $-3.0 \text{ V} - +3.0 \text{ V}$ (Figure 2.19).

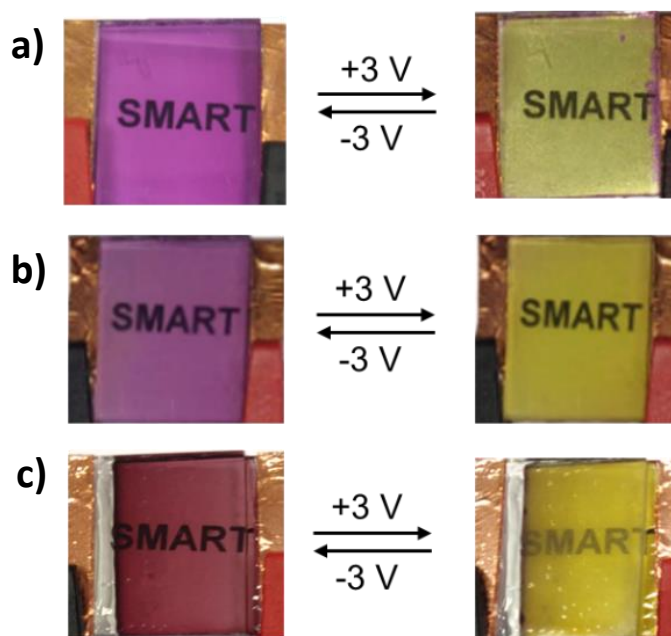


Figure 2.19. Electrochromic switching in solid state devices fabricated from the Fe(II) MPs of a) **Fe(II)-Ph-Tpy**, b) **Fe(II)-TPE-Tpy** and c) **Fe(II)-Thio-Tpy**. The MPs were spray coated on $3 \text{ cm} \times 3 \text{ cm}$ FTO glass substrates. The thickness of the electroactive layer was 165 ± 6 nm. A potential window of $-3.0 \text{ V} - +3.0 \text{ V}$ was used.

As observed for the films, the ECDs also exhibited ligand structure dependent spectroelectrochemical diversification. While the ECD fabricated from **Fe(II)-Ph-Tpy** MPNFs showed the highest optical contrast of $\sim 56\%$ at $\lambda_{\text{MLCT}} = 578$ nm, those from **Fe(II)-TPE-Tpy** ($\sim 35\%$, $\lambda_{\text{MLCT}} = 580$ nm) and **Fe(II)-Thio-Tpy** (46% , $\lambda_{\text{MLCT}} = 584$ nm) exhibited lower values (**Figure 2.20 a-c**).

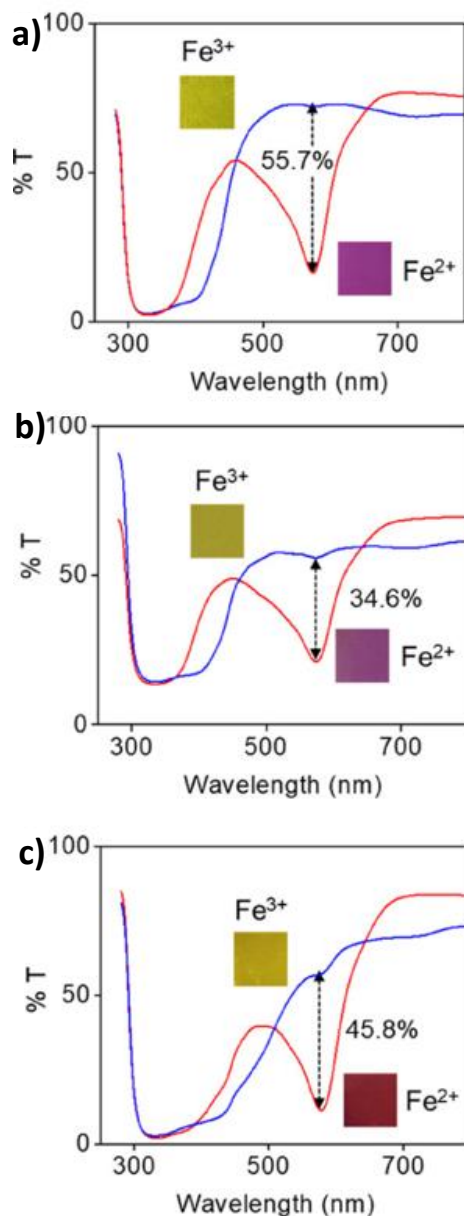


Figure 2.20. Transmittance spectra of the ECDs showing the bleaching of the MLCT bands during electrochemical oxidation of the assemblies constructed from a) **Fe(II)-Ph-Tpy**, b) **Fe(II)-TPE-Tpy** and c) **Fe(II)-Thio-Tpy**. The spectra of the assemblies in their reduced and oxidized states are shown in red and blue, respectively. The corresponding color pallets are shown in the insets.

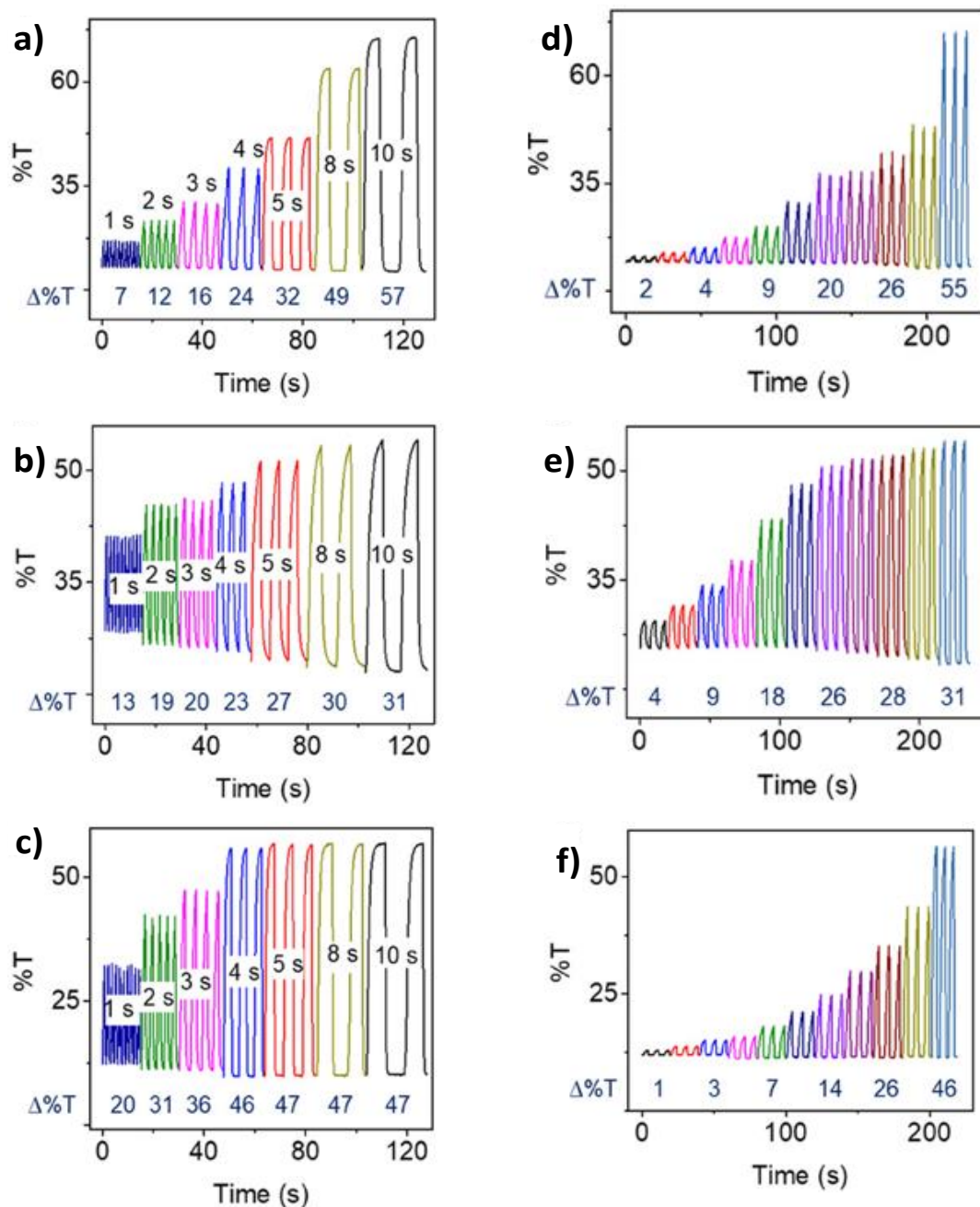


Figure 2.21. Chromoabsorptometry of the assemblies constructed from (a,d) **Fe(II)-Ph-Tpy**, (b,e) **Fe(II)-TPE-Tpy** and (c,f) **Fe(II)-Thio-Tpy** at different pulse widths (a-c) and by applying different double potential steps (d-f). Double potential steps of -2.0 V - +2.0 V and -3.0 V - +3.0 V were used at intervals of ± 0.1 V. The change in %T, rounded to the nearest whole number is given below the corresponding switching cycle.

Lower values for $\Delta(\%T)$ were obtained for the devices as compared to the films due to the use of viscous gel electrolytes. Chromoabsorptometry of the devices using double potential steps measured as change in %T over time confirmed optical contrast values similar to those obtained in the spectral measurements (**Figure 2.21 a-c**). The devices also showed pulse width (switching time) dependent changes in visible light transmittance (**Figure 2.21 a-c**). The devices based on **Fe(II)-Ph-TPy** MPNFs exhibited a linear correlation between the pulse width (1-10 s) and change in %T. The optical contrast for the devices constructed from **Fe(II)-TPE-Tpy** and **Fe(II)-Thio-Tpy** increased linearly with the pulse width until 4-5 s and remained almost constant there after (**Figure 2.22a**).

The potential window used was also found to have an effect on the optical contrast of the devices (**Figure 2.21 d-f**). $\Delta(\%T)$ of the devices of **Fe(II)-Ph-TPy** and **Fe(II)-Thio-Tpy** showed an exponential increase with a ± 0.1 V change in potential windows between -2.0 V - +2.0 V and -3.0 V - +3.0 V. A rather smaller exponential dependence was observed for **Fe(II)-TPE-Tpy** based devices for two-step potentials between -2.0 V - +2.0 V and -2.6 V - +2.6 V, after which a linear correlation was observed (**Figure 2.22b**).

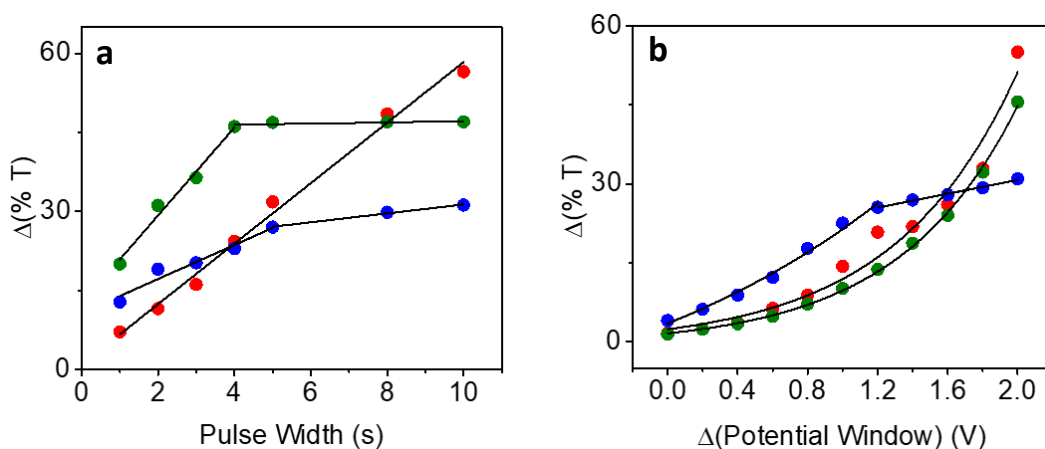


Figure 2.22. The dependence of change in %Transmittance on a) pulse width and b) change in applied potential window for the ECDs of **Fe(II)-Ph-TPy** (red), **Fe(II)-TPE-TPy** (blue) and **Fe(II)-Thio-TPy** (green). A varying pulse width of 1-10 s and a potential window of -3.0 V - +3.0 V was used for a). Potential windows between -2.0 V - +2.0 V and -3.0 V - +3.0 V with ± 0.1 V increments were used for b) at a constant pulse width of 5 s.

The pulse width had a larger repercussion on the bleaching (oxidation) process in devices fabricated from **Fe(II)-Ph-Tpy** and **Fe(II)-Thio-Tpy**, and the coloration (reduction) was rather unaffected as corroborated by an almost constant %T_{min} (**Figure 2.21 a,c**). On the other hand, both coloration and bleaching were affected by these parameters in devices based on **Fe(II)-TPE-Tpy** (**Figure 2.21b**). A similar effect, but to lesser extent, was observed for %T changes upon change in the applied potential window also (**Figure 2.21d-f**). All the devices exhibited faster response times for coloration (reduction), while the bleaching (oxidation) was rather slow. Unlike expected, coloration was considerably faster for the devices as compared to the films, whereas the reverse process was faster in the film state. This unexpectedly faster coloration might be attributed to the larger potential window of operation for the devices (-3.0 V - +3.0 V). Use of smaller potential windows resulted in slower response times as expected. The response times for the devices at a pulse width of 10 s (-3.0 V - +3.0 V, **Figure 2.23a-c**) were as follows. **Fe(II)-Ph-Tpy**: 2.1 s (bleaching), 0.5 s (coloration), **Fe(II)-TPE-Tpy**: 3.5 s (bleaching), 1.1 s (coloration), **Fe(II)-Thio-Tpy**: 2.6 s (bleaching), 0.5 s (coloration). These observations are indicative of an increasingly feasible reductive pathway and strenuous oxidative pathway in the films and devices under specific operational conditions. The coloration efficiency of the devices (at λ_{MLCT}) also followed the order: **Fe(II)-Ph-Tpy** (640.7 cm²/C) > **Fe(II)-TPE-Tpy** (464.6 cm²/C) > **Fe(II)-Thio-Tpy** (351.2 cm²/C), corroborating the ligand structure dependence of almost every measurable spectroelectrochemical property (**Table 2.2**).

The operational stability (5 s pulse width, -3.0 V - +3.0 V), measured as the change in optical contrast over number of switching changes in transmittance of **Fe(II)-Ph-Tpy** ECDs decreased exponentially, and ~20% of the initial contrast was retained after 1000 continuous switchings at room temperature (**Figure 2.24 a,d**). Devices of **Fe(II)-TPE-Tpy** were found to exhibit ~21% reduction in optical contrast after 600 switchings, with no further detectable loss of performance thereafter (**Figure 2.24 b,d**). **Fe(II)-Thio-Tpy** ECDs exhibited no change in performance after 200 switching, 7-8% decrease in optical contrast after 600 switchings and were found to be highly stable with >92% optical contrast after 1000 continuous switchings (**Figure 2.24 c,d**). Presence of multiple aromatic rings in **TPE-Tpy** and **Thio-Tpy** leads to extended conjugation and better delocalization of π -electrons and/or charges. The available electron density on the terpyridine determines the coordination to Fe(II), whereas the presence of two additional heteroatoms (S) in

Thio-Tpy and the lone pairs on these heteroatoms that favors an anticonformation may also play a role in providing exceptional switching stability to the corresponding devices.⁶¹

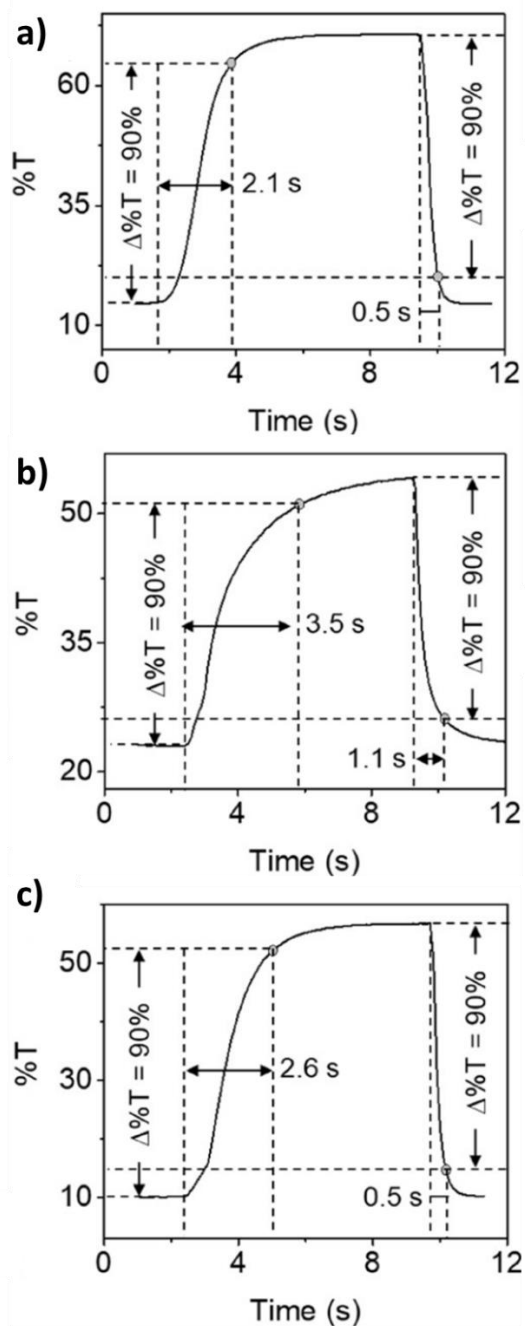


Figure 2.23. The response times for the devices of a) **Fe(II)-Ph-Tpy**, b) **Fe(II)-TPE-Tpy** and c) **Fe(II)-Thio-Tpy** at a pulse width of 10 s. The experiments (at λ_{MLCT} : 578 nm for **Fe(II)-Ph-Tpy**, 580 nm for **Fe(II)-TPE-Tpy** and 584 nm for **Fe(II)-Thio-Tpy**) were carried at potential window of -3 V – 3V for all the experiments.

Table 2.2. Optical and spectroelectrochemical properties of the films and devices

Properties	CPNFs		Fe(II)-TPE-Tpy		Fe(II)-Thio-Tpy	
	Films	Devices	Films	Devices	Films	Devices
λ_{MLCT} (nm)	578	578	580	580	584	584
Optical Contrast (%) ^a	>76	56	40	35	>60	46
Response Time (bl, s) ^b	1.6	2.1	2.6	3.5	2.9	2.6
Response Time (col, s) ^c	1.0	0.5	1.4	1.1	1.4	0.5
Coloration Efficiency (cm ² /C) ^d	1049.5	640.7	756.5	464.6	473.8	351.2

^aDifference in %T at λ_{MLCT} . ^bTime taken to reach 90% of maximum %T. ^cTime taken to reach 90% of minimum %T. ^dCalculated at λ_{MLCT}

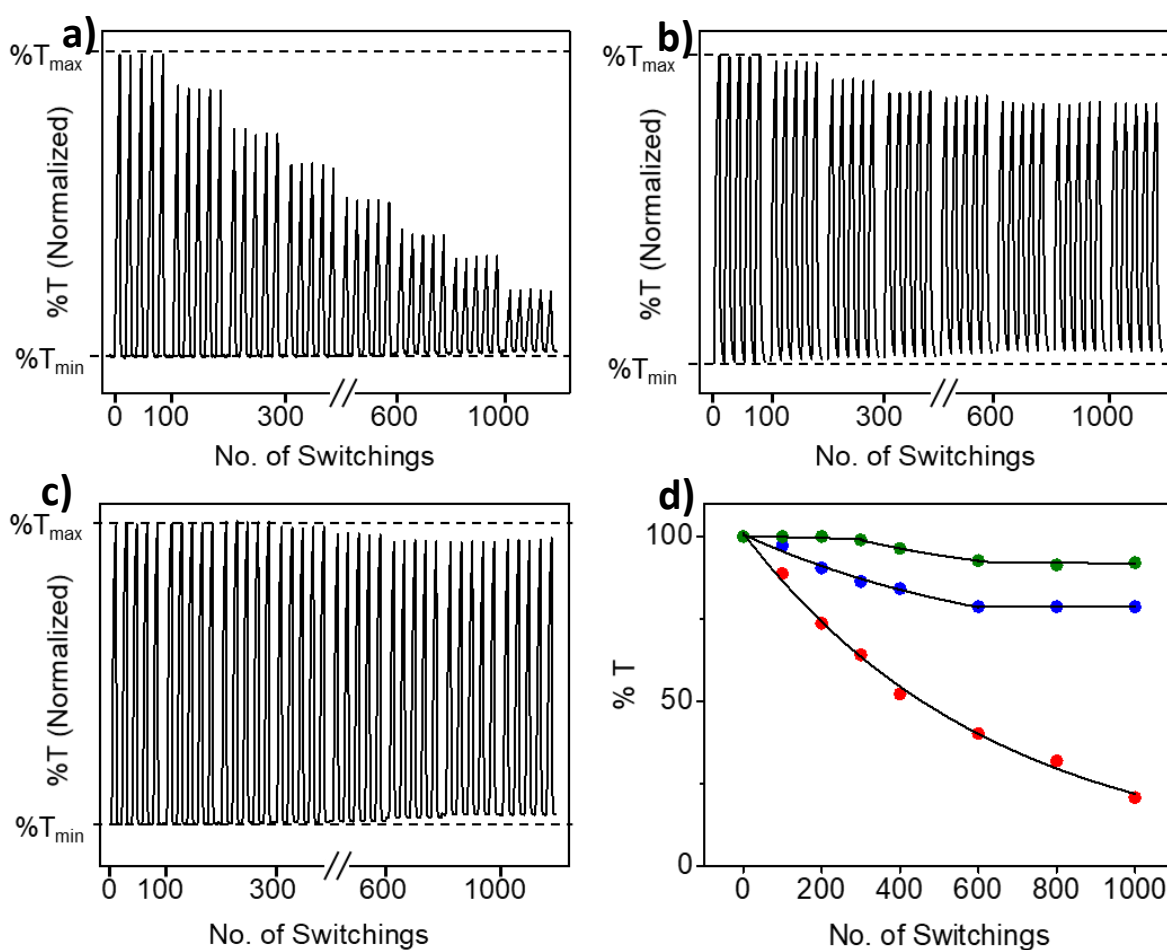


Figure 2.24. Stability of the ECDs constructed from a) **Fe(II)-Ph-Tpy**, b) **Fe(II)-TPE-Tpy** and c) **Fe(II)-Thio-Tpy** up to 1000 continuous switchings at 5 s pulse width and a potential window of -3.0 V - +3.0 V at room temperature. d) The variation in stability with the number of switchings: **Fe(II)-Ph-Tpy**: red, **Fe(II)-TPE-Tpy**: blue and **Fe(II)-Thio-Tpy**: green.

The ECDs were not found to exhibit any memory effect under open circuit conditions. Change in color to yellow upon oxidation was persistent only upon the sustained application of a potential above the corresponding E_{ox} . The devices based on **Fe(II)-TPE-TPy** regained their colored state within 3 min. of withdrawal of potential after complete oxidation. ECDs constructed from **Fe(II)-Ph-TPy** and **Fe(II)-Thio-TPy** required a reasonably longer duration of 10 min. and 8 min., respectively, for complete regaining of color under an open circuit potential (**Figure 2.25**). While the MPNF-modified FTO substrates undergo defined electrochemical reactions, no specific material was introduced in the counter electrode or electrolyte for redox balance. An ion storage layer was also absent. Traces of impurities in the gel electrolyte may undergo reactions at the counter electrode or part of the electrode itself may undergo such reactions.⁶² The presence of oxygen and/or water may also contribute to the counter electrode reactions. The lack of memory under open circuit conditions may be explained based on these undefined reactions at the counter electrode, followed by diffusion of the reaction products into the gel medium. The corresponding cooling efficiency was estimated from a 3×3 cm prototype installed on a cardboard chamber with an outside temperature of $42 \pm 1^\circ\text{C}$ obtained using a commercial lamp combined with a hot air flow. The indoor temperature measured 1.5 cm away from the prototype showed a reduction by $\sim 3^\circ\text{C}$ when compared to a simple glass installation that served as the control.

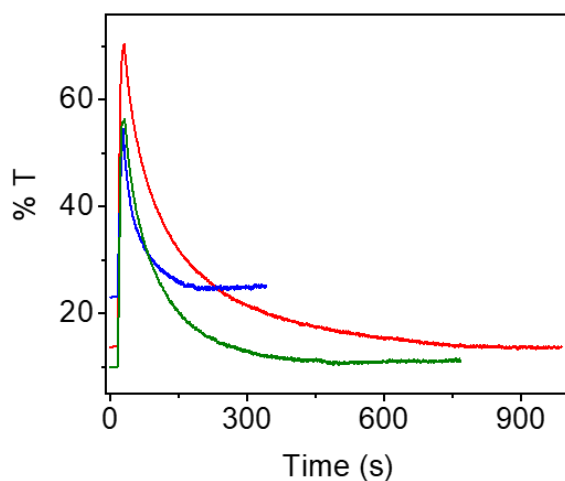


Figure 2.25. Decay of transmittance (%) of the ECDs based on **Fe(II)-Ph-TPy** (red), **Fe(II)-TPE-TPy** (blue) and **Fe(II)-Thio-TPy** (green) under an open circuit potential. All devices were subjected to a potential of +3.0 V for ensuring complete oxidation before switching the potential off.

2.3.5 Creation of Patterns and Images

The spray coating process used for the formation of MPNFs is versatile enough to allow the creation of patterns and images by masking selected areas of the FTO substrate. This process circumvents the requirement for selectively patterned or etched conductive substrates for generating such patterns and images for electrochromic applications. Such images also switch their color under the application of an electric voltage (**Figure 2.26**), and can be realized without the need for selective pixilation, etching or printing.

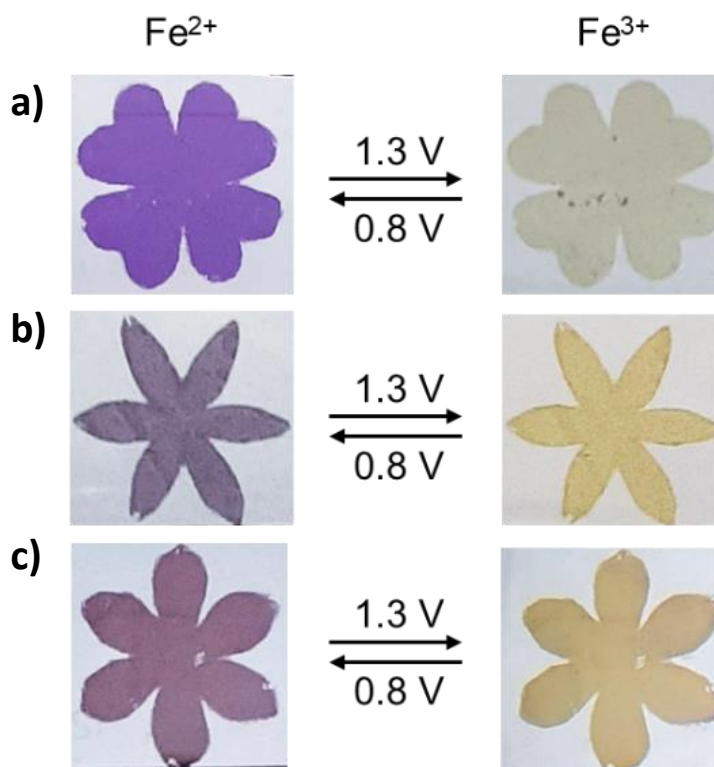


Figure 2.26. Electrochromic images created by masking 3 cm × 3 cm FTO-glass substrates during the spray coating process of a) **Fe(II)-Ph-Tpy**, b) **Fe(II)-TPE-Tpy** and c) **Fe(II)-Thio-Tpy**. The reduced and oxidized states are shown on the left and right, respectively. The modified FTO substrate, Ag/AgCl and platinum wire were used as the working, reference and counter electrodes, respectively. 0.1 M ${}^t\text{Bu}_4\text{NPF}_6$ in acetonitrile was used as the supporting electrolyte.

2.4. Conclusions

Metallosupramolecular assemblies of three different terpyridine ligands having different central core and a common metal center are demonstrated as excellent candidates for making electroactive

coating on TCO substrates. The multilayer electrochromic films of the metallopolymer (MPs) thus obtained exhibited ligand-directed molecular permeability and spectroelectrochemical profiles. The fabricated electrochromic devices exhibited high optical contrasts and coloration efficiencies at low input voltages simultaneous with color-to-color EC transitions. Creation of patterns and images with electro-chromic attributes is facile, without the need for etching or pixilation of TCO substrates. Ligand design plays a key role in controlling the porosity and electrochemical behavior, that are otherwise difficult to achieve in surface confined coordination polymers comprising a single type of metal ion. The combination of designed ligand systems with spray coating process offers a powerful tool for the multilayer deposition of metallosupramolecular assemblies resulting in smart and functional coordination polymer thin films with tunable electrooptical properties for multifarious applications.

2.5. Experimental Section

2.5.1. Materials and Methods

All chemicals and solvents were purchased from Sigma-Aldrich, Merck, Spectrochem and Alfa Aesar. All reagents were used as received, unless otherwise mentioned. All the reactions and experiments were carried out in oven-dried glassware. Moisture and oxygen sensitive reactions were carried out using dry solvents under argon atmosphere. All organic extracts were dried over anhydrous sodium or magnesium sulfate powder, and solvents were removed under reduced pressure using a HEIDOLPH rotary evaporator using a water bath kept below 50 °C.

2.5.2. NMR Spectroscopy

^1H and ^{13}C NMR spectra were recorded at 300 K on a 500 MHz (^1H) Bruker Advance spectrometer using TMS as an internal standard.

2.5.3. FTIR Spectroscopy

Infrared spectra were recorded in the solid state (KBr) using Shimadzu IR Prestige-21 Fourier Transform Infrared Spectrophotometer.

2.5.4. ESI-HRMS and MALDI-TOF Analyses

High-resolution mass spectra were obtained from a JEOL JSM 600. Matrix-assisted laser desorption ionization time-of-flight (MALDI-TOF) mass spectra were performed on an AXIMA-CFR PLUS (SHIMADZU) MALDI-TOF mass spectrometer using α -cyano-4-hydroxycinnamic acid as the matrix.

2.5.5. UV-Vis Spectroscopy

The solution state absorbance measurements were done on a Shimadzu UV–Vis spectrophotometer (UV-2600). Concentration dependent solution studies were carried out in 1 cm quartz cuvette. Temperature (25 °C) was regulated using a Shimadzu temperature controller. The blank experiment with the corresponding solvent provided the baseline. The solution was allowed to come to thermal equilibrium in a Hellma Analytics 10 mm path length quartz cell in the thermostated (± 0.1 °C) cell holder of the spectrophotometer. The UV-vis spectra (25 °C) of the MPNF modified FTO slides were obtained using Ocean Optics UV-vis modular spectrometer (DH-2000-BAL). The blank experiment with the bare FTO slides provided the baseline.

2.5.6. Thickness Measurements

The thickness of the samples was estimated using a Dektak XT profilometer.

2.5.7. X-ray Photoelectron Spectroscopy

The surface chemistry of MPNFs was analyzed using X-ray photoelectron spectroscopy (XPS, PHI 5000 VersaProbe II, ULVAC-PHI Inc., USA) equipped with micro-focused (200 μm , 15KV) monochromatic Al-K α X-Ray source ($h\nu = 1486.6$ eV). Both survey spectra and narrow scan (high-resolution spectra) were recorded. Survey scans were recorded with an X-ray source power of 50W and pass energy of 187.85 eV. High-resolution spectra of the major elements were recorded at 46.95 eV pass energy. XPS data were processed using PHI's Multipak software.

2.5.8. Atomic Force Microscopy and Roughness Estimation

AFM images were recorded at ambient conditions using a Atomic Force Microscopy (AFM; Bruker Multimode Nanoscope V) instrument operating under tapping mode. Micro-fabricated TiN cantilever tips with a resonance frequency of 299 kHz and a spring constant of 20-80 Nm^{-1} was used. Roughness parameter was estimated using Nanoscope Analysis 1.5 software.

2.5.9. Cyclic Voltammetry

Cyclic Voltammetry (CV, BASI CV-50W) for samples in solution state were performed at room temperature using 0.1 M tetrabutylammonium hexafluorophosphate (TBAPF₆) in CH₃CN as supporting electrolyte, glassy carbon as working electrode, Ag/AgCl electrode as reference electrode and platinum wire as counter electrode at room temperature. Cyclic voltammetry of the films and devices were performed on PARSTAT 4000A Potentiostat. MPNF modified FTO served as the working electrode, platinum wire as the counter electrode, Ag/AgCl as the reference, and 0.1 M tetrabutylammonium hexafluorophosphate (TBAPF₆) in CH₃CN was used as the electrolyte for film state electrochemical studies.

2.5.10. Spectroelectrochemical Analysis

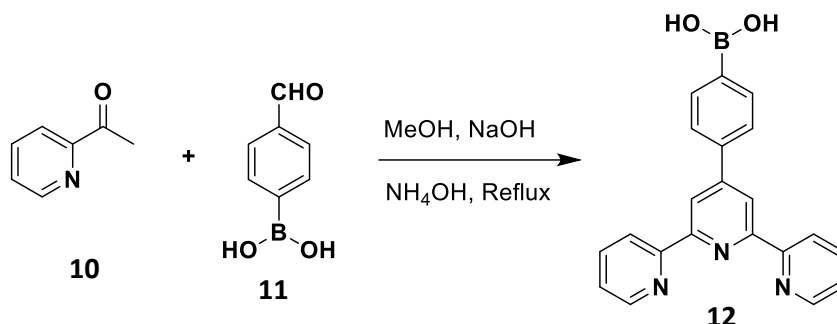
Spectroelectrochemical response of electrochromic devices and films were recorded on Ocean Optics Spectrometer DH-2000-BAL using a PARSTAT 4000A Potentiostat for the electrochemical redox process. Spectroelectrochemistry of films were done by dipping spray coated films on FTO electrodes in 0.1 M TBAPF₆ (in dry acetonitrile) solution (Ag/AgCl electrode and Pt wire as reference and counter electrodes respectively). The blank was done using 0.1 M TBAPF₆ (in anhydrous acetonitrile) solution in a cuvette having 1 cm path length. Transmittance spectra were obtained upon applying double potential steps (-3.0 V and +3.0 V) as a function of time. The change in %T at the MLCT wavelength (578, 580, 584 nm) were monitored at different pulse width (1-10 s) and using different potential windows between -2.0 V - +2.0 V and -3.0 V -+3.0 V at a pulse width of 5 s. Switching stability was investigated by switching between two potential (-3.0 V and +3.0 V) at a pulse width of 5 s for 1000 continuous redox switchings.

2.5.11. Molecular Permeability Studies

Molecular permeability studies were performed using a three-electrode cell configuration consisting of the CPNF modified FTO, Pt wire, and Ag/AgCl as working, counter, and reference electrodes, respectively. The experiments were performed at room temperature using 1.3 mM solutions of the quinones **Q1-Q3** in a 0.05 M solution of TBAPF₆ in dry acetonitrile purged with N₂.

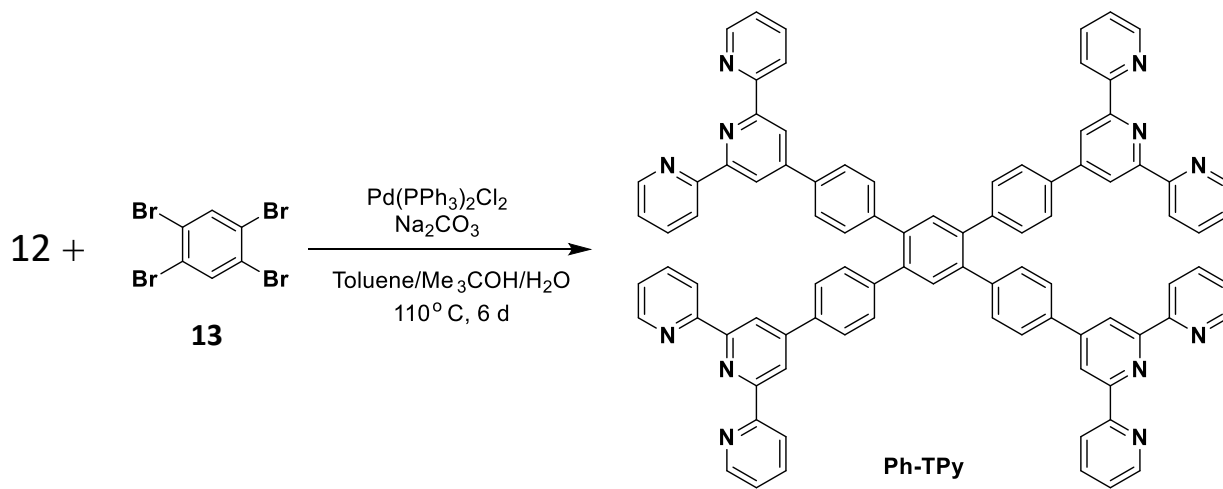
2.6. Synthesis

Synthesis of 4-(2, 2', 6', 2''-terpyridine-4'-yl) phenylboronic acid **12**



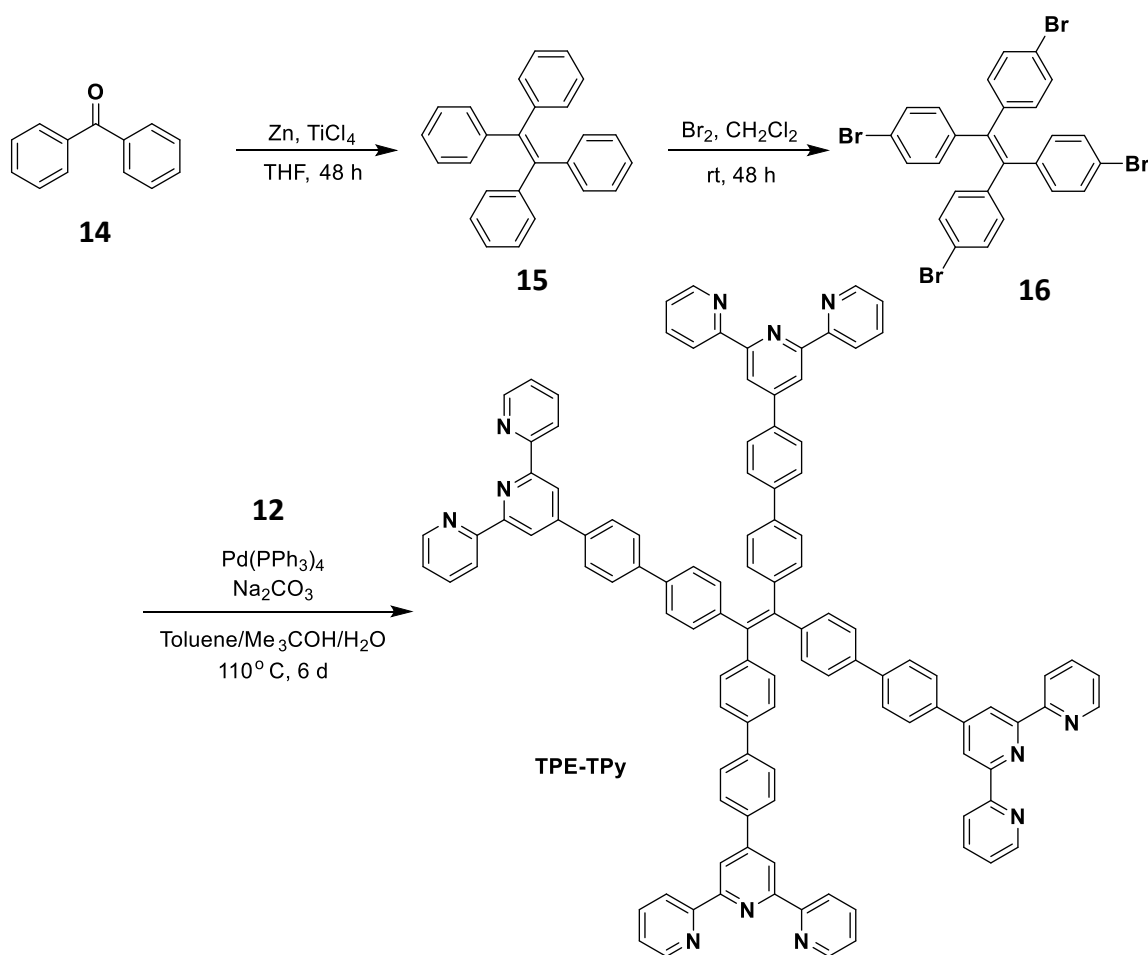
To a solution of NaOH (4.8 g, 0.12 mol) in EtOH (80 mL), 4-Formylphenylboronic acid **10** (3.032 g, 0.02 mol) and 2-acetylpyridine **11** (5.39 g, 0.04 mol) were added. After stirring at room temperature for 24 h, aq. NH₄OH (28%, 75 mL) was added, and the resulting mixture was refluxed for 20 h. The mixture was cooled to room temperature, the solid was collected by filtration and was washed with CHCl₃ to give the product **12** as an off white solid. Yield: 4.686 g, 85%. ¹H NMR (500 MHz, CDCl₃, 300 K) δ: 8.70 – 8.68 (m, 2H, tpy-*H3',5'*), 8.65 – 8.62 (m, 4H, tpy-*H6,6''* and tpy-*H3,3''*), 8.00 (td, *J* = 7.7, 1.8 Hz, 2H, tpy-*H4,4''*), 7.75 (d, *J* = 7.8 Hz, 2H, Ph-*H*), 7.73 (d, *J* = 8.0 Hz, 2H, Ph-*H*), 7.48 (ddd, *J* = 7.5, 4.8, 1.1 Hz, 2H, tpy-*H5,5''*); ESI-MS (*m/z*): Calcd. for [C₂₁H₁₆BN₃O₂+H]⁺: 354.1314. Found: 354.1366.

Synthesis of Ph-TPy



Tetrabromobenzene **13** (100 mg, 0.25 mmol), boronic acid **12** (538 mg, 6 eq), Pd(PPh₃)₂Cl₂ (53.7 mg, 0.3 eq) and Na₂CO₃ (806 mg, 30eq) were added to a glass pressure tube. After three argon/evacuation cycles, H₂O (10 mL), toluene (30 mL) and ¹BuOH (1.5 mL) were added under a flow of argon. The pressure tube was sealed and the mixture was stirred at 110 °C for 6 days. After cooling to room temperature, the mixture was extracted with CHCl₃ (50 mL×2). The combined organic extracts was washed with brine, dried over Na₂SO₄ and concentrated in vacuo. The crude product was purified by column chromatography on silica gel using CHCl₃/MeOH (9:1) as eluent to afford the ligand **Ph-TPy** as a white solid. Yield: 66 mg, 20%. ¹H NMR (500 MHz, CDCl₃, 300 K) δ: 8.70 (s, 8H), 8.63 (d, *J* = 4.6 Hz, 8H), 8.58 (d, *J* = 8.0 Hz, 8H), 7.8-7.70 (m, 16H), 7.67 (s, 2H), 7.41 (d, *J* = 8.3 Hz, 8H), 7.25-7.23 (m, 8H). ¹³C NMR (125 MHz, CDCl₃, 300K) δ: 155.30, 154.89, 148.72, 140.58, 138.49, 135.86, 135.77, 132.03, 129.46, 122.70, 120.29, 117.78. ESI-MS (*m/z*): Calculated for [C₉₀H₅₈N₁₂+H]²⁺: 654.7471, Found: 654.7465.

Synthesis of TPE-TPy



Synthesis of 1,1,2,2-Tetraphenylethylene 15

An ice-cold suspension of zinc powder (6.259 g, 0.095 mol) in dry THF (80 mL) was prepared in a 3-necked flask under argon. TiCl_4 (15 mL, 0.055 mol) was injected slowly over a period of 30 min, the ice-salt-water bath was removed and the reaction mixture was heated under reflux for 4 h. A solution of benzophenone **14** (5.00 g, 0.027 mol) in dry THF (20 mL) was added slowly using a syringe and the mixture was refluxed overnight. The reaction mixture was cooled to room temperature and was quenched with a saturated solution of sodium carbonate (until the effervescence stopped) and was then extracted with chloroform (100 mL \times 3). The organic layer was washed with water (120 mL \times 3) and the combined organic extracts was dried over sodium sulphate and the solvent was removed under reduced pressure. The resulting crude product was purified by column chromatography on silica gel using hexane as eluent. Yield: 4.43 g, 49%. ^1H NMR (500 MHz, CDCl_3 , 300 K) δ : 7.05 – 7.00 (m, 12H), 6.98 – 6.94 (m, 8H). ESI-MS (m/z): Calculated for $[\text{C}_{26}\text{H}_{20}+\text{Na}]^+$: 332.1463. Found: 355.1467.

Synthesis of 1,1,2,2-tetrakis(4-bromophenyl)ethane 16

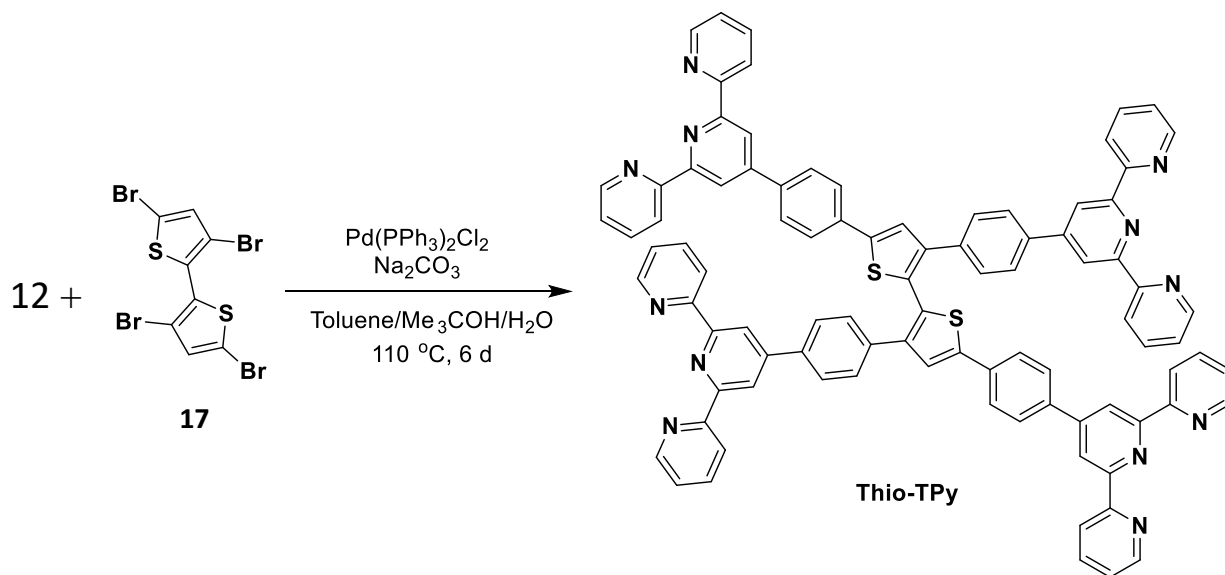
Tetraphenylethylene **15** (1.66 g, 5 mmol) was dissolved in CH_2Cl_2 (100 mL) in a round bottom flask and then Br_2 (3.0 mL) was added dropwise. The mixture was stirred at room temperature for 12 h, and the reaction was quenched by aqueous $\text{Na}_2\text{S}_2\text{O}_3$ (20 mL). The mixture was then extracted using CH_2Cl_2 (50 mL \times 3). The organic layer was washed with water (60 mL \times 3) and the combined organic extracts was dried over MgSO_4 . The solvent was evaporated in vacuo and the residue was purified by column chromatography over silica gel using hexane as eluent. Compound **16** was obtained as a white powder. Yield: 3.05 g, 95%. ^1H NMR (500 MHz, CDCl_3 , 300 K) δ : 7.19 (d, J = 8.2 Hz, 8H), 6.77 (d, J = 8.2 Hz, 8H).

Synthesis of TPE-TPy

1,1,2,2-tetrakis(4-bromophenyl)ethene **16** (100 mg, 0.15 mmol), boronic acid **12** (327 mg, 0.92 mmol), $\text{Pd}(\text{PPh}_3)_2\text{Cl}_2$ (32 mg, 0.046 mmol) and Na_2CO_3 (490.6 mg, 4.62 mmol) were added to a glass pressure tube. After three argon/evacuation cycles, H_2O (10 mL), toluene (30 mL) and $^t\text{BuOH}$ (1.5 mL) were added under a flow of argon. The pressure tube was sealed and the mixture was stirred at 110 $^\circ\text{C}$ for 6 days. After cooling to room temperature, the mixture was extracted with CHCl_3 (50 mL \times 2). The combined organic extracts was washed with brine, dried over Na_2SO_4 , and concentrated in vacuo. The crude product was purified by column chromatography on silica

gel using $\text{CHCl}_3/\text{MeOH}$ (9:1) as eluent to afford the **TPE-TPy** as a white solid. Yield: 68 mg, 28%. ^1H NMR (500 MHz, CDCl_3 , 300 K) δ : 8.78 (s, 8H), 8.74 (s, 8H), 8.68 (d, $J = 7.7$ Hz, 8H), 7.99 (d, $J = 7.3$ Hz, 8H), 7.88 (t, $J = 7.9$ Hz, 8H), 7.79 – 7.72 (m, 8H), 7.56 – 7.50 (m, 8H), 7.39 – 7.27 (m, 16H). ^{13}C NMR (125 MHz, CDCl_3 , 300K) δ : 155.32, 154.98, 148.14, 138.27, 137.53, 135.84, 130.96, 126.70, 126.35, 125.50, 122.79, 120.38, 117.68, 113.04. MALDI TOF: Calculated for $[\text{C}_{110}\text{H}_{72}\text{N}_{12}]$: 1561.60. Found: 1561.69.

Synthesis of Thio-TPy



3,3',5,5'-Tetrabromo-2,2'-bithiophene **17** (100 mg, 0.207 mmol), boronic acid **12** (438 mg, 1.24 mmol), $\text{Pd}(\text{PPh}_3)_2\text{Cl}_2$ (43 mg, 0.062 mmol) and Na_2CO_3 (658 mg, 6.21 mmol) were added to a glass pressure tube. After three argon/evacuation cycles, H_2O (10 mL), toluene (30 mL) and $^t\text{BuOH}$ (1.5 mL) were added under a flow of argon. The pressure tube was sealed and the mixture was stirred at 110 °C for 6 days. After cooling to room temperature, the mixture was extracted with chloroform (50 mL \times 2). The combined organic extracts was washed with brine, dried over Na_2SO_4 , and concentrated in vacuo. The crude product was purified by column chromatography on silica gel using $\text{CHCl}_3/\text{MeOH}$ (9:1) as eluent to afford the product **Thio-TPy** as a white solid. Yield: 56 mg, 17%. ^1H NMR (500 MHz, CDCl_3 , 300 K) δ : 8.78 (s, 8H), 8.74 (s, 8H), 8.68 (d, $J = 7.7$ Hz, 8H), 7.99 (d, $J = 7.3$ Hz, 8H), 7.88 (t, $J = 7.9$ Hz, 8H), 7.79 – 7.72 (m, 8H), 7.56 – 7.50 (m, 8H), 7.39 – 7.27 (m, 16H). ^{13}C NMR (125 MHz, CDCl_3 , 300K) δ : 155.32, 154.98, 148.14, 138.27, 137.53, 135.84, 130.96, 126.70, 126.35, 125.50, 122.79, 120.38, 117.68, 113.04. MALDI TOF: Calculated for $[\text{C}_{110}\text{H}_{72}\text{N}_{12}]$: 1395.44. Found: 1395.85.

2.7. Synthesis of the Coordination Polymers for Spray Coating

A solution of $\text{FeCl}_2 \cdot 4\text{H}_2\text{O}$ (4.97 mg, 2 equiv.) in MeOH (5 mL) was added to a solution of the corresponding ligand (**Ph-TPy**: 6.5 mg, **TPE-TPy**: 7.8 mg, **Bithio-TPy**: 6.97 mg) in CHCl_3 (5 mL). The final concentration of the coordination polymers was 0.3 mM and the freshly prepared solutions were used to spray coated on FTO-glass substrates using the automated spray coater without further purification.

2.8. Fabrication of MPNFs by Spray Coating the MPs on FTO substrates

FTO glass substrates (3.0 cm \times 3.0 cm) were cleaned by washing in soap solution followed by ultrasonication in water, acetone and isopropyl alcohol, each for 15 min. Spray coating was done using Nordson EFD EV Series automated dispensing system that dispenses fluids in a pre-programmed pattern onto a workpiece. Programs were created using the DispenseMotion™ software. A line speed of 150 mm/s and a ptp speed of 200 mm/s was used. 10 sprays of 0.3 mM solutions of the MPs are considered as one deposition step.

2.9. Fabrication of Electrochromic Devices

2.9.1. Synthesis of Gel Electrolyte

LiClO_4 (0.9 g) was added to a mixture of propylene carbonate (6.0 mL) and CH_3CN (10.0 mL) under a flow of argon. To the above stirred solution, PMMA (2.1 g) was added and the mixture was stirred at room temperature until the polymer was completely dissolved (12 h) to obtain a transparent gel electrolyte system.

2.9.2. ECD Fabrication

FTO glass substrates (3.0 cm \times 3.0 cm, for counter/reference electrodes) were cleaned by washing with soap solutions followed by ultrasonication in water, acetone and isopropyl alcohol, each for 15 min. The CPNF-modified FTO substrates (3.0 cm \times 3.0 cm) were rinsed in dry acetonitrile and dried under a flow of argon. The bare FTO substrates were placed on top of these modified substrates and was held tight with an insulating two-sided gorilla tape (thickness < 200 μm) at each end to prevent short circuits as well as to hold the setup together. The gel electrolyte was then injected using a syringe to form a sandwich type architecture and was dried in an air oven at 60 $^\circ\text{C}$ for 10 min. The sandwich cells were then sealed. The ends were connected to a potentiostat/galvanostat and the electrochromic properties of the solid-state set-up were studied.

2.10. References

- (1) Ghosh, S.; Shankar, S.; Susan, D.; Ajayaghosh, A. Diketopyrrolopyrrole-Based Functional Supramolecular Polymers: Next-Generation Materials for Optoelectronic Applications. *Mater. Today Chem.* **2020**, *16*, 100242.
<https://doi.org/10.1016/j.mtchem.2020.100242>.
- (2) Bhattacharyya, A.; De Sarkar, S.; Das, A. Supramolecular Engineering and Self-Assembly Strategies in Photoredox Catalysis. *ACS Catal.* **2021**, *11*, 710–733.
<https://doi.org/10.1021/acscatal.0c04952>.
- (3) Praveen, V. K.; Ajayaghosh, A. CHAPTER 11 Metallosupramolecular Materials for Energy Applications: Light Harvesting. In *Functional Metallosupramolecular Materials*; The Royal Society of Chemistry, **2015**, 318–344.
<https://doi.org/10.1039/9781782622673-00318>.
- (4) Dyer, A. L.; Bulloch, R. H.; Zhou, Y.; Kippelen, B.; Reynolds, J. R.; Zhang, F. A Vertically Integrated Solar-Powered Electrochromic Window for Energy Efficient Buildings. *Adv. Mater.* **2014**, *26*, 4895–4900.
<https://doi.org/10.1002/adma.201401400>.
- (5) Baetens, R.; Jelle, B. P.; Gustavsen, A. Properties, Requirements and Possibilities of Smart Windows for Dynamic Daylight and Solar Energy Control in Buildings: A State-of-the-Art Review. *Sol. Energy Mater. Sol. Cells* **2010**, *94*, 87–105.
<https://doi.org/10.1016/j.solmat.2009.08.021>.
- (6) Llordés, A.; Garcia, G.; Gazquez, J.; Milliron, D. J. Tunable Near-Infrared and Visible-Light Transmittance in Nanocrystal-in-Glass Composites. *Nature* **2013**, *500*, 323–326.
<https://doi.org/10.1038/nature12398>.
- (7) Cai, G.; Eh, A. L. S.; Ji, L.; Lee, P. S. Recent Advances in Electrochromic Smart Fenestration. *Adv. Sustain. Syst.* **2017**, *1*, 1–23.
<https://doi.org/10.1002/adsu.201700074>.
- (8) Rosseinsky, D. R.; Mortimer, R. J. Electrochromic Systems and the Prospects for Devices. *Adv. Mater.* **2001**, *13*, 783–793.
[https://doi.org/10.1002/1521-4095\(200106\)13:11<783::AID-ADMA783>3.0.CO;2-D](https://doi.org/10.1002/1521-4095(200106)13:11<783::AID-ADMA783>3.0.CO;2-D).
- (9) Mortimer, R. J.; Dyer, A. L.; Reynolds, J. R. Electrochromic Organic and Polymeric Materials for Display Applications. *Displays* **2006**, *27*, 2–18.

- <https://doi.org/10.1016/j.displa.2005.03.003>.
- (10) Beaujuge, P. M.; Reynolds, J. R. Color Control in π -Conjugated Organic Polymers for Use in Electrochromic Devices. *Chem. Rev.* **2010**, *110*, 268–320.
<https://doi.org/10.1021/cr900129a>.
- (11) Granqvist, C. G. Electrochromics for Smart Windows: Oxide-Based Thin Films and Devices. *Thin Solid Films* **2014**, *564*, 1–38.
<https://doi.org/10.1016/j.tsf.2014.02.002>.
- (12) García-Jareño, J. J.; Benito, D.; Navarro-Laboulais, J.; Vicente, F. Electrochemical Behavior of Electrodeposited Prussian Blue Films on ITO Electrodes: An Attractive Laboratory Experience. *J. Chem. Educ.* **1998**, *75*, 881–884.
<https://doi.org/10.1021/ed075p881>.
- (13) Christiansen, D. T.; Tomlinson, A. L.; Reynolds, J. R. New Design Paradigm for Color Control in Anodically Coloring Electrochromic Molecules. *J. Am. Chem. Soc.* **2019**, *141*, 3859–3862.
<https://doi.org/10.1021/jacs.9b01507>.
- (14) Yu, X.; Marks, T. J.; Facchetti, A. Metal Oxides for Optoelectronic Applications. *Nat. Mater.* **2016**, *15*, 383–396.
<https://doi.org/10.1038/nmat4599>.
- (15) Banasz, R.; Wałęsa-Chorab, M. Polymeric Complexes of Transition Metal Ions as Electrochromic Materials: Synthesis and Properties. *Coord. Chem. Rev.* **2019**, *389*, 1–18.
<https://doi.org/https://doi.org/10.1016/j.ccr.2019.03.009>.
- (16) Shankar, S.; Lahav, M.; Van Der Boom, M. E. Coordination-Based Molecular Assemblies as Electrochromic Materials: Ultra-High Switching Stability and Coloration Efficiencies. *J. Am. Chem. Soc.* **2015**, *137*, 4050–4053.
<https://doi.org/10.1021/jacs.5b00429>.
- (17) Eloul Dov, N.; Shankar, S.; Cohen, D.; Bendikov, T.; Rechav, K.; Shimon, L. J. W.; Lahav, M.; Van Der Boom, M. E. Electrochromic Metallo-Organic Nanoscale Films: Fabrication, Color Range, and Devices. *J. Am. Chem. Soc.* **2017**, *139*, 11471–11481.
<https://doi.org/10.1021/jacs.7b04217>.
- (18) Park, S.-I.; Quan, Y.-J.; Kim, S.-H.; Kim, H.; Kim, S.; Chun, D.-M.; Lee, C. S.; Taya, M.; Chu, W.-S.; Ahn, S.-H. A Review on Fabrication Processes for Electrochromic Devices. *Int. J. Precis. Eng. Manuf. Technol.* **2016**, *3*, 397–421.
<https://doi.org/10.1007/s40684-016-0049-8>.

- (19) Bera, M. K.; Mori, T.; Yoshida, T.; Ariga, K.; Higuchi, M. Construction of Coordination Nanosheets Based on Tris(2,2'-Bipyridine)-Iron (Fe²⁺) Complexes as Potential Electrochromic Materials. *ACS Appl. Mater. Interfaces* **2019**, *11*, 11893–11903. <https://doi.org/10.1021/acsami.8b22568>.
- (20) Mondal, S.; Ninomiya, Y.; Yoshida, T.; Mori, T.; Bera, M. K.; Ariga, K.; Higuchi, M. Dual-Branched Dense Hexagonal Fe(II)-Based Coordination Nanosheets with Red-to-Colorless Electrochromism and Durable Device Fabrication. *ACS Appl. Mater. Interfaces* **2020**, *12*, 31896–31903. <https://doi.org/10.1021/acsami.0c05921>.
- (21) Lahav, M.; van der Boom, M. E. Polypyridyl Metallo-Organic Assemblies for Electrochromic Applications. *Adv. Mater.* **2018**, *30*, 1706641. <https://doi.org/10.1002/adma.201706641>.
- (22) Higuchi, M. Electrochromic Organic-Metallic Hybrid Polymers: Fundamentals and Device Applications. *Polym. J.* **2009**, *41*, 511–520. <https://doi.org/10.1295/polymj.PJ2009053>.
- (23) Jaffe, A.; Long, J. R. Ordered Absences Observed in Porous Framework Materials. *Nature* **2020**, *578*, 222–223. <https://doi.org/10.1038/d41586-020-00329-5>
- (24) Sun, Y.; Chen, C.; Stang, P. J. Soft Materials with Diverse Suprastructures via the Self-Assembly of Metal-Organic Complexes. *Acc. Chem. Res.* **2019**, *52*, 802–817. <https://doi.org/10.1021/acs.accounts.8b00663>.
- (25) Ding, M.; Flaig, R. W.; Jiang, H. L.; Yaghi, O. M. Carbon Capture and Conversion Using Metal-Organic Frameworks and MOF-Based Materials. *Chem. Soc. Rev.* **2019**, *48*, 2783–2828. <https://doi.org/10.1039/c8cs00829a>.
- (26) Azhar, A.; Li, Y.; Cai, Z.; Zakaria, M. B.; Masud, M. K.; Hossain, M. S. A.; Kim, J.; Zhang, W.; Na, J.; Yamauchi, Y.; Hu, M. Nanoarchitectonics: A New Materials Horizon for Prussian Blue and Its Analogues. *Bull. Chem. Soc. Jpn.* **2019**, *92*, 875–904. <https://doi.org/10.1246/bcsj.20180368>.
- (27) Sun, J. K.; Yang, X. D.; Yang, G. Y.; Zhang, J. Bipyridinium Derivative-Based Coordination Polymers: From Synthesis to Materials Applications. *Coord. Chem. Rev.* **2019**, *378*, 533–560. <https://doi.org/10.1016/j.ccr.2017.10.029>.

- (28) Mizuno, A.; Shuku, Y.; Awaga, K. Recent Developments in Molecular Spin Gyroid Research. *Bull. Chem. Soc. Jpn.* **2019**, *92*, 1068–1093.
<https://doi.org/10.1246/bcsj.20190033>.
- (29) Cui, D.; Perepichka, D. F.; MacLeod, J. M.; Rosei, F. Surface-Confined Single-Layer Covalent Organic Frameworks: Design, Synthesis and Application. *Chem. Soc. Rev.* **2020**, *49*, 2020–2038.
<https://doi.org/10.1039/c9cs00456d>.
- (30) Ariga, K.; Shionoya, M. Nanoarchitectonics for Coordination Asymmetry and Related Chemistry. *Bull. Chem. Soc. Jpn.* **2021**, *94*, 839–859.
<https://doi.org/10.1246/BCSJ.20200362>.
- (31) Pai, S.; Moos, M.; Schreck, M. H.; Lambert, C.; Kurth, D. G. Green-to-Red Electrochromic Fe(II) Metallo-Supramolecular Polyelectrolytes Self-Assembled from Fluorescent 2,6-Bis(2-Pyridyl)Pyrimidine Bithiophene. *Inorg. Chem.* **2017**, *56*, 1418–1432.
<https://doi.org/10.1021/acs.inorgchem.6b02496>.
- (32) Han, F. S.; Higuchi, M.; Kurth, D. G. Metallosupramolecular Polyelectrolytes Self-Assembled from Various Pyridine Ring-Substituted Bisterpyridines and Metal Ions: Photophysical, Electrochemical, and Electrochromic Properties. *J. Am. Chem. Soc.* **2008**, *130*, 2073–2081.
<https://doi.org/10.1021/ja710380a>.
- (33) Hu, C.-W.; Sato, T.; Zhang, J.; Moriyama, S.; Higuchi, M. Three-Dimensional Fe(II)-Based Metallo-Supramolecular Polymers with Electrochromic Properties of Quick Switching, Large Contrast, and High Coloration Efficiency. *ACS Appl. Mater. Interfaces* **2014**, *6*, 9118–9125.
<https://doi.org/10.1021/am5010859>.
- (34) Han, F. S.; Higuchi, M.; Kurth, D. G. Metallo-Supramolecular Polymers Based on Functionalized Bis-Terpyridines as Novel Electrochromic Materials. *Adv. Mater.* **2007**, *19*, 3928–3931.
<https://doi.org/https://doi.org/10.1002/adma.200700931>.
- (35) Laschuk, N. O.; Ahmad, R.; Ebralidze, I. I.; Poisson, J.; Easton, E. B.; Zenkina, O. V. Multichromic Monolayer Terpyridine-Based Electrochromic Materials. *ACS Appl. Mater. Interfaces* **2020**, *12*, 41749–41757.
<https://doi.org/10.1021/acsami.0c11478>.
- (36) Bera, M. K.; Ninomiya, Y.; Higuchi, M. Constructing Alternated Heterobimetallic [Fe(II)/Os(II)] Supramolecular Polymers with Diverse Solubility for Facile Fabrication of

- Voltage-Tunable Multicolor Electrochromic Devices. *ACS Appl. Mater. Interfaces* **2020**, *12*, 14376–14385.
<https://doi.org/10.1021/acsami.9b21966>.
- (37) Jena, S. R.; Choudhury, J. A Fast-Switching Electrochromic Device with a Surface-Confined 3D Metallo-Organic Coordination Assembly. *Chem. Commun.* **2020**, *56*, 559–562.
<https://doi.org/10.1039/C9CC06920H>.
- (38) Deshmukh, M. A.; Gicevicius, M.; Ramanaviciene, A.; Shirsat, M. D.; Viter, R.; Ramanavicius, A. Hybrid Electrochemical/Electrochromic Cu(II) Ion Sensor Prototype Based on PANI/ITO-Electrode. *Sensors Actuators B Chem.* **2017**, *248*, 527–535.
<https://doi.org/https://doi.org/10.1016/j.snb.2017.03.167>.
- (39) Balgley, R.; de Ruiter, G.; Evmenenko, G.; Bendikov, T.; Lahav, M.; van der Boom, M. E. Light-Induced Conversion of Chemical Permeability to Enhance Electron and Molecular Transfer in Nanoscale Assemblies. *J. Am. Chem. Soc.* **2016**, *138*, 16398–16406.
<https://doi.org/10.1021/jacs.6b09781>.
- (40) Mukkatt, I.; Anjana, P. M.; Nirmala, A.; Rakhi, R. B.; Shankar, S.; Ajayaghosh, A. Metal Ion-Induced Capacitance Modulation in near-Isostructural Complexes-Derived Electrochromic Coordination Polymers. *Mater. Today Chem.* **2020**, *16*, 100260.
<https://doi.org/https://doi.org/10.1016/j.mtchem.2020.100260>.
- (41) Balgley, R.; Shankar, S.; Lahav, M.; van der Boom, M. E. Rerouting Electron Transfer in Molecular Assemblies by Redox-Pair Matching. *Angew. Chemie Int. Ed.* **2015**, *54*, 12457–12462.
<https://doi.org/https://doi.org/10.1002/anie.201505290>.
- (42) Takada, K.; Sakamoto, R.; Yi, S.-T.; Katagiri, S.; Kambe, T.; Nishihara, H. Electrochromic Bis(Terpyridine)Metal Complex Nanosheets. *J. Am. Chem. Soc.* **2015**, *137*, 4681–4689.
<https://doi.org/10.1021/ja510788b>.
- (43) Liang, Y.; Strohecker, D.; Lynch, V.; Holliday, B. J.; Jones, R. A. A Thiophene-Containing Conductive Metallopolymer Using an Fe(II) Bis(Terpyridine) Core for Electrochromic Materials. *ACS Appl. Mater. Interfaces* **2016**, *8*, 34568–34580.
<https://doi.org/10.1021/acsami.6b11657>.
- (44) Constable, E. C.; Thompson, A. M. W. C. Multinucleating 2,2':6',2''-Terpyridine Ligands as Building Blocks for the Assembly of Co-ordination Polymers and Oligomers. *J. Chem. Soc., Dalton Trans.* **1992**, 3467–3475.

- <https://doi.org/10.1039/DT9920003467>.
- (45) Vasilopoulou, M.; Aspiotis, G.; Kostis, I.; Argitis, P.; Davazoglou, D. Fabrication of WO₃-Based Electrochromic Displays Using Solid or Gel-like Organic Electrolytes. *J. Phys. Conf. Ser.* **2005**, *10*, 329–332.
<https://doi.org/10.1088/1742-6596/10/1/081>.
- (46) Tong, Z.; Tian, Y.; Zhang, H.; Li, X.; Ji, J.; Qu, H.; Li, N.; Zhao, J.; Li, Y. Recent Advances in Multifunctional Electrochromic Energy Storage Devices and Photoelectrochromic Devices. *Sci. China Chem.* **2017**, *60*, 13–37.
<https://doi.org/10.1007/s11426-016-0283-0>.
- (47) Zhang, Q.; Tsai, C.-Y.; Li, L.-J.; Liaw, D.-J. Colorless-to-Colorful Switching Electrochromic Polyimides with Very High Contrast Ratio. *Nat. Commun.* **2019**, *10*, 1239.
<https://doi.org/10.1038/s41467-019-09054-8>.
- (48) Motiei, L.; Kaminker, R.; Sassi, M.; van der Boom, M. E. Molecule and Electron Transfer through Coordination-Based Molecular Assemblies. *J. Am. Chem. Soc.* **2011**, *133*, 14264–14266.
<https://doi.org/10.1021/ja206179a>.
- (49) Zhao, D.; Timmons, D. J.; Yuan, D.; Zhou, H.-C. Tuning the Topology and Functionality of Metal–Organic Frameworks by Ligand Design. *Acc. Chem. Res.* **2011**, *44*, 123–133.
<https://doi.org/10.1021/ar100112y>.
- (50) Williams, M. E.; Benkstein, K. D.; Abel, C.; Dinolfo, P. H.; Hupp, J. T. Shape-Selective Transport through Rectangle-Based Molecular Materials: Thin-Film Scanning Electrochemical Microscopy Studies. *Proc. Natl. Acad. Sci.* **2002**, *99*, 5171–5177.
<https://doi.org/10.1073/pnas.082643199>.
- (51) Motesharei, K.; Ghadiri, M. R. Diffusion-Limited Size-Selective Ion Sensing Based on SAM-Supported Peptide Nanotubes. *J. Am. Chem. Soc.* **1997**, *119*, 11306–11312.
<https://doi.org/10.1021/ja9727171>.
- (52) Li, S.-S.; Northrop, B. H.; Yuan, Q.-H.; Wan, L.-J.; Stang, P. J. Surface Confined Metallosupramolecular Architectures: Formation and Scanning Tunneling Microscopy Characterization. *Acc. Chem. Res.* **2009**, *42*, 249–259.
<https://doi.org/10.1021/ar800117j>.
- (53) Fujita, M.; Ogura, K. Transition-Metal-Directed Assembly of Well-Defined Organic Architectures Possessing Large Voids: From Macrocycles to [2] Catenanes. *Coord. Chem.*

Rev. **1996**, *148*, 249–264.

[https://doi.org/https://doi.org/10.1016/0010-8545\(95\)01212-5](https://doi.org/https://doi.org/10.1016/0010-8545(95)01212-5).

- (54) Beck, R. E.; Schultz, J. S. Hindered Diffusion in Microporous Membranes with Known Pore Geometry. *Science* **1970**, *170*, 1302–1305.

<https://doi.org/10.1126/science.170.3964.1302>.

- (55) Bélanger, S.; Hupp, J. T.; Stern, C. L.; Slone, R. V.; Watson, D. F.; Carrell, T. G. Thin-Film Molecular Materials Based on Tetrametallic “Squares”: Nanoscale Porosity and Size-Selective Guest Transport Characteristics. *J. Am. Chem. Soc.* **1999**, *121*, 557–563.

<https://doi.org/10.1021/ja9829867>.

- (56) Freeman, B. D. Basis of Permeability/Selectivity Tradeoff Relations in Polymeric Gas Separation Membranes. *Macromolecules* **1999**, *32*, 375–380.

<https://doi.org/10.1021/ma9814548>.

- (57) Robeson, L. M. Correlation of Separation Factor versus Permeability for Polymeric Membranes. *J. Memb. Sci.* **1991**, *62*, 165–185.

[https://doi.org/https://doi.org/10.1016/0376-7388\(91\)80060-J](https://doi.org/https://doi.org/10.1016/0376-7388(91)80060-J).

- (58) Palomaki, P. K. B.; Krawicz, A.; Dinolfo, P. H. Thickness, Surface Morphology, and Optical Properties of Porphyrin Multilayer Thin Films Assembled on Si(100) Using Copper(I)-Catalyzed Azide–Alkyne Cycloaddition. *Langmuir* **2011**, *27*, 4613–4622.

<https://doi.org/10.1021/la104499b>.

- (59) Ellis, C. D.; Murphy, W. R.; Meyer, T. J. Selectivity and Directed Charge Transfer through an Electroactive Metallopolymer Film. *J. Am. Chem. Soc.* **1981**, *103*, 7480–7483.

<https://doi.org/10.1021/ja00415a014>.

- (60) Nishihara, H.; Noguchi, M.; Aramaki, K. Synthesis of Ferrocene and Cobaltocene Electrode Films by Electropolymerization and Their Spectral and Electrochemical Properties. *Inorg. Chem.* **1987**, *26*, 2862–2867.

<https://doi.org/10.1002/chin.198750287>.

- (61) Damrauer, N. H.; Boussie, T. R.; Devenney, M.; McCusker, J. K. Effects of Intraligand Electron Delocalization, Steric Tuning, and Excited-State Vibronic Coupling on the Photophysics of Aryl-Substituted Bipyridyl Complexes of Ru(II). *J. Am. Chem. Soc.* **1997**, *119*, 8253–8268.

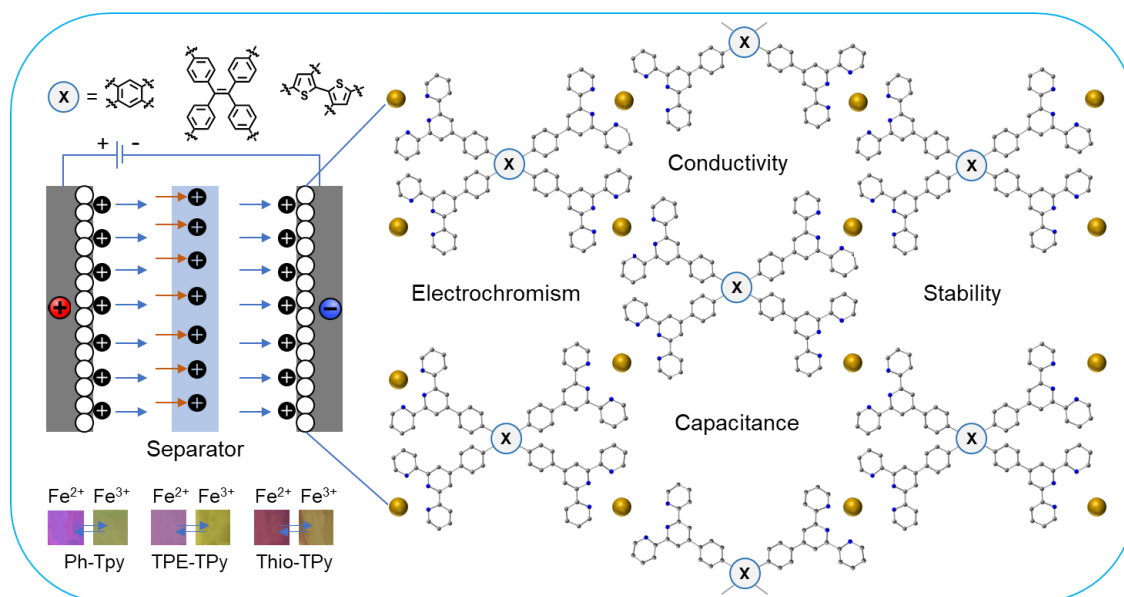
<https://doi.org/10.1021/ja971321m>.

- (62) Cai, G.; Wang, J.; Lee, P. S. Next-Generation Multifunctional Electrochromic Devices. *Acc.*

Chem. Res. **2016**, *49*, 1469–1476.

<https://doi.org/10.1021/acs.accounts.6b00183>.

Electrochromic Energy Storage and Tunable Capacitive Behavior of Fe(II) Coordinated Metallopolymers



3.1. Abstract

Volumetric capacitance is a critical performance parameter for rechargeable power supply in lightweight and microelectronic devices as compared to gravimetric capacitance in larger devices. To this end, we report three electrochromic metallopolymer-based electrode materials containing Fe^{2+} as the coordinating metal ion with high volumetric capacitance and energy densities in a symmetric two-electrode supercapacitor set-up. These metallopolymers exhibited volumetric capacitance up to 866.2 F cm^{-3} at a constant current density of 0.25 A g^{-1} . The volumetric capacitance (**Fe(II)-TPE-TPy**: 544.6 F cm^{-3} > **Fe(II)-Ph-TPy**: 313.8 F cm^{-3} > **Fe(II)-Thio-TPy**: 230.8 F cm^{-3} at 1 A g^{-1}) and energy densities (**Fe(II)-TPE-TPy**: 75.5 mWh cm^{-3} > **Fe(II)-Ph-TPy**: 43.6 mWh cm^{-3} > **Fe(II)-Thio-TPy**: 31.2 mWh cm^{-3}) followed the order of the electrical conductivity of the metallopolymers, and are among the best values reported for metal-organic systems. The variation in ligand structure was key towards achieving different electrical conductivities in these metallopolymers with excellent operational stability under continuous cycling. High volumetric capacitance and energy densities combined with tunable electro-optical properties and electrochromic behavior of these metallopolymers is expected to contribute to high performance and compact micro-energy storage systems. We envision that the integration of smart functionalities with thin film supercapacitors would warrant the surge of miniaturized on-chip micro-supercapacitors integrated in-plane with other microelectronic devices for wearable applications.

3.2. Introduction

Smart materials that respond to changes in environmental conditions are one among the holy grails in current materials science.¹⁻⁵ In this regard, electrochromic materials, capable of exhibiting voltage-dependent optical profiles, are of particular interest.⁶⁻¹⁰ Multifunctional electrochromic systems that regulate heat and light transmission leading to efficient indoor energy management has added several new dimensions to the classical concept of energy saving smart glass technologies.¹¹ Electrochemical energy storage aspects of such smart materials are directed towards combining energy saving and energy storage using a single system.¹²⁻¹⁴ However constructive coupling of smart functions with conventional device technologies is still in its infancy.^{15,16} Electrochromism is operationally similar to the rocking chair type energy storage mechanism and such multifunctional systems, that integrate smart functions with energy storage, are critical towards achieving universal energy access and conservation, energy sustainability and ensuring reliable power supply.^{12,13}

Some electrode materials with inherent electrochromic properties reversibly change their color during the faradaic reactions that occur with charge transfer. Such electrochromic energy storage devices are capable of detecting their state of charge by monitoring the color change and quantified by optical transmittance. Recent interest in the miniaturization of devices and flexible-wearable technologies, facilitated by the innovative design of integrated electronic architectures, have demanded the development of thin-film based energy storage technologies.¹⁷ Therefore, microscale electrochemical energy storage devices have attracted significant attention as alternative power sources in miniaturized electronic devices. The possibilities for optical modulation, fast charge-discharge process and high cycling stabilities make several electrochromic device architectures promising candidates for thin film based micro-electrochemical charge storage applications. In general, low thickness in the range of a few nanometers to less than a micrometer resulting in shorter distances for charge and ion transport allows for faster physical and chemical processes in thin film-based devices. Such ultra-thin supercapacitors are indeed ideal for construction of in-plane micro-storage systems capable of providing on-chip power sources for microelectronic applications. However, applications with large areal energy densities or longer operation times demand reasonably larger thickness for the films.¹⁷

Porous organic polymers with high power density, efficiency and cycling stability have been of contemporary interest as new generation electrode materials for electrochemical energy storage applications. The morphological features play a significant a role in determining the capacitive

behaviour of the material. In this context, Huang *et al.* have synthesized three-dimensional COFs with unique hollow spheres of 500–700 nm size, that was found to be prone to transporting ions more efficiently. Due to the presence of hollow spherical architecture and large surface area, the 3D COF exhibited a high specific capacitance of 251 F g⁻¹ at a current density of 0.5 A g⁻¹, a value superior to most 2D COFs and other porous electrode materials. The specific capacitance increases with the number of cycles, attaining a capacitance of 364 F g⁻¹ after 6000 cycles due to the wetting activation of the hollow spheres (**Figure 3.1**).¹⁸

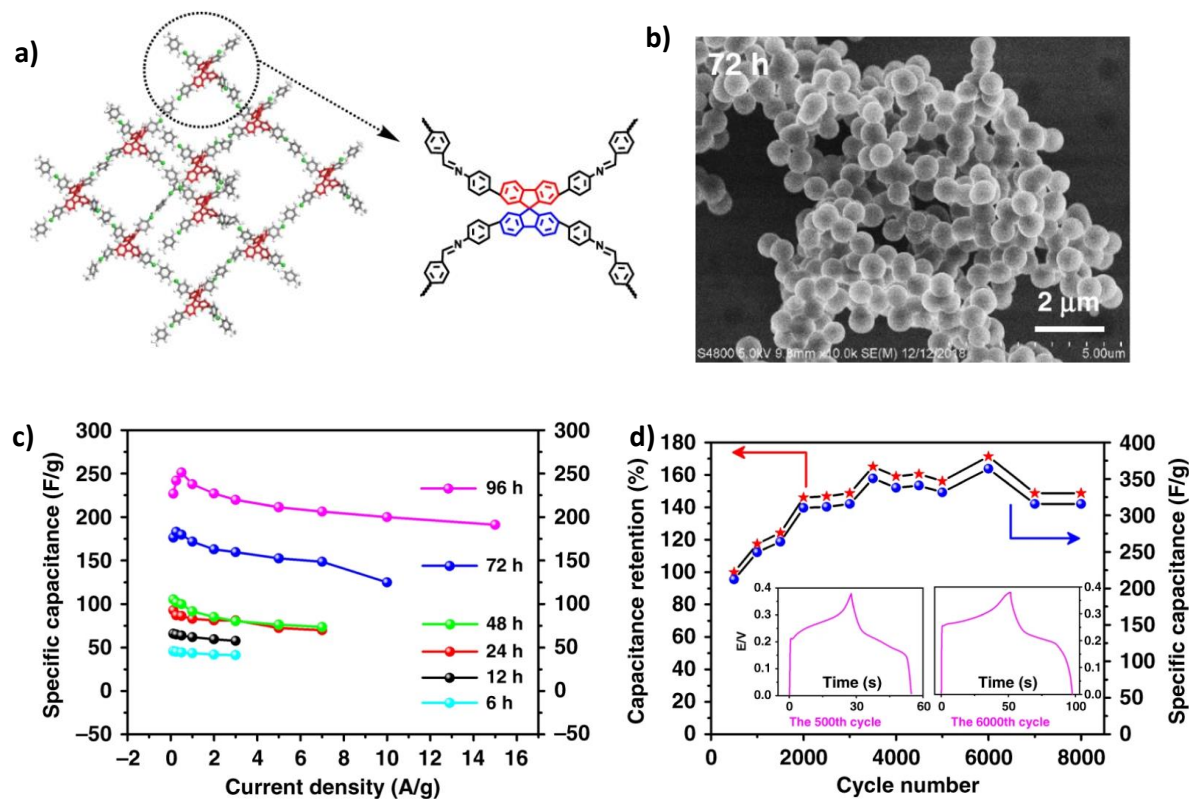


Figure 3.1. a) Schematic illustration of a 3D - COF and the corresponding chemical structure of the monomer. b) SEM image of the hollow spheres. c) Specific capacitance upon varying the current density. d) Cyclic stability of the 3D - COF. Adapted with permission from ref 18.

Incorporating plastic crystals into conjugated 3D COFs was also shown to accelerate ion transport by lowering the barrier for lithium-ion conduction, thereby providing access to solid state electrolytes with high conductivities for better electrochemical energy storage applications.¹⁹ Nitrogen rich conjugated microporous polymers also exhibited high specific capacitance despite having moderate surface areas, thereby corroborating the positive effect of heteroatoms in electrode materials for supercapacitor applications. Conjugated microporous polymers **TAT-CMP-1** and **TAT-CMP-2** based on nitrogen-rich triazatruxene building blocks were synthesized and explored for high-performance supercapacitors. The nitrogen groups

induce pseudocapacitance by enhancing charge mobility as well as introducing negative charges on the polymer surface, resulting in ion doping/de-doping. This polymer showed a high specific capacitance of 183 F g^{-1} at a current density of 1 A g^{-1} and retained 95% capacitance after 10000 cycles (**Figure 3.2**).²⁰

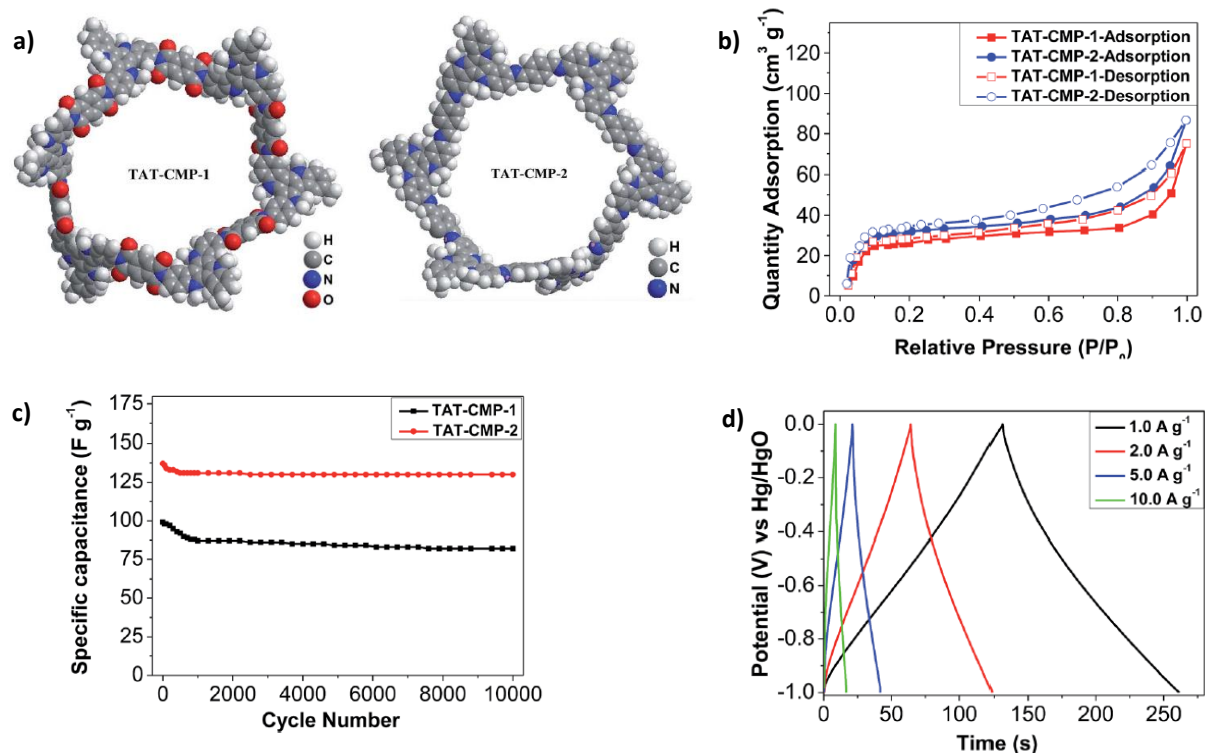


Figure 3.2. a) 3D view of the conjugated microporous polymers **TAT-CMP-1** and **TAT-CMP-2**. b) The corresponding nitrogen adsorption and desorption isotherms. c) Cycling stability at a current density of 10 A/g . d) Galvanostatic charge–discharge curves of **TAT-CMP-1**. Adapted with permission from ref 20.

While inorganic metal oxides are the preferred electrochromic materials, largely due to their high stability, the possible color variations are limited mostly to blue or brown.^{21–24} Many of the conducting polymers and small organic molecules, though provide exceptional color variations, suffer from concerns related to long term stability.^{25,26} Therefore, metal-organic systems that combine the advantages of inorganic and organic counterparts have emerged as a viable alternative in multifunctional electrochromism due to their structural regularity, packing variations, high surface area, tunable porosity and synthetic diversity.^{27–34}

These attributes combined with well-defined redox chemistry and tunable electro-optical properties make this class of materials as for non-carbon electrode materials for electrochemical/electrochromic energy storage applications.^{35–37} Several reports have shown

the significance of the collective properties of the electrode material particles in determining the capacitive performance, whereby material assembly or stacking assumes unprecedented operational significance leading to lower reproducibility and stability under continuous cycling.^{38–40} Therefore, there is an urgent need to develop thin film or micro-supercapacitors with a unique coherence of high volumetric capacitance, energy densities and cycling stability for bridging the gap between batteries and conventional capacitors, particularly for integrated microelectronic device applications.⁴¹

Bao and coworkers have reported conductive 2D metal-organic frameworks **Ni-HAB** based on hexaaminobenzene (**HAB**) ligand, that exhibited high volumetric capacitances up to 760 F cm^{-3} with good chemical stability in both acidic and basic aqueous solutions (**Figure 3.3**).³⁴

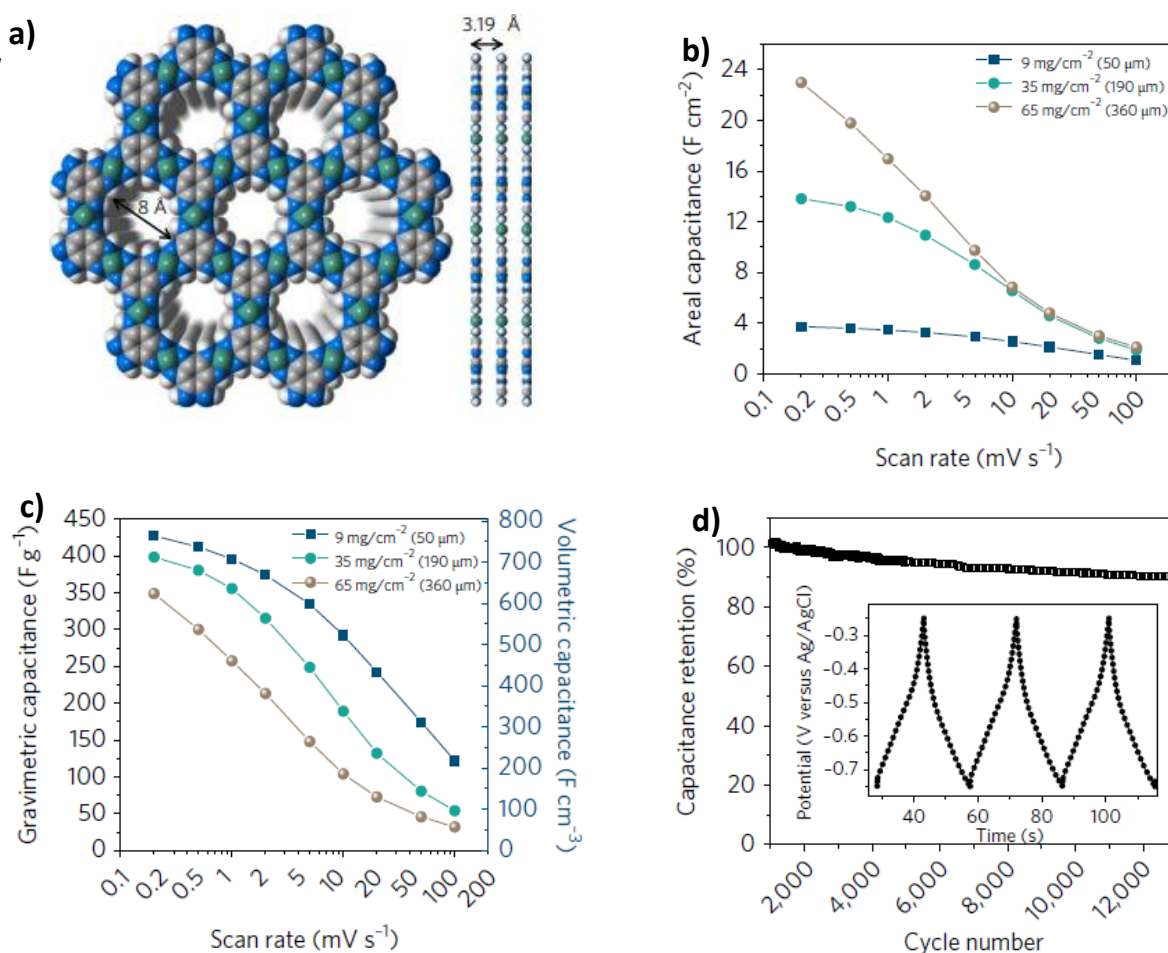


Figure 3.3. a) A space-filling model of the MOF **Ni-HAB**. Blue, grey, green and white spheres represent N, C, Ni and H atoms, respectively. b) Areal capacitance of **Ni-HAB** electrodes at different mass loadings. c) Gravimetric and volumetric capacitance of **Ni-HAB** pellets at different mass loadings of 9, 35 and 65 mg cm^{-2} . d) Cycling stability at 10 A g^{-1} . Adapted with permission from ref 34.

Ni-HAB pellets of 50 μm thickness showed an areal capacitance of 3.7 F cm^{-2} , and on increasing the thickness up to 360 μm , the areal capacitance increased to over 20 F cm^{-2} (**Figure 3.3b**). However, the gravimetric capacitance was found to follow an opposite trend (**Figure 3.3c**) with a capacitance retention of 90% even after 12,000 cycles (**Figure 3.3d**).³⁴

Dinca and coworkers have reported the synthesis of a non-porous coordination polymer (**Ni₃BHT**, **Figure 3.4a**) with high electrical conductivity (500 S m^{-1} , **Figure 3.4b**) and high volumetric capacitance (426 F cm^{-3}) and specific capacitance (245 F g^{-1}) under a reasonably large reductive potential window of 1.7 V using a non-aqueous electrolyte (**Figure 3.4c**).

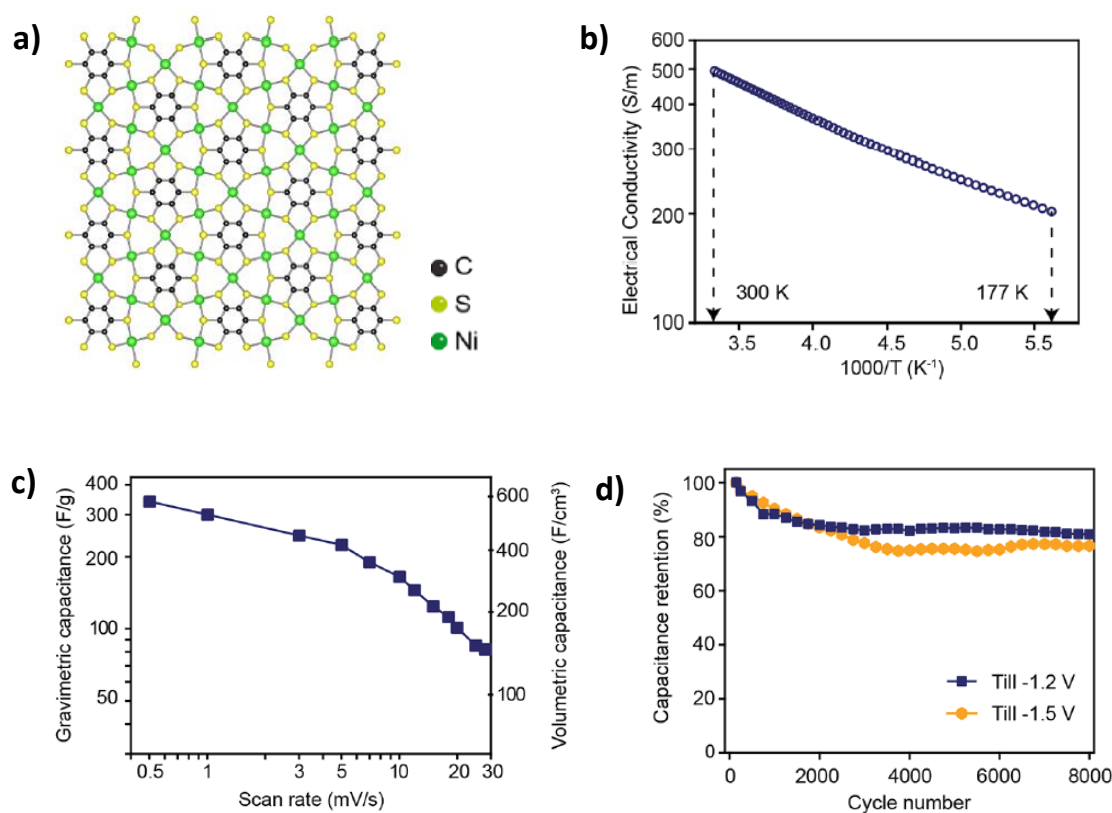


Figure 3.4. a) Simulated structure of of the coordination polymer **Ni₃BHT**. b) Temperature dependent electrical conductivity of **Ni₃BHT** pellets. c) Gravimetric and volumetric capacitance for electrodes fabricated from **Ni₃BHT** at different scan rates and d) the cycling stability at a scan rate of 30 mV s^{-1} . Adapted with permission from ref 42.

The excellent energy storage properties of **Ni₃BHT** was found to be due to pseudocapacitive intercalation of Li^+ ions between the 2D layers of the coordination polymer. Such modes of charge storage are reported only for inorganic metal oxides such as Nb_2O_5 and TiO_2 .⁴² This work is among the first examples for a non-porous coordination polymer showing charge storage due to pseudocapacitive intercalation of ions. **Ni₃BHT** exhibited $>80\%$ capacitance

retention after 8000 cycles (**Figure 3.4d**).⁴² The structure of the electrode most likely controlled the charge transfer resistance at the electrode/electrolyte interface, thereby transferring the charges through the interface.

Gang *et al.* have reported the use of nanowire arrays of the MOF **Cu-CAT** (**Figure 3.5a,b**) as supercapacitor electrodes in the absence of additives. Highly porous and conductive nanowire structures on the electrode surface resulted in high areal capacitance of $22 \mu\text{F cm}^{-2}$.⁴³ **Cu-CAT** based electrode retained 80% capacitive performance after 5000 cycles at 800 mV s^{-1} (**Figure 3.5c**).⁴³ The electrodes based on the nanowire arrays of **Cu-CAT** was found to exhibit two times higher areal capacitance than the powder state (**Figure 3.5d**). In another attempt to investigate MPOF-based composites as active electrodes in supercapacitors, Wang *et al.* have reported the use of cobalt-based MOF crystals interweaved with polyaniline (PANI) chains to reduce the bulk electrical resistance. The composite exhibited an areal capacitance of 2146 mF cm^{-2} at 10 mV s^{-1} and stability up to 2000 cycles with 80% capacitance retention.⁴⁴

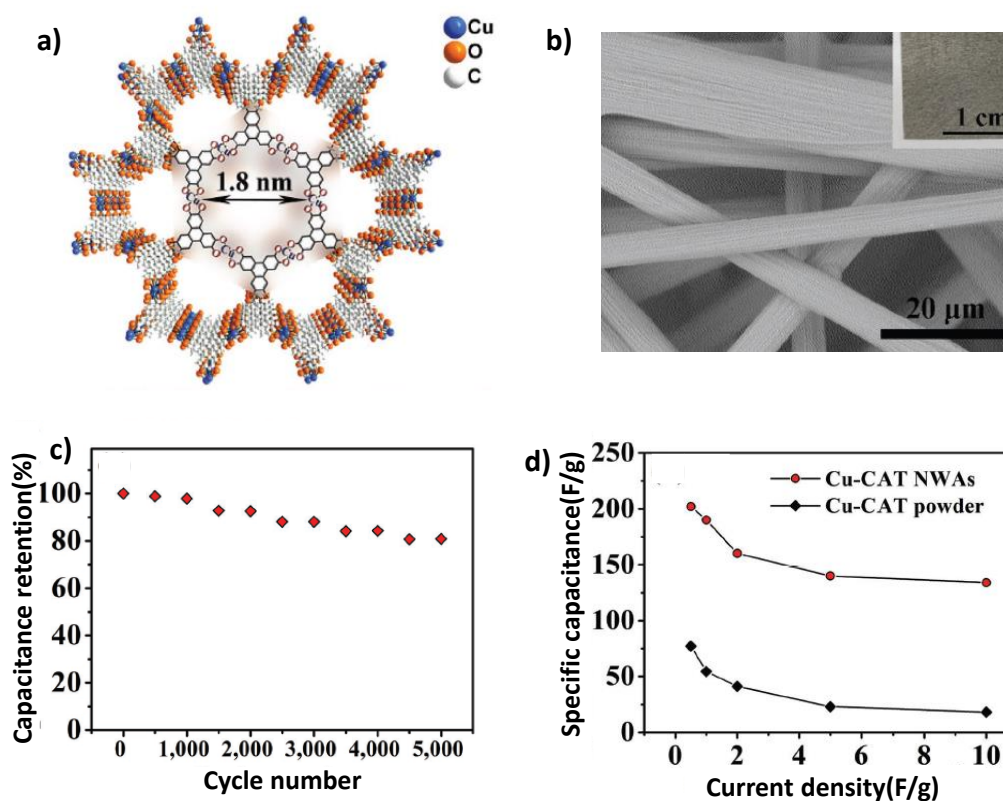


Figure 3.5. a) Crystal structure of the MOF **Cu-CAT** and b) SEM images of nanowire arrays grown on a filter paper. c) Cycling stability of the capacitor electrode at 800 mV s^{-1} . d) Specific capacitance at various current densities for electrodes fabricated from **Cu-CAT** nanowire arrays and **Cu-CAT** powder. (Adapted with permission from ref 43).

Nie *et al.* have constructed an electrochromic supercapacitor device consisting of poly(indole-5-carboxylic acid)/WO₃ (**P5ICA**/WO₃) nanocomposites with excellent electrochromic and energy storage properties. The all-solid electrochromic supercapacitor fabricated using **P5ICA**/WO₃ nanocomposites as working electrode and PEDOT as counter electrode showed specific capacitance of 10.11 mF cm⁻² and coloration efficiency of 608 cm² C⁻¹. **P5ICA**/WO₃ exhibited a visible color change from yellow to blue-green to dark green during charging and on reversibly change to yellow during discharging. A charge-discharge cycling stability up to 3000 cycles with 12% loss in capacitance was also observed (**Figure 3.6**).^{43a}

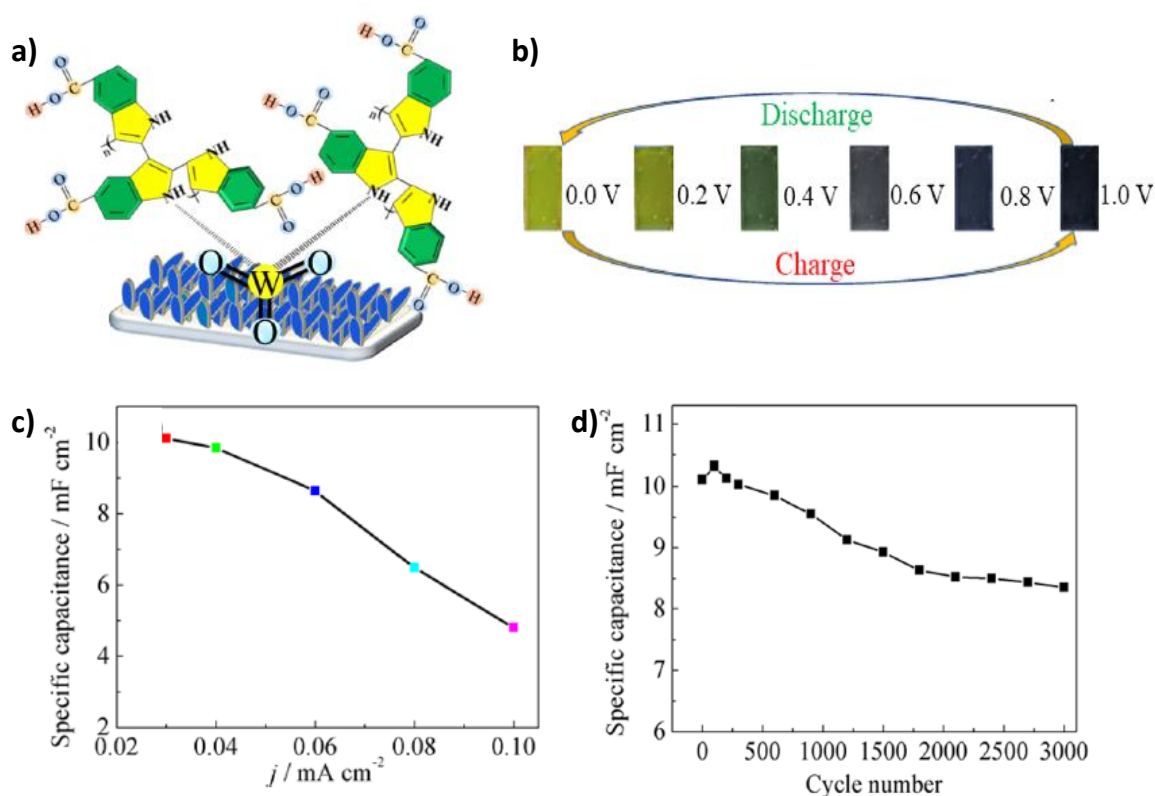


Figure 3.6 a) Schematic representation of **P5ICA**/WO₃ nanocomposites. b) Color change in the electrochromic supercapacitor device during charging and discharging. c) Specific capacitance of the electrode fabricated from **P5ICA**/WO₃ nanocomposites under different current densities. d) Galvanic charge discharge stability at 0.1 mA cm⁻². Adapted with permission from ref 43a.

van der Boom and co-workers have reported an electrochromic-hybrid supercapacitor (EHSC) using iron polypyridyl complexes as electrochromic metal-organic layer and composites of multiwalled carbon nanotubes (MWCNTs) and a conductive polymer PEDOT:PSS as the capacitive layer. The amount of available charge was found to be depicted by the color of the metal complexes. The device showed a specific capacitance of 10.7 F g⁻¹ with high energy and

power densities (2.2 Wh kg^{-1} and 2529 W kg^{-1} , respectively). The device was found to operate with high stability exceeding 1000 consecutive charging–discharging cycles with a short charging time of 2 s (**Figure 3.7**).^{43b}

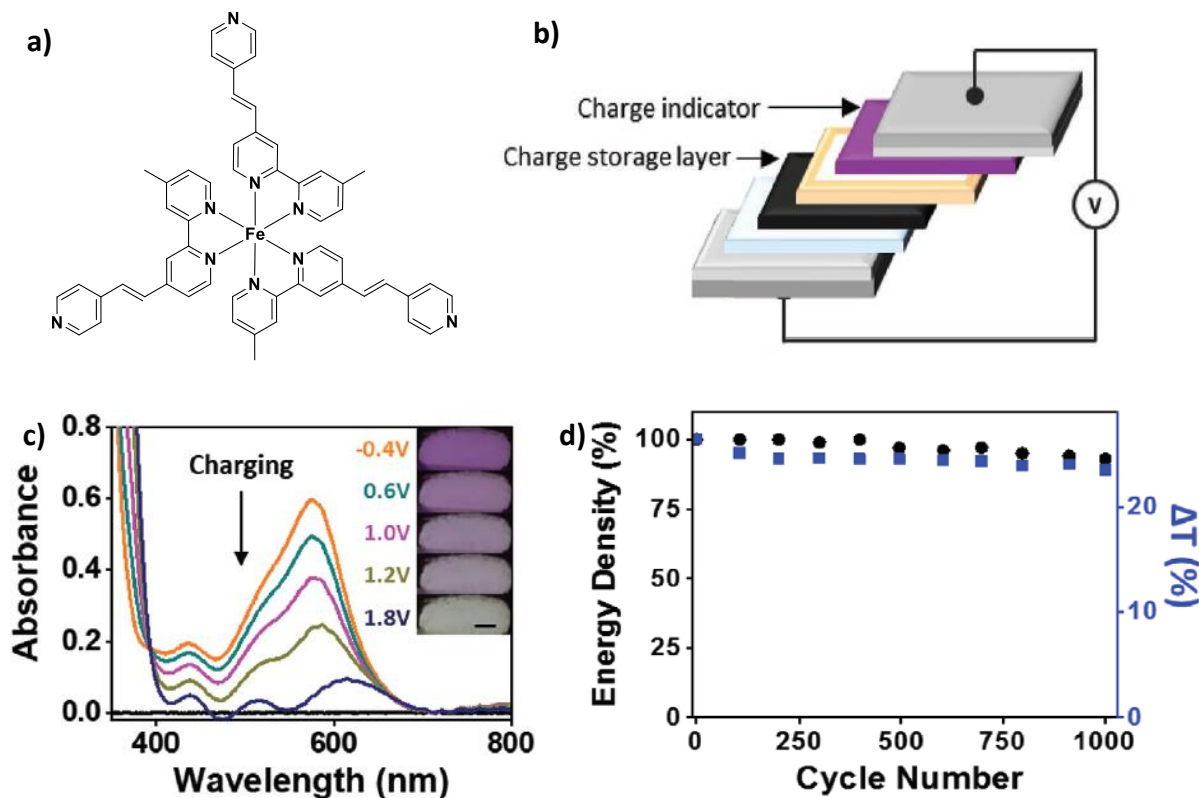


Figure 3.7. a) Structure of the iron polypyridyl complex used as electrochromic layer in an electrochromic–hybrid supercapacitor (EHSC). b) Schematic representation showing the device architecture. c) Absorption spectra and photographs at five different potentials during charging. d) Stability of the electrochromic-hybrid supercapacitor at a current density of 0.88 A g^{-1} . Adapted with permission from ref 43b.

In the previous chapter we reported the electrochromic diversification in metallocupramolecular assemblies and was mainly attributed to the differences in thin film porosity emanating from differences in ligand structure.⁴⁵ However, the electrochemical profiles of the nanoscale spray coated thin films need not be exactly replicated by the isolated metallopolymers. While allowing color-to-color transitions with good efficiency and stability, the electrochemical energy storage properties of such network materials having the same metal ion coordinated to a series of conjugated ligands that differ in their core-structure is not easy to predict. Porosity and surface area of such materials have earlier been shown to dictate the capacitive performance of metal-organic materials.⁴⁶ In this chapter, we demonstrate that electrical conductivity is a

rather more dominant parameter in determining the electrochemical energy storage properties, particularly for low surface area metal-organic materials.⁴⁷ Using electrochromic metallopolymers featuring Fe(II)-terpyridine coordination and high electrical conductivity, supercapacitor electrodes with volumetric capacitance up to 866.2 F cm^{-3} at a current density of 0.25 A g^{-1} and volumetric energy densities up to 75.5 mWh cm^{-3} were fabricated. The capacitive performance, charge-discharge kinetics and charge transfer resistance of the metallopolymers were found to be directly correlated to their electrical conductivity. Further, no deterioration in performance was observed upon multiple cycles of continuous operation and the observed capacitance values and energy densities are superior to or at par with prior literature reports.

3.3 Results and Discussion

3.3.1 Synthesis and Characterization

The ligands **Ph-TPy**, **TPE-TPy** and **Thio-TPy** (**Figure 3.8**) were synthesized using the Suzuki coupling reactions between the boronic acid derivative of terpyridine and the corresponding tetrabromo derivative of benzene, tetraphenyl ethylene or bithiophene.⁴⁵ The detailed synthetic procedure and characterization data are given in the experimental section of Chapter 2.

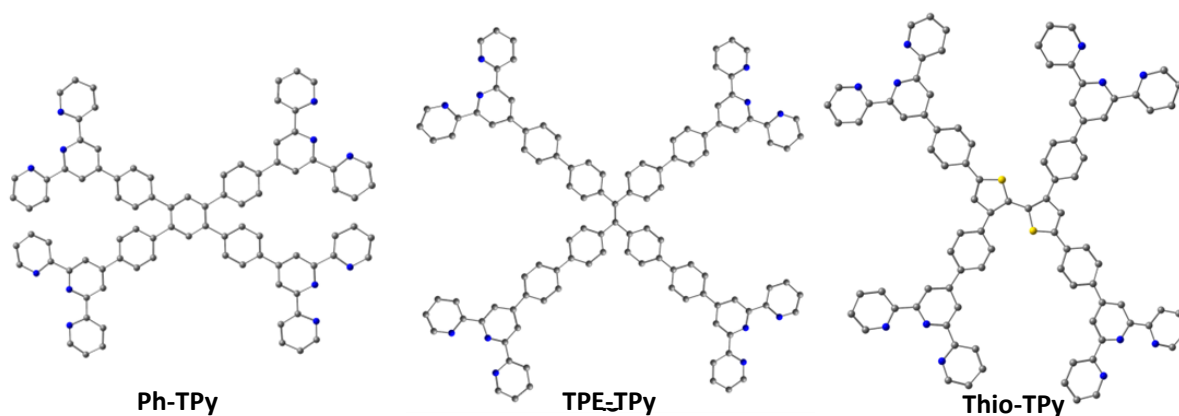


Figure 3.8. A ball-and-stick model showing the molecular structures of the terpyridine ligands a) **Fe(II)-Ph-TPy**, b) **Fe(II)-TPE-TPy** and c) **Fe(II)-Thio-TPy**. The metallopolymers were synthesized by mixing FeCl_2 and the corresponding ligand in a 2:1 molar ratio and were precipitated from water as their PF_6 salts. Hydrogen atom is omitted for clarity. Color codes – grey: carbon, blue: nitrogen, yellow: sulfur.

The metallopolymers **Fe(II)-Ph-TPy**, **Fe(II)-TPE-TPy** and **Fe(II)-Thio-TPy** as their PF₆ salts, with a general formula [Fe(L)₂]_n(PF₆)_{2n} (L = **Ph-TPy**, **TPE-TPy** and **Thio-TPy**), were synthesized by adding a methanolic solution of FeCl₂ to a solution of the corresponding ligand in methanol followed by precipitation from water saturated with ammonium hexafluorophosphate.

¹H NMR spectra of the metallopolymer solutions in CD₃OD exhibited broad and unresolved peaks, most likely due to the paramagnetic nature of the central metal ion. Addition of the metal salt into the ligand solution resulted in an instantaneous purple coloration and the MLCT (metal-to-ligand charge transfer) bands were observed at 570-574 nm for all the three metallopolymers. The extinction coefficients at λ_{MLCT} (MeOH) were found to be 3.43×10⁴ M⁻¹cm⁻¹ for **Fe(II)-Ph-TPy**, 3.40×10⁴ M⁻¹cm⁻¹ **Fe(II)-TPE-TPy** and 5.1×10⁴ M⁻¹cm⁻¹ for **Fe(II)-Thio-TPy** (**Figure 3.9a-c**).

While the ligands exhibited moderate emission in methanol, metal complexation was found to result in near-complete quenching of fluorescence (**Figure 3.9d-f**). FT-IR spectra of all three metallopolymers corroborated the coordination of Fe(II) to the terpyridine ligands as evidenced by the shift in C=C vibrations 1583 ± 1 cm⁻¹ to 1601 ± 2 cm⁻¹, which is characteristic for terpyridine-metal coordination.³⁷ A shift was also observed in the C-H in-plane deformation frequencies, that appeared at 1413 ± 4 cm⁻¹ for the free ligands, which upon metal complexation were shifted to 1407 ± 3 cm⁻¹ (**Figure 3.10**).^{37,45}

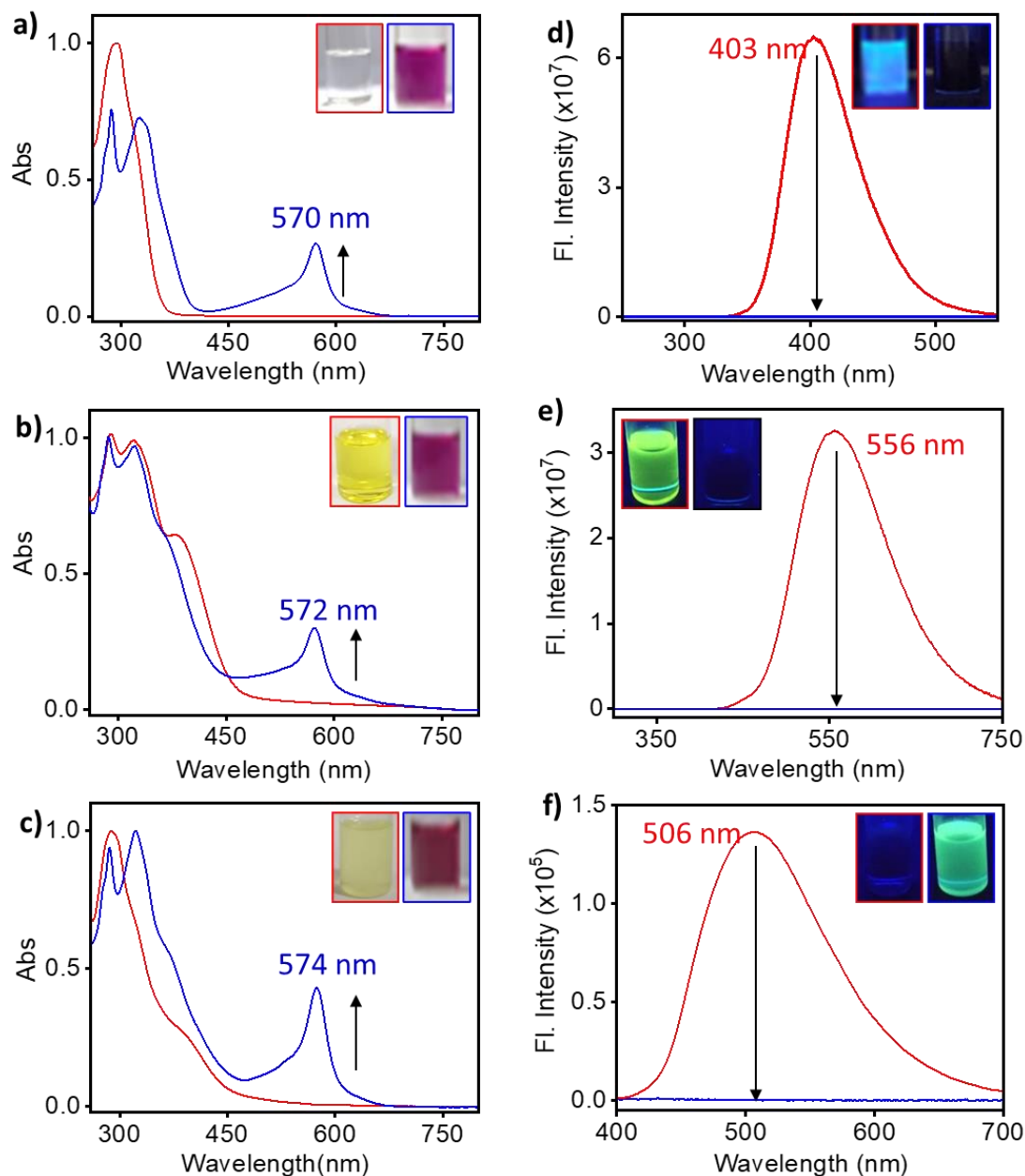


Figure 3.9. UV-Vis spectra of a) **Ph-TPy** (red) and **Fe(II)-Ph-TPy** (blue), b) **TPE-TPy**(red) and **Fe(II)-TPE-TPy** (blue), and c) **Thio-TPy**(red) and **Fe(II)-Thio-TPy** (blue), in methanol ($c = 15 \mu\text{M}$). Photographs of the ligand (red border) and metallopolymer (blue border) solutions under visible light are shown in the insets. Emission spectra of d) **Ph-TPy** (red) and **Fe(II)-Ph-TPy** (blue), e) **TPE-TPy**(red) and **Fe(II)-TPE-TPy** (blue), and f) **Thio-TPy**(red) and **Fe(II)-Thio-TPy** (blue), in methanol ($c = 15 \mu\text{M}$). Insets: Photographs of the ligand (red border) and metallopolymer (blue border) solutions under UV-light. The arrows represent the change upon addition of the metal salt to the corresponding ligand solution. The corresponding λ_{\max} is also shown.

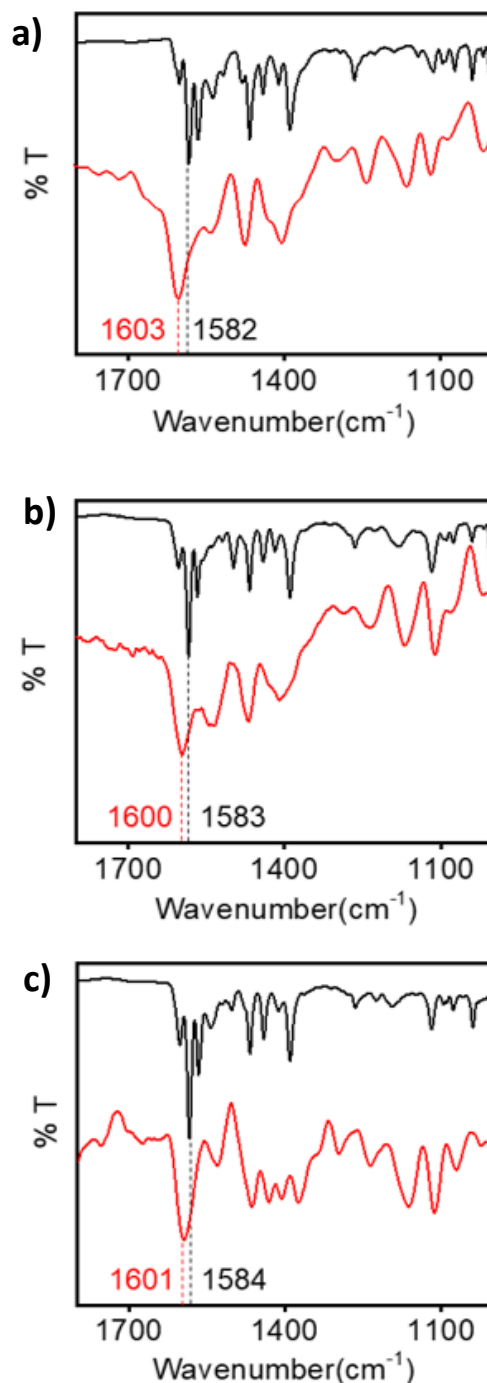


Figure 3.10. FT-IR spectra of a) **Ph-TPy** (black) and **Fe(II)-Ph-TPy** (red), b) **TPE-TPy** (black) and **Fe(II)-TPE-TPy** (red), and c) **Thio-TPy** (black) and **Fe(II)-Thio-TPy** (red). The spectra were recorded in the solid state (KBr, neat). The peaks (wave number in cm^{-1}) corresponding to C=N ring stretching and in plane C-H deformation are provided in each spectrum (black: complex; grey: coordination polymer).

The morphology of the coated films on freshly cleaved mica were obtained using atomic force microscopy (AFM). The AFM images of all three metallopolymer confirmed the formation of

grain-like features densely covering the surface (**Figure 3.11a-c**). The films of **Fe(II)-TPE-TPy** appeared to have fewer open spaces and may likely result in less porous assemblies (**Figure 3.11 b**). The 3D topographies of assemblies confirmed similar roughness of the surfaces (**Figure 3.11 d-f**).

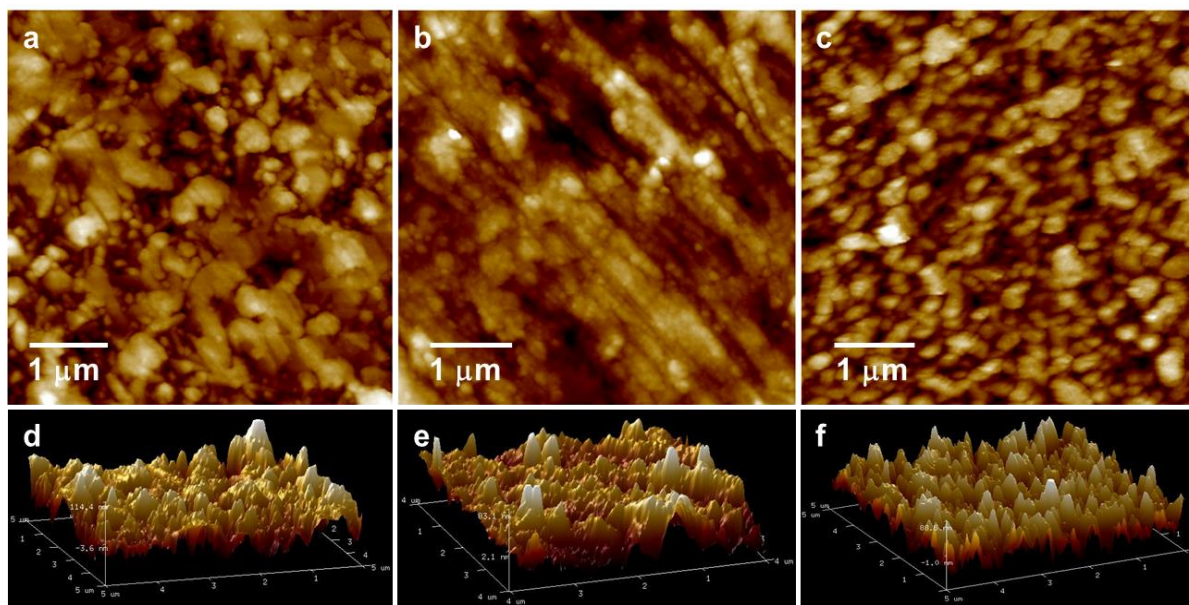


Figure 3.11. AFM images (a-c) and 3D topographies (d-f) of the metallopolymer coatings on freshly cleaved mica: (a,d) **Fe(II)-Ph-TPy**, (b,e) **Fe(II)-TPE-TPy** and (c,f) **Fe(II)-Thio-TPy**.

Powder X-ray diffraction (PXRD) confirmed the amorphous nature of the metallopolymer, that most likely stems from the fast complexation and/or precipitation processes (**Figure 3.12**). Nevertheless, very modest molecular ordering was observed for **Fe(II)-Ph-TPy** as corroborated by low intensity peaks in its PXRD spectrum and the selected area diffraction pattern in TEM (**Figure 3.12 a**).

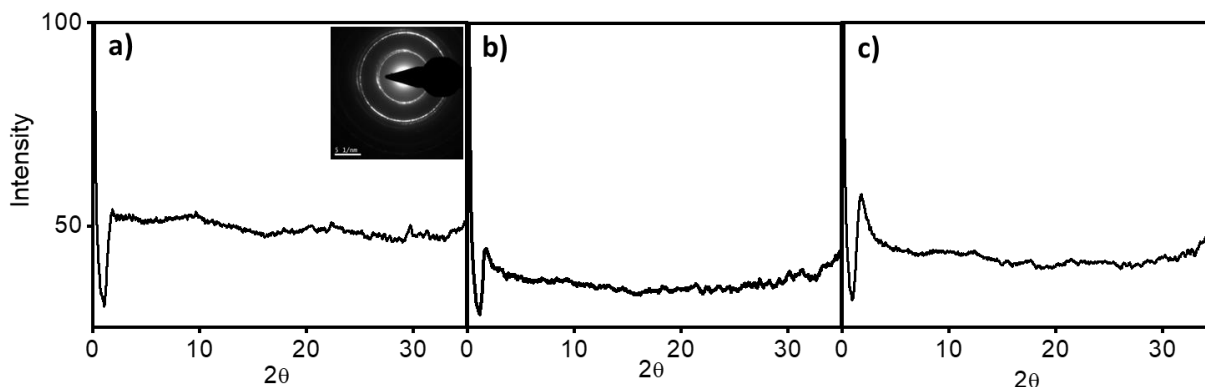
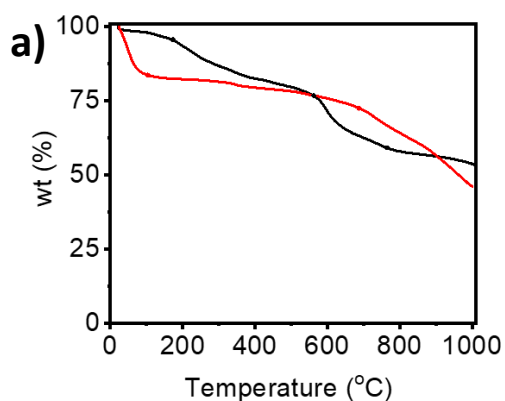
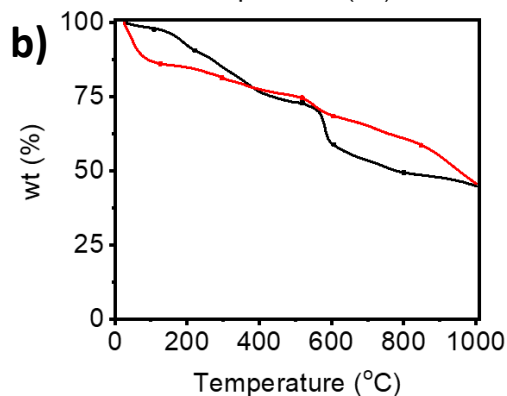


Figure 3.12. Powder X-ray diffraction spectra of a) **Fe(II)-Ph-TPy**, b) **Fe(II)-TPE-TPy**, and c) **Fe(II)-Thio-TPy**. The selected area diffraction pattern from TEM is shown in the inset.

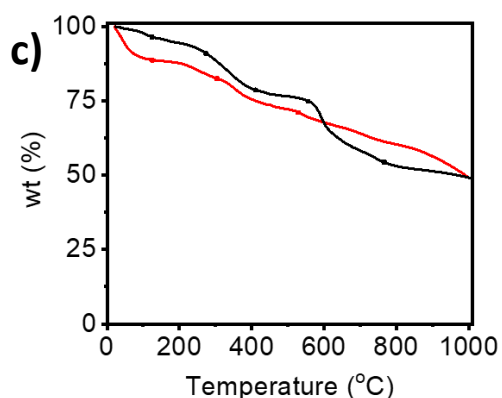
Thermogravimetric analysis under nitrogen atmosphere was conducted to establish the thermal stability of the metallopolymers. Weight loss of approximately half the initial weight of the metallopolymers were observed upon heating to 1000°C. Surprisingly, the ligands and the corresponding metallopolymers exhibited more or less similar thermal stability (**Figure 3.13**).



Ph-TPy		Fe(II)-Ph-TPy	
Temp. (°C)	Wt%	Temp. (°C)	Wt%
172.0	95	110.0	83.5
562.0	84.6	690.0	72.5
764.0	59.2	1000.0	45.5
1000.0	30.0		



TPE-TPy		Fe(II)-TPE-TPy	
Temp. (°C)	Wt%	Temp. (°C)	Wt%
109.0	97.7	126.0	86.0
220.0	90.7	296.0	81.3
519.0	72.8	519.0	74.8
605.0	58.7	605.0	68.5
800.0	49.2	848.0	58.5
1000.0	44.8	1000.0	45.4



Thio-TPy		Fe(II)-Thio-TPy	
Temp. (°C)	Wt%	Temp. (°C)	Wt%
125.0	96.7	125.0	88.7
272.0	90.9	304.0	82.4
410.0	78.8	528.0	71.0
556.0	75	1000.0	48.9
767.0	54.5		
1000.0	48.9		

Figure 3.13. Thermogravimetric curves of a) **Ph-TPy** (black) and **Fe(II)-Ph-TPy** (red), b) **TPE-TPy** (black) and **Fe(II)-TPE-TPy** (red), and c) **Thio-TPy** (black) and **Fe(II)-Thio-TPy** (red). The tables on the right present the decomposition temperature and the corresponding weight retained at each temperature.

The elemental composition of the metallopolymers was qualitatively estimated using X-ray Photoelectron Spectroscopy (XPS). The presence of iron(II) in all the metallopolymers were

confirmed by the $\text{Fe}^{2+} 3p_{3/2}$ (709 eV) and $\text{Fe}^{2+} 3p_{1/2}$ (721-722 eV) in the high resolution XPS data. Characteristic peaks corresponding to N 1s were also observed at binding energies of 399-402 eV in the X-ray photoelectron spectra of the metallopolymers (**Figure 3.14**). A near 2:1 metal to ligand ratio was also observed in the XPS analysis. The characteristic peaks corresponding to the expected chemical structure of the metallopolymers (ring breathing at 1047 cm^{-1} , $\nu(\text{C}=\text{C})$ Inter-ring at $1296\text{-}1298\text{ cm}^{-1}$, $\nu(\text{C}=\text{N})$ and $\nu(\text{C}=\text{C})$ at 1370 cm^{-1} , $1479\text{-}1480\text{ cm}^{-1}$ and $1612\text{-}1614\text{ cm}^{-1}$, $\nu(\text{C}=\text{C})$ at $1320\text{-}1348\text{ cm}^{-1}$ and $1611\text{-}1612\text{ cm}^{-1}$) were also observed in their Raman spectra (**Figure 3.15**).

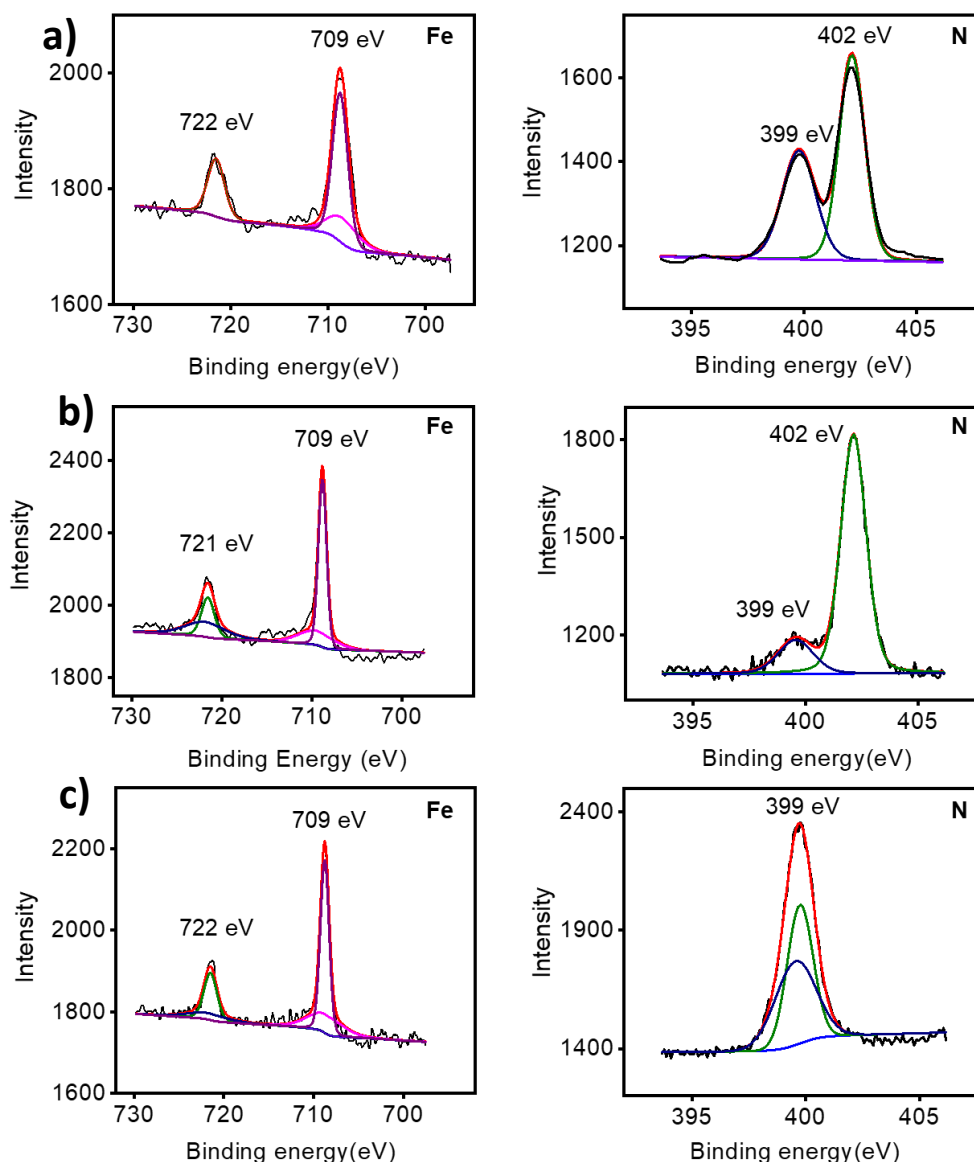


Figure 3.14. High resolution XPS data confirming the Fe $3p_{1/2}$ and Fe $3p_{3/2}$ (left) and N 1s peaks for the metallopolymers: a) **Fe(II)-Ph-TPy**, b) **Fe(II)-TPE-TPy**, and c) **Fe(II)-Thio-TPy**. The binding energy corresponding to each peak is provided in each figure.

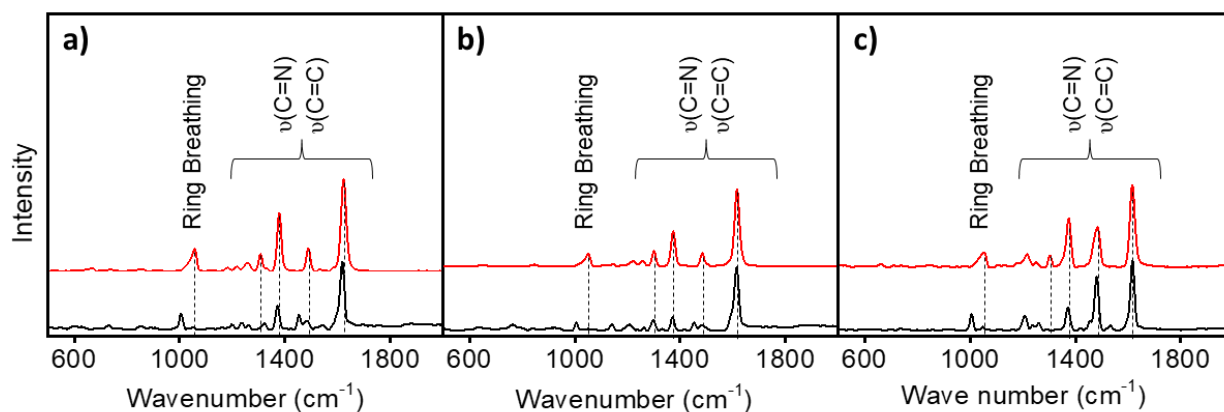


Figure 3.15. Raman spectra of a) **Ph-TPy** (black) and **Fe(II)-Ph-TPy** (red), b) **TPE-TPy** (black) and **Fe(II)-TPE-TPy** (red), and c) **Thio-TPy** (black) and **Fe(II)-Thio-TPy** (red).

3.3.2 Electrochemistry and Spectroelectrochemistry

The metallopolymers were intensely colored due to the MLCT bands in their UV-Vis spectra (**Figure 3.9 a-c**).⁴⁸ The one-electron redox reactions of Fe(II)-terpyridine systems are well documented in the literature.^{49–52} In the previous chapter, we have reported the spectroelectrochemical diversification leading to ligand modulated electrochromic performance in spray-coated metallopolymer assemblies comprising similar metal-ligand combinations.⁴² The metallopolymers in MeOH were drop-cast on transparent conducting oxide (TCO) substrates for investigating their electrochemical redox behaviour. The electrochemical profiles of the metallopolymers were probed using a three-electrode set-up (metallopolymer modified TCO as working, Ag/AgCl as reference and platinum wire as counter electrodes) in 0.1 M lithium perchlorate in acetonitrile as supporting electrolyte. The redox behaviour of the metallopolymer thin films were confirmed at varying scan rates (10 – 300 mV s⁻¹, **Figure 3.16 a-c**) and was further used to validate the possible electron transfer mechanism and elucidate the role of the diffusion of electrolyte ions during the charge storage process in these assemblies. The scan rate dependence of changes in current in the cyclic voltammograms is indicative of the operative electron transfer mechanism in the metallopolymer thin films.^{28,51,53} While the films of **Fe(II)-Ph-TPy** and **Fe(II)-Thio-TPy** exhibited a near-linear increase in cathodic and anodic current with increase in scan rate (**Figure 3.17a,c**), **Fe(II)-TPE-TPy** exhibited a slightly exponential trend (**Figure 3.17b**). An exponential dependence of current with square root of scan rate was observed for **Fe(II)-Ph-TPy** and **Fe(II)-Thio-TPy** (**Figure 3.17d,f**), whereas a linear dependence was observed for **Fe(II)-TPE-TPy** (**Figure 3.17e**).

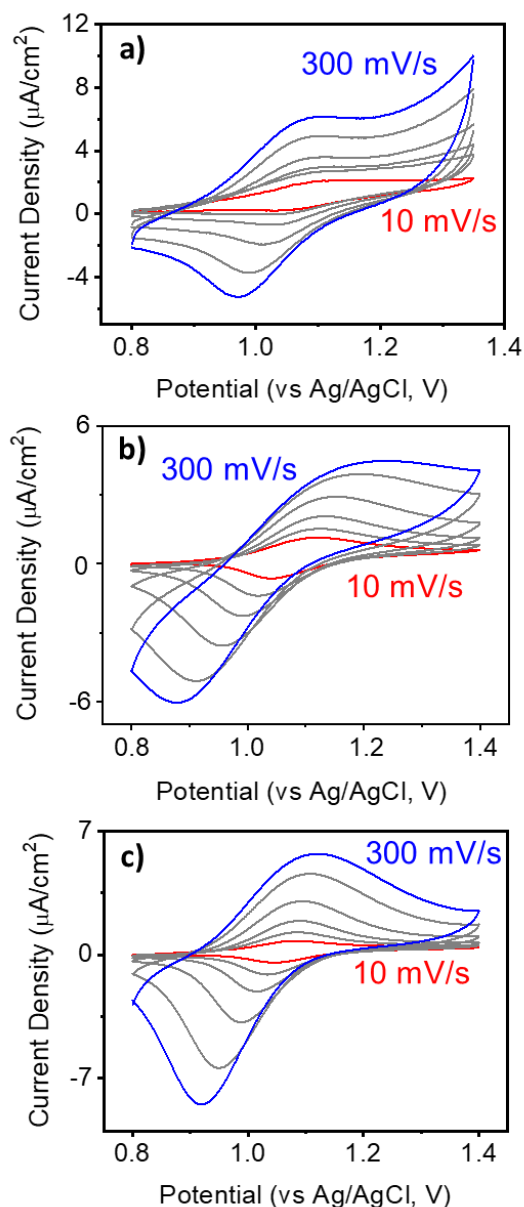


Figure 3.16. Cyclic Voltammograms of a) **Fe(II)-Ph-TPy**, b) **Fe(II)-TPE-TPy**, and c) **Fe(II)-Thio-Tpy** at varying scan rates between 10 (red) and 300 (blue) mV s^{-1} . CVs were obtained using the corresponding metallopolymer modified FTO as working electrode, Ag/AgCl as reference electrode and Pt wire as counter electrode. A 0.1 M solution of lithium perchlorate in dry acetonitrile was used as the supporting electrolyte.

These observations are indicative of different electron transfer mechanisms in operation in these sets of assemblies. The results suggest an electron transfer mechanism limited by slow diffusion in the assemblies formed from **Fe(II)-TPE-TPy**, whereas the diffusion of electrolyte ions may not have a significant effect in the electron transfer rate determining step for the other two assemblies.^{28,51,53} We have previously demonstrated the electrochromic behaviour of these

assemblies using a semi-automated spray coating unit.⁴⁵ While multiple layers of controlled spray coating were required to obtain uniform thin films of the metallopolymers in the previous study, the present work takes advantage of simple drop-casting to form similar films with increased thickness and slightly lower uniformity, without compromising the spectroelectrochemical switching. The single electron redox process, as observed during the electrochemical experiments, was found to be accompanied by a visible change in color. All the metallopolymer assemblies on TCO exhibited color-to-color switching from shades of purple to yellow, when subjected to application of electric potential between 0.7 and 1.5 V (*vs* Ag/AgCl).

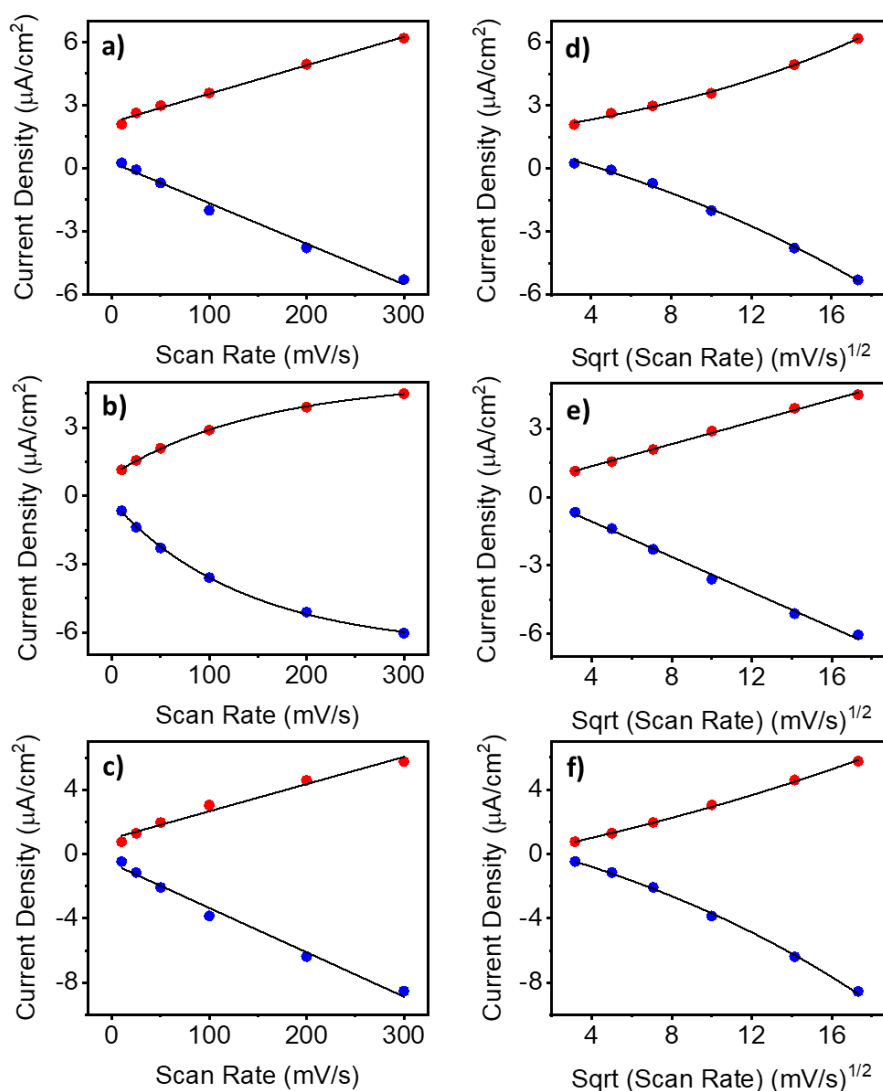


Figure 3.17. The dependence of current on the scan rates (d-f) and square root of the scan rates (g-i) for (d,g) **Fe(II)-Ph-TPy**, (e,h) **Fe(II)-TPE-TPy**, and (f,i) **Fe(II)-Thio-TPy**. CVs (See **Figure 3.14**) were obtained using the corresponding metallopolymer modified FTO as working electrode, Ag/AgCl as reference electrode and Pt wire as counter electrode. A 0.1 M solution of lithium perchlorate in dry acetonitrile was used as the supporting electrolyte.

The electrochromic color switching was quite similar to the corresponding spray coated films and was confirmed by the bleaching of the MLCT bands in the corresponding UV-Vis spectra (**Figure 3.18a-c**). The chromaticity diagram also corroborates the observed color change (**Figure 3.18d-f**), with a response time of less than 3 seconds for all the metallopolymer. We have shown in the previous chapter, via molecular permeability experiments, that spray coated films of **Fe(II)-Ph-TPy** are more porous compared to **Fe(II)-Thio-TPy**, while those of **Fe(II)-TPE-TPy** exhibited the least porosity.⁴²

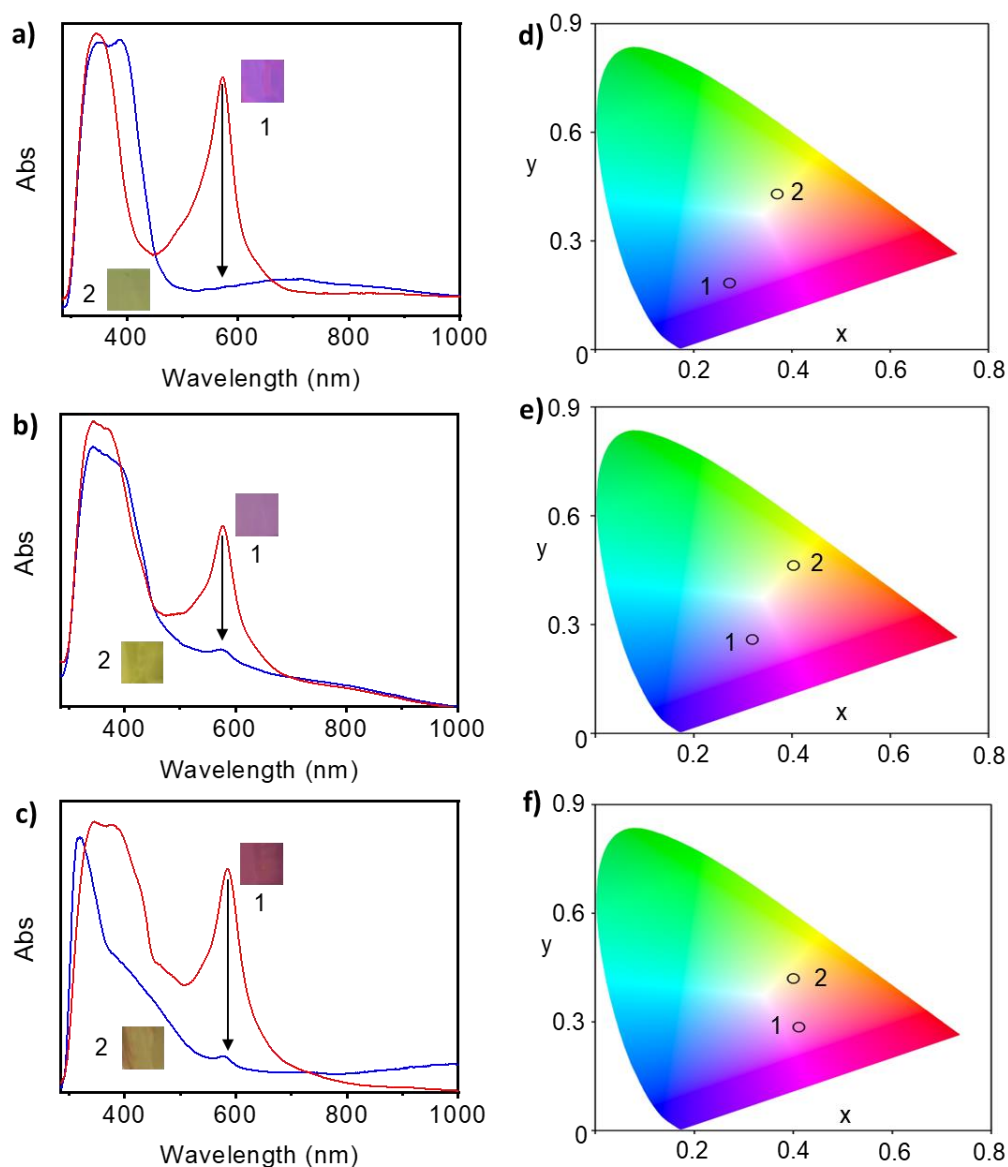


Figure 3.18. UV-Vis spectra of the metallopolymer drop-casted on FTO substrates confirming the bleaching of the MLCT bands during the electrochemical oxidation of the assemblies constructed from a) **Fe(II)-Ph-TPy**, b) **Fe(II)-TPE-TPy**, and c) **Fe(II)-Thio-TPy**. The spectra corresponding to the reduced and oxidized states are shown in red and blue, respectively. The

photographs of the observed color pallets are shown in the insets. 1 represents the reduced ground state and 2 represents the oxidized state. The corresponding chromaticity coordinates obtained upon reversible redox switching for (d) **Fe(II)-Ph-TPy**, (e) **Fe(II)-TPE-TPy** and (f) **Fe(II)-Thio-TPy**. The electrochemical oxidation process was performed using a 3-electrode set-up comprising of the metallopolymer modified FTO as working electrode, Ag/AgCl as reference electrode and Pt wire as counter electrode. A 0.1 M solution of lithium perchlorate in dry acetonitrile was used as the supporting electrolyte at a potential window of 0.7 – 1.5 V.

Interestingly, the response time (time taken for 90% of maximum coloration/bleaching) of these assemblies follow the same order (**Figure 3.19**): **Fe(II)-Ph-TPy** (coloration: 1.8 s, bleaching: 1.0 s), **Fe(II)-Thio-TPy** (coloration: 2.0 s, bleaching: 1.2 s) and **Fe(II)-TPE-TPy** (coloration: 2.3 s, bleaching: 1.6 s). Coloration was found to be faster, in all cases, when compared to the bleaching (**Figure 3.19**). This is most likely due to a comparably more strenuous oxidation pathway in operation, as opposed to an easier reduction pathway in the one-electron redox process mediated by a faster injection of electrons. This process leads to a faster kinetics in $\text{Fe}^{3+/2+}$ redox couple and a probably slower ejection of electrons with a concomitantly slower kinetics in the reverse process ($\text{Fe}^{2+/3+}$).⁵⁴⁻⁵⁶

3.3.3 Capacitance

To evaluate the electrochemical energy storage properties, electrodes (1 cm × 1 cm) were prepared using the corresponding metallopolymer mixed with activated charcoal and polytetrafluoroethylene (PTFE).³⁶ The electrochemical properties of the symmetric two-electrode configuration were studied using cyclic voltammetry (CV), galvanostatic charge-discharge and electrochemical impedance spectroscopy (EIS) at room temperature. The CVs of the electrodes in a symmetric two electrode configuration at different scan rates are shown in **Figure 3.20** and **Figure 3.21**.

An increase in current and area under the curves with increasing scan rate were observed in the cyclic voltammograms for the cells fabricated from all three metallopolymer networks under study (**Figure 3.21**). These observations corroborate the prevalence of redox or faradaic reactions at the electrode – electrolyte interface or within the metallopolymer networks, as required for a favorable capacitive behavior. The cyclic voltammetry loops were predominantly rectangular for the capacitors fabricated from **Fe(II)-Ph-TPy** and **Fe(II)-TPE-TPy**, whereas the CVs obtained for **Fe(II)-Thio-TPy** was rather deviated from the expected rectangular shape,

particularly at higher scan rates (**Figure 3.21**). These data are indicative of comparably slow charge-discharge reactions happening in **Fe(II)-Thio-TPy**, most likely due to higher internal resistance.^{36,57} The deviation from an expected rectangular behavior may also be attributed to the kinetically limited diffusion of electrolyte ions.⁵⁸

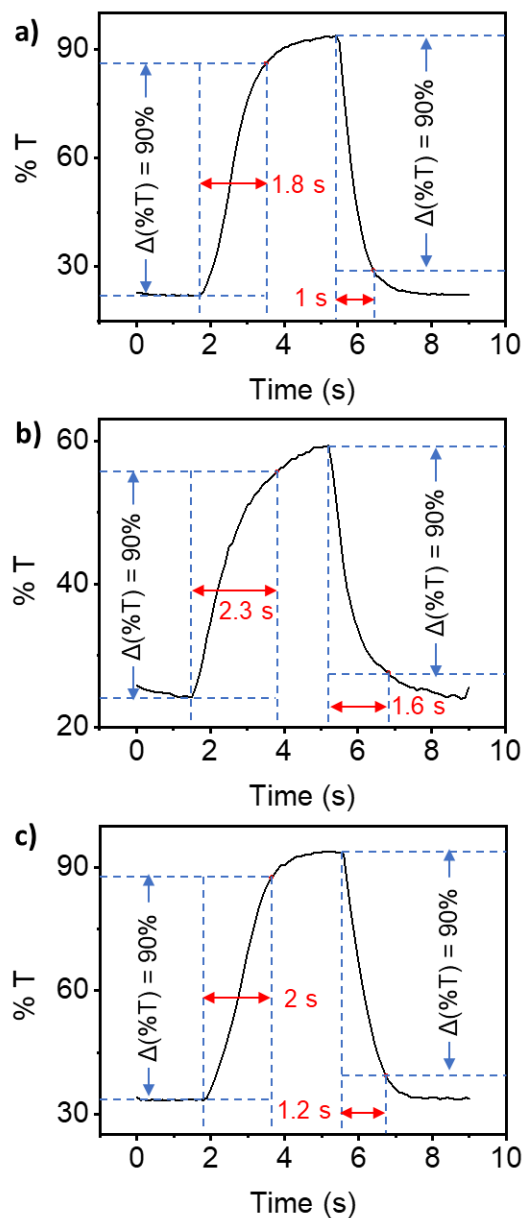


Figure 3.19. The response times obtained upon reversible redox switching for (a) **Fe(II)-Ph-TPy**, (b) **Fe(II)-TPE-TPy** and (c) **Fe(II)-Thio-TPy**. The electrochemical oxidation process was performed using a 3-electrode set-up comprising of the metallopolymer modified FTO as working electrode, Ag/AgCl as reference electrode and Pt wire as counter electrode at a pulse width of 5 s. A 0.1 M solution of lithium perchlorate in dry acetonitrile was used as the supporting electrolyte at a potential window of 0.7 – 1.5 V.

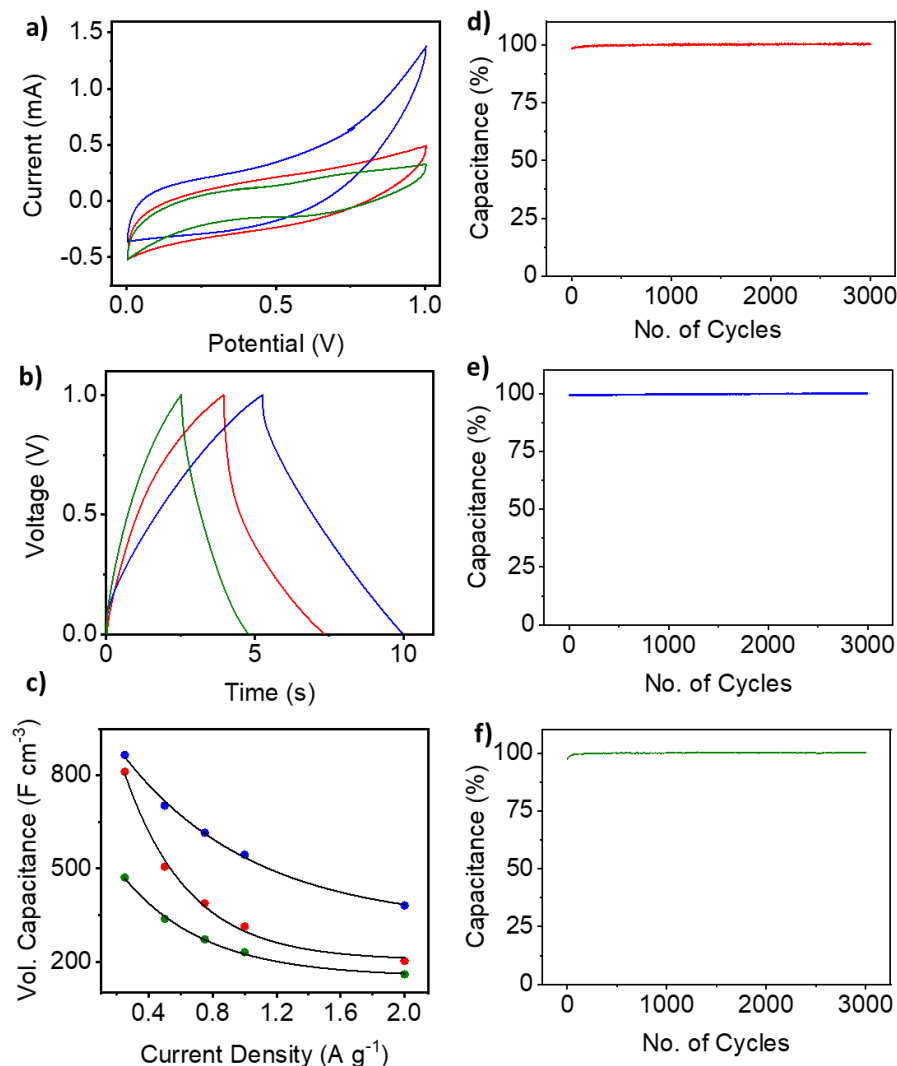


Figure 3.20. a) CV loops obtained from the symmetric supercapacitors fabricated from **Fe(II)-Ph-TPy** (red), **Fe(II)-TPE-TPy** (blue), and **Fe(II)-Thio-TPy** (green) at a scan rate of 100 mV s^{-1} . b) Galvanostatic charge-discharge curves of the supercapacitors fabricated from **Fe(II)-Ph-TPy** (red), **Fe(II)-TPE-TPy** (blue), and **Fe(II)-Thio-TPy** (green) electrodes at a constant potential window ($0.0 - 1.0 \text{ V}$) and current density (1.0 A g^{-1}). c) Comparison of the volumetric capacitance calculated from the GCD curves at different current densities for d) **Fe(II)-Ph-TPy** (red), e) **Fe(II)-TPE-TPy** (blue), and f) **Fe(II)-Thio-TPy** (green). Cycling stability of the symmetric supercapacitors derived from **Fe(II)-Ph-TPy** (red), **Fe(II)-TPE-TPy** (blue), and **Fe(II)-Thio-TPy** (green), at a constant current density of 1.0 A g^{-1} .

These results strongly suggest that the charge storage mechanism does not originate exclusively from the oppositely charged electrical double layer (EDL),⁵⁹ however, small contributions from the EDL cannot be excluded as indicated by reasonably triangular shape of the charge-discharge curves (**Figure 3.20, 3.22**). The current at a given potential in non-carbon electrode systems

may be composed of three components – physically capacitive, pseudocapacitive and diffusive currents.⁶⁰

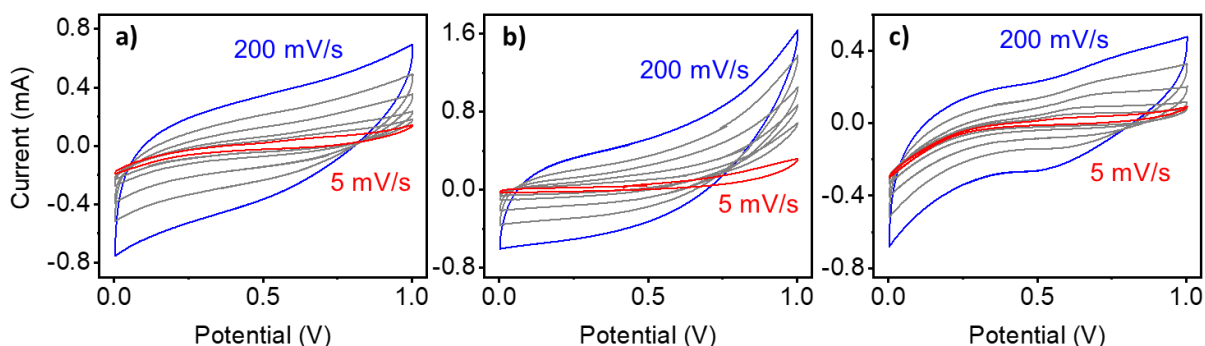


Figure 3.21. CV loops obtained from the symmetric supercapacitors fabricated from a) **Fe(II)-Ph-TPy**, b) **Fe(II)-TPE-TPy**, and c) **Fe(II)-Thio-TPy** at different scan rates. The red traces in (a) – (c) correspond to the CVs obtained at 5 mV s^{-1} and the blue ones correspond to those at 200 mV s^{-1} .

Warburg impedance or charge transfer resistance are generally not observed for ideal polarized electrodes outside the electrochemical redox window.⁶¹ An increase in current above 0.8 V for all the metallopolymer, particularly in the case of **Fe(II)-TPE-TPy**, is due to the onset of the $\text{Fe}^{2+/3+}$ oxidation potential ($1.0\text{-}1.2 \text{ V}$). However, the lower ohmic voltage drop observed for these systems, that most likely originates from the combined effects of isolating barriers developed at the electrode-electrolyte interface leading to mechanical side effects, cannot be rigorously excluded.^{60,61}

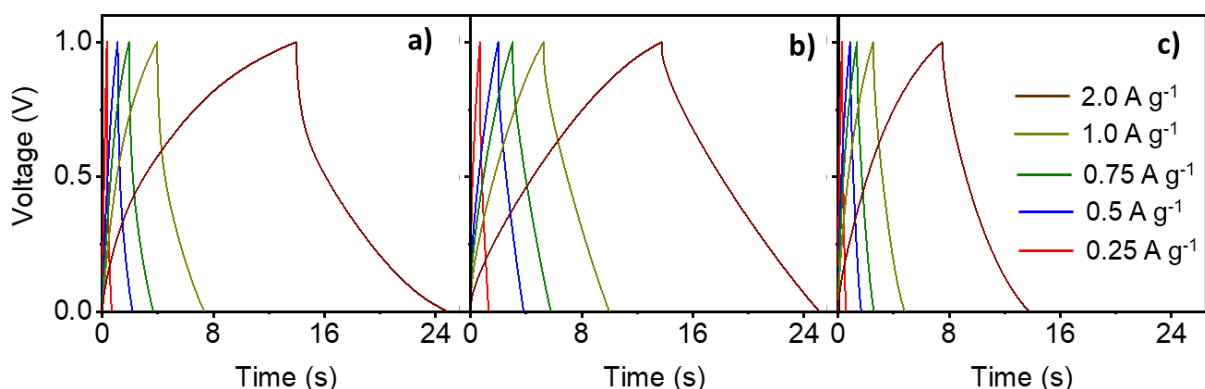


Figure 3.22. Galvanostatic charge-discharge curves of the supercapacitors fabricated from a) **Fe(II)-Ph-TPy**, b) **Fe(II)-TPE-TPy**, and c) **Fe(II)-Thio-TPy** at different current densities at a constant potential window ($0.0 - 1.0 \text{ V}$) and different current densities: 2.0 A g^{-1} (brown), 1.0 A g^{-1} (yellow), 0.75 A g^{-1} (green), 0.50 A g^{-1} (blue), and 0.25 A g^{-1} (red).

While calculation of specific capacitance from the CV loops are technically feasible, the values obtained from the galvanostatic charge-discharge (GCD) curves are more reliable. GCD curves are also useful in predicting the operational efficiency and performance of electrochemical supercapacitors.^{36,62} Nevertheless, capacitive profiles from the cyclic voltammograms were clearly found to increase with increasing scan rates, most likely due to the scan rate dependent diffusion kinetics of electrolytes. Lower scan rates are known to allow sufficient time for the ions to diffuse through the network, leading to an enhanced charge storage behavior.⁶³ Overall, the charge storage performance of the metallopolymer supercapacitors estimated qualitatively from the CV loops was found to follow the order: **Fe(II)-TPE-TPy** > **Fe(II)-Ph-TPy** > **Fe(II)-Thio-TPy**. GCD curves were obtained for all the symmetric capacitors at a constant potential window (0.0 – 1.0 V) by varying the current densities between 0.25 and 2.0 A g⁻¹ (**Figure 3.22**). The data obtained at a current density of 1.0 A g⁻¹ is shown in **Figure 3.20b**. The charge-discharge times for the supercapacitors at every current density followed the order **Fe(II)-TPE-TPy** > **Fe(II)-Ph-TPy** > **Fe(II)-Thio-TPy** (**Figure 3.23a-e**). However, at high current densities (2.0 A g⁻¹), electrodes fabricated from **Fe(II)-Ph-TPy** and **Fe(II)-TPE-TPy** charged and discharged at similar rates, whereas that fabricated from **Fe(II)-Thio-TPy** continued to charge and discharge at a faster rate (**Figure 3.23e**). The earlier reported difference in thin film porosity is the most likely reason for different electron transfer mechanisms exhibited by these assemblies.⁴² The least porous **Fe(II)-TPE-TPy** featured an electron transfer process under a diffusion-controlled mechanism, whereas the electron transfer processes were not found to be limited by slow diffusion in **Fe(II)-Ph-TPy** and **Fe(II)-Thio-TPy**. We envision that these differences in charge storage mechanism is directly correlated to the charge-discharge kinetics as the relatively less porous **Fe(II)-TPE-TPy** charged and discharged at lower rates. While low current densities have been shown to allow the electrolyte ions to penetrate and/or diffuse into the electrode material, high current densities limit the access of the electrolyte ions to the electrode surface only.^{33,56} Deviation from an ideal rectangular shape as well as lack of proper symmetry in the GCD curves points to a predominantly pseudocapacitive origin for the charge storage behavior of these metallopolymer. However, various mass-transport related phenomena as well as Faradaic and non-Faradaic charge storage reactions may also contribute to the observed deviations from ideal supercapacitor profiles.^{36,62} The volumetric capacitance of the supercapacitor electrodes was calculated from the GCD curves at different current densities.

The supercapacitor cells fabricated from **Fe(II)-TPE-TPy** was found to exhibit the highest volumetric capacitance among the three metallopolymers, followed by **Fe(II)-Ph-TPy** and **Fe(II)-Thio-TPy** exhibited the least capacitance values (**Figure 3.23f-j**). The volumetric capacitance was found to decrease exponentially with increasing current densities (**Figure 3.20c**).

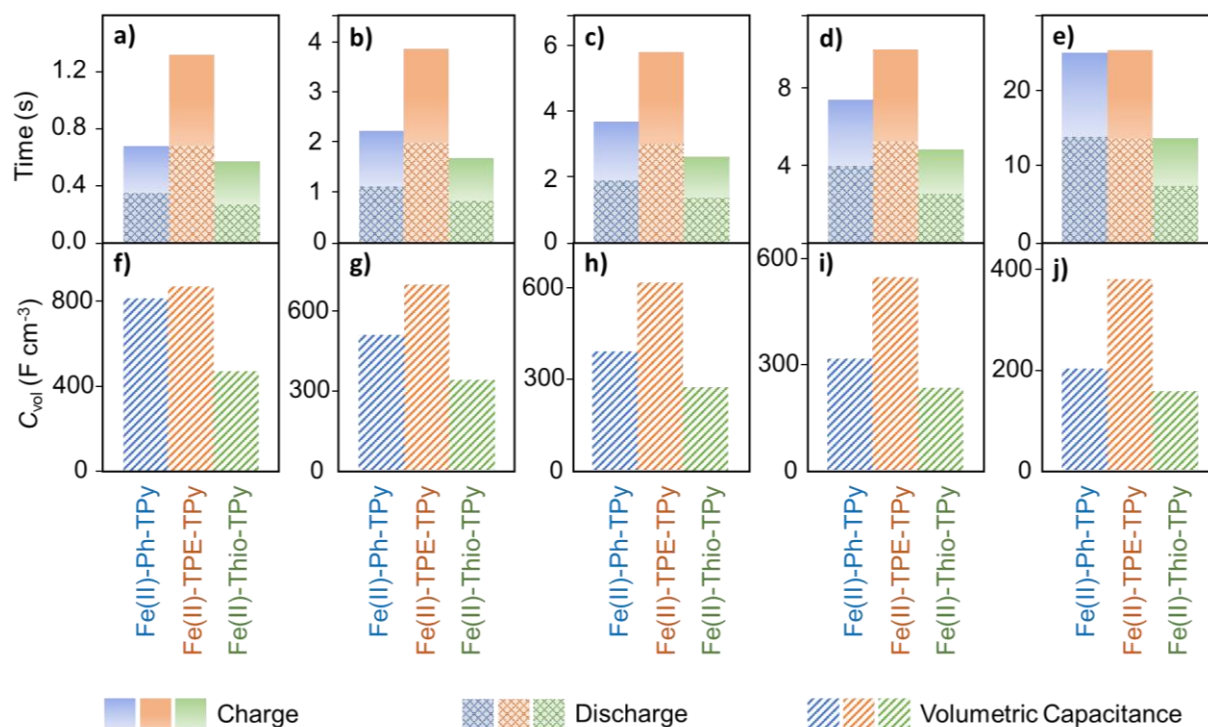


Figure 3.23. Comparison of charge-discharge times (a-e) and volumetric capacitance (f-j) in symmetric supercapacitor cells fabricated from **Fe(II)-Ph-TPy** (blue), **Fe(II)-TPE-TPy** (orange), and **Fe(II)-Thio-TPy** (green). The charge discharge times were obtained at a constant potential window (0.0 – 1.0 V). The current densities were (a,f) 0.25 A g⁻¹, (b,g) 0.50 A g⁻¹, (c,h) 0.75 A g⁻¹, (d,i) 1.0 A g⁻¹, and (e,j) 2.0 A g⁻¹.

At a constant current density of 1.0 A g⁻¹, the calculated volumetric capacitance of the metallopolymers are as follows: **Fe(II)-TPE-TPy** (544.6 F cm⁻³) > **Fe(II)-Ph-TPy** (313.8 F cm⁻³) > **Fe(II)-Thio-TPy** (230.8 F cm⁻³). A maximum volumetric capacitance of 866.2 F cm⁻³ was obtained for the symmetric supercapacitor cell fabricated from **Fe(II)-TPE-TPy** using a potential window between 0 and 1 V operating at a current density of 0.25 A g⁻¹. All the supercapacitor electrodes exhibited excellent stability, most likely due to the extended conjugation within the rigid ligand network,^{28,42,63,64} and no degradation in performance was observed after 3000 cycles of continuous charge-discharge operations at a constant current density of 1.0 A g⁻¹ (**Figure 3.20d-f**). At a constant power density of 0.154 kW cm⁻³, the

metallopolymer based supercapacitors were found to have specific energy densities of 43.6, 75.5 and 31.2 mWh cm⁻³, for **Fe(II)-Ph-TPy**, **Fe(II)-TPE-TPy**, and **Fe(II)-Thio-TPy**, respectively. These volumetric capacitance and energy densities are significantly higher compared to several other electrochromic supercapacitors or conventional systems and is among the best reported for metallopolymer-based systems (**Figure 3.24, Table 3.1**).^{65–68}

Table 3.1. Comparison of the volumetric capacitance (max) and energy density (max) reported for different materials.

Material	Vol. Capacitance F cm ⁻³	Vol. Energy Density mWh cm ⁻³	Vol. Power Density W cm ⁻³	Reference
ITO/NiO _x /Ta ₂ O ₅ /LiNbO ₃ /Ta ₂ O ₅ /WO ₃ /ITO	322	38	71.6	42
Ag NWs/PEDOT:PSS	443	na	na	69
W ₁₈ O ₄₉ NWs / SWCNTs	459	19	0.295	70
EG/V ₂ O ₅ hybrid nanopaper	130.7	20	235	71
Poly Ru	98.5 ± 8	10–18	7	72
Cond. Polymer@MXene	1632	50.6	127	73
LiMn ₂ O ₄ and WO ₃	238	16.2	0.21	74
PANI-18 film	84.4	na		75
Triarylamine / viologen	0.0695	0.03	0.51	76
indacenodithieno[3,2-b]thiophene	230	na	na	77
Polyoxotungstate	135.8	na	na	78
MXene / PEDOT:PSS	754	9.4	0.15	79
TiO ₂ nanowires with POMs	172.3	na	na	80
MoS ₂ nanosheets	700	na	0.62	81
Cu–Al double hydroxide	183.3	10.09	na	82
Fe ₃ O ₄ @graphene fiber	250.75	18.8	4	83
graphene/MnO ₂ hybrid	24	8.44	0.19	84
RuO ₂ /Graphene	1485	50.6	0.033	85
Hexaaminobenzene-@D MOFs	760	na	na	86
CoZnNiS nanosheet	1727.0	65.2	1.31	87
Molybdenum oxide	652	na	na	88
Phosphorus / MOF	506	109.8	0.675	89
Metallopolymers	866.2	75.5	154	This Work

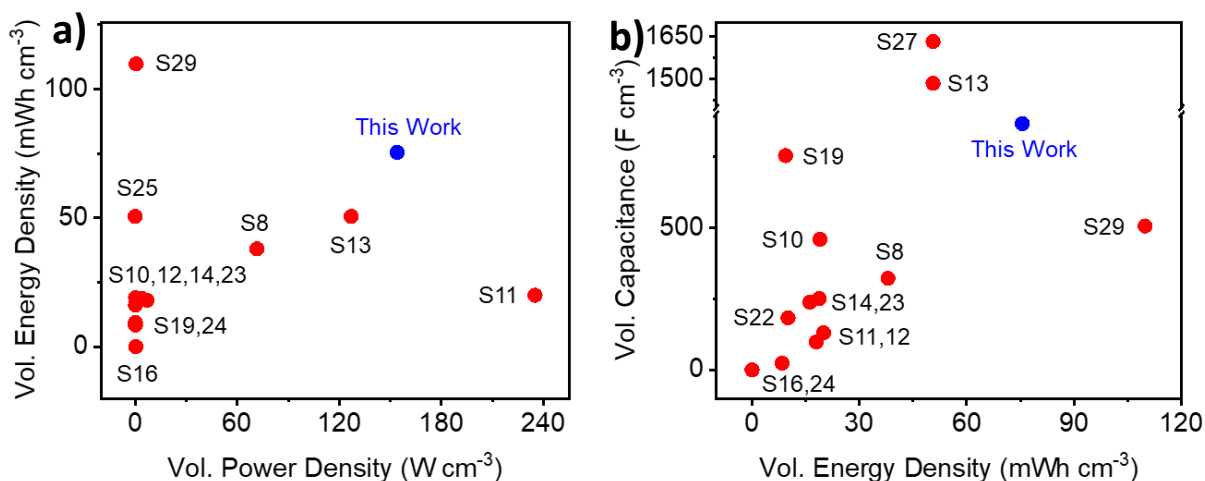


Figure 3.24. Comparison of the supercapacitor performance of different materials reported in literature: a) Ragone Plot (volumetric energy density Vs volumetric power density) and b) volumetric capacitance vs volumetric energy density. The details are provided in Table 3.1.

The electrochemical reactions occurring at the electrode surfaces can be followed using electrochemical impedance spectroscopy (EIS).^{36,62} The presence of a detectable semi-circle region at high frequencies in the Nyquist plot of **Fe(II)-Ph-TPy** indicates a relatively higher charge transfer resistance when compared to **Fe(II)-TPE-TPy** and **Fe(II)-Thio-TPy** (**Figure 3.25**). However, the shortest Warburg diffusion line in the middle-frequency region was observed for the electrodes fabricated from **Fe(II)-TPE-TPy** followed by that from **Fe(II)-Ph-TPy** and the electrodes fabricated from **Fe(II)-Thio-TPy** exhibited the shortest Warburg diffusion line. The contact resistance at the electrode-electrolyte interface, the ionic resistance of the electrolyte and the intrinsic resistance of the metallopolymers may contribute to the overall solution resistance (R_s) or the Equivalent Series Resistance (ESR) and was found to be 3.0, 1.6 and 1.9 Ω for **Fe(II)-Ph-TPy**, **Fe(II)-Thio-TPy**, and **Fe(II)-TPE-TPy**, respectively. The EIS data can be fitted with an equivalent circuit shown in **Figure 3.25a, inset**, with the solution resistance or the equivalent series resistance R_s connected with the charge transfer resistance R_{ct} , the double layer capacitance C_{dl} , and the Warburg Impedance Z_w .

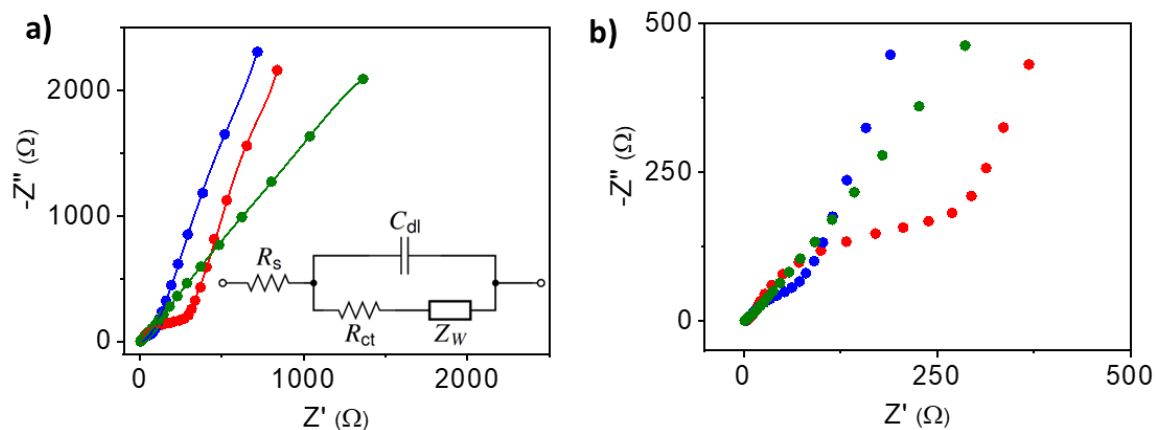


Figure 3.25. a) Nyquist plots of the symmetric supercapacitors derived from **Fe(II)-Ph-TPy** (red), **Fe(II)-TPE-TPy** (blue), and **Fe(II)-Thio-TPy** (green) based electrodes obtained using electrochemical impedance spectroscopy (EIS). Inset: Equivalent Circuit of the best performing **Fe(II)-TPE-TPy** based supercapacitor. b) shows the corresponding zoomed-in image.

3.3.4 BET Surface Area and Conductivity

Porous materials with high surface area have been shown to exhibit better electrochemical energy storage performance. However, such dependence of capacitive performance on BET surface area may not be expected for low surface area materials, particularly metal-organic systems. BET surface areas of the metallopolymers were found to be as follows: $22.3 \pm 2.3 \text{ m}^2 \text{ g}^{-1}$ (**Fe(II)-Ph-TPy**), $13.8 \pm 1.1 \text{ m}^2 \text{ g}^{-1}$ (**Fe(II)-TPE-TPy**), and $16.0 \pm 1.8 \text{ m}^2 \text{ g}^{-1}$ (**Fe(II)-Thio-TPy**), leading to porosity in the order: **Fe(II)-Ph-TPy** > **Fe(II)-Thio-TPy** > **Fe(II)-TPE-TPy**, and is in full agreement with the molecular porosity observed in solution state electrochemical experiments (**Figure 3.26**). The higher porosity of **Fe(II)-Ph-TPy** stems from the presence of mesopores ($d < 50 \text{ nm}$) alongside macropores, while **Fe(II)-TPE-TPy** and **Fe(II)-Thio-TPy** featured only macroporous assemblies (**Figure 3.26**). The BET surface area of the metallopolymers most probably does not contribute to the observed differences in their capacitive performance, since all the materials exhibited rather low surface areas typically less than $10\text{-}25 \text{ m}^2 \text{ g}^{-1}$.^{36,43}

The differences observed in the charge storage properties could be therefore attributed to the difference in electrical conductivity of the metallopolymers and prompted us to investigate their I-V characteristics.⁴⁴⁻⁴⁶ The electrical conductivity of the metallopolymers (thickness: $185 \pm 4 \text{ nm}$) were determined using a 4-probe method (**Figure 3.27**). The charge storage properties and the observed differences between the metallopolymer-based supercapacitors can be justified

based on the differences in conductivity of these metallopolymer thin films. The capacitive performance of the metallopolymer was found to follow the order of their electrical conductivity: **Fe(II)-TPE-TPy** ($2.64 \times 10^{-1} \text{ S cm}^{-1}$) > **Fe(II)-Ph-TPy** ($4.67 \times 10^{-2} \text{ S cm}^{-1}$) > **Fe(II)-Thio-TPy** ($3.88 \times 10^{-2} \text{ S cm}^{-1}$).

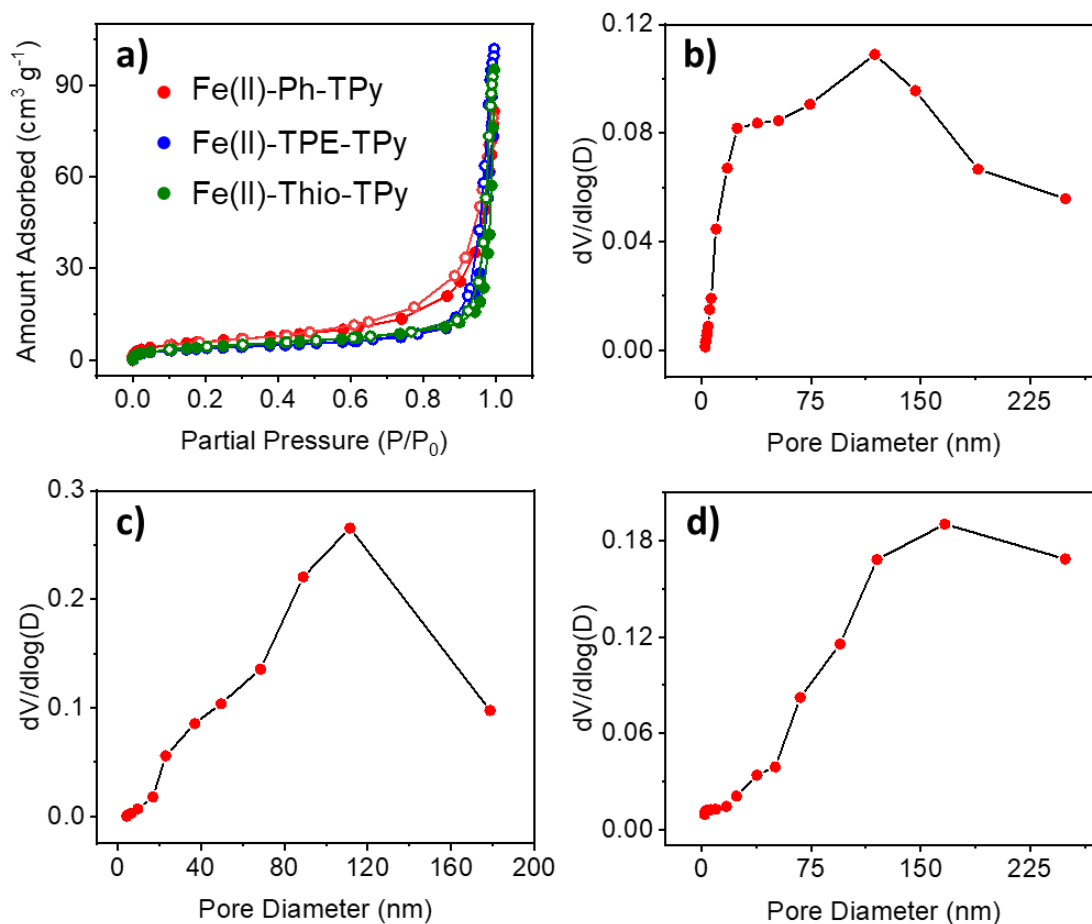


Figure 3.26. (a) BET surface area of the metallopolymer. The pore size distribution obtained from BET surface area analysis for b) **Fe(II)-Ph-TPy**, c) **Fe(II)-TPE-TPy**, and d) **Fe(II)-Thio-TPy**.

Unlike most reported metal-organic materials, metallopolymer used in this study were found to possess significantly high electrical conductivity^{69,70} and may be attributed to high-energy charge transport pathways and enhanced charge carrier mobility, resulting from the presence of extended conjugation and delocalized π -electron systems within the rigid ligand network.³⁸ The continuous metal-chelating pathways along with the presence of heteroatoms have been shown to improve the conductivity of metallopolymer. The comparatively soft-soft interactions between the coordinating nitrogen atoms and Fe^{2+} nodes with its loosely bound β -spin d -band electron also contribute to high conductivity in iron(II) based metal-organic systems.⁷¹

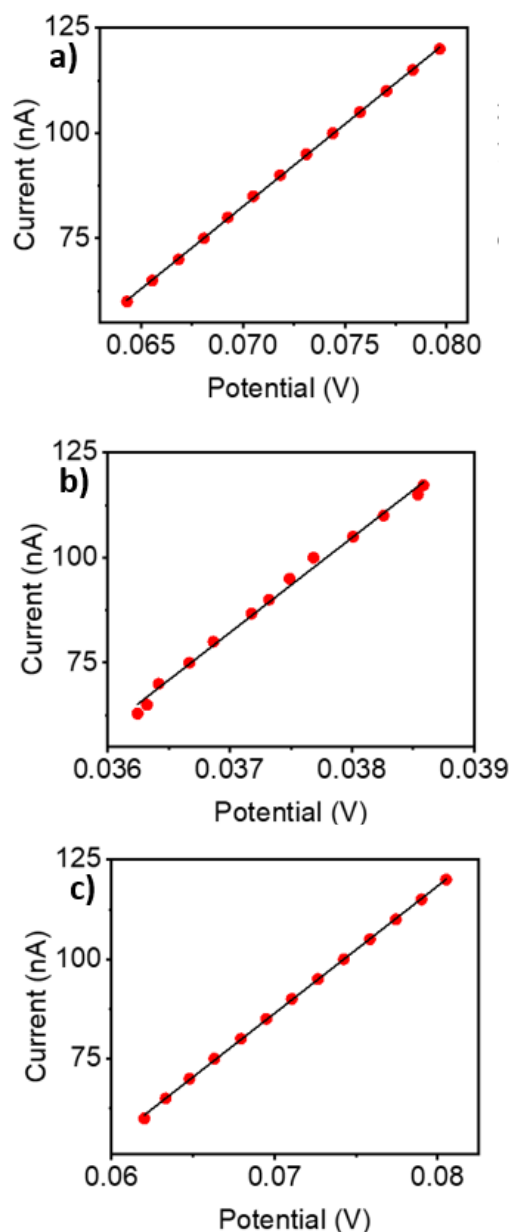


Figure 3.27. I-V characteristics of a) **Fe(II)-Ph-TPy**, b) **Fe(II)-TPE-TPy**, and c) **Fe(II)-Thio-TPy**, obtained from 4-probe measurements.

The extended conjugation in ligand **TPE-TPy**, which is superior compared to **Ph-TPy** and **Thio-TPy**, enhances the through-plane conductivity in **Fe(II)-TPE-TPy** via a better π -d conjugation and efficient charge delocalization pathways. Higher charge delocalization in **Fe(II)-TPE-TPy** also implies better interlayer stacking via π - π interactions leading to enhanced charge transport efficiency and wave function overlap. Though dense grain like morphologies were observed in the AFM images of the metallopolymer (Figure 3.11), **Fe(II)-TPE-TPy** featured fewer open spaces, suggesting a lower resistance arising from smaller number of grain boundaries and related defects, leading to higher conductivity. The high conductivity observed

for all the metallopolymers is also indicative of higher ionic mobility and a plausible redox hopping mechanism, involving the Fe^{2+} centers. It is often difficult to single out the contributions from through-bond, through-plane, through-space and hopping pathways of charge transport, however, a favorable combination of these different pathways that emanates from the structural variations in the ligands accounts for the observed differences in the conductivity of the metallopolymers.⁷¹ Electrochemical addressability of the electrochromic thin films of the metallopolymers was limited at thickness above 250 nm, most likely due to the low porosity that limits the diffusion of the electrolyte ions. However, the capacitive behavior and conductivities were found to be more or less similar at thickness below 200 nm. The contribution from differences in solution or charge transfer resistance, mass transport phenomenon, or faradaic/non-faradaic processes within the metallopolymer network or at the electrode-electrolyte interface to the observed capacitive behavior cannot be rigorously excluded.^{36,62}

The packing densities and amorphous nature of the metallopolymers may also influence the charge storage profile. Theoretical modelling using model ligand systems confirmed similar octahedral coordination modes in the metallopolymers irrespective of the core architecture (**Figure 3.28**). Though the molecular weights of the ligands are different, no direct correlation was observed between the capacitive performance and the molecular weight of the ligands. Nevertheless, variation in the core structure of the ligand is the decisive factor that determines the capacitance and related charge storage signature of these metallopolymer assemblies containing the same metal ion and similar coordinating entities. Such design principles offer excellent opportunities in developing new materials, particularly of metal-organic nature, as promising candidates for electrochemical energy storage applications.

3.4. Conclusions

Electrochromic metallopolymers containing the same metal ion (Fe^{2+}) with varying core structures have been shown to exhibit a ligand modulated capacitive behavior. Fabrication of symmetric supercapacitor cells in a two-electrode configuration using these metallopolymers resulted in high volumetric capacitance up to 544.6 F cm^{-3} at a current density of 1 A g^{-1} , energy densities up to 75.5 mWh cm^{-3} and high cycling stabilities. These values are among the highest reported for metal-organic thin film systems. The volumetric capacitance and charge-discharge properties of the metallopolymer electrodes were found to be in direct correlation with the measured electrical conductivities, that in turn stem from the variations in ligand structure. This

work demonstrates the effect of electrical conductivity in regulating the electrochemical energy storage properties of materials with low to moderate porosity and surface area. The diligence of structural design aiming at enhancing the electrical conductivity in low surface area materials provides a unique strategy to improve the performance of thin film based multifunctional electrochemical energy storage devices. Such thin film systems with stimuli responsive attributes is envisioned to add a new dimension to the emerging smart technologies with application in efficient microscale power sources for miniaturized devices.

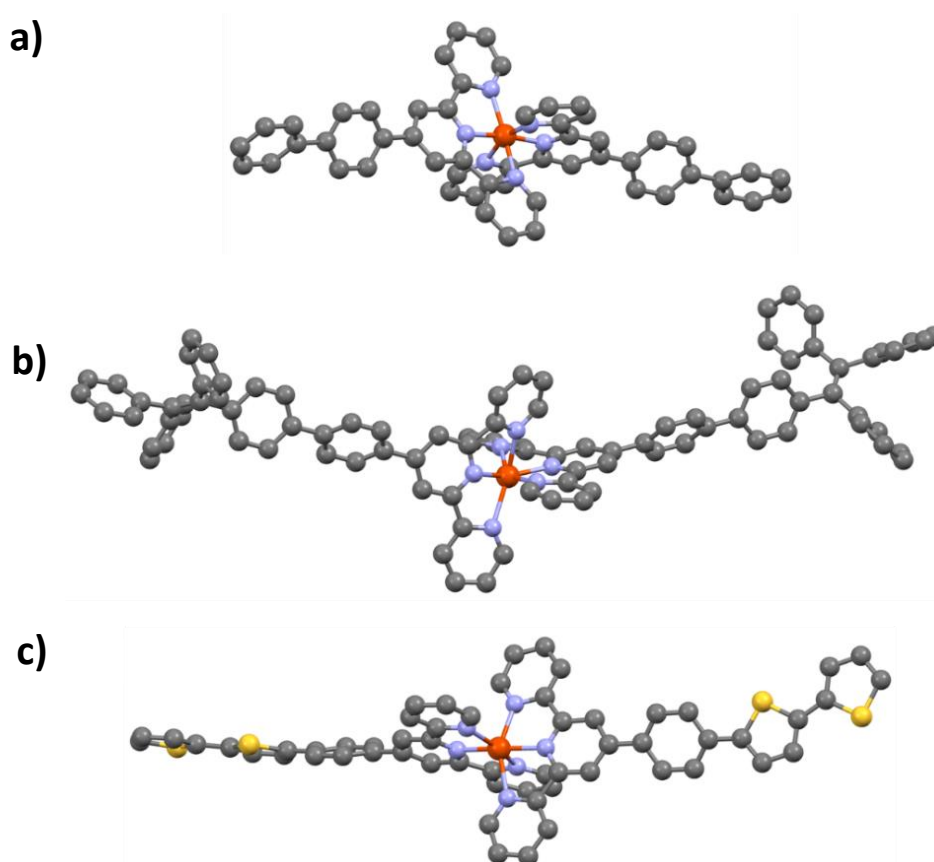


Figure 3.28. Energy-minimized structures confirming the octahedral coordination modes in the metallopolymer using model ligand systems for a) **Fe(II)-Ph-TPy**, b) **Fe(II)-TPE-TPy**, and c) **Fe(II)-Thio-TPy**. Hydrogens are omitted for clarity. Color codes: grey, carbon; blue, nitrogen; yellow, sulfur; red, iron.

3.5. Experimental Section

3.5.1. General Methods and Instrumentation

All reagents were used as received without further purification, unless otherwise noted. Syntheses and experiments were carried out in clean and oven-dried glassware. Reactions were

monitored using silica gel G-60 F254 aluminum TLC (thin layer chromatography) and compounds were visualized by short/long-wavelength UV lamps. Column chromatography was done using silica gel 100-200 mesh as a stationary phase.

3.5.2. Molecular Characterization

^1H and ^{13}C NMR spectra were recorded in deuterated solvents at 300 K on a 500 MHz (^1H) Bruker Avance spectrometer using TMS (tetramethyl silane) as an internal standard. Chemical shifts are presented in ppm (δ) along with the corresponding coupling constants (Hz). HRMS (high resolution mass spectroscopy) data were recorded on a Thermo Scientific Exactive LCMS (liquid chromatography – mass spectrometry) instrument by electrospray ionization method with ions given in m/z using an Orbitrap analyzer. Matrix-assisted laser desorption ionization time-of-flight (MALDI-TOF) mass spectra were obtained using an AXIMA-CFR PLUS (SHIMADZU) MALDI-TOF mass spectrometer using α -cyano-4-hydroxycinnamic acid as the matrix. FT-IR spectra were recorded in the solid state (KBr) using Shimadzu IRPrestige-21 Fourier transform infra-red spectrophotometer.

3.5.3. Absorption and Emission Spectroscopy

Electronic absorption spectra in solution were recorded on a Shimadzu UV-2600 Spectrophotometer, using a clean and dry Hellma Analytics 10 mm quartz cuvette. Temperature was regulated using a Shimadzu temperature controller and a blank experiment with the corresponding solvent provided the baseline. The UV-vis spectra of the metallopolymer modified TCO (transparent conducting oxide) slides were obtained using Ocean Optics UV-vis modular spectrometer (DH-2000-BAL). The blank experiment with the bare TCO slides provided the baseline. Emission spectra were recorded on Horiba Fluorolog – 3 Jovin Yoon with a 1 cm quartz cuvette at room temperature

3.5.4. Morphological Analyses, Thickness Measurements and Thermal Characterization

AFM images were recorded at ambient conditions using an atomic force microscope (AFM; Bruker Multimode Nanoscope V) instrument operating under tapping mode. Micro-fabricated TiN cantilever tips with a resonance frequency of 299 kHz and a spring constant of 20-80 Nm⁻¹ was used. Roughness parameter was estimated using Nanoscope Analysis 1.5 software. The thickness of the thin films was estimated using a Dektak XT profilometer. Thermogravimetric analyses (TGA) were performed at a heating rate of 10 °C/min in nitrogen atmosphere using Shimadzu, DTG-60 equipment.

3.5.5. Powder X-ray Diffraction

Powder X-ray Diffraction (PXRD) analyses were done using XEUSS SAXS/WAXS (small angle x-ray scattering / wide angle x-ray scattering) system by Xenocs, using Ni-filtered Cu K α radiation ($\lambda=0.15405$ nm). Using Fit2D software, 1D pattern were generated from the 2D images obtained from the Mar 345 detector.

3.5.6. X-ray Photoelectron Spectroscopy (XPS)

The elemental composition of the metallopolymers was analyzed using X-ray photoelectron spectroscopy (XPS, PHI 5000 VersaProbe II, ULVAC-PHI Inc., USA) equipped with micro-focused (200 μm , 15 KV) monochromatic Al-K α X-Ray source ($h\nu = 1486.6$ eV). First survey scans were acquired on the samples and for the major detected elements, high-resolution spectra were recorded. Survey scans were recorded with an X-ray source power of 50W and pass energy of 187.85 eV. High-resolution spectra of the major elements were recorded at 46.95 eV pass energy. XPS data were processed using PHI's Multipak software. These spectra were used for qualitative confirmation of elemental compositions and chemical state assignments by curve fitting software XPSPEAK Fit.

3.5.7. Electrochemistry and Spectroelectrochemical Analyses

Cyclic voltammetry of the films was performed on PARSTAT 4000A Potentiostat at room temperature using 0.1 M lithium perchlorate in CH₃CN as supporting electrolyte, metallopolymer modified TCO slides as working electrode, Ag/AgCl as reference electrode and platinum wire as counter electrode at a scan rate of 10-300 mV s⁻¹. Three consecutive scans were performed and the third cycle was selected for analysis. Spectroelectrochemical analyses were recorded on Ocean Optics Spectrometer DH-2000-BAL coupled to a PARSTAT 4000A Potentiostat, by dipping metallopolymer drop-casted FTO electrodes in 0.1 M lithium perchlorate (in dry acetonitrile) solution using Ag/AgCl and Pt wire as reference and counter electrodes, respectively. Absorption spectra were obtained upon applying double potential steps (0.7 V and 1.5 V) as a function of time.

3.5.8. Synthesis

The ligands **Ph-TPy**, **TPE-TPy** and **Thio-TPy** were synthesized using our previously reported procedure. The details are provided in Chapter 2.

3.5.9. Syntheses of the Metallopolymers

A solution of $\text{FeCl}_2 \cdot 4\text{H}_2\text{O}$ (24.9 mg, 2 equiv.) in MeOH (10.0 mL) was added to a solution of the corresponding ligand (**Ph-TPy**: 32.5 mg, **TPE-TPy**: 39.0 mg, **Thio-TPy**: 34.9 mg) in CHCl_3 (10.0 mL). The solution was stirred in the dark at room temperature for 2 h. The solvent was then removed under reduced pressure to 25% of the initial volume. Water (15 mL) saturated with potassium hexafluorophosphate was then added and the reaction mixture was stirred at room temperature for 30 min. The precipitate formed was filtered, washed with DI water (10 mL \times 3) and dried in a vacuum oven to obtain the corresponding metallopolymers in >95% yield. The metallopolymers were characterized by FT-IR spectroscopy, UV-vis spectroscopy, atomic force microscopy (AFM), Powder X-ray diffraction (PXRD), X-ray Photo Electron Spectroscopy (XPS) and Raman spectroscopy and the data are given in the corresponding sections.

3.5.10. Preparation of the Electrodes and Electrochemical Measurements

Supercapacitor electrodes of 1 cm² area were prepared as reported previously using the corresponding metallopolymer (1.0 mg) mixed with activated charcoal and polytetrafluoroethylene and in a mass ratio of 8:1:1.37. The electrochemical properties were studied by cyclic voltammetry (CV), galvanostatic charge-discharge and electrochemical impedance spectroscopy (EIS) using a Modulab (Solartron Analytical) electrochemical workstation. The cell capacitance (C in F) was then calculated from the charge-discharge curves according to Eq. (1)

$$C = \frac{I}{\left(\frac{\Delta V}{\Delta t}\right)} \quad (1)$$

where 'I' is the constant current for charge-discharge, and $\Delta V/\Delta t$ is slope of the discharge curve. The volumetric capacitance (C_{Vol} in F cm⁻³) was then calculated as

$$C_{Vol} = \frac{2C}{At} \quad (2)$$

where 'A' is the area of each electrode and 't' is the thickness of the electrode material.

3.5.11. Determination of Resistivity and Electrical Conductivity by 4-Probe Measurements

Four-probe method (Keithley 2450 source meter) was used to determine the resistivity and the electrical conductivity of the coordination polymers. The corresponding metallopolymer (2 mg) was dissolved in methanol/dichloromethane (1:1 v/v, 200 μL) and was drop-cast on to a glass

substrate. Thickness of the film was measured using a Bruker Dektat XT Profilometer. For a thin layer film, resistivity is calculated from the following equation.

$$\rho = \frac{\pi t V}{\ln 2 I}$$

where t is the thickness of film and resistance $R = V/I$.

Conductivity can be calculated as $\sigma = \frac{1}{\rho}$

3.5.12. Computational Calculations

Optimization and energy calculations of all the molecules were done at the PBE/B level of density functional theory (DFT) using Gaussian 16 program. In BS1, iron center is defined with LANL2DZ basis set and pseudopotentials for core electrons while 6–31G(d) basis set is used to define all other atoms. DFT calculations were done with cluster model illustrating the structure as shown in the **Figure 3.28**. A cluster model was considered for all the DFT calculations, using a system appropriately cut from the chemical structure to fairly describe the ligands.

3.5.13. BET Surface Area Measurements

BET surface area and porosity analysis of the samples were performed with Micromeritics (Tristar 11, USA) surface area analyzer using nitrogen adsorption at 77 K. The samples were degassed at 120°C for 2 h under a N₂ flow before adsorption measurements.

3.6 References

- (1) Su, M.; Song, Y. Printable Smart Materials and Devices: Strategies and Applications. *Chem. Rev.* **2022**, *122*, 5144–5164.
<https://doi.org/10.1021/acs.chemrev.1c00303>.
- (2) Gardan, J. Smart Materials in Additive Manufacturing: State of the Art and Trends. *Virtual Phys. Prototyp.* **2019**, *14*, 1–18.
<https://doi.org/10.1080/17452759.2018.1518016>.
- (3) Yu, X.; Cheng, H.; Zhang, M.; Zhao, Y.; Qu, L.; Shi, G. Graphene-Based Smart Materials. *Nat. Rev. Mater.* **2017**, *2*, 17046.

- <https://doi.org/10.1038/natrevmats.2017.46>.
- (4) Kowalski, P. S.; Bhattacharya, C.; Afewerki, S.; Langer, R. Smart Biomaterials: Recent Advances and Future Directions. *ACS Biomater. Sci. Eng.* **2018**, *4*, 3809–3817. <https://doi.org/10.1021/acsbio.2017.00889>.
- (5) Weng, W.; Yang, J.; Zhang, Y.; Li, Y.; Yang, S.; Zhu, L.; Zhu, M. A Route Toward Smart System Integration: From Fiber Design to Device Construction. *Adv. Mater.* **2020**, *32*, 1902301. <https://doi.org/10.1002/adma.201902301>.
- (6) Jeong, U.; Yin, Y. Smart and Responsive Micro- and Nanostructured Materials. *Adv. Funct. Mater.* **2020**, *30*, 1907059. <https://doi.org/10.1002/adfm.201907059>.
- (7) Dyer, A. L.; Bulloch, R. H.; Zhou, Y.; Kippelen, B.; Reynolds, J. R.; Zhang, F. A Vertically Integrated Solar-Powered Electrochromic Window for Energy Efficient Buildings. *Adv. Mater.* **2014**, *26*, 4895–4900. <https://doi.org/10.1002/adma.201401400>.
- (8) Tong, Z.; Tian, Y.; Zhang, H.; Li, X.; Ji, J.; Qu, H.; Li, N.; Zhao, J.; Li, Y. Recent Advances in Multifunctional Electrochromic Energy Storage Devices and Photoelectrochromic Devices. *Sci. China Chem.* **2017**, *60*, 13–37. <https://doi.org/10.1007/s11426-016-0283-0>.
- (9) Rosseinsky, D. R.; Mortimer, R. J. Electrochromic Systems and the Prospects for Devices. *Adv. Mater.* **2001**, *13*, 783–793. [https://doi.org/10.1002/1521-4095\(200106\)13:11<783::AID-ADMA783>3.0.CO;2-D](https://doi.org/10.1002/1521-4095(200106)13:11<783::AID-ADMA783>3.0.CO;2-D).
- (10) Beaujuge, P. M.; Reynolds, J. R. Color Control in π -Conjugated Organic Polymers for Use in Electrochromic Devices. *Chem. Rev.* **2010**, *110*, 268–320. <https://doi.org/10.1021/cr900129a>.
- (11) Cai, G.; Wang, J.; Lee, P. S. Next-Generation Multifunctional Electrochromic Devices. *Acc. Chem. Res.* **2016**, *49*, 1469–1476. <https://doi.org/10.1021/acs.accounts.6b00183>.
- (12) Lu, Z.; Zhong, X.; Liu, X.; Wang, J.; Diao, X. Energy Storage Electrochromic Devices in the Era of Intelligent Automation. *Phys. Chem. Chem. Phys.* **2021**, *23*, 14126–14145. <https://doi.org/10.1039/D1CP01398J>.
- (13) Wang, H.; Yao, C.-J.; Nie, H.-J.; Yang, L.; Mei, S.; Zhang, Q. Recent Progress in Integrated Functional Electrochromic Energy Storage Devices. *J. Mater. Chem. C* **2020**, *8*, 15507–15525.

- <https://doi.org/10.1039/D0TC03934A>.
- (14) Yu, X.; Chang, M.; Chen, W.; Liang, D.; Lu, X.; Zhou, G. Colorless-to-Black Electrochromism from Binary Electrochromes toward Multifunctional Displays. *ACS Appl. Mater. Interfaces* **2020**, *12*, 39505–39514.
<https://doi.org/10.1021/acsami.0c11840>.
- (15) Marrocchi, A.; Facchetti, A.; Lanari, D.; Petrucci, C.; Vaccaro, L. Current Methodologies for a Sustainable Approach to π -Conjugated Organic Semiconductors. *Energy Environ. Sci.* **2016**, *9*, 763–786.
<https://doi.org/10.1039/C5EE03727A>.
- (16) Gao, S.; Yi, X.; Shang, J.; Liu, G.; Li, R.-W. Organic and Hybrid Resistive Switching Materials and Devices. *Chem. Soc. Rev.* **2019**, *48*, 1531–1565.
<https://doi.org/10.1039/C8CS00614H>.
- (17) Yu, M.; Feng, X. Thin-Film Electrode-Based Supercapacitors. *Joule* **2019**, *3*, 338–360.
<https://doi.org/https://doi.org/10.1016/j.joule.2018.12.012>.
- (18) Liu, Y.-Y.; Li, X.-C.; Wang, S.; Cheng, T.; Yang, H.; Liu, C.; Gong, Y.; Lai, W.-Y.; Huang, W. Self-Templated Synthesis of Uniform Hollow Spheres Based on Highly Conjugated Three-Dimensional Covalent Organic Frameworks. *Nat. Commun.* **2020**, *11*, 5561.
<https://doi.org/10.1038/s41467-020-18844-4>.
- (19) Wang, S.; Li, X.; Cheng, T.; Liu, Y.; Li, Q.; Bai, M.; Liu, X.; Geng, H.; Lai, W.-Y.; Huang, W. Highly Conjugated Three-Dimensional Covalent Organic Frameworks with Enhanced Li-Ion Conductivity as Solid-State Electrolytes for High-Performance Lithium Metal Batteries. *J. Mater. Chem. A* **2022**, *10*, 8761–8771.
<https://doi.org/10.1039/D1TA08771A>.
- (20) Li, X.-C.; Zhang, Y.; Wang, C.-Y.; Wan, Y.; Lai, W.-Y.; Pang, H.; Huang, W. Redox-Active Triazatruxene-Based Conjugated Microporous Polymers for High-Performance Supercapacitors. *Chem. Sci.* **2017**, *8*, 2959–2965.
<https://doi.org/10.1039/C6SC05532J>.
- (21) Wu, W.; Wang, M.; Ma, J.; Cao, Y.; Deng, Y. Electrochromic Metal Oxides: Recent Progress and Prospect. *Adv. Electron. Mater.* **2018**, *4*, 1800185.
<https://doi.org/https://doi.org/10.1002/aelm.201800185>.
- (22) Granqvist, C. G. Electrochromics for Smart Windows: Oxide-Based Thin Films and Devices. *Thin Solid Films* **2014**, *564*, 1–38.
<https://doi.org/https://doi.org/10.1016/j.tsf.2014.02.002>.

- (23) Yu, X.; Marks, T. J.; Facchetti, A. Metal Oxides for Optoelectronic Applications. *Nat. Mater.* **2016**, *15*, 383–396.
<https://doi.org/10.1038/nmat4599>.
- (24) Wu, S.; Liu, J.; Wang, H. A Review of Performance Optimization of MOF - Derived Metal Oxide as Electrode Materials for Supercapacitors. *Int J Energy Res.* **2019**, *43*, 697–716.
<https://doi.org/10.1002/er.4232>.
- (25) Mortimer, R. J.; Dyer, A. L.; Reynolds, J. R. Electrochromic Organic and Polymeric Materials for Display Applications. *Displays* **2006**, *27*, 2–18.
<https://doi.org/10.1016/j.displa.2005.03.003>.
- (26) Banasz, R.; Wałęsa-Chorab, M. Polymeric Complexes of Transition Metal Ions as Electrochromic Materials: Synthesis and Properties. *Coord. Chem. Rev.* **2019**, *389*, 1–18.
<https://doi.org/https://doi.org/10.1016/j.ccr.2019.03.009>.
- (27) Shankar, S.; Lahav, M.; van der Boom, M. E. Coordination-Based Molecular Assemblies as Electrochromic Materials: Ultra-High Switching Stability and Coloration Efficiencies. *J. Am. Chem. Soc.* **2015**, *137*, 4050–4053.
<https://doi.org/10.1021/jacs.5b00429>.
- (28) Eloomov, N.; Shankar, S.; Cohen, D.; Bendikov, T.; Rechav, K.; Shimon, L. J. W.; Lahav, M.; Van Der Boom, M. E. Electrochromic Metallo-Organic Nanoscale Films: Fabrication, Color Range, and Devices. *J. Am. Chem. Soc.* **2017**, *139*, 11471–11481.
<https://doi.org/10.1021/jacs.7b04217>.
- (29) Rai, V.; Singh, R. S.; Blackwood, D. J.; Zhili, D. A Review on Recent Advances in Electrochromic Devices: A Material Approach. *Adv. Eng. Mater.* **2020**, *22*, 2000082.
<https://doi.org/https://doi.org/10.1002/adem.202000082>.
- (30) Bera, M. K.; Mori, T.; Yoshida, T.; Ariga, K.; Higuchi, M. Construction of Coordination Nanosheets Based on Tris(2,2'-Bipyridine)-Iron (Fe²⁺) Complexes as Potential Electrochromic Materials. *ACS Appl. Mater. Interfaces* **2019**, *11*, 11893–11903.
<https://doi.org/10.1021/acsami.8b22568>.
- (31) Xie, Z.; Liu, Q.; Zhang, Q.; Lu, B.; Zhai, J.; Diao, X. Fast-Switching Quasi-Solid State Electrochromic Full Device Based on Mesoporous WO₃ and NiO Thin Films. *Sol. Energy Mater. Sol. Cells* **2019**, *200*, 110017.
<https://doi.org/10.1016/j.solmat.2019.110017>.
- (32) Lahav, M.; van der Boom, M. E. Polypyridyl Metallo-Organic Assemblies for Electrochromic Applications. *Adv. Mater.* **2018**, *30*, 1706641.
<https://doi.org/https://doi.org/10.1002/adma.201706641>.

- (33) Bera, M. K.; Mohanty, S.; Kashyap, S. S.; Sarmah, S. Electrochromic Coordination Nanosheets: Achievements and Future Perspective. *Coord. Chem. Rev.* **2022**, *454*, 214353. <https://doi.org/https://doi.org/10.1016/j.ccr.2021.214353>.
- (34) Feng, D.; Lei, T.; Lukatskaya, M. R.; Park, J.; Huang, Z.; Lee, M.; Shaw, L.; Chen, S.; Yakovenko, A. A.; Kulkarni, A.; Xiao, J.; Fredrickson, K.; Tok, J. B.; Zou, X.; Cui, Y.; Bao, Z. Robust and Conductive Two-Dimensional Metal-Organic Frameworks with Exceptionally High Volumetric and Areal Capacitance. *Nat. Energy* **2018**, *3*, 30–36. <https://doi.org/10.1038/s41560-017-0044-5>.
- (35) Zhao, Z.; Ding, J.; Zhu, R.; Pang, H. The Synthesis and Electrochemical Applications of Core–Shell MOFs and Their Derivatives. *J. Mater. Chem. A* **2019**, *7*, 15519–15540. <https://doi.org/10.1039/C9TA03833G>.
- (36) Mukkatt, I.; Anjana, P. M.; Nirmala, A.; Rakhi, R. B.; Shankar, S.; Ajayaghosh, A. Metal Ion-Induced Capacitance Modulation in near-Isostructural Complexes-Derived Electrochromic Coordination Polymers. *Mater. Today Chem.* **2020**, *16*, 100260. <https://doi.org/https://doi.org/10.1016/j.mtchem.2020.100260>.
- (37) Deshmukh, M. A.; Gicevicius, M.; Ramanaviciene, A.; Shirsat, M. D.; Viter, R.; Ramanavicius, A. Hybrid Electrochemical/Electrochromic Cu(II) Ion Sensor Prototype Based on PANI/ITO-Electrode. *Sensors Actuators B Chem.* **2017**, *248*, 527–535. <https://doi.org/https://doi.org/10.1016/j.snb.2017.03.167>.
- (38) Li, L.; Lou, Z.; Han, W.; Chen, D.; Jiang, K.; Shen, G. Highly Stretchable Micro-Supercapacitor Arrays with Hybrid MWCNT/PANI Electrodes. *Adv. Mater. Technol.* **2017**, *2*, 1600282. <https://doi.org/https://doi.org/10.1002/admt.201600282>.
- (39) El-Kady, M. F.; Kaner, R. B. Scalable Fabrication of High-Power Graphene Micro-Supercapacitors for Flexible and on-Chip Energy Storage. *Nat. Commun.* **2013**, *4*, 1475. <https://doi.org/10.1038/ncomms2446>.
- (40) Tong, Y.-L.; Xu, B.; Du, X.-F.; Cheng, H.-Y.; Wang, C.-F.; Wu, G.; Chen, S. Microfluidic-Spinning-Directed Conductive Fibers toward Flexible Micro-Supercapacitors. *Macromol. Mater. Eng.* **2018**, *303*, 1700664. <https://doi.org/https://doi.org/10.1002/mame.201700664>.
- (41) Mukkatt, I.; Nirmala, A.; Madhavan, N. D.; Shankar, S.; Deb, B.; Ajayaghosh, A. Ligand-Controlled Electrochromic Diversification with Multilayer Coated Metallosupramolecular Polymer Assemblies. *ACS Appl. Mater. Interfaces* **2021**, *13*, 5245–5255. <https://doi.org/10.1021/acsami.0c20428>.

- (42) Banda, H.; Dou, J.-H.; Chen, T.; Libretto, N. J.; Chaudhary, M.; Bernard, G. M.; Miller, J. T.; Michaelis, V. K.; Dincă, M. High-Capacitance Pseudocapacitors from Li⁺ Ion Intercalation in Nonporous, Electrically Conductive 2D Coordination Polymers. *J. Am. Chem. Soc.* **2021**, *143*, 2285–2292.
<https://doi.org/10.1021/jacs.0c10849>.
- (43) Li, W.-H.; Ding, K.; Tian, H.-R.; Yao, M.-S.; Nath, B.; Deng, W.-H.; Wang, Y.; Xu, G. Conductive Metal–Organic Framework Nanowire Array Electrodes for High-Performance Solid-State Supercapacitors. *Adv. Funct. Mater.* **2017**, *27*, 1702067.
<https://doi.org/https://doi.org/10.1002/adfm.201702067>.
- (43a) Guo, Q.; Zhao, X.; Li, Z.; Wang, B.; Wang, D.; Nie, G. High Performance Multicolor Intelligent Supercapacitor and Its Quantitative Monitoring of Energy Storage Level by Electrochromic Parameters. *ACS Appl. Energy Mater.* **2020**, *3*, 2727–2736.
<https://doi.org/10.1021/acsaem.9b02392>.
- (43b) Eisenberg, O.; Algavi, Y. M.; Weissman, H.; Narevicius, J.; Rybtchinski, B.; Lahav, M.; van der Boom, M. E. Dual Function Metallo–Organic Assemblies for Electrochromic–Hybrid Supercapacitors. *Adv. Mater. Interfaces* **2020**, *7*, 1–7.
<https://doi.org/10.1002/admi.202000718>.
- (44) Wang, L.; Feng, X.; Ren, L.; Piao, Q.; Zhong, J.; Wang, Y.; Li, H.; Chen, Y.; Wang, B. Flexible Solid-State Supercapacitor Based on a Metal–Organic Framework Interwoven by Electrochemically-Deposited PANI. *J. Am. Chem. Soc.* **2015**, *137*, 4920–4923.
<https://doi.org/10.1021/jacs.5b01613>.
- (45) Largeot, C.; Portet, C.; Chmiola, J.; Taberna, P.-L.; Gogotsi, Y.; Simon, P. Relation between the Ion Size and Pore Size for an Electric Double-Layer Capacitor. *J. Am. Chem. Soc.* **2008**, *130*, 2730–2731.
<https://doi.org/10.1021/ja7106178>.
- (46) Su, J.; He, W.; Li, X.-M.; Sun, L.; Wang, H.-Y.; Lan, Y.-Q.; Ding, M.; Zuo, J.-L. High Electrical Conductivity in a 2D MOF with Intrinsic Superprotonic Conduction and Interfacial Pseudo-Capacitance. *Matter* **2020**, *2*, 711–722.
<https://doi.org/https://doi.org/10.1016/j.matt.2019.12.018>.
- (47) Gittins, J. W.; Balhatchet, C. J.; Chen, Y.; Liu, C.; Madden, D. G.; Britto, S.; Golomb, M. J.; Walsh, A.; Fairen-Jimenez, D.; Dutton, S. E.; Forse, A. C. Insights into the Electric Double-Layer Capacitance of Two-Dimensional Electrically Conductive Metal–Organic Frameworks. *J. Mater. Chem. A* **2021**, *9*, 16006–16015.
<https://doi.org/10.1039/D1TA04026J>.

- (48) Han, F. S.; Higuchi, M.; Kurth, D. G. Metallo-Supramolecular Polymers Based on Functionalized Bis-Terpyridines as Novel Electrochromic Materials. *Adv. Mater.* **2007**, *19*, 3928–3931.
<https://doi.org/https://doi.org/10.1002/adma.200700931>.
- (49) Hu, C. W.; Sato, T.; Zhang, J.; Moriyama, S.; Higuchi, M. Three-Dimensional Fe(II)-Based Metallo-Supramolecular Polymers with Electrochromic Properties of Quick Switching, Large Contrast, and High Coloration Efficiency. *ACS Appl. Mater. Interfaces* **2014**, *6*, 9118–9125.
<https://doi.org/10.1021/am5010859>.
- (50) Zhu, M.; Huang, Y.; Huang, Y.; Meng, W.; Gong, Q.; Li, G.; Zhi, C. An Electrochromic Supercapacitor and Its Hybrid Derivatives: Quantifiably Determining Their Electrical Energy Storage by an Optical Measurement. *J. Mater. Chem. A* **2015**, *3*, 21321–21327.
<https://doi.org/10.1039/C5TA06237C>.
- (51) Shiryayeva, I. M.; Collman, J. P.; Boulatov, R.; Sunderland, C. J. Nonideal Electrochemical Behavior of Biomimetic Iron Porphyrins: Interfacial Potential Distribution across Multilayer Films. *Anal. Chem.* **2003**, *75*, 494–502.
<https://doi.org/10.1021/ac025918i>.
- (52) Zhang, Q.; Tsai, C.-Y.; Li, L.-J.; Liaw, D.-J. Colorless-to-Colorful Switching Electrochromic Polyimides with Very High Contrast Ratio. *Nat. Commun.* **2019**, *10*, 1239.
<https://doi.org/10.1038/s41467-019-09054-8>.
- (53) Zhu, M.; Huang, Y.; Huang, Y.; Meng, W.; Gong, Q.; Li, G.; Zhi, C. An Electrochromic Supercapacitor and Its Hybrid Derivatives: Quantifiably Determining Their Electrical Energy Storage by an Optical Measurement. *J. Mater. Chem. A* **2015**, *3*, 21321–21327.
<https://doi.org/10.1039/C5TA06237C>.
- (54) Vasilopoulou, M.; Aspiotis, G.; Kostis, I.; Argitis, P.; Davazoglou, D. Fabrication of WO₃-Based Electrochromic Displays Using Solid or Gel-like Organic Electrolytes. *J. Phys. Conf. Ser.* **2005**, *10*, 329–332.
<https://doi.org/10.1088/1742-6596/10/1/081>.
- (55) Molji, C.; Aashish, A.; Neethu, K. S.; Devaki, S. J. Self-Assembled Polyaniline Nanowires Stippled Graphene-3-Pentadecylphenyl Phosphate Hybrid Nanocomposite Based Green Sustainable Electrodes for Supercapacitors. *J. Mater. Chem. A* **2017**, *5*, 16636–16645.
<https://doi.org/10.1039/c7ta05215d>.
- (56) Li, Z.-X.; Zhang, X.; Liu, Y.-C.; Zou, K.-Y.; Yue, M.-L. Controlling the BET Surface Area of Porous Carbon by Using the Cd/C Ratio of a Cd–MOF Precursor and Enhancing

- the Capacitance by Activation with KOH. *Chem. – A Eur. J.* **2016**, *22*, 17734–17747.
<https://doi.org/https://doi.org/10.1002/chem.201603072>.
- (57) Lee, D. Y.; Shinde, D. V.; Kim, E.-K.; Lee, W.; Oh, I.-W.; Shrestha, N. K.; Lee, J. K.; Han, S.-H. Supercapacitive Property of Metal–Organic-Frameworks with Different Pore Dimensions and Morphology. *Microporous Mesoporous Mater.* **2013**, *171*, 53–57.
<https://doi.org/https://doi.org/10.1016/j.micromeso.2012.12.039>.
- (58) Jiang, Y.; Liu, J. Definitions of Pseudocapacitive Materials: A Brief Review. *ENERGY Environ. Mater.* **2019**, *2*, 30–37.
<https://doi.org/https://doi.org/10.1002/eem2.12028>.
- (59) Khademi, M.; Barz, D. P. J. Structure of the Electrical Double Layer Revisited: Electrode Capacitance in Aqueous Solutions. *Langmuir* **2020**, *36*, 4250–4260.
<https://doi.org/10.1021/acs.langmuir.0c00024>.
- (60) Anjana, P. M.; Bindhu, M. R.; Umadevi, M.; Rakhi, R. B. Antibacterial and Electrochemical Activities of Silver, Gold, and Palladium Nanoparticles Dispersed Amorphous Carbon Composites. *Appl. Surf. Sci.* **2019**, *479*, 96–104.
<https://doi.org/10.1016/j.apsusc.2019.02.057>.
- (61) Kondrat, S.; Wu, P.; Qiao, R.; Kornyshev, A. A. Accelerating Charging Dynamics in Subnanometre Pores. *Nat. Mater.* **2014**, *13*, 387–393.
<https://doi.org/10.1038/nmat3916>.
- (62) Schott, M.; Lorrman, H.; Szczerba, W.; Beck, M.; Kurth, D. G. State-of-the-Art Electrochromic Materials Based on Metallo-Supramolecular Polymers. *Sol. Energy Mater. Sol. Cells* **2014**, *126*, 68–73.
<https://doi.org/https://doi.org/10.1016/j.solmat.2014.03.032>.
- (63) Liu, W.; Lu, C.; Wang, X.; Tay, R. Y.; Tay, B. K. High-Performance Microsupercapacitors Based on Two-Dimensional Graphene/Manganese Dioxide/Silver Nanowire Ternary Hybrid Film. *ACS Nano* **2015**, *9*, 1528–1542.
<https://doi.org/10.1021/nn5060442>.
- (64) Yang, J.; Pan, Z.; Yu, Q.; Zhang, Q.; Ding, X.; Shi, X.; Qiu, Y.; Zhang, K.; Wang, J.; Zhang, Y. Free-Standing Black Phosphorus Thin Films for Flexible Quasi-Solid-State Micro-Supercapacitors with High Volumetric Power and Energy Density. *ACS Appl. Mater. Interfaces* **2019**, *11*, 5938–5946.
<https://doi.org/10.1021/acsami.8b18172>.
- (65) Yoo, J.; Byun, S.; Lee, C.-W.; Yoo, C.-Y.; Yu, J. Precisely Geometry Controlled Micro-Supercapacitors for Ultrahigh Areal Capacitance, Volumetric Capacitance, and Energy

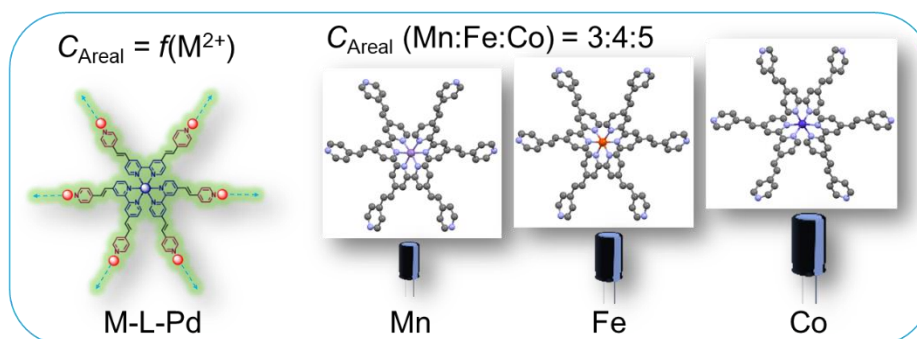
- Density. *Chem. Mater.* **2018**, *30*, 23–27.
<https://doi.org/10.1021/acs.chemmater.7b03786>.
- (66) Peng, Z.; Huang, J.; He, Q.; Li, S.; Tan, L.; Chen, Y. Green Quasi-Solid-State Planar Asymmetric Supercapacitors with High Working Voltage and Extraordinary Volumetric Energy Density. *J. Mater. Chem. A* **2021**, *9*, 14363–14371.
<https://doi.org/10.1039/D1TA04005G>.
- (67) Bhardwaj, S. K.; Bhardwaj, N.; Kaur, R.; Mehta, J.; Sharma, A. L.; Kim, K.-H.; Deep, A. An Overview of Different Strategies to Introduce Conductivity in Metal–Organic Frameworks and Miscellaneous Applications Thereof. *J. Mater. Chem. A* **2018**, *6*, 14992–15009.
<https://doi.org/10.1039/C8TA04220A>.
- (68) Xie, L. S.; Skorupskii, G.; Dincă, M. Electrically Conductive Metal–Organic Frameworks. *Chem. Rev.* **2020**, *120*, 8536–8580.
<https://doi.org/10.1021/acs.chemrev.9b00766>.
- (69) Johnson, E. M.; Ilic, S.; Morris, A. J. Design Strategies for Enhanced Conductivity in Metal–Organic Frameworks. *ACS Cent. Sci.* **2021**, *7*, 445–453.
<https://doi.org/10.1021/acscentsci.1c00047>.
- (70) Xie, L. S.; Alexandrov, E. V.; Skorupskii, G.; Proserpio, D. M.; Dincă, M. Diverse π – π Stacking Motifs Modulate Electrical Conductivity in Tetrathiafulvalene-Based Metal–Organic Frameworks. *Chem. Sci.* **2019**, *10*, 8558–8565.
<https://doi.org/10.1039/C9SC03348C>.
- (71) Clough, A. J.; Orchanian, N. M.; Skelton, J. M.; Neer, A. J.; Howard, S. A.; Downes, C. A.; Piper, L. F. J.; Walsh, A.; Melot, B. C.; Marinescu, S. C. Room Temperature Metallic Conductivity in a Metal–Organic Framework Induced by Oxidation. *J. Am. Chem. Soc.* **2019**, *141*, 16323–16330.
<https://doi.org/10.1021/jacs.9b06898>.
- (72) Liu, L.; Zhang, Q.; Du, K.; He, Z.; Wang, T.; Yi, Y.; Wang, M.; Zhong, X.; Dong, G.; Diao, X. An Intelligent and Portable Power Storage Device Able to Visualize the Energy Status. *J. Mater. Chem. A* **2019**, *7*, 23028–23037.
<https://doi.org/10.1039/C9TA07553D>.
- (73) Ginting, R. T.; Ovhal, M. M.; Kang, J.-W. A Novel Design of Hybrid Transparent Electrodes for High Performance and Ultra-Flexible Bifunctional Electrochromic-Supercapacitors. *Nano Energy* **2018**, *53*, 650–657.
<https://doi.org/https://doi.org/10.1016/j.nanoen.2018.09.016>.

- (74) Li, K.; Shao, Y.; Liu, S.; Zhang, Q.; Wang, H.; Li, Y.; Kaner, R. B. Aluminum-Ion-Intercalation Supercapacitors with Ultrahigh Areal Capacitance and Highly Enhanced Cycling Stability: Power Supply for Flexible Electrochromic Devices. *Small* **2017**, *13*, 1700380.
<https://doi.org/https://doi.org/10.1002/sml.201700380>.
- (75) Zhang, C. (John); Anasori, B.; Seral-Ascaso, A.; Park, S.-H.; McEvoy, N.; Shmeliov, A.; Duesberg, G. S.; Coleman, J. N.; Gogotsi, Y.; Nicolosi, V. Transparent, Flexible, and Conductive 2D Titanium Carbide (MXene) Films with High Volumetric Capacitance. *Adv. Mater.* **2017**, *29*, 1702678.
<https://doi.org/https://doi.org/10.1002/adma.201702678>.
- (76) Mondal, S.; Yoshida, T.; Maji, S.; Ariga, K.; Higuchi, M. Transparent Supercapacitor Display with Redox-Active Metallo-Supramolecular Polymer Films. *ACS Appl. Mater. Interfaces* **2020**, *12*, 16342–16349.
<https://doi.org/10.1021/acsami.9b23123>.
- (77) Li, K.; Wang, X.; Li, S.; Urbankowski, P.; Li, J.; Xu, Y.; Gogotsi, Y. An Ultrafast Conducting Polymer@MXene Positive Electrode with High Volumetric Capacitance for Advanced Asymmetric Supercapacitors. *Small* **2020**, *16*, 1906851.
<https://doi.org/https://doi.org/10.1002/sml.201906851>.
- (78) Liu, L.; Diao, X.; He, Z.; Yi, Y.; Wang, T.; Wang, M.; Huang, J.; He, X.; Zhong, X.; Du, K. High-Performance All-Inorganic Portable Electrochromic Li-Ion Hybrid Supercapacitors toward Safe and Smart Energy Storage. *Energy Storage Mater.* **2020**, *33*, 258–267.
<https://doi.org/https://doi.org/10.1016/j.ensm.2020.08.023>.
- (79) Park, S. H.; Jeong, J.-M.; Kim, S. J.; Kim, K. H.; Lee, S. H.; Bae, N. H.; Lee, K. G.; Choi, B. G. Large-Area and 3D Polyaniline Nanoweb Film for Flexible Supercapacitors with High Rate Capability and Long Cycle Life. *ACS Appl. Energy Mater.* **2020**, *3*, 7746–7755.
<https://doi.org/10.1021/acsaem.0c01140>.
- (80) Zhuang, Y.; Zhao, W.; Wang, L.; Li, F.; Wang, W.; Liu, S.; Huang, W.; Zhao, Q. Soluble Triarylamine Functionalized Symmetric Viologen for All-Solid-State Electrochromic Supercapacitors. *Sci. China Chem.* **2020**, *63*, 1632–1644.
<https://doi.org/10.1007/s11426-020-9789-9>.
- (81) Murto, P.; Elmas, S.; Méndez-Romero, U. A.; Yin, Y.; Genene, Z.; Mone, M.; Andersson, G. G.; Andersson, M. R.; Wang, E. Highly Stable Indacenodithieno[3,2-b]Thiophene-Based Donor–Acceptor Copolymers for Hybrid Electrochromic and Energy Storage

- Applications. *Macromolecules* **2020**, *53*, 11106–11119.
<https://doi.org/10.1021/acs.macromol.0c02212>.
- (82) Chu, D.; Qu, X.; Zhang, S.; Zhang, J.; Yang, Y.; An, W. Polyoxotungstate-Based Nanocomposite Films with Multi-Color Change and High Volumetric Capacitance toward Electrochromic Energy-Storage Applications. *New J. Chem.* **2021**, *45*, 19977–19985.
<https://doi.org/10.1039/d1nj03939c>.
- (83) Ma, J.; Zheng, S.; Cao, Y.; Zhu, Y.; Das, P.; Wang, H.; Liu, Y.; Wang, J.; Chi, L.; Liu, S. (Frank); Wu, Z.-S. Aqueous MXene/PH1000 Hybrid Inks for Inkjet-Printing Micro-Supercapacitors with Unprecedented Volumetric Capacitance and Modular Self-Powered Microelectronics. *Adv. Energy Mater.* **2021**, *11*, 2100746.
<https://doi.org/https://doi.org/10.1002/aenm.202100746>.
- (84) Qu, X.; Fu, Y.; Ma, C.; Yang, Y.; Shi, D.; Chu, D.; Yu, X. Bifunctional Electrochromic-Energy Storage Materials with Enhanced Performance Obtained by Hybridizing TiO₂nanowires with POMs. *New J. Chem.* **2020**, *44*, 15475–15482.
<https://doi.org/10.1039/d0nj02859b>.
- (85) Acerce, M.; Voiry, D.; Chhowalla, M. Metallic 1T Phase MoS₂ Nanosheets as Supercapacitor Electrode Materials. *Nat. Nanotechnol.* **2015**, *10*, 313–318.
<https://doi.org/10.1038/nnano.2015.40>.
- (86) Zhang, M.; Sun, Y.; Song, R. Hierarchical Porous Carbon Materials Obtained by Cu–Al Double Hydroxide Templates with High Gravimetric and Volumetric Capacitance. *Nanotechnology* **2021**, *32*, 235303.
<https://doi.org/10.1088/1361-6528/abe9e8>.
- (87) Xiao, P.; Shi, M.; Xu, L.; Tao, F.; Li, Y.; Zhu, H.; Liu, Y.; Li, Z.; Zhou, Y.; Feng, W. An Efficient Chemical Reduction-Induced Assembly of Fe₃O₄@graphene Fiber for Wire-Shaped Supercapacitors with Ultrahigh Volumetric Energy Density. *Sci. China Technol. Sci.* **2021**, *64*, 2246–2254.
<https://doi.org/10.1007/s11431-020-1896-5>.
- (88) Wu, G.; Yang, X.; Hou, C.; Li, Y.; Zhang, Q.; Wang, H. High Volumetric Energy Density Asymmetric Fibrous Supercapacitors with Coaxial Structure Based on Graphene/MnO₂ Hybrid Fibers. *ChemElectroChem* **2020**, *7*, 4641–4648.
<https://doi.org/https://doi.org/10.1002/celec.202001139>.
- (89) Ma, H.; Kong, D.; Xu, Y.; Xie, X.; Tao, Y.; Xiao, Z.; Lv, W.; Jang, H. D.; Huang, J.; Yang, Q.-H. Disassembly–Reassembly Approach to RuO₂/Graphene Composites for Ultrahigh Volumetric Capacitance Supercapacitor. *Small* **2017**, *13*, 1701026.

<https://doi.org/https://doi.org/10.1002/sml.201701026>.

Metal ion Dependent Capacitance Modulation in Electrochromic Metallopolymers Derived from Near Iso-structural Coordination Complexes



4.1. Abstract

Efficient and stable electrode materials are the prerequisites towards a reliable energy storage technology. The use of metal-organic systems in supercapacitor electrodes was limited as pyrolytic carbon precursors until recently. In this chapter, we report the use of electrochromic metallopolymers obtained from near-isostructural metal (Mn^{2+} , Fe^{2+} , Co^{2+}) bipyridine complexes as electrode materials in a symmetric supercapacitor test cell. The variation in the central metal ion (Mn^{2+} , Fe^{2+} , Co^{2+}) was found to dictate the capacitive performance of the metallopolymers obtained via Pd(II) cross-linking of the otherwise nearly identical parent coordination complexes. The central metal ion not only influences the porosity and BET surface area (6.46 (Mn), 10.36 (Fe) and 29.72 (Co) $\text{m}^2 \text{g}^{-1}$) that affect the areal capacitance, but also the performance parameters like cycling stability and charge discharge kinetics as well as the charge transfer mechanism. A 3:4:5 ratio for the areal capacitance values (9.1 (Mn), 12.2 (Fe), and 15.4 (Co) mF cm^{-2} at a scan rate of 5 mV s^{-1}) corroborates the modulative effect of the metal center in the capacitive characteristics of the metallopolymers. The cycling stabilities of these metallopolymers also followed the same order. The use of larger/smaller ligands is obvious to result in different porosities and surface areas, however, the impact of the central metal ion in near-isostructural coordination complex derived metallopolymers is rather difficult to predict. Though the materials used in this study resulted in modest capacitive performance, the possibilities to improve their surface areas and crystallinity is envisaged to result in the development of new non-carbon electrode materials with efficient electrochemical storage and tunable electro-optical properties.

4.2. Introduction

Limited reserves of fossil fuels and global issues arising from increased carbon dioxide emissions have led to a paradigm shift in energy research, leading to innovative initiatives towards green and cost effective strategies for generation, storage and utilization of energy.¹ Though solar energy conversion provides a serious alternative towards clean energy, the intermittent nature of solar radiation demands for efficient and reliable storage technologies for effectively circumventing the energy requirements. Moreover, the current trends in the evolution of portable electronics are centered around the development of light weight, fast charging, stable and miniaturized storage devices.

Supercapacitors or electrochemical capacitors represent a class of promising electrical energy storage (EES) devices with high power density and long cycle life, compared to the conventional batteries that are not only bulky and rigid, but also require long charging times.² Moreover, the current trends in the evolution of portable electronics are centered around the development of light weight, fast charging, stable and miniaturized storage devices. Supercapacitors can be of two types based on their charge storage mechanism – pseudocapacitors (charge or electron transfer involving faradaic or redox reactions) and electrical double layer capacitors (non-Faradaic electrochemical double layer formed by the electrolyte ions on the electrode surface). Current generation supercapacitors benefit from the use of electrolytes and bridge the gap between batteries and conventional capacitors in terms of their energy and power densities. Until recently, carbon-based materials such as activated carbon, carbon nanotubes, graphite, etc., were exclusively used as active electrode materials in supercapacitors.^{3,4} Nevertheless, the last few years have witnessed the increasing use of non-carbon materials including metal oxides, layered materials, conducting polymers, metal chalcogenides, metal organic frameworks, etc., either exclusively or in combination with carbon as active electrode materials.⁵

Out of all the non-carbon materials, metal organic materials that combine the functional advantages of both organic and inorganic materials, are one of the less investigated class of electrode materials, that too as pyrolytic precursors for carbon in electrochemical storage devices.⁶⁻⁸ Metal-Organic Frameworks (MOFs) and Coordination Polymers (CPs) have emerged as a class of functional materials with multifarious applications over the past couple of decades.⁹⁻¹² With an

unprecedented combination of several characteristic properties such as structural regularity, high surface area, tunable pore size/distribution and synthetic diversity, these materials have instigated diverse realms of science.¹³⁻¹⁵ Porous materials of this class have been shown to have applications in catalysis, separation, sorption, mass transport, sensing, host-guest interactions, etc.,^{10,16,17} of which energy storage and conversion¹⁸ has been of tremendous interest. 2D MOFs and CPs with an inherent porous architecture, accessible active sites and surface areas akin to other 2D materials are indeed potential candidates for electrochemical energy storage and conversion, especially as electrode materials in devices like supercapacitors and batteries.¹⁹⁻²¹ The comparably lower conductivities of metal organic materials most likely hindered their widespread application as electrode materials in supercapacitors.²²⁻²⁵ However, the exceptionally large surface areas and tunable porosity along with structural and morphological versatilities have triggered recent interest to investigate the electrochemical feasibility of using metal organic systems as electrode materials in supercapacitors. The use of redox active metallopolymers with combined electro-optical properties of metals and conjugated organic ligands with a unique coherence of stability and desirable properties as capacitor materials is of tremendous contemporary interest.²¹ Electrochromic devices that combine optical modulation with energy storage allow the real-time monitoring of charge-discharge processes along with providing a visual indication of overcharging.

Dinca *et al.* have reported the first example of a MOF as the sole electrode material in an electrical double layer capacitance (EDLC) without the use of any conductive additives or binders. The MOF $\text{Ni}_3(\text{HITP})_2$ (HITP = 2,3,6,7,10,11-hexamino triphenylene) exhibited an areal capacitance of $18 \mu\text{F cm}^{-2}$ and stability up to 10000 cycles with 90% capacitance retention (**Figure 4.1**).²⁶ The equivalent series resistance was also found to be lower (0.47Ω) than those reported for graphene supercapacitors.

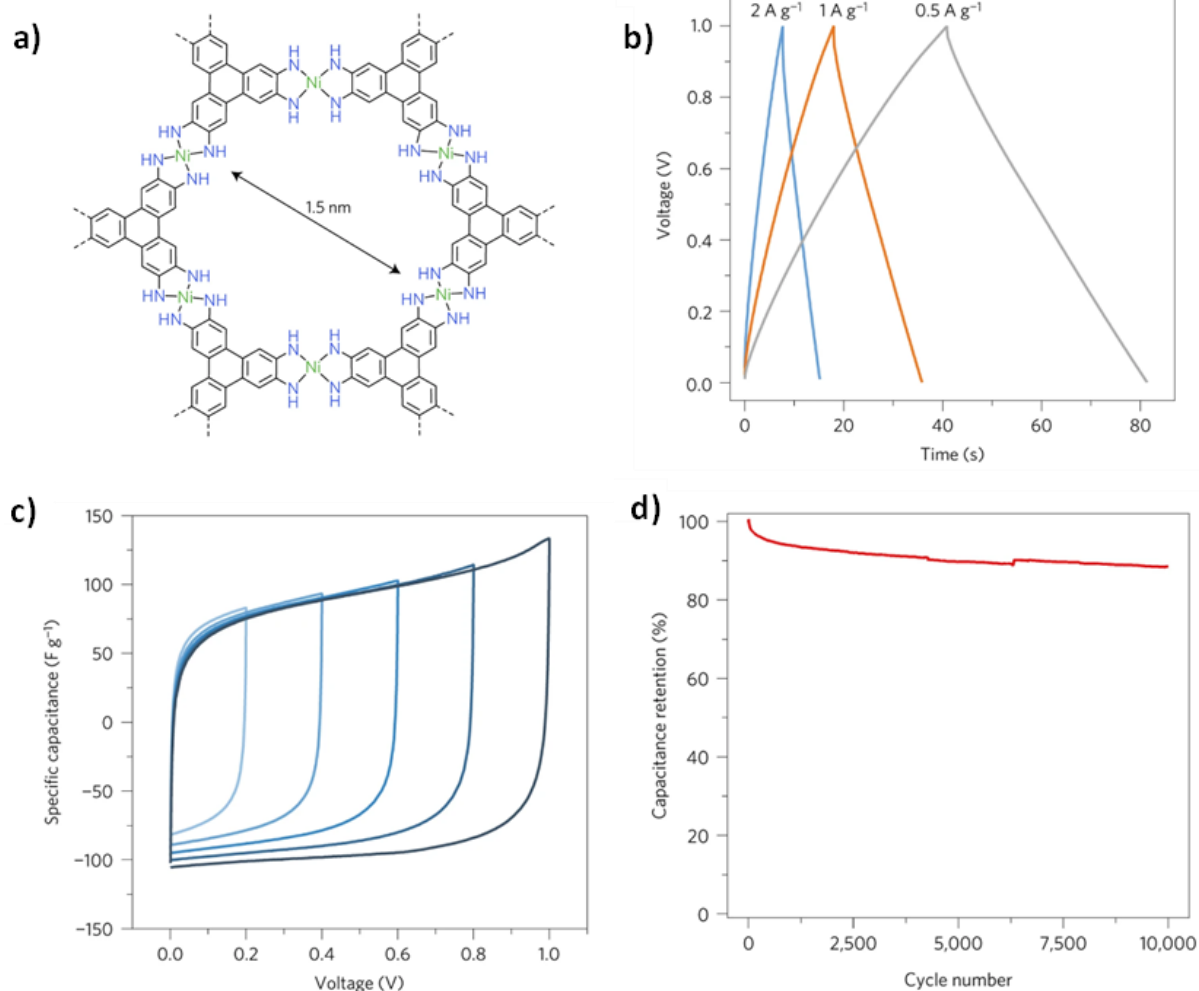


Figure 4.1. a) Structure of the MOF $\text{Ni}_3(\text{HITP})_2$. b) Charge discharge cycles at various current densities. c) CVs at a scan rate of 10 mV s^{-1} with increasing voltage. d) Cycling stability at 2 A g^{-1} . Adapted with permission from reference 26.

Wang and coworkers have evaluated a cobalt based MOF having a layered structure (**Figure 4.2a**) with hexamethylenetetramine and 2,3,5,6-tetrafluoroterephthalic acid as ligands (**Co-LMOF**) as electrode material for energy storage applications. A specific capacitance of 2474 F g^{-1} at a current density of 1 A g^{-1} , and stability up to 2000 cycles with capacitance retention of $>94\%$ was observed for this material. The excellent energy storage property was found to be due to the intrinsic nature of **Co-LMOF** that is spacious enough for the diffusion of the electrolyte and storage of charges (**Figure 4.2**).²⁵

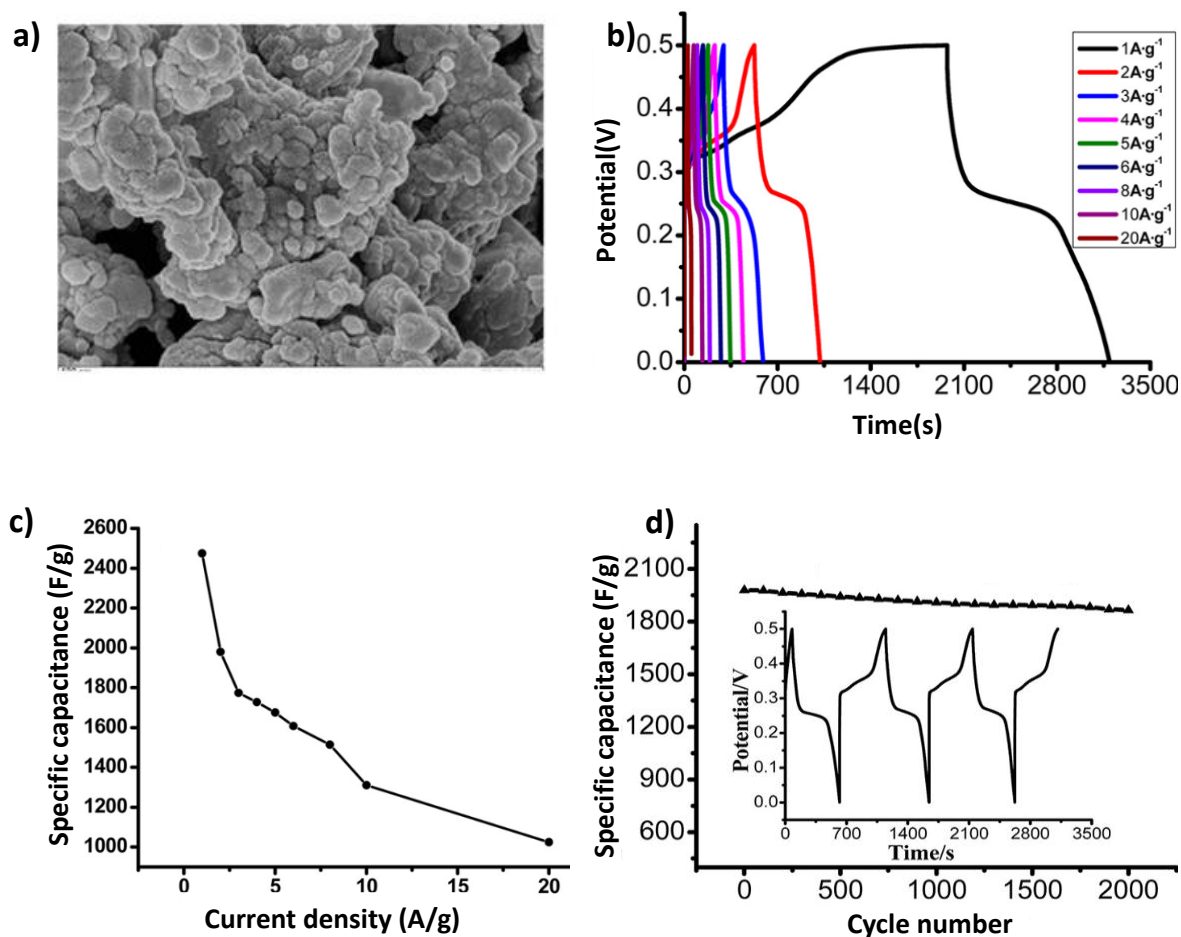


Figure 4.2. a) SEM images of Co-LMOF. b) The charge–discharge curves and c) specific capacitance at different current densities. d) Cycling stability at 2A g⁻¹. Adapted with permission from ref 25.

Gao and co-workers have investigated Ni(OH)₂/graphite nanosheet composites as electrode materials for supercapacitors (**Figure 4.3a,b**). The composite exhibited a specific capacitance of 1956 F g⁻¹ at a current density of 1 A g⁻¹ and a high charge-discharge rate (**Figure 4.3c**). It showed high capacitance retention of 70% after 1000 cycles at the current density of 10 A g⁻¹. The composite showed excellent energy storage properties, good rate capability and long cycle stabilities when compared to pure α -Ni(OH)₂ (**Figure 4.3c,d**).²⁰ The 3D hierarchical porous structure of α -Ni(OH)₂ nanocrystals formed on the matrix of graphite nanosheets was hypothesized to be the reason for the improvement of the reaction kinetics and electrochemical energy storage performance of the composite.

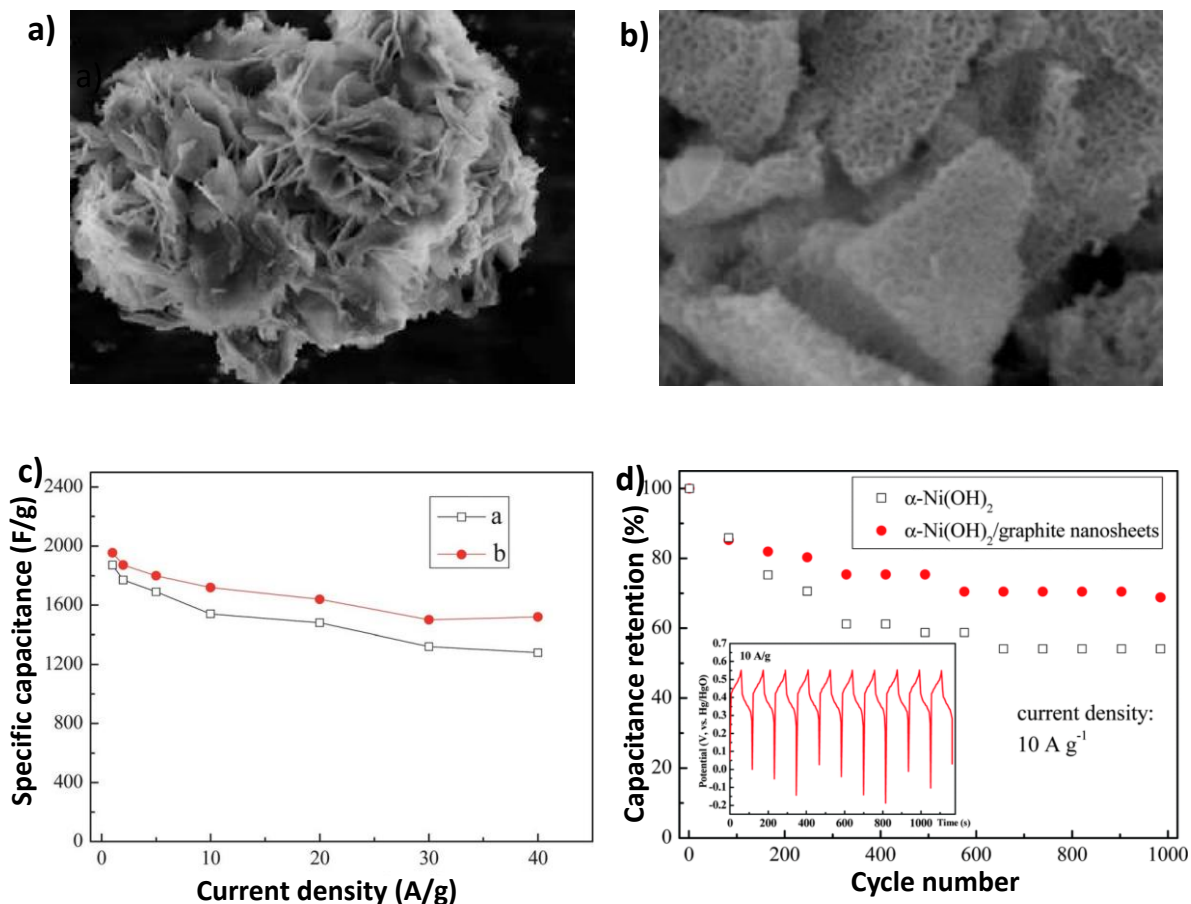


Figure 4.3. a) SEM image of a) pure α -Ni(OH)₂ and b) α -Ni(OH)₂/graphite composite. c) Capacitance vs current density for pure α -Ni(OH)₂ (black) and α -Ni(OH)₂/graphite composite (red). d) Cycling stability at 10A g⁻¹. Adapted with permission from ref 20.

Wei *et al.* have fabricated a 2D-Ni-based MOF (**Figure 4.4a**) and used as supercapacitor electrode material in aqueous alkaline solution. The Ni-based MOF exhibited a capacitance of 668 F g⁻¹ at 10A g⁻¹ and achieved exceptionally high capacitance of 1127 F g⁻¹ at 0.5A g⁻¹ (**Figure 4.4c**).²⁷ It retained 90% of capacitance after 3000 cycles and this excellent energy storage properties are due to intrinsic characteristics of Ni-MOF including its layered structure (**Figure 4.4b,d**).

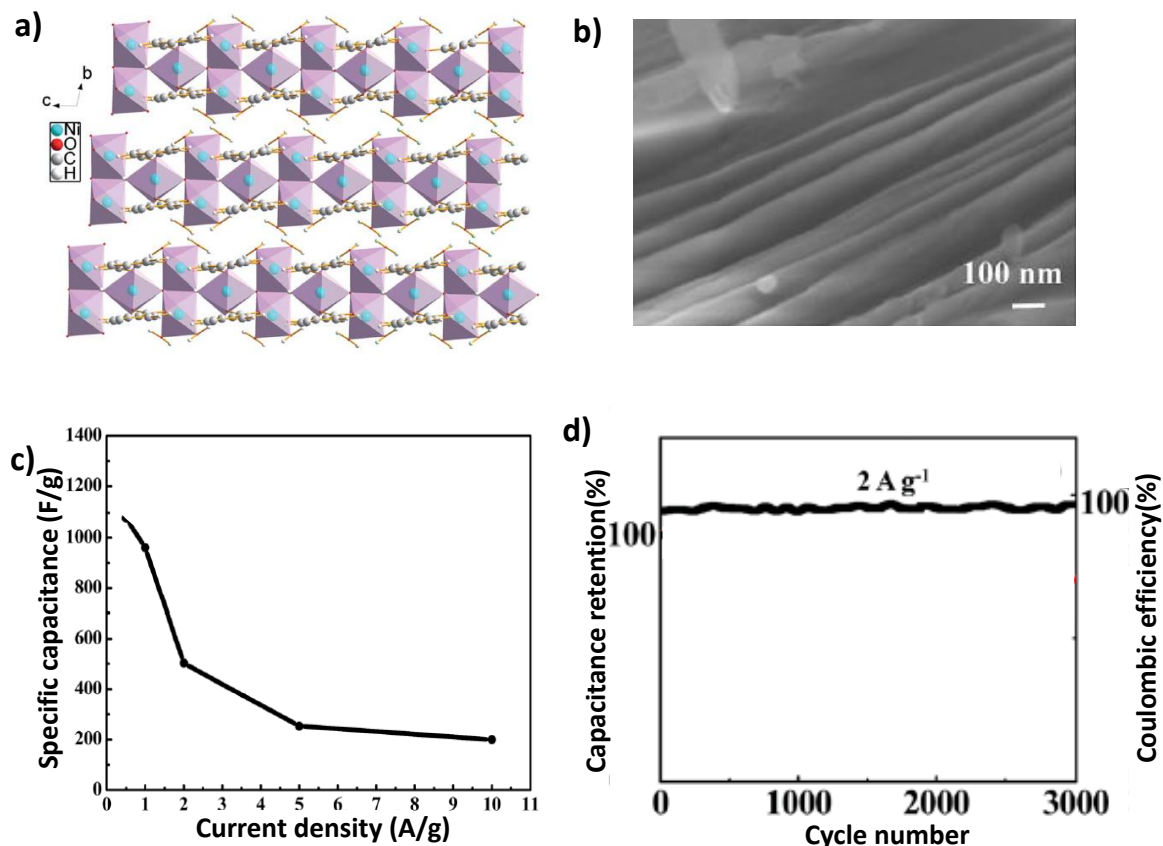


Figure 4.4. a) Structure of Ni-MOF viewed along the a axis. b) SEM image of Ni-MOF showing its layered structure. c) Specific capacitance measured at different current densities for the supercapacitor electrode fabricated from the Ni-MOF. d) Cycling stability of the electrode fabricated from Ni-MOF measured at 2 A g^{-1} . Adapted with permission from reference 27.

Pang and co-workers have reported two-dimensional (2D) cobalt-organic framework (**Co-MOF**) nanosheets using controllable one-step hydrothermal synthesis (**Figure 4.5a,b**). The electrodes fabricated from **Co-MOF** exhibited a specific capacitance of 1159 F g^{-1} at a current density of 0.5 A g^{-1} (**Figure 4.5c**) and showed high cycling stability after 6000 cycles with 96.7% capacitance retention (**Figure 4.5d**).²⁸ The nanosheet-based electrodes exhibited superior specific capacitance than bulk **Co-MOF** and micro-nano **Co-MOF** due to the short ion diffusion length from the ultrathin structure of nanosheet. Liu *et al.* have fabricated asymmetric electrochromic supercapacitors based on terpyridine-Fe (II) coordination polymers with Prussian blue as the

counter electrode. The specific capacitance of the asymmetric device was calculated to be 29.12 F g^{-1} at a current density of 0.4 A g^{-1} .²⁸

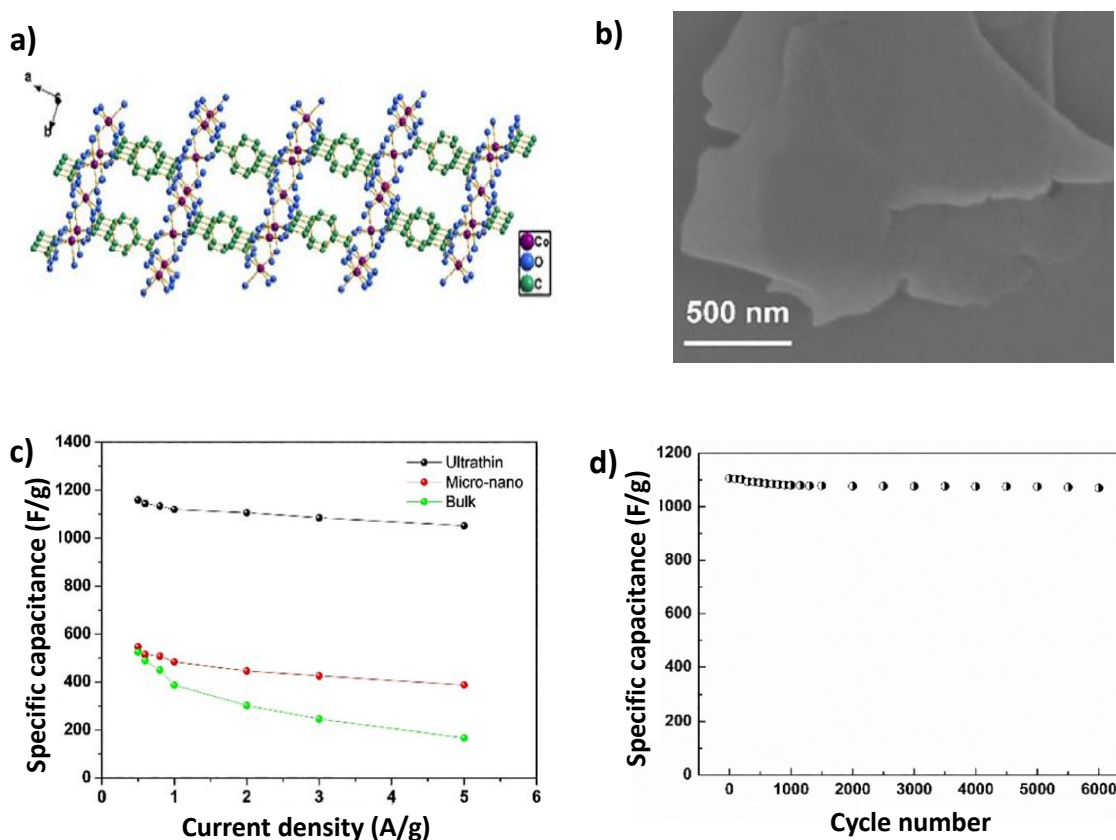


Figure 4.5. a) Molecular structure of ultrathin 2D Co-MOF nanosheet. b) SEM images of the Co-MOF nanosheets. c) Specific capacitances of ultrathin, micro-nano and bulk Co-MOF at different current densities. d) Cycling stability at 2 A g^{-1} using 3.0 M KOH electrolyte. Adapted with permission from ref 28.

Zhang *et al.* have reported a new donor-acceptor molecule containing 3,4-ethylenedioxythiophene (EDOT) as donor and chalcogena-diazolobenzotriazole (CDB) as acceptor. The conjugated polymeric film pCDB-EDOT exhibited both electrochromic and energy storage properties (Figure 4.6a). pCDB-EDOT based thin films showed areal capacitance up to 4.65 mF cm^{-2} at a current density of 0.05 mA cm^{-2} (Figure 4.6b) and 86% retention of capacitance after 2000 charge/discharge cycles. The electrochromic supercapacitor also changed its color from dark green (no power) to blue (fully charged) and was found to power a single yellow LED (1.8 V , 0.04 W) for more than 60 s (Figure 4.6c-d).^{28a}

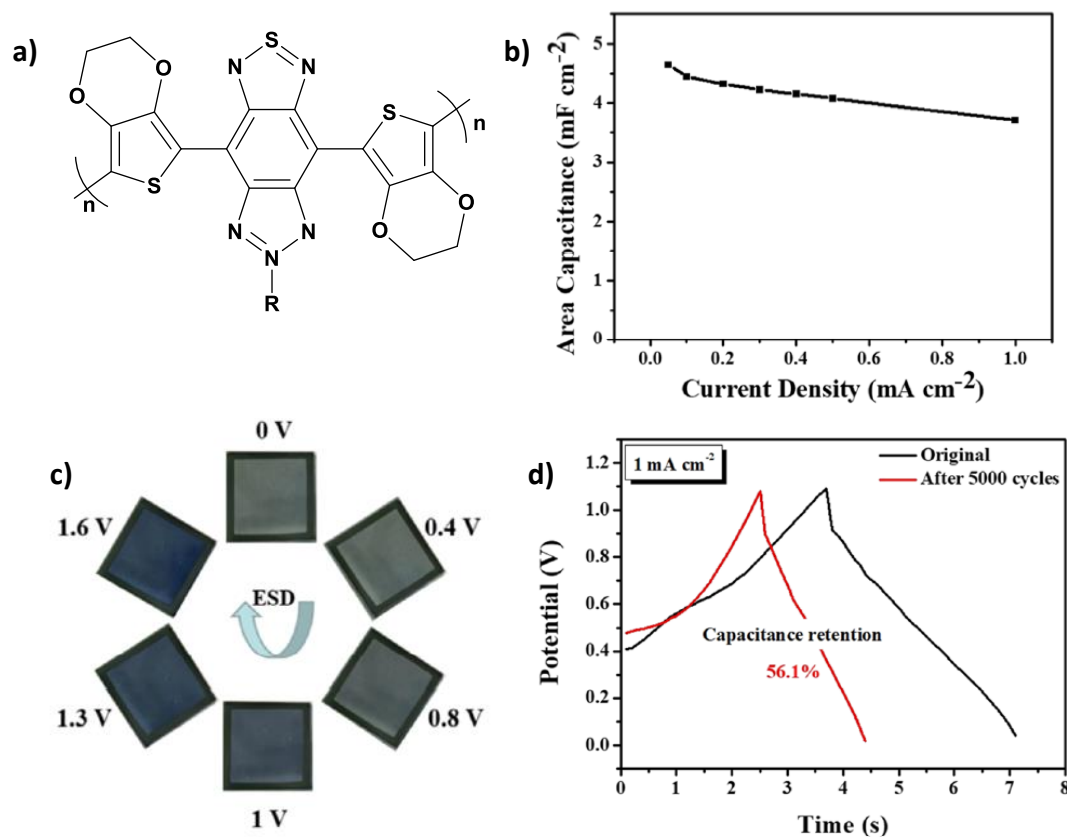


Figure 4.6. Structure of pCDB-EDOT polymer. b) Areal capacitance of pCDB-EDOT at various current densities. c) The color change of the electrochromic supercapacitor device at different voltages. d) The galvanic charge-discharge curves of pCDB-EDOT based electrochromic supercapacitor devices at a current density of 1 mA cm⁻² initially (black) and after 5000 cycles (red). Adapted with permission from ref 28a.

Steiner and co-workers have reported the use of double-gyroid vanadium pentoxide networks for dual function electrochromic supercapacitors with a high specific capacitance of 155 F g⁻¹ and stability up to 100 cycles at 10A g⁻¹. The device showed a corresponding electrochromic color change from green-grey to yellow which further indicated the capacitor's charge status (**Figure 4.7**).^{28b}

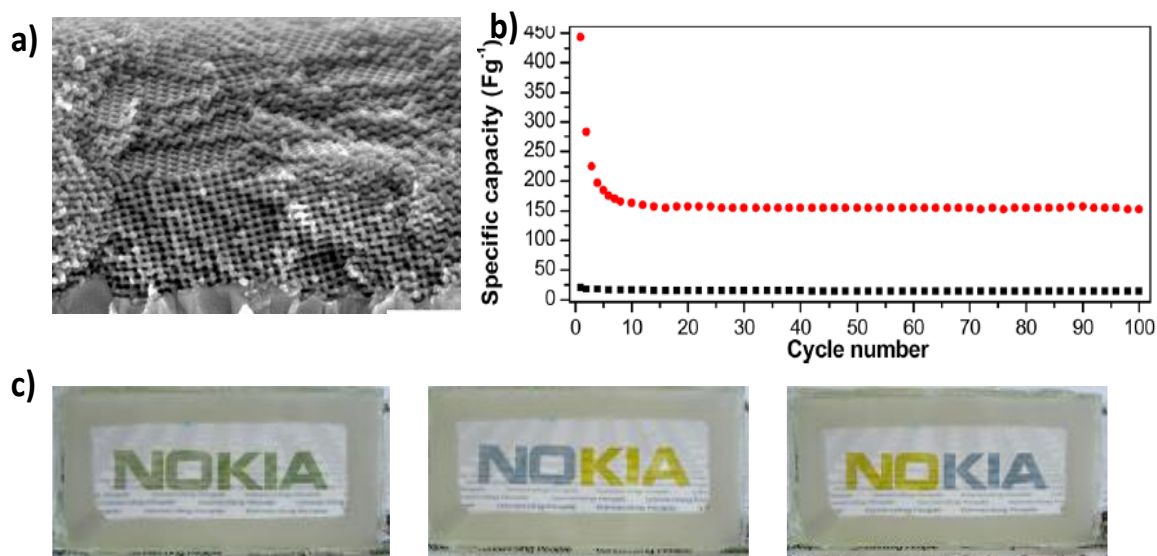


Figure 4.7. a) Scanning electron micrograph of a mesoporous V_2O_5 double-gyroid film on FTO substrate. b) The specific capacitance and charge–discharge cycles at $10 A g^{-1}$. c) Photographs of the electrochromic supercapacitor device displaying color change upon charge (0 V) and discharge (3.5 V). Adapted with permission from ref 28b.

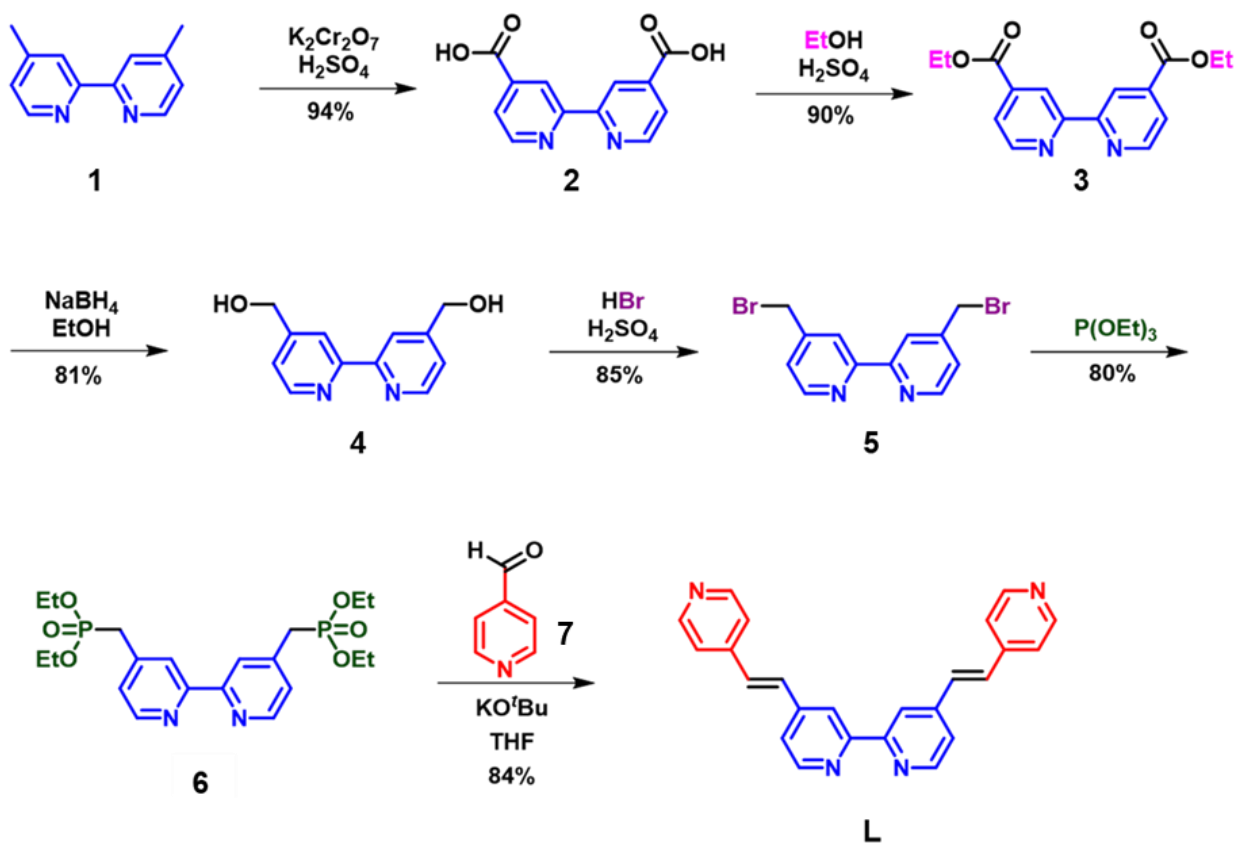
These metallopolymers were used as electrode materials in sandwiched supercapacitor test cells in a symmetric two electrode configuration. The role of the central metal ion in the parent coordination complexes in governing the porosity, surface area and hence the capacitive capabilities of the metallopolymers was investigated. The BET surface areas and the capacitance values were found to be dependent on the central metal ion. The metallopolymer derived supercapacitors exhibited a near 3:4:5 ratio for their areal capacitance (at a scanrate of $5 mV s^{-1}$) for **Mn-L-Pd**, **Fe-L-Pd** and **Co-L-Pd**, respectively. Interestingly, the performance parameters including charge-discharge times and cycling stabilities were also found to follow the same order. Moreover, the central metal ions, due to their characteristic redox potentials, were found to influence the charge transfer mechanism in these symmetric supercapacitors. The Mn and Fe metallopolymer derived devices most likely benefited from the contributions of both pseudocapacitance and EDL mechanisms, whereas a pseudocapacitive mechanism was found to be predominant in the case of cobalt metallopolymer. This study, to the best of our knowledge, is the first on the application of multimetallic all-coordination metallopolymers derived from iso-

structural electrochromic metal complexes as electrode materials with tunable areal capacitance in symmetric supercapacitor devices.

4.3. Results and Discussion

4.3.1. Synthesis and characterization

The ligand **L** (Scheme 4.1) and three isostructural metal complexes were synthesized via the modification of a previously reported procedure.^{31,32} Oxidation of the methyl groups in 4,4'-dimethyl-2,2'-bipyridine **1** followed by esterification and reduction resulted the corresponding diol **4**, which on nucleophilic substitution using Br⁻ and subsequent treatment with P(OEt)₃ followed by Wittig reaction involving pyridine-4-carboxaldehyde **7** afforded the ligand **L** in 39% overall yield. The details regarding the synthetic procedure and characterization are provided in the experimental section.



Scheme 4.1. Synthesis of the ligand **L** from commercially available 4,4'-dimethyl-2,2'-bipyridine **1**. Detailed synthetic procedure and characterization data are provided in the experimental section.

The near octahedral complexes (**Mn-L**: M = Mn, **Fe-L**: M = Fe, **Co-L**: M = Co) were subsequently synthesized by mixing the corresponding metal (II) chlorides with the ligand **L** in methanol in a 1:3 ratio, followed by a PF₆ anion exchange (**Figure 4.8a**).¹⁷ The metal salt and the ligand in solution was stirred for 12 h with occasional heating to 50 °C (every 30 min) to ensure complete reaction. The metallopolymers (**M-L-Pd**, M = Mn, Fe, Co) were obtained from the solutions of the corresponding metal complexes via the cross-linking of the free pyridines with a Pd(II) salt in a 1:3 ratio. The metallopolymer readily precipitated out from solution and were collected by vacuum filtration (**Figure 4.8b**). The schematic representation of the coordination polymer shown in **Figure 4.8b** is an illustration of the possible cross-linking and does not represent a planar 2D structural model.

Typically broad NMR spectra were obtained for all the metal complexes in CD₃OD, DMSO-d₆ or a mixture of CD₃OD and DMSO-d₆. However, similar peak pattern was observed for **Mn-L**, **Fe-L** and **Co-L** in the ¹H NMR spectra, irrespective of the counter anion (Cl⁻ or PF₆⁻). The chemical structure of the metal complexes with a metal to ligand ratio of 1:3 was also confirmed from ESI-MS and MALDI-TOF analysis.

The characteristic FT-IR spectra for metal coordinated pyridines were obtained for all the three complexes and metallopolymers, and the corresponding ring stretching C=N vibrations of pyridines were found to be shifted upon metal coordination (**Figure 4.9**). Two characteristic ring stretching C=N vibrations, one each for non-coordinated (**Mn-L**: 1594 cm⁻¹; **Fe-L**: 1596 cm⁻¹; **Co-L**: 1598 cm⁻¹) and metal coordinated (**Mn-L**: 1609 cm⁻¹; **Fe-L**: 1612 cm⁻¹; **Co-L**: 1612 cm⁻¹) pyridines were evident in the FT-IR spectra of all the complexes. The presence of both non-coordinated and coordinated pyridine C=N peaks in the FT-IR spectra of the metal complexes is indicative of the presence of metal coordinated bipyridines (M = Mn, Fe, Co) and non-coordinated, free terminal pyridines.³¹ However, the peaks corresponding to non-coordinated pyridine C=N vibrations vanished in the spectra of all the metallopolymers, corroborating an almost complete Pd – pyridine coordination in the metallopolymers. The C-H in plane deformation frequencies were also found to be shifted by at least 5 cm⁻¹ (1421 cm⁻¹ to >1426 cm⁻¹) in all the metallopolymers (**Figure 4.9**).

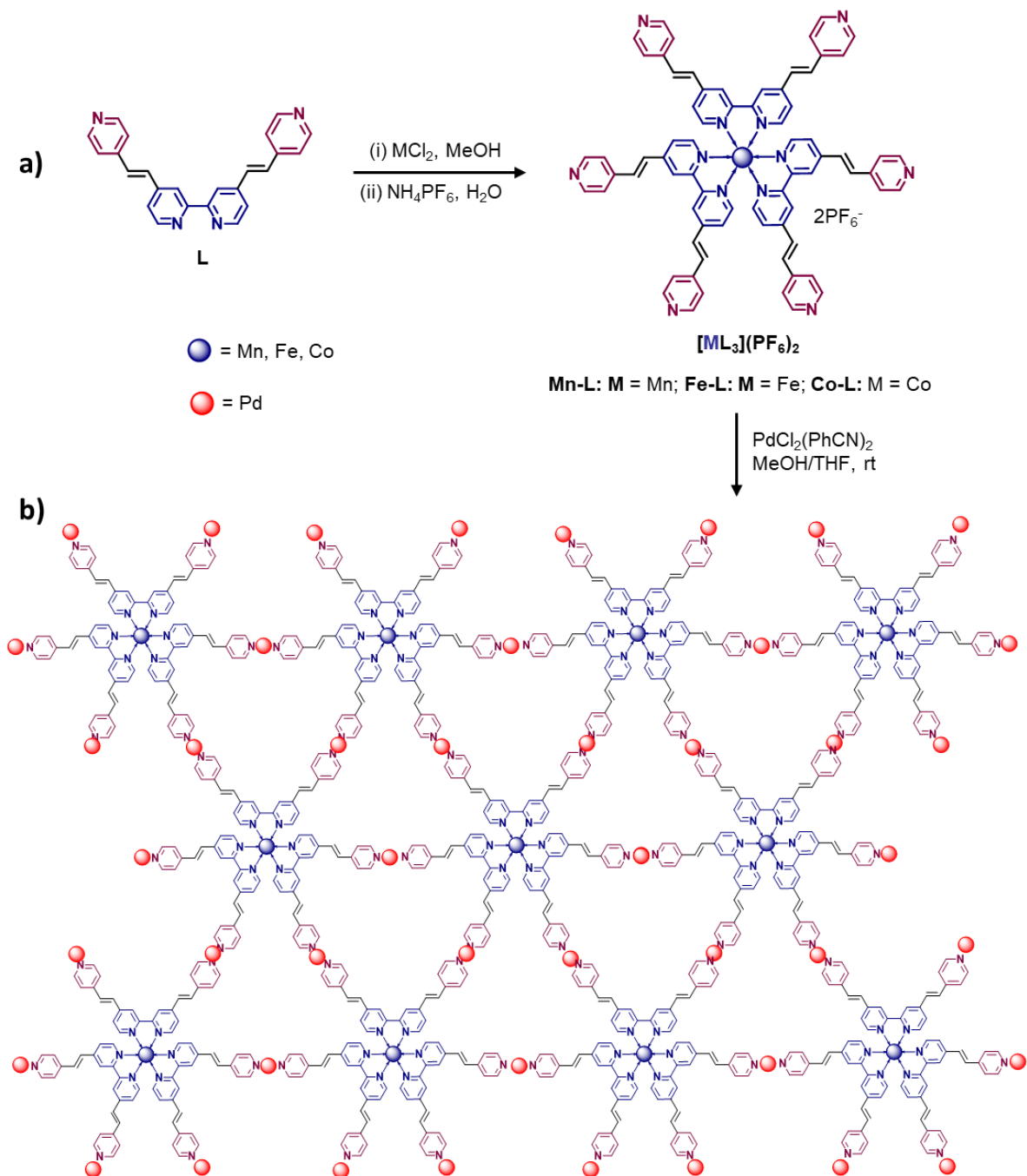


Figure 4.8. a) Scheme showing the molecular structures of the bipyridine ligand **L** and the corresponding coordination complexes $[\text{ML}_3](\text{PF}_6)_2$ ($\text{M} = \text{Mn}, \text{Fe}, \text{Co}$). b) Schematic representation of the formation of the metallopolymers. Three metallopolymers **M-L-Pd** ($\text{M} = \text{Mn}, \text{Fe}, \text{Co}$) were prepared by cross-linking the free pyridines on the complexes **M-L** ($\text{M} = \text{Mn}, \text{Fe}, \text{Co}$) with Pd(II) in a 1:3 ratio.

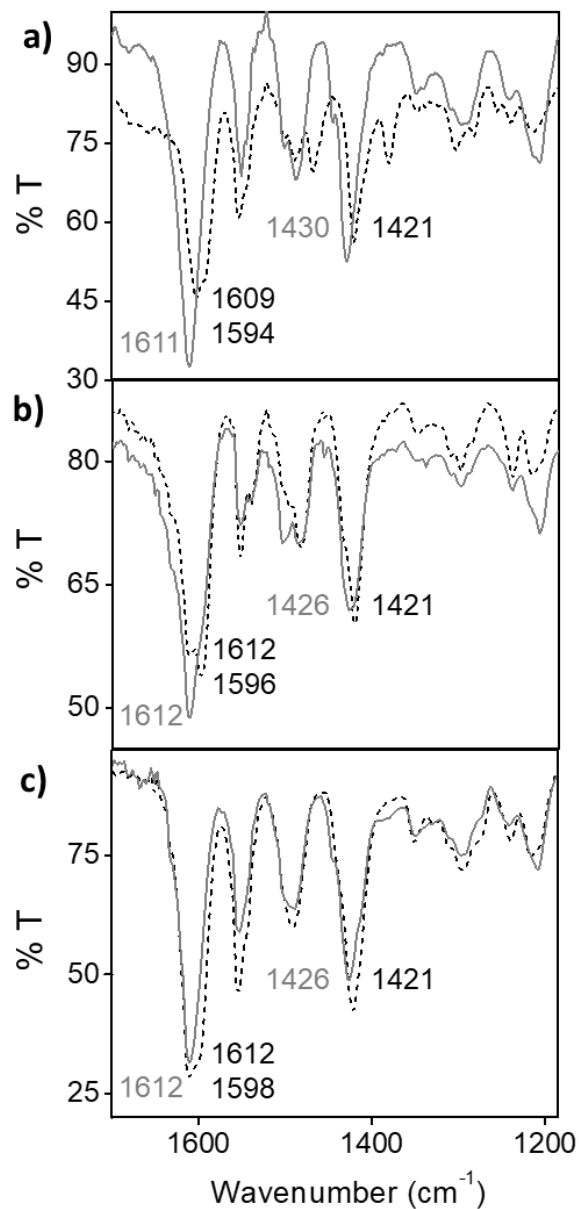


Figure 4.9. FT-IR spectra of (a) **Mn-L** (dotted) and **Mn-L-Pd** (solid), (b) **Fe-L** (dotted) and **Fe-L-Pd** (solid) and (c) **Co-L** (dotted) and **Co-L-Pd** (solid). The spectra were recorded in the solid state (KBr, neat). The peaks (wave number in cm^{-1}) corresponding to C=N ring stretching and in plane C-H deformation are provided in each spectrum (black: complex; grey: coordination polymer).

Thermal stability of complexes and metallopolymer were determined using thermogravimetric analysis (TGA). TGA confirmed higher thermal stability of the metallopolymer compared to their

parent metal-organic complexes (**Figure 4.10**). The Co complex (**Co-L**) and its metallopolymer (**Co-L-Pd**) were found to be the most stable among all the complexes and polymers. The thermal stability was found to be in the order **Co-L** > **Fe-L** > **Mn-L** for the metal bipyridine complexes and in the order **Co-L-Pd** > **Fe-L-Pd** > **Mn-L-Pd** for the metallopolymer.

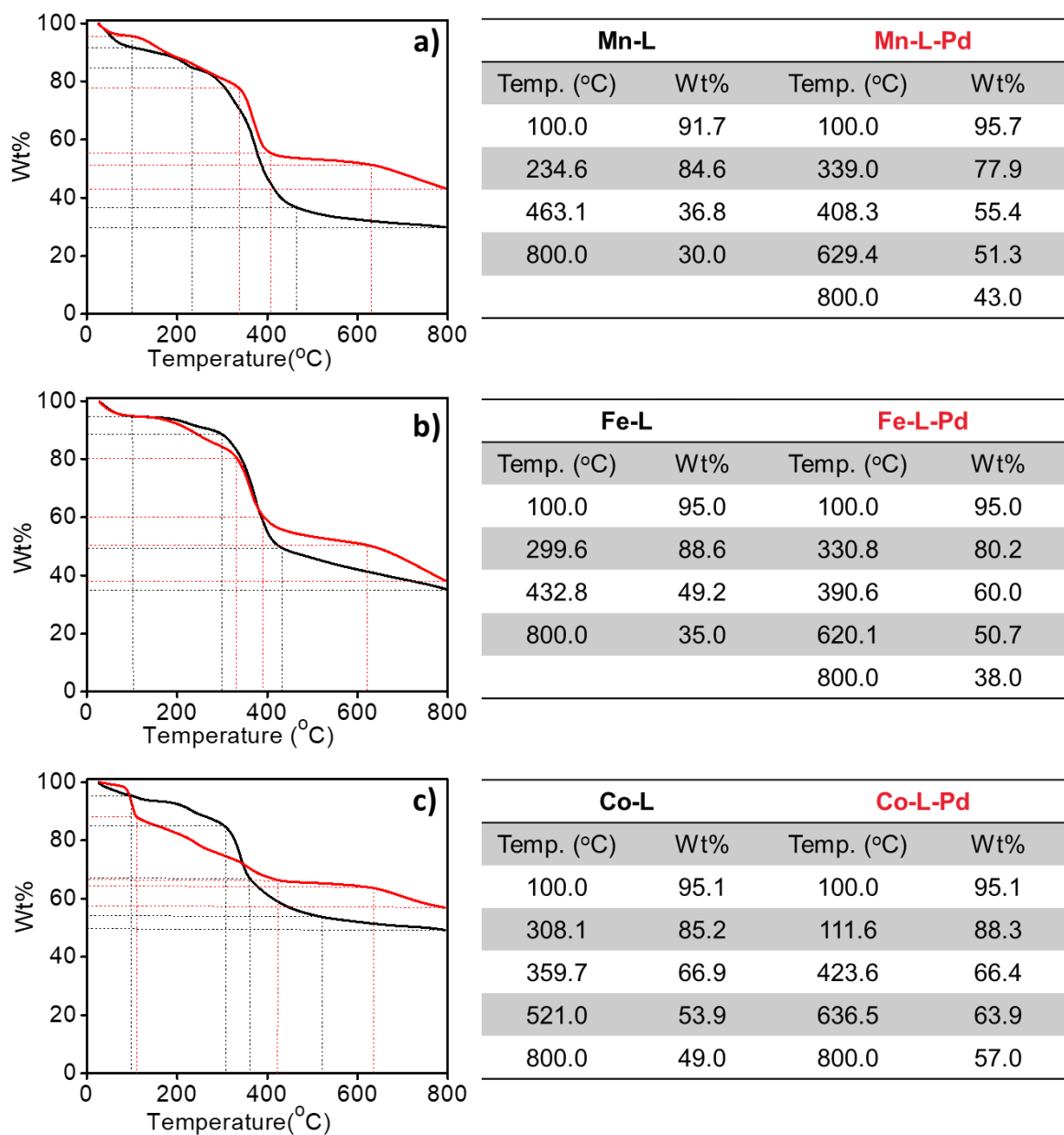


Figure 4.10. Thermogravimetric curves of the metal complexes (black, a) **Mn-L**, b) **Fe-L**, c) **Co-L** and the coordination polymers (red, a) **Mn-L-Pd**, b) **Fe-L-Pd**, c) **Co-L-Pd**). The tables on the right present the decomposition temperature and the corresponding weight loss for each sample.

Molecular ordering in the complexes and polymers were studied using powder XRD analysis (**Figure 4.11**). The polymers were found to be slightly more crystalline than the parent complexes. The Co complex **Co-L** exhibited the highest level of crystallinity among the three complexes, whereas the Mn polymer **Mn-L-Pd** was observed to possess better crystallinity among the polymers. The Fe complex and its polymer were found to be rather barely crystalline, most likely due to the faster reaction kinetics. Comparison with the powder XRD pattern (green) generated from the single crystal data of a structurally related molecule is shown to indicate structural similarity.³²

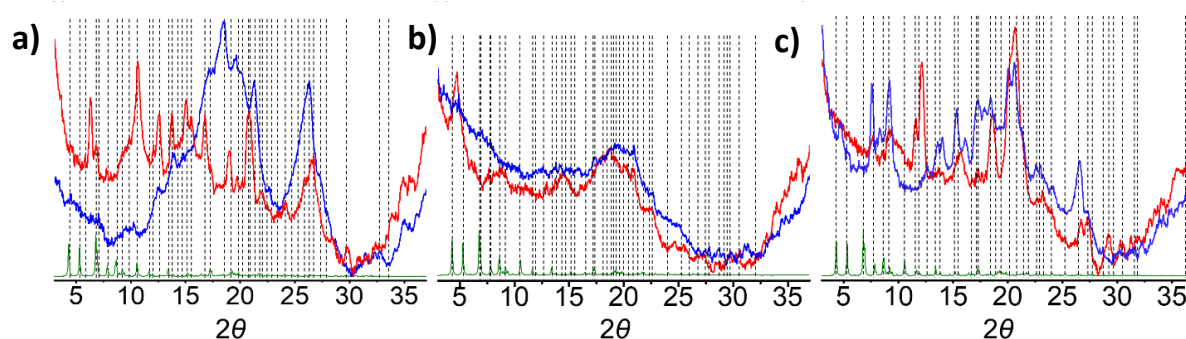


Figure 4.11. Powder X-ray diffraction spectra of a) **Mn-L** (blue) and **Mn-L-Pd** (red), b) **Fe-L** (blue) and **Fe-L-Pd** (red), and c) **Co-L** (blue) and **Co-L-Pd** (red). Comparison with the powder XRD pattern (green) generated from the single crystal data of a structurally related molecule is shown to indicate structural similarity.³²

Morphology of the metallopolymers were investigated using transmission electron microscopy (TEM). No defined morphology was observed for the metallopolymers, however, the formation of irregular sheet like structures co-existing with Pd nanoparticles was evident in the high resolution TEM images (**Figure 4.12**). The elemental composition of the polymers was qualitatively confirmed by energy dispersive X-ray spectroscopy (**Figure 4.13**) and X-ray photoelectron spectroscopy (**Figure 4.14**). The presence of palladium and nitrogen in all the metallopolymers was unanimously substantiated by the Pd 3d_{5/2} (**Mn-L-Pd**: 337.3 eV, **Fe-L-Pd**: 337.3 eV, **Co-L-Pd**: 337.5 eV), Pd 3d_{3/2} (**Mn-L-Pd**: 342.6 eV, **Fe-L-Pd**: 342.5 eV, **Co-L-Pd**: 342.9 eV) and N 1s (**Mn-L-Pd**: 399.1 eV, **Fe-L-Pd**: 399.2 eV, **Co-L-Pd**: 399.5 eV) peaks in the respective survey scan and high resolution XPS data (**Figure 4.14**).

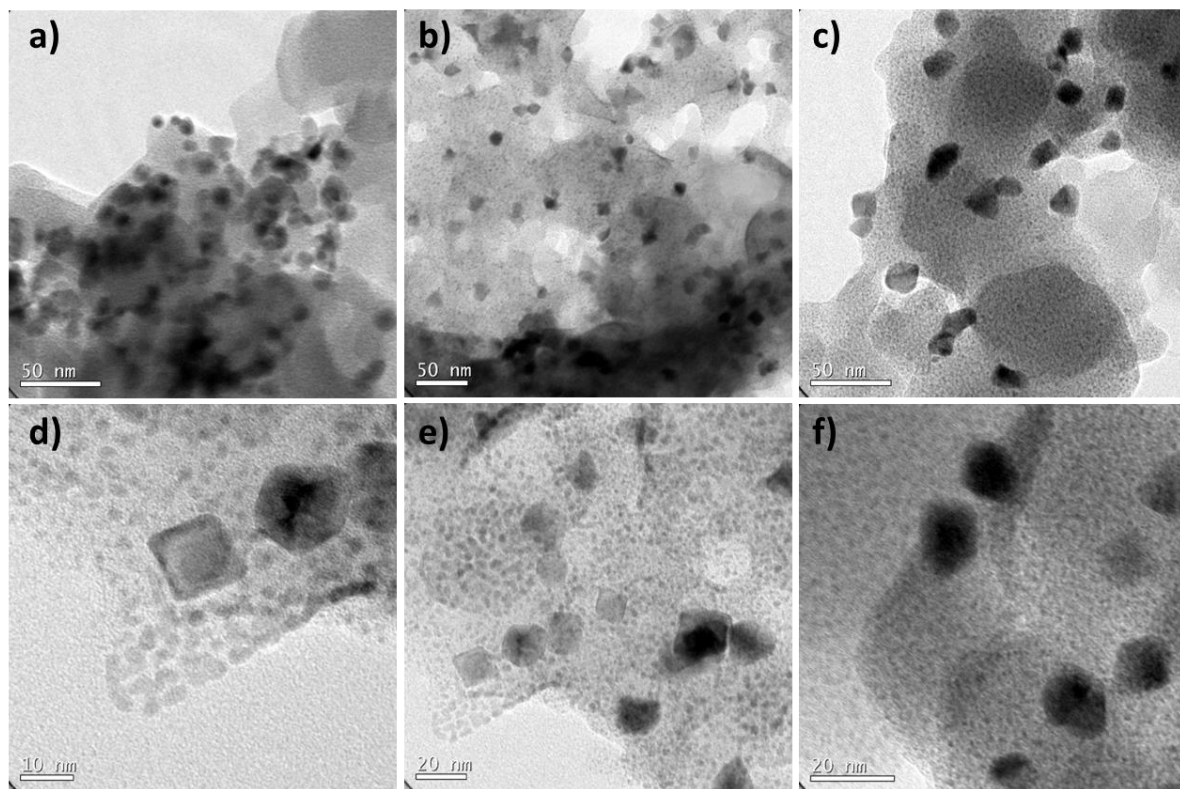


Figure 4.12. TEM and high magnification TEM images of a,d) **Mn-L-Pd**, b,e) **Fe-L-Pd** and c,f) **Co-L-Pd**.

The high resolution XPS of **Mn-L-Pd** exhibited the characteristic Mn $2p_{3/2}$ and $2p_{1/2}$ components, respectively at 641.4 eV and 652.7 eV, each with a corresponding satellite peak at 646.0 eV and 656.8 eV respectively (**Figure 4.14c**). Similarly, $2p_{3/2}$ and $2p_{1/2}$ peaks of Fe with characteristic binding energies corresponding to 707.9 eV (satellite at 711.6 eV) and 720.9 eV respectively were evident from the HR XPS of **Fe-L-Pd** (**Figure 4.14f**). The Co $2p_{3/2}$ and Co $2p_{1/2}$ binding energies at 781.6 eV and 797.0 eV, each with satellite peaks respectively at 787.4 eV and 802.9 eV in the high resolution XPS corroborated the formation of metallopolymers with cobalt centers in **Co-L-Pd** (**Figure 4.14i**). The presence of these elements in the metallopolymers was also confirmed by energy dispersive X-ray spectroscopy on TEM (**Figure 4.13**).

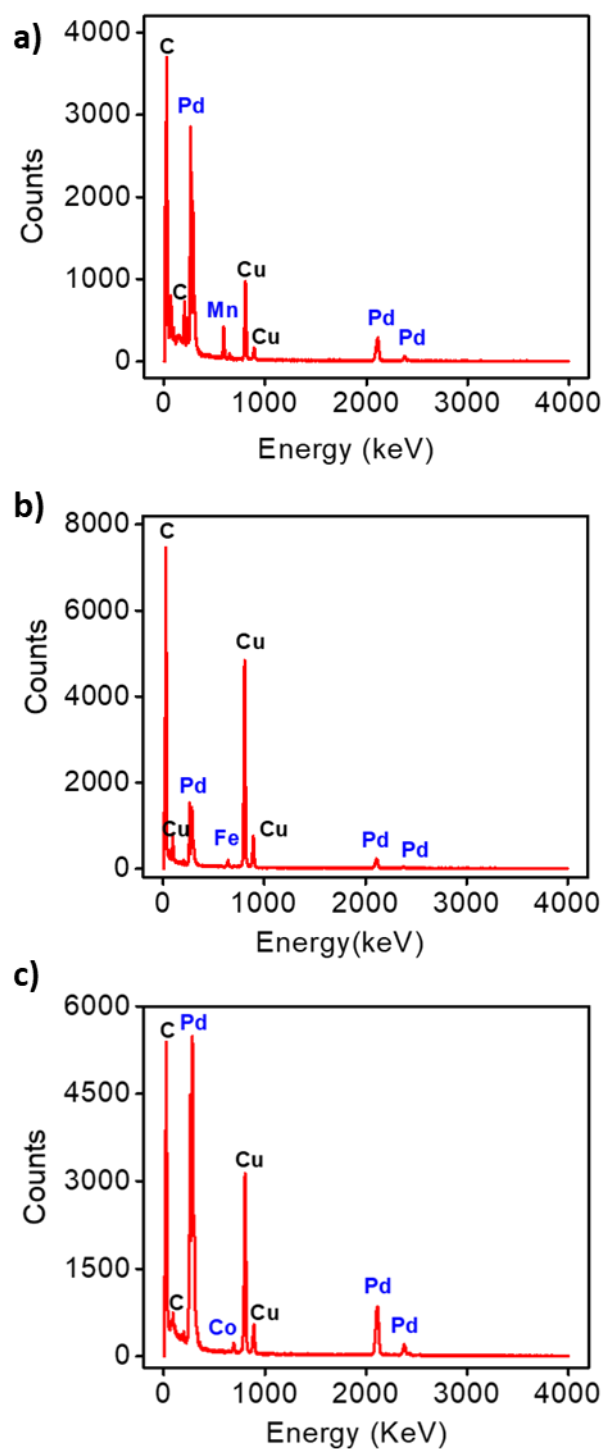


Figure 4.13. Energy dispersive X-ray (EDX) spectra (from TEM) of a) **Mn-L-Pd**, b) **Fe-L-Pd**, c) **Co-L-Pd**, qualitatively confirming the presence of the metal ions (Mn, Fe, Co and Pd) in the metallopolymers.

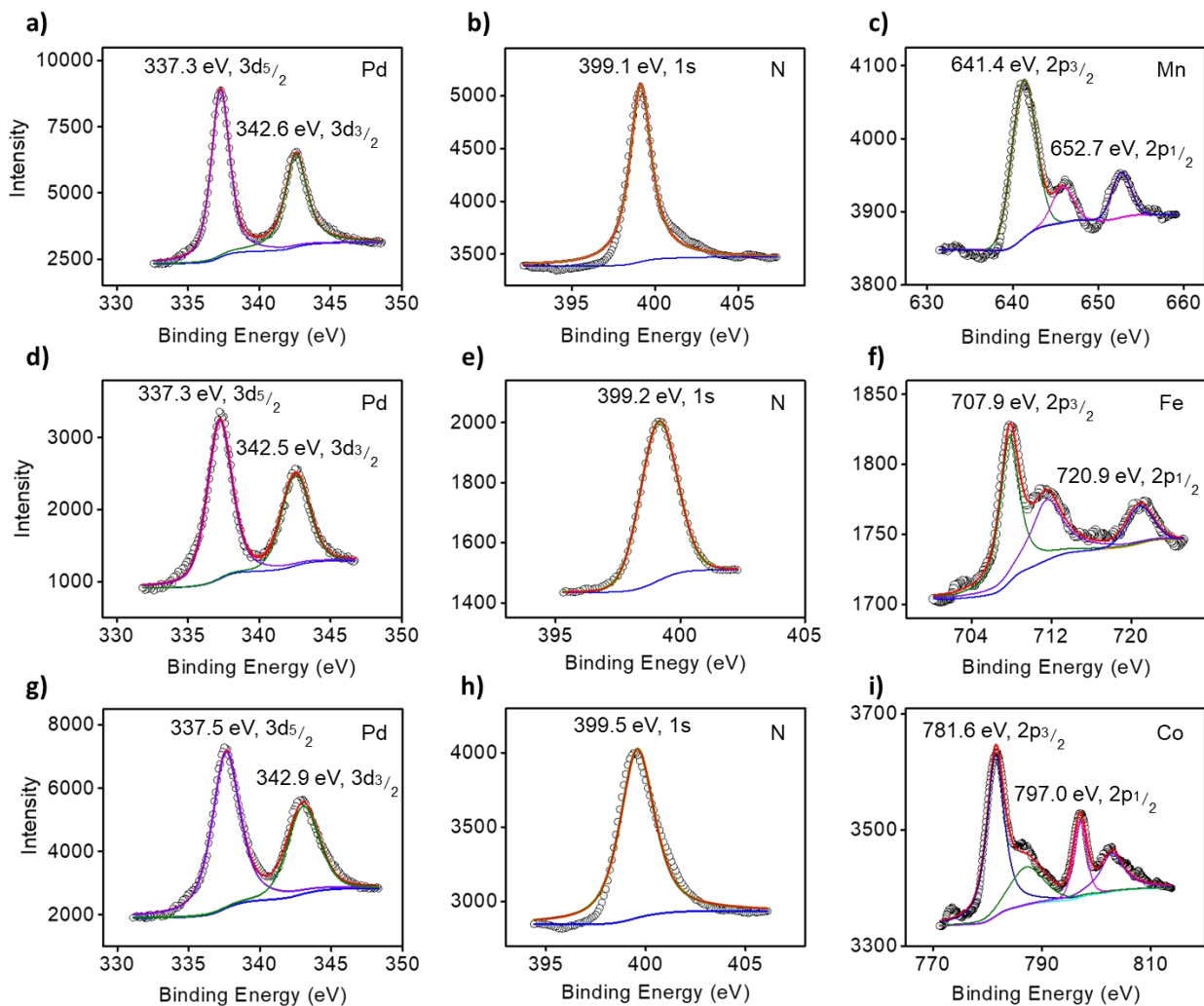


Figure 4.14. High resolution XPS data for (a-c) **Mn-L-Pd**, (d-f) **Fe-L-Pd** and (g-i) **Co-L-Pd**. The left panels (a,d,g) correspond to the high resolution spectra for Pd, the middle ones (b,e,h) correspond to those for N and the right ones (c,f,i) correspond to those for Mn, Fe and Co respectively. The binding energy corresponding to each peak and their assignment are provided in each figure.

Raman spectra also revealed the characteristic peak corresponding to the expected chemical structure of the coordination polymers (ring breathing at 1,015-1,020 cm^{-1} , ν (C=C) inter-ring at 1,202-1,281 cm^{-1} , ν (C=N) at 1,320-1,348 cm^{-1} , 1,483-1,389 cm^{-1} , and 1,634-1,639 cm^{-1} , ν (C=C) at 1,320-1,348 cm^{-1} , and 1,611-1,612 cm^{-1} (**Figure 4.15**).

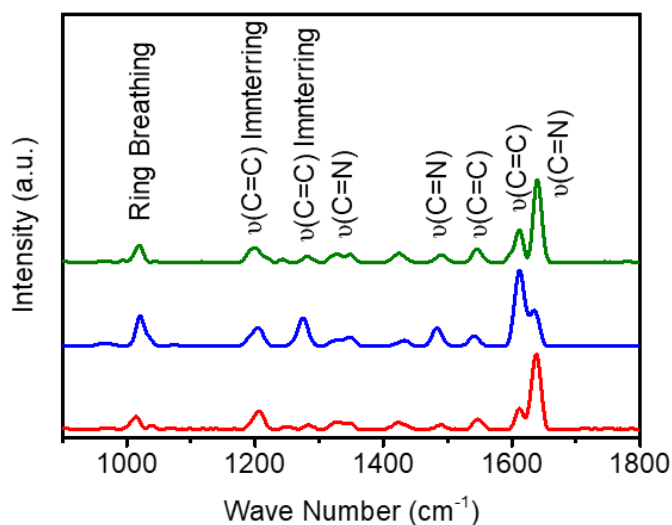


Figure 4.15. Raman spectra of the coordination polymers: **Mn-L-Pd** (red), **Fe-L-Pd** (blue) and **Co-L-Pd** (green).

4.3.2. Photophysical Studies

The iron complex **Fe-L** was intensely colored due to the presence of strong MLCT bands at 571 nm and 428 nm.^{31,32} However, the Mn and Co complexes **Mn-L** and **Co-L** were rather light-yellow colored (**Figure 4.16**) and no detectable charge transfer bands were evident from the corresponding UV-vis spectra (**Figure 4.17a**). The π - π^* bands for all the three complexes were observed in the region of 300-320 nm. Since **Fe-L** was typically colored, we chose this complex to investigate the changes in absorption properties upon cross-linking with Pd(II). Successive addition of increasing amounts of a THF solution of PdCl₂(PhCN)₂ to a solution of **Fe-L** in CH₂Cl₂/MeOH (1:1) resulted in the reduction in intensities of the π - π^* and MLCT bands with a concomitant red shift (**Figure 4.17b**). The visible color of the solution also changed from greyish purple to dark gray upon addition of an excess amount of Pd(II) solution, with the metallopolymer starting to precipitate out, leaving a colorless supernatant liquid. The other two polymers were also precipitated in solution and the filtrate was found to be free of both Pd(II) salt and the metal complex, suggesting a near complete cross-linking of the terminal pyridines in the metallopolymer.

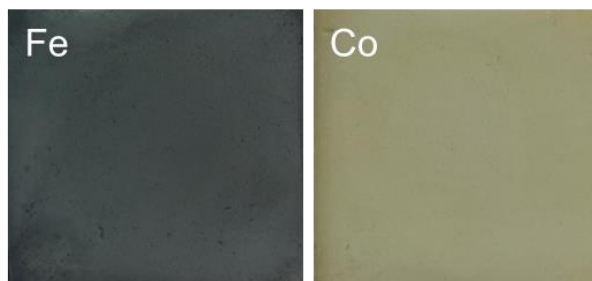


Figure 4.16. Photographs of the thin films obtained by spin-coating the metallopolymer **Fe-L-Pd** (left), and **Co-L-Pd** (right) on FTO substrates.

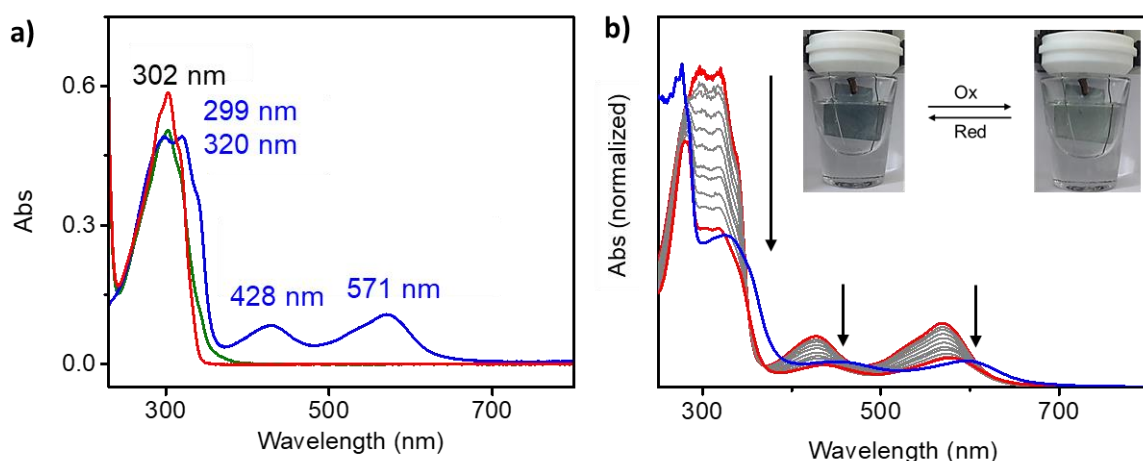


Figure 4.17. a) UV-vis absorption spectra of the metal complexes **Mn-L** (red trace), **Fe-L** (blue trace) and **Co-L** (green trace). The complexes were dissolved in a 1:1 mixture of CD₂Cl₂ and MeOH and the final concentration was adjusted to 15 μM. b) Changes in the UV-vis absorption spectra of a CD₂Cl₂ / MeOH solution (50 μM) of the metal complex **Fe-L** (red trace), upon successive addition of a THF solution (50 μM) of PdCl₂(PhCN)₂. The blue trace represents the spectrum upon addition of an excess of PdCl₂(PhCN)₂ (just before the precipitation of the metallopolymer). Inset: Electrochromic switching of the spin coated films of **Fe-L-Pd** on FTO substrates. The colored state (reduced, Fe²⁺) is shown on the left and the bleached state (single electron oxidized Fe³⁺) is shown on the right. The metallopolymer modified FTO was used as the working electrode and Pt wire and Ag/AgCl were used respectively as the counter and reference electrodes. A potential window of -0.5 V – 2.5V was used for the switching experiments in presence of 0.1 M TBAPF₆ as the supporting electrolyte.

4.3.3. Electrochemical and Electrochromic Studies

Bipyridine complexes of transition metals have been explored widely for their characteristic redox reactions and the complexes used in this study were no exception. All the three complexes, **Mn-L**, **Fe-L** and **Co-L**, exhibited single electron oxidation – reduction peaks in their respective cyclic voltammograms (**Figure 4.18**). Typically, the complexes were drop-cast on to a glassy carbon electrode, dried and was used as the working electrode in a 3-electrode set-up, with a platinum wire and Ag/AgCl as counter and reference electrodes respectively and 0.1 M TBAPF₆ as the supporting electrolyte. At a scan rate of 100 mV s⁻¹, **Mn-L**, **Fe-L** and **Co-L** were found to have their half-wave potentials ($E_{1/2}$) of 1.30, 1.12 and 0.23 V, respectively (**Figure 4.18**). The electrochemical redox potentials of the three complexes are given in **Table 4.1**. To get better insights into the mechanism of electron transfer process in these metal complexes and further to elucidate the role of the diffusion of electrolyte ions during the charge storage process, CVs of the metallopolymer modified electrodes as varying scan rates (50 – 500 mV s⁻¹) were obtained.

Table 4.1. Electrochemical redox potentials of the metal complexes **Mn-L**, **Fe-L** and **Co-L**.

Metal Complex	Potential (V)		
	E_{ox}	E_{red}	$E_{1/2}$
Mn-L-Pd	1.37	1.22	1.30
Fe-L-Pd	1.18	1.06	1.12
Co-L-Pd	0.28	0.17	0.23

CVs were obtained using the corresponding metallopolymer modified glassy carbon as working electrode, Pt wire as counter electrode and Ag/AgCl as reference electrode. A 0.1 M solution of TBAPF₆ in dry acetonitrile was used as the supporting electrolyte.

The scan rate dependence of current in the CVs is indicative of the electron transfer mechanism and hence the role of diffusion in capacitive charge-discharge phenomenon.^{33,34} For all the metallopolymer, the current was found to increase exponentially with the scan rate and linearly with the square root of scan rate (**Figure 4.19**).³⁵

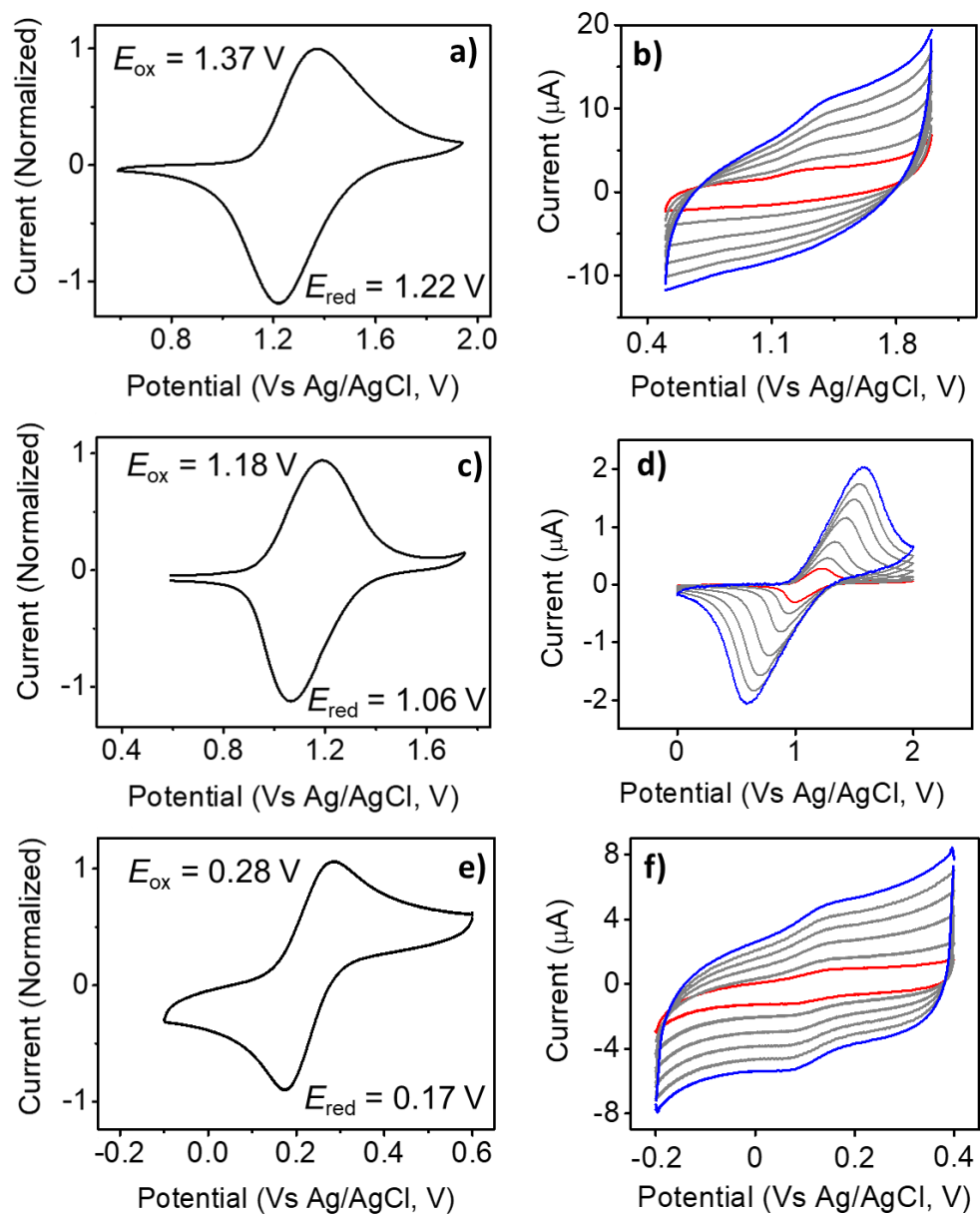


Figure 4.18. Cyclic Voltammograms of a) **Mn-L**, c) **Fe-L**, and e) **Co-L** at a scan rate of 100 mV s^{-1} and b) **Mn-L-Pd**, d) **Fe-L-Pd** and f) **Co-L-Pd** under various scan rates (50 – 500 mV s^{-1}). CVs were obtained using the corresponding metallopolymer modified glassy carbon as working electrode, Pt wire as counter electrode and Ag/AgCl as reference electrode. A 0.1 M solution of TBAPF₆ in dry acetonitrile was used as the supporting electrolyte.

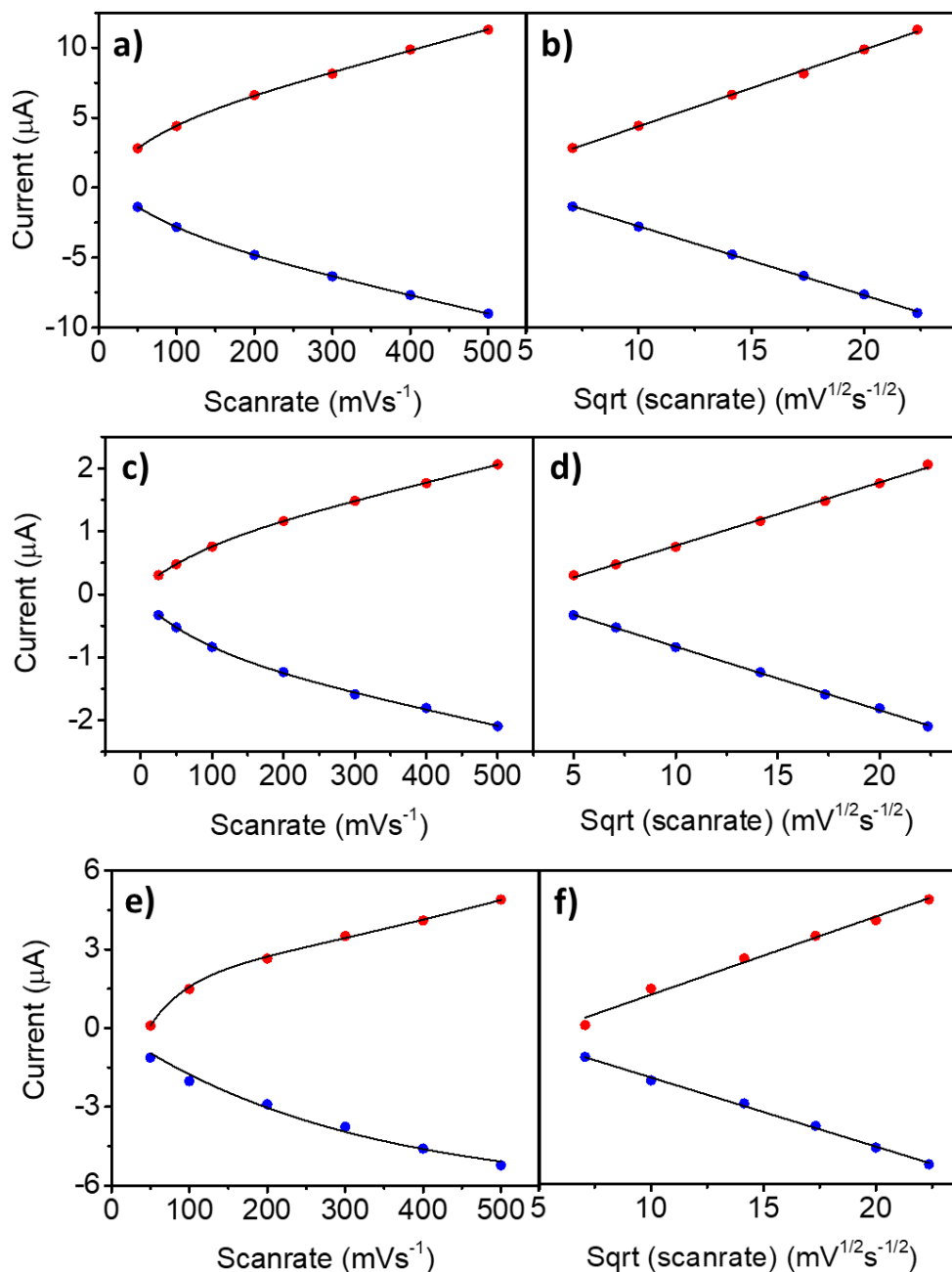


Figure 4.19. The exponential (a,c,e) and linear (b,d,f) dependence of current on the scan rates and square root of the scan rates for (a,b) **Mn-L-Pd**, (c,d) **Fe-L-Pd**, and (e,f) **Co-L-Pd**. The data is derived from the corresponding cyclic voltammograms. CVs were obtained using the corresponding metallopolymer modified glassy carbon as working electrode, Pt wire as counter electrode and Ag/AgCl as reference electrode. A 0.1 M solution of TBAPF₆ in dry acetonitrile was used as the supporting electrolyte.

This observation corroborates the diffusion limited electron transfer in these metallopolymer modified electrodes and hence the diffusion of electrolyte ions may be the rate controlling step in the electrochemical charge-discharge process. The electrochromic behavior of the nanoscale films obtained from **Fe-L** cross-linked by Pd(II) via iterative dip coating on TCO coated glass has been demonstrated by van der Boom and co-workers.³⁵

In this study, the metallopolymer **Fe-L-Pd**, that was formed by mixing the solutions of **Fe-L** and PdCl₂(PhCN)₂, was re-dispersed in MeOH and spin-cast on FTO substrates to obtain switchable electrochromic films, thereby bypassing the need for multiple levels of dip coating and washing cycles in between. While dip coating up to eight bilayers of **Fe-L** and PdCl₂(PhCN)₂ resulted in highly uniform electrochromic nanoscale films, spin coating the preformed metallopolymer led to fast fabrication of switchable electrochromic films of comparable thickness, but with slightly lesser uniformity. The obtained film was found to switch between neutral grey to colorless upon the application of potential (0.0 – 2.0 V, **Figure 4.17b**, inset). Though the electrochemical signature was obtained for **Mn-L-Pd** and **Co-L-Pd**, these films did not exhibit visible electrochromism in the potential window -2.0 – 2.0 V when spin-cast on FTO substrates.

The cycling stability of the spin-coated films of **Fe-L-Pd** was found to be high under electrochemical and electrochromic switching cycles. While the electrochemical experiments under cyclic voltametric conditions did not show significant decrease in the current density or charge density after 50,000 continuous cycles using an electrolyte system comprising 0.1 M TBAPF₆ in propylene carbonate - acetonitrile mixture (**Figure 4.20a**). However, slight decrease in transmittance at 590 nm was observed after 20,000 cycles of electrochromic switching under a potential window of 0.6 V – 1.7 V using the same electrolyte system as above (**Figure 4.20b**). These results are indicative of high cycling stabilities for the spin-coated films that are at par with the layer-by-layer films reported previously. The spin coated films exhibited a response time (time taken for 90% of the maximum transmittance changes to occur during coloration / bleaching) of 2.6 s for bleaching and 1.1 s for coloration (**Figure 4.21**). The pulse width (time for switching time) was also found to have an effect on the changes in transmittance during electrochromic switching of the thin-films of **Fe-L-Pd**. %T was found to increase with increasing pulse width (**Figure 4.22**).

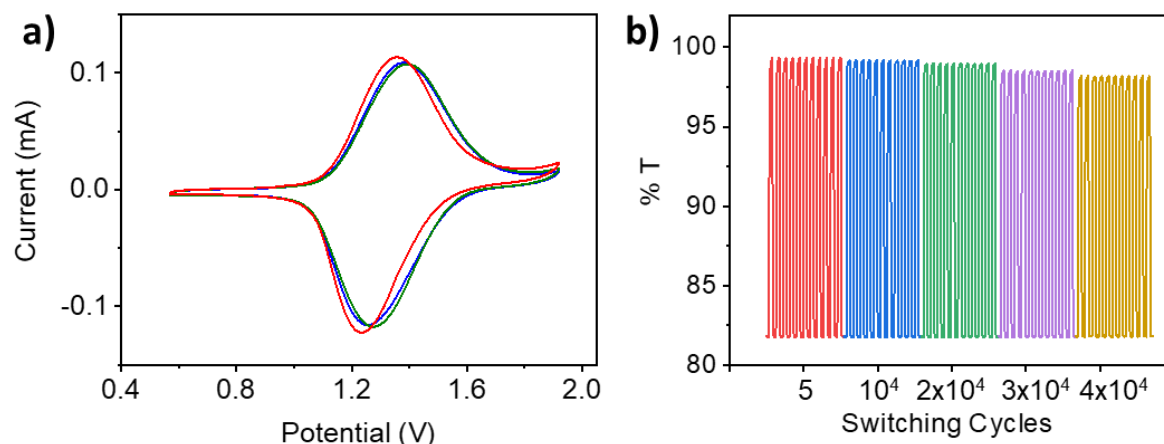


Figure 4.20. a) Cyclic voltammograms of the spin-coated films of **Fe-L-Pd**: as prepared (red), after 25,000 cycles (blue), and after 50,000 cycles (green) of electrochemical switching. b) Electrochromic switching stability of the **Fe-L-Pd** films ($\lambda_{\text{MLCT}} = 590$ nm). The experiments were performed using a 3-electrode set-up comprising of the metallopolymer modified FTO as working electrode, Ag/AgCl as reference electrode and Pt wire as counter electrode at a pulse width of 5 s. A 0.1 M solution of TBAPF₆ in dry PC-acetonitrile was used as the supporting electrolyte.

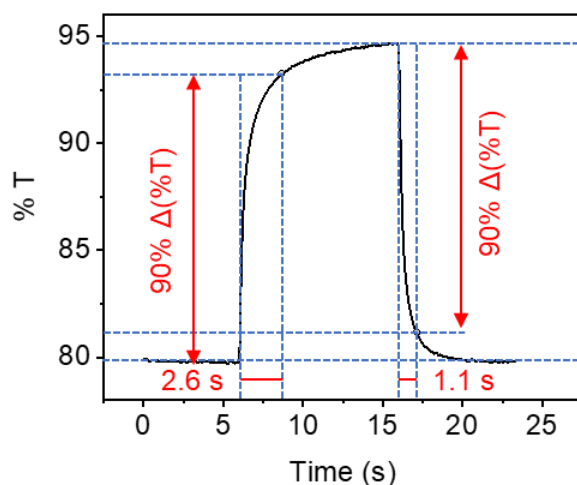


Figure 4.21. The response time obtained upon reversible redox switching of the spin-coated film of **Fe-L-Pd** (thickness = 23 nm). The electrochemical oxidation process was performed using a 3-electrode set-up comprising of the metallopolymer modified FTO as working electrode, Ag/AgCl as reference electrode and Pt wire as counter electrode at a pulse width of 10 s. A 0.1 M solution of TBAPF₆ in dry acetonitrile was used as the supporting electrolyte at a potential window of 0.6 – 1.7 V.

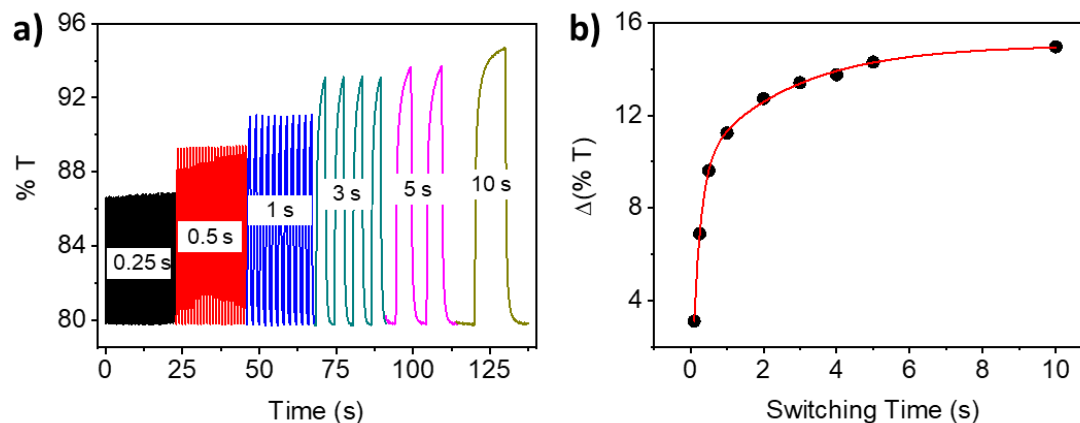


Figure 4.22. a) Chromoabsorptometry of the assemblies constructed by spin-coating **Fe-L-Pd** (thickness = 23 nm) at different switching times (pulse width) and b) the corresponding change in transmittance (%) at different pulse width (0.25-10 s). The experiments (at λ_{MLCT} : 590 nm) were carried out using the modified FTO substrate as the working electrode, Ag/AgCl as reference electrode and platinum wire as counter electrode. 0.1 M TBAPF₆ in acetonitrile was used as the supporting electrolyte. A potential window of 0.6 V – 1.7 V was used for all experiments.

4.3.4. DFT Calculations

In the absence of crystal structures, the energy minimized structures of the complexes were obtained using Density Functional Theory (DFT) at the B3LYP/6-31G (d,p) level (**Figure 4.23**). Near octahedral geometry was obtained for all the three complexes, with three ligands coordinated to the central metal ion through the bipyridine moiety, with similar N-M-N angles (**Mn-L-Pd**: 50.38°, **Fe-L-Pd**: 49.55°, **Co-L-Pd**: 49.09°) and M-N distances (**Mn-L-Pd**: 2.026 Å, **Fe-L-Pd**: 1.993 Å, **Co-L-Pd**: 1.968 Å). Nevertheless, these bond angles and distances in the complexes were found to decrease slightly in the order Mn > Fe > Co. Palladium – pyridine coordination in solution and film states has been extensively reported in literature, with a mutual trans positioning of the pyridine moieties leading to a near square planar geometry.³⁶⁻⁴⁵ The possibilities for the spontaneous formation of square planar Pd(II) centers in these reactions lead to extended networks of the metallopolymers.

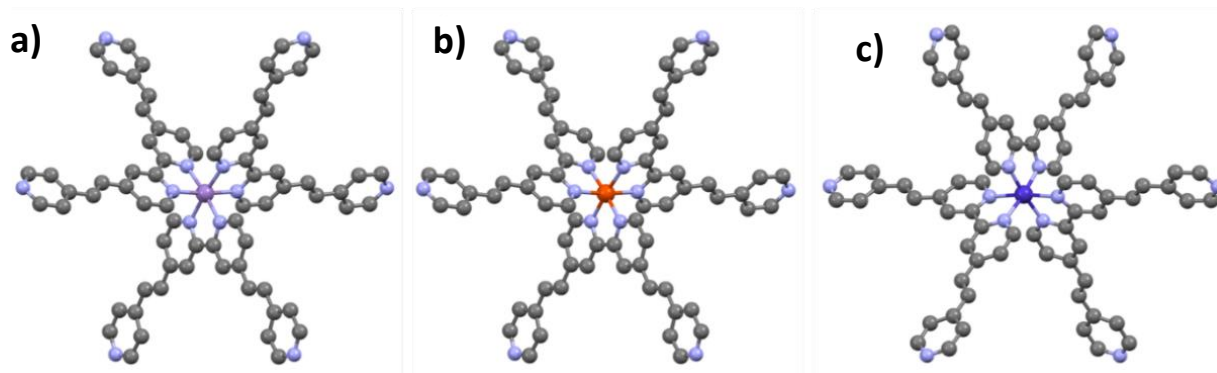


Figure 4.23. Energy minimized structures of a) **Mn-L-Pd**, b) **Fe-L-Pd** and c) **Co-L-Pd** obtained using Density Functional Theory (DFT) at the B3LYP/6-31G (d,p) level, corroborating the near octahedral geometries for all three metal complexes. Color codes: grey: carbon, light blue: nitrogen, purple: manganese, orange: iron, blue: cobalt. Hydrogen atoms have been omitted for clarity.

4.3.5. Capacitance Measurements

Supercapacitor electrodes of 1 cm² area were prepared using the corresponding metallopolymer mixed with polytetrafluoroethylene (PTFE) and activated charcoal in a mass ratio of 8:1:1 in EtOH and was homogenized by ultrasonication before coating onto a conductive carbon cloth substrate. Two symmetric electrodes, separated by a thin polymer separator (Celgard[®] 3400) in 2M KOH aqueous electrolyte, were sandwiched in a supercapacitor test cell. The electrochemical properties of the supercapacitor electrodes fabricated from the three metallopolymer were studied by symmetric assemblies in a two-electrode configuration by cyclic voltammetry (CV), galvanostatic charge-discharge and electrochemical impedance spectroscopy (EIS) at room temperature. A potential window of 0.0 – 1.0 V at 5 – 200 mV/s scan rates, was chosen for CV measurements. The charge-discharge capacity of the electrodes was investigated using the same potential window at current densities of 0.25 – 2.00 mA/g. The EIS measurements were performed at an open circuit voltage of 5 mV in the frequency range 100 kHz - 10 mHz. The measurement parameters were kept constant for all the devices for a rational performance comparison. The cyclic voltammetry (CV) loops of the metallopolymer based electrode materials are presented in **Figures 4.24**.

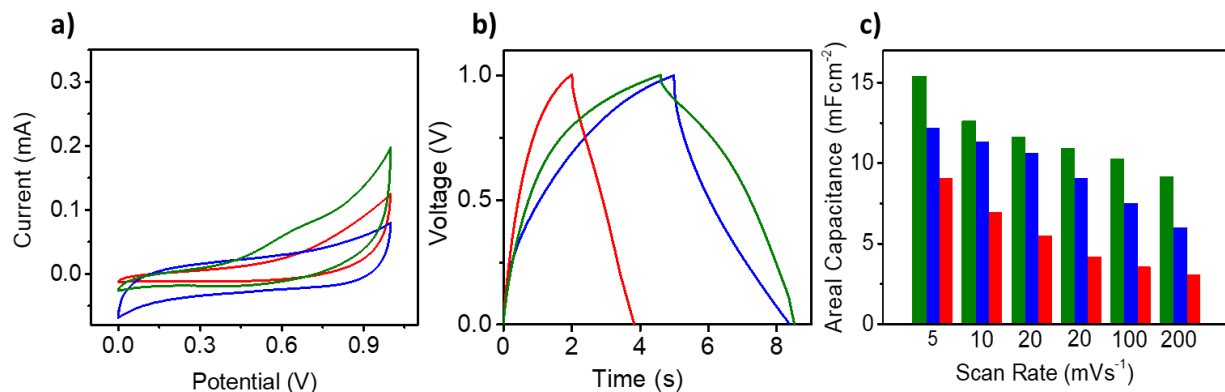


Figure 4.24 a) Cyclic Voltammograms obtained from the symmetric supercapacitors based on **Mn-L-Pd** (red), **Fe-L-Pd** (blue), and **Co-L-Pd** (green) at a scan rate of 5 mV s^{-1} . b) Galvanostatic Charge-Discharge curves of symmetric supercapacitors based on **Mn-L-Pd** (red), b) **Fe-L-Pd** (blue), and **Co-L-Pd** (green) electrodes at a constant potential window (0.0 – 1.0 V) and current density (1.0 mA cm^{-2}). c) Comparison of the areal capacitance obtained for **Mn-L-Pd** (red), **Fe-L-Pd** (blue) and **Co-L-Pd** (green) derived capacitors at different scan rates.

The near rectangular shape of the voltammograms at lower scan rates, more predominant for **Fe-L-Pd** (Figure 4.25b) and lesser for **Mn-L-Pd** (Figure 4.25a), is indicative of comparably lower internal resistance and rapid charge-discharge processes happening within the electrode materials.⁴⁶ The CVs of all the metallopolymer modified electrodes exhibited an increase in current with increasing scan rate. Moreover, the area under the voltammograms and the current were found to increase significantly at higher potentials (Figure 4.25a-c).

These results imply a favorable capacitance behavior as well as the prevalence of redox or faradaic reactions within the porous metallopolymers or at the electrode – electrolyte interface. The cell capacitance (C in F) values were calculated from the cyclic voltammograms (CVs) according to Equation 1.

$$C = \frac{i}{s} \quad (1)$$

where ‘ i ’ is average cathodic current from CV and ‘ s ’ is the corresponding scan rate.

The areal capacitance (C_{Areal}) values were calculated from the cell capacitance values using Equation 2.

$$C_{Areal} = \frac{2}{A} C \quad (2)$$

where A is the area of each electrode.

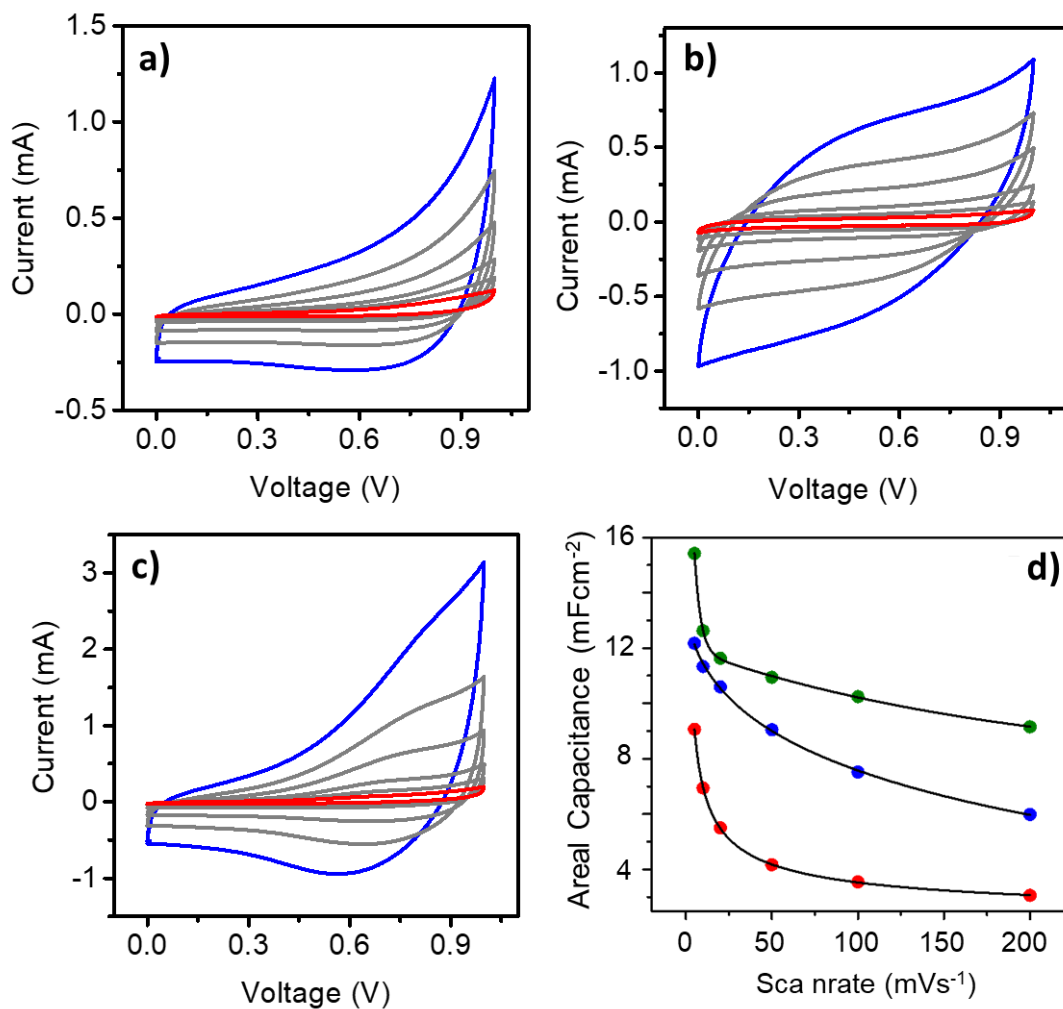


Figure 4.25. Cyclic Voltammograms obtained from the symmetric supercapacitors based on a) **Mn-L-Pd**, b) **Fe-L-Pd**, and c) **Co-L-Pd** at different scan rates. The red traces in (a) – (c) correspond to the CVs obtained at 5 mV s⁻¹ and the blue ones correspond to those at 200 mV s⁻¹. d) Comparison of the areal capacitance obtained for **Mn-L-Pd** (red), **Fe-L-Pd** (blue) and **Co-L-Pd** (green) derived capacitors at different scan rates. $R^2 > 0.99$ for all fits.

Interestingly, the capacitance of the electrodes fabricated from the metallopolymers of near-isostructural complexes with varying metal centers were found to follow the order of the occurrence of the metals in the periodic table ($\text{Mn} < \text{Fe} < \text{Co}$, (**Figure 4.25d**). Maximum areal capacitance (obtained by normalizing the cell capacitance to unit area) values of 9.1, 12.2, and 15.4 mF cm^{-2} were obtained for the symmetric capacitors based on **Mn-L-Pd**, **Fe-L-Pd**, and **Co-L-Pd**, respectively, at a scan rate of 5 mV s^{-1} (**Table 4.2**). The capacitance was found to increase exponentially with decreasing scan rates (**4.24c**, **4.25d**, **Table 4.2**). The scan rate dependence of the capacitance values may be attributed to the kinetics of diffusion of the electrolyte ions into the pores of the metallopolymers at lower scan rates, the electrolytes ions may get longer times to diffuse better into the pores and hence exhibit a higher capacitance value.⁴⁷ The distortion in the rectangular shapes of the CVs at higher scan rates may also be attributed to the limited diffusion of electrolyte ions into the pores of the metallopolymers and the shape of the CVs at higher scan rates resembles the characteristics of redox reactions during charging–discharging cycles, suggesting that the capacitive behavior does not originate from the oppositely charged electrical double layer (EDL).⁴⁷

Table 4.2. Areal capacitance of the metallopolymer derived supercapacitors at varying scanrates.

Scan rate (mV s^{-1})	Areal Capacitance (mF cm^{-2})		
	Mn-L-Pd	Fe-L-Pd	Co-L-Pd
200	3.0609	5.9865	9.1556
100	3.5476	7.5195	10.2451
50	4.166	9.0472	10.9448
20	5.5003	10.5999	11.6344
10	6.9447	11.3357	12.6276
5	9.0621	12.174	15.424

However, contributions from an electric double layer (EDL), especially for **Fe-L-Pd** and **Mn-L-Pd** based supercapacitors, cannot be rigorously excluded. The cyclic voltammograms of **Co-L** and

Co-L-Pd features $\text{Co}^{2+} \leftrightarrow \text{Co}^{3+}$ redox couple in the potential window 0.0 -1.0 V (**Figures 4.18e, 4.25c**), however, the redox couples involving either Mn^{2+} or Fe^{2+} do not occur in the studied potential window (**Figures 4.18a,c, 4.25a,b**). Thus, the characteristics of **Co-L-Pd** is predominantly pseudocapacitive in origin, and that of the Fe and Mn polymers, most likely, have contributions from both electric double layer and pseudocapacitance from redox/faradaic reactions on the electrode surface.

4.3.6. Galvanostatic Charge-Discharge (GCD) Measurements

The practical operation efficiency and performance of supercapacitor materials may be predicted via galvanostatic charge-discharge (GCD) measurements.⁴⁸ GCD curves of the metallopolymer supercapacitors at a constant potential window (0.0 – 1.0 V) under varying current densities (2.00, 1.00, 0.75, 0.50, and 0.25 A g⁻¹) is shown in **Figure 4.24b** and **Figure 4.26**. The obtained GCD curves were not found to be precisely linear or symmetrical, suggesting a pseudocapacitive contribution of the electrochemical behavior. These observations are most likely due to the faradaic charge storage reactions near the electrode surface, and a combination of non-faradaic contributions and mass transport phenomenon involving the porous metallopolymer. The near triangular shapes of the charge – discharge curves suggest additional contributions from an electric double layer to the capacitive behavior. As illustrated from the cyclic voltammograms (**Figure 4.25a, b**), the **Fe-L-Pd** and **Mn-L-Pd** based supercapacitors most likely have contributions from EDL mechanism also.

The cell capacitance (C in mF) values were also calculated from the charge – discharge cycles at a constant current density using Equation 3.

$$C = \frac{I}{\Delta V / \Delta t} \quad (3)$$

where I is the constant current for charge- discharge and $\Delta V / \Delta t$ is slope of the discharge curve. The areal capacitance thus obtained for the symmetric capacitors fabricated from the metallopolymer **Mn-L-Pd**, **Fe-L-Pd**, and **Co-L-Pd**, were 3.64, 6.68 and 7.91 mF cm⁻² respectively. The charge-discharge kinetics were found to be comparable for all the three capacitors at lower current densities (0.25 – 0.50 A g⁻¹) in the potential window 0.0 – 1.0 V (**Figure**

4.26). However, at higher current densities ($>0.50 \text{ A g}^{-1}$), the supercapacitors fabricated from **Mn-L-Pd** were found to charge and discharge at faster rates, compared to those fabricated from **Fe-L-Pd** or **Co-L-Pd** that continued to discharge at similar rates (**4.24b**, **4.26a**). Higher current densities are known to limit the accessibility of the electrolyte ions to the electrode surface only, whereas, lower current densities allow the diffusion/penetration of the ions to access both the electrode surface and the pores of the electrode material. These results are indicative of a similar porosity for the Fe and Co derived metallopolymers and a higher porosity for the Mn-derived polymer.⁴⁹ However, the energy density of these metallopolymer derived supercapacitors were found to be modest (0.5 – 1.1 Wh/kg) at a constant power density of 1 kW/kg, with the trend following the order $\text{Co} > \text{Fe} > \text{Mn}$.

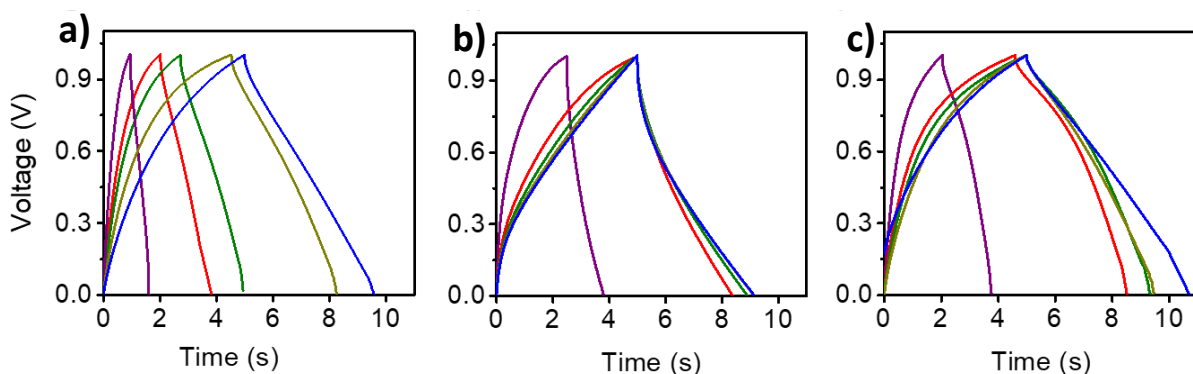


Figure 4.26. Galvanostatic charge-discharge curves of symmetric supercapacitors based on a) **Mn-L-Pd**, b) **Fe-L-Pd**, and c) **Co-L-Pd** electrodes at a constant potential window (0.0 – 1.0 V) and different current densities: 2.0 A g^{-1} (purple), 1.0 A g^{-1} (red), 0.75 A g^{-1} (green), 0.50 A g^{-1} (yellow), and 0.25 A g^{-1} (blue).

4.3.7. Electrochemical Impedance Spectroscopic (EIS) Investigations

Electrochemical impedance spectroscopy (EIS) is generally performed to follow the electrochemical processes occurring at the electrode-electrolyte interface. The Nyquist plots obtained from EIS studies are generally composed of two regions: a semi-circle at high frequencies (charge transfer resistance of the solid electrode) and a straight line (Warburg line) at intermediate to low frequencies (diffusion of electrolyte ions within the porous electrodes and capacitive behavior). The absence of the semi-circular region in the EIS plots at higher frequencies for the

supercapacitors fabricated from **Fe-L-Pd** and **Mn-L-Pd** confirms very low charge transfer resistance in these metallopolymers when compared to **Co-L-Pd** that features a detectable semi-circle at the high frequency region of its Nyquist plot (**Figure 4.27a, 4.27b**). Nevertheless, even with the higher charge transfer resistance and hence the lower electronic conductivity, **Co-L-Pd** exhibited better capacitance behavior, followed by **Fe-L-Pd** and **Mn-L-Pd**. The solution resistance (R_s) or the Equivalent Series Resistance (ESR) could be obtained from the X-intercept on the real axis in the high-frequency region of the Nyquist plot. R_s arises from the combined effect of the ionic resistance of the electrolyte, intrinsic resistance of the metallopolymer and contact resistance at the electrode - electrolyte interface, and was found to be 3.0, 0.5 and 1.5 Ω for **Mn-L-Pd**, **Fe-L-Pd**, and **Co-L-Pd**, respectively. The best model that fits the data for the best performing device fabricated from **Co-L-Pd** is shown in **Figure 4.27a** and consists of R_s in series with R_{ct} , C_{dl} and W , where R_s is the solution resistance or the equivalent series resistance, R_{ct} corresponds to the charge transfer resistance, C_{dl} is the double layer capacitance and W is the Warburg Impedance.

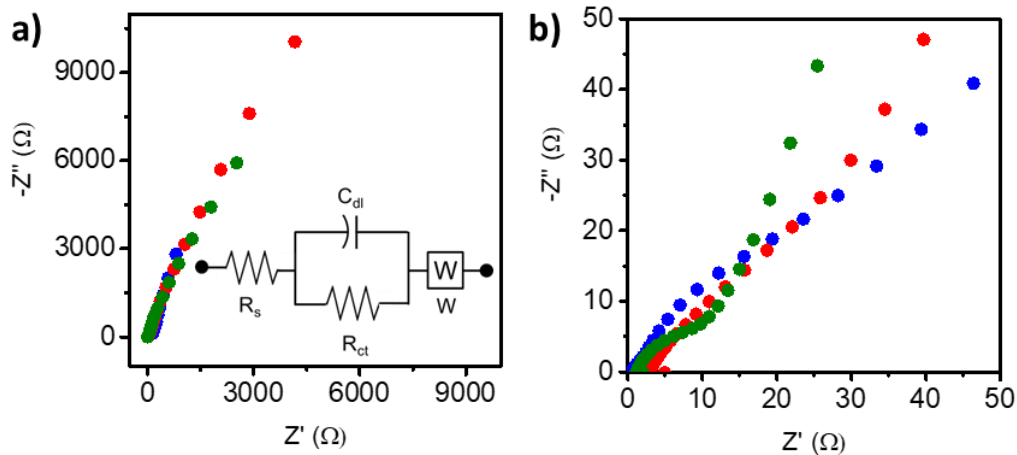


Figure 4.27. a) Nyquist plots of the symmetric supercapacitors derived from **Mn-L-Pd** (red), **Fe-L-Pd** (blue), and **Co-L-Pd** (green) based electrodes obtained using electrochemical impedance spectroscopy (EIS). The inset shows the corresponding equivalent circuit of the best performing **Co-L-Pd** based supercapacitor and b) shows the corresponding zoomed-in image.

The EIS studies indicate the possibilities for a diffusion limited electrochemical and electron transfer processes at the electrode surfaces in these metallopolymer derived symmetric supercapacitors. These results are in complete agreement with the scan rate dependent electrochemical studies of the metallopolymer modified electrodes in solution (**Figure 4.19**). The

cycling stability is of paramount significance in determining the practical applications of the supercapacitors. At a constant current density of 1 mA/g, the **Co-L-Pd** derived device was found to be the most stable with >90% of the areal capacitance retained after 2000 cycles of continuous operation. The Fe and Mn based devices, under identical conditions, retained >88% and >84% areal capacitance, respectively, after 2000 cycles (**Figure 4.28, Table 4.3**). No degradation in performance was observed after 5000 cycles of continuous operation.

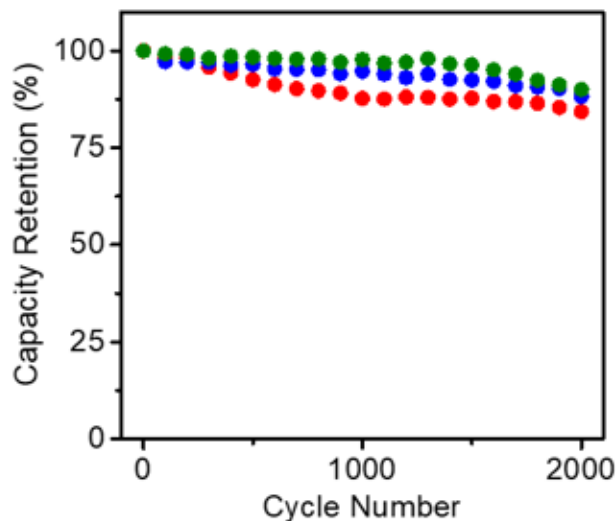


Figure 4.28. Cycling performance (stability) of the symmetric supercapacitors derived from **Mn-L-Pd** (red), **Fe-L-Pd** (blue), and **Co-L-Pd** (green), at a constant current density of 1.0 A g⁻¹.

4.3.8. BET Surface Area Experiments

Interestingly, even though the metallopolymers were obtained from near isostructural complexes of Mn (II), Fe (II) and Co (II), the electrochemical energy storage properties of the metallopolymers are strictly governed by the metal center. To explain the differences in the capacitance behavior of these metallopolymers, their pore volumes and BET surface areas were experimentally determined (**Table 4.3**). As indicated by the charge discharge cycles of the symmetric supercapacitors, **Fe-L-Pd** and **Co-L-Pd** were found to possess pores of similar volume (276 – 277 Å³), whereas the Mn polymer had a comparably larger pore volume of 326 Å³. All three coordination polymers were found to have wide pore size distribution (**Figure 4.29**).

Table 4.3. Characteristics and performance of the coordination polymers and coordination polymer derived supercapacitors.

Coordination Polymer	Capacitance (mF cm ⁻²) ^a	Pore Vol. (Å ³) ^b	BET Surface Area (m ² g ⁻¹)	Stability ^c
Mn-L-Pd	9.06	326.18	6.46	>84%
Fe-L-Pd	12.17	276.23	10.36	>88%
Co-L-Pd	15.42	277.33	29.72	>90%

^a Areal capacitance obtained by normalizing the cell capacitance to unit area for the symmetric capacitors at a scan rate of 5 mV s⁻¹

^b Calculated from BET surface area experiments

^c Capacitance after 5000 cycles of continuous operation

Pore distribution analysis also corroborates the absence of permanent microporosity and the coexistence of macro and mesopores in these coordination polymers. However, significant differences in pore distribution were not observed (**Figure 4.29 b-d**). Larger pores may provide better percolation pathways for faster electron/charge transport during charge discharge cycles. Even with a larger pore volume, **Mn-L-Pd** exhibited the lowest capacitance values among the three metallopolymers (**Table 4.3**). In order to explain this observation, the BET surface area of all the metallopolymers were measured using nitrogen adsorption desorption isotherms at 77 K. All the three metallopolymers exhibited a type IV isotherm with a prominent capillary condensation step at relative pressure close to unity (**Figure 4.29a**). An H1-type hysteresis loop was also observed in all the three isotherms, suggesting the coexistence of macro and mesopores in these metallopolymers (**Figure 4.29**). The BET surface areas were found to be 6.46, 10.36 and 29.72 m²g⁻¹ for **Mn-L-Pd**, **Fe-L-Pd** and **Co-L-Pd**, respectively, which is consistent with the order of areal capacitance of the metallopolymer derived supercapacitors (**Table 4.3**).

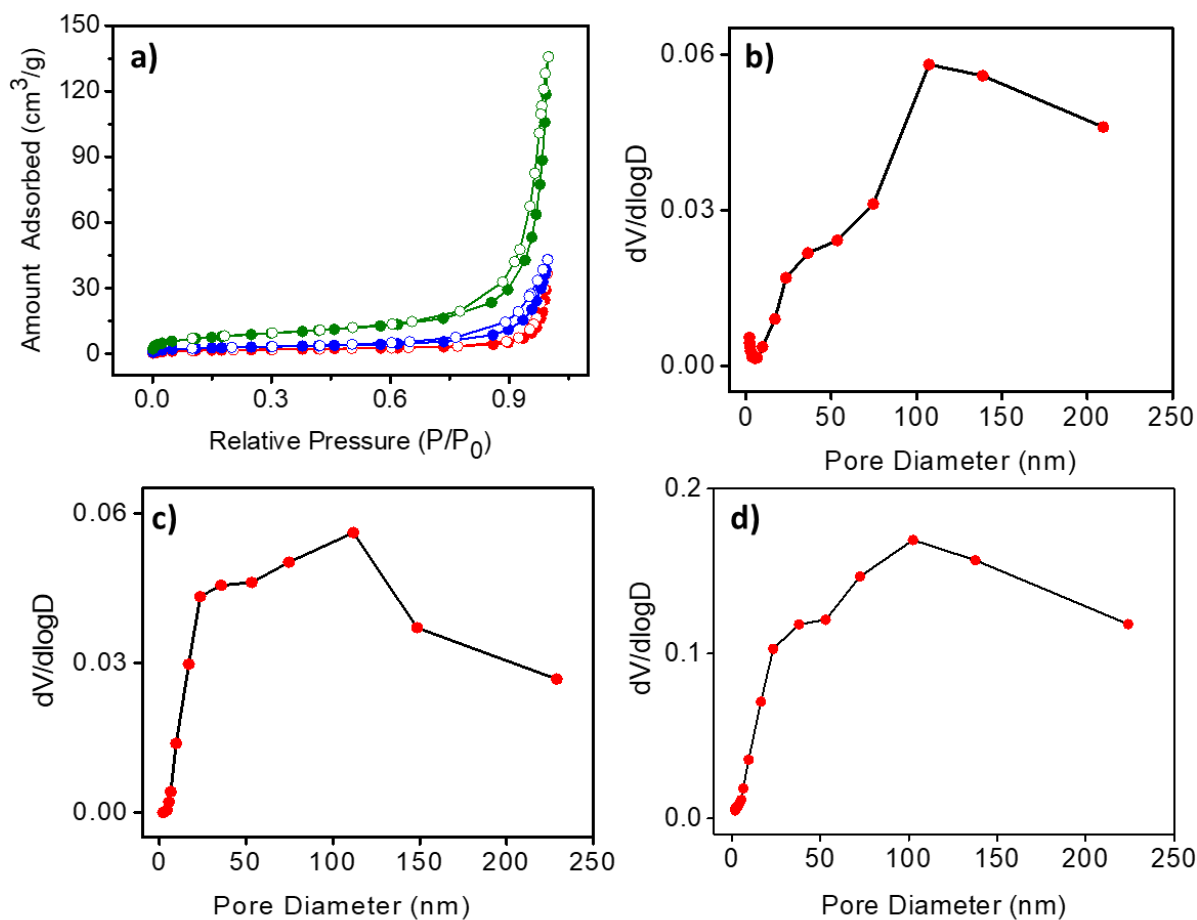


Figure 4.29. (a) BET adsorption (solid circles) and desorption (open circles) isotherms for **Mn-L-Pd** (red), **Fe-L-Pd** (blue), and **Co-L-Pd** (green). Pore size distribution in (a) **Mn-L-Pd**, (b) **Fe-L-Pd** and (c) **Co-L-Pd**, obtained from adsorption isotherms.

The electrical conductivity of **M-L-Pd** (M = Mn, Fe, and Co; thin films, 155 ± 5 nm thickness) was determined using a 4-probe method (**Figure 4.30**). While most of the previously reported pristine MOFs and coordination polymers were found to have more of insulator-like behavior with conductivity in the order of 10^{-10} S/cm, all the three CPs used in this study were found to be more semiconducting in nature with conductivity in the order of 10^{-7} S/cm. The better conductivity most likely originates from the delocalized π -electron systems that in turn offers a rigid network and better stability. Significant differences in conductivity were also not observed among the CPs (**Table 4.4**).

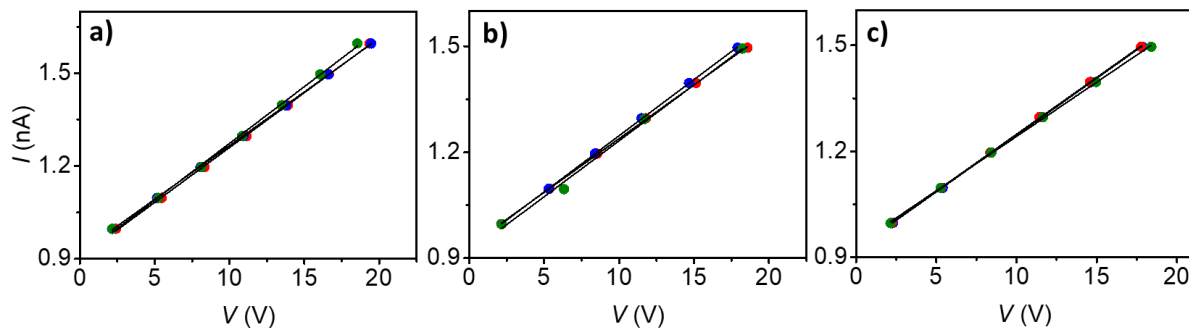


Figure 4.30. I-V characteristics of a) **Mn-L-Pd**, b) **Fe-L-Pd** and c) **Co-L-Pd**, obtained from 4-probe measurements. The red, blue and green colors show the results from three independent measurements.

Table 4.4. Electrical conductivity of the coordination polymers determined from four-probe measurements.

Coordination Polymer	Thickness (nm)	Conductivity ($10^{-7} \text{ S cm}^{-1}$)
Mn-L-Pd	159.0	4.95 ± 0.04
Fe-L-Pd	156.0	4.43 ± 0.04
Co-L-Pd	150.0	4.66 ± 0.04

The charge storage and electrolyte ion mobility of porous electrode materials are primarily determined by their total available surface area and porosity. In the case of metallopolymers currently investigated, there is a trade-off between the surface area and pore volume, and the supercapacitors fabricated from the **Co-L-Pd** with the highest surface area exhibited the highest capacitor performance, followed by **Fe-L-Pd** and **Mn-L-Pd**. However, the effect of other factors including resistance parameters, conductivity, faradaic and non-faradaic contributions, and mass transport in the metallopolymers cannot be rigorously excluded. The observed trends in capacitance behavior may thus be attributed to the combined effect of charge transfer resistance, solution resistance, electronic conductivity, Faradaic and non-Faradaic processes, mass transport, pore volume and more predominantly, the total available surface area of the metallopolymers. The surface area of the metallopolymers increase in the order $\text{Mn} < \text{Fe} < \text{Co}$ and is directly reflected in the capacitance, charge – discharge properties as well as the operational

stability of the supercapacitors. This order of performance follows the order of occurrence of these metals in the periodic table.

Random distribution of Pd nanoparticles in all the three coordination polymers, as evident from TEM images (**Figure 4.12**), may not be expected to contribute differently to the observed modulation of capacitance, its mechanism or kinetics. However, any contribution of these nanoparticles to the value of areal capacitance cannot be completely ruled out. Inter-particle space between the granules observed in the TEM images may also have contributed to the observed capacitance behavior.

The modest values of areal capacitance observed for the supercapacitors can be attributed to the limited order and crystallinity⁵⁰ of these metallopolymers, low surface areas compared to carbon materials as well as their morphological features.⁴⁹ Spontaneous precipitation in solution leads to diminished crystallinity and the presence of larger number of interfaces between the sheet-like non-continuous morphology may act as electron/charge trapping sites, thereby hindering the electrochemical process. However, the capacitance normalized to the BET surface area has been viewed as a parameter to compare the performance of electrode materials. The surface area normalized capacitance values of the metallopolymers are among the highest reported in literature (**Figure 4.31**).⁵⁰⁻⁵⁵ The BET surface area normalized capacitance values of 51.9 - 140.3 $\mu\text{F m}^{-2}$ are at par with the state-of-the-art values reported in literature for metal-organic systems.

Multi-metallic porous coordination polymers (PCPs) are rarely reported as electrode materials in energy storage systems. This study could be the first on the use of novel bimetallic PCPs with modulative capacitance in isostructural metal complexes derived coordination polymers. While these coordination polymers resulted in modest capacitive performance due to several factors discussed above, they were found to possess better electrical conductivity when compared to pristine MOFs or CPs reported in the literature.⁵⁸ The delocalized π electron system in these CPs offers a rigid network with better conductivity and electrochemical stability.³¹ Despite the performance of these materials being less than other reported materials,⁵⁹ modulating the capacitance and its mechanism as well as the charge-discharge kinetics via metal-ion regulated BET surface area disparities, is envisaged to provide new insights in the design of novel non-carbon electrode materials with fine-tuned electrochemical and electro-optical properties.

Variation of the central metal ion while reserving the structural features of the coordination polymers offers promising opportunities to enhance their electrochemical charge storage efficiencies via careful design and manipulation of synthetic strategies leading to higher available surface areas, high packing densities and hence better capacitive performance.^{26,60,61}

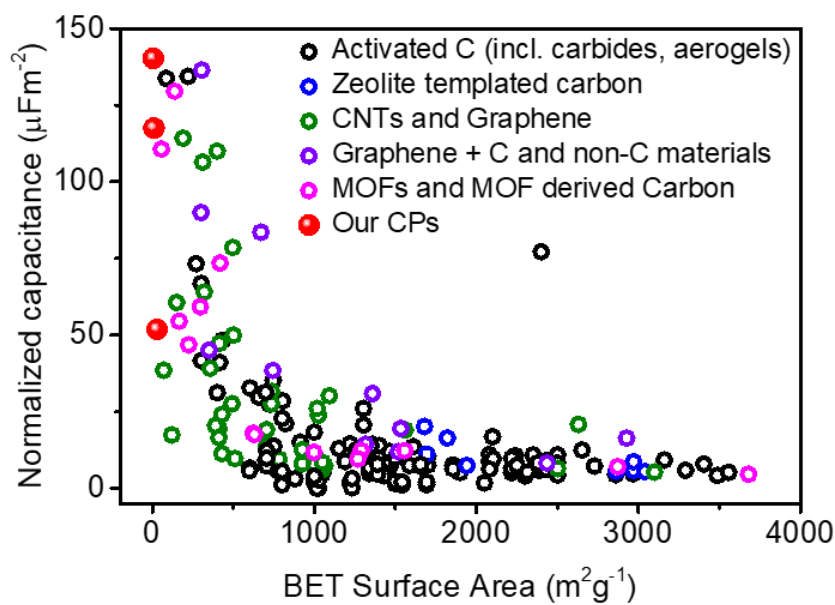


Figure 4.31. Comparison of the capacitance normalized to the BET surface area. The values are plotted directly from the references or calculated from available data on capacitance and specific surface area. The normalized capacitance in the plot is limited to a maximum of $150 \mu\text{Fcm}^{-2}$ for clarity. A few electrode materials with the surface area normalized capacitance $>150 \mu\text{Fcm}^{-2}$ have been reported (CNT: $239.3 \mu\text{Fcm}^{-2}$, 3D porous graphene with noncarbeneous additives: $792.7 \mu\text{Fcm}^{-2}$, $184.0 \mu\text{Fcm}^{-2}$, MOFs and MOF derived carbon: $261.1 \mu\text{Fcm}^{-2}$, $1449.9 \mu\text{Fcm}^{-2}$, $726.0 \mu\text{Fcm}^{-2}$, $869.5 \mu\text{Fcm}^{-2}$, $909.0 \mu\text{Fcm}^{-2}$).

The moderate to low performance of metal-organic materials in a capacitor set-up is generally attributed to the low mobility of charge carriers, originating from weak electron transfer processes involving the metal centers and ligands, leading to rather poor conductivity.⁵⁸ However, better energy storage properties can be imparted to these materials via post-synthetic modifications, composite formation and using host-guest chemistry. Design of conducting ligand molecules as well as mixing with conducting or semiconducting materials at an optimum ratio are also promising strategies towards improving the capacitance characteristics of metal-organic

materials.⁵⁸ The combination of high surface areas, extended ordering, crystallinity, high packing density and favorable morphological features along with several tunable properties makes this class of materials promising candidates for non-carbon electrode materials with excellent performance in electrochemical energy storage systems. With the advent of new energy generation/storage technologies, metal-organic hybrids are potential candidates for active materials for several futuristic applications. The modulation of the capacitance based on the BET surface area of these porous materials offers promising opportunities to enhance their electrochemical charge storage efficiencies via careful manipulation of the synthetic strategies leading to higher available areas and hence better capacitive performance.

4.4. Conclusion

The coordination polymers derived from near isostructural metal complexes consisting of the same ligand that are cross-linked with the same metal ion (Pd^{2+}) exhibited significant effect of the metal center on the porosity, surface area and hence their capacitive performance. Variations in the central metal ion, in otherwise similar coordination polymers with comparable geometry around the metal center, has led to the modulation of charge storage properties and mechanism, cycling stabilities, BET surface area, and charge-discharge kinetics. A 3:4:5 ratio of areal capacitance values (Mn:Fe:Co) at a scan rate of 5 mV s^{-1} substantiates the impact of the central metal ion in determining the capacitive performance of the coordination polymer based electrode materials. Though higher values for BET surface area normalized capacitance were previously obtained for crystalline Co-MOF based systems (5 - 23% drop after 1000 cycles),⁵⁶ better cycling stability was observed for the more or less amorphous cobalt coordination polymer **Co-L-Pd** (<2% drop after 1000 cycles) based supercapacitors. This work demonstrates that the charge storage properties and mechanism, cycling stabilities and charge-discharge kinetics of PCP-based supercapacitors could be effectively modulated by the central metal ion. We envision that the numerous possibilities for incrementing the surface areas as well as the crystallinity of these class of coordination polymers provide enough opportunities to develop non-carbon electrode materials with enhanced performance, stability and charge-discharge kinetics with distinct control over the charge transport mechanism and electro-optical characteristics.

4.5. Experimental Section

4.5.1. Materials and Methods

All reagents were purchased and used as received, unless otherwise noted. All the reactions and experiments were carried out in oven-dried glassware. All reagents were used as received without further purification, unless otherwise noted. Syntheses and experiments were carried out in clean and oven-dried glassware. Reactions were monitored using silica gel G-60 F254 aluminum TLC (thin layer chromatography) and compounds were visualized by short/long-wavelength UV lamps. Column chromatography was done using silica gel 100-200 mesh as a stationary phase.

4.5.2. Molecular Characterization

^1H and ^{13}C NMR spectra were recorded on a 500 MHz Bruker Advance DPX spectrometer using TMS as an internal standard. Chemical shifts are presented in ppm (δ) along with the corresponding coupling constants (Hz). HRMS (high resolution mass spectroscopy) data were recorded on a Thermo Scientific Exactive LCMS (liquid chromatography – mass spectrometry) instrument by electrospray ionization method with ions given in m/z using an Orbitrap analyzer. Matrix-assisted laser desorption ionization time-of-flight (MALDI-TOF) mass spectra were obtained using an AXIMA-CFR PLUS (SHIMADZU) MALDI-TOF mass spectrometer using α -cyano-4-hydroxycinnamic acid as the matrix. FT-IR spectra were recorded in the solid state (KBr) using Shimadzu IRPrestige-21 Fourier transform infra-red spectrophotometer.

4.5.3. Absorption Spectroscopy

Electronic absorption spectra were recorded on a Shimadzu UV-2600 Spectrophotometer. Concentration dependent studies were carried out in 1 cm quartz cuvette. Temperature was regulated using Shimadzu temperature controller. The blank experiment with the corresponding solvent provided the baseline. The solution was allowed to come to thermal equilibrium in a Hellma Analytics 10 mm path length quartz cell in the thermostated (± 0.1 °C) cell holder of the spectrophotometer.

4.5.4. Thermogravimetric Analyses (TGA)

Thermogravimetric analyses (TGA) were performed at a heating rate of 10 °C/min in nitrogen atmosphere using Shimadzu, DTG-60 equipment.

4.5.5. Wide-angle X-ray Diffraction (WAXD) analyses

Wide-angle X-ray Diffraction (WAXD) analyses were done using XEUSS SAXS/WAXS system by Xenocs, using Ni-filtered Cu K α radiation ($\lambda=0.15405$ nm). Using Fit2D software, 1D pattern were generated from the 2D images obtained from the Mar 345 detector.

4.5.6 Transmission Electron Microscopy (TEM)

Transmission Electron Microscopy (TEM) images and TEM-EDX spectra were obtained on a FEI Tecnai G2 30 EDAX microscope with an accelerating voltage of 100 kV and 300 kV respectively. The samples were prepared by drop casting coordination polymers over copper grids.

4.5.7. Raman Spectroscopy

Raman Spectra were recorded in the range of 500-2300 cm⁻¹ using a Handheld Metrohm Raman Mira DS spectrometer using a 785 nm laser (power below 100 mW), with smart acquisition. Base line correction was done using MATLAB. Powder samples were taken on a coverslip for measurement.

4.5.8. Cyclic Voltammetry

Cyclic Voltammetry (CV, BASI CV-50W) for samples were performed at room temperature using 0.1 M tetrabutylammonium hexafluorophosphate (TBAPF6) in CH₃CN as supporting electrolyte, glassy carbon as working electrode, Ag/AgCl electrode as reference electrode and platinum wire as counter electrode with a scan rate of 20-500 mV/s. Three consecutive scans were performed and the third cycle was selected for analysis. 5 mg of complex/coordination polymer in 1 mL CH₂Cl₂ was sonicated to get a dispersion and 5 μ L of this dispersion was drop-casted on to the working electrode and dried before measurements.

4.5.9. X-ray Photoelectron Spectroscopy

The chemical states of coordination polymer was studied by X-ray photoelectron spectroscopy (XPS) using PHI 5000 Versa Probe II (purchased from ULVAC-PHI Inc., USA) equipped with microfocused (200 μm , 15 KV) monochromatic Al-K α X-Ray source ($h\nu = 1486.6 \text{ eV}$). First survey scans were acquired on the samples and for the major detected elements, high-resolution spectra were recorded. These spectra were used for estimating elemental compositions (% At.) and chemical state assignments by curve fitting software XPSPEAK Fit. Survey scans were recorded with X-ray source power of 33 W and pass energy of 187.85 eV. Narrow scans of the elemental lines were recorded at 23.5eV pass energy.

4.5.10. BET Surface Area and Porosity Analysis

BET surface area and porosity analyses of the samples were performed with Micromeritics (Tristar 11, USA) surface area analyzer using nitrogen adsorption at 77 K. The samples were degassed at 200 °C for 2 h in flowing N₂ before adsorption measurements.

4.5.11. Synthesis and Characterization

The ligand **L** was synthesized in six steps from commercially available 4,4'-dimethyl-2,2'-bipyridine using a modified version of an already reported procedure (**Scheme 4.1**).³³

[2,2'-Bipyridine]-4,4'-dicarboxylic acid (2): To a stirred solution of 4,4'-dimethyl-2,2'-bipyridine **1** (10 g, 41 mmol) in sulfuric acid (95-98%, 250 mL) at 0° C was added potassium dichromate (48 g, 163 mmol) in small portions over 20 min. The inside temperature of the mixture was maintained at 70-80° C by occasional cooling using ice/water bath. The resultant mixture was stirred at room temperature until the inside temperature fell below 40° C (3-4 h) while the color turned deep green. The reaction mixture was poured into ice, filtered and washed with cold water until the filtrate became colorless. The solid was dried, refluxed in 50% HNO₃ for 4 h and the solution was poured over ice and diluted with water (2 L). The aqueous mixture was cooled to <5° C and the precipitate was filtered, washed with water (4 × 100 mL), acetone (3 × 30 mL) and dried to give the diacid **2** as an off-white solid (9.51 g, 95%). The crude product obtained was used in the next step without further or purification.

Diethyl [2,2'-bipyridine]-4,4'-dicarboxylate (3): To a suspension of the diacid **2** (9.51 g, 39 mmol) in 1 L of absolute ethanol was added concentrated sulfuric acid (20 mL, 95-98%). The suspension was kept under reflux for 2 days to obtain a clear solution and then cooled to room temperature. The mixture was poured into ice was added and excess ethanol removed under vacuum. The pH was adjusted to neutral with 2M NaOH solution, and the resulting precipitate was filtered, washed with water (5 × 200 mL) and dried to obtain the diester **3** as a yellowish-white solid (10.41 g, 89%). ¹H NMR (300 MHz, CDCl₃) δ 8.98 – 8.92 (m, 2H), 8.87 (d, *J* = 4.9 Hz, 2H), 7.91 (dd, *J* = 5.0, 1.6 Hz, 2H), 4.45 (q, *J* = 7.1 Hz, 4H), 1.44 (t, *J* = 7.1 Hz, 6H). ¹³C NMR (75 MHz, CDCl₃) δ 165.4, 156.7, 150.4, 139.4, 123.7, 121.0, 62.3, 14.6. ESI-MS 301.11 [M+H]⁺, 323.11 [M+Na]⁺, 623.14 [2M+Na]⁺.

[2,2'-Bipyridine]-4,4'-diylldimethanol (4): To a suspension of the diester **3** (10.0 g, 33.3 mmol) in 300 mL of absolute ethanol was added sodium borohydride (25.19 g, 665.9 mmol) in one portion. The mixture was refluxed for 3 h and cooled to room temperature, and excess borohydride was decomposed by the dropwise addition of saturated ammonium chloride solution (300 mL). Ethanol was removed under vacuum and the precipitated solid was filtered. The crude product obtained was dissolved in ethyl acetate (400 mL), washed with water (100 mL), dried over anhy. Na₂SO₄ and the solvent was removed under vacuum to yield the diol **4** as a white powder (5.9 g, 82%). ¹H NMR (300 MHz, CD₃OD) δ 8.63 – 8.56 (m, 2H), 8.30 – 8.21 (m, 2H), 7.53 – 7.38 (m, 2H), 4.76 (s, 4H). ¹³C NMR (75 MHz, CD₃OD) δ 157.2, 154.3, 150.2, 122.7, 120.2, 63.6. ESI-MS 217.08 [M+H]⁺, 239.02 [M+Na]⁺, 455.20 [2M+Na]⁺.

4,4'-Bis(bromomethyl)-2,2'-bipyridine (5): A solution of the diol **4** (10.0 g, 46.2 mmol) in a mixture of HBr (48%, 200 mL) and concentrated H₂SO₄ (95-98%, 67 mL) was refluxed for 6 h and then allowed to cool to room temperature. Water (400 mL) was then added to the mixture and the pH was adjusted to neutral with 2M NaOH solution. The resulting precipitate was filtered, washed with water (4 × 100 mL), and dried. The solid was dissolved in chloroform (200 mL) and the filtrate was dried over anhy. Na₂SO₄ followed by the removal of the solvent under vacuum, yielding the dibromide **5** (13.5 g, 85.4%) as an off-white powder. ¹H NMR (300 MHz, CDCl₃) δ 8.72 (d, *J* = 5.1 Hz, 2H), 8.58 (s, 2H), 7.47 (d, *J* = 5.1 Hz, 2H), 4.52 (s, 4H). ¹³C NMR (75 MHz, CDCl₃) δ 154.2, 149.2, 149.0, 124.8, 122.2, 30.4. ESI-MS 342.90 [M+H]⁺, 364.84 [M+Na]⁺, 706.63 [2M+Na]⁺.

Tetraethyl ([2,2'-bipyridine]-4,4'-diylbis(methylene))bis(phosphonate) (6): To a solution of the dibromide **5** (12.0 g, 35.1 mmol) in dry chloroform (100 mL) was added triethyl phosphite (100 mL) and the resulting mixture was refluxed for 3 h under nitrogen. The excess phosphite was removed under vacuum, and the remaining solid was purified by flash chromatography (Silica gel, 4-8% MeOH/CHCl₃ as eluent) yielding the bisphosphonate **6** as a yellowish-white solid (13.0 g, 81%). ¹H NMR (300 MHz, CDCl₃) δ 8.60 (d, *J* = 5.1 Hz, 2H), 8.38 (s, 2H), 7.37 – 7.32 (m, 2H), 4.05 (dq, *J* = 14.2, 7.1 Hz, 8H), 3.23 (d, *J* = 22.3 Hz, 4H), 1.24 (t, *J* = 7.1 Hz, 12H). ¹³C NMR (75 MHz, CDCl₃) δ 154.9, 148.8, 143.4, 125.5, 125.4, 123.1, 123.0, 62.6, 62.53, 34.7, 32.8, 16.5, 16.4. ³¹P NMR (121 MHz, CDCl₃) δ 25.40. ESI-MS 457.10 [M+H]⁺, 479.04 [M+Na]⁺, 935.07 [2M+Na]⁺, 1391.10 [3M+Na]⁺, 455.20 [M-H]⁻.

4,4'-Bis((E)-2-(pyridin-4-yl)vinyl)-2,2'-bipyridine (L): To a stirred solution of the bisphosphonate **6** (11.8 g, 25.8 mmol) in dry THF (400 mL) under N₂, potassium *tert*-butoxide (7.25 g, 64.6 mmol) was added, followed by pyridine-4-carboxaldehyde **7** (5.5 mL, 58.2 mmol). The mixture was stirred in the dark at room temperature for 3 h, after which triple distilled water (400 mL) was added, and was stirred for another 2 min. The solid was filtered off, washed with water (5 × 100 mL) and diethyl ether (3 × 50 mL), and dried under vacuum to give ligand **L** (9.0 g, 96%) as an off-white solid. ¹H NMR (300 MHz, CD₃OD) δ 8.71 – 8.67 (m, 2H), 8.56 (dd, *J* = 4.7, 1.6 Hz, 4H), 8.54 (d, *J* = 0.9 Hz, 2H), 7.59 (dd, *J* = 4.8, 1.6 Hz, 4H), 7.52 (dd, *J* = 5.2, 1.7 Hz, 2H), 7.44 (s, 4H). ¹³C NMR (75 MHz, CD₃OD) δ 156.2, 149.9, 148.7, 146.0, 145.2, 132.3, 130.8, 122.4, 122.3, 119.4. ESI-MS 363.13 [M+H]⁺, 385.13 [M+Na]⁺, 747.07 [2M+Na]⁺.

Synthesis of the Metal Complexes M-L

The metal complexes **M-L** (M = Mn, Fe, Co) were synthesized by mixing the ligand **L** and the metal (II) chlorides in a 1.1:3 ratio, followed by an anion exchange with ammonium hexafluorophosphate (**Figure 5.6a**). The reaction mixture was occasionally warmed to 50 °C and was stirred overnight (12-16 h) for complete reaction. The coordination polymers were synthesized by mixing a CH₂Cl₂/MeOH (1:1) solution of the corresponding metal complex and a THF solution of PdCl₂(PhCN)₂ in a ratio 1:3. Typically, THF solution of PdCl₂(PhCN)₂ (3 eq) was added to a CH₂Cl₂/MeOH (1:1) solution of the metal complex (1 eq) dropwise and shaken well. The reaction mixture was stirred for 30 min. and then allowed to stand for another 30 min. Addition of the metal

complex to the Pd salt solution resulted in instantaneous precipitation of the coordination polymer. The solid precipitate was filtered and dried to obtain the corresponding coordination polymer (80-90% yield based on the metal complex).

4.5.12. Preparation of Electrodes and Electrochemical Measurements

Supercapacitor electrodes of 1 cm² area were prepared from the coordination polymers using the following procedure. The corresponding metallopolymer was mixed with polytetrafluoroethylene (PTFE) binder and activated charcoal in a mass ratio of 80:10:10 and dispersed in ethanol. The resulting mixture was homogenized by ultrasonication and coated onto the conductive carbon cloth substrate, which was followed by drying at 60 °C for 12 h in a vacuum oven. Each electrode contained ~1 mg of electroactive material. Two symmetric electrodes, separated by a thin polymer separator (Celgard[®] 3400) in 2M KOH aqueous electrolyte, were sandwiched in a supercapacitor test cell (ECC-std, EL-Cell GmbH). The electrochemical properties of the supercapacitor electrodes were studied by symmetric assemblies of each material in a two-electrode configuration by cyclic voltammetry (CV), galvanostatic charge-discharge and electrochemical impedance spectroscopy (EIS) using a Modulab (Solartron Analytical) electrochemical workstation. The cell capacitance (C in F) was then calculated from the cyclic voltammograms (CVs) according to Eq. (1) or from the charge-discharge curves according to Eq. (2)

$$C = \frac{i}{s} \quad (1)$$

where ' i ' is the average cathodic current of CV loop and ' s ' is the scan rate.

$$C = \frac{I}{\left(\frac{\Delta V}{\Delta t}\right)} \quad (2)$$

where ' I ' is the constant current for charge - discharge, $\frac{\Delta V}{\Delta t}$ is slope of the discharge curve. The areal specific capacitance (C_{Areal} in F cm⁻²) was then calculated as

$$C_{sp} = \frac{2C}{A} \quad (3)$$

where 'A' is the area of each electrode.

4.5.13. Determination of Resistivity and Electrical Conductivity via four-Probe Measurements

4-Probe method using a Keithley 2450 source meter was used to determine the resistivity and the electrical conductivity of the coordination polymers. The corresponding CP (2 mg) was dissolved in methanol/dichloromethane (1:1 v/v, 200 μ L) and was drop-cast on to a glass substrate. The thickness of film was measured using a Bruker Dektat XT Profilometer. For a thin layer film, resistivity can be calculated from the following equation.

$$\rho = \frac{\pi t V}{\ln 2 I}$$

where 't' is the thickness of the film and the resistance $R = V/I$.

Conductivity can be calculated as $\sigma = \frac{1}{\rho}$

4.6. References

- (1) Xiang, J.; Ho, C.-L.; Wong, W.-Y. Metallopolymers for Energy Production, Storage and Conservation. *Polym. Chem.* **2015**, *6*, 6905–6930.
<https://doi.org/10.1039/C5PY00941C>.
- (2) Zhang, L. L.; Zhao, X. S. Carbon-Based Materials as Supercapacitor Electrodes. *Chem. Soc. Rev.* **2009**, *38*, 2520–2531.
<https://doi.org/10.1039/B813846J>.
- (3) Xu, Y.; Lin, Z.; Zhong, X.; Huang, X.; Weiss, N. O.; Huang, Y.; Duan, X. Holey Graphene Frameworks for Highly Efficient Capacitive Energy Storage. *Nat. Commun.* **2014**, *5*, 4554.
<https://doi.org/10.1038/ncomms5554>.
- (4) Yanwu, Z.; Shanthi, M.; D., S. M.; J., G. K.; Weiwei, C.; J., F. P.; Adam, P.; M., W. R.; A., C. K.; Matthias, T.; Dong, S.; A., S. E.; S., R. R. Carbon-Based Supercapacitors Produced by Activation of Graphene. *Science*. **2011**, *332*, 1537–1541.
<https://doi.org/10.1126/science.1200770>.

- (5) Das, G. S.; Sarkar, S.; Aggarwal, R.; Sonkar, S. K.; Park, J. W.; Tripathi, K. M.; Kim, T. Y. Fluorescent Microspheres of Zinc 1,2-Dicarbomethoxy-1,2-Dithiolate Complex Decorated with Carbon Nanotubes. *Carbon Lett.* **2019**, *29*, 595–603.
<https://doi.org/10.1007/s42823-019-00058-4>.
- (6) Salunkhe, R. R.; Kaneti, Y. V.; Kim, J.; Kim, J. H.; Yamauchi, Y. Nanoarchitectures for Metal-Organic Framework-Derived Nanoporous Carbons toward Supercapacitor Applications. *Acc. Chem. Res.* **2016**, *49*, 2796–2806.
<https://doi.org/10.1021/acs.accounts.6b00460>.
- (7) Kung, C. W.; Otake, K.; Buru, C. T.; Goswami, S.; Cui, Y.; Hupp, J. T.; Spokoyny, A. M.; Farha, O. K. Increased Electrical Conductivity in a Mesoporous Metal-Organic Framework Featuring Metallacarboranes Guests. *J. Am. Chem. Soc.* **2018**, *140*, 3871–3875.
<https://doi.org/10.1021/jacs.8b00605>.
- (8) Wang, H.; Zhu, Q. L.; Zou, R.; Xu, Q. Metal-Organic Frameworks for Energy Applications. *Chem* **2017**, *2*, 52–80.
<https://doi.org/10.1016/j.chempr.2016.12.002>.
- (9) Furukawa, H.; Cordova, K. E.; O’Keeffe, M.; Yaghi, O. M. The Chemistry and Applications of Metal-Organic Frameworks. *Science*. **2013**, *341*, 1230444.
<https://doi.org/10.1126/science.1230444>.
- (10) Zhou, H.-C.; Long, J.R.; Yaghi, O.M. Introduction to Metal–Organic Frameworks. *Chem. Rev.* **2012**, *112*, 673–674.
<https://doi.org/10.1021/cr300014x>.
- (11) Yuan, S.; Feng, L.; Wang, K.; Pang, J.; Bosch, M.; Lollar, C.; Sun, Y.; Qin, J.; Yang, X.; Zhang, P.; Wang, Q.; Zou, L.; Zhang, Y.; Zhang, L.; Fang, Y.; Li, J.; Zhou, H.-C. Stable Metal–Organic Frameworks: Design, Synthesis, and Applications. *Adv. Mater.* **2018**, *30*, 1704303.
<https://doi.org/https://doi.org/10.1002/adma.201704303>.
- (12) Zhou, H.-C.; Kitagawa, S. Metal–Organic Frameworks (MOFs). *Chem. Soc. Rev.* **2014**, *43*, 5415–5418.
<https://doi.org/10.1039/C4CS90059F>.
- (13) Kitagawa, S.; Kitaura, R.; Noro, S. Functional Porous Coordination Polymers. *Angew. Chem., Int. Ed.* **2004**, *43*, 2334–2375.

- <https://doi.org/https://doi.org/10.1002/anie.200300610>.
- (14) Bureekaew, S.; Shimomura, S.; Kitagawa, S. Chemistry and Application of Flexible Porous Coordination Polymers. *Sci. Technol. Adv. Mater.* **2008**, *9*, 14108.
<https://doi.org/10.1088/1468-6996/9/1/014108>.
- (15) Bureekaew, S.; Shimomura, S.; Kitagawa, S. Chemistry and Application of Flexible Porous Coordination Polymers. *Sci. Technol. Adv. Mater.* **2008**, *9*, 14108.
<https://doi.org/10.1088/1468-6996/9/1/014108>.
- (16) Mukhopadhyay, R. D.; Das, G.; Ajayaghosh, A. Stepwise Control of Host–Guest Interaction Using a Coordination Polymer Gel. *Nat. Commun.* **2018**, *9*, 1987.
<https://doi.org/10.1038/s41467-018-04303-8>.
- (17) Sun, F.; Li, Q.; Xue, H.; Pang, H. Pristine Transition-Metal-Based Metal-Organic Frameworks for Electrocatalysis. *ChemElectroChem* **2019**, *6*, 1273–1299.
<https://doi.org/https://doi.org/10.1002/celec.201801520>.
- (18) Xiao, P.; Xu, Y. Recent Progress in Two-Dimensional Polymers for Energy Storage and Conversion: Design, Synthesis, and Applications. *J. Mater. Chem. A* **2018**, *6*, 21676–21695.
<https://doi.org/10.1039/C8TA02820F>.
- (19) Zhang, L. L.; Zhao, X. S. Carbon-Based Materials as Supercapacitor Electrodes. *Chem. Soc. Rev.* **2009**, *38*, 2520–2531.
<https://doi.org/10.1039/B813846J>.
- (20) Lu, W.; Guo, X.; Luo, Y.; Li, Q.; Zhu, R.; Pang, H. Core-Shell Materials for Advanced Batteries. *Chem. Eng. J.* **2019**, *355*, 208–237.
<https://doi.org/https://doi.org/10.1016/j.cej.2018.08.132>.
- (21) Zhang, H.; Nai, J.; Yu, L.; Lou, X. W. (David). Metal-Organic-Framework-Based Materials as Platforms for Renewable Energy and Environmental Applications. *Joule* **2017**, *1*, 77–107.
<https://doi.org/https://doi.org/10.1016/j.joule.2017.08.008>.
- (22) Cao, X.; Tan, C.; Sindoro, M.; Zhang, H. Hybrid Micro-/Nano-Structures Derived from Metal-Organic Frameworks: Preparation and Applications in Energy Storage and Conversion. *Chem. Soc. Rev.* **2017**, *46*, 2660–2677.
<https://doi.org/10.1039/c6cs00426a>.

- (23) Wang, L.; Han, Y.; Feng, X.; Zhou, J.; Qi, P.; Wang, B. Metal-Organic Frameworks for Energy Storage: Batteries and Supercapacitors. *Coord. Chem. Rev.* **2016**, *307*, 361–381. <https://doi.org/10.1016/j.ccr.2015.09.002>.
- (24) Xu, G.; Nie, P.; Dou, H.; Ding, B.; Li, L.; Zhang, X. Exploring Metal Organic Frameworks for Energy Storage in Batteries and Supercapacitors. *Mater. Today* **2017**, *20*, 191–209. <https://doi.org/10.1016/j.mattod.2016.10.003>.
- (25) Liu, X.; Shi, C.; Zhai, C.; Cheng, M.; Liu, Q.; Wang, G. Cobalt-Based Layered Metal-Organic Framework as an Ultrahigh Capacity Supercapacitor Electrode Material. *ACS Appl. Mater. Interfaces* **2016**, *8*, 4585–4591. <https://doi.org/10.1021/acsami.5b10781>.
- (26) Feng, D.; Lei, T.; Lukatskaya, M. R.; Park, J.; Huang, Z.; Lee, M.; Shaw, L.; Chen, S.; Yakovenko, A. A.; Kulkarni, A.; Xiao, J.; Fredrickson, K.; Tok, J. B.; Zou, X.; Cui, Y.; Bao, Z. Robust and Conductive Two-Dimensional Metal-organic Frameworks with Exceptionally High Volumetric and Areal Capacitance. *Nat. Energy* **2018**, *3*, 30–36. <https://doi.org/10.1038/s41560-017-0044-5>.
- (27) Yang, J.; Xiong, P.; Zheng, C.; Qiu, H.; Wei, M. Metal-Organic Frameworks: A New Promising Class of Materials for a High Performance Supercapacitor Electrode. *J. Mater. Chem. A* **2014**, *2*, 16640–16644. <https://doi.org/10.1039/C4TA04140B>.
- (28) Zheng, Y.; Zheng, S.; Xu, Y.; Xue, H.; Liu, C.; Pang, H. Ultrathin Two-Dimensional Cobalt-Organic Frameworks Nanosheets for Electrochemical Energy Storage. *Chem. Eng. J.* **2019**, *373*, 1319–1328. <https://doi.org/https://doi.org/10.1016/j.cej.2019.05.145>.
- (28a) Huang, Q.; Chen, J.; Yan, S.; Shao, X.; Dong, Y.; Liu, J.; Li, W.; Zhang, C. New Donor-Acceptor-Donor Conjugated Polymer with Twisted Donor-Acceptor Configuration for High-Capacitance Electrochromic Supercapacitor Application. *ACS Sustain. Chem. Eng.* **2021**, *9*, 13807–13817. <https://doi.org/10.1021/acssuschemeng.1c04498>.
- (28b) Wei, D.; Scherer, M. R. J.; Bower, C.; Andrew, P.; Ryhänen, T.; Steiner, U. A Nanostructured Electrochromic Supercapacitor. *Nano Lett.* **2012**, *12*, 1857–1862. <https://doi.org/10.1021/nl2042112>.

- (29) Chen, H.; Xing, J.; Wang, W.; Li, X.; Shu, M.; Gao, P.; Pan, Y.; Liu, J. Electrochromic and Energy Storage Properties of Novel Terpyridine-Fe(II) Coordination Polymers: Improving Performance by Molecular Engineering of Nonconjugated Linkers from Linear to Three-Arm Star Configuration. *Sol. Energy Mater. Sol. Cells* **2022**, *248*, 111967.
<https://doi.org/10.1016/j.solmat.2022.111967>.
- (30) Lee, D. Y.; Shinde, D. V.; Kim, E. K.; Lee, W.; Oh, I. W.; Shrestha, N. K.; Lee, J. K.; Han, S. H. Supercapacitive Property of Metal-Organic-Frameworks with Different Pore Dimensions and Morphology. *Microporous Mesoporous Mater.* **2013**, *171*, 53–57.
<https://doi.org/10.1016/j.micromeso.2012.12.039>.
- (31) Shankar, S.; Lahav, M.; Van Der Boom, M. E. Coordination-Based Molecular Assemblies as Electrochromic Materials: Ultra-High Switching Stability and Coloration Efficiencies. *J. Am. Chem. Soc.* **2015**, *137*, 4050–4053.
<https://doi.org/10.1021/jacs.5b00429>.
- (32) Eloomov, N.; Shankar, S.; Cohen, D.; Bendikov, T.; Rechav, K.; Shimon, L. J. W.; Lahav, M.; Van Der Boom, M. E. Electrochromic Metallo-Organic Nanoscale Films: Fabrication, Color Range, and Devices. *J. Am. Chem. Soc.* **2017**, *139*, 11471–11481.
<https://doi.org/10.1021/jacs.7b04217>.
- (33) Wang, Y.; Hong, Z.; Wei, M.; Xia, Y. Layered H₂Ti₆O₁₃-Nanowires: A New Promising Pseudocapacitive Material in Non-Aqueous Electrolyte. *Adv. Funct. Mater.* **2012**, *22*, 5185–5193.
<https://doi.org/10.1002/adfm.201200766>.
- (34) Zhang, J. T.; Liu, S.; Pan, G. L.; Li, G. R.; Gao, X. P. A 3D Hierarchical Porous α -Ni(OH)₂/Graphite Nanosheet Composite as an Electrode Material for Supercapacitors. *J. Mater. Chem. A* **2014**, *2*, 1524–1529.
<https://doi.org/10.1039/c3ta13578k>.
- (35) Yang, J.; Xiong, P.; Zheng, C.; Qiu, H.; Wei, M. Metal–Organic Frameworks: A New Promising Class of Materials for a High Performance Supercapacitor Electrode. *J. Mater. Chem. A* **2014**, *2*, 16640–16644.
<https://doi.org/10.1039/C4TA04140B>.

- (36) Kaminker, R.; Motiei, L.; Gulino, A.; Fragalà, I.; Shimon, L. J. W.; Evmenenko, G.; Dutta, P.; Iron, M. A.; van der Boom, M. E. Stepwise Assembly of Coordination-Based Metal–Organic Networks. *J. Am. Chem. Soc.* **2010**, *132*, 14554–14561.
<https://doi.org/10.1021/ja105518n>.
- (37) Choudhury, J.; Kaminker, R.; Motiei, L.; De Ruiter, G.; Morozov, M.; Lupo, F.; Gulino, A.; Van Der Boom, M. E. Linear vs Exponential Formation of Molecular-Based Assemblies. *J. Am. Chem. Soc.* **2010**, *132*, 9295–9297.
<https://doi.org/10.1021/ja104203v>.
- (38) Altman, M.; Shukla, A. D.; Zubkov, T.; Evmenenko, G.; Dutta, P.; Van Der Boom, M. E. Controlling Structure from the Bottom-up: Structural and Optical Properties of Layer-by-Layer Assembled Palladium Coordination-Based Multilayers. *J. Am. Chem. Soc.* **2006**, *128*, 7374–7382.
<https://doi.org/10.1021/ja061026e>.
- (39) Gao, S.; Zheng, Z.; Lü, J.; Cao, R. Progressive Release of a Palladium-Pyridyl Complex from a Layer-by-Layer Multilayer and Illustrative Application to Catalytic Suzuki Coupling. *Chem. Commun.* **2010**, *46*, 7584–7586.
<https://doi.org/10.1039/c0cc01986k>.
- (40) Northrop, B. H.; Zheng, Y.-R.; Chi, K.-W.; Stang, P. J. Self-Organization in Coordination-Driven Self-Assembly. *Acc. Chem. Res.* **2009**, *42*, 1554–1563.
<https://doi.org/10.1021/ar900077c>.
- (41) Stone, M. T.; Moore, J. S. Supramolecular Chelation Based on Folding. *J. Am. Chem. Soc.* **2005**, *127*, 5928–5935.
<https://doi.org/10.1021/ja050713n>.
- (42) Tominaga, M.; Suzuki, K.; Kawano, M.; Kusukawa, T.; Ozeki, T.; Sakamoto, S.; Yamaguchi, K.; Fujita, M. Finite, Spherical Coordination Networks That Self-Organize from Small Components. *Angew. Chemie - Int. Ed.* **2004**, *43*, 5621– 5625.
<https://doi.org/10.1002/anie.200461422>.
- (43) You, C. C.; Wüthner, F. Self-Assembly of Ferrocene-Functionalized Perylene Bisimide Bridging Ligands with Pt(II) Corner to Electrochemically Active Molecular Squares. *J. Am. Chem. Soc.* **2003**, *125*, 9716–9725.
<https://doi.org/10.1021/ja029648x>.

- (44) Leininger, S.; Olenyuk, B.; Stang, P. J. Self-Assembly of Discrete Cyclic Nanostructures Mediated by Transition Metals. *Chem. Rev.* **2000**, *100*, 853–907.
<https://doi.org/10.1021/cr9601324>.
- (45) Kaminker, R.; Popovitz-Biro, R.; van der Boom, M. E. Coordination-Polymer Nanotubes and Spheres: A Ligand-Structure Effect. *Angew. Chem., Int. Ed.* **2011**, *50*, 3224–3226.
<https://doi.org/10.1002/ange.201008193>.
- (46) Molji, C.; Aashish, A.; Neethu, K. S.; Devaki, S. J. Self-Assembled Polyaniline Nanowires Stippled Graphene-3-Pentadecylphenyl Phosphate Hybrid Nanocomposite Based Green Sustainable Electrodes for Supercapacitors. *J. Mater. Chem. A* **2017**, *5*, 16636–16645.
<https://doi.org/10.1039/c7ta05215d>.
- (47) Kondrat, S.; Wu, P.; Qiao, R.; Kornyshev, A. A. Accelerating Charging Dynamics in Subnanometre Pores. *Nat. Mater.* **2014**, *13*, 387–393.
<https://doi.org/10.1038/nmat3916>.
- (48) Li, Z. X.; Zhang, X.; Liu, Y. C.; Zou, K. Y.; Yue, M. L. Controlling the BET Surface Area of Porous Carbon by Using the Cd/C Ratio of a Cd–MOF Precursor and Enhancing the Capacitance by Activation with KOH. *Chem. - A Eur. J.* **2016**, *22*, 17734–17747.
<https://doi.org/10.1002/chem.201603072>.
- (49) Anjana, P. M.; Bindhu, M. R.; Umadevi, M.; Rakhi, R. B. Antibacterial and Electrochemical Activities of Silver, Gold, and Palladium Nanoparticles Dispersed Amorphous Carbon Composites. *Appl. Surf. Sci.* **2019**, *479*, 96–104.
<https://doi.org/10.1016/j.apsusc.2019.02.057>.
- (50) Choi, K. M.; Jeong, H. M.; Park, J. H.; Zhang, Y.-B.; Kang, J. K.; Yaghi, O. M. Supercapacitors of Nanocrystalline Metal–Organic Frameworks. *ACS Nano* **2014**, *8*, 7451–7457.
<https://doi.org/10.1021/nn5027092>.
- (51) Wu, S.; Liu, J.; Wang, H.; Yan, H. A Review of Performance Optimization of MOF-Derived Metal Oxide as Electrode Materials for Supercapacitors. *Int. J. Energy Res.* **2019**, *43*, 697–716.
<https://doi.org/https://doi.org/10.1002/er.4232>.

- (52) Yu, M.; Liu, R.; Liu, J.; Li, S.; Ma, Y. Polyhedral-Like NiMn-Layered Double Hydroxide/Porous Carbon as Electrode for Enhanced Electrochemical Performance Supercapacitors. *Small* **2017**, *13*, 1702616.
<https://doi.org/https://doi.org/10.1002/sml.201702616>.
- (53) Wang, R.; Jayakumar, A.; Xu, C.; Lee, J.-M. Ni(OH)₂ Nanoflowers/Graphene Hydrogels: A New Assembly for Supercapacitors. *ACS Sustain. Chem. Eng.* **2016**, *4*, 3736–3742.
<https://doi.org/10.1021/acssuschemeng.6b00362>.
- (54) Yan, Y.; Gu, P.; Zheng, S.; Zheng, M.; Pang, H.; Xue, H. Facile Synthesis of an Accordion-like Ni-MOF Superstructure for High-Performance Flexible Supercapacitors. *J. Mater. Chem. A* **2016**, *4*, 19078–19085.
<https://doi.org/10.1039/C6TA08331E>.
- (55) Xu, J.; Yang, C.; Xue, Y.; Wang, C.; Cao, J.; Chen, Z. Facile Synthesis of Novel Metal-Organic Nickel Hydroxide Nanorods for High Performance Supercapacitor *Electrochim. Acta* **2016**, *211*, 595–602.
<https://doi.org/https://doi.org/10.1016/j.electacta.2016.06.090>.
- (56) Hua, Y.; Li, X.; Chen, C.; Pang, H. Cobalt Based Metal-Organic Frameworks and Their Derivatives for Electrochemical Energy Conversion and Storage. *Chem. Eng. J.* **2019**, *370*, 37–59.
<https://doi.org/https://doi.org/10.1016/j.cej.2019.03.163>.
- (57) Largeot, C.; Portet, C.; Chmiola, J.; Taberna, P.-L.; Gogotsi, Y.; Simon, P. Relation between the Ion Size and Pore Size for an Electric Double-Layer Capacitor. *J. Am. Chem. Soc.* **2008**, *130*, 2730–2731.
<https://doi.org/10.1021/ja7106178>.
- (58) Bhardwaj, S. K.; Bhardwaj, N.; Kaur, R.; Mehta, J.; Sharma, A. L.; Kim, K.-H.; Deep, A. An Overview of Different Strategies to Introduce Conductivity in Metal–Organic Frameworks and Miscellaneous Applications Thereof. *J. Mater. Chem. A* **2018**, *6*, 14992–15009.
<https://doi.org/10.1039/C8TA04220A>.

- (59) Siwal, S. S.; Zhang, Q.; Sun, C.; Thakur, V. K. Graphitic Carbon Nitride Doped Copper–Manganese Alloy as High–Performance Electrode Material in Supercapacitor for Energy Storage. *Nanomaterials*. **2020**, *10*, 2.
<https://doi.org/10.3390/nano10010002>.
- (60) Vedhanarayanan, B.; Babu, B.; Shaijumon, M. M.; Ajayaghosh, A. Exfoliation of Reduced Graphene Oxide with Self-Assembled π -Gelators for Improved Electrochemical Performance. *ACS Appl. Mater. Interfaces* **2017**, *9*, 19417–19426.
<https://doi.org/10.1021/acsami.6b09418>.
- (61) Zhao, Z.; Ding, J.; Zhu, R.; Pang, H. The Synthesis and Electrochemical Applications of Core–Shell MOFs and Their Derivatives. *J. Mater. Chem. A* **2019**, *7*, 15519–15540.
<https://doi.org/10.1039/C9TA03833G>.

ABSTRACT

Name of the Student: **Ms. Indulekha M.**

Registration No.: 10CC17A39014

Faculty of Study: Chemical Sciences

Year of Submission: 2023

AcSIR Academic centre/CSIR Lab: CSIR-National Institute for Interdisciplinary Science and Technology (CSIR-NIIST)

Name of the Supervisors: **Dr. A Ajayaghosh and Dr. Sreejith Shankar**

Title of the thesis: *Metal-organic Assemblies for Multifunctional Electrochromic Materials and Devices*

Electrochromic materials are a family of smart materials that change their optical properties in terms of absorbance, reflectance, or emission via an electrochemical redox process under the application of an electric voltage. Coordination-based metal-organic thin films are relatively less investigated class of electrochromic materials, with excellent prospects in terms of optical contrast, ease of switching, redox reversibility, facile processibility, low power consumption, and high cycle life. The current thesis aims at developing new metal-organic systems with highly efficient EC properties and the fabrication of the corresponding solid-state electrochromic devices as well as applying them for developing micro-supercapacitors with a unique coherence of high volumetric capacitance, energy densities and cycling stability.

The thesis has been divided into four chapters. In the **first chapter**, an overview of electrochromism, its applications, and different type of electrochromic materials have been discussed. In the **second chapter**, we synthesized three tetrapyridine ligands with variations in their core architecture (phenyl vs. tetraphenylethynyl vs. bithiophene) to create spray-coated electrochromic assemblies of iron(II) based coordination polymer network films on transparent conducting oxide substrates. These thin films exhibited molecular permeability and spectroelectrochemical properties that are in turn dictated by the ligand structure. Electrochromic films with high coloration efficiencies (up to 1050 cm²/C) and superior optical contrast (up to 76%) with a concomitant color-to-color redox transition were readily achieved. In the **third chapter**, we report three electrochromic metallopolymer-based electrode materials containing Fe²⁺ with high volumetric capacitance and energy densities in a symmetric two-electrode supercapacitor set-up. These metallopolymers exhibited volumetric capacitance up to 866.2 F cm⁻³ at a constant current density of 0.25 A g⁻¹. The volumetric capacitance (Fe(II)-TPE-TPy: 544.6 F cm⁻³ > Fe(II)-Ph-TPy: 313.8 F cm⁻³ > Fe(II)-Thio-TPy: 230.8 F cm⁻³ at 1 A g⁻¹) and energy densities (Fe(II)-TPE-TPy: 75.5 mWh cm⁻³ > Fe(II)-Ph-TPy : 43.6 mWh cm⁻³ > Fe(II)-Thio-TPy: 31.2 mWh cm⁻³) followed the order of the electrical conductivity of the metallopolymers, and are among the best values reported for metal-organic systems. In the **fourth chapter**, we report the use of electrochromic metallopolymers obtained from near-isostructural metal (Mn²⁺, Fe²⁺, Co²⁺) bipyridine coordination complexes as electrode materials in a symmetric supercapacitor test cell. The central metal ion not only influences the porosity, BET surface area (6.46 (Mn), 10.36 (Fe) and 29.72 (Co) m²g⁻¹) and hence the areal capacitance, but also the performance parameters like cycling stability and charge-discharge kinetics as well as the charge transfer mechanism. A 3:4:5 ratio for the areal capacitance values (9.1 (Mn), 12.2 (Fe), and 15.4 (Co) mFcm⁻² at a scan rate of 5 mVs⁻¹) corroborates the modulative effect of the metal center in the capacitive characteristics of the metallopolymers.

List of Publications Emanating from Thesis Work

1. **Mukkatt, I.**; Anjana, P. M.; Nirmala, A.; Rakhi, R. B.; Shankar, S.; Ajayaghosh, A. Metal Ion-Induced Capacitance Modulation in near-Isostructural Complexes-Derived Electrochromic Coordination Polymers. *Mater. Today Chem.* **2020**, *16*, 100260. <https://doi.org/https://doi.org/10.1016/j.mtchem.2020.100260>.
2. **Mukkatt, I.**; Nirmala, A.; Madhavan, N. D.; Shankar, S.; Deb, B.; Ajayaghosh, A. Ligand-Controlled Electrochromic Diversification with Multilayer Coated Metallosupramolecular Polymer Assemblies. *ACS Appl. Mater. Interfaces* **2021**, *13*, 5245–5255. <https://doi.org/10.1021/acsami.0c20428>.
3. **Mukkatt, I.**; Mohanachandran, A. P.; Nirmala, A.; Patra, D.; Sukumaran, P. A.; Pillai, R. S.; Rakhi, R. B.; Shankar, S.; Ajayaghosh, A. Tunable Capacitive Behavior in Metallopolymer-Based Electrochromic Thin Film Supercapacitors. *ACS Appl. Mater. Interfaces* **2022**, *14*, 31900–31910. <https://doi.org/10.1021/acsami.2c05744>.

List of Publications not Related to Thesis Work

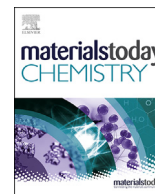
1. Nirmala, A.; **Mukkatt, I.**; Shankar, S.; Ajayaghosh, A. Thermochromic Color Switching to Temperature Controlled Volatile Memory and Counter Operations with Metal–Organic Complexes and Hybrid Gels. *Angew. Chemie Int. Ed.* **2021**, *60*, 455–465. <https://doi.org/10.1002/anie.202011580>.

List of Conferences Presented/Participated

1. Indulekha Mukkatt, Anjana Padmaja Mohanachandran, Anjali Nirmala, R. B. Rakhi, Sreejith Shankar and Ayyappanpillai Ajayaghosh, Metal Dependent Capacitance Modulation in Electrochromic Metallopolymers Derived from Near Iso-structural Coordination Polymers, 14th International Conference on Ecomaterial, National Institute for Interdisciplinary Science and Technology (NIIST), Trivandrum, February, 2020 (**Poster presentation**).

2. Indulekha Mukkatt, Anjana Padmaja Mohanachandran, Anjali Nirmala, R. B. Rakhi, Sreejith Shankar and Ayyappanpillai Ajayaghosh, Capacitance Variations in Electrochromic Metallopolymers Derived from Near Iso-structural Coordination Complexes, Frontiers in Chemical Sciences – FCS 2020 National Seminar advances in electrochemistry and material science, Calicut university, Calicut, January, 2020 (**Oral Presentation, Best Oral Presentation Award**).
3. Indulekha Mukkatt, Anjali Nirmala, Sreejith Shankar and Ayyappanpillai Ajayaghosh, Ligand Controlled Molecular Permeability and Spectroelectrochemical Diversification in Electrochromic Metal-Organic Assemblies, The 22nd RIES-Hokudai International Symposium, Japan, November, 2021 (**Poster Presentation, Symposium Chair Poster Award**).
4. Indulekha Mukkatt, Anjali Nirmala, Sreejith Shankar and Ayyappanpillai Ajayaghosh, Ligand Controlled Spectroelectrochemical Diversification and Molecular Permeability in Electrochromic Metal-Organic Assemblies, National Conference on Materials Science and Technology (NCMST-2021), National Institute for Interdisciplinary Science and Technology (NIIST), Thiruvananthapuram, December, 2021 (**Poster presentation**).
5. Indulekha Mukkatt, Anjali Nirmala, Sreejith Shankar and Ayyappanpillai Ajayaghosh, Molecular Permeability and Spectroelectrochemical Diversification in Metal-Organic Electrochromic Assemblies – A Ligand Structure Effect, National Symposium on Recent Advances in the Physics of Materials, National Institute for Interdisciplinary Science and Technology (NIIST), Thiruvananthapuram, December, 2021 (**Poster Presentation, Best Poster Award**).
6. Indulekha Mukkatt, Anjali Nirmala, Sreejith Shankar and Ayyappanpillai Ajayaghosh, Ligand Controlled Spectroelectrochemical Diversification and Molecular Permeability in Electrochromic Metal-Organic Assemblies, Kerala Science Congress, Thiruvananthapuram, February, 2022 (**Poster Presentation**).
7. Indulekha Mukkatt, Anjana Padmaja Mohanachandran, Anjali Nirmala, R. B. Rakhi, Sreejith Shankar and Ayyappanpillai Ajayaghosh, Tunable Electrochromic and Capacitive Behaviour in Metallosupramolecular Polymer Assemblies, International Conference on

Chemistry and Applications of Soft Materials (CASM 2022), National Institute for Interdisciplinary Science and Technology (NIIST), Trivandrum, 2022 (**Poster Presentation, Best Poster Award**).



Metal ion-induced capacitance modulation in near-isostructural complexes-derived electrochromic coordination polymers

I. Mukkatt^{a, b}, P.M. Anjana^a, A. Nirmala^a, R.B. Rakhi^{a, c}, S. Shankar^{a, b, *},
A. Ajayaghosh^{a, b, **}

^a Photosciences and Photonics Section, Chemical Sciences and Technology Division, CSIR-National Institute for Interdisciplinary Sciences and Technology (CSIR-NIIST), Thiruvananthapuram, 695019, India

^b Academy of Scientific and Innovative Research (AcSIR), CSIR-Human Resource Development Centre, Ghaziabad, 201002, India

ARTICLE INFO

Article history:

Received 3 January 2020
Received in revised form
18 February 2020
Accepted 19 February 2020
Available online xxx

Keywords:

Metal-organic
Supercapacitors
Bipyridine complexes
BET surface area
3-electrode set-up

ABSTRACT

Coordination polymers and metal–organic frameworks have attracted immense attention across different fields of science as materials with numerous functional applications. Herein, we report the use of coordination polymers obtained from near-isostructural metal (Mn^{2+} , Fe^{2+} , and Co^{2+}) bipyridine complexes as electrode materials in a symmetric supercapacitor test cell. The variation in the central metal ion (Mn^{2+} vs. Fe^{2+} vs. Co^{2+}) in these nearly identical coordination complexes was found to dictate the capacitive performance of the coordination polymers obtained via Pd(II) cross-linking. The central metal ion not only influences the porosity, Brunauer–Emmett–Teller (BET) surface area (6.5 (Mn), 10.4 (Fe), and 29.7 (Co) m^2/g), and the areal capacitance, but also the performance parameters such as the cycling stability and charge–discharge kinetics as well as the charge transfer mechanism. A 3:4:5 ratio for the areal capacitance values (9.1 (Mn), 12.2 (Fe), and 15.4 (Co) $mF\ cm^{-2}$ at a scan rate of 5 mV/s) corroborates the modulative effect of the metal center. The cycling stabilities of these coordination polymers also followed the same order. At higher current densities ($>0.50\ mA\ cm^{-2}$), the supercapacitors fabricated from the Mn-coordination polymer were found to charge and discharge at faster rates, whereas those fabricated from Fe- or Co-coordination polymers continued to discharge at similar rates, indicating similar pore volumes for the latter as confirmed by BET surface area measurements. Although the materials used in this study resulted in modest capacitive performance, the possibilities to enhance their surface area and crystallinity is envisaged to result in the development of new, multifunctional non-carbon electrode materials with efficient electrochemical storage characteristics and tunable electro-optical properties.

© 2020 Elsevier Ltd. All rights reserved.

1. Introduction

Metal–organic frameworks (MOFs) and coordination polymers (CPs) have emerged as a class of functional materials with multifarious applications over the past couple of decades [1–4]. With an unprecedented combination of several characteristic properties,—structural regularity, high surface area, tunable pore size/distribution, and synthetic diversity—these materials have

instigated diverse realms of science [5–7]. Porous materials of this class have been shown to have applications in catalysis, separation, sorption, mass transport, sensing, host–guest interactions, etc. [2,8,9], of which energy storage and conversion [10] has been of tremendous interest. Two-dimensional (2D) MOFs and CPs with an inherent porous architecture, accessible active sites, and surface areas akin to other 2D materials are indeed potential candidates for electrochemical energy storage and conversion, especially as electrode materials in devices like supercapacitors and batteries [11,12]. Until recently, carbon-based materials were exclusively used as active electrode materials in supercapacitors [13–18]. Out of all non-carbon materials, metal–organic CPs [19] that combine the functional advantages of both inorganic and organic components [1,20] are one of the relatively less investigated class of electrode materials, generally as pyrolytic precursors for carbon [21–24]. The

* Corresponding author.

** Corresponding author.

E-mail addresses: sreejith.shankar@niist.res.in (S. Shankar), ajayaghosh@niist.res.in (A. Ajayaghosh).

^c Present Address: Department of Physics, University of Kerala, Kariavattom Campus, Thiruvananthapuram, Kerala - 695581, India.

comparably lower conductivities most likely hindered their widespread application as electrode materials [22,25–27]. However, exceptionally large surface areas and tunable porosity along with structural and morphological versatility [21,28–30] have triggered recent attention toward metal–organic coordination polymers for electrochemical energy storage applications [22,31–34]. The use of redox active coordination polymers with combined electro-optical properties of metals and conjugated organic ligands possessing a unique coherence of stability and desirable properties as capacitor materials is of tremendous contemporary interest [34–36]. For instance, high volumetric capacitance (760 F cm^{-3}) and areal (20 F cm^{-2}) capacitance using conductive hexaaminobenzene-derived 2D MOFs and stable supercapacitors with a specific capacitance of 977.04 F/g using a hexagonal Ni-MOF have been recently reported [37,38].

The capacitive performance of porous materials is primarily governed by their porosity and total available surface area [39]. Ligands of different sizes have been earlier reported to obviously modulate the pore size and surface area of MOFs and hence regulate their capacitance behavior [40]. However, the effect of central metal ions in determining the porosity/surface areas and hence the electrochemical energy storage performance of isostructural metal complex-derived electrode materials is hard to foresee. In this work, we used near-isostructural bipyridine (**L**) complexes (**M–L**) of Mn^{2+} , Fe^{2+} , and Co^{2+} with free terminal pyridines to synthesize three coordination polymers (**M–L–Pd**) via a Pd^{2+} -mediated crosslinking strategy (Fig. 1, Schemes S1–S3). These coordination polymers were used as electrode materials in sandwiched supercapacitor test cells in a two-electrode configuration and the role of the central metal ion in the parent coordination complexes in governing the porosity, surface area, and hence the capacitive capabilities of the coordination polymers was investigated. The Brunauer–Emmett–Teller (BET) surface areas and the capacitance values were found to be dependent on the central metal ion. The coordination polymer-derived supercapacitors exhibited a near 3:4:5 ratio for their areal capacitance (at a scan rate of 5 mV/s) for **Mn–L–Pd**, **Fe–L–Pd**, and **Co–L–Pd**, respectively. Moreover, the central metal ions, due to their characteristic redox potentials, were found to influence the charge transfer mechanism in these symmetric supercapacitors. This study could be the first on the application of multimetallic coordination polymers derived from isostructural metal complexes as electrode materials with tunable areal capacitance in symmetric supercapacitor devices.

2. Materials and methods

2.1. General methods and instrumentation

All reagents were purchased and used as received, unless otherwise noted. All the reactions and experiments were carried out in oven-dried glasswares.

^1H and ^{13}C nuclear magnetic resonance (NMR) spectra were recorded on a 500 MHz Bruker Advance DPX spectrometer using tetramethylsilane as an internal standard. Matrix-assisted laser desorption ionization time-of-flight (MALDI-TOF) mass spectra were obtained using a Shimadzu AXIMA-CFR PLUS spectrometer using α -cyano-4-hydroxycinnamic acid as the matrix. Electronic absorption spectra were recorded on a Shimadzu UV-2600 spectrophotometer. Concentration-dependent studies were carried out in 1 cm quartz cuvettes. Temperature was regulated using a Shimadzu temperature controller. The blank experiment with the corresponding solvent provided the baseline. The solution was allowed to come to thermal equilibrium in a Hellma Analytics 10 mm path length quartz cell in the thermostated ($\pm 0.1 \text{ }^\circ\text{C}$) cell holder of the spectrophotometer. Thermogravimetric analyses

(TGA) were performed at a heating rate of $10 \text{ }^\circ\text{C/min}$ in nitrogen atmosphere using Shimadzu DTG-60 equipment. Wide-angle X-ray diffraction (WAXD) analyses were carried out using a XEUS SAXS/WAXS system by Xenocs, using Ni-filtered $\text{Cu K}\alpha$ radiation ($\lambda = 0.15405 \text{ nm}$). Using Fit2D software, 1D patterns were generated from the 2D images obtained from the Mar 345 detector. Transmission electron microscopy (TEM) images and TEM-EDX spectra were obtained using a FEI Tecnai G2 30 EDAX microscope with accelerating voltages of 100 kV and 300 kV, respectively. The samples were prepared by drop-casting coordination polymers over copper grids. Cyclic voltammetry (CV, BASI CV-50W) for samples was performed at room temperature using 0.1 M tetrabutylammonium hexafluorophosphate (TBAPF_6) in CH_3CN as supporting electrolyte, glassy carbon as working electrode, Ag/AgCl electrode as reference electrode, and platinum wire as counter electrode with a scan rate of $20\text{--}500 \text{ mV/s}$. Three consecutive scans were performed and the third cycle was selected for analysis. 5 mg of complex/coordination polymer in 1 mL CH_2Cl_2 was sonicated to get a dispersion and 5 μL of this dispersion was drop-casted onto the working electrode and dried before measurements. The chemical states of the coordination polymers were studied by X-ray photoelectron spectroscopy (XPS) using PHI 5000 Versa Probe II (purchased from ULVAC-PHI Inc., USA) equipped with a micro-focused (200 μm , 15 KV) monochromatic Al-K α X-ray source ($h\nu = 1,486.6 \text{ eV}$). First survey scans were acquired on the samples and for the major detected elements, high-resolution spectra were recorded. These spectra were used for estimating elemental compositions (% At.) and chemical state assignments by curve fitting software XPSPEAK Fit. Survey scans were recorded with an X-ray source power of 33 W and a pass energy of 187.85 eV. Narrow scans of the elemental lines were recorded at 23.5 eV pass energy. FT-IR spectra were recorded in the solid state (KBr) using a Shimadzu IRPrestige-21 Fourier transform infra-red spectrophotometer. BET surface area and porosity analysis of the samples were performed with a Micromeritics (Tristar 11, USA) surface area analyzer using nitrogen adsorption at 77 K. The samples were degassed at $200 \text{ }^\circ\text{C}$ for 2 h in flowing N_2 before adsorption measurements.

2.2. Synthesis

The ligand **L** was synthesized in six steps from commercially available 4,4'-dimethyl-2,2'-bipyridine using a reported procedure (Scheme S1) [41,42]. The metal complexes **M–L** (**M** = Mn, Fe, Co) were synthesized by mixing the ligand **L** and the metal(II) chlorides in a 1:1:3 ratio, followed by an anion exchange using a reported procedure (Scheme S2) [41,42]. The reaction mixture was occasionally warmed to $50 \text{ }^\circ\text{C}$ and was stirred overnight (12–16 h) for complete reaction. The coordination polymers were synthesized by mixing a $\text{CH}_2\text{Cl}_2/\text{MeOH}$ (1:1) solution of the corresponding metal complex and a THF solution of $\text{PdCl}_2(\text{PhCN})_2$ in a ratio of 1:3. Typically, THF solution of $\text{PdCl}_2(\text{PhCN})_2$ (3 eq.) was added to a $\text{CH}_2\text{Cl}_2/\text{MeOH}$ (1:1) solution of the metal complex (1 eq.) dropwise and shaken well. The reaction mixture was stirred for 30 min and then allowed to stand for another 30 min. Addition of the metal complex to the Pd salt solution resulted in instantaneous precipitation of the coordination polymer. The solid precipitate was filtered and dried to obtain the corresponding coordination polymer (80–90% yield based on the metal complex).

2.3. Preparation of the electrodes and electrochemical measurements

Supercapacitor electrodes of 1 cm^2 area were prepared using the coordination polymers by the following procedure. The corresponding metallopolymer was mixed with the

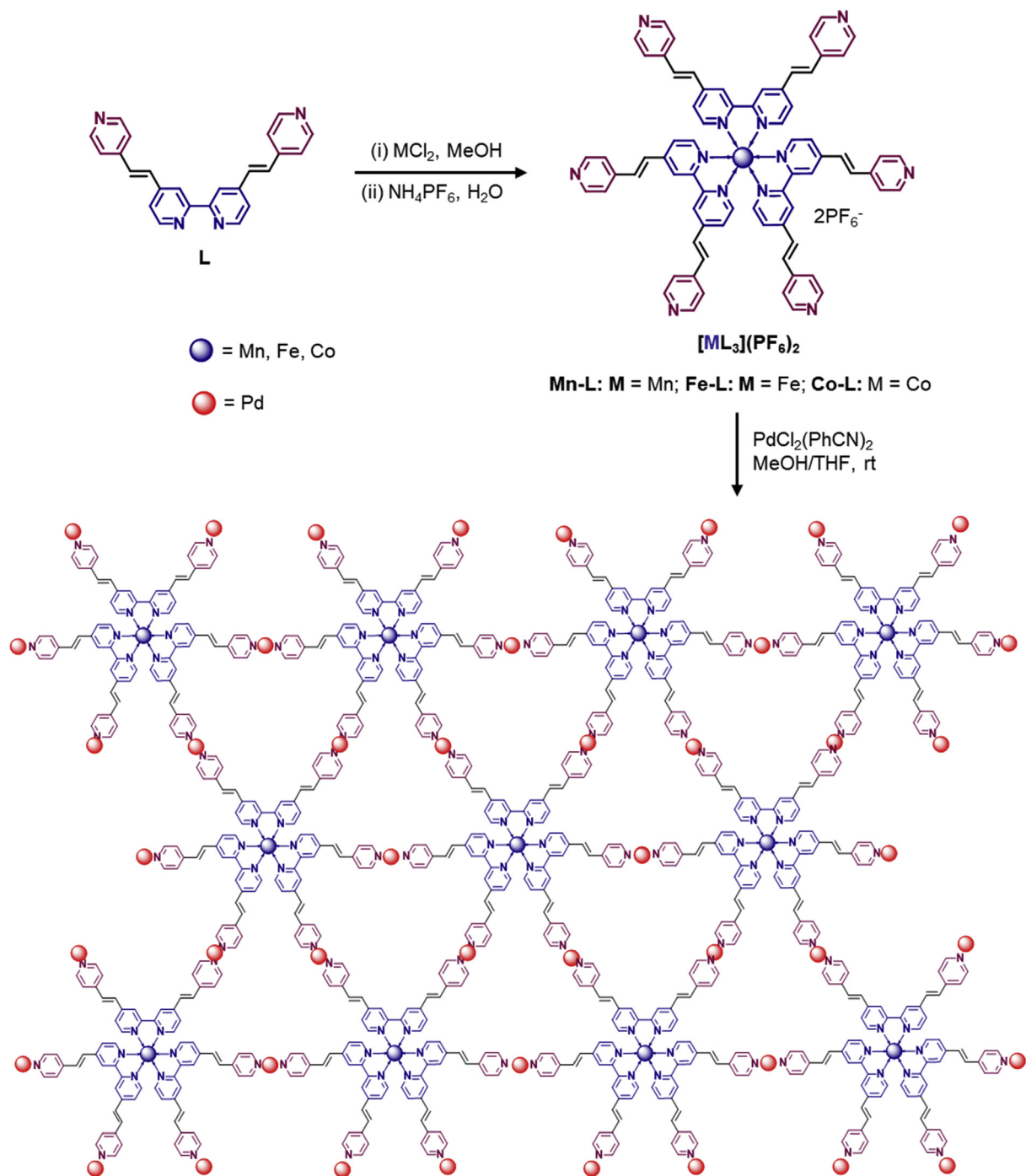


Fig. 1. Scheme showing the molecular structures of the bipyridine ligand **L** and the corresponding coordination complexes $[\text{ML}_3](\text{PF}_6)_2$ ($\text{M} = \text{Mn, Fe, and Co}$) and a schematic representation of the formation of the coordination polymers. Three coordination polymers **M-L-Pd** ($\text{M} = \text{Mn, Fe, and Co}$) were prepared by cross-linking the free pyridines on the complexes **M-L** ($\text{M} = \text{Mn, Fe, and Co}$) with Pd(II) in a 1:3 ratio. See the experimental section for more details. The schematic representation of the coordination polymer is an illustration of the possible cross-linking and does not represent a planar 2D structural model.

polytetrafluoroethylene (PTFE) binder and activated charcoal in a mass ratio of 80:10:10 and dispersed in ethanol. The resulting mixture was homogenized by ultrasonication and coated onto the conductive carbon cloth substrate, which was followed by drying at 60 °C for 12 h in a vacuum oven. Each electrode contained ~1 mg of electroactive material. Two symmetric electrodes, separated by a thin polymer separator (Celgard® 3400) in 2 M KOH aqueous electrolyte, were sandwiched in a supercapacitor test cell (ECC-std,

EL-Cell GmbH). The electrochemical properties of the supercapacitor electrodes were studied by symmetric assemblies of each material in a two-electrode configuration by CV, galvanostatic charge–discharge (GCD) measurements, and electrochemical impedance spectroscopy (EIS) using a Modulab (Solartron Analytical) electrochemical workstation. The cell capacitance (C in F) was then calculated from the cyclic voltammograms according to Eq. (1) or from the charge–discharge curves according to Eq. (2)

$$C = \frac{i}{s} \quad (1)$$

where 'i' is the average cathodic current of CV loop and 's' is the scan rate.

$$C = \frac{I}{\left(\frac{\Delta V}{\Delta t}\right)} \quad (2)$$

where 'I' is the constant current for charge–discharge and $\Delta V/\Delta t$ is the slope of the discharge curve. The areal specific capacitance (C_{Areal} in $F\text{ cm}^{-2}$) was then calculated as

$$C_{sp} = \frac{2C}{A} \quad (3)$$

where 'A' is the area of each electrode.

2.4. Determination of resistivity and electrical conductivity via 4-probe measurements

The 4-probe method using a Keithley 2450 source meter was used to determine the resistivity and the electrical conductivity of the coordination polymers. The corresponding CP (2 mg) was dissolved in methanol/dichloromethane (1:1 v/v, 200 μL) and was drop-cast onto a glass substrate. The thickness of film was measured using a Bruker Dektak XT profilometer. For a thin layer film, resistivity can be calculated from the following equation.

$$\rho = \frac{\pi t}{\ln 2} \frac{V}{I}$$

where t is the thickness of film and resistance $R = V/I$.

Conductivity can be calculated as $\sigma = \frac{1}{\rho}$.

3. Results and discussion

3.1. Synthesis and characterization

The ligand **L** and its isostructural metal complexes were synthesized according to a previously reported procedure (Fig. 1, see Supporting information for details) [41,42]. The near octahedral complexes (**Mn–L**: $M = \text{Mn}$, **Fe–L**: $M = \text{Fe}$, and **Co–L**: $M = \text{Co}$) were subsequently synthesized by mixing the corresponding metal(II) chlorides with the ligand **L** in methanol in a 1:3 ratio, followed by a PF_6^- anion exchange (Fig. 1). The metal salt and the ligand in solution was stirred for 12 h with occasional heating to 50 $^\circ\text{C}$ to ensure complete reaction. The coordination polymers (**M–L–Pd**, $M = \text{Mn}$, Fe , and Co) were obtained from their respective solutions via the cross-linking of the free pyridines on the complexes with a Pd(II) salt in a 1:3 ratio. The coordination polymers (Fig. 1) readily precipitated out from solution and were collected by vacuum filtration.

Typically broad NMR spectra were obtained for all the metal complexes in deuterated methanol (CD_3OD), deuterated dimethyl sulfoxide ($\text{DMSO-}d_6$), or a mixture of CD_3OD and $\text{DMSO-}d_6$. However, a similar peak pattern was observed for **Mn–L**, **Fe–L**, and **Co–L** in the ^1H NMR spectra, irrespective of the counter anion being Cl^- or PF_6^- . ESI-MS and MALDI-TOF analysis were also indicative of the chemical structure of the metal complexes with a metal to ligand ratio of 1:3.

The characteristic FT-IR spectra of the metal coordinated pyridines were obtained for all the three complexes and coordination polymers. The corresponding ring stretching $\text{C}=\text{N}$ vibrations of pyridines were found to be shifted upon metal coordination

(Fig. S1). Two characteristic ring stretching $\text{C}=\text{N}$ vibrations, one each for non-coordinated (**Mn–L**: 1,594 cm^{-1} ; **Fe–L**: 1,596 cm^{-1} ; and **Co–L**: 1,598 cm^{-1}) and metal-coordinated (**Mn–L**: 1,609 cm^{-1} ; **Fe–L**: 1,612 cm^{-1} ; and **Co–L**: 1,612 cm^{-1}) pyridines, were evident in the FT-IR spectra of all the complexes. The presence of both non-coordinated and coordinated pyridine $\text{C}=\text{N}$ peaks in the FT-IR spectra of the metal complexes is indicative of the presence of metal coordinated bipyridines ($M = \text{Mn}$, Fe , and Co) and non-coordinated, free terminal pyridines [41]. However, the peaks corresponding to non-coordinated pyridine $\text{C}=\text{N}$ vibrations vanished in the spectra of all the coordination polymers, corroborating an almost complete Pd –pyridine coordination in the coordination polymers. The $\text{C}-\text{H}$ in-plane deformation frequencies were also found to be shifted by at least 5 cm^{-1} (1,421 cm^{-1} in **M–L** to 1,426 cm^{-1} or higher in **M–L–Pd**) in all the coordination polymers (Fig. S1). Digesting the CPs using concentrated HCl followed by neutralization with triethylamine resulted in the recovery of ligand **L**, confirming its presence in all the CPs.

Thermogravimetric analysis under an inert atmosphere revealed slightly higher thermal stability of the coordination polymers compared to their parent metal–organic complexes (Fig. S2). The Co complex (**Co–L**) and its coordination polymer (**Co–L–Pd**) were found to be more stable among all the complexes and polymers. The thermal stability was found to be in the order of **Co–L** > **Fe–L** > **Mn–L** for the metal–bipyridine complexes and in the order of **Co–L–Pd** > **Fe–L–Pd** > **Mn–L–Pd** for the coordination polymers. Modest levels of molecular ordering in the complexes and polymers were confirmed by powder XRD analysis (Fig. S3). Nevertheless, the polymers were found to be more crystalline than the parent complexes. The Co complex **Co–L** exhibited the highest level of crystallinity among the three complexes, whereas the Mn polymer **Mn–L–Pd** was observed to possess better crystallinity among the polymers. The Fe complex and its polymer were found to be rather barely crystalline, most likely due to the faster reaction kinetics. Existence of several diffraction peaks at similar 2θ values in the XRD spectra of **M–L** and **M–L–Pd**, as in the powder pattern generated from the single crystal data of a reported metal–bipyridine system, is indicative of near-octahedral geometry of the central metal ion in the metal complexes and their coordination polymers [42]. No defined morphology was observed for the coordination polymers; however, the formation of irregular sheet-like structures co-existing with Pd nanoparticles was evident in the high-resolution TEM images (Figs. 2a–c and S4).

The elemental composition of the polymers was confirmed by X-ray photoelectron spectroscopy (XPS, Figs. 3 and S5) and energy dispersive X-ray spectroscopy (EDS, Fig. S6). The presence of palladium and nitrogen in all the coordination polymers was unanimously substantiated by the $\text{Pd } 3d_{5/2}$ (**Mn–L–Pd**: 337.3 eV, **Fe–L–Pd**: 337.3 eV, and **Co–L–Pd**: 337.5 eV), $\text{Pd } 3d_{3/2}$ (**Mn–L–Pd**: 342.6 eV, **Fe–L–Pd**: 342.5 eV, and **Co–L–Pd**: 342.9 eV), and $\text{N } 1s$ (**Mn–L–Pd**: 399.1 eV, **Fe–L–Pd**: 399.2 eV, and **Co–L–Pd**: 399.5 eV) peaks in the respective survey scan and high-resolution XPS data (Figs. 3a–c and S5) [43]. The high-resolution XPS of **Mn–L–Pd** exhibited the characteristic $\text{Mn } 2p_{3/2}$ and $2p_{1/2}$ components, respectively at 641.4 eV and 652.7 eV, each with a corresponding satellite peak at 646.0 eV and 656.8 eV (Figs. 3c and S5a) [43]. Similarly, $2p_{3/2}$ and $2p_{1/2}$ peaks of Fe with characteristic binding energies corresponding to 707.9 eV (satellite at 711.6 eV) and 720.9 eV respectively were evident from the HR XPS of **Fe–L–Pd** (Figs. 3f and S5b) [43]. The $\text{Co } 2p_{3/2}$ and $\text{Co } 2p_{1/2}$ binding energies at 781.6 eV and 797.0 eV, each with satellite peaks respectively at 787.4 eV and 802.9 eV in the high-resolution XPS, corroborated the formation of coordination polymers with cobalt centers in **Co–L–Pd** (Figs. 3i and S5c) [43]. Further, a near 1:3 ratio of M ($M = \text{Mn}$, Fe , and Co): Pd was also observed from the XPS

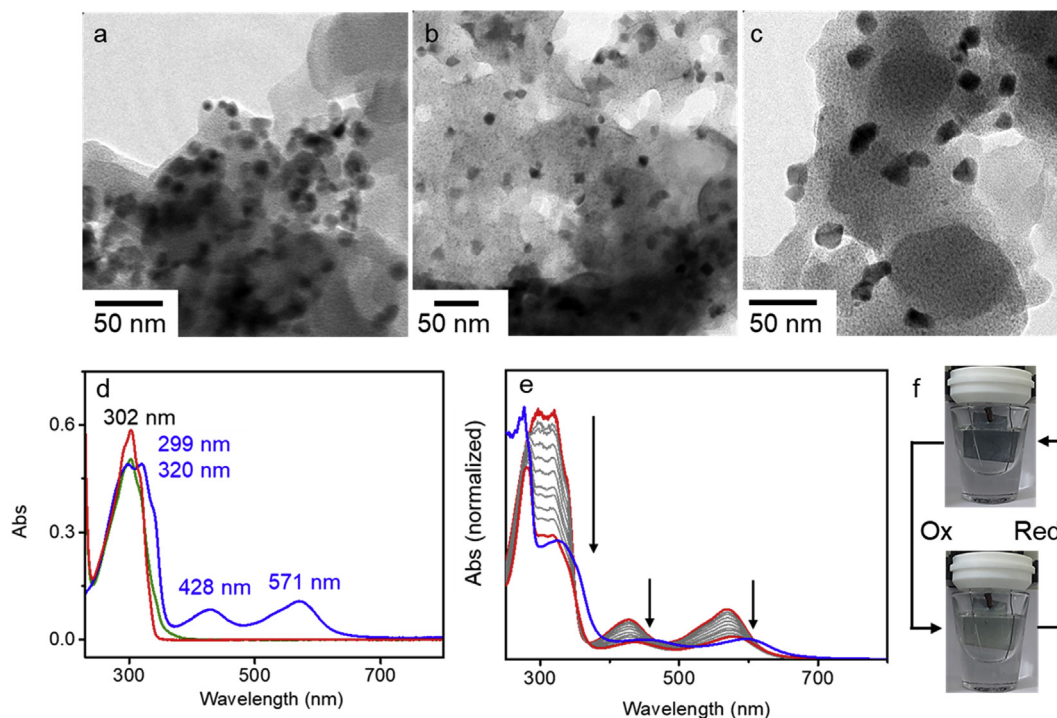


Fig. 2. Transmission electron microscopy (TEM) images (a) **Mn-L-Pd**, (b) **Fe-L-Pd**, and (c) **Co-L-Pd**. (d) UV-vis absorption spectra of the metal complexes **Mn-L** (red trace), **Fe-L** (blue trace), and **Co-L** (green trace). The complexes were dissolved in a 1:1 mixture of CH_2Cl_2 and MeOH and the final concentration was adjusted to $15 \mu\text{M}$. (e) Changes in the UV-vis absorption spectra of a $\text{CH}_2\text{Cl}_2/\text{MeOH}$ solution ($50 \mu\text{M}$) of the metal complex **Fe-L** (red trace), upon successive addition of a THF solution ($50 \mu\text{M}$) of $\text{PdCl}_2(\text{PhCN})_2$. The blue trace represents the spectrum upon addition of an excess of $\text{PdCl}_2(\text{PhCN})_2$ (just before the precipitation of the coordination polymer). (f) Electrochromic switching of the spin-coated films of **Fe-L-Pd** on FTO substrates. The colored state (reduced, Fe^{2+}) is shown on the left and the bleached state (single electron oxidized Fe^{3+}) is shown on the right. The coordination polymer-modified FTO was used as the working electrode and Pt wire and Ag/AgCl were used respectively as the counter and reference electrodes. A potential window of -0.5 – 2.5 V was used for the switching experiments in the presence of 0.1 M TBAPF_6 as the supporting electrolyte.

measurements, indicating a 1:3 metal–ligand ratio and hence the isostructural nature of the parent coordination complexes. The presence of these elements in the coordination polymers was also confirmed by energy dispersive X-ray spectroscopy on TEM (Fig. S6). Raman spectra also revealed the characteristic peaks corresponding to the expected chemical structure of the coordination polymers (ring breathing at $1,015$ – $1,020 \text{ cm}^{-1}$, $\nu(\text{C}=\text{C})$ interring at $1,202$ – $1,281 \text{ cm}^{-1}$, $\nu(\text{C}=\text{N})$ at $1,320$ – $1,348 \text{ cm}^{-1}$, $1,483$ – $1,389 \text{ cm}^{-1}$, and $1,634$ – $1,639 \text{ cm}^{-1}$, $\nu(\text{C}=\text{C})$ at $1,320$ – $1,348 \text{ cm}^{-1}$, and $1,611$ – $1,612 \text{ cm}^{-1}$, Fig. S7).

The Fe complex **Fe-L** was intensely colored due to the presence of strong MLCT bands at 571 nm and 428 nm [41,42]. However, the Mn and Co complexes **Mn-L** and **Co-L** were rather light yellow colored (Fig. S8) and no detectable charge transfer bands were evident from the corresponding UV-vis spectra (Fig. 2d). The π – π^* bands for all the three complexes were observed in the region 300 – 320 nm. Because **Fe-L** was typically colored, we chose this complex to investigate the changes in absorption properties upon cross-linking with Pd(II). Successive addition of increasing amounts of a THF solution of $\text{PdCl}_2(\text{PhCN})_2$ to a solution of **Fe-L** in $\text{CH}_2\text{Cl}_2/\text{MeOH}$ (1:1) resulted in the reduction in intensities of the π – π^* and MLCT bands with a concomitant red shift (Figs. 2e and S9). The visible color of the solution also changed from grayish purple to dark gray upon addition of an excess of Pd(II) solution, with the coordination polymer starting to precipitate out, leaving a colorless supernatant liquid. The other two polymers were also precipitated in solution and the filtrate was found to be free of both Pd(II) salt and the metal complex, suggesting a near complete cross-linking of the terminal pyridines in the coordination polymers.

3.2. Electrochemistry

Bipyridine complexes of transition metals have been explored widely for their characteristic redox reactions and the complexes used in this study were no exception. All the three complexes, **Mn-L**, **Fe-L**, and **Co-L**, exhibited single electron oxidation–reduction peaks in their respective cyclic voltammograms (Fig. 4a,c,e). Typically, the complexes were drop-cast onto a glassy carbon electrode, dried, and used as the working electrode in a three-electrode set-up, with a platinum wire and Ag/AgCl as counter and reference electrodes and 0.1 M TBAPF_6 as the supporting electrolyte. At a scan rate of 100 mV/s , **Mn-L**, **Fe-L**, and **Co-L** were found to have their half-wave potentials ($E_{1/2}$) of 1.30 , 1.12 , and 0.23 V, respectively (Fig. 4a,c,e). The electrochemical redox potentials of the three complexes are given in Table S1.

To get better insights into the mechanism of electron transfer process in these metal complexes and further to elucidate the role of the diffusion of electrolyte ions during the charge storage process, CVs of the coordination polymer-modified electrodes as varying scan rates (50 – 500 mV/s) were obtained. The scan rate dependence of current in the CVs is indicative of the electron transfer mechanism and hence the role of diffusion in capacitive charge–discharge phenomenon [44,45]. For all the coordination polymers, the current was found to increase exponentially with scan rate and linearly with the square root of scan rate (Figs. 4b,d,f and S10). This observation corroborates the diffusion-limited electron transfer in these coordination polymer-modified electrodes and hence the diffusion of electrolyte ions may be the rate-controlling step in the electrochemical charge–discharge process [46].

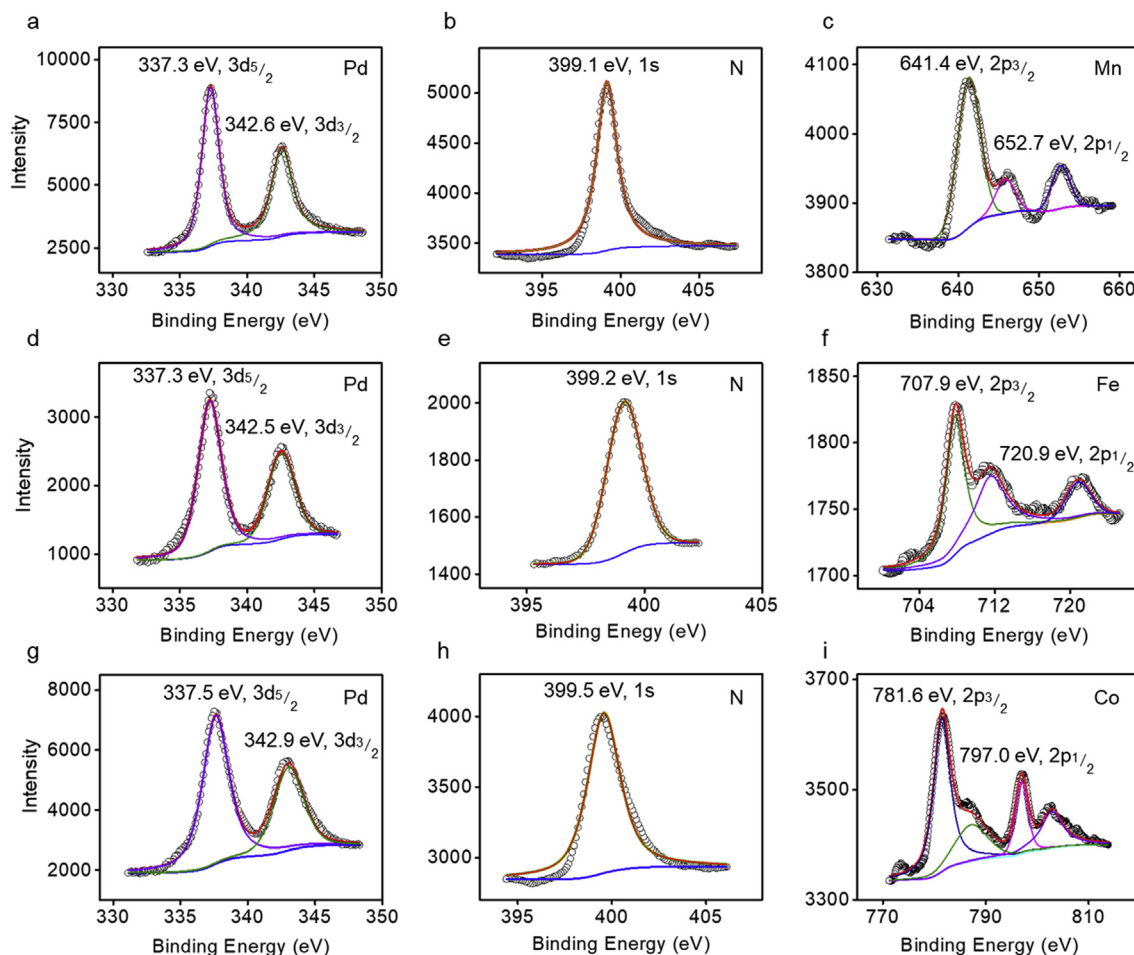


Fig. 3. High-resolution XPS data for (a–c) **Mn–L–Pd**, (d–f) **Fe–L–Pd**, and (g–i) **Co–L–Pd**. The left panels (a, d, and g) correspond to the high-resolution spectra for Pd, the middle ones (b, e, and h) correspond to those for N, and the right ones (c, f, and i) correspond to those for Mn, Fe, and Co respectively. The binding energies corresponding to the peaks and their assignment are provided in each figure.

The electrochromic behavior of nanoscale films obtained from **Fe–L** cross-linked by Pd(II) via iterative dip coating on TCO-coated glass has been demonstrated by van der Boom and co-workers [41]. In this study, the coordination polymer **Fe–L–Pd** that was formed by mixing the solutions of **Fe–L** and PdCl₂(PhCN)₂ was re-dispersed in MeOH and spin-cast on FTO substrates to obtain switchable electrochromic films, thereby bypassing the need for multiple levels of dip coating and washing cycles in between. While dip coating up to eight bilayers of **Fe–L** and PdCl₂(PhCN)₂ resulted in highly uniform electrochromic nanoscale films, spin coating the preformed coordination polymer led to fast fabrication of switchable electrochromic films of comparable thickness, but with slightly lesser uniformity. The obtained film was found to switch between neutral gray to colorless upon the application of potential (0.0–2.0 V, Fig. 2f). Though the electrochemical signature was obtained for **Mn–L–Pd** and **Co–L–Pd**, these films did not exhibit visible electrochromism in the potential window of –2.0–2.0 V when spin-cast on FTO substrates.

3.3. DFT calculations

In the absence of crystal structures, the energy minimized structures of the complexes were studied using density functional theory (DFT) at the B3LYP/6-31G (d,p) level (Fig. S11). Near octahedral geometry was obtained for all the three complexes, with

three ligands coordinated to the central metal ion through the bipyridine moiety, with similar N–M–N angles (**Mn–L–Pd**: 50.38°, **Fe–L–Pd**: 49.55°, and **Co–L–Pd**: 49.09°) and M–N distances (**Mn–L–Pd**: 2.026 Å, **Fe–L–Pd**: 1.993 Å, and **Co–L–Pd**: 1.968 Å). Nevertheless, these bond angles and distances in the complexes were found to decrease slightly in the order of Mn > Fe > Co. Palladium–pyridine coordination in solution and film states has been extensively reported in literature, with a mutual *trans* positioning of the pyridine moieties leading to a near square planar geometry [47–52]. The possibilities for the spontaneous formation of square planar Pd(II) centers in these reactions lead to extended networks of the coordination polymers [48].

3.4. Capacitance

Supercapacitor electrodes of 1 cm² area were prepared using the corresponding metallopolymer mixed with PTFE and activated charcoal in a mass ratio of 8:1:1 (see Supporting information for details). The electrochemical properties were studied using symmetric assemblies in a two-electrode configuration by CV, GCD measurements, and EIS at room temperature.

The CV loops of the coordination polymer-based electrode materials are presented in Figs. 5a and S12. The near rectangular shape of the voltammograms at lower scan rates, more predominant for **Fe–L–Pd** (Figs. 5a and S12b) and lesser for **Mn–L–Pd** (Figs. 5a and

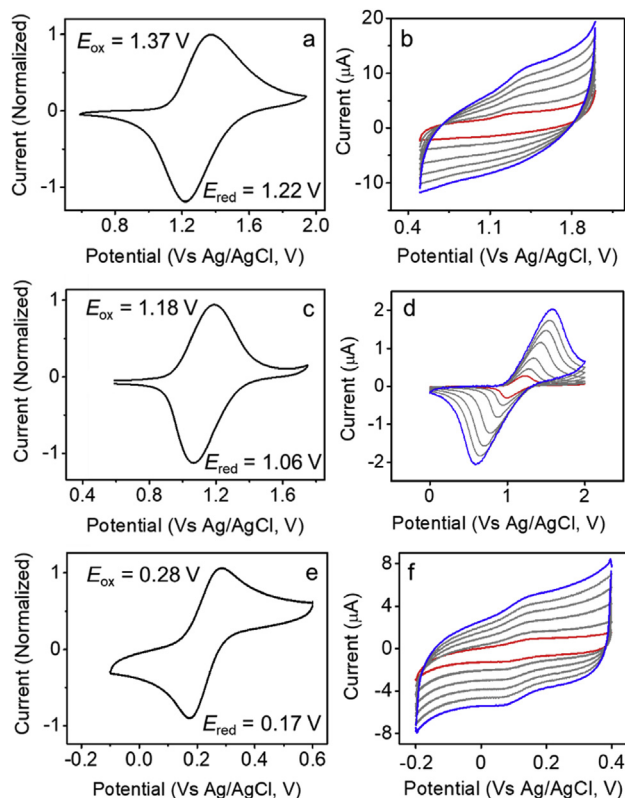


Fig. 4. Cyclic voltammograms of (a) **Mn-L**, (c) **Fe-L**, and (e) **Co-L** at a scan rate of 100 mV/s and (b) **Mn-L-Pd**, (d) **Fe-L-Pd**, and (f) **Co-L-Pd** under various scan rates (50–500 mV/s), showing the increase in current with increasing scan rates. The exponential and linear dependence of current on the scan rates and square root of the scan rates is provided in the Supporting information. The voltammograms were obtained using the corresponding coordination polymer-modified glassy carbon as the working electrode, Pt wire as the counter electrode, and Ag/AgCl as the reference electrode. A 0.1 M solution of tetrabutylammonium hexafluorophosphate in dry acetonitrile was used as the supporting electrolyte.

(Fig. S12a), is indicative of comparably lower internal resistance and rapid charge–discharge processes happening within the electrode materials [53]. The CVs of all the coordination polymer-modified electrodes exhibited an increase in current with increasing scan rate. Moreover, the area under the voltammograms and the current were found to increase significantly at higher potentials (Fig. S12a–c). These results imply a favorable capacitance behavior

as well as the prevalence of redox or faradaic reactions within the porous coordination polymers (PCPs) or at the electrode–electrolyte interface.

Interestingly, the capacitance of the electrodes fabricated from the coordination polymers of near-isostructural complexes with varying metal centers was found to follow the order of the occurrence of the metals in the periodic table ($\text{Mn} < \text{Fe} < \text{Co}$, Figs. 5a and S12). Maximum areal capacitance values (normalized per unit area) of 9.1, 12.2, and 15.4 mF cm^{-2} were obtained for the symmetric capacitors based on **Mn-L-Pd**, **Fe-L-Pd**, and **Co-L-Pd**, respectively, at a scan rate of 5 mV/s (Table 1). The capacitance was found to increase exponentially with decreasing scan rates (Figs. 5a inset, 5c, S12d, Table S2). The scan rate dependence of the capacitance values is attributed to the kinetics of diffusion of the electrolyte ions into the pores of the coordination polymers. At lower scan rates, the electrolyte ions may get longer times to diffuse into the pores and hence exhibit a higher capacitance value [54]. The distortion in the rectangular shapes of the CVs at higher scan rates is attributed to the limited diffusion of electrolyte ions into the pores of the coordination polymers [55]. The shape of the CVs at higher scan rates resembles the characteristics of redox reactions during charging–discharging cycles, suggesting that the capacitive behavior does not originate exclusively from the oppositely charged electrical double layer [40]. However, near triangular shapes of the charge–discharge curves suggest some contribution from an electric double layer also to the capacitive behavior and hence cannot be rigorously excluded [55].

The cyclic voltammograms of **Co-L** and **Co-L-Pd** feature $\text{Co}^{2+} \leftrightarrow \text{Co}^{3+}$ redox couple in the range of 0.0–1.0 V (Figs. 4c, 5a, S10c and S12c); however, the redox couples involving either Mn^{2+} or Fe^{2+} do not occur in the selected potential window (Figs. 4a, b, 5a and S12a,b). Thus, the characteristics of **Co-L-Pd** are predominantly pseudocapacitive in origin and those of the Fe and Mn polymers, most likely, have contributions from both electric double layer and pseudocapacitance arising from redox/faradaic reactions on the electrode surface.

The practical operation efficiency and performance of supercapacitor materials may be predicted via GCD measurements [56]. GCD curves of the coordination polymer supercapacitors at a constant potential window (0.0–1.0 V) under varying current densities (2.00, 1.00, 0.75, 0.50, and 0.25 mA cm^{-2}) are shown in Figs. 5b and S13. The obtained GCD curves were not found to be precisely linear or symmetrical, suggesting a pseudocapacitive behavior. A combination of faradaic charge storage reactions near the electrode surface, non-faradaic contributions, and mass transport phenomenon

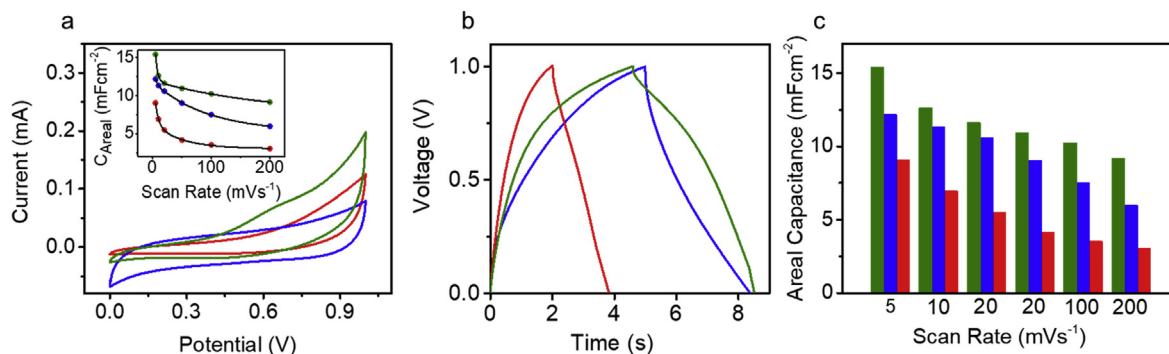


Fig. 5. (a) Cyclic voltammograms obtained from the symmetric supercapacitors based on **Mn-L-Pd** (red), **Fe-L-Pd** (blue), and **Co-L-Pd** (green) at a scan rate of 5 mV/s. Inset: comparison of the areal capacitance obtained for **Mn-L-Pd** (red), **Fe-L-Pd** (blue), and **Co-L-Pd** (green)-derived capacitors at different scan rates. $R^2 > 0.99$ for all fits. (b) Galvanostatic charge–discharge curves of symmetric supercapacitors based on **Mn-L-Pd** (red), **Fe-L-Pd** (blue), and **Co-L-Pd** (green) electrodes at a constant potential window (0.0–1.0 V) and current density (1.0 mA cm^{-2}). (c) Comparison of the areal capacitance obtained for **Mn-L-Pd** (red), **Fe-L-Pd** (blue), and **Co-L-Pd** (green)-derived capacitors at different scan rates.

Table 1
Characteristics and performance of the coordination polymers and coordination polymer-derived supercapacitors.

Coordination Polymer	Capacitance (mF cm ⁻²) ^a	Pore Vol. (Å ³) ^b	BET Surface Area (m ² /g)	Stability ^c
Mn-L-Pd	9.06	326.18	6.46	>84%
Fe-L-Pd	12.17	276.23	10.36	>88%
Co-L-Pd	15.42	277.33	29.72	>90%

^a Areal capacitance obtained by normalizing the cell capacitance to unit area for the symmetric capacitors at a scan rate of 5 mV/s.

^b Calculated from BET surface area experiments.

^c Capacitance after 5,000 cycles of continuous operation.

involving the porous active materials has been previously shown to result in such observations [56].

The charge–discharge kinetics were found to be comparable for all the three capacitors at lower current densities (0.25–0.50 mA cm⁻²) in the potential window of 0.0–1.0 V (Fig. S13). However, at higher current densities (>0.50 mA cm⁻²), the supercapacitor cells fabricated from **Mn-L-Pd** were found to charge and discharge at faster rates, compared to those fabricated from **Fe-L-Pd** or **Co-L-Pd** that continued to discharge at similar rates (Fig. S13). Higher current densities are known to limit the accessibility of the electrolyte ions to the electrode surface only, whereas, lower current densities allow the diffusion/penetration of the ions to access both the electrode surface and the pores of the electrode material [56]. These results are indicative of a similar porosity for the Fe- and Co-derived coordination polymers and a higher porosity for the Mn-derived polymer and have been confirmed by BET surface area measurements. However, the energy densities of these coordination polymer-derived supercapacitors were found to be modest (0.5–1.1 Wh/kg) at a constant power density of 1 kW/kg [57], in the following order: Co > Fe > Mn.

EIS investigations are performed to follow the electrochemical processes occurring at the electrode–electrolyte interface [56]. The absence of the semi-circular region in the EIS plots at higher frequencies for the supercapacitors fabricated from **Fe-L-Pd** and **Mn-L-Pd** confirms very low charge transfer resistance in these coordination polymers compared to **Co-L-Pd** that features a detectable semi-circle at the high-frequency region of its Nyquist plot (Figs. S14a and S15). Nevertheless, even with the higher charge transfer resistance and hence the lower electronic conductivity, **Co-L-Pd** exhibited better capacitance behavior, followed by **Fe-L-Pd** and **Mn-L-Pd**. The solution resistance (R_s) or the equivalent series resistance arises from the combined effect of the ionic resistance of the electrolyte, intrinsic resistance of the coordination polymer, and contact resistance at the electrode–electrolyte interface and was found to be 3.0, 0.5, and 1.5 Ω for **Mn-L-Pd**, **Fe-L-Pd**, and **Co-L-Pd**, respectively.

The best model that fits the data for the best performing device fabricated from **Co-L-Pd** is shown in Fig. S16 and consists of R_s in series with R_{ct} , C_{dl} , and W , where R_s is the solution resistance or the equivalent series resistance, R_{ct} corresponds to the charge transfer resistance, C_{dl} is the double layer capacitance, and W is the Warburg impedance. The EIS studies indicate the possibilities for diffusion-limited electrochemical and electron transfer processes at the electrode surfaces in these coordination polymer-derived symmetric supercapacitors. These results are in complete agreement with the scan rate-dependent electrochemical studies of the coordination polymer-modified electrodes in solution (Fig. 4).

The cycling stability is of paramount significance in determining the practical applications of supercapacitors. At a constant current density of 1 mA cm⁻², the **Co-L-Pd**-derived device was found to be the most stable with >90% of the areal capacitance retained after 2,000 cycles of continuous operation. The Fe- and Mn-based

devices, under identical conditions, retained >88% and >84% areal capacitance, respectively, after 2,000 cycles (Fig. S14b, Table 1). No detectable changes in capacitive performance was observed at least until 5,000 cycles of continuous operation.

3.5. BET surface area experiments

Although the coordination polymers were obtained from near isostructural complexes of Mn(II), Fe(II), and Co(II), the electrochemical energy storage properties of the coordination polymers are strictly governed by the metal center. To explain the differences in the capacitance behavior of these coordination polymers, their pore volumes and BET surface areas were experimentally determined (Fig. 6a, Table 1). As indicated by the charge–discharge cycles of the symmetric supercapacitors, **Fe-L-Pd** and **Co-L-Pd** were found to possess pores of similar volume (276–277 Å³), whereas the Mn polymer had a comparably larger pore volume of 326 Å³. All three coordination polymers were found to have wide pore size distribution (Fig. 6b–d). Pore distribution analysis also corroborates the absence of permanent microporosity and the coexistence of macro and mesopores in these coordination polymers. However, significant differences in pore distribution was not observed. With comparably larger pore volume of **Mn-L-Pd**, better percolation pathways may have led to faster electron/charge transport during charge–discharge cycles. Even with a larger pore volume, **Mn-L-Pd** exhibited the lowest capacitance values among the three coordination polymers (Table 1). In order to explain this observation, the BET surface areas of all the coordination polymers were measured using nitrogen adsorption–desorption isotherms at 77 K. All the three coordination polymers exhibited a type IV isotherm with a prominent capillary condensation step at a relative pressure close to unity (Fig. 6a). An H1-type hysteresis loop was also observed in all the three isotherms, suggesting the coexistence of macro and mesopores in these coordination polymers (Fig. 6a) [55]. The BET surface areas were found to be 6.5, 10.4, and 29.7 m²/g for **Mn-L-Pd**, **Fe-L-Pd**, and **Co-L-Pd**, respectively, which is consistent with the order of areal capacitance of the coordination polymer-derived supercapacitors (Table 1). The steep rising of the uptake in the BET isotherm may have originated from the interparticle condensation and may have contributions to the observed differences in capacitive performance. However, determination of the individual contributions is rather beyond the scope of this study.

The electrical conductivity of **M-L-Pd** (M = Mn, Fe, and Co; thin films, 155 ± 5 nm thickness) was determined using a 4-probe method (Fig. S17). While most of the previously reported pristine MOFs and coordination polymers were found to have more of insulator-like behavior with conductivity in the order of 10⁻¹⁰ S/cm [58], all the three CPs used in this study were found to be more semiconducting in nature with conductivity in the order of 10⁻⁷ S/cm. The better conductivity most likely stems from the delocalized π-electron systems that in turn offers a rigid network and better stability. Significant differences in conductivity were also not observed among the CPs (Table S3).

The charge storage and electrolyte ion mobility of porous electrode materials are primarily determined by their total available surface area and porosity [59]. In the coordination polymers currently investigated, there is a trade-off between the surface area and pore volume, and the supercapacitors fabricated from the **Co-L-Pd** with the highest surface area exhibited the highest capacitor performance, followed by **Fe-L-Pd** and **Mn-L-Pd**. However, the effect of other factors including resistance parameters, conductivity, faradaic and non-faradaic contributions, and mass transport in the coordination polymers cannot be rigorously excluded. The observed trends in capacitance behavior may thus be

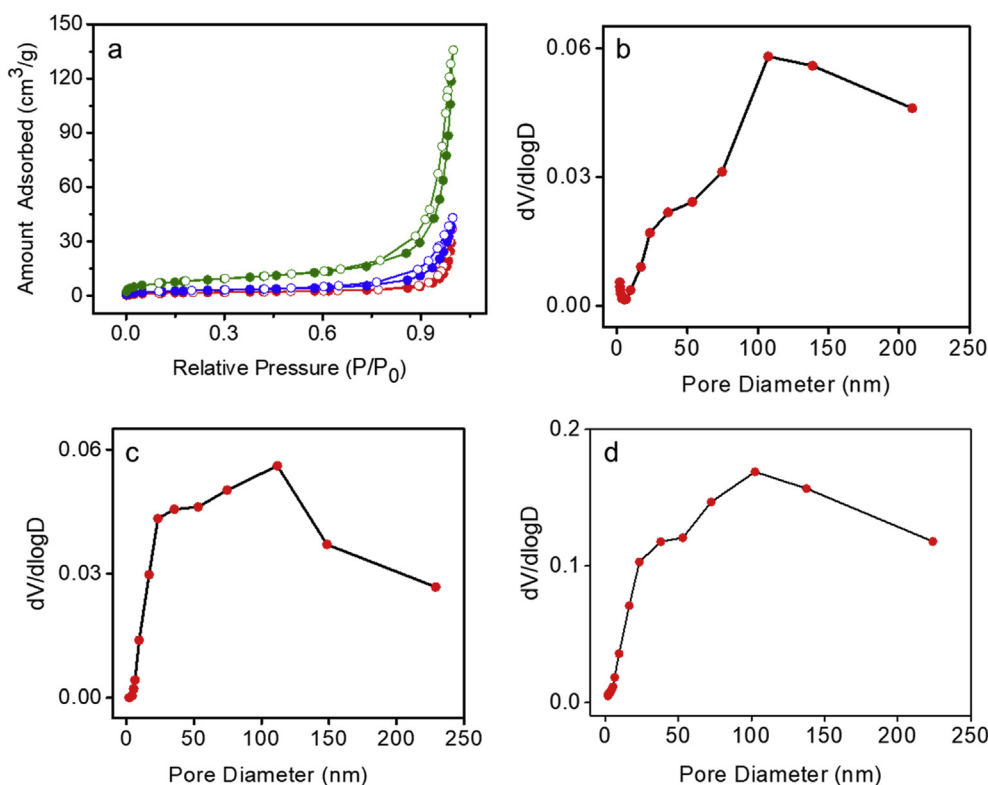


Fig. 6. (a) BET adsorption (solid circles) and desorption (open circles) isotherms for **Mn-L-Pd** (red), **Fe-L-Pd** (blue), and **Co-L-Pd** (green). Pore size distribution in (a) **Mn-L-Pd**, (b) **Fe-L-Pd**, and (c) **Co-L-Pd**, obtained from adsorption isotherms.

attributed to the combined effect of charge transfer resistance, solution resistance, electronic conductivity, faradaic and non-faradaic processes, mass transport, pore volume, and more predominantly, the total available surface area of the coordination polymers. The surface area of the coordination polymers increases in the order of $\text{Mn} < \text{Fe} < \text{Co}$ and is directly reflected in the capacitance, charge-discharge properties and the operational stability of the supercapacitors. Amazing enough, this order of performance follows the order of occurrence of these metals in the periodic table. Random distribution of Pd nanoparticles in all the three coordination polymers, as evident from TEM images (Fig. 2a–c), may not be expected to contribute differently to the observed modulation of capacitance, its mechanism, or kinetics. However, any contribution of these nanoparticles to the value of areal capacitance cannot be completely ruled out. Inter-particle space between the granules observed in the TEM images may also have contributed to the observed capacitance behavior.

The modest values of areal capacitance observed for the supercapacitors can be attributed to the limited order and crystallinity [60] of these coordination polymers, low surface areas compared to carbon materials, low packing density as well as their morphological features [37]. Spontaneous precipitation in solution leads to diminished crystallinity and the presence of larger number of interfaces between the sheet-like non-continuous morphology may act as electron/charge trapping sites, thereby hindering the electrochemical process. The capacitance normalized to the BET surface area is chosen as a parameter to compare the performance of electrode materials. The surface area-normalized capacitance values of the coordination polymers are among the highest reported in literature (Fig. S18) [40,55,61–66]. The BET surface area-normalized capacitance values of 51.9–140.3 $\mu\text{F m}^{-2}$ are at par with the state-of-the-art values reported in literature for metal-organic systems.

Multi-metallic PCPs are rarely reported as electrode materials in energy storage systems. This study could be the first on the use of novel bimetallic PCPs with modulative capacitance in isostructural metal complexes-derived coordination polymers. While these coordination polymers resulted in modest capacitive performance due to several factors discussed above, they were found to possess better electrical conductivity compared to pristine MOFs or CPs reported in the literature [58]. The delocalized π electron system in these CPs offers a rigid network with better conductivity and electrochemical stability [41]. Despite the performance of these materials being less than other reported materials [67], modulating the capacitance and its mechanism, as well as the charge-discharge kinetics via metal-ion regulated BET surface area disparities, is envisaged to provide new insights into the design of novel non-carbon electrode materials with fine-tuned electrochemical and electro-optical properties. Variation of the central metal ion while reserving the structural features of the coordination polymers offers promising opportunities to enhance their electrochemical charge storage efficiencies via careful design and manipulation of synthetic strategies leading to higher available surface areas, high packing densities, and hence better capacitive performance [37,68,69].

The moderate-to-low performance of metal-organic materials in a capacitor set-up is generally attributed to the low mobility of charge carriers, originating from weak electron transfer processes involving the metal centers and ligands, leading to rather poor conductivity [58]. However, better energy storage properties can be imparted to these materials via post-synthetic modifications, composite formation, and using host-guest chemistry. Design of conducting ligand molecules and mixing with conducting or semiconducting materials at an optimum ratio are also promising strategies toward improving the capacitance characteristics of metal-organic materials [58]. The combination of high surface

areas, extended ordering, crystallinity, high packing density, and favorable morphological features along with several tunable properties makes this class of materials promising candidates for non-carbon electrode materials with excellent performance in electrochemical energy storage systems. With the advent of new electrocatalysts [70] and energy generation/storage technologies, metal–organic hybrids are potential candidates for active materials for several futuristic applications.

4. Conclusions

The coordination polymers derived from near isostructural metal complexes consisting of the same ligand and cross-linked with the same metal ion (Pd^{2+}) exhibited significant effect of the metal center on the porosity, surface area, and hence their capacitive performance. Variations in the central metal ion, in otherwise similar coordination polymers with comparable geometry around the metal center, has led to the modulation of charge storage properties and mechanism, cycling stabilities, BET surface area, and charge–discharge kinetics. A 3:4:5 ratio of areal capacitance values ($\text{Mn}:\text{Fe}:\text{Co}$) at a scan rate of 5 mV/s substantiates the impact of the central metal ion in determining the capacitive performance of the coordination polymer-based electrode materials. Though higher values for BET surface area-normalized capacitance were previously obtained for crystalline Co-MOF-based systems (5–23% drop after 1,000 cycles) [40,71], better cycling stability was observed for the more or less amorphous cobalt coordination polymer **Co–L–Pd** (<2% drop after 1,000 cycles)-based supercapacitors. This work demonstrates that the charge storage properties and mechanism, cycling stabilities, and charge–discharge kinetics of PCP-based supercapacitors could be effectively modulated by the central metal ion. We envision that the numerous possibilities for incrementing the surface areas as well as the crystallinity of these class of coordination polymers provide enough opportunities to develop non-carbon electrode materials with enhanced performance, stability, and charge–discharge kinetics with distinct control over the charge transport mechanism and electro-optical characteristics [72–76].

Author contributions

The manuscript was written through contributions of all authors. All authors have given approval to the final version of the manuscript.

Declaration of competing interest

The authors declare that they have no known competing financial interests or personal relationships that could have appeared to influence the work reported in this paper.

Acknowledgment

IM is grateful to DST, Government of India for an INSPIRE Fellowship. SS and RRB are grateful to DST-SERB, Government of India for Ramanujan Fellowships (SB/S2/RJN-058/2016, SB/S2/RJN-098/2015). AA thanks DST-SERB, Government of India, for a J. C. Bose National Fellowship (SB/S2/JCB-11/2014). This work was supported by CSIR, Government of India (MLP 0022 and MLP 0030). Dr. C. H. Suresh is gratefully acknowledged for discussions on DFT calculations. The authors are thankful to Dr. Saju Pillai, Dr. U. S. Hareesh, and Dr. E. Bhoje Gowd for XPS, TGA, and XRD experiments, respectively.

Appendix A. Supplementary data

Supplementary data to this article can be found online at <https://doi.org/10.1016/j.mtchem.2020.100260>.

References

- [1] H. Furukawa, K.E. Cordova, M. O’Keeffe, O.M. Yaghi, The chemistry and applications of metal–organic frameworks, *Science* 341 (2013) 1230444, <https://doi.org/10.1126/science.1230444>.
- [2] H.-C. Zhou, J.R. Long, O.M. Yaghi, Introduction to metal–organic frameworks, *Chem. Rev.* 11 (2012) 673–674, <https://doi.org/10.1021/cr300014x>.
- [3] S. Yuan, L. Feng, K. Wang, J. Pang, M. Bosch, C. Lollar, Y. Sun, J. Qjin, Y. Yang, P. Zhang, Q. Wang, L. Zou, Y. Zhang, L. Zhang, Y. Fang, J. Li, H.-C. Zhou, Stable metal–organic frameworks: design, synthesis, and applications, *Adv. Mater.* 30 (2018) 1704303, <https://doi.org/10.1002/adma.201704303>.
- [4] H.-C. Zhou, S. Kitagawa, Metal–organic frameworks (MOFs), *Chem. Soc. Rev.* 43 (2014) 5415–5418, <https://doi.org/10.1039/C4CS90059F>.
- [5] S. Kitagawa, R. Kitaura, S.I. Noro, Functional porous coordination polymers, *Angew. Chem. Int. Ed.* 43 (2004) 2334–2375, <https://doi.org/10.1002/anie.200300610>.
- [6] S. Bureekaew, S. Shimomura, S. Kitagawa, Chemistry and application of flexible porous coordination polymers, *Sci. Technol. Adv. Mater.* 9 (2008), 014108, <https://doi.org/10.1088%2F1468-6996%2F9%2F1%2F014108>.
- [7] S.R. Batten, N.R. Champness, Coordination polymers and metal–organic frameworks: materials by design, *Phil. Trans. R. Soc. A.* 375 (2017) 20160032, <https://doi.org/10.1098/rsta.2016.0032>.
- [8] R.D. Mukhopadhyay, G. Das, A. Ajayaghosh, Stepwise control of host–guest interaction using a coordination polymer gel, *Nat. Commun.* 9 (2018) 1987, <https://doi.org/10.1038/s41467-018-04303-8>.
- [9] F. Sun, Q. Li, H. Xue, H. Pang, Pristine transition-metal-based metal–organic frameworks for electrocatalysis, *ChemElectroChem* 6 (2019) 1273–1299, <https://doi.org/10.1002/celec.201801520>.
- [10] P. Xiao, Y. Xu, Recent progress in two-dimensional polymers for energy storage and conversion: design, synthesis, and applications, *J. Mater. Chem. A.* 6 (2018) 21676–21695, <https://doi.org/10.1039/C8TA02820F>.
- [11] L.L. Zhang, X.S. Zhao, Carbon-based materials as supercapacitor electrodes, *Chem. Soc. Rev.* 38 (2009) 2520–2531, <https://doi.org/10.1039/b813846j>.
- [12] W. Lu, X. Guo, Y. Luo, Q. Li, R. Zhu, H. Pang, Core-shell materials for advanced batteries, *Chem. Eng. J.* 355 (2019) 208–237, <https://doi.org/10.1016/j.cej.2018.08.132>.
- [13] W. Gu, G. Yushin, Review of nanostructured carbon materials for electrochemical capacitor applications: advantages and limitations of activated carbon, carbide-derived carbon, zeolite-templated carbon, carbon aerogels, carbon nanotubes, onion-like carbon, and graphene, *Wiley Interdiscip. Rev. Energy Environ.* 3 (2014) 424–473, <https://doi.org/10.1002/wene.102>.
- [14] Y. Xu, Z. Lin, X. Zhong, X. Huang, N.O. Weiss, Y. Huang, X. Duan, Holey graphene frameworks for highly efficient capacitive energy storage, *Nat. Commun.* 5 (2014) 4554, <https://doi.org/10.1038/ncomms5554>.
- [15] Y. Zhu, S. Murali, M.D. Stoller, K.J. Ganesh, W. Cai, P.J. Ferreira, A. Pirkle, R.M. Wallace, K.A. Cyhosh, M. Thommes, D. Su, E.A. Stach, R.S. Ruoff, Carbon-based supercapacitors produced by activation of graphene, *Science* 332 (2011) 1537–1541, <https://doi.org/10.1126/science.1200770>.
- [16] P. Simon, Y. Gogotsi, Materials for electrochemical capacitors, *Nat. Mater.* 7 (2008) 845–854, <https://doi.org/10.1038/nmat2297>.
- [17] Y. Myung, S. Jung, T.T. Tung, K.M. Tripathi, T.Y. Kim, Graphene-based aerogels derived from biomass for energy storage and environmental remediation, *ACS Sustain. Chem. Eng.* 7 (2019) 3772–3782, <https://doi.org/10.1021/acssuschemeng.8b04202>.
- [18] T.S. Tran, K.M. Tripathi, B.N. Kim, I.-K. You, B.J. Park, Y.H. Han, T.Y. Kim, Three-dimensionally assembled Graphene/ α -MnO₂ nanowire hybrid hydrogels for high performance supercapacitors, *Mater. Res. Bull.* 96 (2017) 395–404, <https://doi.org/10.1016/j.materresbull.2017.04.012>.
- [19] S. Zheng, H. Xue, H. Pang, Supercapacitors based on metal coordination materials, *Coord. Chem. Rev.* 373 (2018) 2–21, <https://doi.org/10.1016/j.ccr.2017.07.002>.
- [20] G.S. Das, S. Sarkar, R. Aggarwal, S.K. Sonkar, J.-W. Park, K.M. Tripathi, T.Y. Kim, Fluorescent microspheres of zinc 1,2-dicarbomethoxy-1,2-dithiolate complex decorated with carbon nanotubes, *Carbon Lett.* 29 (2019) 595–603, <https://doi.org/10.1007/s42823-019-00058-4>.
- [21] A. Zheng, X. Li, B. Yan, Q. Hu, Y. Xu, X. Xiao, H. Xue, H. Pang, Transition-metal (Fe, Co, Ni) based metal–organic frameworks for electrochemical energy storage, *Adv. Energy. Mater.* 7 (2017) 1602733, <https://doi.org/10.1002/aenm.201602733>.
- [22] F. Marpaung, M. Kim, J.H. Khan, K. Konstantinov, Y. Yamauchi, M.S.A. Hossain, J. Na, J. Kim, Metal–organic framework (MOF)-Derived nanoporous carbon materials, *Chem. Asian J.* 14 (2019) 1331–1343, <https://doi.org/10.1002/asia.201900026>.
- [23] R.R. Salunkhe, Y.V. Kaneti, Y. Yamauchi, Metal–organic framework-derived nanoporous metal oxides toward supercapacitor applications: progress and prospects, *ACS Nano* 11 (2017) 5293–5308, <https://doi.org/10.1021/acsnano.7b02796>.

- [24] X.-C. Xie, K.-J. Huang, X. Wu, Metal–organic framework derived hollow materials for electrochemical energy storage, *J. Mater. Chem. A* 6 (2018) 6754–6771, <https://doi.org/10.1039/C8TA00612A>.
- [25] L. Sun, M.G. Campbell, M. Dinca, Electrically conductive porous metal–organic frameworks, *Angew. Chem. Int. Ed.* 55 (2016) 3566–3579, <https://doi.org/10.1002/anie.201506219>.
- [26] C.-W. Kung, K. Otake, C.T. Buru, S. Goswami, Y. Cui, J.T. Hupp, A.M. Spokoyny, O.K. Farha, Increased electrical conductivity in a mesoporous metal–organic framework featuring metallocarboranes guests, *J. Am. Chem. Soc.* 140 (2018) 3871–3875, <https://doi.org/10.1021/jacs.8b00605>.
- [27] H. Wang, Q.-L. Zhu, R. Zou, Q. Xu, Metal–organic frameworks for energy applications, *Inside Chem.* 2 (2017) 52–80, <https://doi.org/10.1016/j.chempr.2016.12.002>.
- [28] X. Cao, C. Tan, M. Sindoro, H. Zhang, Hybrid micro-/nano-structures derived from metal–organic frameworks: preparation and applications in energy storage and conversion, *Chem. Soc. Rev.* 46 (2017) 2660–2677, <https://doi.org/10.1039/c6cs00426a>.
- [29] R.D. Mukhopadhyay, V.K. Praveen, A. Hazra, T.K. Maji, A. Ajayaghosh, Light driven mesoscale Assembly of a coordination polymeric gelator into flowers and stars with distinct properties, *Chem. Sci.* 6 (2015) 6583–6591, <https://doi.org/10.1039/c5sc02233a>.
- [30] S. Shankar, R. Balgley, M. Lahav, S.R. Cohen, R. Popovitz-Biro, M.E. van der Boom, Metal–organic microstructures: from rectangular to stellated and interpenetrating polyhedra, *J. Am. Chem. Soc.* 137 (2015) 226–231, <https://doi.org/10.1021/ja509428a>.
- [31] L. Wang, Y. Han, X. Feng, J. Zhou, P. Qi, B. Wang, Metal–organic frameworks for energy storage: batteries and supercapacitors, *Coord. Chem. Rev.* 307 (2016) 361–381, <https://doi.org/10.1016/j.ccr.2015.09.002>.
- [32] G. Xu, P. Nie, H. Dou, B. Ding, L. Li, X. Zhang, Exploring metal organic frameworks for energy storage in batteries and supercapacitors, *Mater. Today* 20 (2017) 191–209, <https://doi.org/10.1016/j.mattod.2016.10.003>.
- [33] X. Liu, C. Shi, C. Zhai, M. Cheng, Q. Liu, G. Wang, Cobalt-based layered metal–organic framework as an ultrahigh capacity supercapacitor electrode material, *ACS Appl. Mater. Interfaces* 8 (2016) 4585–4591, <https://doi.org/10.1021/acsami.5b10781>.
- [34] H. Zhang, J. Nai, L. Yu, X.W.D. Lou, Metal–organic–framework-based materials as platforms for renewable energy and environmental applications, *Joule* 1 (2017) 77–107, <https://doi.org/10.1016/j.joule.2017.08.008>.
- [35] A. Morozan, F. Jaouen, Metal organic frameworks for electrochemical applications, *Energy Environ. Sci.* 5 (2012) 9269–9290, <https://doi.org/10.1039/C2EE22989G>.
- [36] Z. Liang, C. Qu, W. Guo, R. Zou, Q. Xu, Pristine metal–organic frameworks and their composites for energy storage and conversion, *Adv. Mater.* 30 (2018) 1702891, <https://doi.org/10.1002/adma.201702891>.
- [37] D. Feng, T. Lei, M.R. Lukatskaya, J. Park, Z. Huang, M. Lee, L. Shaw, S. Chen, A.A. Yakovenko, A. Kulkarni, J. Xiao, K. Fredrickson, J.B. Tok, X. Zou, Y. Cui, Z. Bao, Robust and conductive two-dimensional Metal–Organic frameworks with exceptionally high volumetric and areal capacitance, *Nat. Energy* 3 (2018) 30–36, <https://doi.org/10.1038/s41560-017-0044-5>.
- [38] Y. Li, Y. Xu, Y. Liu, H. Pang, Exposing {001} crystal plane on hexagonal Ni-MOF with surface-grown cross-linked mesh-structures for electrochemical energy storage, *Small* (2019) 1902463, <https://doi.org/10.1002/smll.201902463>.
- [39] R.R. Salunkhe, Y.V. Kaneti, J. Kim, J.H. Kim, Y. Yamauchi, Nanoarchitectures for metal–organic framework-derived nanoporous carbons toward supercapacitor applications, *Acc. Chem. Res.* 49 (2016) 2796–2806, <https://doi.org/10.1021/acs.accounts.6b00460>.
- [40] D.Y. Lee, D.V. Shinde, E.-K. Kim, W. Lee, I.-W. Oh, N.K. Shrestha, J.K. Lee, S.-H. Han, Supercapacitive property of metal–organic-frameworks with different pore dimensions and morphology, *Microporous Mesoporous Mater.* 171 (2013) 53–57, <https://doi.org/10.1016%2Fj.micromeso.2012.12.039>.
- [41] S. Shankar, M. Lahav, M.E. van der Boom, Coordination-based molecular assemblies as electrochromic materials: ultra-high switching stability and coloration efficiencies, *J. Am. Chem. Soc.* 137 (2015) 4050–4053, <https://doi.org/10.1021/jacs.5b00429>.
- [42] N. Ellool-Dov, S. Shankar, D. Cohen, T. Bendikov, K. Rehav, L. Shimon, M. Lahav, M.E. van der Boom, Electrochromic metallo–organic nanoscale films: fabrication, color range, and devices, *J. Am. Chem. Soc.* 139 (2017) 11471–11481, <https://doi.org/10.1021/jacs.7b04217>.
- [43] J.F. Moulder, W.F. Stickle, P.E. Sobol, K.D. Bomben, in: J. Chastain (Ed.), *Handbook of X-ray Photoelectron Spectroscopy*, Perkin-Elmer Corporation, Minnesota, USA, 1992.
- [44] Y. Wang, Z. Hong, M. Wei, Y. Xia, Layered H₂Ti₆O₁₃-nanowires: a new promising pseudocapacitive material in non-aqueous electrolyte, *Adv. Funct. Mater.* 22 (2012) 5185–5193, <https://doi.org/10.1002/adfm.201200766>.
- [45] J.T. Zhang, S. Liu, G.L. Pan, G.R. Li, X.P. Gao, A 3D hierarchical porous α -Ni(OH)₂/Graphite nanosheet composite as an electrode material for supercapacitors, *J. Mater. Chem. A* 2 (2014) 1524–1529, <https://doi.org/10.1039/C3TA13578K>.
- [46] J. Yang, P. Xiong, C. Zheng, H. Qiu, M. Wei, Metal–organic frameworks: a new promising class of materials for a high performance supercapacitor electrode, *J. Mater. Chem. A* 2 (2014) 16640–16644, <https://doi.org/10.1039/C4TA04140B>.
- [47] R. Kaminker, L. Motiei, A. Gulino, I. Fragalà, L.J.W. Shimon, G. Evmenenko, P. Dutta, M.A. Iron, M.E. van der Boom, Stepwise assembly of coordination-based metal–organic networks, *J. Am. Chem. Soc.* 132 (2010) 14554–14561, <https://doi.org/10.1021/ja105518n>.
- [48] J. Choudhury, R. Kaminker, L. Motiei, G. de Ruiter, M. Morozov, F. Lupo, A. Gulino, M.E. van der Boom, Linear vs exponential formation of molecular-based assemblies, *J. Am. Chem. Soc.* 132 (2010) 9295–9297, <https://doi.org/10.1021/ja104203v>.
- [49] M. Altman, A.D. Shukla, T. Zubkov, G. Evmenenko, P. Dutta, M.E. van der Boom, Controlling structure from the bottom-up: structural and optical properties of layer-by-layer assembled palladium coordination-based multilayers, *J. Am. Chem. Soc.* 128 (2006) 7374–7382, <https://doi.org/10.1021/ja061026e>.
- [50] M.T. Stone, J.S. Moore, Supramolecular chelation based on folding, *J. Am. Chem. Soc.* 127 (2005) 5928–5935, <https://doi.org/10.1021/ja050713n>.
- [51] S. Leininger, B. Olenyuk, P.J. Stang, Self-assembly of discrete cyclic nanostructures mediated by transition metals, *Chem. Rev.* 100 (2000) 853–908, <https://doi.org/10.1021/cr960132a>.
- [52] R. Kaminker, R. Popovitz-Biro, M.E. van der Boom, Coordination-polymer nanotubes and spheres: a ligand-structure effect, *Angew. Chem. Int. Ed.* 50 (2011) 3224–3226, <https://doi.org/10.1002/anie.201008193>.
- [53] C. Molji, A. Aashish, A.S. Neethu, S.J. Devaki, Self-assembled polyaniline nanowires stippled graphene-3-pentadecylphenyl phosphate hybrid nanocomposite based green sustainable electrodes for supercapacitors, *J. Mater. Chem. A* 5 (2017) 16636–16645, <https://www.x-mol.com/paperRedirect/339420>.
- [54] S. Kondrat, P. Wu, R. Qiao, A.A. Kornyshev, Accelerating charging dynamics in subnanometre pores, *Nat. Mater.* 13 (2014) 387–393, <https://doi.org/10.1038/nmat3916>.
- [55] Z.-X. Li, X. Zhang, Y.-C. Liu, K.-Y. Zou, M.-L. Yue, Controlling the BET surface area of porous carbon by using the Cd/C ratio of a Cd–MOF precursor and enhancing the capacitance by activation with KOH, *Chem. Eur. J.* 22 (2016) 17734–17747, <https://doi.org/10.1002/chem.201603072>.
- [56] P.M. Anjana, M.R. Bindhu, M. Umadevi, R.B. Rakhi, Antibacterial and electrochemical activities of silver, gold, and palladium nanoparticles dispersed amorphous carbon composites, *Appl. Surf. Sci.* 479 (2019) 96–104, <https://doi.org/10.1016/j.apsusc.2019.02.057>.
- [57] Y. Hao, K. Santhakumar, S.P. Amareesh, J. Jae-Hyung, S.L. Yun, L. Wu, Graphene supercapacitor with both high power and energy density, *Nanotechnology* 28 (2017) 445401, <https://doi.org/10.1088/1361-6528/aa8948>.
- [58] S.K. Bhardwaj, N. Bhardwaj, R. Kaur, J. Mehta, A.L. Sharma, K.-H. Kim, A. Deep, An overview of different strategies to introduce conductivity in metal–organic frameworks and miscellaneous applications thereof, *J. Mater. Chem. A* 6 (2018) 14992–15009, <https://doi.org/10.1039/c8ta04220a>.
- [59] C. Largeot, C. Portet, J. Chmiola, P.-L. Taberna, Y. Gogotsi, P. Simon, Relation between the ion size and pore size for an electric double-layer capacitor, *J. Am. Chem. Soc.* 130 (2008) 2730–2731, <https://doi.org/10.1021/ja7106178>.
- [60] K.M. Choi, H.M. Jeong, J.H. Park, Y.-B. Zhang, J.K. Kang, O.M. Yaghi, Supercapacitors of nanocrystalline metal–organic frameworks, *ACS Nano* 8 (2014) 7451–7457, <https://doi.org/10.1021/nn502709z>.
- [61] S. Wu, J. Liu, H. Wang, H. Yan, A review of performance optimization of MOF-derived metal oxide as electrode materials for supercapacitors, *Int. J. Energy Res.* 43 (2019) 697–716, <https://doi.org/10.1002/er.4143>.
- [62] B.J. Yoon, S.-H. Jeong, K.-H. Lee, H.S. Kim, C.G. Park, J.H. Han, Electrical properties of electrical double layer capacitors with integrated carbon nanotube electrodes, *Chem. Phys. Lett.* 388 (2004) 170–174, <https://doi.org/10.1016/j.cplett.2004.02.071>.
- [63] H.Y. Chen, X. Chang, D.M. Chen, J.B. Liu, P. Liu, Y. Xue, H.L. Lin, S. Han, Graphene-karst cave flower-like Ni–Mn layered double oxides nanoarrays with energy storage electrode, *Electrochim. Acta* 220 (2016) 36–46, <https://doi.org/10.1016/j.electacta.2016.10.019>.
- [64] R.H. Wang, A. Jayakumar, C. Xu, J.M. Lee, Ni(OH)₂ nanoflowers/graphene hydrogels: a new assembly for supercapacitors, *ACS Sustain. Chem. Eng.* 4 (2016) 3736–3742, <https://doi.org/10.1021/acsschemeng.6b00362>.
- [65] Y. Yan, P. Gu, S. Zheng, M. Zheng, H. Pang, H. Xue, Facile synthesis of an accordion-like Ni-MOF superstructure for high-performance flexible supercapacitors, *J. Mater. Chem. A* 4 (2016) 19078–19085, <https://doi.org/10.1039/c6ta08331e>.
- [66] J. Xu, C. Yang, Y. Xue, C. Wang, Cao, Z.J. Chen, Facile synthesis of novel metal-organic nickel hydroxide nanorods for high performance supercapacitor, *Electrochim. Acta* 211 (2016) 595–602, <https://doi.org/10.1016/j.electacta.2016.06.090>.
- [67] S.S. Siwal, Q. Zhang, C. Sun, V.K. Thakur, Graphitic carbon nitride doped copper–manganese alloy as high–performance electrode material in supercapacitor for energy storage, *Nanomaterials* 10 (2020) 2, <https://doi.org/10.3390/nano10010002>.
- [68] B. Vedhanarayanan, B. Babu, M.M. Shaijumon, A. Ajayaghosh, Exfoliation of reduced graphene oxide with self-assembled π -gelators for improved electrochemical performance, *ACS Appl. Mater. Interfaces* 9 (2017) 19417–19426, <https://doi.org/10.1021/acsami.6b09418>.
- [69] Z. Zhao, J. Ding, R. Zhu, H. Pang, The synthesis and electrochemical applications of core–shell MOFs and their derivatives, *J. Mater. Chem. A* 7 (2019) 15519–15540, <https://doi.org/10.1039/C9TA03833G>.
- [70] S.S. Siwal, S. Thakur, Q.B. Zhang, V.K. Thakur, Electrocatalysts for electro-oxidation of direct alcohol fuel cell: chemistry and applications, *Mater. Today Chem.* 14 (2019) 100182, <https://doi.org/10.1016/j.mtchem.2019.06.004>.
- [71] Y. Hua, L. Li, C. Chen, H. Pang, Cobalt based metal–organic frameworks and their derivatives for electrochemical energy conversion and storage, *Chem. Eng. J.* 370 (2019) 37–59, <https://doi.org/10.1016/j.cej.2019.03.163>.

- [72] R. Abazari, S. Sanati, A. Morsali, A.M.Z. Slawin, C.L. Carpenter-Warren, W. Chen, A. Zheng, Ultrafast post-synthetic modification of a pillared cobalt(II)-based metal-organic framework via sulfurization of its pores for high-performance supercapacitors, *J. Mater. Chem. A* 7 (2019) 11953–11966, <https://doi.org/10.1039/C9TA01628G>.
- [73] B.Y. Guan, X.Y. Yu, H.B. Wu, X.W. Lou, Complex nanostructures from materials based on metal-organic frameworks for electrochemical energy storage and conversion, *Adv. Mater.* 29 (2017) 1703614, <https://doi.org/10.1002/adma.201703614>.
- [74] H. Huang, J.R. Li, K. Wang, T. Han, M. Tong, L. Li, Y. Xie, Q. Yang, D. Liu, C. Zhong, An *in situ* self-assembly template strategy for the preparation of hierarchical-pore metal-organic frameworks, *Nat. Commun.* 6 (2015) 8847, <https://doi.org/10.1038/ncomms9847>.
- [75] J. Zhou, B. Wang, Emerging crystalline porous materials as a multifunctional platform for electrochemical energy storage, *Chem. Soc. Rev.* 46 (2017) 6927–6945, <https://doi.org/10.1039/c7cs00283a>.
- [76] A.A. Talin, A. Centrone, A.C. Ford, M.E. Foster, V. Stavila, P. Haney, R.A. Kinney, V. Szalai, F. El Gabaly, H.P. Yoon, F. Leonard, M.D. Allendorf, Tunable electrical conductivity in metal-organic framework thin-film devices, *Science* 343 (2014) 66–69, <https://doi.org/10.1126/science.1246738>.

Ligand-Controlled Electrochromic Diversification with Multilayer Coated Metallosupramolecular Polymer Assemblies

Indulekha Mukkatt, Anjali Nirmala, Nayan Dev Madhavan, Sreejith Shankar,* Biswapriya Deb, and Ayyappanpillai Ajayaghosh*



Cite This: <https://dx.doi.org/10.1021/acsami.0c20428>



Read Online

ACCESS |



Metrics & More



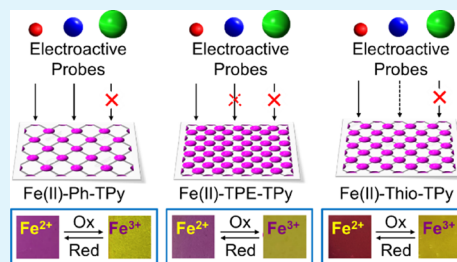
Article Recommendations



Supporting Information

ABSTRACT: Designing surface-confined molecular systems capable of expressing changes in functional properties as a result of slight variations in chemical structure under the influence of an external stimulus is of contemporary interest. In this context, we have designed three tetraterpyridine ligands with variations in their core architecture (phenyl vs tetraphenylethynyl vs bithiophene) to create spray-coated electrochromic assemblies of iron(II)-based metallosupramolecular polymer network films on transparent conducting oxide substrates. These assemblies exhibited molecular permeability and spectroelectrochemical properties that are in turn dictated by the ligand structure. Electrochromic films with high coloration efficiencies (up to 1050 cm²/C) and superior optical contrast (up to 76%) with a concomitant color-to-color redox transition were readily achieved. These functional switching elements were integrated into sandwich-type electrochromic cells (CE up to 641 cm²/C) that exhibited high contrast ratios of up to 56%, with attractive ON–OFF ratios, fast switching kinetics, and high operational stability. Every measurable spectroelectrochemical property of the films and devices is an associated function of the ligand structure that coordinates the same metal ion to different extents. While exhibiting a ligand-structure-induced differential metal coordination leading to porosity and spectroelectrochemical diversification, these assemblies allow the creation of electrochromic patterns and images by a simple spray-coating technique.

KEYWORDS: electrochromism, metallosupramolecular polymers, molecular permeability, ligands, supramolecular assembly, spectroelectrochemistry



1. INTRODUCTION

New and improved molecular and supramolecular systems with designed functions are being actively explored for driving next-generation clean and energy-efficient technologies.^{1–3} In this context, smart electrochromic devices (ECDs) with a low energy footprint are envisioned to contribute to efficient energy management.^{4,5} The tunable color and transparency of electrochromic (EC) coatings can regulate light and heat transmission properties, leading to efficient indoor lighting and cooling.^{6–8} Though several materials are being explored for electrochromic color switching, the real-world applications of such systems are hindered by the exorbitant cost, moderate to low efficiency, laborious processibility, slow color switching, and relatively low cycle life. Metal oxides and conjugated polymers have been extensively investigated as efficient electrochromic materials.^{9–13} The large-scale application of metal oxides, though one of the best reported EC systems,^{9,14} is limited by the high cost of vacuum processing. Therefore, solution processible materials that change color efficiently with low applied voltage are of significant commercial interest.¹⁰ Coordination-based metal–organic thin films are a relatively less investigated class of electrochromic materials, with excellent prospects in terms of optical contrast, redox reversibility, processibility, power consumption, and cycle life.^{15–22}

While the rational design of porous materials has opened up exciting avenues for several applications,^{23,24} nanoscopic control over the internal structure of surface-confined porous metal–organic networks with in-plane periodicity is scarcely reported.²⁵ Owing to their rich structural diversities, metallosupramolecular coordination polymers have attracted immense attention in catalysis, carbon capture, color switching, sensing, adsorption and separation, nanoarchitectonics, etc.^{26–30} Electrochromic color tunability in metallosupramolecular polymers has been achieved using modular approaches, and their structure–property relationship has been established.^{31–34} Tunable spectroelectrochemical properties are also achieved using multimetalated surface-confined assemblies.^{35,36} Ditopic terpyridine ligand systems are extensively investigated as EC materials; nevertheless, the metal ion induced electrochromic self-assembly of tetratopic terpyridines has been rarely reported.^{31–36} Structural modification using electron-with-

Received: November 16, 2020

Accepted: January 11, 2021

63 drawing/donating groups may have a predictable impact on the
64 electrochromic attributes of such materials.^{13,32–34} The effect of
65 the interaction of metal ions with conducting polymers on their
66 electrochromic activity for the detection of Cu(II) has also been
67 reported.³⁷ However, electrochemical diversification based on
68 small variations in the core architecture of otherwise similar
69 molecular components in their thin film states is hard to predict.
70 A fundamental understanding of the internal structure, porosity,
71 and transport of electrons or materials in electrochromic thin
72 films mandated at effectively modulating their properties is in
73 need of attention.^{38,39} Combined with complex electron and
74 mass transfer processes, a diverse electro-optical behavior of
75 such systems, while efficiently modulating their smart response,
76 is extremely difficult to achieve.⁴⁰

77 In this study, we demonstrate the use of simple Fe(II)-
78 metallosupramolecular polymer network films (MPNFs)⁴¹
79 derived from different core-linked tetraterpyridine ligands
80 leading to electrochromic redox-active interfaces with molec-
81 ular-level control over their permeability and electro-optical
82 properties. Exceptionally high optical contrast (up to 76%) and
83 coloration efficiencies (up to 1050 cm²/C) were obtained for
84 these spray-coated films that exhibited color-to-color transitions.
85 The electrochromic devices (ECDs) fabricated from these
86 nanoscopic films (165 ± 6 nm thick) also exhibited high
87 coloration efficiencies (up to 641 cm²/C), cycling stability
88 (1000 redox switchings), and optical contrast (up to 56%). The
89 films and devices were found to switch color with relatively low
90 response times (0.5–3 s). This study provides one of the first
91 examples for metallosupramolecular assemblies with a similar
92 solution electrochemistry, wherein designed variations in ligand
93 structure dictate the extent of metal coordination and
94 differential molecular permeability, leading to spectroelectro-
95 chemical diversification (redox potential, optical contrast,
96 response time, voltage response, cycling stability, coloration
97 efficiency) in both film and device configurations.

2. EXPERIMENTAL SECTION

98 **2.1. Materials and Methods.** All chemicals and solvents were
99 purchased from Sigma-Aldrich, Merck, Spectrochem, and Alfa Aesar.
100 All reagents were used as received unless otherwise noted. All the
101 reactions and experiments were carried out in oven-dried glassware.
102 Moisture- and oxygen-sensitive reactions were carried out using dry
103 solvents and under an argon atmosphere. All organic extracts were dried
104 over anhydrous sodium or magnesium sulfate powder, and solvents
105 were removed under reduced pressure using a HEIDOLPH rotary
106 evaporator using a water bath below 50 °C.

107 **2.2. Instrumentation and Experimental Procedure.** ¹H and
108 ¹³C NMR spectra were recorded at 300 K on a 500 MHz (¹H) Bruker
109 Advance DPX spectrometer using TMS as an internal standard.
110 Chemical shifts are presented in ppm. High-resolution mass spectra
111 were obtained from a JEOL JSM 600. Matrix-assisted laser desorption
112 ionization time-of-flight (MALDI-TOF) mass spectra were obtained
113 using an AXIMA-CFR PLUS (SHIMADZU) MALDI-TOF mass
114 spectrometer using α -cyano-4-hydroxycinnamic acid as the matrix. The
115 solution state absorbance measurements were done on a Shimadzu
116 UV–vis spectrophotometer (UV-2600). Concentration-dependent
117 solution studies were carried out in a 1 cm quartz cuvette. Temperature
118 (25 °C) was regulated using a Shimadzu temperature controller. The
119 blank experiment with the corresponding solvent provided the baseline.
120 The solution was allowed to come to thermal equilibrium in a Hellma
121 Analytics 10 mm path length quartz cell in the thermostated (±0.1 °C)
122 cell holder of the spectrophotometer. The UV–vis spectra (25 °C) of
123 the MPNF modified FTO slides were obtained using an Ocean Optics
124 UV–vis modular spectrometer (DH-2000-BAL). The blank experi-
125 ment with the bare FTO slides provided the baseline. The thickness of

the samples was estimated using a Dektak XT profilometer. The surface
126 chemistry of MPNFs was analyzed using X-ray photoelectron
127 spectroscopy (XPS, PHI 5000 VersaProbe II, ULVAC-PHI Inc.,
128 USA) equipped with a microfocused (200 μ m, 15 KV) monochromatic
129 Al-K α X-ray source ($h\nu = 1486.6$ eV). Both survey spectra and narrow
130 scan (high-resolution spectra) were recorded. Survey scans were
131 recorded with an X-ray source power of 50 W and pass energy of 187.85
132 eV. High-resolution spectra of the major elements were recorded at
133 46.95 eV pass energy. XPS data were processed using PHI's Multipak
134 software. AFM images were recorded at ambient conditions using an
135 atomic force microscopy (AFM; Bruker Multimode Nanoscope V)
136 instrument operating under tapping mode. Microfabricated TiN
137 cantilever tips with a resonance frequency of 299 kHz and a spring
138 constant of 20–80 Nm⁻¹ was used. The roughness parameter was
139 estimated using the Nanoscope Analysis 1.5 software. Cyclic
140 voltammetry (CV, BASI CV-50 W) for samples in a solution state
141 was performed at room temperature using 0.1 M tetrabutylammonium
142 hexafluorophosphate (TBAPF₆) in CH₃CN as the supporting electro-
143 lyte, glassy carbon as the working electrode, the Ag/AgCl electrode as
144 the reference electrode, and a platinum wire as the counter electrode at
145 room temperature. Cyclic voltammetry of the films and devices was
146 performed on a PARSTAT 4000A Potentiostat. The MPNF modified
147 FTO served as the working electrode, platinum wire as the counter
148 electrode, Ag/AgCl as the reference electrode, and 0.1 M
149 tetrabutylammonium hexafluorophosphate (TBAPF₆) in CH₃CN as
150 the electrolyte for film state electrochemical studies.
151

2.3. Spectroelectrochemical Analysis. The spectroelectrochem-
152 ical response of the electrochromic devices and films was recorded on
153 an Ocean Optics Spectrometer DH-2000-BAL using a PARSTAT
154 4000A Potentiostat for the electrochemical redox process. Spectroelectro-
155 chemistry of films was done by dipping spray-coated films on FTO
156 electrodes in a 0.1 M TBAPF₆ (in dry acetonitrile) solution (Ag/AgCl
157 electrode and Pt wire as reference and counter electrodes, respectively).
158 The blank was done using a 0.1 M TBAPF₆ (in anhydrous acetonitrile)
159 solution in a cuvette having a 1 cm path length. Transmittance spectra
160 were obtained upon applying double potential steps (−3.0 and +3.0 V)
161 as a function of time. The change in %T at the MLCT wavelength (578,
162 580, and 584 nm) was monitored at different pulse widths (1–10 s) and
163 using different potential windows between −2.0 and +2.0 V and −3.0
164 and +3.0 V at a pulse width of 5 s. Switching stability was investigated by
165 switching between two potentials (−3.0 and +3.0 V) at a pulse width of
166 5 s for 1000 continuous redox switchings.
167

2.4. Molecular Permeability Studies. Molecular permeability
168 studies were performed using a three-electrode cell configuration
169 consisting of the MPNF modified FTO, Pt wire, and Ag/AgCl as
170 working, counter, and reference electrodes, respectively. The experi-
171 ments were performed at room temperature using 1.3 mM solutions of
172 the quinones **Q1–Q3** in a 0.05 M solution of TBAPF₆ in dry
173 acetonitrile purged with N₂.
174

2.5. Synthesis. **2.5.1. Synthesis of the Ligands.** **2.5.1.1. Synthesis**
175 **of 4-(2,2',6',2''-Terpyridine-4'-yl)phenylboronic Acid 1.** To a solution
176 of NaOH (4.8 g, 0.12 mol) in EtOH (80 mL), 4-formylphenylboronic
177 acid **2** (3.032 g, 0.02 mol) and 2-acetylpyridine **1** (5.39 g, 0.04 mol)
178 were added. After stirring at room temperature for 24 h, aq NH₄OH
179 (28%, 75 mL) was added, and the resulting mixture was refluxed for 20
180 h. The mixture was cooled to room temperature, and the solid was
181 collected by filtration and was washed with CHCl₃ to give the product **3**
182 as an off-white solid (Scheme S1). Yield: 4.686 g, 85%. ¹H NMR (500
183 MHz, CDCl₃, 300 K) δ : 8.70–8.68 (m, 2H, tpy-H3',5'), 8.65–8.62 (m,
184 4H, tpy-H6,6''), 8.00 (td, $J = 7.7, 1.8$ Hz, 2H, tpy-H4,4''),
185 7.75 (d, $J = 7.8$ Hz, 2H, Ph-H), 7.73 (d, $J = 8.0$ Hz, 2H, Ph-H), 7.48
186 (ddd, $J = 7.5, 4.8, 1.1$ Hz, 2H, tpy-H5,5''). ESI-MS (m/z): calcd for
187 [C₂₁H₁₆BN₃O₂ + H]⁺: 354.1314; found: 354.1366.
188

2.5.1.2. Synthesis of Ph-TPy. Tetrabromobenzene **4** (100 mg, 0.25
189 mmol), boronic acid **3** (538 mg, 6 equiv), Pd(PPh₃)₂Cl₂ (53.7 mg, 0.3
190 equiv), and Na₂CO₃ (806 mg, 30 equiv) were added to a glass pressure
191 tube. After three argon/evacuation cycles, H₂O (10 mL), toluene (30
192 mL), and *tert*-butyl alcohol (1.5 mL) were added under a flow of argon.
193 The pressure tube was sealed, and the mixture was stirred at 110 °C for
194 6 days. After cooling to room temperature, the mixture was extracted
195

196 with chloroform (50 mL × 2). The combined organic extracts were
197 washed with brine, dried over Na₂SO₄, and concentrated in vacuo. The
198 crude product was purified by column chromatography on a silica gel
199 using CHCl₃/MeOH (9:1) as the eluent to afford the ligand **Ph-TPy** as
200 a white solid (Scheme S2). Yield: 66 mg, 20%. ¹H NMR (500 MHz,
201 CDCl₃, 300 K) δ: 8.70 (s, 8H), 8.63 (d, J = 4.6 Hz, 8H), 8.58 (d, J = 8.0
202 Hz, 8H), 7.8–7.70 (m, 16H), 7.67 (s, 2H), 7.41 (d, J = 8.3 Hz, 8H),
203 7.25–7.23 (m, 8H). ¹³C NMR (125 MHz, CDCl₃, 300 K) δ: 155.30,
204 154.89, 148.72, 140.58, 138.49, 135.86, 135.77, 132.03, 129.46, 122.70,
205 120.29, 117.78. ESI-MS (*m/z*): calcd for [C₉₀H₅₈N₁₂ + H]²⁺: 654.7471;
206 found: 654.7465.

207 **2.5.1.3. Synthesis of TPE-TPy.** Step 1: synthesis of 1,1,2,2-
208 tetraphenylethylene **6**

209 An ice-cold suspension of zinc powder (6.259 g, 0.095 mol) in dry
210 THF (80 mL) was prepared in a three-necked flask under argon. TiCl₄
211 (15 mL, 0.055 mol) was injected slowly over a period of 30 min, the
212 ice–salt–water bath was removed, and the reaction mixture was heated
213 under reflux for 4 h. A solution of benzophenone **5** (5.00 g, 0.027 mol)
214 in dry THF (20 mL) was added slowly using a syringe, and the mixture
215 was refluxed overnight. The reaction mixture was cooled to room
216 temperature and was quenched with a saturated solution of sodium
217 carbonate (until the effervescence stopped) and was then extracted with
218 chloroform (100 mL × 3). The organic layer was washed with water
219 (120 mL × 3), the combined organic extracts were dried over sodium
220 sulfate, and the solvent was evaporated under reduced pressure. The
221 resulting crude product was purified by column chromatography on a
222 silica gel using hexane as the eluent (Scheme S3). Yield: 4.43 g, 49%. ¹H
223 NMR (500 MHz, CDCl₃, 300 K) δ: 7.05–7.00 (m, 12H), 6.98–6.94
224 (m, 8H). ESI-MS (*m/z*): calcd for [C₂₆H₂₀ + Na]⁺: 332.1463; found:
225 355.1467.

226 Step 2: synthesis of 1,1,2,2-tetrakis(4-bromophenyl)ethane **7**⁵³
227 Tetraphenylethylene **6** (1.66 g, 5 mmol) was dissolved in CH₂Cl₂
228 (100 mL) in a round-bottom flask, and then Br₂ (3.0 mL) was added
229 dropwise. The mixture was stirred at room temperature for 12 h, and
230 the reaction was quenched by aqueous Na₂S₂O₃ (20 mL). The mixture
231 was then extracted using CH₂Cl₂ (50 mL × 3). The organic layer was
232 washed with water (60 mL × 3), and the combined organic extracts
233 were dried over MgSO₄. The solvent was evaporated in vacuo, and the
234 residue was purified by column chromatography over a silica gel using
235 hexane as the eluent. Compound **7** was obtained as a white powder.
236 Yield: 3.05 g, 95%. ¹H NMR (500 MHz, CDCl₃, 300 K) δ: 7.19 (d, J =
237 8.2 Hz, 8H), 6.77 (d, J = 8.2 Hz, 8H).

238 Step 3: synthesis of TPE-TPy
239 1,1,2,2-Tetrakis(4-bromophenyl)ethane **7** (100 mg, 0.15 mmol),
240 boronic acid **3** (327 mg, 0.92 mmol), Pd(PPh₃)₂Cl₂ (32 mg, 0.046
241 mmol), and Na₂CO₃ (490.6 mg, 4.62 mmol) were added to a glass
242 pressure tube. After three argon/evacuation cycles, H₂O (10 mL),
243 toluene (30 mL), and *tert*-butyl alcohol (1.5 mL) were added under a
244 flow of argon. The pressure tube was sealed, and the mixture was stirred
245 at 110 °C for 6 days. After cooling to room temperature, the mixture
246 was extracted with CHCl₃ (50 mL × 2). The combined organic extracts
247 were washed with brine, dried over Na₂SO₄, and concentrated in vacuo.
248 The crude product was purified by column chromatography on a silica
249 gel using CHCl₃/MeOH (9:1) as the eluent to afford the TPE-TPy as a
250 white solid. Yield: 68 mg, 28%. ¹H NMR (500 MHz, CDCl₃, 300 K) δ:
251 8.78 (s, 8H), 8.74 (s, 8H), 8.68 (d, J = 7.7 Hz, 8H), 7.99 (d, J = 7.3 Hz,
252 8H), 7.88 (t, J = 7.9 Hz, 8H), 7.79–7.72 (m, 8H), 7.56–7.50 (m, 8H),
253 7.39–7.27 (m, 16H). ¹³C NMR (125 MHz, CDCl₃, 300 K) δ: 155.32,
254 154.98, 148.14, 138.27, 137.53, 135.84, 130.96, 126.70, 126.35, 125.50,
255 122.79, 120.38, 117.68, 113.04. MALDI TOF: calcd for [C₁₁₀H₇₂N₁₂]:
256 1561.60; found: 1561.69.

257 **2.5.1.4. Synthesis of Thio-TPy.** 3,3',5,5'-Tetrabromo-2,2'-bithio-
258 phene **8** (100 mg, 0.207 mmol), boronic acid **3** (438 mg, 1.24 mmol),
259 Pd(PPh₃)₂Cl₂ (43 mg, 0.062 mmol), and Na₂CO₃ (658 mg, 6.21
260 mmol) were added to a glass pressure tube. After three argon/
261 evacuation cycles, H₂O (10 mL), toluene (30 mL), and *tert*-butyl
262 alcohol (1.5 mL) were added under a flow of argon. The pressure tube
263 was sealed, and the mixture was stirred at 110 °C for 6 days. After
264 cooling to room temperature, the mixture was extracted with
265 chloroform (50 mL × 2). The combined organic extracts were washed

with brine, dried over Na₂SO₄, and concentrated in vacuo. The crude
product was purified by column chromatography on a silica gel using
CHCl₃/MeOH (9:1) as the eluent to afford the product **Thio-TPy** as a
white solid (Scheme S4). Yield: 56 mg, 17%. ¹H NMR (500 MHz,
CDCl₃, 300 K) δ: 8.78 (s, 8H), 8.74 (s, 8H), 8.68 (d, J = 7.7 Hz, 8H),
7.99 (d, J = 7.3 Hz, 8H), 7.88 (t, J = 7.9 Hz, 8H), 7.79–7.72 (m, 8H),
7.56–7.50 (m, 8H), 7.39–7.27 (m, 16H). ¹³C NMR (125 MHz,
CDCl₃, 300 K) δ: 155.32, 154.98, 148.14, 138.27, 137.53, 135.84,
130.96, 126.70, 126.35, 125.50, 122.79, 120.38, 117.68, 113.04.
MALDI TOF: calcd for [C₁₁₀H₇₂N₁₂]: 1395.44; found: 1395.85.

256 **2.5.2. Synthesis of the Metallosupramolecular Polymers for Spray
257 Coating.** A solution of FeCl₂·4H₂O (4.97 mg, 2 equiv) in MeOH was
258 added to a solution of the corresponding ligand (**Ph-TPy**: 6.5 mg, **TPE-
259 TPY**: 7.8 mg, **Bihio-TPY**: 6.97 mg) in CHCl₃ (5 mL). The final
260 concentration of the metallosupramolecular polymers was 0.3 mM, and
261 the freshly prepared solutions were spray coated on FTO glass
262 substrates using the automated spray coater without further
263 purification.

264 **2.6. Fabrication of MPNFs by Spray Coating the MPs on FTO
265 Substrates.** FTO glass substrates (2.5 × 2.5 cm) were cleaned by
266 washing in a soap solution followed by ultrasonication in water,
267 acetone, and isopropyl alcohol, each for 15 min. Spray coating was done
268 using the Nordson EFD EV Series automated dispensing system that
269 dispenses fluids in a preprogrammed pattern onto a workpiece.
270 Programs were created using the DispenseMotion software. A line
271 speed of 150 mm/s and a ptp speed of 200 mm/s were used. Ten sprays
272 of 0.3 mM solutions of the MPs are considered as one deposition step.

273 **2.7. Fabrication of Electrochromic Devices.** **2.7.1. Step 1:
274 Synthesis of the Gel Electrolyte**⁵⁴. LiClO₄ (0.9 g) was added to a
275 mixture of propylene carbonate (6.0 mL) and CH₃CN (10.0 mL) under
276 a flow of argon. To the above stirred solution, PMMA (2.1 g) was added
277 and the mixture was stirred at room temperature until the polymer was
278 completely dissolved (12 h) to obtain a transparent gel electrolyte
279 system.

280 **2.7.2. Step 2: ECD Fabrication.** FTO glass substrates (2.5 × 2.5 cm,
300 for counter/reference electrodes) were cleaned by washing with soap
301 solutions followed by ultrasonication in water, acetone, and isopropyl
302 alcohol, each for 15 min. The MPNF-modified FTO substrates (2.5 ×
303 2.5 cm) were rinsed in dry acetonitrile and dried under a flow of argon.
304 The bare FTO substrates were placed on top of these modified
305 substrates and was held tight with an insulating two-sided gorilla tape
306 (thickness < 200 μm) at each end to prevent short circuits as well as to
307 hold the setup together. The gel electrolyte was then injected using a
308 syringe to form a sandwich-type architecture and was dried in an air
309 oven at 60 °C for 10 min. The sandwich cells were then sealed. The
310 ends were connected to a potentiostat/galvanostat, and the electro-
311 chromic properties of the solid-state setup were studied. 312

3. RESULTS AND DISCUSSION

313 **3.1. Synthesis, Fabrication, and Characterization of
314 Thin Films.** Metallosupramolecular polymers (MPs) of three
315 tetraterpyridine-based ligands (**Ph-TPy**, **TPE-TPy**, and **Thio-
316 TPY**; Figure 1) with variations in their core architecture (phenyl
317 vs tetraphenylethynyl vs bithiophene) were prepared using
318 Fe(II) as the coordinating metal. Details of the synthesis and
319 characterization of the ligands are shown in the Supporting
320 Information. The formation of the metallopolymers was
321 confirmed by the emergence of characteristic MLCT bands in
322 the UV–vis spectra along with a concomitant decrease in ligand
323 emission. Increasing the concentration above 300 μM in
324 methanol led to instantaneous precipitation, further corroborat-
325 ing the formation of the metallosupramolecular polymers. FT-IR
326 showed a shift of C=C stretching vibrations from 1582–1585
327 to 1600–1603 cm⁻¹, which is characteristic for the metal
328 complexation of terpyridine ligands.

329 Methanol solutions of the Fe(II) MPs (0.3 mM) were spray
330 coated to generate multilayer electrochromic assemblies on
331 TCO substrates. The electroactive components of these 331

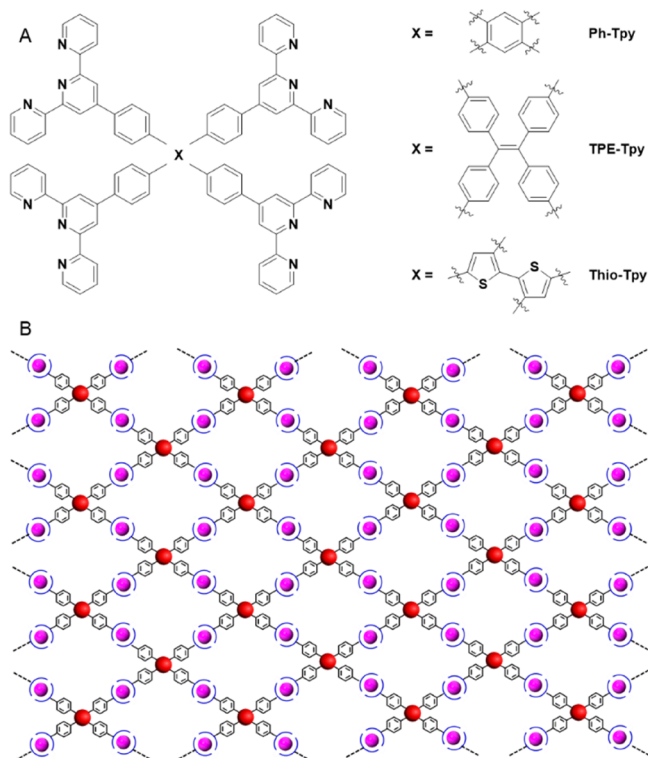


Figure 1. (A) Molecular structures of the terpyridine ligands used in this study. (B) A schematic illustration of the structure of the metallosupramolecular polymers. The core (Ph, TPE, and Thio) is shown in red, the coordinating terpyridines are shown in blue, and Fe(II) is shown in pink. The corresponding MPs are denoted as Fe(II)-Ph-Tpy, Fe(II)-TPE-Tpy, and Fe(II)-Thio-Tpy.

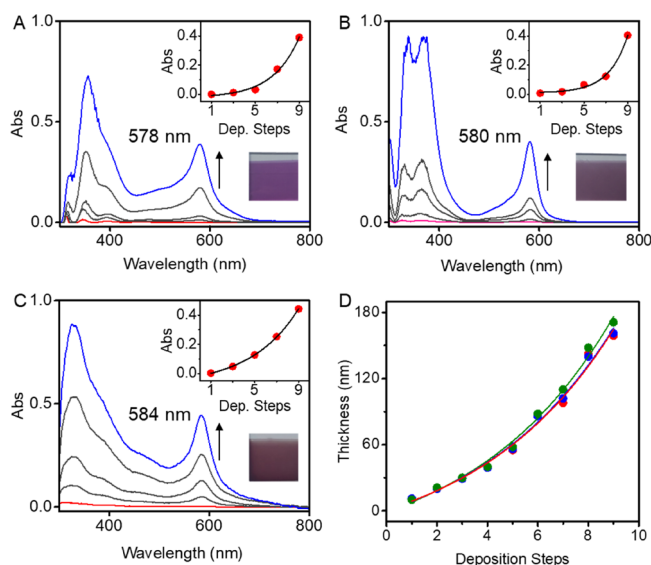


Figure 2. UV-vis spectra of the assemblies formed by spray coating the methanol solutions (0.3 mM) of the ligands containing 2 equiv of FeCl₂: (A) Ph-Tpy, (B) TPE-Tpy, and (C) Thio-Tpy. The MLCT bands are also shown. The exponential increase in the absorbance of the MLCT bands with the number of deposition steps and the corresponding photographs of the FTO glass substrates (3 × 3 cm) after nine deposition steps are shown in the insets. R² > 0.99 for all fits. (D) The change in the thickness of the spray-coated films with the number of deposition steps for the assemblies obtained using Fe(II) MPs of Ph-Tpy (red), TPE-Tpy (blue), and Thio-Tpy (green). R² > 0.99 for all fits.

assemblies are the well-defined coordination entities bridged by Fe(II) centers.^{21,32,34,42} Terpyridine ligands generally bind divalent metal ions to form bis(terpyridine) complexes with a defined *D*_{2d} symmetry.⁴⁰ Such assemblies are known to exhibit a one-electron redox behavior.^{21,32,34} The intense color in the ground state of these MPs is characterized by a strong metal-to-ligand charge transfer (572–575 nm) with high molar extinction coefficients ($\epsilon \sim 3\text{--}5 \text{ M}\cdot\text{cm}^{-1}$ in methanol, Figure S1).⁴³ The assemblies were characterized using UV-vis spectroscopy, atomic force microscopy (AFM), X-ray photoelectron spectroscopy (XPS), electrochemistry and spectroelectrochemistry, and thickness measurements using a profilometer. *Ex situ* absorption spectra measured after alternate deposition steps and thickness measurements confirmed a ligand-structure-independent exponential growth model for these nanoscopic assemblies (Figure 2). The intensity of the characteristic λ_{MLCT} (578 nm for Fe(II)-Ph-Tpy, 580 nm for Fe(II)-TPE-Tpy, and 584 nm for Fe(II)-Thio-Tpy) and thickness of the 350 MPNFs increased exponentially with deposition steps (Figure 2, insets). A second MLCT band at wavelengths < 400 nm was also observed for all these thin films (Figure 2A–C). The initial coating process most likely resulted in a single layer or bilayer of the metallosupramolecular polymers as corroborated by the absorption spectra and a thickness of ~ 10 nm. The subsequent spray coating leads to a uniform single-layer coating before additional layers start to assemble. However, after the formation of a near-complete single layer, multiple spray coatings facilitate the self-assembly of the metallosupramolecular polymers via intermolecular/interlayer interactions, leading to the observed exponential growth of the film. The variations in the core group

resulted in different shades of purple to brownish colors for these metallosupramolecular polymer network films (Figure 2A–C insets, D).

AFM images showed grainlike morphologies for all the MPNFs (Figure S2).¹⁷ The films of Fe(II)-Thio-Tpy were found to be composed of uniformly sized grains (45 ± 5 nm), while the others exhibited a larger size distribution. The films obtained from Fe(II)-TPE-Tpy revealed the prevalence of clustered grains. Consequently, these films had a comparably higher roughness ($R_{\text{rms}} \sim 35$ nm), while those based on Fe(II)-Ph-Tpy and Fe(II)-Thio-Tpy exhibited a slightly lower roughness ($R_{\text{rms}} = 23 \pm 2$ nm), after nine deposition steps. All the MPNFs appeared rather free of defects to the naked eye (Figure 2, insets).

The cyclic voltammograms of the assemblies exhibited an exponential increase in the current density with the number of deposition steps (Figure 3). A linear correlation between the thickness of the assemblies and current densities up to nine deposition steps suggests that nearly all metal centers remain electroactive at least until a thickness of 165 ± 6 nm (Figure S3). The current densities vary linearly with scan rate (10–600 mV s⁻¹) and exponentially with the square root of scan rate (Figure S4). This observation is indicative of a surface-confined electrochemical redox process that is not limited by slow diffusion.^{16,33,44}

The growth models, thickness, and overall morphologies of the metallosupramolecular assemblies were found to be more or less unaffected by the variations in the core structure of the parent ligands. In contrast to the reports by Kurth and co-workers, these observations suggest a negligible effect of the molecular mass and viscosity of the metallosupramolecular MPs on the formation and electro-optical properties of the MPNFs.³¹

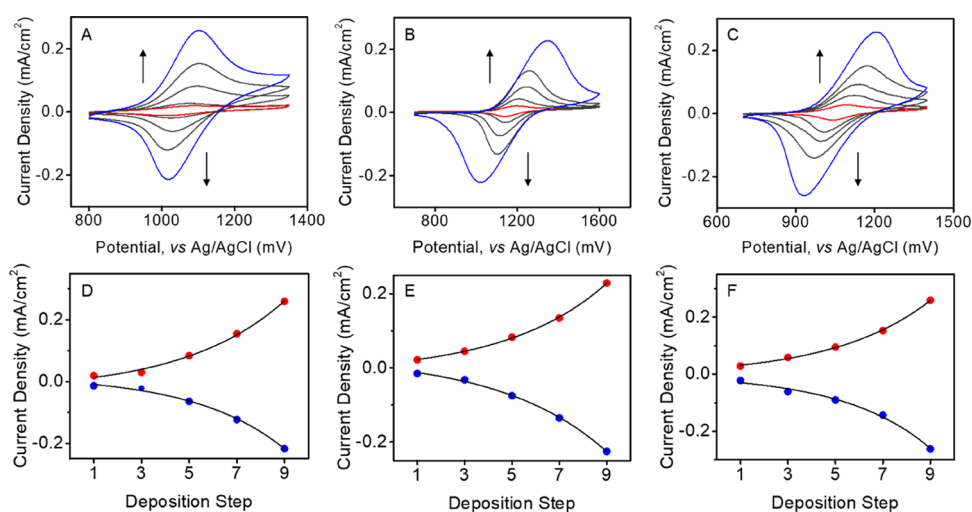


Figure 3. Cyclic voltammograms of the assemblies formed by spray coating the methanol solutions (0.3 mM) of the ligands containing 2 equiv of FeCl₂: (A) Ph-Tpy, (B) TPE-Tpy, and (C) Thio-Tpy. The exponential increase in the current densities for the assemblies constructed from (D) Fe(II)-Ph-Tpy, (E) Fe(II)-TPE-Tpy, and (F) Fe(II)-Thio-Tpy with the number of deposition steps. The current densities in the oxidative and reductive directions are shown in red and blue circles, respectively. $R^2 > 0.99$ for all fits. The experiments were carried out using the modified FTO substrate as the working electrode, Ag/AgCl as the reference electrode, and platinum wire as the counter electrode. Bu₄PF₆ (0.1 M) in acetonitrile was used as the supporting electrolyte.

394 However, the electrochemical and spectroelectrochemical
395 profiles indeed depend on the ligand structure. For instance,
396 all the Fe(II) MPs in the solution (acetonitrile, 15 μ M)
397 exhibited similar redox potentials; however, the oxidation and
398 reduction potentials of the films obtained after nine deposition
399 steps were distinctly different, with a larger peak-to-peak
400 separation (Figure S5, Table S1).

401 After nine deposition steps, the molecular assemblies
402 constructed using Fe(II)-Ph-Tpy, Fe(II)-TPE-Tpy, and Fe-
403 (II)-Thio-Tpy exhibited a characteristic Fe^{2+/3+} redox couple
404 with half-wave potentials ($E_{1/2}$) of 1.06, 1.12, and 1.14 V,
405 respectively (Figure S4B, Table S1). This single-electron redox
406 process is accompanied by a visually perceivable change in color.
407 While many Fe-oligopyridine systems generally exhibit a color-
408 to-colorless redox behavior,^{16–18} we observed typical color-to-
409 color transitions. Electrochemical oxidation leads to a decrease
410 in the intensity of the MLCT bands with a concomitant increase
411 in ligand-centered charge transfer transitions, leading to a yellow
412 color in the oxidized state (Figure S6). The effect of the
413 variations in ligand structure was evident in the optical contrast
414 at λ_{MLCT} and was found to be higher for the assemblies
415 constructed from Fe(II)-Ph-Tpy (>76%) followed by those
416 from Fe(II)-Thio-Tpy (>60%) and Fe(II)-TPE-Tpy (~40%,
417 Figure S6).

418 **3.2. Spectroelectrochemical Diversification in the Film**
419 **State.** The spectroelectrochemical properties of the assemblies
420 were investigated using double potential steps and were
421 recorded as optical changes over time (Figure S7). The overall
422 pulse width dependent changes in the contrast ratios of Fe(II)-
423 TPE-Tpy MPNFs are due to the combined effect of an increase
424 in %T during bleaching (oxidation) and a concomitant decrease
425 in %T during coloration (reduction, Figures S7B and S8B).
426 However, %T during the coloration of Fe(II)-Ph-Tpy- and
427 Fe(II)-Thio-Tpy-based films was found to be more or less
428 independent of pulse width (>2 s, Figures S7A,C and S8A,C).
429 Therefore, the overall changes in contrast ratios for these films
430 stem almost exclusively from the increase in %T during
431 bleaching (oxidation). Thus, the ligand structure is directly

expressed in the ease of redox reactions in these MPNFs within a
defined potential window: oxidation and reduction are equally
demanding for the films of Fe(II)-TPE-Tpy; the near-complete
reduction of Fe³⁺ centers to Fe²⁺ is facile even at low switching
times (2 s) in Fe(II)-Ph-Tpy- and Fe(II)-Thio-Tpy-based
films; the oxidation process (Fe²⁺ \rightarrow Fe³⁺), on the other hand, is
rather difficult when the pulse width is low.

The response time (time taken for >90% of the color to switch
in oxidative and reductive directions) was also found to be an
associated function of the ligand structure. The MPNFs based
on Fe(II)-Ph-Tpy exhibited response times of 1.6 and 1 s for
bleaching and coloration, respectively, at a pulse width of 10 s
(Figure S9A). The response times, under identical operational
conditions, for Fe(II)-TPE-Tpy- and Fe(II)-Thio-Tpy-based
assemblies were comparably higher: 2.6 s (bleaching) and 1.4 s
(coloration), and 2.9 s (bleaching) and 1.4 s (coloration),
respectively (Figure S9B,C). The observed fast coloration may
be attributed to the rapid injection of electrons (reduction, Fe³⁺
 \rightarrow Fe²⁺) and counter ions into the films as compared to the
electrochemically slower rejection of electrons (oxidation, Fe²⁺
 \rightarrow Fe³⁺) and counter ions during bleaching.^{45–47}

An equally important parameter that determines the perform-
ance of electrochromic systems is their coloration efficiency.
Coloration efficiency is defined as the change in optical density
per unit charge ejected or injected per unit area of the active
electrode. The molecular assemblies were found to have high
coloration efficiencies (at λ_{MLCT}) but dictated by the core
architecture of the parent ligands: Fe(II)-Ph-Tpy (1049.5 cm²/
C) > Fe(II)-TPE-Tpy (756.5 cm²/C) > Fe(II)-Thio-Tpy
(473.8 cm²/C).

The subtle differences in the (spectro)electrochemical
properties of the assemblies with similar modes of deposition
may be attributed to the differences in their internal arrange-
ment and structure. XPS data of all three ligands (Ph-Tpy, TPE-
Tpy, and Thio-Tpy) showed the characteristic peak corre-
sponding to the binding energy of N 1s at 398.8 eV (Figure
S10A,D,G). Characteristic peaks corresponding to Fe²⁺ 2p_{3/2}
(708.85 \pm 0.05 eV) and Fe²⁺ 2p_{1/2} (721.55 \pm 0.05 eV) were

470 unambiguously observed in the XPS spectra of Fe(II)-Ph-Tpy,
 471 Fe(II)-TPE-Tpy, and Fe(II)-Thio-Tpy (Figure S10B,E,H).
 472 However, two peaks corresponding to N 1s (398.65 ± 0.15 and
 473 399.75 ± 0.15 eV) were observed for the MPs as opposed to a
 474 single peak in the spectra of the parent ligands (Figure
 475 S10C,F,I). This observation is indicative of incomplete
 476 coordination of the terminal terpyridines. The N 1s peak at
 477 398.65 ± 0.15 eV corresponds to the free tpy-nitrogen, while
 478 that at 399.75 ± 0.15 eV represents the Fe(II)-coordinated
 479 nitrogen. The ratio of the two N 1s peak areas is a direct measure
 480 of the extent of coordination in these assemblies. While the
 481 MPNFs of Fe(II)-Ph-Tpy and Fe(II)-Thio-Tpy showed an
 482 approximately 1:1 ratio of the coordinated and free tpy-
 483 nitrogens, Fe(II)-TPE-Tpy exhibited a ratio of $\sim 1:2.5$. There-
 484 fore, the ligand structure determines the extent of coordination
 485 of the terminal terpyridines, which in turn is most likely
 486 expressed in the electro-optical properties of the assemblies. The
 487 possible effect of the signal depth (~ 20 nm vs film thickness of
 488 165 ± 6 nm) is excluded as comparable data were obtained from
 489 both the films and isolated powders of the metallosupramo-
 490 lecular polymers.¹⁷

491 **3.3. Molecular Permeability in the Film State.** These
 492 observations prompted us to explore their differential molecular
 493 permeability using the cyclic voltammetric response of three
 494 quinone-based redox probes of different molecular dimensions
 495 at identical concentration (1.3 mM, Figure 4A).⁴⁸ The size-
 496 selective transfer of molecular probes through surface-confined
 497 thin films has been explored based on known cavity size and
 498 molecular dimensions of the probes.^{48–51} However, MPNFs
 499 with small variations in their core architecture as in this study,
 500 which do not necessarily reflect their internal arrangements and
 501 resulting pore sizes, are generally challenging as thin-film
 502 molecular sieves.^{49,52,53} Three sets of MPNFs with varying
 503 thicknesses were used to assess their molecular sieving
 504 properties.⁵⁴

505 The current density corresponding to the redox peaks of the
 506 molecular probes gives a direct evidence for the extent of
 507 permeation. The small-sized 1,4-benzoquinone **Q1** was found to
 508 permeate all the assemblies irrespective of their thickness (up to
 509 39.5 ± 0.5 nm, Figure 4B,D,F) and porosity, whereas the bulkier
 510 3,3',5,5'-tetra-*tert*-butyldiphenylquinone **Q3** was found not to
 511 traverse through any of the thin films (minimum thickness of 10
 512 nm, Figure S11). This size exclusion is indicative of a porosity of
 513 the assemblies that ranges between the molecular dimensions of
 514 the probes **Q1** and **Q3**. A high degree of selective permeation
 515 was observed for a probe **Q2** of a molecular size in between that
 516 of **Q1** and **Q3** (Figure 4C,E,G).

517 The amount of **Q1** that reached the FTO surface was
 518 dependent on both the film thickness^{55–57} and the core
 519 structure of the ligand. At a thickness of 10.5 ± 0.5 nm (one
 520 deposition step), the films constructed from Fe(II)-Ph-Tpy
 521 allowed more of **Q1** to permeate as compared to those of Fe(II)-
 522 TPE-Tpy and Fe(II)-Thio-Tpy (Figure 4B). As the thickness of
 523 the films increased (29.5 ± 0.5 and 39.5 ± 0.5 nm), their
 524 permeability decreased. However, a higher extent of perme-
 525 ability was consistently observed for Fe(II)-Ph-Tpy-based films
 526 followed by Fe(II)-Thio-Tpy, and the lowest permeability was
 527 observed for the films of Fe(II)-TPE-Tpy (Figure 4D,F),
 528 irrespective of the film thickness.

529 This result gave a first indication of the higher porosity for the
 530 films based on Fe(II)-Ph-Tpy followed by Fe(II)-Thio-Tpy
 531 and Fe(II)-TPE-Tpy and was further confirmed by using a
 532 second molecular probe **Q2** of a slightly larger dimension. At a

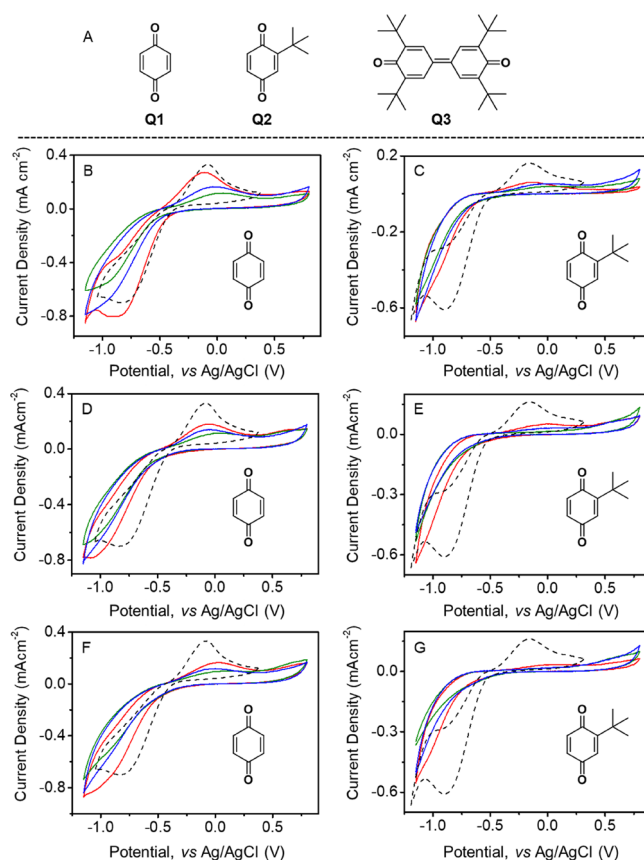


Figure 4. (A) Molecular structures of the redox probes **Q1–Q3**. Cyclic voltammograms of the molecular probes **Q1** and **Q2** (1.3 mM) obtained using MPNFs of Fe(II)-Ph-Tpy (red), Fe(II)-TPE-Tpy (blue), and Fe(II)-Thio-Tpy (green) as working electrodes at a film thickness of (B, C) 10.5 ± 0.5 nm, (D, E) 29.5 ± 0.5 nm, and (F, G) 39.5 ± 0.5 nm. Ag/AgCl and platinum wire were used as the reference and counter electrodes, respectively. Bu₄PF₆ (0.05 M) in acetonitrile was used as the supporting electrolyte. The thickness of the assemblies was estimated from profilometer measurements.

533 thickness of 10.5 ± 0.5 nm (one deposition step), all the films
 534 were permeable to the probe **Q2** in the order Fe(II)-Ph-Tpy >
 535 Fe(II)-Thio-Tpy > Fe(II)-TPE-Tpy (Figure 4C). Increasing
 536 the thickness to 29.5 ± 0.5 nm (three deposition steps) resulted
 537 in the selective permeation of the probe **Q2**. The films based on
 538 Fe(II)-Ph-Tpy and Fe(II)-Thio-Tpy were still permeable
 539 (Fe(II)-Ph-Tpy > Fe(II)-Thio-Tpy), and those based on
 540 Fe(II)-TPE-Tpy did not allow the probe to penetrate as
 541 indicated by the absence of the peaks in the corresponding CV
 542 (Figure 4E). At a still higher film thickness (39.5 ± 0.5 nm, four
 543 deposition steps), only the films based on Fe(II)-Ph-Tpy were
 544 found to be permeable (Figure 4G). The size-selective
 545 permeation achieved in these molecular assemblies suggests
 546 their porosity to be in the order Fe(II)-Ph-Tpy > Fe(II)-Thio-
 547 Tpy > Fe(II)-TPE-Tpy.

548 The distorted shapes of the cyclic voltammograms are most
 549 likely due to the diffusive nature of mass transport.⁴⁸ Two
 550 mechanisms may be operating under these experimental
 551 conditions: a charge transfer mechanism, whereby the probes
 552 get oxidized at the thin film–solution interface, or a diffusive
 553 mechanism, whereby the probes get oxidized at the thin film–
 554 FTO interface.^{48,58–60} The former mechanism may be excluded
 555 based on the following observations: (i) redox peaks of the
 556 probes are observed in most of the CVs, and (ii) other charge

transfer peaks are absent in the CVs. The selective molecular sieving is achieved by a favorable interplay of differential porosity that emerged from a combined effect of available percolation pathways and the interconnection of pores of varying diameters, which underlines the ligand structure effect on the internal structure of these MPNFs.⁴⁸

3.4. Electrochromic Devices. Electrochromic devices (ECDs) were fabricated from these MPNFs (thickness = 165 ± 6 nm) to investigate the effect of ligand structure on electrochromic performance (see the Supporting Information for the details).^{16,17} The devices switched reversibly between a characteristic transparent colored state (Fe^{2+}) and a transparent yellow state (Fe^{3+}) upon the application of double step potentials between -3.0 and $+3.0$ V (Figure 5, Supporting

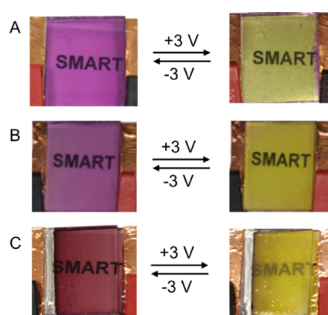


Figure 5. Electrochromic color switching in solid-state devices fabricated from the Fe(II) MPs of (A) Fe(II)-Ph-Tpy, (B) Fe(II)-TPE-Tpy, and (C) Fe(II)-Thio-Tpy. The MPs were spray coated on 3×3 cm FTO glass substrates. The thickness of the electroactive layer was 165 ± 6 nm. A potential window of -3.0 to $+3.0$ V was used.

Information: Video S1). As observed for the films, the ECDs also exhibited a ligand-structure-dependent spectroelectrochemical diversification. While the ECD fabricated from Fe(II)-Ph-Tpy MPNFs showed the highest optical contrast of $\sim 56\%$ at $\lambda_{\text{MLCT}} = 578$ nm, those from Fe(II)-TPE-Tpy ($\sim 35\%$, $\lambda_{\text{MLCT}} = 580$ nm) and Fe(II)-Thio-Tpy (46% , $\lambda_{\text{MLCT}} = 584$ nm) exhibited lower

values (Figure 6A–C). Lower values were obtained for the devices as compared to the films due to the use of viscous gel electrolytes.

3.5. Spectroelectrochemical Diversification in Devices. Chromoabsorptometry of the devices using double potential steps measured as the change in %T over time confirmed optical contrast values similar to those obtained in the spectral measurements. All the devices exhibited faster response times for coloration (reduction), while the bleaching (oxidation) was rather slow.^{45–47} Unlike expected, coloration was considerably faster for the devices as compared to the films, whereas the reverse process was faster in the film state. This unexpectedly faster coloration might be attributed to the larger potential window of operation for the devices (-3.0 to $+3.0$ V). Use of smaller potential windows resulted in slower response times as expected. The response times for the devices at a pulse width of 10 s (-3.0 to $+3.0$ V, Figure 6D–F) were as follows: Fe(II)-Ph-Tpy, 2.1 s (bleaching) and 0.5 s (coloration); Fe(II)-TPE-Tpy, 3.5 s (bleaching) and 1.1 s (coloration); and Fe(II)-Thio-Tpy, 2.6 s (bleaching) and 0.5 s (coloration). These observations are indicative of an increasingly feasible reductive pathway and strenuous oxidative pathway in the films and devices under the specific operational conditions.

The devices also showed pulse width (switching time) dependent changes in visible light transmittance (Figure 7A–C). The devices based on Fe(II)-Ph-Tpy MPNFs exhibited a linear correlation between the pulse width (1–10 s) and change in %T. The optical contrast for the devices constructed from Fe(II)-TPE-Tpy and Fe(II)-Thio-Tpy increased linearly with the pulse width until 4–5 s and remained almost constant thereafter (Figure S12A). The potential window used was also found to have an effect on the optical contrast of the devices (Figure 7D–F). The $\Delta(\%T)$ of the devices of Fe(II)-Ph-Tpy and Fe(II)-Thio-Tpy showed an exponential increase with a ± 0.1 V change in potential windows between -2.0 and $+2.0$ V and -3.0 and $+3.0$ V. A rather smaller exponential dependence was observed for Fe(II)-TPE-Tpy-based devices for two-step potentials between -2.0 and $+2.0$ V and -2.6 and $+2.6$ V, after

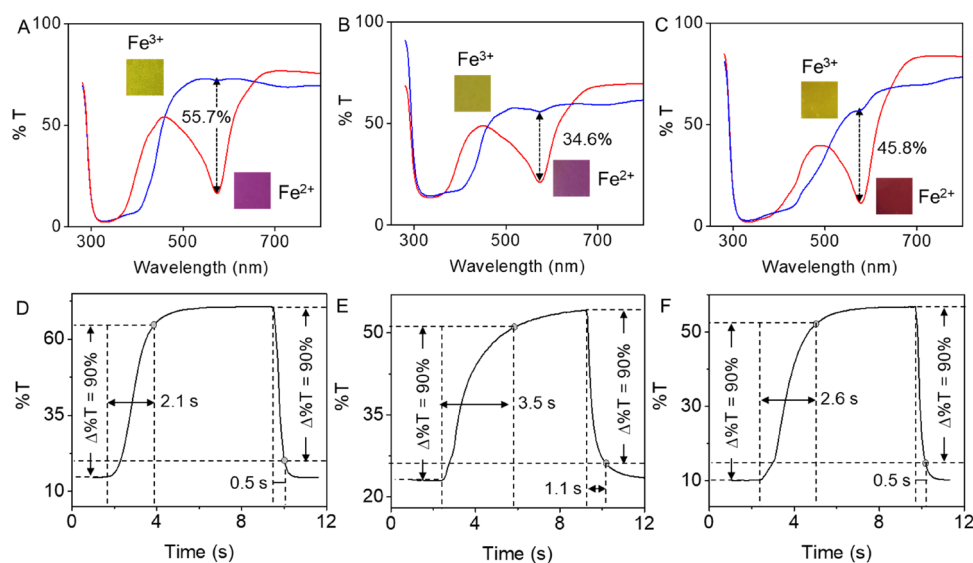


Figure 6. Transmittance spectra of the ECDs showing the bleaching of the MLCT bands during the electrochemical oxidation of the assemblies constructed from (A) Fe(II)-Ph-Tpy, (B) Fe(II)-TPE-Tpy, and (C) Fe(II)-Thio-Tpy. The spectra of the assemblies in their reduced and oxidized states are shown in red and blue, respectively. The corresponding color pallets are shown in the insets. The response times for the devices of (D) Fe(II)-Ph-Tpy, (E) Fe(II)-TPE-Tpy, and (F) Fe(II)-Thio-Tpy at a pulse width of 10 s.

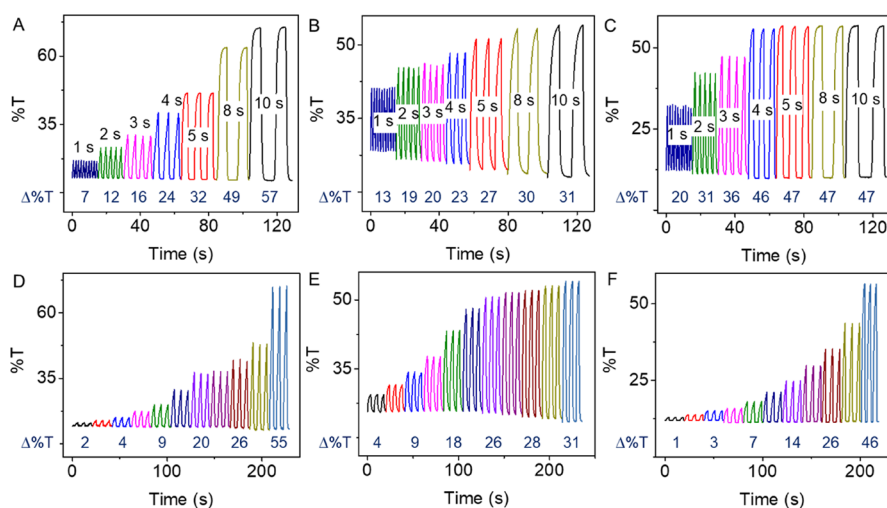


Figure 7. Chromoabsorptometry of the assemblies constructed from (A) Fe(II)-Ph-Tpy, (B) Fe(II)-TPE-Tpy, and (C) Fe(II)-Thio-Tpy at different pulse widths. Chromoabsorptometry of the assemblies constructed from (D) Fe(II)-Ph-Tpy, (E) Fe(II)-TPE-Tpy, and (F) Fe(II)-Thio-Tpy by applying different double potential steps. Double potential steps of -2.0 to $+2.0$ V and -3.0 to $+3.0$ V were used at intervals of ± 0.1 V. The change in $\%T$, rounded to the nearest whole number, is given below the corresponding switching cycle.

615 which a linear correlation was observed (Figure S12B). The
616 pulse width had a larger repercussion on the bleaching
617 (oxidation) process in devices fabricated from Fe(II)-Ph-Tpy
618 and Fe(II)-Thio-Tpy, and the coloration (reduction) was rather
619 unaffected as corroborated by an almost constant $\%T_{\min}$ (Figure
620 7A,C). On the other hand, both coloration and bleaching were
621 affected by these parameters in devices based on Fe(II)-TPE-
622 Tpy (Figure 7B). A similar effect, but to lesser extent, was
623 observed for $\%T$ changes upon change in the applied potential
624 window also (Figure 7D–F).

625 The coloration efficiency of the devices (at λ_{MLCT}) also
626 followed the order Fe(II)-Ph-Tpy ($640.7 \text{ cm}^2/\text{C}$) > Fe(II)-
627 TPE-Tpy ($464.6 \text{ cm}^2/\text{C}$) > Fe(II)-Thio-Tpy ($351.2 \text{ cm}^2/\text{C}$),
628 corroborating the ligand structure dependence of almost every
629 measurable spectroelectrochemical property (Table S2). These
630 electrochromic devices exhibited high coloration efficiencies
631 and contrast ratios that are at par with the related systems
632 reported in the literature (Figure S13, Table S3). High contrast
633 ratios and coloration efficiencies are associated with a
634 combination of the high extinction coefficient, near-perfect
635 electrochemical accessibility and bistability of the metal centers
636 at a low voltage window, use of compatible electrochemical
637 components, and structural features arising from a high degree
638 of conjugation and delocalization of electrons and charges.

639 The operational stability (5 s pulse width, -3.0 to $+3.0$ V),
640 measured as the change in optical contrast over number of
641 switchings, of Fe(II)-Ph-Tpy ECDs decreased exponentially,
642 and $\sim 20\%$ of the initial contrast was retained after 1000
643 continuous switchings at room temperature (Figure S14A,D).
644 Devices of Fe(II)-TPE-Tpy were found to exhibit an $\sim 21\%$
645 reduction in optical contrast after 600 switchings, with no
646 further detectable loss of performance thereafter (Figure
647 S14B,D). Fe(II)-Thio-Tpy ECDs exhibited no change in
648 performance after 200 switchings and a 7–8% decrease in
649 optical contrast after 600 switchings and were found to be highly
650 stable with a $>92\%$ optical contrast after 1000 continuous
651 switchings (Figure S14C,D). The presence of multiple aromatic
652 rings in TPE-Tpy and Thio-Tpy leads to an extended
653 conjugation and better delocalization of π electrons and/or
654 charges. The available electron density on the terpyridine

determines the coordination to Fe(II), whereas the presence of 655
two additional heteroatoms (S) in Thio-Tpy and the lone pairs 656
on these heteroatoms that favors an anticonformation may also 657
play a role in providing exceptional switching stability to the 658
corresponding devices.^{16,31,61} The corresponding cooling 659
efficiency was estimated from a 3×3 cm prototype installed 660
on a cardboard chamber with an outside temperature of 42 ± 1 661
 $^\circ\text{C}$ obtained using a commercial lamp combined with a hot air 662
flow. The indoor temperature measured 1.5 cm away from the 663
prototype showed a reduction by ~ 3 $^\circ\text{C}$ compared to a simple 664
glass installation that served as the control. 665

The ECDs were not found to exhibit any memory effect under 666
open circuit conditions.¹⁷ The change in color to yellow upon 667
oxidation was persistent only upon the sustained application of a 668
potential above the corresponding E_{ox} . The devices based on 669
Fe(II)-TPE-Tpy regained their colored state within 3 min of 670
withdrawal of potential after complete oxidation. ECDs 671
constructed from Fe(II)-Ph-Tpy and Fe(II)-Thio-Tpy re- 672
quired a reasonably longer duration of 10 and 8 min, 673
respectively, for the complete regaining of color under an 674
open circuit potential (Figure S15). While the MPNF-modified 675
FTO substrates undergo defined electrochemical reactions, no 676
specific material was introduced in the counter electrode or 677
electrolyte for redox balance. An ion-storage layer was also 678
absent. Traces of impurities in the gel electrolyte may undergo 679
reactions at the counter electrode, or a part of the electrode itself 680
may undergo such reactions.^{17,62,63} The presence of oxygen 681
and/or water may also contribute to the counter electrode 682
reactions.¹⁷ The lack of memory under open circuit conditions 683
may be explained based on these undefined reactions at the 684
counter electrode, followed by diffusion of the reaction products 685
into the gel medium.¹⁷ 686

3.6. Creation of Patterns and Images. The spray-coating 687
process used for the formation of MPNFs is versatile enough to 688
allow the creation of patterns and images by masking selected 689
areas of the FTO substrate. This circumvents the requirement 690
for selectively patterned or etched conductive substrates for 691
generating such patterns and images for electrochromic 692
applications. Such images also switch their color under the 693

694 application of an electric voltage (Figure 8) and can be realized
695 without the need for selective pixilation, etching, or printing.

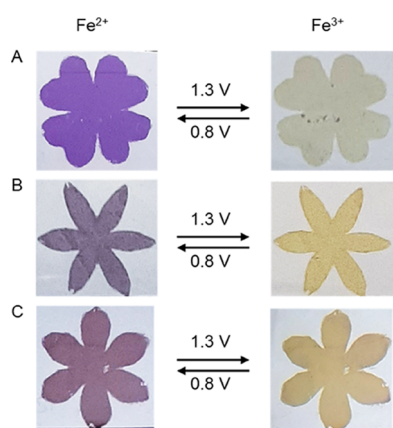


Figure 8. Electrochromic images created by masking 3×3 cm FTO glass substrates during the spray-coating process of (A) Fe(II)-Ph-Tpy, (B) Fe(II)-TPE-Tpy, and (C) Fe(II)-Thio-Tpy. The reduced and oxidized states are shown on the left and right, respectively. The modified FTO substrate, Ag/AgCl, and platinum wire were used as the working, reference, and counter electrodes, respectively. Bu₄PF₆ (0.1 M) in acetonitrile was used as the supporting electrolyte.

4. CONCLUSIONS

696 Metallosupramolecular polymer assemblies of three different
697 terpyridine ligands having a different central core and a common
698 metal center are demonstrated as excellent candidates for
699 making electroactive coating on TCO substrates. The multilayer
700 electrochromic films thus obtained exhibited ligand-directed
701 molecular permeability and spectroelectrochemical profiles. The
702 fabricated electrochromic devices exhibited high optical
703 contrasts and coloration efficiencies at low input voltages
704 simultaneous with color-to-color EC transitions. The creation of
705 patterns and images with electrochromic attributes is facile,
706 without the need for etching or pixilation of TCO substrates.
707 The ligand design plays a key role in controlling the porosity,
708 which in turn dictates the electrochemical behavior, which is
709 otherwise difficult to achieve in surface-confined metal-
710 losupramolecular polymers comprising a single type of metal
711 ion. The combination of a *de novo* ligand design with a spray-
712 coating process offers a powerful tool for the multilayer
713 deposition of metallosupramolecular assemblies resulting in
714 smart and functional metallosupramolecular polymer network
715 films with tunable electro-optical properties for multifarious
716 applications.

ASSOCIATED CONTENT

Supporting Information

717 The Supporting Information is available free of charge at
718 <https://pubs.acs.org/doi/10.1021/acsami.0c20428>.

721 Materials and methods, synthesis (Schemes S1–S4),
722 experimental procedure, UV–vis spectra (Figure S1),
723 AMF images (Figure S2), linear correlation (Figure S3),
724 CVs of the MPNFs (Figure S4), CVs of the metal-
725 losupramolecular polymers (Figure S5), transmittance
726 spectra of the metal–organic assemblies (Figure S6),
727 chromoabsorptometry of the assemblies (Figure S7),
728 change in transmittance (Figure S8), response times
729 (Figure S9), high-resolution XPS data (Figure S10), cyclic

voltammograms of the molecular probe Q3 (Figure S11),
730 dependence of change in %transmittance (Figure S12),
731 plot of coloration efficiency vs optical contrast (Figure
732 S13), stability of the ECDs (Figure S14), decay of
733 transmittance (Figure S15), redox potentials (Table S1),
734 optical and spectroelectrochemical properties (Table S2),
735 optical contrast and coloration efficiency (Table S3)
(PDF)

736 Devices switching reversibly between a characteristic
738 transparent colored state (Fe²⁺) and a transparent yellow
739 state (Fe³⁺) (MP4)

AUTHOR INFORMATION

Corresponding Authors

741 **Sreejith Shankar** – Photosciences and Photonics Section,
742 Chemical Sciences and Technology Division, CSIR-National
743 Institute for Interdisciplinary Science and Technology (CSIR-
744 NIIST), Thiruvananthapuram 695019, India; Academy of
745 Scientific and Innovative Research (AcSIR), CSIR-Human
746 Resource Development Centre, Ghaziabad 201002, India;
747 orcid.org/0000-0002-1158-5935;
748 Email: sreejith.shankar@niist.res.in

749 **Ayyappanpillai Ajayaghosh** – Photosciences and Photonics
750 Section, Chemical Sciences and Technology Division, CSIR-
751 National Institute for Interdisciplinary Science and Technology
752 (CSIR-NIIST), Thiruvananthapuram 695019, India;
753 Academy of Scientific and Innovative Research (AcSIR), CSIR-
754 Human Resource Development Centre, Ghaziabad 201002,
755 India; orcid.org/0000-0001-8574-5391;
756 Email: ajayaghosh@niist.res.in

Authors

757 **Indulekha Mukkatt** – Photosciences and Photonics Section,
758 Chemical Sciences and Technology Division, CSIR-National
759 Institute for Interdisciplinary Science and Technology (CSIR-
760 NIIST), Thiruvananthapuram 695019, India; Academy of
761 Scientific and Innovative Research (AcSIR), CSIR-Human
762 Resource Development Centre, Ghaziabad 201002, India

763 **Anjali Nirmala** – Photosciences and Photonics Section,
764 Chemical Sciences and Technology Division, CSIR-National
765 Institute for Interdisciplinary Science and Technology (CSIR-
766 NIIST), Thiruvananthapuram 695019, India

767 **Nayan Dev Madhavan** – Photosciences and Photonics Section,
768 Chemical Sciences and Technology Division, CSIR-National
769 Institute for Interdisciplinary Science and Technology (CSIR-
770 NIIST), Thiruvananthapuram 695019, India

771 **Biswapriya Deb** – Photosciences and Photonics Section,
772 Chemical Sciences and Technology Division, CSIR-National
773 Institute for Interdisciplinary Science and Technology (CSIR-
774 NIIST), Thiruvananthapuram 695019, India; Academy of
775 Scientific and Innovative Research (AcSIR), CSIR-Human
776 Resource Development Centre, Ghaziabad 201002, India;
777 orcid.org/0000-0001-7954-9386

778 Complete contact information is available at:
779 <https://pubs.acs.org/doi/10.1021/acsami.0c20428>

Author Contributions

780 The manuscript was written through the contributions of all
781 authors. All authors have given approval to the final version of
782 the manuscript.

Notes

783 The authors declare no competing financial interest.

789 ■ ACKNOWLEDGMENTS

790 I.M. is grateful to DST-INSPIRE for a research fellowship. S.S. is
791 grateful to DST-SERB, Government of India, for a Ramanujan
792 Fellowship (SB/S2/RJN-058/2016). A.A. thanks DST-SERB,
793 Government of India, for a J.C. Bose National Fellowship (SB/
794 S2/JCB-11/2014). This work was also supported by CSIR
795 (HCP0030, MLP 0049), Government of India. We thank Dr.
796 Saju Pillai and Mr. Peer Mohammed for the XPS measurements.

797 ■ REFERENCES

798 (1) Ghosh, S.; Shankar, S.; Philips, D. S.; Ajayaghosh, A.
799 Diketopyrrolopyrrole-Based Functional Supramolecular Polymers:
800 Next-Generation Materials for Optoelectronic Applications. *Mater.*
801 *Today Chem.* **2020**, *16*, 100242.
802 (2) Dumele, O.; Chen, J.; Passarelli, J. V.; Stupp, S. I. Supramolecular
803 Energy Materials. *Adv. Mater.* **2020**, *32*, 1907247.
804 (3) Praveen, V. K.; Ajayaghosh, A. CHAPTER 11. Metallosupramo-
805 lecular Materials for Energy Applications: Light Harvesting, In
806 *Functional Metallosupramolecular Materials*, J. G., Hardy, F. H.,
807 Schacvolher, (Eds.), RSC Smart Materials 2–15, 2015.
808 (4) Dyer, A. L.; Bulloch, R. H.; Zhou, Y.; Kippelen, B.; Reynolds, J. R.;
809 Zhang, F. A Vertically Integrated Solar-Powered Electrochromic
810 Window for Energy Efficient Buildings. *Adv. Mater.* **2014**, *26*, 4895–
811 4900.
812 (5) Baetens, R.; Jelle, B. P.; Gustavsen, A. Properties, Requirements
813 and Possibilities of Smart Windows for Dynamic Daylight and Solar
814 Energy Control in Buildings: A State-Of-The-Art Review. *Sol. Energy*
815 *Mat. Sol. Cells* **2010**, *94*, 87–105.
816 (6) Llordes, A.; Garcia, G.; Gazquez, J.; Milliron, D. J. Tunable Near-
817 Infrared and Visible-Light Transmittance in Nanocrystal-in-Glass
818 Composites. *Nature* **2013**, *500*, 323–326.
819 (7) Cai, G.; Eh, A. L.-S.; Ji, L.; Lee, P. S. Recent Advances in
820 Electrochromic Smart Fenestration. *Adv. Sustainable Syst.* **2017**, *1*,
821 1700074.
822 (8) Rosseinsky, D. R.; Mortimer, R. J. Electrochromic Systems and the
823 Prospects for Devices. *Adv. Mater.* **2001**, *13*, 783–793.
824 (9) Mortimer, R. J.; Dyer, A. L.; Reynolds, J. R. Electrochromic
825 Organic and Polymeric Materials for Display Applications. *Displays*
826 **2006**, *27*, 2–18.
827 (10) Beaujuge, P. M.; Reynolds, J. R. Color Control in Pi-Conjugated
828 Organic Polymers for Use in Electrochromic Devices. *Chem. Rev.* **2010**,
829 *110*, 268–320.
830 (11) Granqvist, C. G. Electrochromics for Smart Windows: Oxide-
831 Based Thin Films and Devices. *Thin Solid Films* **2014**, *564*, 1–38.
832 (12) Garcia-Jareno, J. J.; Benito, D.; Navarro-Laboulais, J.; Vicente, F.
833 Electrochemical Behavior of Electrodeposited Prussian Blue Films on
834 ITO Electrode: An Attractive Laboratory Experience. *J. Chem. Educ.*
835 **1998**, *75*, 881.
836 (13) Christiansen, D. T.; Tomlinson, A. L.; Reynolds, J. R. New
837 Design Paradigm for Color Control in Anodically Coloring Electro-
838 chromic Molecules. *J. Am. Chem. Soc.* **2019**, *141*, 3859–3862.
839 (14) Yu, X.; Marks, T. J.; Facchetti, A. Metal Oxides for
840 Optoelectronic Applications. *Nat. Mater.* **2016**, *15*, 383–396.
841 (15) Banasz, R.; Wałęsa-Chorab, M. Polymeric Complexes of
842 Transition Metal Ions as Electrochromic Materials: Synthesis and
843 Properties. *Coord. Chem. Rev.* **2019**, *389*, 1–18.
844 (16) Shankar, S.; Lahav, M.; van der Boom, M. E. Coordination-Based
845 Molecular Assemblies as Electrochromic Materials: Ultra-High Switch-
846 ing Stability and Coloration Efficiencies. *J. Am. Chem. Soc.* **2015**, *137*,
847 4050–4053.
848 (17) Eloul Dov, N.; Shankar, S.; Cohen, D.; Bendikov, T.; Rechav, K.;
849 Shimon, L. J. W.; Lahav, M.; van der Boom, M. E. Electrochromic
850 Metallo-Organic Nanoscale Films: Fabrication, Color Range, and
851 Devices. *J. Am. Chem. Soc.* **2017**, *139*, 11471–11481.
852 (18) Zhong, Y.-W. Electrochromism within Transition-Metal
853 Coordination Complexes and Polymers. In *Electrochromic Materials*
854 *and Devices*; Mortimer, R. J., Rosseinsky, D. R., Monk, P. M. S., Eds.;

WileyVCH Verlag GmbH & Co. KGaA: Weinheim, Germany, 2013; 855
Chapter 6. 856
(19) Bera, M. K.; Mori, T.; Yoshida, T.; Ariga, K.; Higuchi, M. 857
Construction of Coordination Nanosheets Based on Tris(2,2'- 858
bipyridine)–Iron (Fe²⁺) Complexes as Potential Electrochromic 859
Materials. *ACS Appl. Mater. Interfaces* **2019**, *11*, 11893–11903. 860
(20) Mondal, S.; Ninomiya, Y.; Yoshida, T.; Mori, T.; Bera, M. K.; 861
Ariga, K.; Higuchi, M. Dual-Branched Dense Hexagonal Fe(II)-Based 862
Coordination Nanosheets with Red-to-Colorless Electrochromism and 863
Durable Device Fabrication. *ACS Appl. Mater. Interfaces* **2020**, *12*, 864
31896–31903. 865
(21) Lahav, M.; van der Boom, M. E. Polypyridyl Metallo-Organic 866
Assemblies for Electrochromic Applications. *Adv. Mater.* **2018**, 867
1706641. 868
(22) Higuchi, M. Electrochromic Organic–Metallic Hybrid Poly- 869
mers: Fundamentals and Device Applications. *Polym. J.* **2009**, *41*, 511– 870
520. 871
(23) Jaffe, A.; Long, J. R. Ordered Absences Observed in Porous 872
Framework Materials. *Nature* **2020**, *578*, 222–223. 873
(24) Sun, Y.; Chen, C.; Stang, P. J. Soft Materials with Diverse 874
Suprastructures via the Self-Assembly of Metal–Organic Complexes. 875
Acc. Chem. Res. **2019**, *52*, 802–817. 876
(25) Ding, M.; Flaig, R. W.; Jiang, H.-L.; Yaghi, O. M. Carbon Capture 877
and Conversion Using Metal–Organic Frameworks and MOF-Based 878
Materials. *Chem. Soc. Rev.* **2019**, *48*, 2783–2828. 879
(26) Azhar, A.; Li, Y.; Cai, Z.; Zakaria, M. B.; Masud, M. F.; Hossain, 880
M. S. A.; Kim, J.; Zhang, W.; Na, J.; Yamauchi, Y.; Hu, M. 881
Nanoarchitectonics: A New Materials Horizon for Prussian Blue and 882
Its Analogues. *Bull. Chem. Soc. Japan* **2019**, *92*, 875–904. 883
(27) Sun, J.-K.; Yang, X.-D.; Yang, G.-Y.; Zhang, J. Bipyridinium 884
Derivative-Based Coordination Polymers: From Synthesis to Materials 885
Applications. *Coord. Chem. Rev.* **2019**, *378*, 533–560. 886
(28) Mizuno, A.; Shuku, Y.; Awaga, K. Recent Developments in 887
Molecular Spin Gyroid Research. *Bull. Chem. Soc. Japan* **2019**, *92*, 888
1068–1093. 889
(29) Cui, D.; Perepichka, D. F.; MacLeod, J. M.; Rosei, F. Surface- 890
Confined Single-Layer Covalent Organic Frameworks: Design, Syn- 891
thesis and Application. *Chem. Soc. Rev.* **2020**, *49*, 2020–2038. 892
(30) Ariga, K.; Shionoya, M. Nanoarchitectonics for Coordination 893
Asymmetry and Related Chemistry. *Bull. Chem. Soc. Japan* **2021**, 894
DOI: 10.1246/bcsj.20200362. Advance Publication, 895
(31) Pai, S.; Moos, M.; Schreck, M. H.; Lambert, C.; Kurth, D. G. 896
Green-to-Red Electrochromic Fe(II) Metallo-Supramolecular Poly- 897
electrolytes Self-Assembled from Fluorescent 2,6-Bis(2-pyridyl)- 898
pyrimidine Bithiophene. *Inorg. Chem.* **2017**, *56*, 1418–1432. 899
(32) Han, F. S.; Higuchi, M.; Kurth, D. G. Metallosupramolecular 900
Polyelectrolytes Self-Assembled from Various Pyridine Ring-Substi- 901
tuted Bisterpyridines and Metal Ions: Photophysical, Electrochemical, 902
and Electrochromic Properties. *J. Am. Chem. Soc.* **2008**, *130*, 2073– 903
2081. 904
(33) Hu, C. W.; Sato, T.; Zhang, J.; Moriyama, S.; Higuchi, M. Three- 905
Dimensional Fe(II)-based Metallo-Supramolecular Polymers with 906
Electrochromic Properties of Quick Switching, Large Contrast, and 907
High Coloration Efficiency. *ACS Appl. Mater. Interfaces* **2014**, *6*, 9118– 908
9125. 909
(34) Han, F. S.; Higuchi, M.; Kurth, D. G. Metallo-Supramolecular 910
Polymers Based on Functionalized Bis-terpyridines as Novel Electro- 911
chromic Materials. *Adv. Mater.* **2007**, *19*, 3928–3931. 912
(35) Laschuk, N. O.; Ahmad, R.; Ebraldize, I. I.; Poisson, J.; Easton, E. 913
B.; Zenkina, O. V. Multichromic Monolayer Terpyridine-Based 914
Electrochromic Materials. *ACS Appl. Mater. Interfaces* **2020**, *12*, 915
41749–41757. 916
(36) Bera, M. K.; Ninomiya, Y.; Higuchi, M. Constructing Alternated 917
Heterobimetallic [Fe(II)/Os(II)] Supramolecular Polymers with 918
Diverse Solubility for Facile Fabrication of Voltage-Tunable Multicolor 919
Electrochromic Devices. *ACS Appl. Mater. Interfaces* **2020**, *12*, 14376– 920
14385. 921
(37) Deshmukh, M. A.; Gicevicius, M.; Ramanaviciene, A.; Shirsat, M. 922
D.; Viter, R.; Ramanavicius, A. Hybrid Electrochemical/Electro- 923

- 924 chromic Cu(II) Ion Sensor Prototype Based on PANI/ITO-Electrode.
925 *Sensors and Actuators B Chemical* **2017**, *248*, 527–535.
- 926 (38) Balgley, R.; de Ruiter, G.; Evmenenko, G.; Bendikov, T.; Lahav,
927 M.; van der Boom, M. E. Light-Induced Conversion of Chemical
928 Permeability to Enhance Electron and Molecular Transfer in Nanoscale
929 Assemblies. *J. Am. Chem. Soc.* **2016**, *138*, 16398–16406.
- 930 (39) Mukkatt, L.; Anjana, P. M.; Nirmala, A.; Rakhi, R. B.; Shankar, S.;
931 Ajayaghosh, A. Metal Ion-Induced Capacitance Modulation in Near-
932 Isostructural Complexes-Derived Electrochromic Coordination Poly-
933 mers. *Mater. Today Chem.* **2020**, *16*, 100260.
- 934 (40) Balgley, R.; Shankar, S.; Lahav, M.; van der Boom, M. E.
935 Rerouting Electron Transfer in Molecular Assemblies by Redox-Pair
936 Matching. *Angew. Chem., Int. Ed.* **2015**, *54*, 12457–12462.
- 937 (41) Takada, K.; Sakamoto, R.; Yi, S.-T.; Katagiri, S.; Kambe, T.;
938 Nishihara, H. Electrochromic Bis(terpyridine)metal Complex Nano-
939 sheets. *J. Am. Chem. Soc.* **2015**, *137*, 4681–4689.
- 940 (42) Liang, Y.; Strohecker, D.; Lynch, V.; Holliday, B. J.; Jones, R. A. A
941 Thiophene-Containing Conductive Metallopolymer Using an Fe(II)
942 Bis(terpyridine) Core for Electrochromic Materials. *ACS Appl. Mater.*
943 *Interfaces* **2016**, *8*, 34568–34580.
- 944 (43) Constable, E. C.; Thompson, A. M. W. C. Multinucleating 2,2' :
945 6',2''-Terpyridine Ligands as Building Blocks for the Assembly of Co-
946 ordination Polymers and Oligomers. *J. Chem. Soc., Dalton Trans.* **1992**,
947 3467–3475.
- 948 (44) Shiryaeva, I. M.; Collman, J. P.; Boulatov, R.; Sunderland, C. J.
949 Nonideal Electrochemical Behavior of Biomimetic Iron Porphyrins:
950 Interfacial Potential Distribution across Multilayer Films. *Anal. Chem.*
951 **2003**, *75*, 494–502.
- 952 (45) Vasilopoulou, M.; Aspiotis, G.; Kostis, I.; Argitis, P.; Davazoglou,
953 D. Fabrication of WO₃-Based Electrochromic Displays Using Solid or
954 Gel-Like Organic Electrolytes. *J. Phys. Conf. Series* **2005**, *10*, 329–332.
- 955 (46) Tong, Z.; Tian, Y.; Zhang, H.; Li, X.; Ji, J.; Qu, H.; Li, N.; Zhao, J.;
956 Li, Y. Recent Advances in Multifunctional Electrochromic Energy
957 Storage Devices and Photoelectrochromic Devices. *Sci. China Chem.*
958 **2017**, *60*, 13–37.
- 959 (47) Zhang, Q.; Tsai, C.-Y.; Li, L.-J.; Liaw, D.-J. Colorless-to-Colorful
960 Switching Electrochromic Polyimides with Very High Contrast Ratio.
961 *Nature Commun.* **2019**, *10*, 1239.
- 962 (48) Motiei, L.; Kaminker, R.; Sassi, M.; van der Boom, M. E.
963 Molecule and Electron Transfer through Coordination-Based Molec-
964 ular Assemblies. *J. Am. Chem. Soc.* **2011**, *133*, 14264–14266.
- 965 (49) Zhao, D.; Timmons, D. J.; Yuan, D.; Zhou, H.-C. Tuning the
966 Topology and Functionality of Metal–Organic Frameworks by Ligand
967 Design. *Acc. Chem. Res.* **2011**, *44*, 123–133.
- 968 (50) Williams, M. E.; Benkstein, K. D.; Abel, C.; Dinolfo, P. H.; Hupp,
969 J. T. Shape-Selective Transport through Rectangle-Based Molecular
970 Materials: Thin-Film Scanning Electrochemical Microscopy Studies.
971 *Proc. Natl. Acad. Sci. U. S. A.* **2002**, *99*, 5171–5177.
- 972 (51) Motesharei, K.; Ghadiri, M. R. Diffusion-Limited Size-Selective
973 Ion Sensing Based on SAM-Supported Peptide Nanotubes. *J. Am.*
974 *Chem. Soc.* **1997**, *119*, 11306–11312.
- 975 (52) Li, S. S.; Northrop, B. H.; Yuan, Q. H.; Wan, L. J.; Stang, P. J.
976 Surface Confined Metallosupramolecular Architectures: Formation
977 and Scanning Tunneling Microscopy Characterization. *Acc. Chem. Res.*
978 **2009**, *42*, 249–259.
- 979 (53) Fujita, M.; Ogura, K. Transition-Metal-Directed Assembly of
980 Well-Defined Organic Architectures Possessing Large Voids: From
981 Macrocycles to [2] Catenanes. *Coord. Chem. Rev.* **1996**, *148*, 249–264.
- 982 (54) Beck, R. E.; Schultz, J. S. Hindered Diffusion in Microporous
983 Membranes with Known Pore Geometry. *Science* **1970**, *170*, 1302–
984 1305.
- 985 (55) Belanger, S.; Hupp, J. T.; Stern, C. L.; Slone, R. V.; Watson, D. F.;
986 Carrell, T. G. Thin-Film Molecular Materials Based on Tetrametallic
987 “Squares”: Nanoscale Porosity and Size-Selective Guest Transport
988 Characteristics. *J. Am. Chem. Soc.* **1999**, *121*, 557–563.
- 989 (56) Freeman, B. D. Basis of Permeability/Selectivity Tradeoff
990 Relations in Polymeric Gas Separation Membranes. *Macromolecules*
991 **1999**, *32*, 375–380.
- (57) Robeson, L. M. Correlation of Separation Factor Versus
Permeability for Polymeric Membranes. *J. Membr. Sci.* **1991**, *62*, 993
165–185. 994
- (58) Palomaki, P. K. B.; Krawicz, A.; Dinolfo, P. H. Thickness, Surface
Morphology, and Optical Properties of Porphyrin Multilayer Thin
Films Assembled on Si(100) Using Copper(I)-Catalyzed Azide–
Alkyne Cycloaddition. *Langmuir* **2011**, *27*, 4613–4622. 998
- (59) Ellis, C. D.; Murphy, W. R.; Meyer, T. J. Selectivity and Directed
Charge Transfer through an Electroactive Metallopolymer Film. *J. Am.*
Chem. Soc. **1981**, *103*, 7480–7483. 1000
- (60) Nishihara, H.; Noguchi, M.; Aramaki, K. Synthesis of Ferrocene
and Cobaltocene Electrode Films by Electropolymerization and Their
Spectral and Electrochemical Properties. *Inorg. Chem.* **1987**, *26*, 2862–
2867. 1004
- (61) Damrauer, N. H.; Boussie, T. R.; Devenney, M.; McCusker, J. K.
Effects of Intraligand Electron Delocalization, Steric Tuning, and
Excited-State Vibronic Coupling on the Photophysics of Aryl-
Substituted Bipyridyl Complexes of Ru(II). *J. Am. Chem. Soc.* **1997**,
119, 8253–8268. 1008
- (62) Cai, G.; Wang, J.; Lee, P. S. Next-Generation Multifunctional
Electrochromic Devices. *Acc. Chem. Res.* **2016**, *49*, 1469–1476. 1012
- (63) Stanco, A.; Marszalek, K. W.; Swatowska, B.; Sobkow, Z.
Electronic Materials and Components. In *Microelectronic Material and*
Technologies; Suszynski, Z., Ed.; Koszalin University of Technology:
Koszalin, Poland, 2012; pp. 191–203. 1015

Tunable Capacitive Behavior in Metallopolymer-based Electrochromic Thin Film Supercapacitors

Indulekha Mukkatt, Anjana Padmaja Mohanachandran, Anjali Nirmala, Dipak Patra, Priyanka A. Sukumaran, Renjith S. Pillai, R. B. Rakhi, Sreejith Shankar,* and Ayyappanpillai Ajayaghosh*



Cite This: *ACS Appl. Mater. Interfaces* 2022, 14, 31900–31910



Read Online

ACCESS |



Metrics & More



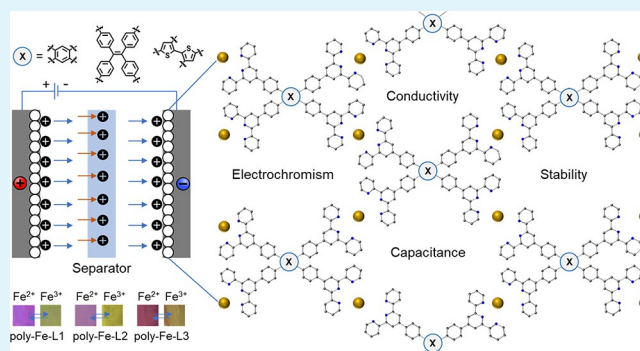
Article Recommendations



Supporting Information

ABSTRACT: Volumetric capacitance is a more critical performance parameter for rechargeable power supply in lightweight and microelectronic devices as compared to gravimetric capacitance in larger devices. To this end, we report three electrochromic metallopolymer-based electrode materials containing Fe^{2+} as the coordinating metal ion with high volumetric capacitance and energy densities in a symmetric two-electrode supercapacitor setup. These metallopolymers exhibited volumetric capacitance up to 866.2 F cm^{-3} at a constant current density of 0.25 A g^{-1} . The volumetric capacitance (**poly-Fe-L2**: 544.6 F cm^{-3} > **poly-Fe-L1**: 313.8 F cm^{-3} > **poly-Fe-L3**: 230.8 F cm^{-3} at 1 A g^{-1}) and energy densities (**poly-Fe-L2**: 75.5 mWh cm^{-3} > **poly-Fe-L1**: 43.6 mWh cm^{-3} > **poly-Fe-L3**: 31.2 mWh cm^{-3}) followed the order of the electrical conductivity of the metallopolymers and are among the best values reported for metal–organic systems. The variation in the ligand structure was key toward achieving different electrical conductivities in these metallopolymers with excellent operational stability under continuous cycling. High volumetric capacitances and energy densities combined with tunable electro-optical properties and electrochromic behavior of these metallopolymers are expected to contribute to high performance and compact microenergy storage systems. We envision that the integration of smart functionalities with thin film supercapacitors would warrant the surge of miniaturized on-chip microsupercapacitors integrated in-plane with other microelectronic devices for wearable applications.

KEYWORDS: coordination polymers, electrochromic, metal–organic, supercapacitors, capacitance



1. INTRODUCTION

Smart materials that respond to changes in environmental conditions are one among the holy grails in current materials science.^{1–6} In this regard, electrochromic materials, capable of exhibiting different optical profiles at different applied voltages, are of particular interest.^{7–10} Multifunctional electrochromic systems that regulate heat and light transmission leading to efficient indoor energy management have added several new dimensions to the classical concept of energy-saving smart glass technologies.^{11–14} Electrochemical energy storage aspects of such smart materials are directed toward combining energy saving and energy storage using a single system.^{12,13} However constructive coupling of smart functions with conventional device technologies is still in its infancy.^{15,16} Electrochromism is operationally similar to the rocking chair-type energy storage mechanism, and such multifunctional systems that integrate smart functions with energy storage are critical towards achieving universal energy access and conservation, energy sustainability and ensuring reliable power supply.^{12,13}

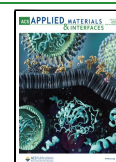
Porous organic polymers with high power density, efficiency, and cycling stability have been of contemporary interest as

new-generation electrode materials for electrochemical energy storage applications.¹⁷ The significance of morphological features in determining the capacitive behavior of such materials was demonstrated using hollow spherical structures of 3D covalent organic frameworks with enhanced surface area and specific capacitance (251 F g^{-1} at 0.5 A g^{-1}) that further increased with cycling.¹⁸ Incorporating plastic crystals into conjugated 3D COFs was shown to accelerate ion transport by lowering the barrier for lithium ion conduction, thereby providing access to solid-state electrolytes with high conductivities for better electrochemical energy storage applications.¹⁹ Nitrogen-rich conjugated microporous polymers also exhibited high specific capacitance (up to 183 F g^{-1} at 1.0 A g^{-1}), despite having moderate surface areas, thereby corrob-

Received: April 1, 2022

Accepted: June 23, 2022

Published: July 6, 2022



orating the positive effect of heteroatoms in electrode materials for supercapacitor applications.²⁰

While inorganic metal oxides are preferred electrochromic materials, largely due to their high stability, the possible color variations are limited mostly to blue or brown.^{21–24} Many of the conducting polymers and small organic molecules, though provide exceptional color variations, suffer from concerns related to long-term stability.^{10,25} Therefore, metal–organic systems that combine the advantages of inorganic and organic counterparts have emerged as a viable alternative in multifunctional electrochromism due to their structural regularity, packing variations, high surface area, tunable porosity, and synthetic diversity.^{26–33} These attributes combined with well-defined redox chemistry and tunable electro-optical properties make this class of materials promising candidates as non-carbon electrode materials for electrochemical/electrochromic energy storage applications.^{34–36} Several reports have shown the significance of the collective properties of the electrode material particles in determining the capacitive performance, whereby material assembly or stacking assumes unprecedented operational significance leading to lower reproducibility and stability under continuous cycling.^{37–40} Therefore, there is an urgent need to develop thin film or microsupercapacitors with a unique coherence of high volumetric capacitance, energy densities, and cycling stability for bridging the gap between batteries and conventional capacitors, particularly for integrated microelectronic device applications.

We have previously reported the electrochromic diversification in metallosupramolecular assemblies, which was mainly attributed to the differences in thin film porosity emanating from differences in the ligand structure.⁴¹ However, the electrochemical profiles of the nanoscale spray-coated thin films need not be exactly replicated by the isolated metallopolymer. While allowing color-to-color transitions with good efficiency and stability, the electrochemical energy storage properties of such network materials having the same metal ion coordinated to a series of conjugated ligands that differ in their core structure are not easy to predict. Porosity and surface area of such materials have earlier been shown to dictate the capacitive performance of metal–organic materials.^{36,42} In the present work, we demonstrate that electrical conductivity is a rather more dominant parameter in determining the electrochemical energy storage properties, particularly for low surface area metal–organic materials.^{34,43,44} Using electrochromic metallopolymer featuring Fe(II)-terpyridine coordination and high electrical conductivity, supercapacitor electrodes with volumetric capacitance up to 866.2 F cm⁻³ at a current density of 0.25 A g⁻¹ and volumetric energy densities up to 75.5 mWh cm⁻³ were fabricated. The capacitive performance, charge–discharge kinetics, and charge transfer resistance of the metallopolymer were found to be directly correlated to their electrical conductivity. Further, no deterioration in performance was observed upon multiple cycles of continuous operation and the observed capacitance values and energy densities are superior to or at par with prior literature reports.

2. MATERIALS AND METHODS

2.1. General Methods and Instrumentation. All reagents were used as received without further purification, unless otherwise noted. Syntheses and experiments were carried out in clean and oven-dried glassware. Reactions were monitored using silica gel G-60 F254 aluminum TLC (thin layer chromatography) and compounds were

visualized by short/long-wavelength UV lamps. Column chromatography was done using silica gel 100–200 mesh as a stationary phase.

2.1.1. Molecular Characterization. ¹H and ¹³C NMR spectra were recorded in deuterated solvents at 300 K on a 500 MHz (¹H) Bruker Avance spectrometer using TMS (tetramethyl silane) as an internal standard. Chemical shifts are presented in ppm (δ) along with the corresponding coupling constants (Hz). HRMS (high-resolution mass spectrometry) data were recorded on a Thermo Scientific Exactive LCMS (liquid chromatography–mass spectrometry) instrument by an electrospray ionization method with ions given in *m/z* using an Orbitrap analyzer. Matrix-assisted laser desorption ionization time-of-flight (MALDI-TOF) mass spectra were obtained using an AXIMA-CFR PLUS (SHIMADZU) MALDI-TOF mass spectrometer using α -cyano-4-hydroxycinnamic acid as the matrix. FT-IR spectra were recorded in the solid state (KBr) using a Shimadzu IRPrestige-21 Fourier transform infrared spectrophotometer.

2.1.2. Absorption and Emission Spectroscopy. Electronic absorption spectra in solution were recorded on a Shimadzu UV-2600 Spectrophotometer, using a clean and dry Hellma Analytics 10 mm quartz cuvette. Temperature was regulated using a Shimadzu temperature controller and a blank experiment with the corresponding solvent provided the baseline. The UV–vis spectra of the metallopolymer-modified TCO (transparent conducting oxide) slides were obtained using an Ocean Optics UV–vis modular spectrometer (DH-2000-BAL). The blank experiment with the bare TCO slides provided the baseline. Emission spectra were recorded on a Horiba Fluorolog-3 Jovin Yoon with a 1 cm quartz cuvette at room temperature.

2.1.3. Morphological Analyses, Thickness Measurements, and Thermal Characterization. AFM images were recorded in ambient conditions using an atomic force microscope (AFM; Bruker Multimode Nanoscope V) instrument operating under tapping mode. Microfabricated TiN cantilever tips with a resonance frequency of 299 kHz and spring constant of 20–80 N m⁻¹ were used. The roughness parameter was estimated using Nanoscope Analysis 1.5 software. The thickness of the thin films was estimated using a Dektak XT profilometer. Thermogravimetric analyses (TGA) were performed at a heating rate of 10 °C/min in a nitrogen atmosphere using Shimadzu DTG-60 equipment.

2.1.4. Powder X-ray Diffraction. Powder X-ray Diffraction (PXRD) analyses were done using a XEUSS SAXS/WAXS (small-angle X-ray scattering/wide angle X-ray scattering) system by Xenocs, using Ni-filtered Cu K α radiation ($\lambda = 0.15405$ nm). Using Fit2D software, 1D patterns were generated from the 2D images obtained from the Mar 345 detector.

2.1.5. X-ray Photoelectron Spectroscopy (XPS). The elemental composition of the metallopolymer was analyzed using X-ray photoelectron spectroscopy (XPS, PHI 5000 VersaProbe II, ULVAC-PHI Inc., USA) equipped with a micro-focused (200 μ m, 15 KV) monochromatic Al K α X-ray source ($h\nu = 1486.6$ eV). First survey scans were acquired on the samples, and for the major detected elements, high-resolution spectra were recorded. Survey scans were recorded with an X-ray source power of 50 W and pass energy of 187.85 eV. High-resolution spectra of the major elements were recorded at 46.95 eV pass energy. XPS data were processed using PHI's Multipak software. These spectra were used for qualitative confirmation of elemental compositions and chemical state assignments by curve fitting software XPSPEAK Fit.

2.1.6. Electrochemistry and Spectroelectrochemical Analyses. Cyclic voltammetry of the films was performed on a PARSTAT 4000A potentiostat at room temperature using 0.1 M lithium perchlorate in CH₃CN as the supporting electrolyte, metallopolymer-modified TCO slides as the working electrode, Ag/AgCl as the reference electrode, and a platinum wire as the counter electrode at a scan rate of 10–300 mV s⁻¹. Three consecutive scans were performed, and the third cycle was selected for analysis. Spectroelectrochemical analyses were recorded on an Ocean Optics Spectrometer DH-2000-BAL coupled to the PARSTAT 4000A potentiostat by dipping metallopolymer drop-cast FTO electrodes in 0.1 M lithium perchlorate (in dry acetonitrile) solution using Ag/

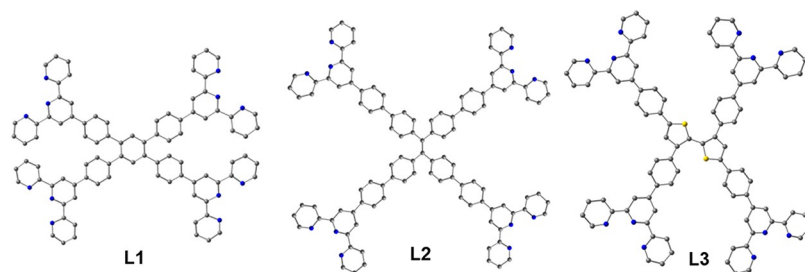


Figure 1. A ball-and-stick model showing the molecular structures of the terpyridine ligands **L1**–**L3** used for the synthesis of the Fe(II) metallopolymers **poly-Fe-L1**, **poly-Fe-L2**, and **poly-Fe-L3**. The metallopolymers were synthesized by mixing FeCl₂ and the corresponding ligand in a 2:1 molar ratio and were precipitated from water as their PF₆ salts. The hydrogen atom is omitted for clarity. Color codes – gray: carbon, blue: nitrogen, yellow: sulfur.

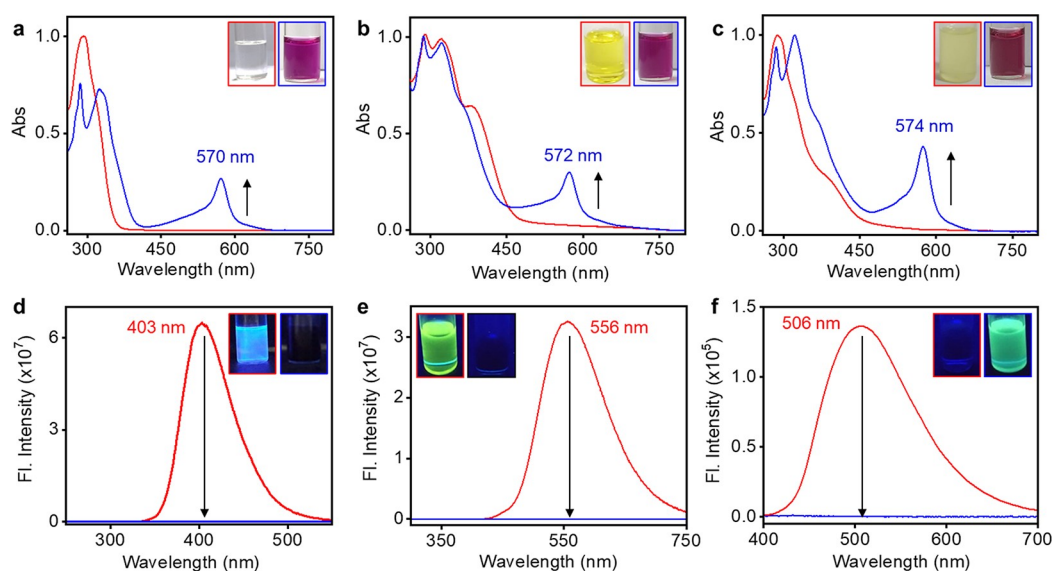


Figure 2. UV–Vis spectra of (a) **L1** (red) and **poly-Fe-L1** (blue), (b) **L2** (red) and **poly-Fe-L2** (blue), and (c) **L3** (red) and **poly-Fe-L3** (blue), in methanol ($c = 15 \mu\text{M}$). Photographs of the ligand (red border) and metallopolymer (blue border) solutions under visible light. Emission spectra of (d) **L1** (red) and **poly-Fe-L1** (blue), (e) **L2** (red) and **poly-Fe-L2** (blue), and (f) **L3** (red) and **poly-Fe-L3** (blue) in methanol ($c = 15 \mu\text{M}$). Insets: photographs of the ligand (red border) and metallopolymer (blue border) solutions under UV light. The arrows represent the change upon addition of the metal salt to the corresponding ligand solution. The corresponding λ_{max} is also shown.

AgCl and a Pt wire as the reference and counter electrodes, respectively. Absorption spectra were obtained upon applying double potential steps (0.7 and 1.5 V) as a function of time.

2.2. Synthesis. The ligands **L1**, **L2**, and **L3** were synthesized using our previously reported procedure.⁴¹ The details are provided in the Supporting Information.

2.2.1. Syntheses of the Metallopolymers. A solution of FeCl₂·4H₂O (24.9 mg, 2 equiv) in MeOH (10.0 mL) was added to a solution of the corresponding ligand (**L1**: 32.5 mg, **L2**: 39.0 mg, **L3**: 34.9 mg) in CHCl₃ (10.0 mL). The solution was stirred in the dark at room temperature for 2 h. The solvent was then removed under reduced pressure to 25% of the initial volume. Water (15 mL) saturated with potassium hexafluorophosphate was then added, and the reaction mixture was stirred at room temperature for 30 min. The precipitate formed was filtered, washed with DI water (10 mL × 3), and dried in a vacuum oven to obtain the corresponding metallopolymers in >95% yield.

2.3. Preparation of the Electrodes and Electrochemical Measurements. Supercapacitor electrodes of 1 cm² area were prepared as reported previously using the corresponding metallopolymer (1.0 mg) mixed with activated charcoal and polytetrafluoroethylene in a mass ratio of 8:1:1.³⁶ The electrochemical properties were studied by cyclic voltammetry (CV), galvanostatic charge–discharge, and electrochemical impedance spectroscopy (EIS) using a Modulab (Solartron Analytical) electrochemical

workstation. The cell capacitance (C in F) was then calculated from the charge–discharge curves according to eq 1

$$C = \frac{I}{(\Delta V/\Delta t)} \quad (1)$$

where I is the constant current for charge–discharge and $\Delta V/\Delta t$ is the slope of the discharge curve. The volumetric capacitance (C_{Vol} in F cm⁻³) was then calculated as

$$C_{\text{sp}} = \frac{2C}{At} \quad (2)$$

where A is the area of each electrode and t is the thickness of the electrode material.

2.4. Determination of Resistivity and Electrical Conductivity by 4-Probe Measurements. The four-probe method (Keithley 2450 source meter) was used to determine the resistivity and the electrical conductivity of the coordination polymers. The corresponding metallopolymer (2 mg) was dissolved in methanol/dichloromethane (1:1 v/v, 200 μL) and was drop-cast on to a glass substrate. The thickness of the film was measured using a Bruker Dektat XT Profilometer. For a thin layer film, resistivity is calculated from the following equation:

$$\rho = \frac{\pi t V}{\ln 2 I}$$

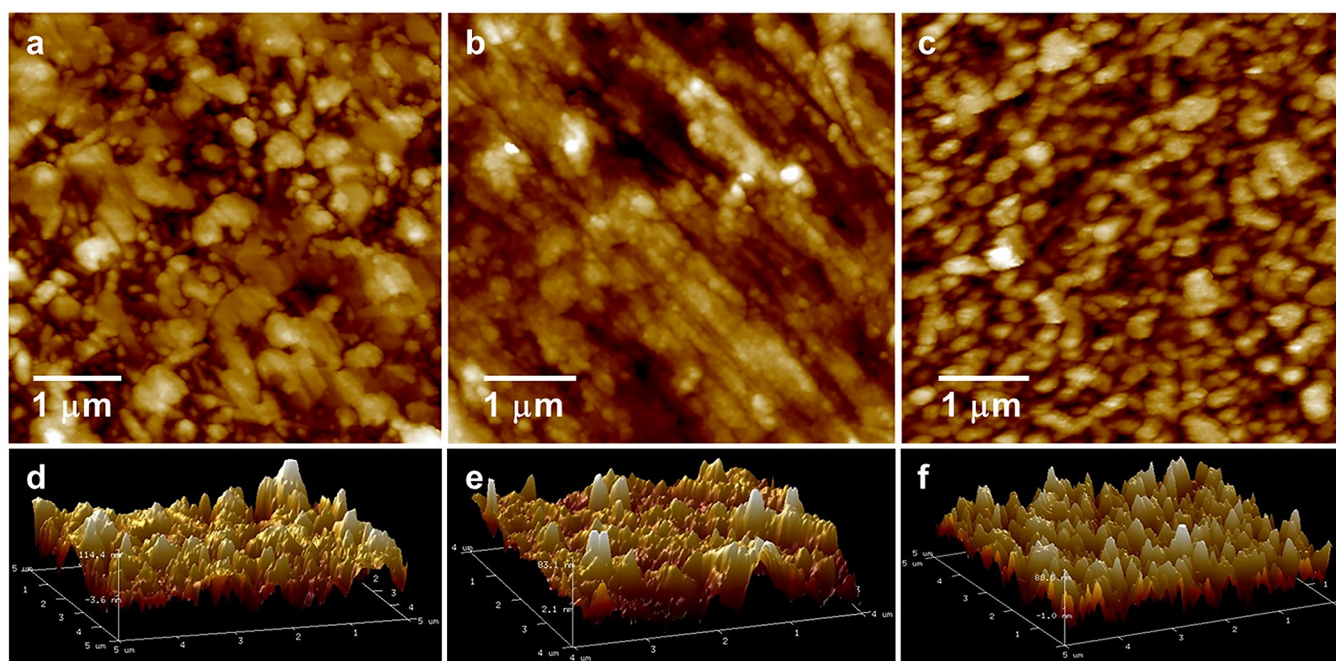


Figure 3. AFM images (a–c) and 3D topographies (d–f) of the metallopolymer coatings on freshly cleaved mica: (a,d) poly-Fe-L1, (b,e) poly-Fe-L2, and (c,f) poly-Fe-L3.

where t is the thickness of film and resistance $R = V/I$.

Conductivity can be calculated as $\sigma = \frac{1}{\rho}$

3. RESULTS AND DISCUSSION

3.1. Synthesis and Characterization. The ligands L1–L3 (Figure 1) were synthesized using the Suzuki coupling reactions between the boronic acid derivative of terpyridine and the corresponding tetrabromo derivative of benzene, tetraphenyl ethylene, or bithiophene.⁴¹ The detailed synthetic procedure and characterization data are given in the experimental section. The metallopolymer poly-Fe-L1, poly-Fe-L2, and poly-Fe-L3 as their PF₆ salts, with a general formula Fe(L)₂]_n(PF₆)_{2n} (L = L1–L3), were synthesized by adding a methanolic solution of FeCl₂ to a solution of the corresponding ligand in methanol followed by precipitation from water saturated with ammonium hexafluorophosphate. ¹H NMR of the metallopolymer solutions in CD₃OD exhibited broad and unresolved peaks, most likely due to the paramagnetic nature of the central metal ion.

Addition of the metal salt into the ligand solution resulted in an instantaneous purple coloration, and the MLCT (metal-to-ligand charge transfer) bands were observed at 570–574 nm for all the three metallopolymer. The extinction coefficients at λ_{MLCT} (MeOH) were found to be $3.4 \times 10^4 \text{ M}^{-1} \text{ cm}^{-1}$ for poly-Fe-L1 and poly-Fe-L2 and $5.1 \times 10^4 \text{ M}^{-1} \text{ cm}^{-1}$ for poly-Fe-L3 (Figure 2a–c). While the ligands L1–L3 exhibited moderate emission in their methanol solutions, metal complexation was found to result in near-complete quenching of fluorescence (Figure 2d–f). FT-IR spectra of all three metallopolymer corroborated the coordination of Fe(II) to the terpyridine ligands as evidenced by the shift in C=C vibrations from 1583 ± 1 to $1601 \pm 2 \text{ cm}^{-1}$, which is characteristic for terpyridine–metal coordination. A shift was also observed in the C–H in-plane deformation frequencies that appeared at $1413 \pm 4 \text{ cm}^{-1}$ for the free ligands, which

upon metal complexation were shifted to $1407 \pm 3 \text{ cm}^{-1}$ (Figure S1).^{36,41}

The morphologies of the coated films on freshly cleaved mica were obtained using atomic force microscopy (AFM). The AFM images of all three metallopolymer confirmed the formation of grain-like features densely covering the surface (Figure 3a–c). The films of poly-Fe-L2 appeared to have fewer open spaces and may likely result in less porous assemblies (Figure 3b). The 3D topographies of assemblies confirmed roughness of the surface (Figure 3d–f). Powder X-ray diffraction (PXRD) confirmed the amorphous nature of the metallopolymer that most likely stems from the fast complexation and/or precipitation processes (Figure S2). Nevertheless, very modest molecular ordering was observed for poly-Fe-L1 as corroborated by low intensity peaks in its PXRD spectrum and the selected area diffraction pattern in TEM (Figure S2a). Thermogravimetric analysis under a nitrogen atmosphere was conducted to establish the thermal stability of the metallopolymer. A weight loss of approximately half the initial weight of the metallopolymer was observed upon heating to 1000 °C. Surprisingly, the ligands and the corresponding metallopolymer exhibited more or less similar thermal stability (Figure S3). The elemental composition of the metallopolymer was qualitatively estimated using X-ray photoelectron spectroscopy (XPS). The presence of iron(II) in all the metallopolymer was confirmed by the Fe²⁺ 3p_{3/2} (709 eV) and Fe²⁺ 3p_{1/2} (721–722 eV) peaks in the high-resolution XPS data. Characteristic peaks corresponding to N 1s were also observed at binding energies of 399–402 eV in the X-ray photoelectron spectra of the metallopolymer (Figure S4). A near 2:1 metal to ligand ratio was also observed in the XPS analysis. The characteristic peaks corresponding to the expected chemical structure of the metallopolymer (ring breathing at 1047 cm^{-1} , $\nu(\text{C}=\text{C})$ inter-ring at $1296\text{--}1298 \text{ cm}^{-1}$, $\nu(\text{C}=\text{N})$ and $\nu(\text{C}=\text{C})$ at 1370 cm^{-1} , $1479\text{--}1480$ and $1612\text{--}1614 \text{ cm}^{-1}$, and $\nu(\text{C}=\text{C})$ at $1320\text{--}1348$ and 1611--

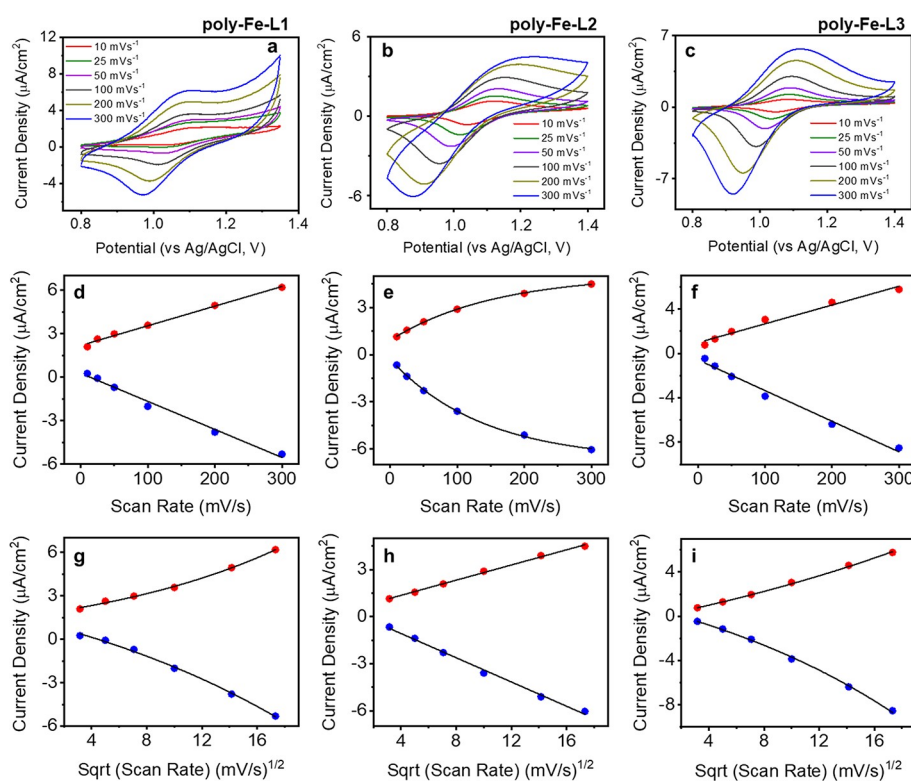


Figure 4. Cyclic voltammograms of (a) **poly-Fe-L1**, (b) **poly-Fe-L2**, and (c) **poly-Fe-L1** at varying scan rates between 10 (red) and 300 (blue) mV s^{-1} . The dependence of current on the scan rates (d–f) and square root of the scan rates (g–i) for (d,g) **poly-Fe-L1**, (e,h) **poly-Fe-L2**, and (f,i) **poly-Fe-L3**. CVs were obtained using the corresponding metallopolymer-modified FTO as the working electrode, Ag/AgCl as the reference electrode, and a Pt wire as the counter electrode. A 0.1 M solution of lithium perchlorate in dry acetonitrile was used as the supporting electrolyte.

1612 cm^{-1}) were also observed in their Raman spectra (Figure S5).

3.2. Electrochemistry and Spectroelectrochemistry.

The metallopolymers were intensely colored due to the MLCT bands in their UV–Vis spectra (Figure 2a–c).^{27,28,41} The one-electron redox reactions of Fe(II)–terpyridine systems are well documented in the literature.^{41,45–47} We have recently reported the spectroelectrochemical diversification leading to ligand-modulated electrochromic performance in spray-coated metallopolymer assemblies comprising similar metal–ligand combinations.⁴¹ The metallopolymers in MeOH were drop-cast on transparent conducting oxide (TCO) substrates for investigating their electrochemical redox behavior. The electrochemical profiles of the metallopolymers were probed using a three-electrode setup (metallopolymer-modified TCO as the working electrode, Ag/AgCl as the reference electrode, and a platinum wire as the counter electrode) in 0.1 M lithium perchlorate in acetonitrile as the supporting electrolyte. The redox behavior of the metallopolymer thin films was confirmed at varying scan rates (10–300 mV s^{-1} , Figure 4a–c) and was further used to validate the possible electron transfer mechanism and elucidate the role of the diffusion of electrolyte ions in the charge storage process in these assemblies.

The scan rate dependence of changes in current in the cyclic voltammograms is indicative of the operative electron transfer mechanism in the metallopolymer thin films.^{27,46,48} While the films of **poly-Fe-L1** and **poly-Fe-L3** exhibited a near-linear increase in cathodic and anodic current with an increase in scan rate (Figure 4d,f), **poly-Fe-L2** exhibited a slightly exponential trend (Figure 4e). An exponential dependence of current with the square root of the scan rate was observed for

poly-Fe-L1 and **poly-Fe-L3** (Figure 4g,i), whereas a linear dependence was observed for **poly-Fe-L2** (Figure 4h). These observations are indicative of different electron transfer mechanisms in operation in these sets of assemblies. The results suggest an electron transfer mechanism limited by slow diffusion in the assemblies formed from **poly-Fe-L2**, whereas the diffusion of electrolyte ions may not have a significant effect in the electron transfer rate-determining step for the other two assemblies.^{27,46,48}

We have previously demonstrated the electrochromic behavior of these assemblies using a semi-automated spray coating unit.⁴¹ While multiple layers of controlled spray coating were required to obtain uniform thin films of the metallopolymers in the previous study, the present work takes advantage of simple drop-casting to form similar films with increased thickness and slightly lower uniformity, without compromising the spectroelectrochemical switching. The single electron redox process, as observed during the electrochemical experiments, was found to be accompanied by a visible change in color. All the metallopolymer assemblies on TCO exhibited color-to-color switching from shades of purple to yellow when subjected to application of an electric potential between 0.7 and 1.5 V (vs Ag/AgCl). The electrochromic color switching was quite similar to the corresponding spray-coated films and was confirmed by the bleaching of the MLCT bands in the corresponding UV–Vis spectra (Figure 5a–c). The chromaticity diagram also corroborates the observed color change (Figure 5d–f), with a response time of less than 3 s for all the metallopolymers.

We have earlier shown, via molecular permeability experiments, that spray-coated films of **poly-Fe-L1** are more porous

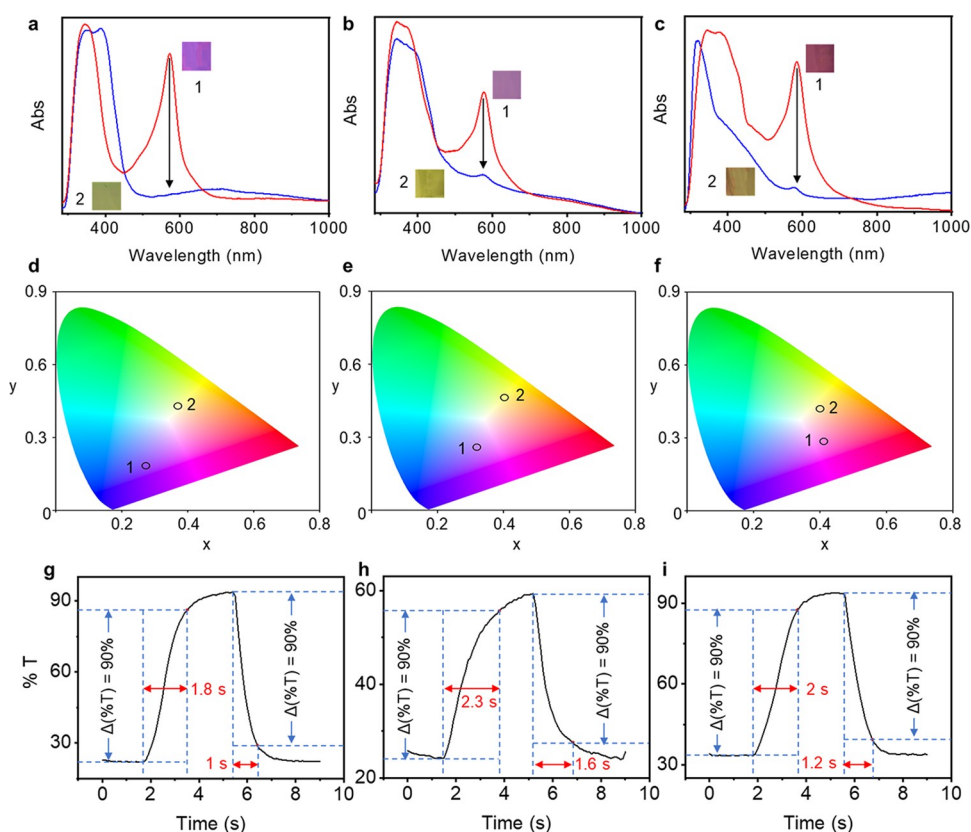


Figure 5. UV–Vis spectra of the metallopolymers drop-casted on FTO substrates confirming the bleaching of the MLCT bands during the electrochemical oxidation of the assemblies constructed from (a) **poly-Fe-L1**, (b) **poly-Fe-L2**, and (c) **poly-Fe-L3**. The spectra corresponding to the reduced and oxidized states are shown in red and blue, respectively. The photographs of the observed color pallets are shown in the insets. 1 represents the reduced ground state and 2 represents the oxidized state. Corresponding chromaticity coordinates (d–f) and response times (g–i) obtained upon reversible redox switching for (d,g) **poly-Fe-L1**, (e,h) **poly-Fe-L2**, and (f,i) **poly-Fe-L3**. The electrochemical oxidation process was performed using a 3-electrode setup comprising the metallopolymer-modified FTO as the working electrode, Ag/AgCl as the reference electrode, and a Pt wire as the counter electrode at a pulse width of 5 s. A 0.1 M solution of lithium perchlorate in dry acetonitrile was used as the supporting electrolyte at a potential window of 0.7–1.5 V.

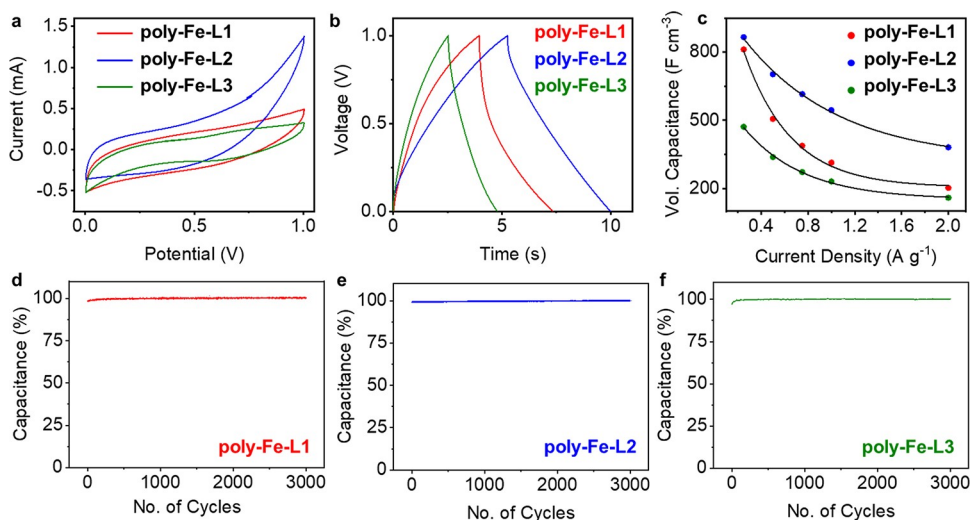


Figure 6. (a) CV loops obtained from the symmetric supercapacitors fabricated from **poly-Fe-L1** (red), **poly-Fe-L2** (blue), and **poly-Fe-L3** (green) at a scan rate of 100 mV s^{-1} . (b) Galvanostatic charge–discharge curves of the supercapacitors fabricated from **poly-Fe-L1** (red), **poly-Fe-L2** (blue), and **poly-Fe-L3** (green) electrodes at a constant potential window (0.0–1.0 V) and current density (1.0 A g^{-1}). (c) Comparison of the volumetric capacitance calculated from the GCD curves at different current densities for (d) **poly-Fe-L1** (red), (e) **poly-Fe-L2** (blue), and (f) **poly-Fe-L3** (green). Cycling stability of the symmetric supercapacitors derived from **poly-Fe-L1** (red), **poly-Fe-L2** (blue), and **poly-Fe-L3** (green), at a constant current density of 1.0 A g^{-1} .

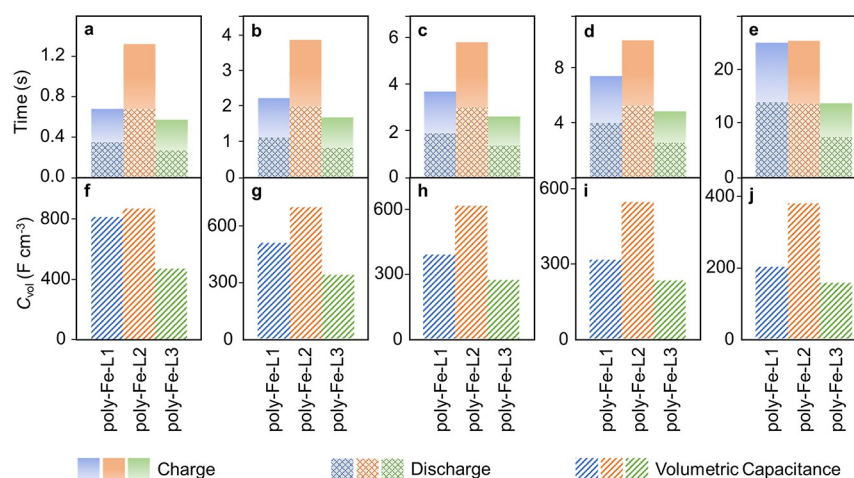


Figure 7. Comparison of charge–discharge times (a–e) and volumetric capacitance (f–j) in symmetric supercapacitor cells fabricated from **poly-Fe-L1** (blue), **poly-Fe-L2** (orange), and **poly-Fe-L3** (green). The charge discharge times were obtained at a constant potential window (0.0–1.0 V). The current densities were (a,f) 0.25 A g^{-1} , (b,g) 0.50 A g^{-1} , (c,h) 0.75 A g^{-1} , (d,i) 1.0 A g^{-1} , and (e,j) 2.0 A g^{-1} .

compared to **poly-Fe-L3**, while those of **poly-Fe-L2** exhibited the least porosity.⁴¹ Interestingly, the response time (time taken for 90% of maximum coloration/bleaching) of these assemblies also followed the same order (Figure Sg–i): **poly-Fe-L1** (coloration: 1.8 s, bleaching: 1.0 s), **poly-Fe-L3** (coloration: 2.0 s, bleaching: 1.2 s), and **poly-Fe-L2** (coloration: 2.3 s, bleaching: 1.6 s). Coloration was found to be faster, in all cases, compared to bleaching (Figure Sg–i). This is most likely due to a comparably more strenuous oxidation pathway in operation, as opposed to an easier reduction pathway in the one-electron redox process mediated by a faster injection of electrons. This process leads to a faster kinetics in the $\text{Fe}^{3+/2+}$ redox couple and a probably slower ejection of electrons with a concomitantly slower kinetics in the reverse process ($\text{Fe}^{2+/3+}$).^{49–51}

3.3. Capacitance. To evaluate the electrochemical energy storage properties, electrodes ($1 \text{ cm} \times 1 \text{ cm}$) were prepared using the corresponding metallopolymer mixed with activated charcoal and polytetrafluoroethylene (PTFE).³⁶ The electrochemical properties of the symmetric two-electrode configuration were studied using cyclic voltammetry (CV), galvanostatic charge–discharge, and electrochemical impedance spectroscopy (EIS) at room temperature (see the Supporting Information for details).

The CVs of the electrodes in a symmetric two-electrode configuration at different scan rates are shown in Figure 6a and Figure S6. An increase in current and area under the curves with increasing scan rate was observed in the cyclic voltammograms for the cells fabricated from all three metallopolymer (Figure S6). These observations corroborate the prevalence of redox or faradaic reactions at the electrode–electrolyte interface or within the metallopolymer networks, as required for a favorable capacitive behavior. The cyclic voltammetry loops were predominantly rectangular for the capacitors fabricated from **poly-Fe-L1** and **poly-Fe-L2**, whereas the CVs obtained for **poly-Fe-L3** rather deviated from the expected rectangular shape, particularly at higher scan rates (Figure S6). These data are indicative of comparably slow charge–discharge reactions happening in **poly-Fe-L3**, most likely due to higher internal resistance.^{36,52} The deviation from an expected rectangular behavior may also be attributed to the kinetically limited diffusion of electrolyte ions.⁵³ These results

strongly suggest that the charge storage mechanism does not originate exclusively from the oppositely charged electrical double layer (EDL);⁵⁴ however, small contributions from the EDL cannot be rigorously excluded as indicated by the reasonably triangular shape of the charge–discharge curves (Figure 6b and Figure S7).

The current at a given potential in non-carbon electrode systems may be composed of three components – physically capacitive, pseudocapacitive, and diffusive currents.⁵⁵ Warburg impedance or charge transfer resistance is generally not observed for ideal polarized electrodes outside the electrochemical redox window.⁵⁶ An increase in current above 0.8 V for all the metallopolymer, particularly in the case of **poly-Fe-L2**, is due to the onset of the $\text{Fe}^{2+/3+}$ oxidation potential (1.0–1.2 V). However, the lower ohmic voltage drop observed for these systems, which most likely stems from the combined effects of isolating barriers developed at the electrode–electrolyte interface leading to mechanical side effects, cannot be rigorously excluded.^{55,56}

While calculations of specific capacitance from the CV loops are technically feasible, the values obtained from the galvanostatic charge–discharge (GCD) curves are more reliable. GCD curves are also useful in predicting the operational efficiency and performance of electrochemical supercapacitors.^{36,57} Nevertheless, capacitive profiles from the cyclic voltammograms were clearly found to increase with increasing scan rates, most likely due to the scan rate-dependent diffusion kinetics of electrolytes. Lower scan rates are known to allow sufficient time for the ions to diffuse through the network, leading to an enhanced charge storage behavior.⁵⁸ Overall, the charge storage performance of the metallopolymer supercapacitors estimated qualitatively from the CV loops was found to follow the order **poly-Fe-L2** > **poly-Fe-L1** > **poly-Fe-L3**.

GCD curves were obtained for all the symmetric capacitors at a constant potential window (0.0–1.0 V) by varying the current densities between 0.25 and 2.0 A g^{-1} (Figure S7). The data obtained at a current density of 1.0 A g^{-1} is shown in Figure 6b. The charge–discharge times for the supercapacitors at every current density followed the order **poly-Fe-L2** > **poly-Fe-L1** > **poly-Fe-L3** (Figure 7a–e). However, at high current densities (2.0 A g^{-1}), electrodes fabricated from **poly-Fe-L1**

and **poly-Fe-L2** charged and discharged at similar rates, whereas that fabricated from **poly-Fe-L3** continued to charge and discharge at a faster rate (Figure 7e). The earlier reported difference in thin film porosity is the most likely reason for different electron transfer mechanisms exhibited by these assemblies.⁴¹ The least porous **poly-Fe-L2** featured an electron transfer process under a diffusion-controlled mechanism, whereas the electron transfer processes were not found to be limited by slow diffusion in **poly-Fe-L1** and **poly-Fe-L3**. We envision that these differences in charge storage mechanism are directly correlated to the charge–discharge kinetics as the relatively less porous **poly-Fe-L2** charged and discharged at lower rates. While low current densities have been shown to allow the electrolyte ions to penetrate and/or diffuse into the electrode material, high current densities limit the access of the electrolyte ions to the electrode surface only.^{32,51} Deviation from an ideal rectangular shape as well as the lack of proper symmetry in the GCD curves points to a predominantly pseudocapacitive origin for the charge storage behavior of these metallopolymers. However, various mass transport-related phenomena as well as faradaic and non-faradaic charge storage reactions may also contribute to the observed deviations from ideal supercapacitor profiles.^{36,57}

The volumetric capacitance of the supercapacitor electrodes was calculated from the GCD curves at different current densities. The supercapacitor cells fabricated from **poly-Fe-L2** was found to exhibit the highest volumetric capacitance among the three metallopolymers followed by **poly-Fe-L1**, and **poly-Fe-L3** exhibited the least capacitance values (Figure 7f–j). The volumetric capacitance was found to decrease exponentially with increasing current densities (Figure 6c). At a constant current density of 1.0 A g⁻¹, the calculated volumetric capacitance of the metallopolymers is as follows: **poly-Fe-L2** (544.6 F cm⁻³) > **poly-Fe-L1** (313.8 F cm⁻³) > **poly-Fe-L3** (230.8 F cm⁻³). A maximum volumetric capacitance of 866.2 F cm⁻³ was obtained for the symmetric supercapacitor cell fabricated from **poly-Fe-L2** using a potential window between 0 and 1 V operating at a current density of 0.25 A g⁻¹. All the supercapacitor electrodes exhibited excellent stability, most likely due to the extended conjugation within the rigid ligand network,^{27,41,59} and no degradation in performance was observed after 3000 cycles of continuous charge–discharge operations at a constant current density of 1.0 A g⁻¹ (Figure 6d–f). At a constant power density of 0.154 kW cm⁻³, the metallopolymers-based supercapacitors were found to have specific energy densities of 43.6, 75.5, and 31.2 mWh cm⁻³, for **poly-Fe-L1**, **poly-Fe-L2**, and **poly-Fe-L3**, respectively. These volumetric capacitance and energy density values are significantly higher compared to several other electrochromic supercapacitors or conventional systems and are among the best reported for metallopolymers-based systems (Figure S8 and Table S1).^{60–63}

The electrochemical reactions occurring at the electrode surfaces can be followed using electrochemical impedance spectroscopy (EIS).^{36,57} The presence of a detectable semi-circle region at high frequencies in the Nyquist plot of **poly-Fe-L1** indicates a relatively higher charge transfer resistance compared to those of **poly-Fe-L2** and **poly-Fe-L3** (Figure S9). However, the shortest Warburg diffusion line in the middle-frequency region was observed for the electrodes fabricated from **poly-Fe-L2** followed by that from **poly-Fe-L1** and the electrodes fabricated from **poly-Fe-L3** exhibited the longest Warburg diffusion line. The contact resistance at the

electrode–electrolyte interface, the ionic resistance of the electrolyte, and the intrinsic resistance of the metallopolymers may contribute to the overall solution resistance (R_s) or the equivalent series resistance (ESR), which was found to be 3.0, 1.6, and 1.9 Ω for **poly-Fe-L1**, **poly-Fe-L2**, and **poly-Fe-L3**, respectively. The EIS data can be fitted with an equivalent circuit shown in Figure S10, with the solution resistance or the equivalent series resistance R_s connected with the charge transfer resistance R_{ct} , the double layer capacitance, C_{dl} , and the Warburg Impedance Z_w .

3.4. BET Surface Area and Conductivity. Porous materials with high surface areas have been shown to exhibit better electrochemical energy storage performance. However, such dependence of capacitive performance on BET surface area may not be expected for low surface area materials, particularly metal–organic systems. BET surface areas of the metallopolymers were found to be as follows: 22.3 ± 2.3 m² g⁻¹ (**poly-Fe-L1**), 13.8 ± 1.1 m² g⁻¹ (**poly-Fe-L2**), and 16.0 ± 1.8 m² g⁻¹ (**poly-Fe-L3**), leading to porosity in the order **poly-Fe-L1** > **poly-Fe-L3** > **poly-Fe-L2**, which are in full agreement with the molecular porosity observed in solution-state electrochemical experiments (Figure S11a). The higher porosity of **poly-Fe-L1** stems from the presence of mesopores ($d < 50$ nm) alongside macropores, while **poly-Fe-L2** and **poly-Fe-L3** featured only macroporous assemblies (Figure S11b–d).

The BET surface area of the metallopolymers most probably does not contribute to the observed differences in their capacitive performance since all the materials exhibited rather low surface areas typically less than 10–25 m² g⁻¹.^{36,42} The differences observed in the charge storage properties could be therefore attributed to the difference in electrical conductivity of the metallopolymers and prompted us to investigate their I – V characteristics.^{34,43,44} The electrical conductivities of the metallopolymers (thickness: 185 ± 4 nm) were determined using a 4-probe method (Figure S12). The charge storage properties and the observed differences between the metallopolymers-based supercapacitors can be justified based on the differences in conductivity of these metallopolymers thin films. The capacitive performance of the metallopolymers was found to follow the order of their electrical conductivity: **poly-Fe-L2** (2.64×10^{-1} S/cm) > **poly-Fe-L1** (4.67×10^{-2} S/cm) > **poly-Fe-L3** (3.88×10^{-2} S/cm). Unlike most reported metal–organic materials, the metallopolymers used in this study were found to possess significantly high electrical conductivity,^{64,65} which may be attributed to high-energy charge transport pathways and enhanced charge carrier mobility resulting from the presence of extended conjugation and delocalized π -electron systems within the rigid ligand network.³⁷ The continuous metal-chelating pathways along with the presence of heteroatoms have been shown to improve the conductivity of metallopolymers. The comparatively soft–soft interactions between the coordinating nitrogen atoms and Fe²⁺ nodes with their loosely bound β -spin d-band electron also contribute to high conductivity in iron(II)-based metal–organic systems.⁶⁶ The extended conjugation in ligand L2, which is superior to those in L1 and L3, enhances the through-plane conductivity in **poly-Fe-L2** via a better π –d conjugation and efficient charge delocalization pathways. Higher charge delocalization in **poly-Fe-L2** also implies better interlayer stacking via π – π interactions, leading to enhanced charge transport efficiency and wave function overlap. Though dense grain-like morphologies were observed in the AFM images of the

metallopolymers (Figure 3), poly-Fe-L2 featured fewer open spaces, suggesting a lower resistance arising from a smaller number of grain boundaries and related defects, leading to higher conductivity. The high conductivity observed for all the metallopolymers is also indicative of higher ionic mobility and a plausible redox hopping mechanism involving the Fe^{2+} centers. It is often difficult to single out the contributions from through-bond, through-plane, through-space, and hopping pathways of charge transport; however, a favorable combination of these different pathways that emanates from the structural variations in the ligands accounts for the observed differences in the conductivity of the metallopolymers.⁶⁶

Electrochemical addressability of the electrochromic thin films of the metallopolymers was limited at thicknesses above 250 nm, most likely due to the low porosity that limits the diffusion of the electrolyte ions. However, the capacitive behavior and conductivities were found to be more or less similar at thicknesses below 200 nm. The contribution from differences in solution or charge transfer resistance, mass transport phenomena, or faradaic/non-faradaic processes within the metallopolymer network or at the electrode–electrolyte interface to the observed capacitive behavior cannot be rigorously excluded.^{36,57} The packing densities and amorphous nature of the metallopolymers may also influence the charge storage profile. Theoretical modeling using model ligand systems confirmed similar octahedral coordination modes in the metallopolymers irrespective of the core architecture (Figure S13). Though the molecular weights of the ligands are different, no direct correlation was observed between the capacitive performance and the molecular weight of the ligands. Nevertheless, variation in the core structure of the ligand is the decisive factor that determines the capacitance and related charge storage signature of these metallopolymer assemblies containing the same metal ion and similar coordinating entities. Such design principles offer excellent opportunities in developing new materials, particularly of a metal–organic nature, as promising candidates for electrochemical energy storage applications.

4. CONCLUSIONS

Electrochromic metallopolymers containing the same metal ion (Fe^{2+}) with varying core structures have been shown to exhibit a ligand modulated capacitive behavior. Fabrication of symmetric supercapacitor cells in a two-electrode configuration using these metallopolymers resulted in high volumetric capacitance up to 544.6 F cm^{-3} at a current density of 1 A g^{-1} , energy densities up to 75.5 mWh cm^{-3} , and high cycling stabilities. These values are among the highest reported for metal–organic thin film systems. The volumetric capacitance and charge–discharge properties of the metallopolymer electrodes were found to be in direct correlation with the measured electrical conductivities that in turn stem from the variations in the ligand structure. This work demonstrates the effect of electrical conductivity in regulating the electrochemical energy storage properties of materials with low to moderate porosity and surface area. The diligence of structural design aiming at enhancing the electrical conductivity in low surface area materials provides a unique strategy to improve the performance of thin film-based multifunctional electrochemical energy storage devices. Such thin film systems with stimuli-responsive attributes are envisioned to add a new

dimension to the emerging smart technologies with application in efficient microscale power sources for miniaturized devices.

■ ASSOCIATED CONTENT

SI Supporting Information

The Supporting Information is available free of charge at <https://pubs.acs.org/doi/10.1021/acsami.2c05744>.

Materials and methods, synthesis, experimental procedure, FT-IR, PXRD, high-resolution XPS, and Raman spectra, thermogravimetric and galvanostatic charge–discharge curves, CV loops, comparison of supercapacitor performance, Nyquist plots, equivalent circuit of the best performing poly-Fe-L2-based supercapacitor, BET surface area of the metallopolymers, I – V characteristic plot, and energy-minimized structures (PDF)

■ AUTHOR INFORMATION

Corresponding Authors

Sreejith Shankar – Photosciences and Photonics Section, Chemical Sciences and Technology Division, CSIR - National Institute for Interdisciplinary Sciences and Technology (CSIR - NIIST), Thiruvananthapuram 695019, India; Academy of Scientific and Innovative Research (AcSIR), Ghaziabad 201002, India; orcid.org/0000-0002-1158-5935; Email: sreejith.shankar@niist.res.in

Ayyappanpillai Ajayaghosh – Photosciences and Photonics Section, Chemical Sciences and Technology Division, CSIR - National Institute for Interdisciplinary Sciences and Technology (CSIR - NIIST), Thiruvananthapuram 695019, India; Academy of Scientific and Innovative Research (AcSIR), Ghaziabad 201002, India; orcid.org/0000-0001-8574-5391; Email: ajayaghosh@niist.res.in

Authors

Indulekha Mukkatt – Photosciences and Photonics Section, Chemical Sciences and Technology Division, CSIR - National Institute for Interdisciplinary Sciences and Technology (CSIR - NIIST), Thiruvananthapuram 695019, India; Academy of Scientific and Innovative Research (AcSIR), Ghaziabad 201002, India

Anjana Padmaja Mohanachandran – Material Sciences and Technology Division, CSIR - National Institute for Interdisciplinary Sciences and Technology (CSIR - NIIST), Thiruvananthapuram 695019, India; Department of Physics, University of Kerala, Thiruvananthapuram, Kerala 695581, India

Anjali Nirmala – Photosciences and Photonics Section, Chemical Sciences and Technology Division, CSIR - National Institute for Interdisciplinary Sciences and Technology (CSIR - NIIST), Thiruvananthapuram 695019, India; Academy of Scientific and Innovative Research (AcSIR), Ghaziabad 201002, India

Dipak Patra – Photosciences and Photonics Section, Chemical Sciences and Technology Division, CSIR - National Institute for Interdisciplinary Sciences and Technology (CSIR - NIIST), Thiruvananthapuram 695019, India; Academy of Scientific and Innovative Research (AcSIR), Ghaziabad 201002, India

Priyanka A. Sukumaran – Photosciences and Photonics Section, Chemical Sciences and Technology Division, CSIR - National Institute for Interdisciplinary Sciences and Technology (CSIR - NIIST), Thiruvananthapuram 695019,

India; Academy of Scientific and Innovative Research (AcSIR), Ghaziabad 201002, India

Renjith S. Pillai – Department of Chemistry, Christ University, Bangalore 560029 Karnataka, India

R. B. Rakhi – Academy of Scientific and Innovative Research (AcSIR), Ghaziabad 201002, India; Material Sciences and Technology Division, CSIR - National Institute for Interdisciplinary Sciences and Technology (CSIR - NIIST), Thiruvananthapuram 695019, India; orcid.org/0000-0002-0207-8595

Complete contact information is available at:
<https://pubs.acs.org/10.1021/acsami.2c05744>

Author Contributions

The manuscript was written through contributions of all authors. All authors have given approval to the final version of the manuscript.

Funding

DST, DST-SERB, CSIR (Government of India)

Notes

The authors declare no competing financial interest.

ACKNOWLEDGMENTS

I.M. is grateful to DST-INSPIRE for a senior research fellowship. S.S. and R.R.B. are grateful to DST-SERB, Government of India for Ramanujan Fellowships (SB/S2/RJN-058/2016, SB/S2/RJN-098/2015). A.A. thanks DST-SERB, Government of India, for a J. C. Bose National Fellowship (SB/S2/JCB-11/2014). This work was also supported by CSIR (HCP 0030, MLP 0037 and MLP 0049) and DST (Nanomission, GAP 162939), Government of India. We thank Dr. Saju Pillai and Mr. Peer Mohammed for XPS measurements, Dr. Bhoje Gowd for PXRD measurements, and Dr. K. Yoosaf for Raman spectroscopy.

REFERENCES

- (1) Su, M.; Song, Y. Printable Smart Materials and Devices: Strategies and Applications. *Chem. Rev.* **2022**, *122*, 5144–5164.
- (2) Gardan, J. Smart Materials in Additive Manufacturing: State of the Art and Trends. *Virtual Phys. Prototyp.* **2019**, *14*, 1–18.
- (3) Yu, X.; Cheng, H.; Zhang, M.; Zhao, Y.; Qu, L.; Shi, G. Graphene-Based Smart Materials. *Nat. Rev. Mater.* **2017**, *2*, 17046.
- (4) Kowalski, P. S.; Bhattacharya, C.; Afewerki, S.; Langer, R. Smart Biomaterials: Recent Advances and Future Directions. *ACS Biomater. Sci. Eng.* **2018**, *4*, 3809–3817.
- (5) Wang, W.; Yang, J.; Zhang, Y.; Li, Y.; Yang, S.; Zhu, L.; Zhu, M. A Route Toward Smart System Integration: From Fiber Design to Device Construction. *Adv. Mater.* **2020**, *32*, 1902301.
- (6) Jeong, U.; Yin, Y. Smart and Responsive Micro- and Nanostructured Materials. *Adv. Funct. Mater.* **2020**, *30*, 1907059.
- (7) Dyer, A. L.; Bulloch, R. H.; Zhou, Y.; Kippelen, B.; Reynolds, J. R.; Zhang, F. A Vertically Integrated Solar-Powered Electrochromic Window for Energy Efficient Buildings. *Adv. Mater.* **2014**, *26*, 4895–4900.
- (8) Cai, G.; Eh, A. L.-S.; Ji, L.; Lee, P. S. Recent Advances in Electrochromic Smart Fenestration. *Adv. Sustainable Syst.* **2017**, *1*, 1700074.
- (9) Rosseinsky, D. R.; Mortimer, R. J. Electrochromic Systems and the Prospects for Devices. *Adv. Mater.* **2001**, *13*, 783–793.
- (10) Beaujuge, P. M.; Reynolds, J. R. Color Control in π -Conjugated Organic Polymers for Use in Electrochromic Devices. *Chem. Rev.* **2010**, *110*, 268–320.
- (11) Cai, G.; Wang, J.; Lee, P. S. Next-Generation Multifunctional Electrochromic Devices. *Acc. Chem. Res.* **2016**, *49*, 1469–1476.

(12) Lu, Z.; Zhong, X.; Liu, X.; Wang, J.; Diao, X. Energy Storage Electrochromic Devices in the Era of Intelligent Automation. *Phys. Chem. Chem. Phys.* **2021**, *23*, 14126–14145.

(13) Wang, H.; Yao, C.-J.; Nie, H.-J.; Yang, L.; Mei, S.; Zhang, Q. Recent Progress in Integrated Functional Electrochromic Energy Storage Devices. *J. Mater. Chem. C* **2020**, *8*, 15507–15525.

(14) Yu, X.; Chang, M.; Chen, W.; Liang, D.; Lu, X.; Zhou, G. Colorless-to-Black Electrochromism from Binary Electrochromes toward Multifunctional Displays. *ACS Appl. Mater. Interfaces* **2020**, *12*, 39505–39514.

(15) Assunta, M.; Facchetti, A.; Lanari, D.; Petruccia, C.; Luigi, V. Current Methodologies for a Sustainable Approach to π -Conjugated Organic Semiconductors. *Energy Environ. Sci.* **2016**, *9*, 763–786.

(16) Gao, S.; Yi, X.; Shang, J.; Liu, G.; Li, R. W. Organic and Hybrid Resistive Switching Materials and Devices. *Chem. Soc. Rev.* **2019**, *48*, 1531–1565.

(17) Liu, X.; Liu, C.-F.; Xu, S.; Cheng, T.; Wang, S.; Lai, W.-Y.; Huang, W. Porous organic polymers for high-performance supercapacitors. *Chem. Soc. Rev.* **2022**, *51*, 3181–3225.

(18) Liu, Y.-Y.; Li, X.-C.; Wang, S.; Cheng, T.; Yang, H.; Liu, C.; Gong, Y.; Lai, W.-Y.; Huang, W. Self-Templated Synthesis of Uniform Hollow Spheres Based on Highly Conjugated Three-Dimensional Covalent Organic Frameworks. *Nature Commun.* **2020**, *11*, 5561.

(19) Wang, S.; Li, X.; Cheng, T.; Liu, Y.; Li, Q.; Bai, M.; Liu, X.; Geng, H.; Lai, W.-Y.; Huang, W. Highly Conjugated Three-Dimensional Covalent Organic Frameworks with Enhanced Li-Ion Conductivity as Solid-State Electrolytes for High-Performance Lithium Metal Batteries. *J. Mater. Chem. A* **2022**, *10*, 8761–8771.

(20) Li, X.-C.; Zhang, Y.; Wang, C.-Y.; Wan, Y.; Lai, W.-Y.; Pang, H.; Huang, W. Redox-Active Triazatruxene-based Conjugated Microporous Polymers for High-Performance Supercapacitors. *Chem. Sci.* **2017**, *8*, 2959–2965.

(21) Wu, W.; Wang, M.; Ma, J.; Cao, J.; Deng, Y. Electrochromic Metal Oxides: Recent Progress and Prospect. *Adv. Electronic Mater.* **2018**, *4*, 1800185.

(22) Granqvist, C. G. Electrochromics for Smart Windows: Oxide-Based Thin Films and Devices. *Thin Solid Films* **2014**, *564*, 1–38.

(23) Yu, X.; Marks, T. J.; Facchetti, A. Metal Oxides for Optoelectronic Applications. *Nat. Mater.* **2016**, *15*, 383–396.

(24) Wu, S.; Liu, J.; Wang, H.; Yan, H. A Review of Performance Optimization of MOF-derived Metal Oxide as Electrode Materials for Supercapacitors. *Int. J. Energy Res.* **2019**, *43*, 697–716.

(25) Mortimer, R. J.; Dyer, A. L.; Reynolds, J. R. Electrochromic Organic and Polymeric Materials for Display Applications. *Displays* **2006**, *27*, 2–18.

(26) Banasz, R.; Wałęsa-Chorab, M. Polymeric Complexes of Transition Metal Ions as Electrochromic Materials: Synthesis and Properties. *Coord. Chem. Rev.* **2019**, *389*, 1–18.

(27) Shankar, S.; Lahav, M.; van der Boom, M. E. Coordination-Based Molecular Assemblies as Electrochromic Materials: Ultra-High Switching Stability and Coloration Efficiencies. *J. Am. Chem. Soc.* **2015**, *137*, 4050–4053.

(28) Eloom Dov, N.; Shankar, S.; Cohen, D.; Bendikov, T.; Rechav, K.; Shimon, L. J. W.; Lahav, M.; van der Boom, M. E. Electrochromic Metallo-Organic Nanoscale Films: Fabrication, Color Range, and Devices. *J. Am. Chem. Soc.* **2017**, *139*, 11471–11481.

(29) Zhong, Y.-W. Electrochromism within Transition-Metal Coordination Complexes and Polymers. In *Electrochromic Materials and Devices*; Mortimer, R. J.; Rosseinsky, D. R.; Monk, P. M. S. (Eds.), WileyVCH Verlag GmbH & Co. KGaA: Weinheim, Germany, 2015; Chapter 6, p 185–210.

(30) Bera, M. K.; Mori, T.; Yoshida, T.; Ariga, K.; Higuchi, M. Construction of Coordination Nanosheets Based on Tris(2,2'-bipyridine)-Iron (Fe²⁺) Complexes as Potential Electrochromic Materials. *ACS Appl. Mater. Interfaces* **2019**, *11*, 11893–11903.

(31) Jena, S. R.; Choudhury, J. A Fast-Switching Electrochromic Device with a Surface-Confined 3D Metallo-Organic Coordination Assembly. *Chem. Commun.* **2020**, *56*, 559–562.

- (32) Lahav, M.; van der Boom, M. E. Polypyridyl Metallo-Organic Assemblies for Electrochromic Applications. *Adv. Mater.* **2018**, 1706641.
- (33) Bera, M. K.; Mohanty, S.; Kashyap, S. S.; Sarmah, S. Electrochromic Coordination Nanosheets: Achievements and Future Perspective. *Coord. Chem. Rev.* **2022**, 454, No. 214353.
- (34) Feng, D.; Lei, T.; Lukatskaya, M. R.; Park, J.; Huang, Z.; Lee, M.; Shaw, L.; Chen, S.; Yakovenko, A. A.; Kulkarni, A.; Xiao, J.; Fredrickson, K.; Tok, J. B.; Zou, X.; Cui, Y.; Bao, Z. Robust and Conductive Two-Dimensional Metal–Organic Frameworks with Exceptionally High Volumetric and Areal Capacitance. *Nature Energy* **2018**, 3, 30–36.
- (35) Zhao, Z.; Ding, J.; Zhu, R.; Pang, H. The Synthesis and Electrochemical Applications of Core–Shell MOFs and their Derivatives. *J. Mater. Chem. A* **2019**, 7, 15519–15540.
- (36) Indulekha, M.; Anjali, N.; Rakhi, R. B.; Shankar, S.; Ajayaghosh, A. Metal Ion Induced Capacitance Modulation in Near-Isostructural Complexes Derived Electrochromic Coordination Polymers. *Mater. Today Chem.* **2020**, 16, No. 100260.
- (37) Kim, C.; Moon, J. H. Hierarchical Pore-Patterned Carbon Electrodes for High-Volumetric Energy Density Micro-Supercapacitors. *ACS Appl. Mater. Interfaces* **2018**, 10, 19682–19688.
- (38) Li, L.; Lou, Z.; Han, W.; Chen, D.; Jiang, K.; Shen, G. Highly Stretchable Micro-Supercapacitor Arrays with Hybrid Mwcnt/Pani Electrodes. *Adv. Mater. Technol.* **2017**, 2, 1600282.
- (39) El-Kady, M. F.; Kaner, R. B. Scalable Fabrication of High-Power Graphene Micro-Supercapacitors for Flexible and on-Chip Energy Storage. *Nat. Commun.* **2013**, 4, 1475.
- (40) Tong, Y.-L.; Xu, B.; Du, X.-F.; Cheng, H.-Y.; Wang, C.-F.; Wu, G.; Chen, S. Microfluidic-Spinning-Directed Conductive Fibers toward Flexible Micro-Supercapacitors. *Macromol. Mater. Eng.* **2018**, 28, 1700664.
- (41) Indulekha, M.; Anjali, N.; Madhavan, N. D.; Shankar, S.; Deb, B.; Ajayaghosh, A. Ligand Controlled Electrochromic Diversification with Multi-Layer Coated Metallosupramolecular Polymer Assemblies. *ACS Appl. Mater. Interfaces* **2021**, 13, 5245–5255.
- (42) Largeot, C.; Portet, C.; Chmiola, J.; Taberna, P.-L.; Gogotsi, Y.; Simon, P. Relation between the Ion Size and Pore Size for an Electric Double-Layer Capacitor. *J. Am. Chem. Soc.* **2008**, 130, 2730–2731.
- (43) Su, J.; He, W.; Li, X. M.; Sun, L.; Wang, H. Y.; Lan, Y. Q.; Ding, M.; Zuo, J. L. High Electrical Conductivity in a 2D MOF with Intrinsic Superprotonic Conduction and Interfacial Pseudo-capacitance. *Matter* **2020**, 2, 711–722.
- (44) Gittins, J. W.; Balhatchet, C. J.; Chen, Y.; Liu, C.; Madden, D. G.; Britto, S.; Golomb, M. J.; Walsh, A.; Fairen-Jimenez, D.; Dutton, S. E.; Forse, A. C. Insights into the Electric Double-Layer Capacitance of Two-Dimensional Electrically Conductive Metal–Organic Frameworks. *J. Mater. Chem. A* **2021**, 9, 16006–16015.
- (45) Han, F. S.; Higuchi, M.; Kurth, D. G. Metallo-Supramolecular Polymers Based on Functionalized Bis-terpyridines as Novel Electrochromic Materials. *Adv. Mater.* **2007**, 19, 3928–3931.
- (46) Hu, C. W.; Sato, T.; Zhang, J.; Moriyama, S.; Higuchi, M. Three-Dimensional Fe(II)-based Metallo-Supramolecular Polymers with Electrochromic Properties of Quick Switching, Large Contrast, and High Coloration Efficiency. *ACS Appl. Mater. Interfaces* **2014**, 6, 9118–9125.
- (47) Han, F. S.; Higuchi, M.; Kurth, D. G. Metallosupramolecular Polyelectrolytes Self-Assembled from Various Pyridine Ring-Substituted Bisterpyridines and Metal Ions: Photophysical, Electrochemical, and Electrochromic Properties. *J. Am. Chem. Soc.* **2008**, 130, 2073–2081.
- (48) Shiryayeva, I. M.; Collman, J. P.; Boulatov, R.; Sunderland, C. J. Nonideal Electrochemical Behavior of Biomimetic Iron Porphyrins: Interfacial Potential Distribution across Multilayer Films. *Anal. Chem.* **2003**, 75, 494–502.
- (49) Zhang, Q.; Tsai, C.-Y.; Li, L.-J.; Liaw, D.-J. Colorless-to-Colorful Switching Electrochromic Polyimides with Very High Contrast Ratio. *Nature Commun.* **2019**, 10, 1239.
- (50) Tong, Z.; Tian, Y.; Zhang, H.; Li, X.; Ji, J.; Qu, H.; Li, N.; Zhao, J.; Li, Y. Recent Advances in Multifunctional Electrochromic Energy Storage Devices and Photoelectrochromic Devices. *Sci. China Chem.* **2017**, 60, 13–37.
- (51) Vassilopoulou, M.; Pappas, D.; Raptis, I.; Davazoglou, D.; Kostis, I. Fabrication of WO₃-Based Electrochromic Displays Using Solid or Gel-Like Organic Electrolytes. *J. Phys. Conf. Series* **2005**, 10, 329–332.
- (52) Molji, C.; Aashish, A.; Neethu, A. S.; Devaki, S. J. Self-Assembled Polyaniline Nanowires Stippled Graphene-3-Pentadecylphenyl Phosphate Hybrid Nanocomposite based Green Sustainable Electrodes for Supercapacitors. *J. Mater. Chem. A* **2017**, 5, 16636–16645.
- (53) Li, Z.-X.; Zhang, X.; Liu, Y.-C.; Zou, K.-Y.; Yue, M.-L. Controlling the BET Surface Area of Porous Carbon by Using the Cd/C Ratio of a Cd–MOF Precursor and Enhancing the Capacitance by Activation with KOH. *Chem. Eur. J.* **2016**, 22, 17734–17747.
- (54) Lee, D. Y.; Shinde, D. V.; Kim, E.-K.; Lee, W.; Oh, I.-W.; Shrestha, N. K.; Lee, J. K.; Han, S.-H. Supercapacitive Property of Metal–Organic-Frameworks with Different Pore Dimensions and Morphology. *Microporous Mesoporous Mater.* **2013**, 171, 53–57.
- (55) Jiang, Y.; Liu, J. Definitions of Pseudocapacitive Materials: A Brief Review. *Energy Environ. Mater.* **2019**, 2, 30–37.
- (56) Khademi, M.; Barz, D. P. J. Structure of the Electrical Double Layer Revisited: Electrode Capacitance in Aqueous Solutions. *Langmuir* **2020**, 36, 4250–4260.
- (57) Anjana, P. M.; Bindhu, M. R.; Umadevi, M.; Rakhi, R. B. Antibacterial and Electrochemical Activities of Silver, Gold, and Palladium Nanoparticles Dispersed Amorphous Carbon Composites. *Appl. Surface Sci.* **2019**, 479, 96–104.
- (58) Kondrat, S.; Wu, P.; Qiao, R.; Kornyshev, A. A. Accelerating Charging Dynamics in Subnanometre Pores. *Nature Mater.* **2014**, 13, 387–393.
- (59) Pai, S.; Moos, M.; Schreck, M. H.; Lambert, C.; Kurth, D. G. Green-to-Red Electrochromic Fe(II) Metallo-Supramolecular Polyelectrolytes Self-Assembled from Fluorescent 2,6-Bis(2-pyridyl)pyrimidine Bithiophene. *Inorg. Chem.* **2017**, 56, 1418–1432.
- (60) Liu, W.; Lu, C.; Wang, X.; Tay, R. Y.; Tay, B. K. High-Performance Microsupercapacitors Based on Two-Dimensional Graphene/Manganese Dioxide/Silver Nanowire Ternary Hybrid Film. *ACS Nano* **2015**, 9, 1528–1542.
- (61) Yang, J.; Pan, Z.; Yu, Q.; Zhang, Q.; Ding, X.; Shi, X.; Qiu, Y.; Zhang, K.; Wang, J.; Zhang, Y. Free-Standing Black Phosphorus Thin Films for Flexible Quasi-Solid-State Micro-Supercapacitors with High Volumetric Power and Energy Density. *ACS Appl. Mater. Interfaces* **2019**, 11, 5938–5946.
- (62) Yoo, J.; Byun, S.; Lee, C.-W.; Yoo, C.-Y.; Yu, J. Precisely Geometry Controlled Microsupercapacitors for Ultrahigh Areal Capacitance, Volumetric Capacitance, and Energy Density. *Chem. Mater.* **2018**, 30, 3979–3990.
- (63) Peng, Z.; Huang, J.; He, Q.; Li, S.; Tan, S.; Chen, Y. Green Quasi-Solid-State Planar Asymmetric Supercapacitors with High Working Voltage and Extraordinary Volumetric Energy Density. *J. Mater. Chem. A* **2021**, 9, 14363–14371.
- (64) Bhardwaj, S. K.; Bhardwaj, N.; Kaur, R.; Mehta, J.; Sharma, A. L.; Kim, K.-H.; Deep, A. An Overview of Different Strategies to Introduce Conductivity in Metal–Organic Frameworks and Miscellaneous Applications Thereof. *J. Mater. Chem. A* **2018**, 6, 14992–15009.
- (65) Xie, L. S.; Skorupskii, G.; Dincă, M. Electrically Conductive Metal–Organic Frameworks. *Chem. Rev.* **2020**, 120, 8536–8580.
- (66) Johnson, E. M.; Ilic, S.; Morris, A. J. Design Strategies for Enhanced Conductivity in Metal–Organic Frameworks. *ACS Cent. Sci.* **2021**, 7, 445–453.